

Tulay Aygan Atesin
Sajid Bashir
Jingbo Louise Liu *Editors*

Nanostructured Materials for Next-Generation Energy Storage and Conversion

Photovoltaic and Solar Energy

[MATERIALS.SPRINGER.COM](https://www.materials.springer.com)

 Springer

Nanostructured Materials for Next-Generation Energy Storage and Conversion

Tulay Aygan Atesin • Sajid Bashir
Jingbo Louise Liu
Editors

Nanostructured Materials for Next-Generation Energy Storage and Conversion

Photovoltaic and Solar Energy

With 208 Figures and 43 Tables

 Springer

Editors

Tulay Aygan Atesin
Department of Chemistry, College of
Sciences
University of Texas Rio Grande Valley
Edinburg, TX, USA

Sajid Bashir
Department of Chemistry
Texas A&M University Kingsville
Kingsville, TX, USA

Jingbo Louise Liu
Department of Chemistry
Texas A&M University Kingsville
Kingsville, TX, USA

ISBN 978-3-662-59592-3

ISBN 978-3-662-59594-7 (eBook)

<https://doi.org/10.1007/978-3-662-59594-7>

© Springer-Verlag GmbH Germany, part of Springer Nature 2019, corrected publication 2023

This work is subject to copyright. All rights are reserved by the Publisher, whether the whole or part of the material is concerned, specifically the rights of translation, reprinting, reuse of illustrations, recitation, broadcasting, reproduction on microfilms or in any other physical way, and transmission or information storage and retrieval, electronic adaptation, computer software, or by similar or dissimilar methodology now known or hereafter developed.

The use of general descriptive names, registered names, trademarks, service marks, etc. in this publication does not imply, even in the absence of a specific statement, that such names are exempt from the relevant protective laws and regulations and therefore free for general use.

The publisher, the authors, and the editors are safe to assume that the advice and information in this book are believed to be true and accurate at the date of publication. Neither the publisher nor the authors or the editors give a warranty, expressed or implied, with respect to the material contained herein or for any errors or omissions that may have been made. The publisher remains neutral with regard to jurisdictional claims in published maps and institutional affiliations.

This Springer imprint is published by the registered company Springer-Verlag GmbH, DE, part of Springer Nature.

The registered company address is: Heidelberger Platz 3, 14197 Berlin, Germany

Preface

Solar Energy Drying Systems: A Preview

The purpose of this book is to answer questions related to the substitution of fossil fuels for electricity generation for the home or industry using solar platform. The projections are that in the next 50 years, mobility and energy/electrical demand will increase, necessitating a contribution of renewable energy sources including solar energy that will become a significant mix in the energy portfolio. Part of this portfolio will utilize thermal, metal or metal oxide for storage energy, and part is direct energy generation and usage. The application of renewables such as solar energy is attractive because it further addresses the need to lower greenhouse gas emissions, which in turn leads to lower environmental pollution and further reduce our dependency on oil from foreign governments.

Anatomy of This Book

Each author brings his or her vision to solar energy, the technical merits of the approach, and benefits within an overview. We as editors use this preface space to incorporate tangential ideas discussed by the other authors or inclusion of policy, infrastructure, cost analysis, and data on the practical feasibility of using solar cells at any place on the globe. Any errors, omissions, and faults are ours, and we welcome feedback and comment.

Any project, be it a white paper to legislatures, a doctoral thesis, a book chapter, a review article, and a grant proposal, is an intense endeavor and almost always a team effort; this book is no different, which we acknowledge here: Antje Endemann for the day-to-day management and preprint layout of the various manuscripts; George and Sharon, both at Springer (Springer Science+Business Media, LLC), for taking an idea based on our work within the American Chemical Society (ACS) Division of Energy and Fuels (ENFL, Liu and Bashir) and Division of Colloid and Surface Chemistry (COLL, Liu and Bashir); and Texas A&M University-Kingsville for the support.

Lastly, we pay our respect to Peter J. Derrick (1945–2017) who died recently. He was my doctoral thesis advisor and my academic father, whose presence is missed. He lived his life to make this planet a better place for us and our children's children through science, training, mentoring, and education including ethics. Peter's short biography can be found here: <https://doi.org/10.1177/1469066717739174>. Thank you, Peter, your legacy will endure.

We will begin with a brief look ahead to why solar energy is an important energy component and transplant the use of photovoltaics to likely changes in energy demand over the next 50 years. We also briefly and tangentially discuss allied areas such as why research in solar energy should be conducted, its potential to world population growth, demand for electrical energy, contributions toward global greenhouse gases (or assistance in lowering greenhouse gases), and whether carbon dioxide is harmful to human health. This is followed by a very brief primer on sunlight, solar irradiance on this planet's surface with a simplistic explanation on why we have daily, monthly, and seasonal changes in sunlight.

The book can be thought of consisting of three general thrusts. In the first thrust, we covered energy policy, toxicity, and primer on photovoltaics (► Chap. 1, "Solar Energy: Potential and Toxicology", Bashir), simulation (► Chap. 2, "First Principles Simulations for CuInGaSe₂ (CIGS) Solar Cells", Tang), and design of photovoltaic-based manufacturing system using computer-aided design (► Chap. 3, "Design of Photovoltaics-Based Manufacturing System Using Computer-Aided Design", Ezequiel Santibañez-Aguilar). In the middle thrust, we cover energy harvesting, conversion, and use of Group III–IV materials for energy harvesting (► Chap. 4, "Solar Energy Harvesting by Perfect Absorbers Made of Natural Hyperbolic Material", Wang; ► Chap. 5, "Strategies for Improving Solar Energy Conversion: Nanostructured Materials and Processing Techniques", So-Yoon; ► Chap. 6, "The Recent Research and Growth in Energy Efficiency in Cu₂ZnSnS₄ (CZTS) Solar Cells", Deokata; ► Chap. 7, "Counter Electrode Materials for Organic-Inorganic Perovskite Solar Cells", He), electron transport (► Chap. 8, "Impact of Electron Transport Layers (ETLs) and Hole Transport Layer (HTLs) on Perovskite Solar Cells Performance", Farhana), and energy storage (► Chap. 9, "Thermal Management Techniques for Concentrating Photovoltaic Modules", Xu), as well as thermal management (► Chap. 10, "Thermal Energy Storage Systems Based on Metal Hydride Materials", Corgnate), coupling of energy storage to photovoltaics (► Chap. 11, "Advanced Coupling of Energy Storage and Photovoltaics", Qiao), recent advances in dye-sensitized solar cells (► Chap. 12, "Design, Engineering, and Evaluation of Porphyrins for Dye-Sensitized Solar Cells", He), and use of the metal-organic framework as energy materials (► Chap. 13, "Insights into the Application of Metal-Organic Frameworks for Molecular Photovoltaics", Morris). The last thrust is related to actual applications including solar industrial process heat (► Chap. 14, "Industry-Specific Utilization of Solar Industrial Process Heat (SHIP)", Huda) and applications of solar energy in building management and desalination (► Chap. 15, "Comparative Analysis of Water Quality of Different Types of Feed Water in Solar Energy Based Desalting System", Wang) applications.

“All things are poisons, for there is nothing without poisonous qualities. It is only the dose which makes a thing poison.” Paracelsus (Borzelleca, 2000)

It could be argued that the ever-increasing demand for energy and emission of carbon dioxide, greenhouse gases, nitrogen oxides, and sulfur oxides are a kind of poison. It is our central thesis that the outcomes of these maladies can be remedied by a thoughtful transition to solar energy.

Why Pivot Toward Solar Energy?

This volume addresses recent advances in solar energy, where light energy is captured and used directly or indirectly to heat water and buildings or provide heat from the Sun. The Sun is the most efficient nuclear fusion reactor, approximately converting 700 million tons of hydrogen-2 into 695 tons of helium-4 each second through fusion. The missing mass of 5 million tons is converted into energy corresponding to 3.83×10^{26} joules per second, corresponding to the following: $[M = (3.83 \times 10^{26}) / (9 \times 10^{16})] = 4.26 \times 10^9$ kilograms of mass [1]. The attention to the utilization of solar diffuse sources is threefold:

- Burning of carbon-based fossil fuels including methane generates carbon dioxide, which is a greenhouse gas [2].
- Fossil fuels generate particulate matter which is also harmful to human health, as well as the environment [3].
- Fossil fuels could be better used in the manufacturing of plastics, drugs, and commodities, rather than for transport, heating, or generation of electricity [4].

It has been shown that greenhouse gases such as carbon dioxide (CO₂) and methane (CH₄) absorb longwave radiation and retain that energy, resulting in temperature fluctuations in the troposphere resulting in areas of increased “hotness” and areas of increased “coldness” in the short term. In the long term, this repartition will lead to an increase in the global temperature, causing frozen ice caps to melt, raising sea levels, generating localized tsunamis, and promoting more desert-like regions due to rapid evaporation of water [5].

Carbon dioxide is a nonpolar linear molecule with a D infinity h symmetry and can absorb infrared wavelengths of 4 and 15 microns; therefore, it has the potential to trap heat and reradiate it to the atmosphere, trapping energy. There are three terrestrial bodies which have carbon dioxide, Venus and Mars, which has approximately 96% carbon dioxide, and Pluto, which has 0.5% carbon dioxide. The temperature at the surface is related to the atmospheric pressure and illumination from the Sun. Venus has an atmospheric pressure approximately 96 times that of the Earth, while Mars has about 5.9×10^{-3} atm and Pluto approximately 1 atm. The surface temperature on Venus is higher than what would be expected from the Sun, while the atmospheric pressure on Mars is too low to redistribute heat efficiently, giving rise to the notation that increasing CO₂ levels can lead to increased global temperatures [6].

Are Carbon Dioxide Levels Rising?

The current CO₂ concentration is 400 parts per million corresponding to a partial pressure of 0.3 mmHg ($0.04/100 \times 760$), with oxygen at 160 mmHg and nitrogen at 593 mm Hg, and would not be directly toxic until the atmospheric concentration is around 5% of ($5/100 \times 760=$) 38 mmHg. At these levels blood CO₂ would exhibit hypercapnia, leading to hypoventilation, confusion, flushed skin, and muscle twitches. Prolonged exposure will lead to respiratory, cardiovascular, and nerve damage; for this reason, it was imperative that the Apollo 13 astronauts adopted the CO₂ scrubbers (lithium hydroxide canisters) from the Command Module to fit the Lunar Module Systems. At 3% (30,000 ppm) electrolyte imbalance changes are expected due to prolonged exposures, and at 4% unconsciousness is possible, which becomes critical at 5%. Therefore, while CO₂ is not a direct threat, it is a concern with respect to absorption of heat and its contribution toward global warming. Other gases are due to combustion such as a nitrous oxide (N₂O) and fluorinated gases. Since CO₂ is central to respiration and burning of carbon, it has a greater influence than the other greenhouse gases [7].

Is Solar the Way Forward Toward a Global Energy Mix?

Global warming is a long-term progression and cannot be reserved with any rapidity; therefore, society needs to act today, to see positive changes within our lifetimes (50-year time frame). Since 1980 the annual global temperature has increased alongside global CO₂ levels [8]. Since nuclear fusion reactors are not viable at the present time, capturing of sunlight is a viable alternative which is just as efficient as shown by photosynthetic plant life that absorbs the red and blue spectrum of light. Therefore, an energy mix with solar energy in the portfolio should be a priority, due to its centrality. While wind, geothermal energy, and hydropower are important, they are not equally accessible across this planet, whereas sunlight reaches almost every region of this planet [9]. The other realization is that if nothing is done, fossil fuels will decline and will not be economically viable to extract. Land can be used for mining, planting crops, and buildings habitats, and extraction to burn is a short-term option [10].

Utilization of solar radiation is central to a coherent energy plan, as the nuclear reactor provides continuous energy at least. The Sun is about 4.5 billion years old. It has used up about half of its nuclear fuel, and in about 5 billion years, the Sun will begin to transform into a Red Giant as the inner core expands into planetary nebulae and then contracts into a dwarf over a period of 75,000 years. This timescale is infinite relative to our age, and therefore, solar radiation energy can be considered abundant and indefinite [11]. To reduce particulate matter and CO₂ emissions and to re-task carbon for the production of materials as opposed to use for energy, sustainable energy sources such as solar should be integral to energy policy. Here solar energy will affect both the demand side and the energy side as energy utilities can sell the surplus to neighboring countries or neighboring districts; the lowering of global CO₂ should stabilize global temperature fluctuations. Most of the population reside in metropolitan cities where a population concentration has occurred since the

Modern Industrial Revolution of the 1960s in the United States. The major source of cooling (or heating) is electricity which is expected to increase as global temperatures increase in some areas. Coupled to this are seasonal variations; therefore, summers will be warmer and winters slightly warmer, placing infrastructure limitations, where peak energy demand exceeds the maximum capacity of the transmission systems. A decentralized approach where a community or houses have their own solar panels can alleviate this infrastructure overloading. In addition, new designs include buildings with more efficient heating and cooling designs [36].

Would Transition to Solar Energy Increase Its Benefit in the World Population?

Changes to the climate will result in alternations in energy demand, and it appears that the demand for electricity will increase, although this is not certain. The energy demands in India and China from 1980 to 2018 have increased but currently have slowed down or flattened, whereas in Japan, North America, and the European Union, there is a flat or slight increase in energy demands. Most of this energy demand has been met by coal-fired power stations where coal is converted to particulate matter and coal emissions to carbonic acid, as well as SO_x and NO_x depending on the composition of coal. These affect buildings, freshwater lakes, and forests due to the increased acidity of the rain [37]. If the increase in world population is compared with energy demands, there has been a positive correlation, although the demand for energy is less in the less developed world than in China/India, North America/Japan, and the European Union; in the latter the population increases are less than in Africa or Asia. This is shown in the table below and correlated with the “doubling time” using $T = 69G - 0.98$, where G is the population growth rate (%), T is the doubling time (years), and 69 and 0.98 are empirically derived coefficients by plotting the world populations from 1950 to an anticipated population in 2050, a year time span [38].

The current world population of 7.6 billion is expected to reach 9.8 billion in 2050. The largest growth is anticipated from India, Nigeria, the Democratic Republic of the Congo, Pakistan, Ethiopia, the United Republic of Tanzania, the United States, Uganda, and Indonesia [12]. This is similar to but not identical with the countries with the highest population, which are China, India, the United States, and Indonesia with populations of 200 million or greater (cf. Table 1).

Table 1 Breakdown of world population by area

	% population increase
First World countries	12
Central and Eastern Europe	5
Least developed countries	137
World	52

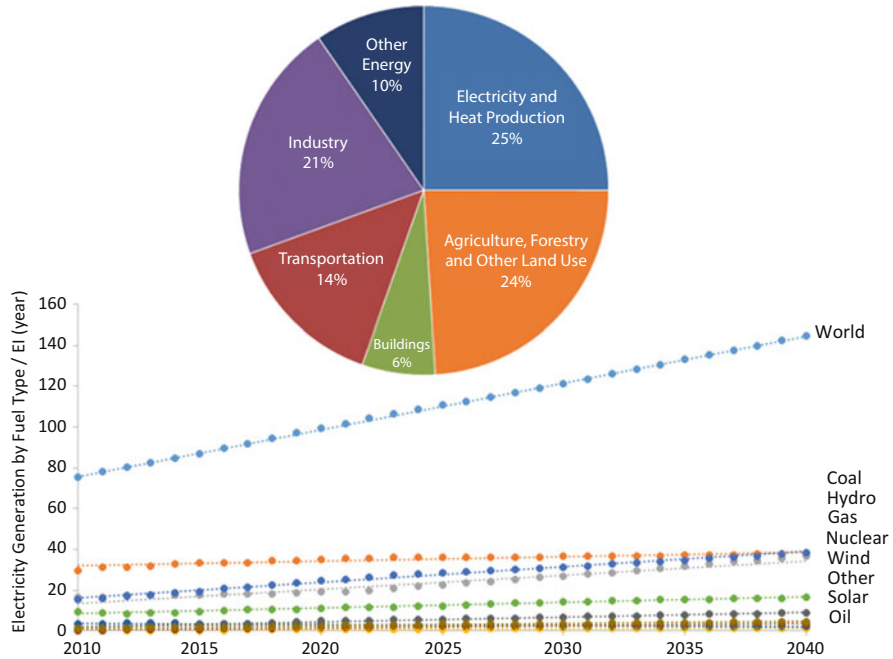


Fig. 1 Summary of carbon dioxide emissions by sector (IPCC 2014, top panel) and world electricity demand by energy type from 2010 to 2040 (bottom panel, [14])

Everyone needs chemical energy and water to survive; this, in turn, requires energy from the Sun (photosynthesis) or coal to transport food and water from farms to the cities. The world demand for energy will increase until at least 2020 and is increasing at 1.7% requiring $\sim 15 \times 10^9$ tons of oil equivalent (toe) or 75×10^6 barrels of oil per day to 120×10^6 barrels of oil per day, of which three-quarters is consumed by the transport section (IEA 2002). The incorporation of solar will lead to diversity, decentralization, and lower dependence on nonrenewable resources, lowering stress on the environment and enabling access to energy (water and food) to the marginalized groups.

The rationale for renewable energy portfolio is based on two assumptions, the first is that global demands for energy will continue to rise in absolute terms, although the rate of increase may not, and the second is that energy production from fossil fuels will generate carbon dioxide and other greenhouse gases. The sectors which produce the most are evenly split between agricultural and electricity generation with a nonsignificant contribution from building air-conditioning (Fig. 1). In addition, global greenhouse gas emissions are dominated by carbon dioxide emissions (Figs. 2 and 3), with China and the United States dominating the emissions (Fig. 3); therefore, energy policy from these countries will affect the world balance. Solar energy can play a major role in both areas, that is, first transition from fossil fuels and second meeting the energy demands in electricity generation and building air-conditioning, which is accountable for almost one third of the emissions.

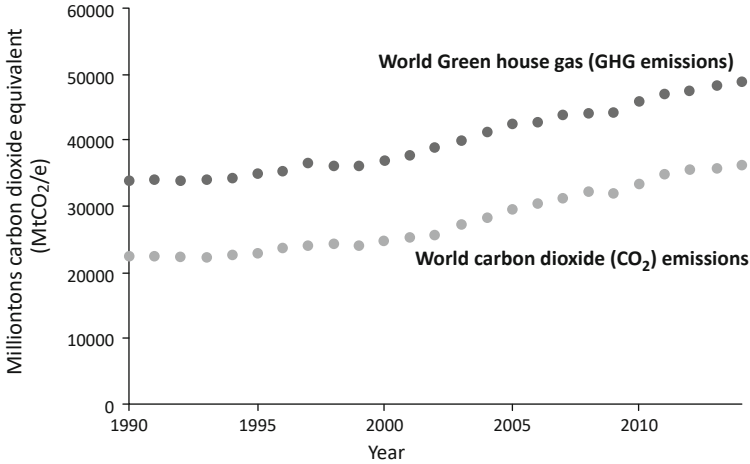


Fig. 2 Summary of world greenhouse gas emissions in million ton equivalence [15] and world carbon dioxide emissions (ORNL 2016)

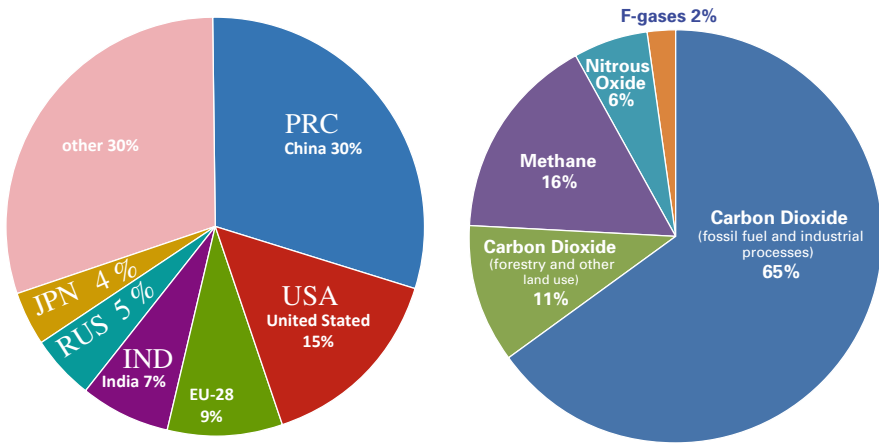


Fig. 3 Summary of greenhouse gas emissions by countries or economic alliance (left, IPCC, 2014) and by greenhouse gas (right, IPCC 2014)

Planet Earth is an oval-shaped body, and approximating it as a sphere, we can use $4 \times \pi \times r^2$ to calculate its surface area. Its amount of sunlight (solar flux) which is intercepted will depend on the body's cross section and can be estimated using $\pi \times r^2$; therefore, the total amount of light intercepted by the Earth is total flux/4 and is 340 w/m^2 at 0° north. The amount of solar radiation incident on the Earth is not the amount utilized, but the difference between radiation and amount reflected or planetary albedo (reflected/incident) and would vary depending on the degree of latitude, season and degree of clouds, and rain and weather patterns. The highest/lowest would be January/

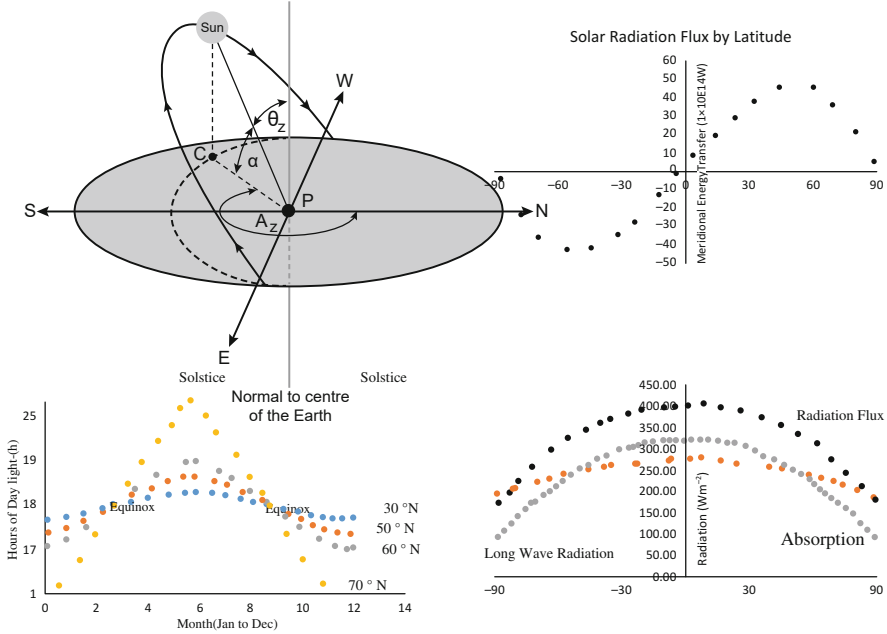
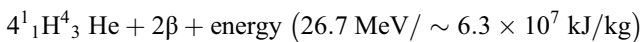


Fig. 4 The zenith angle (θ_z), the altitude angle (α), and the azimuth angle (A_z) of the Sun when viewed from point P (top left, ITACANET), the fluctuation of solar radiation by latitude (top right, ITACANET), hours of daylight as a function of angle (bottom left, ITACANET), and the amount of radiation which falls on the Earth, amount reflected and amount absorbed (ITACANET) <https://www.itacanet.org/the-sun-as-a-source-of-energy/part-1-solar-astronomy/> and <https://www.itacanet.org/the-sun-as-a-source-of-energy/part-2-solar-energy-reaching-the-earths-surface/>

July with emissions dominated by the lower troposphere. At altitudes less than 30° , the planetary albedo is around 25% and does not fluctuate, but between 40° north and south, the solar absorption exceeds the planetary emission, giving rise to a volcanic type of waveform if the latitude is plotted against the radiative flux; if a meridional energy transfer versus the latitude is plotted, a sinusoidal relationship is observed and is summarized in Fig. 4 [16].

Life requires chemical energy, and this may be derived from light energy supplied by the Sun through nuclear fusion. The Sun is the most massive object in our solar system with a radius of 1.39×10^6 km (or 175 Earth’s diameters) with varying temperature zones at different R values. Approximately 90% of the fusion energy is generated within 0.23 R, the surface at 1.0 R is dominated by convection cells of up to 3,000 km in diameter whose life is a few minutes, with smaller cells ($<1,000$ km) forming pores and larger cells forming darker sunspots, with the outermost photosphere having a lower density than air at sea level and being the source of solar radiation. The photosphere is surrounded by the chromosphere and corona which contribute to solar radiation flux [17]:



The large temperature gradient enables the Sun to radiate electromagnetic energy in the form of photons, receiving 4.1×10^{15} kWh daily or 5.2×10^{11} coal equivalent tons per day, which is slightly more than the annual global energy demand of 1×10^{10} coal equivalent tons. Therefore, the daily energy emissions from the Sun if harvested could easily satisfy the world's energy demand. The amount of solar energy per unit area is the radiant flux density or irradiance and varies by latitude and season. The greatest irradiance is in the tropics and decreases outward (0–90°). Between 35° north and 35° south reside the most populous regions which received approximately 2,000 kWh/year or 0.25 coal equivalent tons annually [18].

This light can be used for direct electricity generation (photovoltaics), generation of fuels by electrolysis (photochemical) or sugars (photosynthesis) depending on the system. The light reaching the atmosphere from the Sun in terms of emission represents a blackbody [19].

The solar energy spectrum is equivalent to a blackbody temperature of 5,800 K, where the energy (irradiation per wavelength) depends on the temperature of the body and not its composition. At higher temperatures, the energy-wavelength profile is shifted to shorter wavelength for higher temperatures. The maximum wavelength of light is around $\lambda = 0.5 \mu\text{m}$, which is a yellow-green light [20]. The atmosphere is sensitive to the wavelength of light, with shorter wavelengths of gamma, X-rays, and ultraviolet being absorbed and not penetrating the surface. Infrared radiation is absorbed by water vapor and carbon dioxide and visible by dust and silica particles, whereas longer wavelengths like radio waves are not usually absorbed and do not reach the surface. Therefore, the blackbody temperature approximates absorption profile equivalent to an air mass coefficient of zero, defined as the path length L through the atmosphere, and solar radiation incident at angle z relative to the normal Earth's surface (L/L_0), where L_0 is the light path taken at the normal Earth's surface and AM1.5 corresponds to the solar panel of 1.5 atmosphere thickness and corresponds to a solar zenith angle of $\theta_z = 48.2^\circ$ (cf. Fig. 5) [21].

The reason for the air coefficients (AM) is that the Earth is not flat but curved and also has a tilt (angle between the Earth's orbit and the plane of the equator), which affects seasons at the poles as they do not receive sunlight. The Earth also follows an elliptical orbit around the Sun, in addition to rotation about its own axis and a wobble around its axis [22]. This means over the period of 100,000 years, the actual rotational path will vary and the amount of sunlight reaching the surface will also alter as the Earth's orbit causes its distance to vary, accounting for the Southern/Northern Hemisphere dichotomy as well as seasonal changes from the current maximum of $1,360 \text{ W/m}^2$ [23]. As sunlight has no normal impact to the surface but at an angle, due to the Earth's tilt and taking account the curvature of the Earth, the attenuation (lowering) of absorbed energy at the surface can be approximated using Cartwright's model:

$$m = \left[1, 229 + (614 \sin \alpha)^2 \right]^{1/2} - 614 \sin \alpha,$$

where m is the air mass ratio (optical path at the zenith and optical path at an angle; if the angle is 90° , then $m = 1$; if the angle is less than 90° , then $m > 1$) [24]. Thus, at an air mass of 0 (AM0) atmospheres, the total amount of radiance is $1,353 \text{ W/m}^2$ ([25];

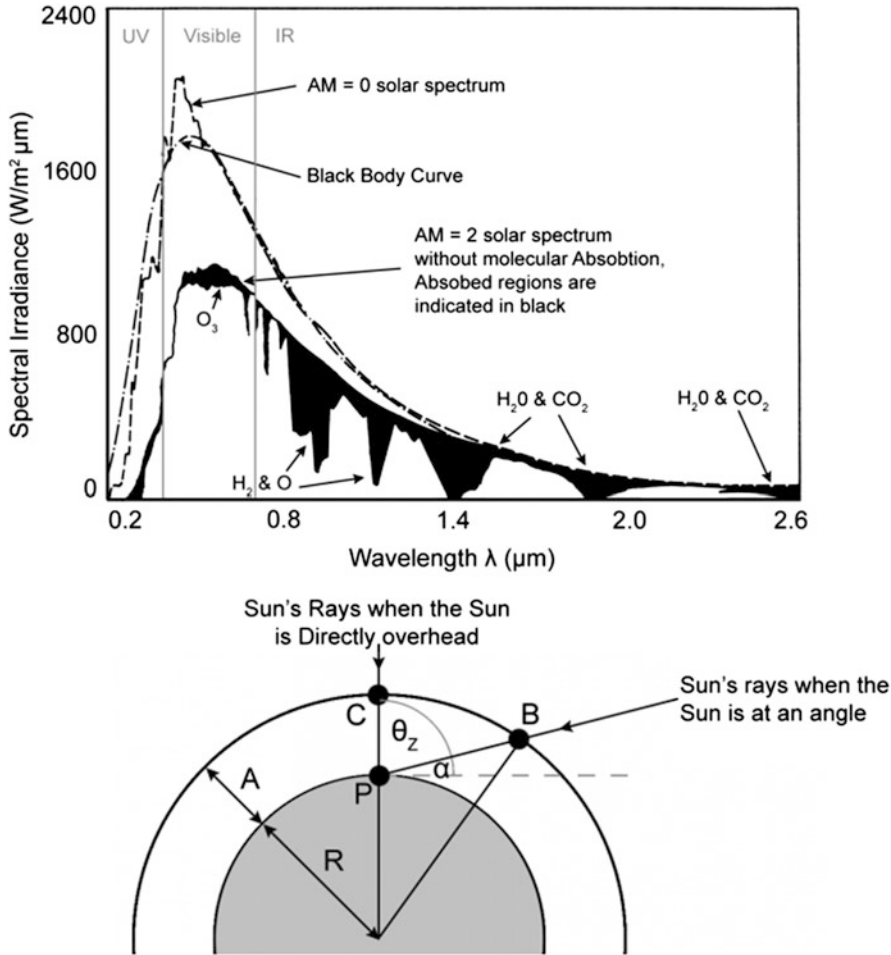


Fig. 5 (Top) the extraterrestrial solar spectrum (AM = 0), the theoretical blackbody curve, and the solar spectrum at the Earth's surface for AM = 2 and the absorbed regions shown in black (ITACANET) and (bottom) the distance traveled through the atmosphere by the Sun's rays at the path AM = BP/CP, an angle $\cos \theta_z$ (ITACANET) <https://www.itacanet.org/the-sun-as-a-source-of-energy/part-2-solar-energy-reaching-the-earths-surface/>

however, for simplicity we will use the value 1,360 W/m²). The actual irradiance at the surface at AM1.5 or greater is influenced by atmospheric conditions (clear sky or cloudy) or geometric effects including rotations and tilt. It should be emphasized the AM0 flux will change as the distance/eccentricity/tilt/wobble and distance between the Sun and the Earth vary over the next 100,000 years [26].

Thus, solar flux (I) is the radiant energy which is incident on a surface, and its variation over a specific time is known as the insolation. The incident light which falls on the flat surface is related to the azimuth angle (θ_z), $I_z = I \cos \theta_z$, where θ_z is the angle between the normal to the surface [27].

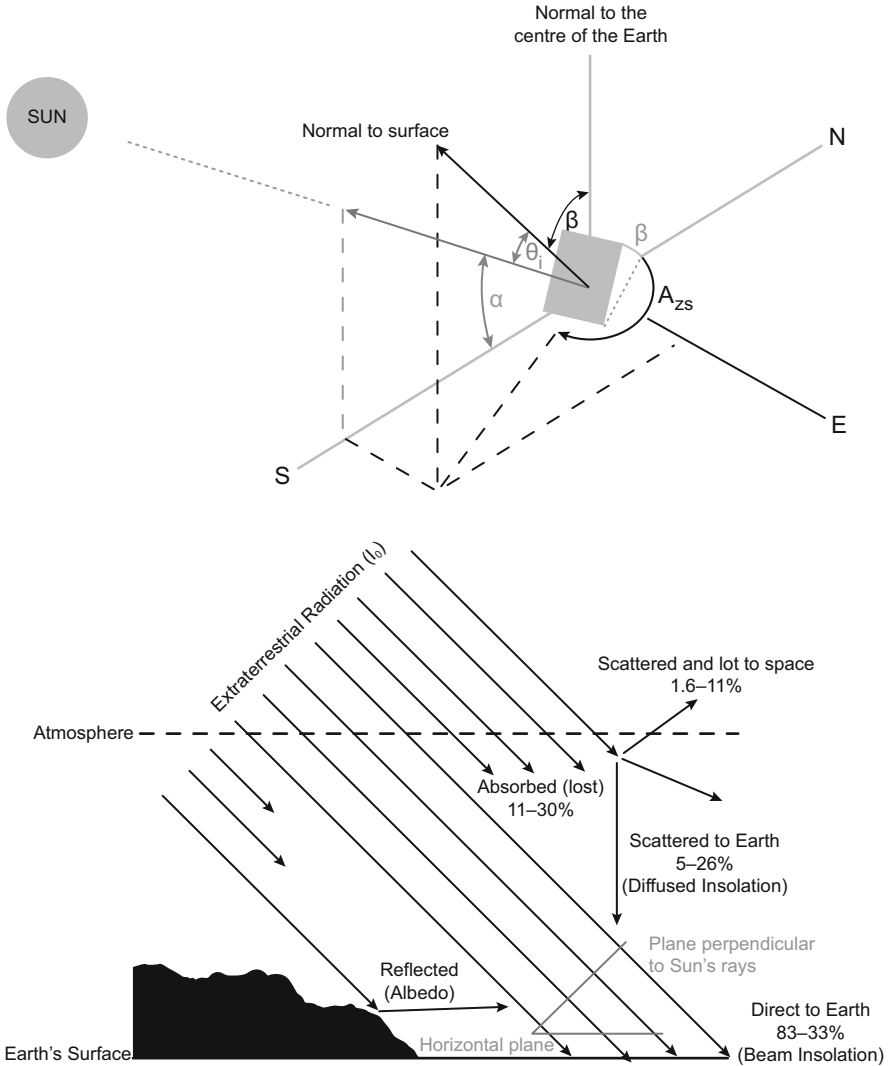


Fig. 6 (Top) the angle of incidence (θ_i) of the Sun on a surface tilted at an angle from the horizontal (β) and with any surface azimuth angle (AZS) (AZS is measured clockwise from north, $\theta_i > 90^\circ$ at any point in the Sun is behind the surface and the surface will be shading), and (bottom) the effect of the atmosphere on the solar radiation reaching the Earth's surface (ITACANET) <https://www.itacanet.org/the-sun-as-a-source-of-energy/part-2-solar-energy-reaching-the-earths-surface/>

Therefore, the solar flux impinging on the surface is related to the distance from the light source, dispersion through the media, and angle of irradiance. The diffusion can be uniform in all directions, or can be directional, as summarized in Fig. 6 [28].

The flux per unit area at distance R is thus $I_t \tau / 4 \pi R^2$, and assuming a distance of 150×10^9 m, the solar flux is around 3.8×10^{26} W. Since the Earth orbits around the

Sun, the fraction falling on this “disc” is $R/4$ or $1,360/4 = 340 \text{ W/m}^2$. The solar radiation at the surface can be approximated using Bouguer’s law as $I = I_0 e^{-\tau}$, where I_0 is the incident (extraterrestrial) radiance, I is the transmitted (terrestrial) radiance, and τ is the path length, related to the air mass (m) ratio [29].

Lastly, the diffusivity of light is related to the number of photons which are absorbed in the atmospheric gases, Rayleigh scattering, and Mie scattering due to particulate matter or dust in the atmosphere. Atmospheric scattering is not constant but varies to the λ^{-4} power, which means that the shorter wavelengths are scattered more than the longer wavelengths and can be considered constant for a cloudiness sky. Mie scattering also has a wavelength (λ^{-n} , where $n = 1-2$) dependence and is not constant, whereas Rayleigh scattering is the dominant form of scattering (Fig. 7). The measured light flux at the surface is lower than the values calculated using the approximation by Cartwright [24] since the distance between the Sun and Earth follows a wobble and eccentric pattern and the rotation of the Earth about its axis but also on the Earth’s revolution around the Sun is not uniform in the elliptical disc [30].

The orbit affects the light flux which would result in a year-to-year variation at the same declination angle (δ) due to the Earth’s tilt (axis relative to the plane of the ecliptic) and the angle swept out by the Earth’s orbit around the Sun, resulting in varying distances depending on whether the Earth is at the solstice, equinox, and the aphelion pattern as the Sun does not occupy the center of this orbital eclipse (Fig. 7, left), requiring solar cells to be repositioned at a specific tilt angle (θ , Fig. 7, right) [31].

In summary, the position of the Sun-Earth vector is defined by the elevated angle above the azimuth and the azimuth angle projected along with the Earth to the Sun (ecliptic circle). The combined sum of both angles equals 90° , with a maximum declination of 23° and 45 min on the summer or winter solstice. The other factors which alter light intensity at the surface are weather and landscape changes (cloudy versus cloudless and flat versus mountainous) and are also affected by the hour angle ($15^\circ \times 24 \text{ h} = 360^\circ$) [32]. The maximum sunshine duration (S) can be estimated as a function of solid angle of irradiance and can be loosely expressed as $2/15 \cos^{-1}(-\tan \varphi \tan \delta)$, where φ is the latitude, δ is the declination angle, and hour angle (ω) is $= 15(12 - h)$, where h is the current hour, where $I_h = I \cos \theta_z$, and where I is the solar irradiance, θ_z is the zenith angle, and I_h is the flux which is perpendicular to a horizontal surface [34]. For non-horizontal surfaces, the slope angle and aspect ratio need to be taken into account, using cos and sine rule ($A \cos \varphi + B \sin \varphi + C = 0$, where the constants depend on the slope (α), aspect (Ω), latitude (φ), and solar declination (δ)) [33]. This variation coupled with weather accounts for the differences in irradiance between the hemispheres and territories is shown in Fig. 8 [35].

Author Contributions

S. Bashir completed the initial draft including equations relating to thermodynamics, J.L. Liu the data for figures and figures from *itacanet.org*, and N.K. Sanders the final draft which was submitted by J. Liu for review.

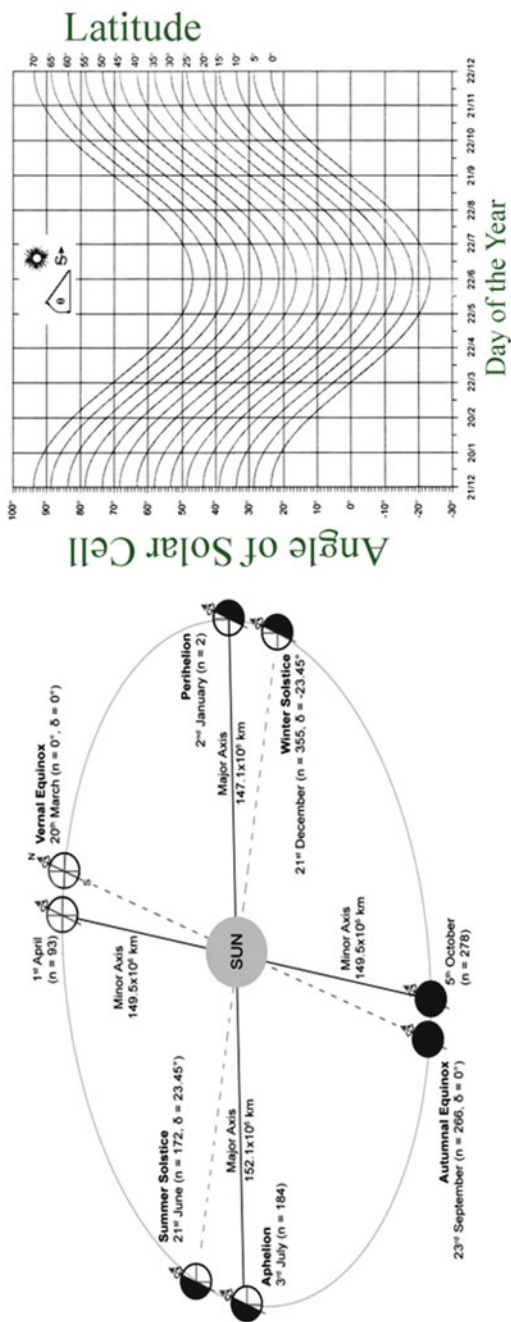


Fig. 7 (Left) the orbit of the world around the Sun: n is the day number where on January 1 $n = 1$ and δ is the declination angle (ITACANET) and (right) panel angles for latitudes from 70° to -70° ; negative panel angles indicate that panel is inclined to face north (ITACANET) <https://www.itacanet.org/solar-panel-angles-for-various-latitudes/> and <https://www.itacanet.org/the-sun-as-a-source-of-energy/part-1-solar-astronomy/>

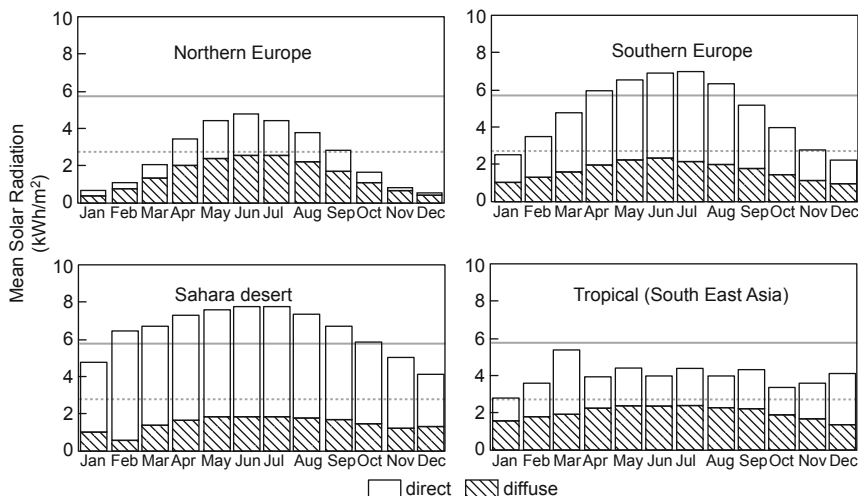


Fig. 8 The yearly profile of mean solar radiation for different locations around the world. The solid gray line shows the value of 5.75 kWh/day, and the dashed gray line shows 2.88 kWh/day (ITACANET) <https://www.itacanet.org/the-sun-as-a-source-of-energy/part-2-solar-energy-reaching-the-earths-surface/>

Acknowledgments

This work is supported by the Petroleum Research Fund of the American Chemical Society (53827-UR10) and the Robert A. Welch Foundation (Departmental Grant, AC-0006). We thank the program chairs of the ENFL and COLL divisions of the America Chemical Society for the opportunity to run or moderate symposia at the technical sessions. Lastly, we would like to thank Springer Science+Business Media and LLC technical staff for their assistance in copy editing this preface and other book chapters.

Department of Chemistry
Texas A&M University-Kingsville
Kingsville, TX, USA

S. Bashir
N. K. Sanders
J. Liu

References

1. D.J. Rose, Controlled nuclear fusion: Status and outlook. *Science* **172**(3985), 797–808 (1971)
2. W. Fulkerson, R.R. Judkins, M.K. Sanghvi, Energy from fossil fuels. *Sci. Am.* **263**(3), 128–135 (1990)

3. M.Z. Jacobson, Control of fossil-fuel particulate black carbon and organic matter, possibly the most effective method of slowing global warming. *J. Geophys. Res. Atmos.* **107**(D19), ACH-16 (2002)
4. K.G. Harding, J.S. Dennis, H. Von Blottnitz, S.T.L. Harrison, Environmental analysis of plastic production processes: comparing petroleum-based polypropylene and polyethylene with biologically-based poly- β -hydroxybutyric acid using life cycle analysis. *J. Biotechnol.* **130**(1), 57–66 (2007)
5. H. Rodhe, A comparison of the contribution of various gases to the greenhouse effect. *Science* **248**(4960), 1217–1219 (1990)
6. F.H. Hedlund, The extreme carbon dioxide outburst at the Menzengraben potash mine 7 July 1953. *Saf. Sci.* **50**(3), 537–553 (2012)
7. P.M. Vitousek, Beyond global warming: ecology and global change. *Ecology* **75**(7), 1861–1876 (1994)
8. J. Hansen, M. Sato, R. Ruedy, K. Lo, D.W. Lea, M. Medina-Elizade, Global temperature change. *Proc. Natl. Acad. Sci.* **103**(39), 14288–14293 (2006)
9. W. Gates, Federally supported commercial technology development: solar thermal technologies 1970–1982. *Res. Policy* **17**(1), 27–42 (1988)
10. G.T. Miller, Energy and environment: the four energy crises (No. 04; HD9502. A2, M5 1980) (1980)
11. T. Ohnishi, Nucleosynthesis of superheavy elements in the universe. *Prog. Theor. Phys.* **47**(3), 845–866 (1972)
12. UN WPP, 2017 Revision of world population prospects (2017), <https://www.un.org/development/desa/en/news/population/world-population-prospects-2017.html>. ORNL
13. T.A. Boden, G. Marland, R.J. Andres, National CO₂ emissions from fossil-fuel burning, cement manufacture, and gas flaring: 1751–2014. Carbon Dioxide Information Analysis Center, Oak Ridge National Laboratory, U.S. Department of Energy (2017). https://doi.org/10.3334/CDIAC/00001_V2017. IPCC (2014a)
14. IEO, The International Energy Outlook 2016 world energy projection system plus climate (2016). <http://watchdev.s3.amazonaws.com/production/models/8/EIA.jpg?1523910494>
15. CAIT, *Climate Data Explorer. 2017. Country Greenhouse Gas Emissions* (World Resources Institute, Washington, DC, 2017). <http://cait.wri.org>
16. D.T. Reindl, W.A. Beckman, J.A. Duffie, Evaluation of hourly tilted surface radiation models. *Sol. Energy* **45**(1), 9–17 (1990)
17. P. Foukal, What determines the relative areas of spots and faculae on sun-like stars? *Astrophys. J.* **500**(2), 958 (1998)
18. G. Bellini, J. Benziger, D. Bick, G. Bonfini, D. Bravo, B. Caccianiga, . . . A. Chavarria, Neutrinos from the primary proton-proton fusion process in the Sun. *Nature* **512**(7515), 383 (2014)
19. C.A. Gueymard, The sun’s total and spectral irradiance for solar energy applications and solar radiation models. *Sol. Energy* **76**(4), 423–453 (2004)
20. E.A. Anderson, D.R. Baker, Estimating incident terrestrial radiation under all atmospheric conditions. *Water Resour. Res.* **3**(4), 975–988 (1967)

21. S. Twomey, Aerosols, clouds, and radiation. *Atmos. Environ. Part A* **25**(11), 2435–2442 (1991)
22. A. Toomre, On the ‘nearly diurnal wobble’ of the Earth. *Geophys. J. Int.* **38**(2), 335–348 (1974)
23. J.L. Monteith, Attenuation of solar radiation: a climatological study. *Q. J. R. Meteorol. Soc.* **88**(378), 508–521 (1962)
24. T.J. Cartwright, *Modeling the World in a Spreadsheet: Environmental Simulation on a Microcomputer (No. JHUP-0095/XAB)* (Johns Hopkins University Press, Baltimore, 1993)
25. H. Li, Y. Lian, X. Wang, W. Ma, L. Zhao, Solar constant values for estimating solar radiation. *Energy* **36**(3), 1785–1789 (2011)
26. A.M. Noorian, I. Moradi, G.A. Kamali, Evaluation of 12 models to estimate hourly diffuse irradiation on inclined surfaces. *Renew. Energy* **33**(6), 1406–1412 (2008)
27. L. Kumar, A.K. Skidmore, E. Knowles, Modeling topographic variation in solar radiation in a GIS environment. *Int. J. Geogr. Inf. Sci.* **11**(5), 475–497 (1997)
28. R.E. Bird, C. Riordan, Simple solar spectral model for direct and diffuse irradiance on horizontal and tilted planes at the earth’s surface for cloudless atmospheres. *J. Clim. Appl. Meteorol.* **25**(1), 87–97 (1986)
29. M. Vollmer, S.D. Gedzelman, Colors of the Sun and Moon: the role of the optical air mass. *Eur. J. Phys.* **27**(2), 299 (2006)
30. Y. Harada, T. Asakura, Radiation forces on a dielectric sphere in the Rayleigh scattering regime. *Opt. Commun.* **124**(5–6), 529–541 (1996)
31. M. Collares-Pereira, A. Rabl, The average distribution of solar radiation—correlations between diffuse and hemispherical and between daily and hourly insolation values. *Sol. Energy* **22**(2), 155–164 (1979)
32. A. Berger, M.F. Loutre, C. Tricot, Insolation and Earth’s orbital periods. *J. Geophys. Res. Atmos.* **98**(D6), 10341–10362 (1993)
33. L.W. Swift Jr., Algorithm for solar radiation on mountain slopes. *Water Resour. Res.* **12**(1), 108–112 (1976)
34. D.A. Teets, Predicting sunrise and sunset times. *Coll. Math. J.* **34**(4), 317–321 (2003)
35. T. Huld, R. Müller, A. Gambardella, A new solar radiation database for estimating PV performance in Europe and Africa. *Sol. Energy* **86**(6), 1803–1815 (2012)
36. International Energy Agency, *Technology Roadmap: Solar Heating and Cooling*. International Energy Agency (2012)
37. G.E. Likens, F.H. Bormann, Acid rain: a serious regional environmental problem. *Science* **184**(4142), 1176–1179 (1974)
38. P.R. Ehrlich, A.H. Ehrlich, The population bomb revisited. *The electronic journal of sustainable development*, **1**(3), 63–71 (2009)

Contents

1 Solar Energy: Potential and Toxicology	1
Bhumika Ancha, Sajid Bashir, Nancy KingSanders, and Jingbo Louise Liu	
2 First-Principles Simulations for CuInGaSe₂ (CIGS) Solar Cells	45
Yu-Wen Cheng, Hong-Tao Xue, Fu-Ling Tang, and Jingbo Louise Liu	
3 Design of Photovoltaics-Based Manufacturing System Using Computer-Aided Design	75
José Ezequiel Santibañez-Aguilar, Sergio Castellanos, Benjamin B. Shapiro, Douglas M. Powell, Ian M. Peters, Tonio Buonassisi, Daniel M. Kammen, and Antonio Flores-Tlacuahuac	
4 Solar Energy Harvesting by Perfect Absorbers Made of Natural Hyperbolic Material	89
Zhaolong Wang and Ping Cheng	
5 Strategies for Improving Solar Energy Conversion: Nanostructured Materials and Processing Techniques	111
Monica C. So, Sung Won Yoon, and Nicole D. Mackie	
6 The Recent Research and Growth in Energy Efficiency in Cu₂ZnSnS₄ (CZTS) Solar Cells	137
R. J. Deokate	
7 Counter Electrode Materials for Organic-Inorganic Perovskite Solar Cells	165
Zonghao Liu and Hongshan He	
8 Impact of Electron Transport Layers (ETLs) and Hole Transport Layer (HTLs) on Perovskite Solar Cells Performance	227
Shakhawan Ahmad Mhamad, Abdussamad Mukhtar Mohammed, Madzlan Aziz, and Farhana Aziz	

9 Thermal Management Techniques for Concentrating Photovoltaic Modules	247
Xiaoru Zhuang, Xinhai Xu, and Jianpeng Cui	
10 Thermal Energy Storage Systems Based on Metal Hydride Materials	283
Claudio Corngale and Bruce Hardy	
11 Advanced Coupling of Energy Storage and Photovoltaics	317
Ashim Gurung, Ke Chen, and Qiquan Qiao	
12 Design, Engineering, and Evaluation of Porphyrins for Dye-Sensitized Solar Cells	351
Wenhui Li, Mahmoud Elkhalfifa, and Hongshan He	
13 Insights into the Application of Metal-Organic Frameworks for Molecular Photovoltaics	383
Matthew C. Kessinger and Amanda J. Morris	
14 Industry-Specific Utilization of Solar Industrial Process Heat (SHIP)	409
Shahjadi Hisan Farjana, Nazmul Huda, and M. A. Parvez Mahmud	
15 Comparative Analysis of Water Quality of Different Types of Feed Water in Solar Energy Based Desalting System	439
Arunkumar Thirugnanasambantham, Jiaqiang Wang, and David Denkenberger	
16 Toward Economically Rational Hydrogen Production from Solar Energy: From Battery Versus Hydrogen to Battery × Hydrogen	457
Michihisa Koyama	
17 Postface: China in the New Policies Scenario	471
Yongjun Gao, Yuliang Zhang, Jingbo Louise Liu, and Sajid Bashir	
Correction to: Design, Engineering, and Evaluation of Porphyrins for Dye-Sensitized Solar Cells	C1
Wenhui Li, Mahmoud Elkhalfifa, and Hongshan He	
Index	497

About the Editors



Tulay Aygan Atesin received her Ph.D. in 2007 from the University of Rochester under the supervision of Professor William D. Jones working on the mechanisms of strong bond activation reactions. She was a Postdoctoral Research Associate at the University of Wisconsin-Madison from 2007 to 2009 and at Northwestern University from 2009 to 2011. After being a Lecturer at the University of Wisconsin-Whitewater, she moved to the University of Texas Rio Grande Valley (formally the University of Texas-Pan American) in 2013. She completed the UTPA ADVANCE Leadership Institute in spring of 2014 and UTPA ADVANCE Administrative Fellow in the Office of Undergraduate Research and Service Learning in 2014–2015. She was a DOE Visiting Faculty at the Iowa State University and the Ames Laboratory in summer of 2016. She completed the ACS Leadership Institute in 2017 and chaired the ACS South Texas Local Section in 2018. She is a recipient of a 2008 Young Investigator Award from the ACS Division of Inorganic Chemistry.



Sajid Bashir received his Ph.D. in Analytical Chemistry from the University of Warwick, England, in 2001. He was a Postgraduate Research Associate at Cornell University who conducted research in the field of plant genetics. Currently, he is Full Professor at Texas A&M University-Kingsville (TAMUK) and a Faculty Fellow at the US Air Force. He has directed and participated in more than 20 projects supported by the Welch Foundation, TAMUK, Texas Workforce Commission, and US National Institutes of Health. He has coauthored more than 80 book chapters and peer-reviewed journal

articles. He is a Fellow of the Royal Society of Chemistry and Chartered Chemist and Chartered Scientist of the Science Council. Currently, he collaborated with the local law enforcement as a consultant.



Jingbo Louise Liu received her Ph.D. in Materials Science and Engineering from the University of Science and Technology Beijing in 2001. She is Full Professor at the Texas A&M University-Kingsville (TAMUK) and focuses on materials preparation, characterization, and applications. She is a Fellow of Royal Society of Chemistry and DEBI Faculty Fellow at the US Air Force Research Laboratory. She has authored and coauthored books, book chapters, and peer-reviewed journal articles (more than 100). During her 12.5-year services in the TAMUK, she taught more than 8,700 students and trained about 150 students and scholars to conduct leading-edge research. She directed and/or participated in the projects (more than 40) supported by the NSF (USA and China), NSERC (CANADA), ACS Petroleum Research Funds, and Department of Education as PI, Co-PI, and senior personnel. She was recently elected as the Chairwoman in the Division of Energy and Fuels, American Chemical Society.

About the Authors



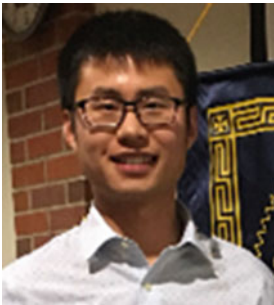
Dr. Farhana Aziz is currently a Senior Lecturer in the Department of Energy Engineering, School of Chemical and Energy Engineering, and Senior Associate Research Fellow in the Advanced Membrane Technology Research Center (AMTEC), Universiti Teknologi Malaysia (UTM). She already led a few research grants and is a member of more than 25 research projects. Her specialized research area includes nanomaterial synthesis and characterizations for gas separation, wastewater treatment, and energy applications.



Madzlan Aziz received his B.Sc. from the Newcastle-U-Tyne Polytechnic, UK; M.Sc. from the University of Manchester, UK; and Ph.D. from De Montfort University, Leicester, UK. He is currently Director of Research and Management Center, Universiti Teknologi Malaysia. His research interests include electrochemistry material, advanced material, and nanomaterial.



Dr. Sergio Castellanos received his Ph.D. in Mechanical Engineering from the Massachusetts Institute of Technology in 2015. He is a researcher at the California Institute for Energy and Environment and the Energy and Resources Group in the University of California, Berkeley. His current research areas are in energy systems modeling, sustainable transportation, solar photovoltaics deployment analysis, and environmental and energy justice.



Ke Chen is currently pursuing his Ph.D. under the guidance of Professor Qiquan Qiao at the Department of Electrical Engineering and Computer Science, South Dakota State University (SDSU), USA. He obtained his master's degree in Textile Engineering at Jiangnan University, China, in 2016. His research interests focus on solar rechargeable energy storage systems, lithium metal and lithium-ion batteries, and perovskite solar cells.



Dr. Ping Cheng, a Member of the Chinese Academy of Sciences, received his M.S. degree in Mechanical Engineering from MIT and Ph.D. in Aeronautics and Astronautics from Stanford University. He is Chair Professor in the School of Mechanical Engineering at Shanghai Jiao Tong University. Professor Cheng is an internationally renowned specialist in heat transfer. He has done seminal research work in porous-media heat transfer, radiative gas dynamics, and microscale boiling/condensation heat transfer. Professor Cheng has received four top international honors, including ASME/AICHE Max Jakob Memorial Award, ASME Heat Transfer Memorial Award, AIAA Thermophysics Award, and ASME Heat Transfer Division Classic Paper Award. Professor Cheng is also a Fellow of both [ASME](#) and [AIAA](#). He serves as an Editor for *International Journal of Heat*

and Mass Transfer and International Communications in Heat and Mass Transfer and is a Member of the editorial board of 12 international heat transfer journals.



Yu-Wen Cheng is currently a Ph.D. candidate in the Harbin Institute of Technology (HIT). He joined Dr. Tang's groups in 2014 and has been working in nano-functional materials (thin-film solar cell). He received his master's degree in Material Science and Technology at Lanzhou University of Technology (LUT) in 2017. Now, his research involves nano-structured functional materials and their applications in sustainable energy.



Claudio Corgnale received his Ph.D. in Mechanical and Industrial Engineering from Roma Tre University (Italy). Dr. Corgnale has more than 15 years of experience and expertise in hydrogen energy systems and thermal energy storage systems. He has been involved in the design and assessment of hydrogen production systems, developing process and detailed transport models for thermochemical and electrochemical hydrogen production plants. Dr. Corgnale has also been working on hydrogen storage, thermochemical energy storage systems, and hydrogen compression systems.



Jianpeng Cui is currently a master's degree student in the School of Mechanical Engineering and Automation at Harbin Institute of Technology, Shenzhen, People's Republic of China. He received his bachelor's degree from Harbin Engineering University, Harbin, China, in 2017. His research interest is on the thermal management of concentrated photovoltaic cells.



David Denkenberger received his Ph.D. from the University of Colorado at Boulder in the Building Systems Program. He is Assistant Professor at the University of Alaska Fairbanks in Mechanical Engineering. He received the National Science Foundation Graduate Research Fellowship; he is a Leader in Energy and Environmental Design (LEED), a Distinguished Alumnus in Penn State University, and a Registered Professional Engineer. He has authored or coauthored 95 publications (more than 1,400 citations, more than 50,000 downloads, h-index = 18), including two books. He has given over 90 technical presentations.



Dr. R. J. Deokate received his Ph.D. in Materials Science from the Shivaji University, Kolhapur (MS), India, in 2010. He is Assistant Professor at Vidya Pratishthan's Arts Science and Commerce College, Baramati, Pune (MS), India. His research interests include the nano-structured thin-film materials preparation, characterization, and understanding of fundamental physical and chemical properties and applications in alternative energy science.



Shahjadi Hisan Farjana received her Master of Science in Ocean Systems Engineering from the Korea Advanced Institute of Science and Technology (KAIST), South Korea, in 2015. After graduating from KAIST, she joined the Korea Research Institute of Standards and Science (KRISS), Daejeon, Korea, as a Researcher. She is currently a Ph.D. candidate under the supervision of Dr. Nazmul Huda in the School of Engineering at Macquarie University, Sydney, Australia. Her research interests include solar process heat integration and sustainability analysis in the mining industries. Farjana has authored and coauthored more than 25 peer-reviewed journals and conference articles.



Yongjun Gao has been working on energy research and policy for the long term. He received the awards on the provincial and municipal levels. He is an advisor on energy policy of the scientific and technology industries. His research achievements were recognized by the China Electric Power Association. He has published dozens of papers in different peer-reviewed journals.



Ashim Gurung received his Ph.D. in Electrical Engineering from South Dakota State University (SDSU) in 2017 and is currently a Postdoctoral Research Associate in Professor Qiquan Qiao's research group at SDSU. His major research expertise embodies research in different avenues of promising sustainable technologies based on energy generation and storage that includes battery charging designs with photovoltaics, third-generation solar cells, lithium ion, lithium metal batteries, solid-state batteries, supercapacitors, sensors, and microgrids.



Bruce Hardy is an expert in modeling transport processes and thermodynamics for hydrogen storage and thermochemical energy storage systems. He has led modeling teams for several large-scale DOE EERE programs involving media-based hydrogen storage, novel solar energy storage systems, and a number of other applications. Models that he developed have been used and referenced by the international community of hydrogen energy experts.



Hongshan He received his Ph.D. in Inorganic Chemistry from Sun Yat-sen University in 1996 and is Associate Professor at Eastern Illinois University. His research is focused on the design and synthesis of photoactive materials for solar energy conversion, bioimaging, and photocatalysis. Currently, he is Associate Editor for *RSC Advances*.



Nazmul Huda is a Senior Lecturer in Mechanical Engineering at Macquarie University, Sydney, Australia. His research interests include sustainable energy systems for novel engineering applications, high-temperature processing, computational fluid dynamic (CFD) modeling of high-temperature systems, energy materials, solar thermal processing, extractive metallurgy of light metals, and renewable energy. He completed his bachelor's degree in Mechanical Engineering and then continued his postgraduate research leading to a Ph.D. at the Swinburne University of Technology, Melbourne, Australia.



Matthew C. Kessinger is a native of Princeton, WV. He received his B.S. in Chemistry at Concord University in 2015. He began his graduate studies at Virginia Tech in 2015 under the guidance of Prof. Amanda Morris. His research interests include the fabrication and characterization of photovoltaic devices, electrochemical redox electrolytes, and charge transfer-induced spin crossover complexes.



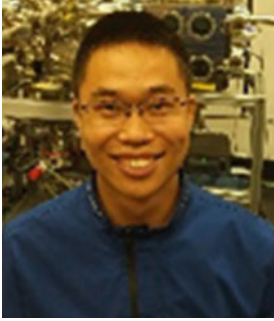
Nancy KingSanders has an extensive background in higher education that spans more than 30 years to include her current appointment as Executive Director, Center for Teaching and Learning at Austin Peay State University. Previously, she served as a tenured Full Professor in the Music Department; Graduate Music Education Coordinator; Administrative Intern for Academic Affairs, Associate Dean for Graduate Studies, and Associate Vice President for Student Success all at Texas A&M University – Kingsville. In her former capacity as Academic Affairs, Associate Dean for Graduate Studies, she coordinated research policy at Texas A&M University – Kingsville and become familiar with the topic of sustainable energy-related policies at State, Federal, and Government levels as well as the importance of energy policy dissemination to a wider audience of nonexperts.



Dr. Michihisa Koyama received his Ph.D. in Chemical System Engineering from the University of Tokyo in 2002. After serving as Assistant Professor at Tohoku University, he moved to INAMORI Frontier Research Center, Kyushu University, as Professor. He is now serving as the Unit Director at the National Institute for Materials Science as well as Professor at Shinshu University and Visiting Professor at Hiroshima University. Dr. Koyama has authored and coauthored more than 290 review articles, books and book chapters, and peer-reviewed journal articles. His research activities cover the wide aspects of energy from materials to systems, further to future energy vision. He was awarded the SCEJ Young Investigator Researcher Award, the Society of Chemical Engineers, Japan, in 2009, and the Young Scientists' Prize, the Commendation for Science and Technology by the Minister of Education, Culture, Sports, Science and Technology, in 2014. He directed and participated in more than 60 projects after being promoted as Full Professor, which are supported by the Japan Science and Technology Agency, Japan Society for the Promotion of Science, New Energy and Industrial Technology Development Organization of Japan, Ministry of the Environment of Japan, leading private companies, etc. He served as Committee Member in various panels of public organizations for the science policymaking or proposal reviews.



Wenhui Li obtained his Ph.D. in Optoelectronic Information Engineering from Huazhong University of Science and Technology in 2015. Currently, he is a Faculty Member at Jiangxi University of Science and Technology. His research interests include the design and synthesis of organic and organic-inorganic hybrid materials for solar energy conversion and luminescent devices applications, surface chemistry of semiconductor nanomaterials, and engineering of the organic-semiconductor interface.



Zonghao Liu received his Ph.D. in Opto-electronic Information Engineering at Wuhan National Laboratory for Optoelectronics, Huazhong University of Science and Technology, in 2016. Currently, he works as a Postdoctoral Research Fellow at the Okinawa Institute of Science and Technology Graduate University, Japan. His research is focused on the design and synthesis of functional materials for solar energy conversion devices, such as dye-sensitized solar cells and perovskite solar cells.



Nicole D. Mackie is majoring in Physics and minoring in Chemistry. She interned at Sandia National Laboratories in Energy Nanomaterials Division and earned scholarships for her work in self-assembling nanomaterials. She aspires to be a STEM teacher.



M. A. Parvez Mahmud received his B.Sc. degree in Electrical and Electronic Engineering at Khulna University of Engineering and Technology (KUET), Bangladesh, in 2011, and his Master of Engineering degree in Nano-Mechatronics at the University of Science and Technology (UST), Korea, in 2015. After graduating from UST, he joined the Korea Institute of Machinery and Materials (KIMM), Daejeon, Korea, as a Researcher. He is currently a Ph.D. candidate under the supervision of Professor Candace Lang and Dr. Nazmul Huda in the School of Engineering at Macquarie University, Sydney, Australia. His research interests include the economic optimization of microgrids and cleaner production of renewable energy.



Shakhawan Ahmad Mhamad is Lecturer in the College of Education, Chemistry Department, the University of Sulaimani in Kurdistan Region of Iraq. He received his master's degree in Physical Chemistry from Universiti Teknologi Malaysia in 2014. He completed his Ph.D. at Universiti Teknologi Malaysia. His current research focuses on lead-free and stable perovskite solar cell.



Abdussamad Mukhtar Mohammed is a Ph.D. student of Physical Chemistry with interest in perovskite solar cell at Universiti Teknologi Malaysia (UTM). He obtained his M.Sc. and B.Sc. in Industrial Chemistry from Jodhpur National University, India, and Bayero University Kano, Nigeria, in 2016 and 2013. Abdussamad is Lecturer in the Department of Chemistry, Yobe State University, Damaturu, Yobe State, Nigeria.



Dr. Ian M. Peters is a Scholar working on solar energy and solar photovoltaic concepts. He received his Ph.D. in Physics from the Albert Ludwigs University of Freiburg, Germany, in 2009. He has held positions at the Fraunhofer Institute for Solar Energy Systems (ISE) in Freiburg, Germany, at the Solar Energy Research Institute of Singapore (SERIS) and the Massachusetts Institute of Technology (MIT). He is Associate Editor for the journal *Solar Energy* and has coauthored more than 200 papers in scientific journals and at conferences. His research interests lie in novel photovoltaic concepts, optics and photonic, system adoption of renewable energies, tandem solar cells, techno-economic modeling, and simulation and modeling.



Qiquan Qiao is Harold C. Hohbach Professor and Graduate Coordinator in Electrical Engineering at South Dakota State University (SDSU). His current research interests focus on biomedical sensors, agriculture sensors, polymer photovoltaics, dye-sensitized solar cells, perovskite solar cells, and lithium-ion batteries. He received the Faculty Award for Global Engagement: Excellence in International Research in 2016, the F.O. Butler Award for Excellence in Research at SDSU in 2014, the US NSF CAREER Award in 2010, and the Bergmann Memorial Award from the US-Israel Binational Science Foundation in 2009.



Monica C. So earned her Ph.D. from the Northwestern University in Inorganic Solid-State Chemistry. In 2015, she became Assistant Professor of Physical/Materials Chemistry at California State University, Chico, where she is currently studying the structure and properties of 2D and 3D nanomaterials for sustainability applications. These range from energy conversion and water decontamination to electronics and thermoelectrics. Her work is supported by the Department of Energy, Department of Education, California State University (CSU) Program for Education and Research in Biotechnology.



Fu-Ling Tang is Full Professor at the School of Materials Science and Engineering, Lanzhou University of Technology. He received his Ph.D. in Materials Science and Technology from Tsinghua University in 2007. His research expertise focuses on solar energy and materials study. He published more than 100 peer-reviewed manuscripts and directed about 10 projects supported by the Chinese National Science Foundation.



Arunkumar Thirugnanasambantham received his Ph.D. in Physics from Bharathiar University in 2012. He received a Junior Research Fellowship (JRF) during his Ph.D. from the Ministry of New and Renewable Energy (MNRE). He was a recipient of an Indian National Science Academy (INSA) Visiting Scientist Fellowship during the year 2014. He was awarded a Dr. D.S. Kothari Post-Doctoral Fellowship during 2015 under the supervision of Professor R. Velraj, Director and Head in the Institute for Energy Studies, Anna University, India. His research interests are solar desalination, broadband energy absorbing materials, and wastewater treatment.



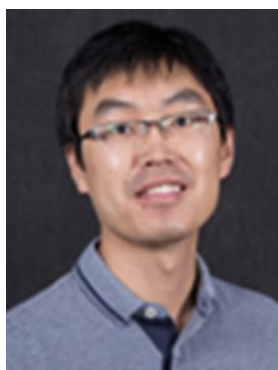
Jiaqiang Wang received his Ph.D. in Physical Chemistry from the University of Leeds in 2000. He is Director of the National Center for International Research on Photoelectric and Energy Materials, Yunnan Province Engineering Research Center of Photocatalytic Treatment of Industrial Wastewater and Key Laboratory of Advanced Materials for Wastewater Treatment of Kunming Yunnan University. His research includes the study of water resources and transportation.



Dr. Zhaolong Wang Assistant Professor at Hunan University, received his B.S. degree from Huazhong University of Science and Technology and his Ph.D. from Shanghai Jiao Tong University, and his supervisors are Professors Ping Cheng and Zhuomin M. Zhang. He worked at the School of Mechanical Engineering at Georgia Institute of Technology in Professor Zhuomin Zhang's research group as a Visiting Scholar from 2016 to 2017. His research interests are in the area of nano-optics of nanoparticles and metamaterials, photo-thermal conversion, radiation heat transfer, solar-thermal energy harvesting, and nanoscale boiling in a nanofluid. He has published more than 10 journal papers and conference papers in the past 6 years, and his work on perfect absorber is highlighted by the *Advance in Engineering* journal. He has participated in eight projects funded by NSF of China and research institutes.



Sung Won Yoon earned her B.S. in Chemistry and minored in Mathematics from the California State University, Chico. She interned at Sandia National Laboratories in the Energy Nanomaterials Division and worked at Nanotech Energy, a startup company focusing on graphene-based batteries. She is currently pursuing a doctoral degree in the Department of Chemistry, University of Houston.



Xinhai Xu is presently Associate Professor in the School of Mechanical Engineering and Automation at the Harbin Institute of Technology, Shenzhen, China. He received his Ph.D. in Mechanical Engineering from the University of Arizona in 2014. His research interests include multi-physics analysis of fuel cells, reforming to produce hydrogen, molten salt heat transfer fluids, and thermal management of batteries. He directed research projects funded by the National Natural Science Foundation of China and Shenzhen Science and Technology Innovation Commission as PI.



Hong-Tao Xue received his Ph.D. in Materials Processing Engineering from Lanzhou University of Technology in 2017 and has authored and coauthored more than 30 peer-reviewed journal articles on the structural, electronic, optical, thermodynamics, and mechanical properties of organic, inorganic, and organic-inorganic hybrid thin-film solar cell materials as well as their heterointerfaces using the first-principles calculation method based on density functional theory (DFT). His doctoral dissertation was selected as an excellent doctoral dissertation of Gansu Province in 2017 by the Gansu Provincial Department of Education. He is a Full-Time Research Worker of the State Key Laboratory of Advanced Processing and Recycling of Nonferrous Metals at the Lanzhou University of Technology.



Xiaoru Zhuang is a Postdoctoral Fellow at the School of Mechanical Engineering and Automation, Harbin Institute of Technology, Shenzhen, China. She received her bachelor's degree in Thermal Energy and Power Engineering from Central South University, Changsha, China, in 2012, and her Ph.D. major in Cryogenic and Refrigeration Engineering from the Technical Institute of Physics and Chemistry, Chinese Academy of Sciences, Beijing, China, in 2017. Her research areas focus on heat transfer and hydrogen production. She has published 17 papers in peer-reviewed journals and conferences.

Contributors

Bhumika Ancha Department of Chemistry, Texas A&M University-Kingsville, Kingsville, TX, USA

Farhana Aziz Advanced Membrane Technology Research Centre (AMTEC), School of Chemical and Energy Engineering, Faculty of Engineering, UniversitiTeknologi Malaysia, Johor Bahru, Malaysia

Madzlan Aziz Faculty of Sciences, UniversitiTeknologi Malaysia, Johor Bahru, Malaysia

Sajid Bashir Department of Chemistry, Texas A&M University-Kingsville, Kingsville, TX, USA

Tonio Buonassisi Massachusetts Institute of Technology, Massachusetts Avenue, Cambridge, MA, USA

Sergio Castellanos Energy and Resources Group and Berkeley Energy and Climate Institute, University of California, Berkeley, USA

Ke Chen Center for Advanced Photovoltaics, Department of Electrical Engineering and Computer Sciences, South Dakota State University, Brookings, SD, USA

Ping Cheng MOE Key Laboratory for Power Machinery and Engineering, School of Mechanical and Power Engineering, Shanghai Jiao Tong University, Shanghai, China

Yu-Wen Cheng Department of Materials Science and Engineering, Lanzhou University of Technology, Lanzhou, China

Claudio Corgnale Greenway Energy, LLC, Aiken, SC, USA
Savannah River National Laboratory, Aiken, SC, USA

Jianpeng Cui School of Mechanical Engineering and Automation, Harbin Institute of Technology, Shenzhen, China

David Denkenberger Mechanical Engineering and the Alaska Center for Energy and Power, University of Alaska Fairbanks, Fairbanks, AK, USA

R. J. Deokate Vidya Pratishthan's Arts Science and Commerce College, Baramati, India

Mahmoud Elkhalfifa Department of Chemistry and Biochemistry, Eastern Illinois University, Charleston, IL, USA

Shahjadi Hisan Farjana Sustainable Energy Systems Engineering Group, Macquarie University, Sydney, Australia

Antonio Flores-Tlacuahuac School of Engineering and Science, Tecnológico de Monterrey, Monterrey, Mexico

Yongjun Gao Zhejiang Triangle Qing Energy Enterprise Management Co., Ltd., Hangzhou, People's Republic of China

Zhejiang Yangtze River Delta Clean Energy, Conservation and Environmental Protection Development Research Center, Hangzhou, People's Republic of China

Ashim Gurung Center for Advanced Photovoltaics, Department of Electrical Engineering and Computer Sciences, South Dakota State University, Brookings, SD, USA

Bruce Hardy Savannah River National Laboratory, Aiken, SC, USA

Hongshan He Department of Chemistry and Biochemistry, Eastern Illinois University, Charleston, IL, USA

Nazmul Huda Sustainable Energy Systems Engineering Group, Macquarie University, Sydney, Australia

Daniel M. Kammen Energy and Resources Group and Berkeley Energy and Climate Institute, University of California, Berkeley, USA

Matthew C. Kessinger Virginia Tech, Blacksburg, VA, USA

Nancy KingSanders Austin Peay State University, Clarksville, TN, USA

Michihisa Koyama Center for Green Research on Energy and Environmental Materials, National Institute for Materials Science, Tsukuba, Ibaraki, Japan
Research Initiative for Supra-Materials, Shinshu University, Nagano, Japan
Graduate School of Engineering, Hiroshima University, Higashi-Hiroshima, Japan

Wenhui Li School of Information Engineering, Jiangxi University of Science and Technology, Ganzhou, Jiangxi, China

Jingbo Louise Liu Department of Chemistry, Texas A&M University-Kingsville, Kingsville, TX, USA

Department of Chemistry, Texas A&M University (TAMU), College Station, TX, USA

Zonghao Liu Wuhan National Laboratory for Optoelectronics, School of Optical and Electronic Information, Huazhong University of Science and Technology, Wuhan, P. R. China

Nicole D. Mackie Department of Chemistry and Biochemistry, California State University, Chico, Chico, CA, USA

M. A. Parvez Mahmud Sustainable Energy Systems Engineering Group, Macquarie University, Sydney, Australia

Shakhawan Ahmad Mhamad Faculty of Sciences, UniversitiTeknologi Malaysia, Johor Bahru, Malaysia

Chemistry Department, Faculty of Education, University of Sulaimani, Kurdistan, Iraq

Abdussamad Mukhtar Mohammed Faculty of Sciences, UniversitiTeknologi Malaysia, Johor Bahru, Malaysia

Department of Chemistry, Yobe State University, Damaturu, Yobe State, Nigeria

Amanda J. Morris Virginia Tech, Blacksburg, VA, USA

Ian M. Peters MIT Photovoltaic Research Laboratory, Cambridge, MA, USA

Douglas M. Powell Golman School of Public Policy, University of California, Berkeley, CA, USA

Qiquan Qiao Center for Advanced Photovoltaics, Department of Electrical Engineering and Computer Sciences, South Dakota State University, Brookings, SD, USA

José Ezequiel Santibañez-Aguilar School of Engineering and Science, Tecnológico de Monterrey, Monterrey, Mexico

Benjamin B. Shapiro E3 Consulting, San Francisco, CA, USA

Monica C. So Department of Chemistry and Biochemistry, California State University, Chico, Chico, CA, USA

Arunkumar Thirugnanasambantham National Center for International Research on Photoelectric and Energy Materials, Yunnan Provincial Collaborative Innovation Center of Green Chemistry for Lignite Energy, Yunnan Province Engineering Research Center of Photocatalytic Treatment of Industrial Wastewater, The Universities' Center for Photocatalytic Treatment of Pollutants in Yunnan Province, School of Chemical Sciences and Technology, Yunnan University, Kunming, China

Fu-Ling Tang Department of Materials Science and Engineering, Lanzhou University of Technology, Lanzhou, China

Department of Chemistry, Texas A&M University, Kingsville, TX, USA

Jiaqiang Wang National Center for International Research on Photoelectric and Energy Materials, Yunnan Provincial Collaborative Innovation Center of Green Chemistry for Lignite Energy, Yunnan Province Engineering Research Center of Photocatalytic Treatment of Industrial Wastewater, The Universities' Center for Photocatalytic Treatment of Pollutants in Yunnan Province, School of Chemical Sciences and Technology, Yunnan University, Kunming, China

Zhaolong Wang College of Mechanical and Vehicle Engineering, Hunan University, Changsha, China

Xinhai Xu School of Mechanical Engineering and Automation, Harbin Institute of Technology, Shenzhen, China

Institute of Hydrogen and Fuel Cell, Harbin Institute of Technology, Shenzhen, China

Hong-Tao Xue Department of Materials Science and Engineering, Lanzhou University of Technology, Lanzhou, China

Sung Won Yoon Department of Chemistry and Biochemistry, California State University, Chico, Chico, CA, USA

Yuliang Zhang Zhejiang Triangle Qing Energy Enterprise Management Co., Ltd., Hangzhou, People's Republic of China

Zhejiang Yangtze River Delta Clean Energy, Conservation and Environmental Protection Development Research Center, Hangzhou, People's Republic of China

Xiaoru Zhuang School of Mechanical Engineering and Automation, Harbin Institute of Technology, Shenzhen, China

Common Abbreviations

θ	Azimuth angle (deviation from the north)
δ	Density
φ	Elevation angle
α	Thermal volumetric expansion coefficient
α	Absorption coefficient
ϵ	Dielectric constant
η	Reflection coefficient
μ	Thermal conductivity
κ	Thermal conductivity
\parallel	Electrical field vector parallel to the plane of incidence
\perp	Electrical field vector perpendicular to the plane of incidence
a	An area
Ac	Alternating current
Albedo	Irradiance caused by reflections from the ground
AM	Relative air mass
Arc	Anti-reflective coating
aSi	Amorphous silicon
b	Length of the path passed by irradiance
Bi_2Te_3	Bismuth telluride
C	Permittivity constant
CdS	Cadmium-sulfite
CdTe	Cadmium-telluride
CIGS	Copper indium gallium selenide
CNTs	Carbon nanotubes
Cp	Heat capacity
cSi	Single crystal silicon
CuInSe_2	Copper-indium-diselenide
CVD	Chemical vapor deposition
d	Number of the day of a year
d	Thickness of a layer
DC	Direct current
di	Thickness of layer no. i
DSSC	Dye-sensitized solar cell

E_0	Extraterrestrial irradiance
EDS	X-ray energy dispersive spectrometer
EDX	Energy-dispersive X-ray spectroscopy
ESR	Electron spin resonance spectroscopy
FESEM	Field emission scanning electron microscopy
FF	Form-factor of the I-V characteristics
GaA	Gallium-arsenide
Ge	Germanium
h	Height (above sea level)
h	Planck's constant
hr	Relative humidity
I_d	Conducting-state current
I_{mp}	Current at the maximum power point
I_{photo}	Photo-induced current
IR	Infrared radiation
I_r	Irradiance of the diffuse component
I_{sc}	Short circuit current
K	Boltzmann constant
k	Imaginary part of the optical refractive index
l	Length
MOFs	Metal-organic frameworks
M_p	Maximum power
mSi	Mono- or single-crystalline silicon
n	Optical refractive index
Noc	Nominal operating conditions
Noct	Nominal operating cell temperature
Nu	Nusselt number
Oc	Open circuit
Ocv	Open circuit voltage
p	Air pressure
P	Power, heat flow
PC	Polycarbonate
PCE	Photovoltaic conversion efficiency
PE	Polyethylene
PMMA	Polymethylmethacrylate
Pr	Prandtl's number
pSi	Poly-(multi)-crystalline silicon
PTFE	Polytetrafluoroethylene
Pv	Photovoltaic
PVC	Polyvinyl chloride
PVF	Polyvinyl fluoride
q	Charge of an electron
q	Heat transfer coefficient
q	Quantity of heat

r	Electrical resistance
Ra	Rayleigh's number
Re	Reynold's number
S	Emittance of a surface
SC	Short circuit
Si	Silicon
sSi	Solar-grade silicon
STC	Standard test conditions
T	Temperature
t	Time of day in hours
T	Transmittance
Tc	Temperature coefficient
TEM	Transmission electron microscopy
TiO ₂	Titanium dioxide
U	Normalized voltage
UV-vis	Ultraviolet-visible spectroscopy
W	Watts
XRD	X-ray powder diffraction
y	Year
ZnO	Zinc oxide
ZnS	Zinc sulfate
ZrO ₂	Zinc dioxide



Solar Energy: Potential and Toxicology

1

Bhumika Ancha, Sajid Bashir, Nancy KingSanders, and
Jingbo Louise Liu

This chapter is dedicated to Professor Peter J. Derrick who passed away in March 2017 during the writing of this chapter.

Contents

1.1	Introduction	3
1.2	Solar Energy	5
1.3	Solar Thermal Electricity (STE) and Solar Photovoltaics (PV)	9
1.4	Solar Cell Primer	13
1.5	Toxicological Evaluation	18
1.6	Photocatalytic Reactivity	21

Author Contribution

BA completed all the experimental research, and the experimental, result, and conclusion sections with the first draft of the introduction were written by LL. The data in the figures and charts in the introduction were supplied by SB and LL. The final draft was reviewed and edited by NKS and LL.

B. Ancha · S. Bashir

Department of Chemistry, Texas A&M University-Kingsville, Kingsville, TX, USA

e-mail: bhumika.ancha@students.tamuk.edu; kfsb005@tamuk.edu

N. KingSanders

Austin Peay State University, Clarksville, TN, USA

e-mail: kingsandersn@apsu.edu

J. L. Liu (✉)

Department of Chemistry, Texas A&M University-Kingsville, Kingsville, TX, USA

Department of Chemistry, Texas A&M University (TAMU), College Station, TX, USA

e-mail: kfjll00@tamuk.edu; jingbo.liu@tamu.edu

1.7	Bactericidal Properties	22
1.7.1	Experimental Procedure	22
1.7.2	Synthesis Overview	23
1.7.3	Colloidal Synthesis	23
1.7.4	Solid State Chemistry to Produce CTO-NPs	24
1.7.5	Characterization of Titania	24
1.7.6	X-Ray Powder Diffraction	24
1.7.7	Transmission and Scanning Electron Microscopy	25
1.7.8	Spectroscopic Analyses	25
1.7.9	Bactericidal Performance of CTO-NPs	26
1.8	Results	27
1.8.1	Synthesis of CTO-NPs	27
1.8.2	Characterization of Titania	27
1.8.3	X-Ray Powder Diffraction	27
1.8.4	Transmission and Scanning Electron Microscopy	28
1.8.5	X-Ray Energy Dispersive Spectroscopy	28
1.8.6	Applications of Nanomaterials	31
1.8.7	Photocatalytical Reactivities of CTO-NPs	31
1.8.8	Bactericidal Performance of CTO-NPs	33
1.9	Discussion	34
1.9.1	Colloidal and Solid State Chemistry	34
1.9.2	Characterization of Titania	36
1.9.3	Application of Nanomaterials	38
1.10	Conclusion	38
	References	39

Abstract

Global energy demands towards 100 PW necessitated a rethink of approaches to generate the required demand through accelerated use of sustainable resources for both heating and generation of electricity. This is to degrade the global warming potential, lower greenhouses gases, and ultimately ensure against depletion of natural resources which may be required for habituation, agro-use or extraction for construction, catalysis, and fabrication of new materials instead of energy. Of the newer types of sustainable resources, solar energy has drawn considerable interest, due to the ability of the sun (a nuclear fusion reactor) to potentially meet all the demands with regard to heating and electrical generation. Current global production of electricity via solar only top 100 GW (less than 10% of the required load) but show promise. Current solar technologies are dominated by crystal silicon solar cells, although newer approaches using thin-films, CdTe, organic photopolymers, and composite devices have come online to meet the anticipated share for energy and heating, in diverse applications (satellite communication, heating, desalination, pumping of water, and electricity generation). While solar cells directly do not generate carbon dioxide and contribute towards global warming, the manufacturing of these devices does expend considerable energy and generates carbon dioxide, although leveled costs (dollar-per-kilowatt hour) are comparable to a coal-derived generation of energy and the roll-out and market deployment of solar cells is expected to increase. Likewise the environmental and

health hazard of disposal of solar components at end-of-life is unknown due to their longevity (25–30 year life cycle), although preliminary studies have shown that semiconductor components such as titania (TiO_2) are toxic to human cells, micro-organism, and freshwater algae, there is considerable variation in lethality of titania, due to exposure, concentration, and type of titania (anatase or rutile, nano or bulk) and microorganism (Gram-negative or Gram-positive).

To address the question of toxicity, we undertook synthesis, characterization, photocatalyticity, and cytotoxicity of Ce-doped TiO_2 (CTO-NPs). An environmental-friendly and cost-effective sol-gel approach was used to prepare different formulations of CTO-NPs. The starting materials of $\text{Ce}(\text{NO}_3)_3$ and $\text{Ti}(\text{O}i\text{Bu})_4$ were used, and a water-isopropanol mixture was used as a solvent to ensure the solubility of the above starting materials. The fabrication variables of CTO-NPs were optimized according to the photocatalytic reactivity and anti-bacterial activities. The powders of CTO-NPs were prepared after calcination at 200–400 °C with an increment of 50 °C for 2 h. These so-prepared CTO-NPs were characterized using X-ray powder diffraction, scanning and transmission electron microscopy, and ultraviolet and Raman spectroscopy, to evaluate their crystalline structure, morphology, and vibrational modes. It was found that the TiO_2 tetragonal anatase structure (PDF 01-086-1157, $3.7852 \times 9.5139 \text{ \AA}$ and $90 \times 90^\circ$) was obtained. The cerium cation-substituted the lattice Ti, leading to one phase formation. These CTO-NPs were found to be effective at decomposing methylene blue under visible light. Both Gram-negative (*S. marcescens*, ATCC 49732) and Gram-positive (*M. luteus*, ATCC 13880) bacteria were also tested using CTO-NPs as disinfectants. The maximum bactericidal concentrations (MBCs) were found to be 0.6 ppm to inactivate both bacteria within 1 h.

1.1 Introduction

The total energy needs of the planet are approximately 14,200 million metric tons of oil equivalent (TOE) or 165 PW/h in 2017 ($1 \text{ PW/h} = 1 \times 10^{15} \text{ W/h}$) [1]. Of this approximately 3.9% is from renewable resources (excluding hydro and nuclear), 4.6% from nuclear, 7.0% from hydro, 24.2% from gas, 27.9% from coal, and 32.4% from oil [2]. Relative to 1972 when almost 50% of the energy was from oil, all primary energy sources have declined except gas and renewables. Coal has fluctuated up and is expected to decline after 2020 to be surpassed by gas as the primary energy resource (after oil) as the next highest source [3]. Nuclear source spiked from approximately 1980s to 2010 and is now stable at 4%. It is the significant rise of renewables that is of interest, this rise becoming significant around 2020 and by 2040 comprising 14% of global energy.

Where does solar fit in? Solar and wind is the major primary energy sources for renewables accounting for 1.4% compared to 2.3% for wind or 0.07 million TOE for solar and 0.14 million TOE for wind, however. This current capacity is a fraction of the actual energy output of our sun, a yellow dwarf star that has a surface temperature

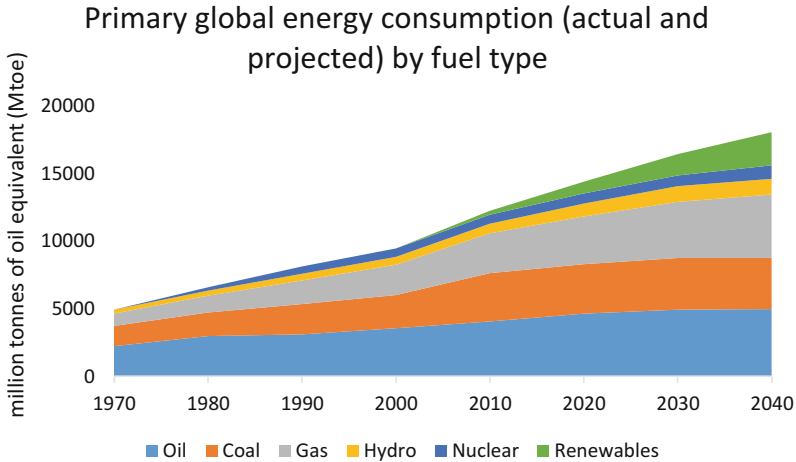


Fig. 1.1 Summary of global energy by fuel type by decade. (Sources: [5–7])

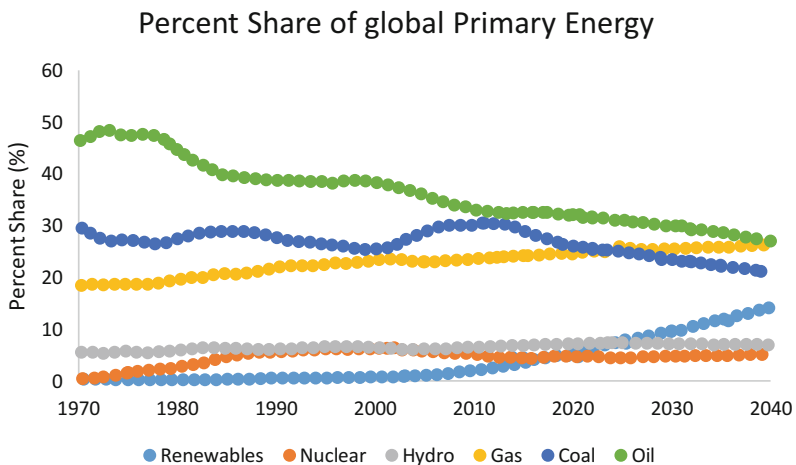


Fig. 1.2 Summary of percent share of global energy by fuel type by decade. (Sources: [5–8])

of approximately 5700 K and an energy of almost 3,300,000 YWh ($1 \text{ YWh} = 1 \times 10^{24} \text{ Wh}$), which is less than the entire combined energy need of the plant [4] shown in Figs. 1.1 and 1.2.

The vast majority of energy is derived from fossil fuels (~92%), leaving nuclear and hydro with 8% in the 1980s to an anticipated 12% by 2020 with other renewables being less than 0.1% in the 1970s rising to 17% by 2020 (nuclear, hydro, solar, wind, and thermal storage). While not significant in statistical terms, it is a great increase relative to initial usage [9–11].

Primary energy can broadly be classified as non-renewables and includes fossil fuels, minerals and biomass, and renewables that include solar, wind, thermal, and hydro.

The former category is dependent upon mining, extraction, purification (or fractionation), and usage, whereas the renewables resources rely on weather and rainfall to generate energy [12]. Oil exploration peaked in 2006 and is expected to decline slowly until 2040 for conventional oil. Moving to natural gas liquids, utilization of horizontal drilling and hydraulic fracturing into liquids-rich sweet spots of shale and tight gas will extend the utility of fossil fuels, but this is a tradeoff between economics of extraction, cracking, transportation, compliance, and resale, and as reserves dwindle, the more technically challenging “expensive” pockets would need to be explored, driving up costs. The extraction process is also expensive in terms of brine used, and combustion of fuels to generate energy and carbon dioxide and water [13].

1.2 Solar Energy

Sunlight is a resource that could be further tapped and utilized. Plants and certain algae utilize sunlight to generate sugars during photosynthesis. Unfortunately, not all sunlight is used to the same degree [14]. The planet Earth is oval shaped with a natural curvature. Some of the irradiances are reflected (30%), another 29% is absorbed by the atmosphere or reflected by clouds or the atmosphere, in addition to being radiated into space from the atmosphere or the land. Some of the sunlight is used in conduction and rising air (6.8%), another 22.9% is used to heat water (latent heat of vaporization) leaving 51% to be absorbed by surface (plants, land or oceans); approximately 15 PW/h is available for heating and conversion into biomass, or electricity [15]. The global demand for energy was 138 TW/h meaning the solar could supply all planetary energy needs, even at 75% emission loss [16].

The fraction of light energy that falls on the surface is a factor of longitude and latitude as well as the time of year. This is because the planet is oval and the sun is spherical, with the planet orbiting the sun once every 365 days (~ 4380 h of illumination per year) with an axis of rotation of 23.45° to the orbital plane [17]. The light rays travel a greater distance when the sun is “lower” in the sky than its zenith. The light intensity falling on the surface can be approximated using a cosine function (irradiance is equal to irradiance on a surface perpendicular to the direction of the sun \times the cosine of the irradiance angle) of 23.45° and is independent on atmospheric adsorption [4].

For example, sunlight impact at a 60° angle has to travel twice as far as overhead. This “air mass” (value of 2) relative to a value of 1 (overhead at zenith) would also lower the light energy due to absorption, refraction, and scattering by the atmosphere, which absorbs most if not all of the shorter wavelengths such as ultraviolet radiation. The sunlight of the most practical use is visible, near infrared. Taking water as an example to illustrate how the electromagnetic radiation affects chemical processes, the dissociation bond energy is approximately 290 kJ/mol [18] shown in Fig. 1.3a, b.

Light absorption would excite electrons into higher electronic states, and in Fig. 1.3c it can be seen that ultraviolet radiation would have sufficient energy, it can also be seen that the bulk of this energy is screened (e.g., by ozone) and never

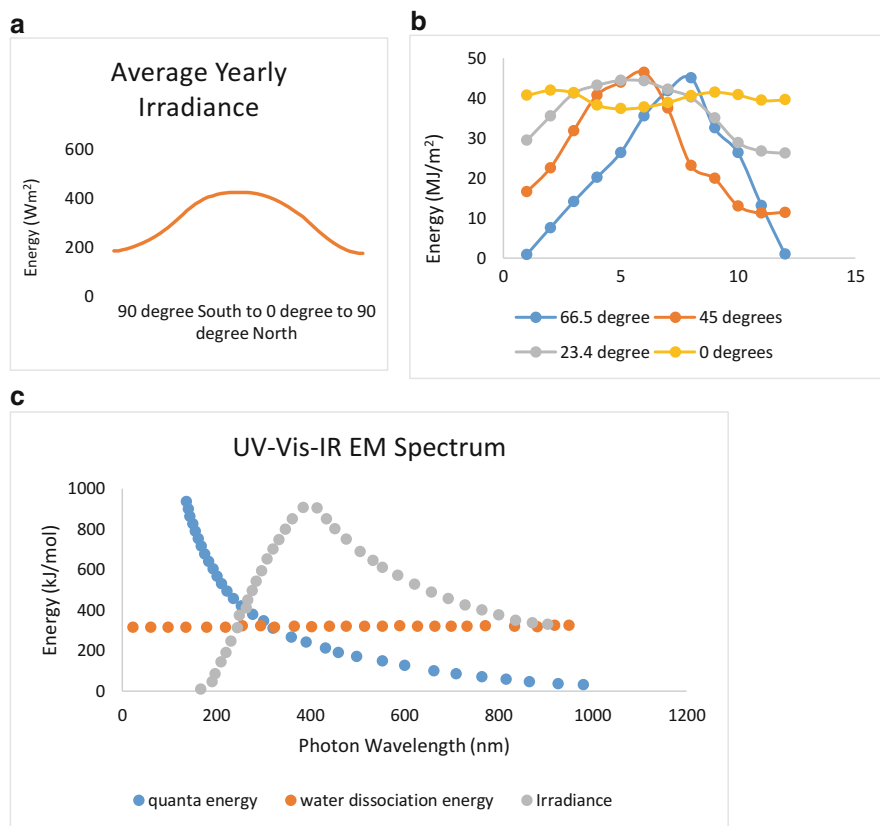


Fig. 1.3 Breakdown of electromagnetic radiation by (a) latitude, (b) tilt angle, (c) and function of quanta energy versus wavelength, irradiance, and energy required to dissociate water by one or multiple photon-absorption events. (Source: [18])

reaches the surface. Therefore, although UV radiation is capable of bond dissociation, statistically this is an unlikely event due to the lower intensity reaching oceans and lakes near the surface, whereas visible light photons do not have sufficient energy if a one-step process is considered. For visible light to be effective, a multi-step process is required, where multiple quanta of energy are required. This, in turn, will lower the efficiency of the reaction. Although the absorption of blue and red light by plants is a multi-step process and is inefficient relative to a single quantum process efficiencies, the sheer quantity of photons and plants enable this to be a productive process. The last point is an important consideration; water, for example, is transparent to visible light and would require a photocatalyst to absorb the incident light energy to transfer this energy to the molecule to facilitate bond cleavage. For an efficient process, this would also require the catalyst to have high absorptivity and broad spectral response. Since the plant is curved and spinning on its axis, the average irradiance is not constant but depends on the tilt angle. The regions which

receive the highest flux are Africa (7 °N and 21 °E), South America (23 °N/102 °W), and Australia (27 °S/133 °E). The optimal tilt angle for light collection can be defined either as global normal irradiance (GNI) or direct normal irradiance (DNI). The former relates to a measure of the maximum solar energy that can be used, while the latter relates to the irradiance received on a surface perpendicular to the sun's light (in the form of electromagnetic (EM) radiation) [19]. Tilt angles can become significant between 30 °S and 30 °N and may be up to 15° lower than latitude, affecting design and construction. The difference in collected energy between no tilt angle and where the sun's rays are tracked could be as much as threefold, and this difference is expected to be more pronounced in Europe, and less in Africa, Australia, and South Pacific. The average sunlight is dependent upon the broad longitude/latitude instead of a constant and also highly dependent upon the season. It varies from 1200 kWh/m²/year in Europe to 1800 kWh/m²/year in Central America, Australia, and Africa to 2300 kWh/m² during the summer months [20]. The irradiation of sunlight on the earth's surface is not uniform or constant over one rotation and thus needs to be averaged to decide if a specific location is suitable to harvest sunlight. This is accomplished by using global normal irradiance as a starting point in the calculation to determine the actual sunlight at a specific location over a specified period (day, week, month or year). The GNI value is approximated as 500 kWh/m²/year, from which the "average" is calculated around 1300 W/m². This value is estimated using the expression (1.1):

$$I = F_c \left[1 + x \cos \left(2\pi \frac{\text{day} - 3}{365} \right) \right] \quad (1.1)$$

where I is the solar irradiance, adjusted for eccentricity which in turn is related to Earth's position relative to the sun, as it orbits the sun (day 1–365). The solar flux constant (F_c) is 128×10^3 lux. The DNI correction for the atmosphere is $\text{DNI} = F_c e^{-cm}$, where c is the atmospheric extinction coefficient (e.g., 4.61 m^{-1}) and varies by depth, while m is the relative optical air mass (e.g., AM1.5 W/m²; Fig. 1.4). A day is defined as the time interval between two successive transits by the sun over a specific location (for example, the meridian) corresponding to one diurnal cycle or full rotation of the Earth to the sun. This rotation corresponding to one 24-h interval. However, the light intensity which falls on a specific location is not constant, and to determine the "average" daily value, the sunlight over 1 year is factored to determine the daily flux. Under these conditions, 1 year is 365 97/400 days, with January 1st, February 1st, and December 31st representing the 1st, 32nd and 365th day of the year. The highest flux (perihelion) would be when the sun and earth are the closest, and this is approximately the 3rd of January (2016, 2018, 2019, and 2021, and the 5th of 2017, 2020, and 2022), but the dates can differ by a day depending on the position facing away or towards the sun and the position of the moon relative to the earth.

The Earth's orbit around the sun is approximately circular. The minimum and maximum distance from the sun do not differ by more than three million miles (3%); a more significant influence on sunlight is the earth's axial tilt (23.4° on its vertical axis,

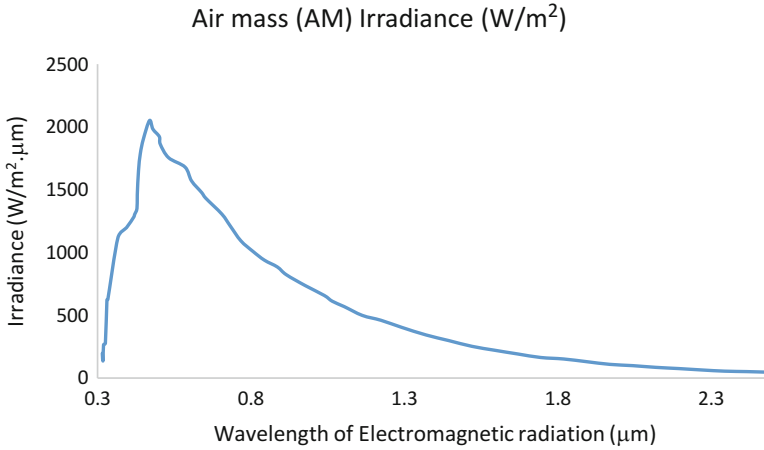


Fig. 1.4 Approximation of dependence of surface irradiance to air mass and wavelength of electromagnetic (EM) irradiance. (Sources: [21, 22])

eccentricity of less than 0.02) that determines the seasons, as the earth tilts towards/away from the sun (summer or winter solstices) or direction of the tilt and the direction to the Sun are perpendicular (equinoxes, Vernal & Autumnal) seasons [23].

The Earth receives a fraction of the possible irradiance of the sun, as it has a smaller cross section ($\pi \times R_E^2$) and tilt cosine angle (θ), which would correspond to approximately 340 W/m^2 . As orbital eccentricity increases, the solar irradiance difference becomes significant. The planets Mercury, Mars, and Pluto show significant eccentricity, and therefore there is a magnitude of difference between solar irradiances (2.15-1.36-0.34 respectively relative to $R_E = 1.00$), whereas the other planets show less eccentricity and the ratio of highest and lowest solar irradiance is similar (0.96 (Venus, lowest) – 1.16 (Saturn, highest), relative to $R_E = 1.00$) [24].

The spectrum of light from the sun resembles Blackbody radiation (5800 K) of which one-half is in the visible spectrum of the electromagnetic spectrum. The ultraviolet (UV) component of light which is mainly absorbed by ozone can further be classified by the wavelength band which corresponds to “short,” “intermediate,” and “long” UV wavelengths. These correspond to band “C” (100–280 nm); “B” (280–315 nm); and “A” (315–400 nm). Sunlight comprising of UV radiation has wavelengths which can reach the surface of the Earth (7%). The UV radiation has sufficient energy to promote radical formation and bond weakening in deoxyribonucleic acid (DNA). All major lifeforms on Earth (bacteria, archaea, and eukaryotes) possess DNA and are susceptible to its harmful effects; fortunately, the level of UV radiation exposure at the surface is not high enough to cause permanent damage without prolonged exposure. Wavelengths of lesser photon energy are visible light, infrared (IR, 750– 1×10^6 nm), microwave, and radio wave of which visible light (400–750 nm, 46%) are the main sources of solar radiation for heating and energy. Longer wavelengths past visible light include infrared (IR) radiation and are also classified by wavelength band. IR bands “A” (700–1400 nm), “B”

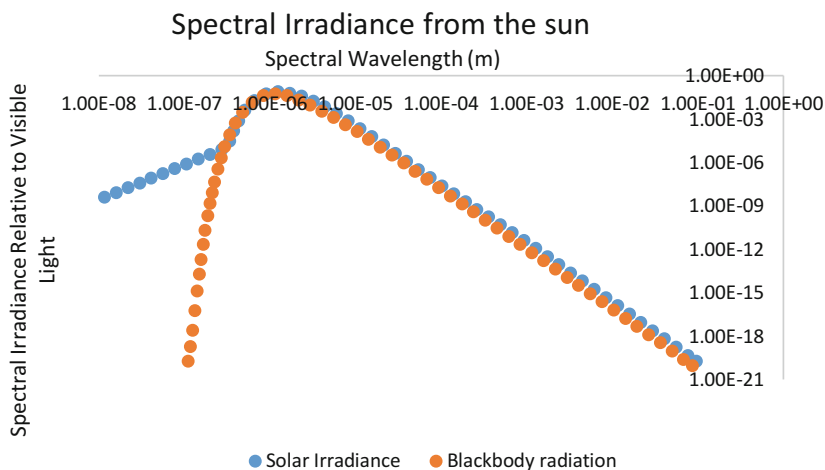


Fig. 1.5 Summary of electromagnetic radiation from the sun and from a blackbody versus wavelength. (Sources: [25, 26])

(1400–3000 nm), and “C” (3000 nm – 1 mm) are used for solar heating (47%). Other bands such as radio waves are too low in energy to be of use. A plot of the EM irradiance from the sun and energy emitted by a “blackbody” having a surface temperature (approximately 5800 Kelvin) is also shown. For practical purposes, most of “useful energy” falls in the visible to infrared wavelength of light, summarized in Figs. 1.3c and 1.5.

While the approximate irradiance is around 1.3 kW/m^2 , not all of the irradiance is utilized for heat or electrical current generation due to reflection, absorption, and scattering. As the volume of air becomes greater (air mass, AM), the fraction of useful light reaching the surface diminishes; at its zenith the irradiance is around 1.3 kW/m^2 , but as the sun arcs along the sky, the degree of useful light diminishes (e.g., is $\sim 900 \text{ W/m}^2$ at AM1 and $\sim 230 \text{ W/m}^2$ at AM10) as well as latitude (30° “belt”) and season (20% lower in the winter relative to the summer).

Solar technologies can be passive or active. In passive, the orientation of the building, water container, and windows relative to sunlight promotes illumination and heating, whereas active utilize sunlight to generate electricity or reactive oxygen species for disinfection or thermal storage for water heating. Even if 1% of available sunlight was used for energy generation, this would be 70-fold more than the entire global energy demand in 2005 [27].

1.3 Solar Thermal Electricity (STE) and Solar Photovoltaics (PV)

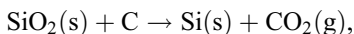
Sunlight can be used to boil water to generate steam, which in turn can be used to generate electricity. In addition, photons can be converted to electrons using semiconductors to generate electricity. Thin film silica wafers are used as photovoltaic

surfaces with microcrystalline and amorphous structures. Amorphous silicon has a band gap of 1.7 eV, whereas crystalline silicon has a band gap of 1.1 eV [28]. These bands gaps reflect the ability to absorb different parts of the EM spectrum. Although these cells have lower efficiencies (6%), their greater usage has increased global electricity generating capacity. Global solar capacity in 2035 is expected to be 150% greater than the BP Energy analysis due to falling costs and stronger policy support in China and India, two of the largest solar markets [5]. The average irradiance of 7 kWh/m²/day can be utilized by heating or photovoltaic systems, which couple the collector to solar arrays that generate direct current (DC). Typically an inverter is used to convert the DC to alternating current (AC) to be used in the general electrical grid [29]. Taking the EIA estimates, it appears that solar PV will become significant in the electricity generation sector in 2030, with wind as a significant provider of US electricity, providing 160 GW by 2050 (relative to 40 GW in 2020, with wind energy proving a constant 120 GW over the 2020–2050 time period), making up 48% of the world's installed capacity and 33% of electricity generation by 2040. In 2017, solar and wind global electricity generation was 1447 TW/h out of 24,860 TW/h or 5.8%; in 2040, it is anticipated to be 12,461 TW/h out of 37,510 TW/h or 33.2% [3].

While Solar PV array capacity factors operate below 25% efficiency, relative to fossil fuel-based power stations (36% Carnot cycle efficiency), their cost per kilowatt is similar, and unlike for fossil fuels, costs are falling for solar PV [30]. In addition, solar panels can be installed as thin film cell integrated to a flexible polymer roofing membrane, or as roof tiles or shingles, to facades of building exteriors, glazing or semi-transparent glass windows, and skylights. The “levelized cost of energy” is a measure of US cents per kilowatt-hour of electricity generated. Fossil fuel-derived energy in the form of conventional and advanced natural gas combined-cycle entering service in 2017 with appropriate tax credits are by 2040 anticipated to generate energy at \$53/MWh (at 2017 \$ value), while energy from advanced combustion turbine is anticipated to cost around \$85/MWh and energy from coal with 30% carbon capture and sequestration at \$114/MWh. Energy generation from renewables such as advanced nuclear is estimated to cost around \$78/MWh; for biomass \$85/MWh; and for onshore wind, at \$50/MWh; while offshore wind is anticipated to cost \$111/MWh, due to the greater infrastructure costs. Traditional renewables such as geothermal the anticipated cost are \$45/MWh; hydroelectric at \$58/MWh, while the solar thermal cost is anticipated at \$132/MWh and solar PV at \$48/MWh. As the earlier cost list highlights, energy production is highly sensitive to the type of fuel and the method employed to generate energy. Using \$52/MWh as a benchmark, only advanced combined-cycle turbines, using fossil fuels or renewable fuels such as geothermal, wind, onshore, and solar PV are price-competitive with geothermal being the “cheapest” and solar PV being the most “expensive” within the select energy resources [31]. These capacity-weighted averages also incorporated current costs with available tax credits that are not uniform across all energy mixes, capacities, and efficiencies.

The energy returned on energy invested is a net balance of energy utilized in the construction and operation of an energy resource including environmental impact. The carbon dioxide per kilowatt-hour of electricity varies depending on the system but is generally greater than 15 g/kWh for solar PV over its operating lifetime and is

lower than coal-fired power stations (915 g/kWh), nuclear (6 g/kWh), or wind (11 g/kWh). Heavy metals used as dopants or in cadmium telluride solar cells (CdTe) are toxic (5 g/m², 0.3–0.9 µg/kWh over its operating lifetime). Life-cycle cadmium emissions from coal are 3.1 µg/kWh, lignite 6.2 and natural gas 0.2 µg/kWh [32]. The time period before the investment costs are recouped is also different on technology type and varies between 1.5 and 11 years for different types of solar PV systems, assuming a 30-year operating lifetime [33]. The lifecycle analysis also factors in carbon dioxide obtained in the crystallization process:



Therefore, one mole of silicon will generate 1.5 moles of carbon dioxide at 1700° requiring energy. Approximately 13 MWh of electricity is used to produce 1 t of pure silicon. Approximately 50 tons (tn) of pure silicon (\$84,500 per tn) is required to meet the global energy requirements in 2005, and this was approximately 1/100th of the global production of silicon. The harvested silica is used for direct heating of homes, roof solar water heating, solar furnaces, and a sun-concentrated solar thermal power plant. The efficiency of light collection to electricity production is on par with photosynthesis (6–12%). In photosynthesis, light, carbon dioxide, and water are used to generate sugars (C₆H₁₂O₆, known as biomass); however, unlike photosynthesis, photovoltaics (PV) cannot alone meet expected demand nor decarbonize electricity generation without input from other renewables. These above physical constraints of silicon process to “commercial grade silicon,” cost of energy, and carbon dioxide emission limit the percent mix of solar towards global energy, and it will never meet 100% of the requirement, due to the low production of pure silicon and the energy-intensive processes required; however, solar PV can be a significant contributor towards sustainable energy alongside wind, geothermal, biomass, and nuclear [34].

The energy flow (exergy) and energy efficiency are related to light irradiance which is captured to varying degrees of success by different solar collector designs. In a semiconductor, the valence band is where the electrons are located and the conduction band is where the electrons end up separated by a band gap. The magnitude of this gap will reflect if the material exhibits more conductor-like or insulator-like properties and the spectrum of light that is absorbed [35].

Silicon is a group IV element having four valence electrons, which can be excited by a specific quantum of sunlight (1.12 eV); however, in a semiconductor to facilitate electron movement, the element is doped with electron-rich (group 5, 6, 7) and electron-deficient (group 1, 2, or 3) elements [36]. This creates a potential for electrons to migrate from the electron-rich areas to “holes” in the electron-deficient area, as silicon requires four electrons [37]. This can create positive and negative types which meet at the PN junction and forms the PV cell, with a light receiving antenna at the N-type of the device, illustrated in Fig. 1.6 [38].

The photovoltaic module charge controlled the inverter and storage battery. The photovoltaic module consists of photovoltaic cells which absorb light and generate electricity. The inverter converts direct current to alternating current and the charge controller prevents the battery from being overcharged or discharged to increase

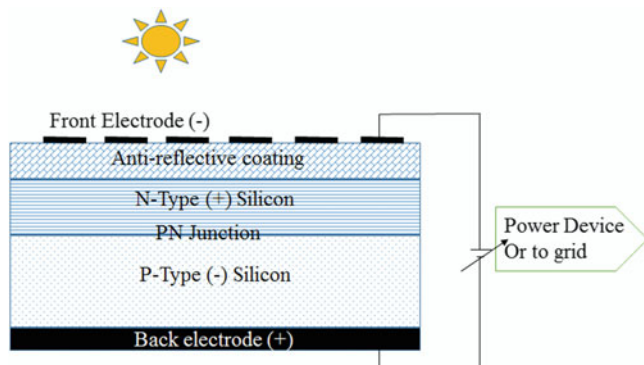


Fig. 1.6 Schematic of Si-based PV cell. (Source: [39, 40])

battery life. Lastly, the battery stores the surplus current. The most common type of solar cells are based on crystalline simplified silicon (sc-Si) or multi-crystalline silicon (mc-Si), thin-film micro amorphous silicon (a-Si), cadmium telluride (CdTe), copper indium selenide (CIS), and copper indium gallium selenide (CIGS) [41]. Recent advances have included organic photovoltaics based on carbon polymers. The above category of semiconductors has band gaps between 1.1 and 1.7 eV [42]. The most common are silicon-based cells that have a band gap of 1.12 eV and are between 11% and 20% efficient, where single silicon crystals are cured by the Czochralski process [43]. In recent years, manufacturers have moved towards thin-film cells that utilized 99% less material than crystalline solar cells, with a light efficiency of 12% and a service life of 25–30 years [44]. The major components are based on either a-Si, CdTe, CIS, or CIGS. The films convert 5–13% of light to electricity [45]. Researches to increase the solar efficiencies of silicon-based solar cells have incorporated hybrid perovskite ((CH₃NH₃)PbI₃), organic materials, nanotubes, graphenes, and quantum dots [46].

Moving from inorganic to organic systems offers advantages in terms of flexibility and panel area as well as fabrication [47]. The light absorbing layer is sandwiched between a glass coated with semitransparent indium tin oxide (ITO) on top and a conducting layer underneath (e.g., Al electrode) and a mixture of two ionomers such as poly(3,4-ethylene dioxythiophene) [PEDOT] polystyrene sulfonate [PSS] as a conducting polymer [48]. The wide band gap of 2 eV limits the spectrum of EM radiation that can be absorbed and the overall cell efficiency [49] with graphene support to extend efficiency and absorption range [50]. Other types of solar cells include dye-sensitized cells.

In a dye-sensitized cell, the absorption of light is separated from the transport of charge carriers. The “front electrode” can be thought of glass with transparent conductive tin oxide (TCO), with nanocrystalline titania adjacent to the TCO later separated by a conducting counter electrode. In between the titania and the counter electrode is the electrolyte where the redox chemistries occur. The electrons are fed into this redox cycle by the counter electrode and channeled to the titania, where

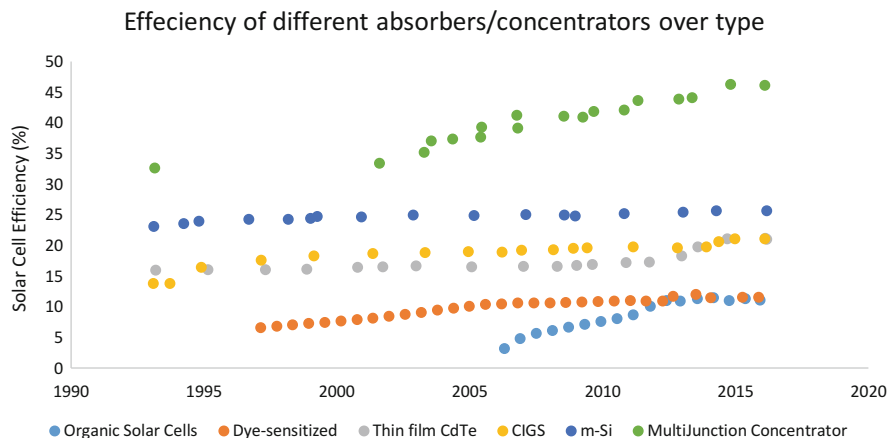


Fig. 1.7 Summary of improving light absorption efficiency of different solar cell/concentrator types of the last three decades. (Sources: [6, 55])

electron transport can occur [51]. This simplified design limits the efficiencies to 7–11% [52]. Other dyes such as ruthenium and zinc complexes have also been used, increasing efficiency with cost. Recently semiconductors such as perovskite-based trialkyl lead halides as light absorption materials have been used and can be 20% efficient [53]. Other areas have focused on metal-free organic dyes based on coumarin, quinoline, or indolines [54]. The differing design and solar cell/concentrator efficiencies are summarized in Fig. 1.7.

Factors that affect solar cell efficiency include surface temperature, solar irradiance, and intermittency, and clouds or dust. This, in turn, affects the cost of kilowatt/hour and has dropped almost 100-fold over the last three decades resulting in lower carbon dioxide emissions relative to coal-fired power stations [56]. A trend appears to be a migration away from silicon towards a-Si, CdTe, or CIGS and organic solar cells, due to their faster payback cycle and wider usage of solar in areas of lighting, water pumping, desalination, and communication [57].

1.4 Solar Cell Primer

Upon absorption of light, electrons are excited to higher orbitals and decay back to their initial states, generating heat but not causing bond cleavage. In electromagnetic radiation, a photon at higher energy, such as in the ultraviolet, can be used to promote bond cleavage. Upon absorption of light energy, an electron residing in a chemical bond may be promoted to a higher vacant orbital creating a “hole” that is “positively” charged [58]. An electron in the conduction band is, therefore, “free” to move within the crystal generating current. Similarly, hole (or charge carriers) can move by sequential “filling” from adjacent electron, which creates a new “hole” in their former location. The movement of charge carriers is related to temperature and band gap of the material.

For a cell to generate current, a circuit needs to be completed in the “opposite” direction to the movement of electrons. A potential barrier selectively separates the two charge carriers that are generated using light energy. The charge separation sets up a voltage difference between the ends of the cell which is used to drive an electric current in an external circuit [59]. To construct a cell, a positive and a negative terminals need to be constructed, and this may be accomplished through selective doping of the silicon crystal. By incorporating an atom with one additional electron relative to Si, such as P, a negative carrier is introduced and the “additional” electron can be used in the crystal’s conduction band to form part of an electric current [60].

In addition to the donor dopant atom, an acceptor dopant or positive carrier is also required. The acceptor has one less electron than Si (e.g. B) and would generate a hole. Connecting both n-type and p-type materials at an np junction would enable the charge carriers to migrate in opposite directions. As they move, an “intrinsic” barrier is setup limiting the total number that can migrate and form electron-hole pairs (Fig. 1.8a). Since light irradiance on the surface promotes charge separation, an excess of electrons

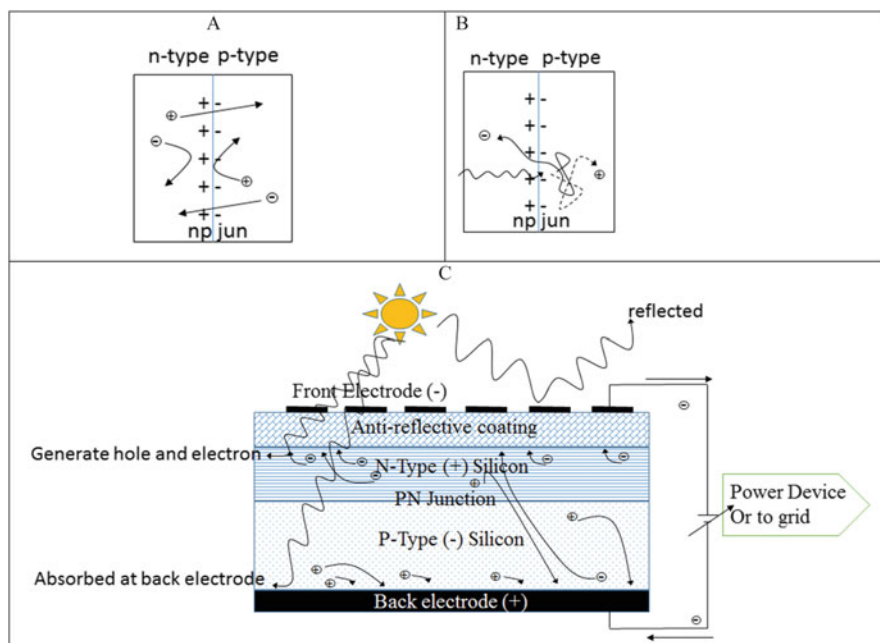


Fig. 1.8 Schematic of a solar cell. (a) During junction, electrons move from the n-type Si to p-type, while holes move in the counter direction. The movement of charge carriers in Si builds up an intrinsic barrier at the junction (np-jun) inhibiting further movement of free charge carriers and creates an equilibrium. (b) Upon absorption of a quantum of energy, an electron is excited on the p-type of Si and migrates across the np junction (np-jun) before it can recombine with a hole. (c) Light irradiance and absorption yields (electron-hole pairs) charge carriers that migrate in opposite direction, separated by the potential barrier, generating a voltage that drives a current through an external circuit from which useful work is undertaken. Some light is lost through reflection or absorbed from the back electrode. (Sources: [39, 40, 64–68])

(on n-side) and holes (on p-side) is generated, creating a charge imbalance in the cell (Fig. 1.8b). Negative charges flow out of the electrode on the n-type side through a load and perform useful work (Fig. 1.8c). The electrons flow into the p-type side, where they recombine with holes [61]. Thus light energy absorbed by the electrons is consumed during electron migration across the external circuit, generating an equilibrium between incident light which creates electron-hole pairs generating a charge imbalance and the PN junction and external circuit which facilitate movement and useful work at the expense of giving up the initially absorbed energy [62]. The incident light is used to generate charge carriers that move in opposite directions across the junction, creating a charge imbalance to drive a current through a circuit [63].

A number of phenomena lead to energy processes that do not lead to useful work. A major source of cell inefficiencies is a loss of light by reflection, ignoring latitude and seasonal changes. Approximately 5% of light is lost through coating the glass to minimize losses through reflection. Light of energies other than that required for excitation of electrons is also not efficiently utilized. Therefore a “useful” material is a material whose valance and conductance bands are separated by less than 2.6 electron-volts (eV) of energy. This corresponds to energy accessible in the visible wavelength spectrum of compatible materials including pure silicon (Si) and the semiconductor gallium arsenide (GaAs). Pure Si has a bandgap of 1.1 eV while that of GaAs is 1.4 eV. Quanta of energies equivalent between 1 and 2.6 eV will promote electrons from the valence to conduction bands and thereby potentially contribute towards energy production. Other factors are direct and indirect electron-hole recombination. The free charge carrier energy can be reduced through collisions, leading to lower charge mobility and lesser current (Fig. 1.9a). These may be related to surface inhomogeneities related to the Si and dopants (Fig. 1.9b). The flow of electrons and holes is related to the resistance of the material summarized using Ohm’s law ($R = V/I$) but is not true for materials where recombination losses are not proportional to resistance. Resistance occurs in the bulk of the material, top-surface of the material, and at the interface between the cell and electrical contacts leading to the external circuit (Fig. 1.9c). At higher temperatures, electrons have more energy, but the lattice vibrations also increase and interfere with charge carriers; the increase in temperature lowers the barrier at the junction to separate charges, which for Si occurs around 300 °C (Fig. 1.9d) where thermally excited ions undergo collisions and reduced ion mobility. Resistance losses can be offset through higher doping, at the expense of increased lattice inhomogeneities leading to an excess of free carriers which can overcome the potential barrier at the junction and eliminate any charge imbalance and the ability to generate current in the external circuit.

In the area of solar thermal, concentrated solar thermal are used for heating and concentrated solar power for the generation of electricity, where high magnification mirrors concentrate solar energy to heat to generate steam from water and electricity from steam-driven generators. The designs are parabolic troughs to focus light and heat into a receiver and Fresnel-type mirrors to focus onto receiver tube, towers that are an array of small mirrors which track the sunlight and focus the energy to a specific point, and solar dish collectors that focus light above a reflector dish. The strengths and weaknesses of these designs are summarized in Table 1.1.

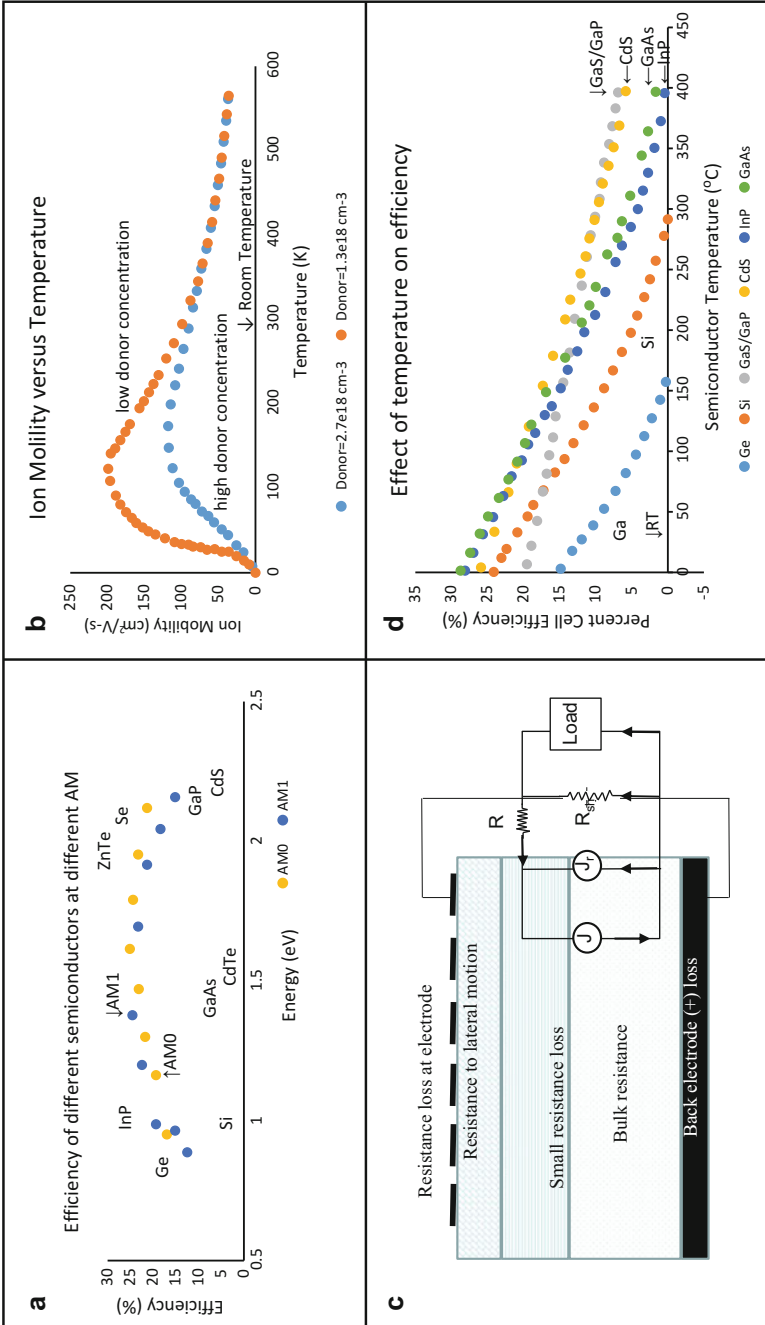


Fig. 1.9 Summary of effects which lead to cell inefficiencies related to (a) different semiconductor materials and light absorption at different air mass; (b) the effect of donor concentration on ion mobility; (c) intrinsic and bulk factors contributing to resistance within the device and circuit; and (d) effect of semiconductor temperature on cell inefficiencies. (Sources: [39, 40, 69–73]; Russell 2018)

Table 1.1 Summary of concentrating solar power technologies [74]

Parameter	Parabolic trough	Solar tower	Linear Fresnel	Dish-Stirling
Maturity	High	Intermediate	Intermediate	Low
Operating temperature (°C)	290–550	250–650	250–390	550–750
Max efficiency (%)	20	35	18	30
Max electricity efficiency (%)	16	20	13	25
“Engine”	Superheated steam Rankine	Superheated steam Rankine	Saturated steam Rankine	Stirling
Assembly	Absorber attached to collector and moves with collector	External surface with a fixed receiver	Fixed absorber with a secondary reflector	Absorber attached to a collector, and moves with collector
Storage system	Two-tank molten salt at 380 °C or 550 °C	Two-tank molten salt at 550 °C	Pressurized steam storage (<10 min)	Storage under development
Steam conditions (°C/bar)	380–540/100	540/100–160	260/50	N/A
Capacity/h	7	10	< 7	< 7

Solar energy by 2020 will be available, economic, and competitive with natural gas for heating and coal for generation of electricity in dollar-per-British thermal unit or dollar-per-kilowatt/hour, respectively, particularly by mimicking some design elements from photosynthetic plant apparatus [75] or through incorporation of molybdenum disulfide flakes (MoS_2) into an active buffer layer [76] to extend efficiencies beyond 25% [77] and sixfold increase from the first introduction of perovskite solar cells over the last decade [78] with the potential of semi-transparent solar cells as windows which transmit visible light and utilize IR light for energy [77]. By incorporating flexible hole transporting agents such as 3, 4-ethylenedioxythiophene, efficiencies can be increased [79]. Other approaches to increase efficiency have incorporated tungsten and alumina layers to absorb a wider spectrum of electromagnetic radiation [80], or biopolymers based on chitosan [81], or careful adjustment of redox centers in dye-sensitized solar cells [82]. The major materials will remain Si/CdTe between now and at least 2040 (Fig. 1.10) with other materials becoming significant.

Current solar technology primarily focuses on improvement of absorption to the generation of energy efficiencies, with c-Si as the dominant material. Although Si itself is not a limiting material, the other metals potentially can be limited, requiring recycling of silver, indium, gallium, and germanium which have considerable value.

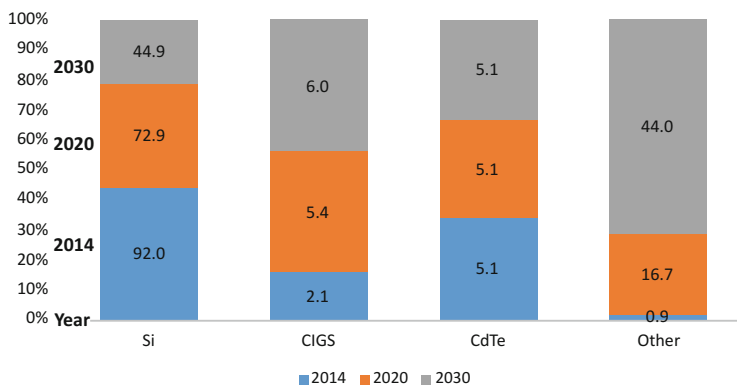


Fig. 1.10 Projected and actual market share of solar panels based on Si, CdTe materials. (Source: [83])

The current recycling technologies also generate energy and utilize harmful solvents, which in turn need to be captured, condensed, distilled, and purified. Currently, few policies cover the entire lifecycle and take account end-of-life scenarios after 25 years of estimated usage. For example, China, India, European Union, and the United States, the dominant regions for solar energy, do not have government-level policies on recycling, nor are the effects of disposal of solar panels in landfills known. In view of the increasing use of solar for the generation of energy (thermal and electrical), the effects of disposal of materials are not undertaken except in a few studies.

1.5 Toxicological Evaluation

Titania (TiO_2) is a common material in DSSC solar cells, as well as an additive in cosmetics and sunscreens and a nano disinfectant [84]. Titania has three geometric forms with rutile (space group: P42/mnm, bulk density 0.04–0.41 g/mL, specific area 130–190 m^2/g) [85] being the most abundant in optical applications [86]. The anatase form (space group: I41/amd, bulk density 0.04–0.06 g/mL, specific area 45–55 m^2/g) [87] is used in organic photovoltaics as an electron collecting layer catalyst, while the Brookite (space group: Pbcu, bulk density 0.06–0.10 g/mL, specific area 150–400 m^2/g) [88]. Brookite form has limited commercial usage. The disposal of devices such as solar cells containing titania into landfills often leads to leaching of these ions into the water table, streams, or lakes. While the concentration of leaches is unknown, it is estimated to be less than 1 parts-per-million (ppm) [89]. Previously it was reported that 0.05–1.0 ppm of titania and alumina were toxic to algae over 72 h [90] and did not affect chromium Cr (VI) ion toxicity which increased in a dose-dependent manner [91]. The general observations from the literature are that titania (morphology undefined) or anatase/rutile (4.5:1 c/c) lowers the population of freshwater algae at losses as low as 1 ppm, due to membrane

damage resulting from reactive oxygen species (ROS)-induced membrane weakening [92]. In other studies, it was reported that titania under ultraviolet A radiation was detrimental to algae relative to algae with titania but non-irradiated, presumably due to UV-A-assisted photocatalysis of TiO_2 generating ROS [93]. Since titania has three allotropes with anatase and rutile being the most abundant, it has been demonstrated that the anatase phase is more cytotoxic to mouse keratinocyte than the rutile form. It has also been demonstrated that while both forms are toxic, the mode of action is different. The rutile form initiates apoptosis via ROS, whereas the anatase (P25 type) forms initiate cell necrosis and membrane disassembly [94].

To evaluate the photocatalysis of titania, UV-A, UV-B, and UV-C have been evaluated, with titania with UV-C irradiation being the most toxic to microalgae than only UV-C exposure, as well as human skin fibroblasts. Solar panels also have silver metal-based contacts [95].

In a study silver and titania nanoparticles were investigated on ciliated protozoans, and it was shown that the cytotoxicity was greater with both materials than either one alone (additivity or potentiation) [95]. The effective dose at 50% lethality of titania to *Chlorella* sp. was determined to be 3.36 g/L for the anatase (25 nm nanoparticles) form and 6.26 mg/L for the rutile (10 nm diameter \times 40 nm length rods) form under UV irradiation at 72 h exposure. The reduction in chlorophyll was 31.6% for the anatase form and 29.76% for the rutile form. Surprisingly, additive (same direction) and antagonistic (opposite direction) responses were also found when both forms were co-mixed in varying mixtures. The 0.25, 0.25 mg/L and 0.5, 0.5 mg/L were antagonistic, whereas the 1, 1 mg/L was additive when chlorophyll yield was measured. For example, titania uptakes into the algal cells varied as a function of dose and type. At 0.5 mg/L concentration, there was approximately 25% (\pm 5%) uptake of the anatase form; for rutile form, the uptake was almost 80% (\pm 1%), and for the combined (0.5:0.5 c/c) anatase:rutile, the uptake was almost 60% (\pm 30%) [96]. The toxic effects of titania and other metal ions on bacteria or tissue are dependent on the ionic charge and the type of metal, as well as mode of toxicity [97]. In general metal ions such as silver (Ag^+), zinc (Zn^{2+}), and mercury (Hg^{2+}) [98] demonstrate strong cytotoxicity at 11 ppm (Hg and Ag) and 16 ppm (Cu). Cobalt (Co^{3+}) demonstrates intermediate cytotoxicity in human tissues but not in microorganisms; aluminum (Al^{3+}) exhibits no toxicity to either human tissues or microorganisms [99]. Thus metals that can behave as disinfectants are limited to Cu^{2+} , Ag^+ , and TiO_2 . Human osteoblast-like (MC3T3-E1) cells appear to be tolerant to titania (Ti6Al4V) alloy including titania doped with copper (4xCu-TiO₂) [100].

The most common mechanism for toxicity is intracellular ROS production, triggering of antioxidative and inflammatory gene expression in a concentration-dependent and time-dependent manner. For example, Si nanoparticles are cytotoxic and initiate inflammatory response through increased expression in cyclooxygenase-2 (COX-2), tumor necrosis factor alpha (TNF- α), interleukin 1 beta (IL-1 β), interleukin-5 (IL-5), and interleukin-8 (IL-8) which is distinct to iron (Fe^{3+}) and titania which do not induce broad array of inflammatory mediators. TNF- α mRNA levels in adenocarcinomic human alveolar basal epithelial cells (A549) and inducible nitric oxide synthase (iNOS) in macrophages were elevated [101]. The levels of ROS

and cytotoxicity or degree of inflammation does not positively correspond, suggesting a distinct biochemical signaling mechanism. Titania, for example, will increase ROS without increased cytotoxicity. Bio-coating of silica with serum proteins would eliminate their inflammatory and cytotoxicity potential. The murine macrophage cell line RAW264 exhibited delayed toxicity upon incubation with Si which was detected after 72 h exposure with a slight increase in ROS [102]. Titania nanoparticles were not found to be toxic in the same cell line, but increased ROS levels and induced TNF- α expression and detection of macrophage inflammatory protein II (MIP-2) were detected [103]. Titania induced enhanced ROS and DNA damage [104], but at 300 ppm did induce interleukin-8 expression in A549 cells [105]. While effects at a high dose may be observed within 24 h, lower doses, such as 50 ppm, may exhibit a response at 72–96 h time period in A549 cell [106]. The mechanism by which titania is taken into the cell is via passive diffusion, active transport, and phagocytosis and to a lesser degree by clathrin-dependent endocytosis [107], but is highly dependent on nanomaterial morphology, dimension, cell type, media, serum, and incubation time, as well as dose. Incubation between 50 and 400 ppm at 24–168 h has shown toxicity under different experimental conditions. A comparison of Fe³⁺, Si^{0,4+}, and Ti⁴⁺ has shown that uncoated Si⁰ is the most toxic in eliciting an inflammation response as a result of elevated ROS and activation of other proteins, such as stress-activated protein c-Jun N-terminal kinase (JNK), which result in apoptosis. Induction of inflammatory cytokines like interleukin-6 and interleukin-8 and chemokines by amorphous Si⁰ can lead to damage to human lung epithelial cells [108]. Silicon is also known to trigger the release of TNF- α and increased expression of MIP-2 in RAW264.7 macrophages, the response related to the specific surface area of the nanomaterials rather than the diameter [109]. Both titania and silica lead to inflammation in human monocytic (THP-1) cell line and murine macrophages [110] and may be related to the degree of agglomeration rather than initial diameter which in turn affects surface area. Elevated interleukin-8 can also lead to lysosomal damage [110] in a number of different cell systems [111]. The amelioration of the cytotoxicity exhibited by silica after coating suggests that the sites of interaction are phospholipids in the cell membrane, wherein media silica forms silanol intermediate where the negatively charged oxygen [O⁻] interact with the positively charged [R⁽⁺⁾NCH₃R] trimethyl-ammonium head group of the membrane lipid, leading to increased membrane plasticity and unzipping or membrane degradation. Other possible mechanisms include uptake mediated by scavenger receptor (SR-A) as shown in Si uptake in RAW264.7 macrophages [112]. Silica binding to SR-A might trigger p38 kinase downstream and release of TNF- α and inflammation [113].

Titania in primary human dermal fibroblasts (HDF) and human lung carcinoma (A549) cells will facilitate the generation of interleukin-8 which in turn will increase lactate dehydrogenase (LDH) activity, a measure of cytotoxicity. Dose-dependent toxicity was observed at 1500 ppm, which is a much higher dose than observed with carbon (C₆₀) nanoparticles [114] with the phase (and not surface area) being related to toxicity. Here, anatase form (153 m²/g) was found to induce cytotoxicity, whereas rutile form (123 m²/g) did not, and mixed forms appeared to be additive in terms of

toxicity. The differences in toxicity might be explained by the degree of hydration and water splitting catalysis by the different titania types. For example, it appears that the anatase phase is able to adsorb dissociatively [115], whereas rutile phases adsorb non-dissociatively [116]. Upon UV radiation, hydroxyl radical is generated on the surface of anatase titania via Ti-OH and OH⁻ interactions. The hydroxyl (HO[•]) radical is the primary reactive oxygen species and is able to degrade organic dyes via first-order kinetics. The half-life ($t_{1/2}$) for Congo red degradation by anatase phase titania was 1.5 min, whereas it was 120 min for rutile phase and 3.5 min for Degussa formulation (80:20 anatase:rutile) form and not related to differences in surface area. Reactive oxygen species, in turn, lead to cellular damage, such as measured by LDH release (at 1500 ppm in the dark or 30 ppm with UV radiation, whereas the rutile form was not active at any concentrations up to 1500 ppm). Unlike fullerenes (C₆₀), titania can also affect the mitochondria, as examined by the (1-(4,5-dimethylthiazol-2-yl)-3,5-diphenylformazan [MTT]) assay. Mitochondrial toxicity was observed using anatase at 1500 ppm but not rutile. General inflammation by measuring interleukin-8 was also shown to be effective for anatase (at 300 ppm) but not for rutile form, which correlated with the ability of the nanomaterial to generate ROS. Reactive species were observed for anatase but not for rutile and this, in turn, was related to illumination with UV-A for anatase that appeared to potentiate the response but not for rutile [117]. While this study contradicts several other studies in showing no toxicity for rutile form of titania, it is consistent with the general literature which indicates that the toxicity of titania is highly dependent on the type, morphology, concentration, matrix, media, incubation time, and cell type. To weigh the difference between these studies, we investigated the effects of titania without modification and embedded in ceria and their toxicological effects in bacteria.

Cerium oxide (CeO₂) has been widely used for catalysis because of its high catalytic properties. From the fluorite-type structure of ceria, the catalytic properties and oxide ion conductivity has been originated, and the partial reduction of Ce⁴⁺ to Ce³⁺ gives rise to oxygen vacancies. Titania (TiO₂) is the chemically stable, environmentally compatible, and functionally versatile oxide materials. The modified material properties and functions of TiO₂ are determined by their nanostructures, which are influenced by many external factors, predominantly pressure, temperature, and the surrounding environment. The nano TiO₂ materials are also having some mechanical properties such as elasticity and deformation behavior. They also have some bulk properties which include a high refractive index and ultraviolet light absorption.

1.6 Photocatalytic Reactivity

The photocatalysis is a process to accelerate a photochemical reaction in the presence of light, which is absorbed by the catalyst. The photo-reactivity is highly dependent on the catalyst reactivity to generate an electron-hole pair. Through the electron-hole pair, free radicals can be generated when a secondary reaction occurs. This photocatalysis is

practically used in water purification, such as removal of pharmaceutical waste. This study uses methylene blue as a model molecule to evaluate the photocatalytic reactivity of TiO₂ nanomaterials, which are the most commonly used semiconductor photocatalyst. The photocatalytic properties of TiO₂ utilized in various environmental applications was investigated in this research.

1.7 Bactericidal Properties

Nanoparticles have various biological applications; they can be used as sensors, for analyte detection, drug targets, pathogen detection, etc. NPs have been employed in sensors for a variety of applications including detecting analytes at very low concentrations, detecting and separating pathogens, detecting and capturing cells, and detecting molecular and cellular functions. By taking the advantage of the unique properties of the nanoparticles such as high surface area, small size, and composition-dependent properties enables the use of surface ligands as a way to amplify the detection threshold or provide more rapid detection. The nanoparticle biosensors are mainly focused on using inorganic materials particularly metal or magnetic nanoparticles. Gold nanoparticles have been used as sensor due to their surface chemistry. TiO₂ has a capability of killing both Gram-positive and Gram-negative bacteria, although Gram-positive bacteria are less sensitive because of their ability to form spores. The concentration of the TiO₂ which is required to kill the bacteria will range from 100 to 1000 ppm depending on their size, intensity, and wavelength of light used. Recent studies indicate that the TiO₂ nanoparticles are able to kill viruses such as Hepatitis B virus, Poliovirus 1, and herpes simplex virus. The antibacterial activity of TiO₂ nanoparticles is related to the production of hydroxyl free and peroxide radicals formed under UV irradiation by the oxidative and reductive pathways. A strong absorbance of UV renders activation of TiO₂ under solar irradiation, significantly enhancing solar disinfection. The inhibitory effect of nanomaterials on the microorganisms such as bacteria is through various processes such as membrane lysis and inhibition of critical proteins (sources of carbon, nitrogen, sulfur, and oxygen) and nucleic acids. They will affect both outer and inner membranes, phospholipid peroxidation, cell wall weakening and lysis, interaction with lipoproteins, Omp carrier proteins and LP in the periplasm resulting in plasma membrane peeling and rupture, as well as DNA fragmentation.

1.7.1 Experimental Procedure

The aim is threefold, for (1) material synthesis of Ce-doped TiO₂ nanoparticles (CTO-NPs) and fabrication variable optimization; (2) characterization of these CTO-NPs; and (3) photocatalytic and biological applications of these CTO-NPs. All chemicals, solvents, and reagents unless otherwise specified were obtained from VWR International (West Chester, PA) or Sigma-Aldrich (St. Louis, MO). Double-distilled, filtered ultrapure water was used (Ultrapure™, Barnstead,

Dubuque, IA, referred to as distilled water) where water-based solvents were necessary, and all solvents were a reagent or high-performance liquid chromatography (HPLC) grade.

1.7.2 Synthesis Overview

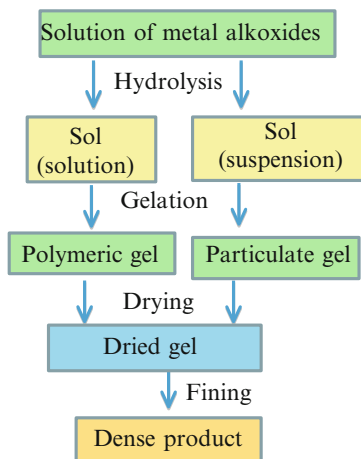
In this section, the colloidal and solid-state chemistry was employed to produce CTO colloids and powders. The optimal variables of fabrications were studied.

1.7.3 Colloidal Synthesis

The nanoparticles are fabricated by the sol-gel method, a wet chemical method, which is also called as chemical solution deposition. This process is a series of chemical reactions which irreversibly converts a homogeneous solution of reactant precursors (a sol) into a three-dimensional polymer (a gel) forming an elastic solid as the same volume of the solution. Through this process, uniform in size, fixed shape, crystalline nanoparticles were fabricated with defined optical, magnetic, and physical properties. The procedure of the CTO-NP synthesis and the optimal variables are summarized below (Fig. 1.11):

1. Drop-wise addition of titanium butoxide ($\text{Ti}^{\text{n}}\text{OBU}_4$) to 40 mL of isopropanol.
2. Agitation on a magnetic plate at room temperature (RT) for 60 min.
3. Specific mass of cerium oxide nitrate is added to 10 mL of distilled water.
4. After 60 min stirring of the titania slurry, the cerium oxide nitrate stock is added in drops to the TiO_2 and isopropanol mixture.
5. The binary mixture is stirred for an additional 60 min.

Fig. 1.11 The schematic of the synthesis of CTO-NPs and the key fabrication variables



Fabrication variables:

Concentration:

0.01, 0.03, and 0.1 mol/L (M);

Calcination

Temperature:

200–400 °C (50 °C increments); &

Ce dopant: 5–30

mol % (5 % increments).

1.7.4 Solid State Chemistry to Produce CTO-NPs

A solution of titanium butoxide and isopropyl alcohol was mixed and kept under constant stirring for about 45 min at room temperature. The desired weight percentage of 0.05–0.35 (+0.05 increments) of cerium nitrate was mixed with water and this was added to the gelling solution to obtain a doped gel of titania. The solution was then converted to gel, which was calcinated at desired temperatures of 200 °C, 250 °C, 300 °C, 350 °C, 400 °C for 2 h to obtain a powder. A solution of titanium butoxide [$C_{16}H_{36}O_4Ti$] and isopropyl alcohol [C_3H_8O] were mixed and kept under constant stirring for about 45 min at room temperature (also shown in Fig. 1.11). The desired weight percentage (% wt) of 0.05–0.35 (+0.05 increments) of cerium nitrate [$Ce(NO_3)_3$] was mixed with water [H_2O]. This ternary system was mixed for initially forming a gelling solution to obtain a doped gel of titania [TiO_2]. The gel was calcinated at desired temperatures of 200 °C, 250 °C, 300 °C, 350 °C, and 400 °C for 2 h to obtain a white powder.

1.7.5 Characterization of Titania

To evaluate the cerium-doped TiO_2 nanoparticles (CTO-NPs), a series of advanced instrumental techniques was employed to achieve information on morphology, vibration modes, and crystalline structures. X-ray powder diffraction (XRD, Bruker D8 Advantage) was used to collect the crystalline structure and crystallite size (*X-ray powder diffraction*). The electron microscopic analyses, namely transmission electron microscope (TEM, FEI G2-F20) and scanning electron microscopy (SEM, JEOL 6700F), were used to evaluate the crystalline structures and porosity under ultrahigh vacuum (*transmission and scanning electron microscopy*). The spectroscopic analyses, such as ultraviolet-visible spectroscopy (UV-VIS, Beckman Coulter DU 800), were used to determine the functional groups in the CTO-NPs. X-ray energy dispersive spectrometry (EDS) was used to determine the chemical components and elemental composition. The characterization methods and associated technique variables are discussed in the following sections.

1.7.6 X-Ray Powder Diffraction

A Bruker D8 advantage diffractometer equipped with Germanium bent crystal monochromator, using copper radiation ($\lambda = 1.5414 \text{ \AA}$, $K_{\alpha 1}$), was also used to identify the crystalline structure with superior resolution. In the cavity of the glassy sample holder, the specimen is placed and is allowed to be naturally dried. From the diffraction angle range of 20–80°, the XRD patterns were recorded. The data were collected using JOB data collection software and analyzed by Jade 7.0 package. The background was removed and the XRD pattern was indexed with the standard PDF files. The operational variables were controlled at 40 kV and 44 mA. The data collection was carried out at ambient condition.

1.7.7 Transmission and Scanning Electron Microscopy

An FEI Tecnai G²-F20 transmission electron microscope (TEM) (FEI Company, Hillsboro, Oregon) equipped with X-ray energy dispersive spectrometer (EDS) capabilities was employed to obtain nanostructure information and crystalline phase about the colloid-derived nanoparticles. The instrument was operated in the TEM mode to obtain the high-resolution images of crystals, as well as scanning TEM (STEM) mode. The spherical aberration coefficient and resolution were approximately 2.0 and 0.27 nm, respectively. A probe size of 1 nm was used for EDS. Although a simplification, the collected image contrast is related to the atomic number (Z) squared, with elements with higher Z contributing to brighter contrast. The surface morphology and texture of the crystalline materials were also examined using a JEOL 6701F field emission scanning electron microscope (FESEM, JEOL Ltd., Plano, TX). The surface morphology and texture of the CTO-NPs were also examined by a Quanta 600 FEG field emission scanning electron microscopy (SEM) (FEI Company, Hillsboro, OR). FESEM is capable of generating and collecting high-resolution and low-vacuum images. The FESEM was equipped with a field emission gun and a Schottky emitter. The voltage was controlled at 5 or 15 kV and beam current at 100 nA. The chamber pressure and gun pressure were controlled at 3.5×10^{-5} Torr and 3.0×10^{-9} Torr for high resolution. A thin layer (4.0 nm) of gold (Au) metal was sputtered onto the sample surface to improve conductivity.

1.7.8 Spectroscopic Analyses

Ultraviolet visible spectroscopy: The UV-VIS spectrophotometer (Beckman Coulter, DU 800) is used to measure the optical absorbance spectrum of the synthesized nanoparticles. Deuterium and Tungsten light sources are the main compositions of this spectrophotometer. UV-VIS spectrophotometer is also provided with a grating to filter the selected wavelengths between 190 and 1100 nm spectral bandwidth with less than 1.8 nm bandwidth. The DU acquisition and analysis software for wavelength (RediScan) was used which exports to Excel functionality, with post-processing carried out within Excel. The absorbance spectrum data that is obtained can be tested by estimating it with a Gaussian distribution. The estimation was done using RediScan and Excel software to analyze the data.

X-ray energy dispersive spectroscopy: As stated previously, this EDS is equipped with Quanta 600 FEG field emission scanning electron microscopy (SEM) (FEI Company, Hillsboro, OR). EDS was used to evaluate the elements and their composition based on the principle of emission.

Photocatalytic reactivities of CTO-NPs: Photocatalytic $Ce_xTi_{1-x}O_2$ NPs to decompose MB was tested under visible light and darkness, respectively. The Log reduction analyses were used to determine photocatalytic reactivities of NPs to decompose MB under visible light. $Ce_xTi_{1-x}O_2$ NPs was introduced into the diluted MB aqueous solution and UV-VIS data were collected every hour to estimate the

Table 1.2 Absorbance calibration curve of methylene blue (MB, stock solution: 20 ppm)

NP volume	Concentration of nanoparticles (9500 ppm)	Volume of methylene blue (mL)	Concentration of methylene blue (20 ppm)	Total volume (mL)
9	7500	2	3.6	11
9	750	2	3.6	11
9	75	2	3.6	11
9	7.5	2	3.6	11
9	0.75	2	3.6	11

photocatalytic efficiency of CTO-NPs under visible light and in the dark, respectively. Methylene blue a cationic thiazine dye with molecular weight 319.86 g/mol was further diluted 20 ppm (parts per million). The $Ce_xTi_{1-x}O_2$ NPs with 7500 ppm (0.3 M) were used to test the photocatalytic activity. Serial dilutions of the nanoparticles were made until the concentration became 0.75 ppm as shown in Table 1.2. The MB was diluted from 20 to 3.6 ppm, and this concentration is used to test the photocatalytic activity. The CTO-NPs and methylene blue are mixed in specified volumes as shown in the table below and each sample is tested both under the visible light and in dark with no visible light. Therefore, we can observe the percentage of methylene blue degradation of the samples in both visible light and dark, respectively. Comparative studies can be made by observing the degradation under two different conditions. The samples should be kept under sunlight and the intensity of the light should also be noted. For every 1 h, the samples are tested with UV/Vis spectrophotometer at 200–800 wavelength.

1.7.9 Bactericidal Performance of CTO-NPs

The bactericidal activity assays were performed using *Serratia marcescens* (*S. marcescens*, commercially available strains ATCC 13880 were used) as the model organism to evaluate the bioactivity of CTO-NPs. Gram-positive bacteria, *Micrococcus luteus* (*M. luteus*, Gram-positive, ATCC 49732) was also used to test the bioactivity of CTO-NPs. Both types of bacteria (5.0 mL) were cultured in Difco™ nutrient LB broth (Miller Luria-Bertani, Becton-Dickinson, Franklin Lakes, NJ) in an incubator shaker (Innova® 43, Incubator Shaker Series, New Brunswick Scientific, NJ) at 37 °C for 24 h. The cultured bacteria were then diluted to 50 mL. The CTO-NPs (0.050 M, 2 mL) were tested against the above bacteria. After the treatment, an aliquot (0.5 mL) was collected and tested using ultraviolet visible spectroscopy to identify the absorbance every hour to determine the optical density (OD) at 600 nm. Control experiments were carried out under identical conditions in the absence of the CTO-NPs, which is used as a disinfectant. In this study, it is defined that no growth of bacteria cells indicates full bactericidal activity and growth indicates partial or no bactericidal activity. Our previous experience in

determining number of colonies per milliliter (CFU) for *bacteria* using dilute samples ($\text{abs} < 0.6$) approximates to 1 OD unit corresponding to 10^9 bacteria per mL, therefore OD_{600} is an excellent implicit comparative technique in assessing bacterial viability, whereas plate dilution and counting of colonies is explicit and more accurate where bacterial growth phase is not known or new strains are used for the first time.

1.8 Results

In this chapter, synthesis and characterization of CTO-NPs and their photocatalytic and biological application will be discussed in sections related to the *Synthesis of CTO-NPs*, *Characterization of CTO-NPs (X-ray powder diffraction, Spectroscopic analyses, and Electron microscopic analyses)*, and *Application of Nanomaterials (Photocatalytical reactivities and Bactericidal performance)*, respectively.

1.8.1 Synthesis of CTO-NPs

In this study, sol-gel chemistry was used due to its benefits, such as low processing cost, energy efficiency, high production rate, rapid productivity of fine homogeneous powder, achievable uniformity at low temperatures, and high purity of the final products. However, this method displays some demerits, for example, large volume shrinkage and cracking during drying.

1.8.2 Characterization of Titania

In this chapter, the instrumentation analyses (X-ray diffraction, electron microscopy, and spectroscopy) were discussed. These methods were used to evaluate the morphological and crystalline structure and elemental composition of the CTO-NPs.

1.8.3 X-Ray Powder Diffraction

X-ray powder diffraction (XRD, Bruker D8 Advantage) was used to collect the crystalline structure and crystallite size. The XRD results (Fig. 1.12) indicated that the CTO-NPs with different formulations were well-indexed with tetragonal anatase TiO_2 structure (PDF 01-086-1157). The lattice constants were $3.7852 \times 9.5139 \text{ \AA}$ and $90 \times 90^\circ$, respectively. XRD indicated that there is no second phase, suggesting that Ce^{4+} cations replace the Ti in the lattice. This study indicated that dopant of Ce with a lower amount than 0.35 shows no effect on the crystalline structure. However, it is hypothesized that the band gap may be reduced due to the inner transition metal doping from the photocatalytic study.

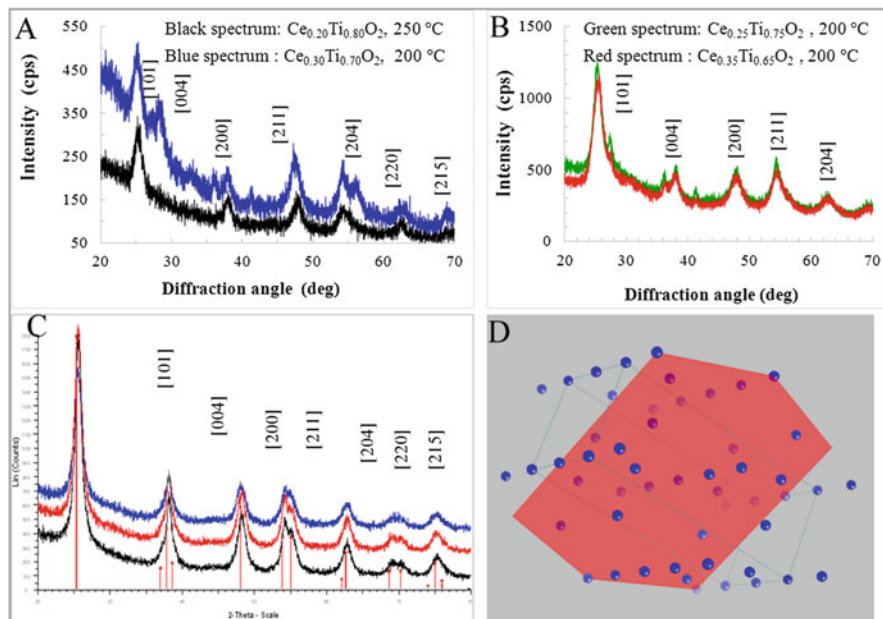


Fig. 1.12 The XRD analyses of CTO-NPs. (a and b) CTO-NPs with four different formulations (different Ce dopants and calcination temperatures); (c) TiO_2 anatase structure as a reference (Liu's previous data); (d) Anatase TiO_2 structure

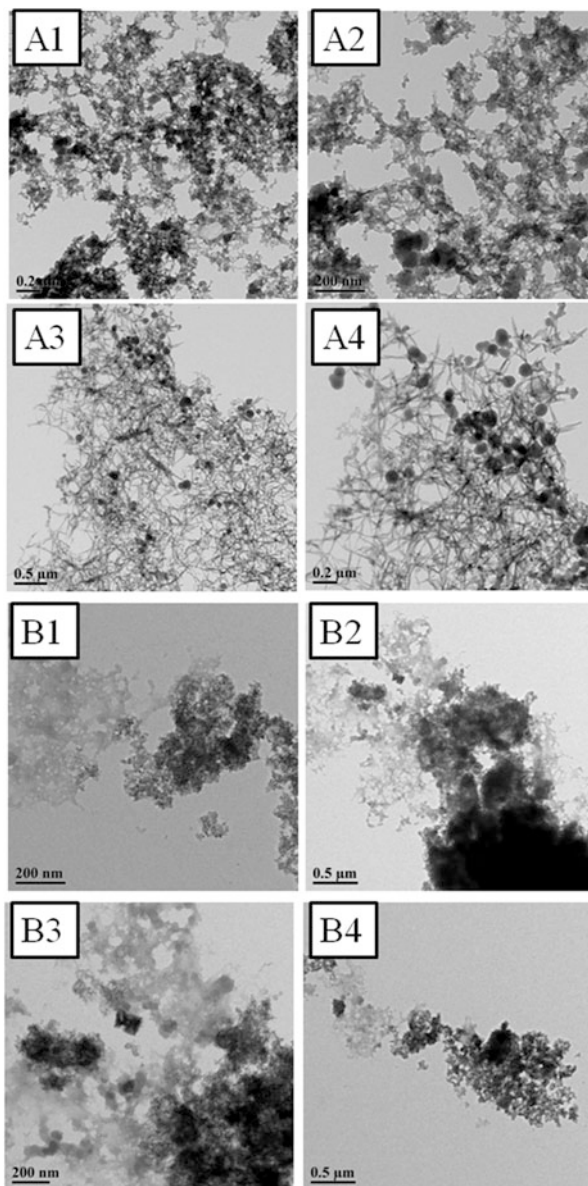
1.8.4 Transmission and Scanning Electron Microscopy

In this study, the transmission electron microscope (TEM, FEI G2-F20) was used to evaluate the morphology and particle size distribution of the CTO-NPs with different doping amounts (Fig. 1.13a, b). TEM images indicate that the fibrous networks were formed. Nanoparticles were found to be agglomerated due to heat treatment, sized at 125 nm. The dark spots were found to be resulting from Ti and Ce heavy elements. Scanning electron microscopy (SEM, JEOL 6700F) was also used to evaluate the morphology of the CTO-NPs (Fig. 1.13). It was found that the charging of samples occurred, due to the existence of organic residue. Coating electronic conductive layer onto the sample surface will remove electrons, further to resolve the charging.

1.8.5 X-Ray Energy Dispersive Spectroscopy

X-ray energy-dispersive spectroscopic (EDS) chemical analyses of three regions (Fig. 1.14) also confirmed Ce and Ti molar ratios were maintained in the final CTO-NPs as experimental design. The principal emission of Ti occurred at

Fig. 1.13 The TEM analyses of CTO-NPs. (a) $\text{Ce}_{0.35}\text{Ti}_{0.65}\text{O}_2$ NPs and (b) $\text{Ce}_{0.30}\text{Ti}_{0.70}\text{O}_2$ NPs



4.510 keV ($\text{K}_{\alpha 1}$) while that of Ce occurred at 4.840 keV ($\text{L}_{\alpha 1}$). Two elements Pt and Pd were also observed which result from the conductive coating layers. Figure 1.14a, b are obtained from EDS equipped with TEM and Fig. 1.14c from EDS equipped with SEM. Both analyses confirmed that the Ti and Ce amount totaled at 100%.

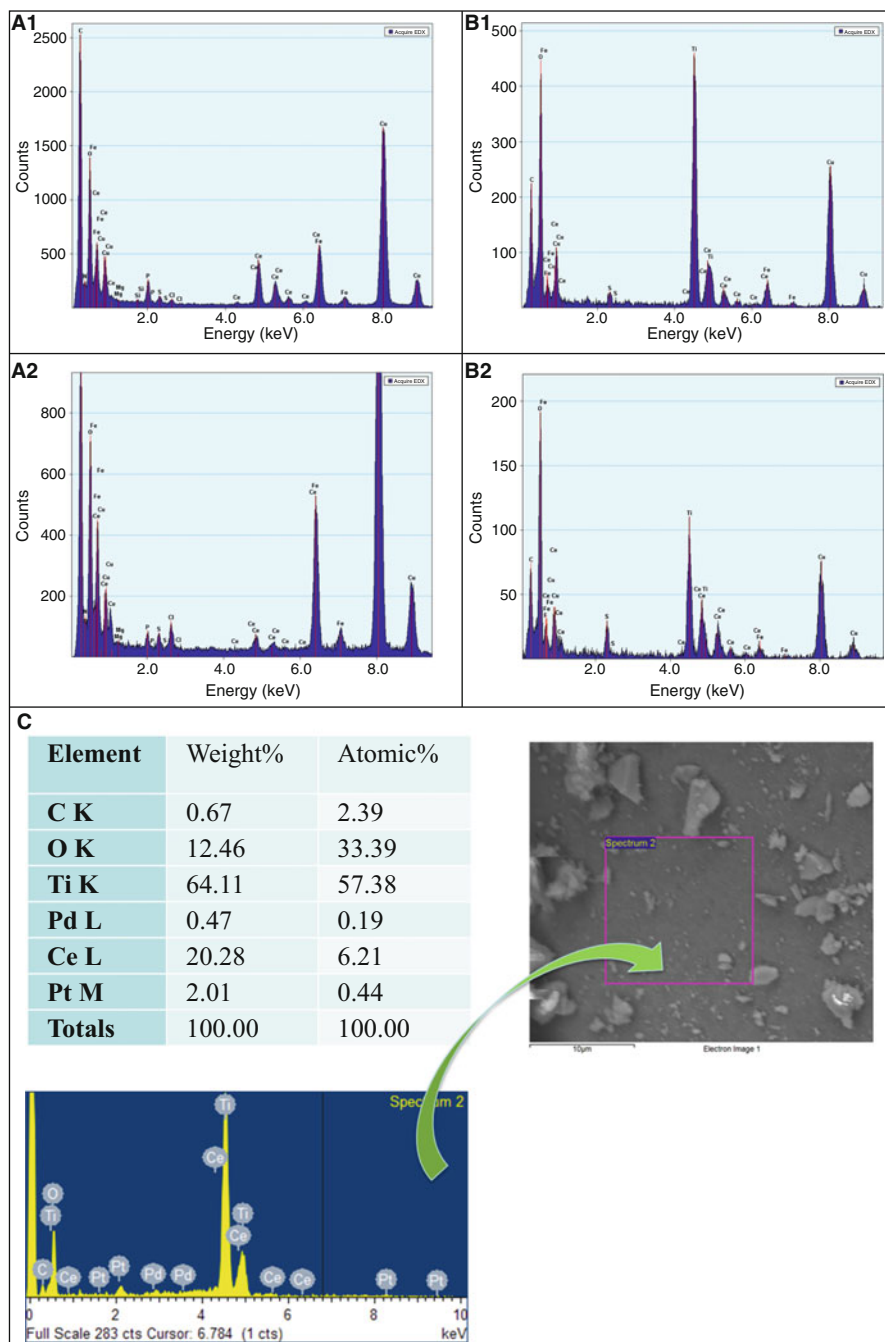


Fig. 1.14 The EDS analyses of CTO-NPs (equipped with TEM). (a) $\text{Ce}_{0.35}\text{Ti}_{0.65}\text{O}_2$ NPs and (b) $\text{Ce}_{0.30}\text{Ti}_{0.70}\text{O}_2$ NPs. (c) EDS analyses of CTO-NPs, equipped with TEM

1.8.6 Applications of Nanomaterials

The Ce-doped TiO₂ nanoparticles (CTO-NPs) were found to be effective at photocatalyst and disinfectant. This chapter will discuss the photocatalytic reactivity and bactericidal efficacy of CTO-NPs with different formulations, respectively.

1.8.7 Photocatalytical Reactivities of CTO-NPs

Standardization: A methylene blue (MB) dye stock solution was prepared with a concentration of 20 ppm, which is further diluted from 2.4 to 0.4 by using isopropanol as a solvent. The absorbance of these dilutions (Fig. 1.15a) was then measured by using UV-Visible spectroscopy (Fig. 1.15b). It can be observed that the major absorbance peak occurred at 292 nm and 652 nm due to a benzene ring and hetero poly aromatic linkage, respectively. A calibration curve was also plotted using the absorbance of decomposed MB solution as a function of the concentrations. The results showed good linearity of the standard curve was received from the high correlation coefficient (R) (Fig. 1.15c).

Photocatalytical reactivities: A series of methylene blue (MB) decomposition tests were carried out with CTO-NPs. Initially, two concentrations of CTO-NPs were tested, indicating MB decomposition occurs instantaneously at high CTO-NPs

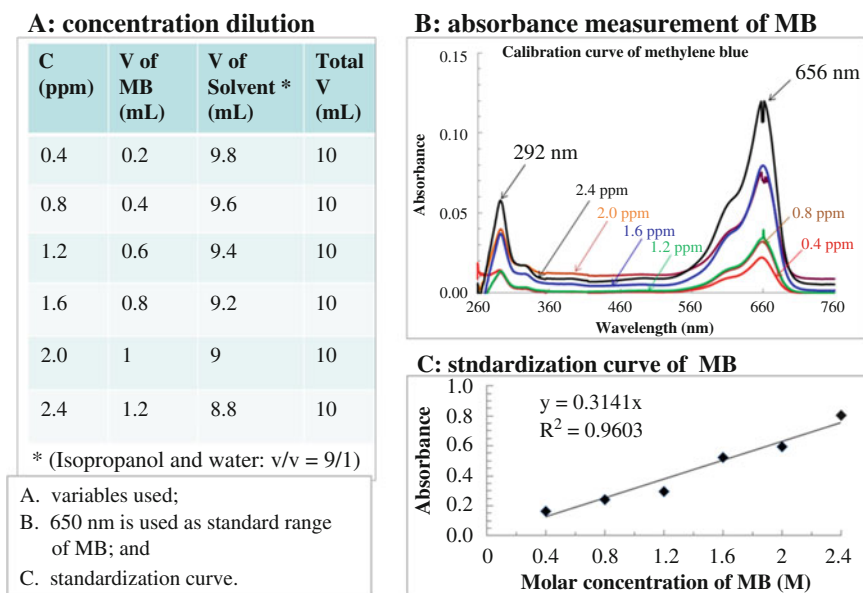


Fig. 1.15 Absorbance calibration curve of methylene blue (MB, stock solution: 20 ppm), (a) different dilutions of MB solution; (b) absorbance of the MB under decomposition; and (c) the standardization curve

concentrations (Fig. 1.16). Therefore, further dilution was carried out from 7500 to 0.75 ppm to determine the lowest concentration of CTO-NPs. The decomposition efficiency was tested under different conditions, namely visible light and darkness. The absorbance was measured at different time intervals 60, 120, and 180 min with UV-VIS spectroscopy (Fig. 1.16b). From the figure, we can see that the methylene blue decomposition rate seems to increase with the increase in the concentration of $Ce_{0.35}Ti_{0.65}O_2$. The Log reduction analyses indicated that MB degradation was catalyzed using CTO-NPs under visible light. The NPs with $Ce_{0.35}Ti_{0.65}O_2$ formulation displayed the highest efficiency compared with another doping amount. It was also found that the lower efficiency of MB degradation in the dark compared with under visible light was as expected.

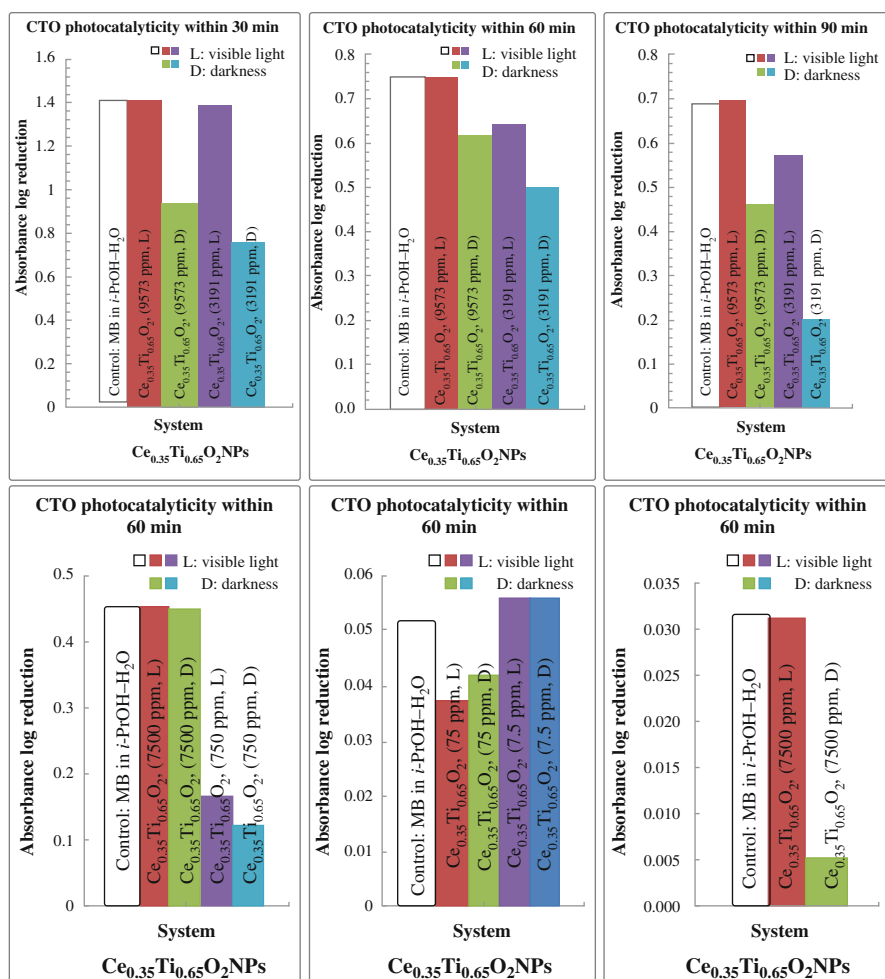


Fig. 1.16 (continued)

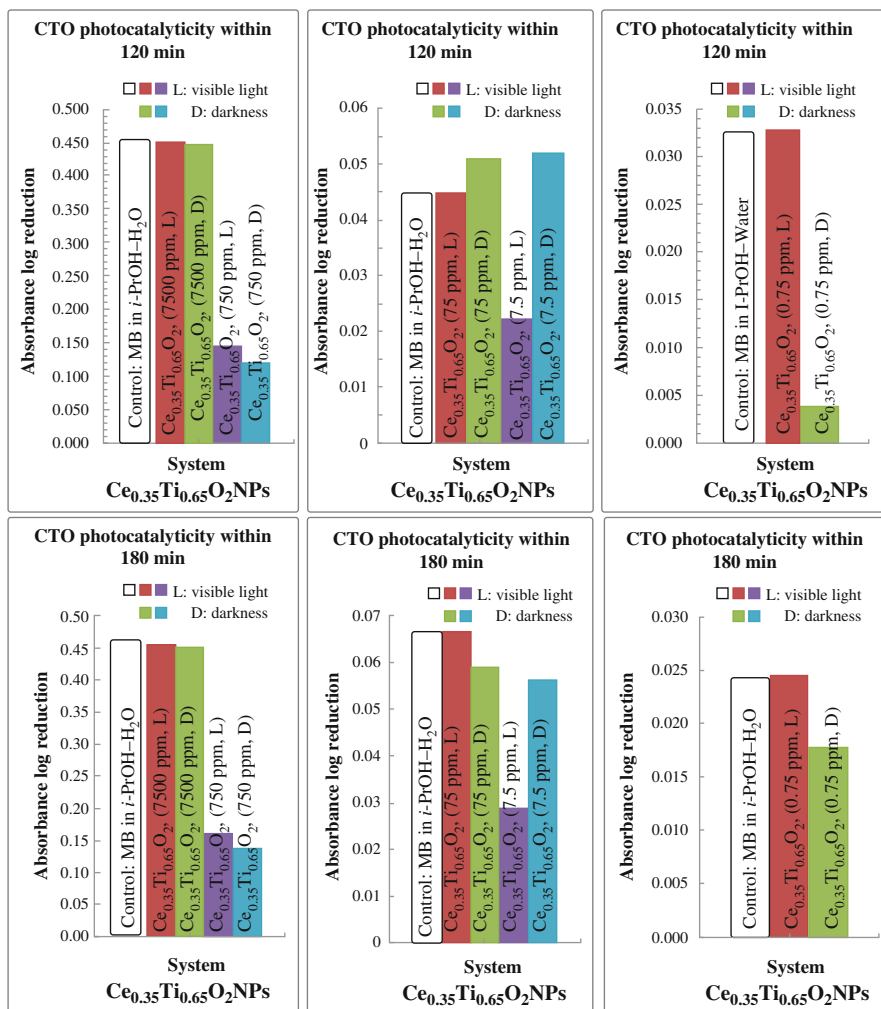


Fig. 1.16 (a) The photocatalytic reactivities of CTO-NPs ($x = 0.35$): two different concentrations were tested in either darkness or under visible light, indicating the MB decomposition occurred instantaneously. (b) The photocatalytic reactivities of CTO-NPs ($x = 0.35$): diluted concentrations were tested to evaluate the decomposition of MB with a prolonged time period

1.8.8 Bactericidal Performance of CTO-NPs

The bactericidal activity assays were performed using Gram-negative bacteria, *Serratia marcescens* (*S. marcescens*, commercially available strains ATCC 13880), and Gram-positive bacteria, *Micrococcus luteus* (*M. luteus*, Gram-positive, ATCC 49732), to evaluate the bactericidal performance of CTO-NPs. Both types of bacteria (5.0 mL) were cultured in Difco™ nutrient LB broth (Miller Luria-Bertani, Becton-

Dickinson, Franklin Lakes, NJ) in an incubator shaker (Innova[®] 43, Incubator Shaker Series, New Brunswick Scientific, NJ) at 37 °C for 24 h.

The cultured bacteria (*S. marcescens* and *M. luteus*) were then diluted to 50 mL. The CTO-NPs (10, 100, and 1000 ppm) were tested against the above bacteria. After the treatment, an aliquot (0.5 mL) was collected and tested using ultraviolet visible spectroscopy (Lambda 35 ultraviolet-visible (UV-Vis) spectrophotometer (PerkinElmer, Fremont, CA)) to identify the absorbance every hour to determine the optical density (OD) at 600 nm (Fig. 1.17). Three doping amounts were tested in this study, indicating CTO-NPs are highly effective at inactivating bacteria under visible light. The observation indicated that Ce doping may result in the band gap of TiO₂ decrease (this assumption will be tested by synchronous X-ray).

The TEM images indicated high effectiveness using Ce_{0.3}Ti_{0.7}O₂ NPs on inactivation of both Gram-negative and Gram-positive bacteria, shown in Fig. 1.18. It can be seen that the cell membranes were peeling off and flagella disappeared, indicating the death of bacteria. Due to the active interaction between NPs and bacteria, it was assumed that the DNA fragmentation in cytosol was the mechanism to inactivate the bacteria. Although the Gram-positive bacteria (*M. luteus*) are generally considered more resilient to sterilization, this study showed similar trends observed for Gram-negative bacteria (*S. marcescens*). It was safe to conclude that minimal damage to the cell wall was observed, causing termination of cell division and damage of intact cell wall.

Elemental composition analyses by EDS (Fig. 1.19) also indicated cell death due to the permeability of calcium (Ca) and potassium (K) cations, and phosphorus (P) and nitrogen (N) anions across the cell membrane into the extracellular matrix for both microbes. “Ce” and “Ti” are from NPs used to inactivate bacteria; “P,” “O,” and “Cl” are from lipids on the membrane; “K” from the plasma membrane; and Cu is from the copper grid.

The CTO-NPs effectively inactivated Gram-negative microbes under visible light (TiO₂ requires UV). The kinetic study (Fig. 1.20) indicated that the Ce_{0.35}Ti_{0.65}O₂ photocatalyst follows the near-zero order reaction. The reaction orders for both Ce_{0.20}Ti_{0.80}O₂ and Ce_{0.30}Ti_{0.70}O₂ photocatalysts were found to be second order, approximately. However, the future work will be carried out to confirm the reaction order using CTO-NPs as disinfectants.

1.9 Discussion

1.9.1 Colloidal and Solid State Chemistry

Both colloidal and solid-state chemistry approaches were used to prepare Ce⁴⁺ ions doped TiO₂ nanoparticles (CTO-NPs). Different molar ratios between Ce and Ti were used to form 40 formulations of CTO-NPs. The temperatures to form CTO colloids were controlled at room temperature, while the calcination temperatures to produce CTO powders were controlled at 200–400 °C with an increment of 50 °C.

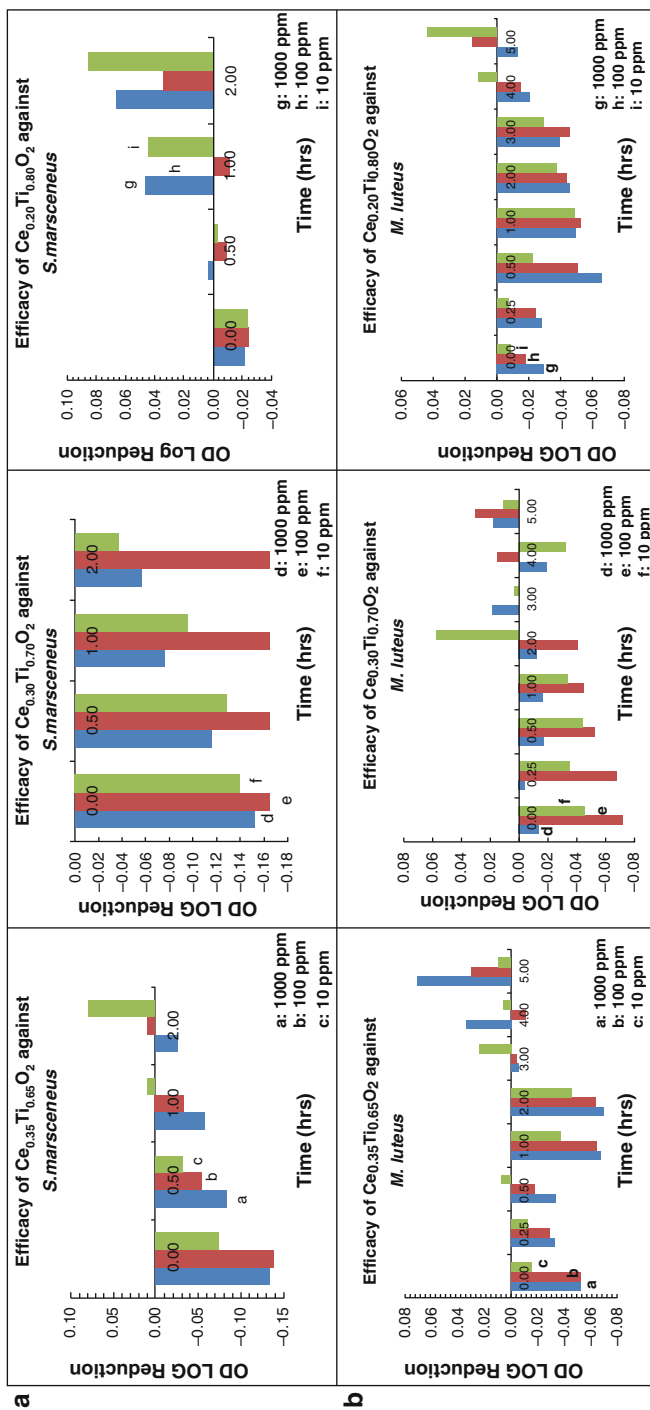


Fig. 1.17 (a) The bactericidal analyses of CTO-NPs: Gram-negative bacteria, *S. marcescens* cells were found to be damaged by CTO-NPs due to high particle-bacteria interaction. (b) The bactericidal analyses of CTO-NPs (three different Ce doping): Gram-positive bacteria, *M. luteus* cells were found to be damaged due to high particle-bacteria interaction

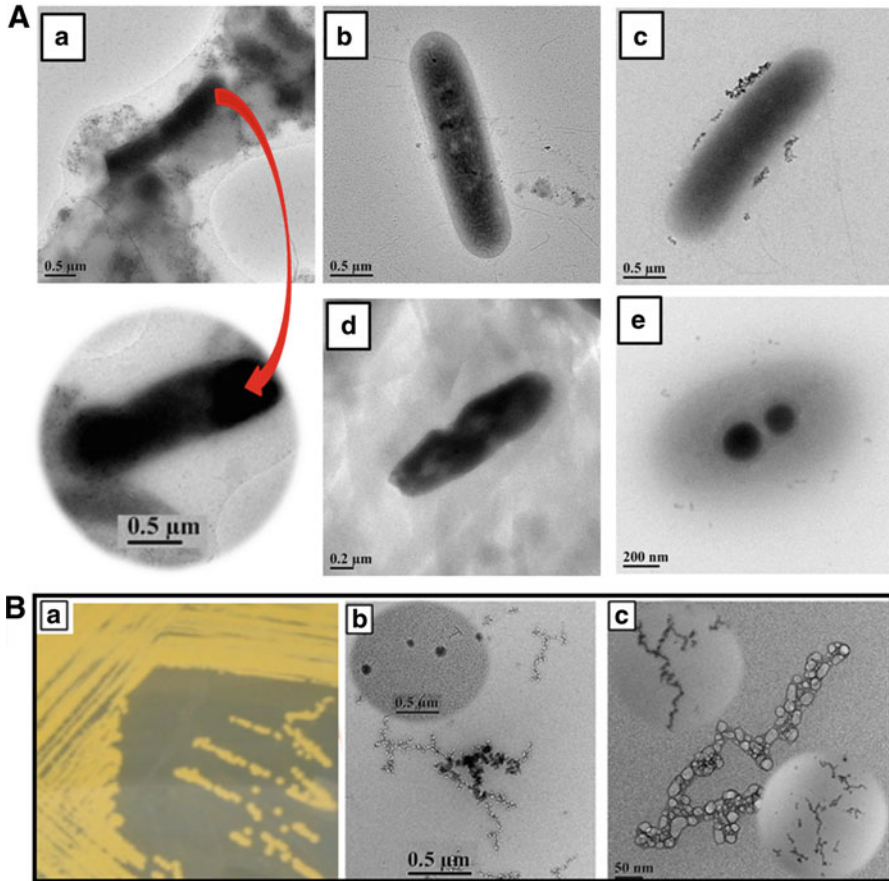


Fig. 1.18 (a) Transmission electron microscopy (TEM) image of a cluster of *S. marcescens* in varying stages of cell damage from B to E. The rod-shaped bacteria (A) were observed; B and C, the cell membrane was peeling out; and D and E, the flagella disappeared and DNA fragmented. (b) Optical Image of *M. luteus* adopted from A Ouverney and Zavala [118]; transmission electron microscopy (TEM) image of cluster of *M. luteus* in varying stages of cell damage from B to C. The potential residue of cells is observed; aggregation of microbial cell components and membrane sugars form the networks shaped structure

1.9.2 Characterization of Titania

Nano-characterization was employed to understand the in-depth structure of CTO-NPs. A series of the state-of-the-art techniques (five instrumental techniques) were used to characterize nanostructure. X-ray powder diffraction indicated highly crystalline anatase CTO-NPs were obtained, and crystallite sizes were tunable by varying the calcination temperatures. Spectroscopic and

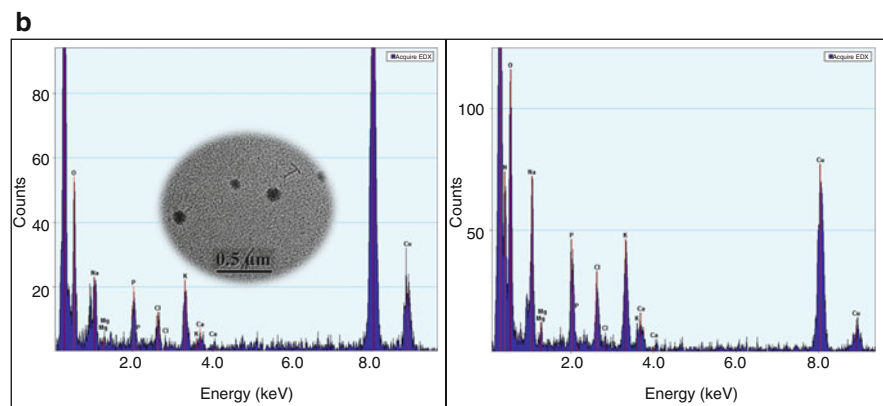
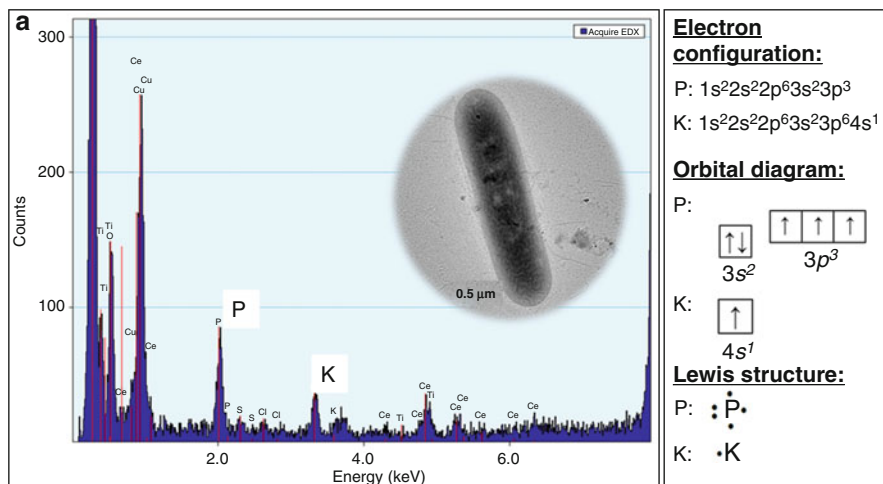


Fig. 1.19 (a) X-ray energy dispersive spectroscopy of elemental composition of *S. marcescens*. (b) X-ray energy dispersive spectroscopy of elemental composition of *M. luteus*

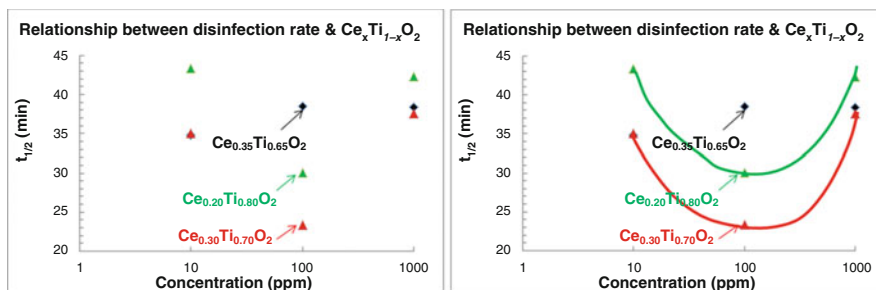


Fig. 1.20 Kinetic study by half-life to evaluate the bacteria inactivation reaction using CTO-NPs

microscopic analyses collectively provide instructive information to understand the fine structure of the CTO-NPs. To summarize, the characterization data provided a guideline to improve material design based on the end application.

1.9.3 Application of Nanomaterials

A recent study indicated that the dimensionality, particle size distribution, and crystallinity of TiO₂ nanoparticles are increasingly important to determine the electronic, optical, and biological properties and end applications of these nanoparticles. Traditionally, TiO₂-based nanomaterials have been extensively studied; however, photocatalytic and bactericidal activities under visible light have not been reported. The originality of this study lies in the application of CTO-NPs under visible light.

1.10 Conclusion

The following conclusions can be drawn from this study:

1. Ce_xTi_{1-x}O₂ NPs were fabricated using an ecologically friendly colloidal chemistry approach.
2. The nanoparticles were characterized as being monodisperse and crystalline (PDF 01-086-1157, 3.7852 × 9.5139 Å and 90 × 90°).
3. Although agglomeration of Ce_xTi_{1-x}O₂ NPs was detected, the photocatalytic reactivities and bactericidal performance were found to be too effective.
4. Breaking down of methylene blue was observed under visible light without any UV light. The catalysts can be used in treating pharmaceutical wastes.
5. Inactivating both Gram-negative (*S. marcescens*) and Gram-positive (*M. luteus*) bacteria without introducing ultraviolet light. This study will provide a practical method for water disinfection.

Acknowledgments The authors wish to thank the National Science Foundation (CBET-0930079 and 0821370), Graduate Scholarship from the Department of Chemistry, Texas A&M University-Kingsville (TAMUK), the College of Arts and Sciences (CoA&S, Dr. Bashir, 160336-00002), ACS-PRF (53827-UR10, Liu), SFFP (Bashir) and Welch Departmental Grant (AC-0006, Dr. Hahn), NSF-MRI acquisition (Liu), URA (160315-00015, Liu) and RDF grants (160345-00005, Liu), at Texas A&M University-Kingsville (TAMUK) for funding.

Drs. E. Massa and J. Escudero (Department of Biological and Health Sciences, Texas A&M University-Kingsville, TAMUK) are acknowledged for providing bacteria. Dr. H. Kim and Ms. Y. Chen (Dr. H.-C. Zhou's group), Texas A&M University, College Station, are also duly acknowledged for image collection and analyses. The technical support from the TAMUK and the use of TAMU Center of Microscopy Imaging and Materials Characterization Facility are also duly acknowledged.

References

1. IAE Outlook, W.E., *International Energy Agency* (2017), pp. 1–782/782 pages, <https://www.ica.org/weo2017/>
2. M. Hasanuzzaman, U.S. Zubir, N.I. Ilham, H. Seng Che, Global electricity demand, generation, grid system, and renewable energy policies: a review. *Wiley Interdisciplinary Rev. Energy Environ.* 6(3), e222 (2017)
3. EIA Outlook, A. E., Outlook with projections to 2050. January 5, 2017. *US Energy Information Administration* (2017), pp. 3–100/127 pages, [https://www.eia.gov/outlooks/aeo/pdf/0383\(2017\).pdf](https://www.eia.gov/outlooks/aeo/pdf/0383(2017).pdf)
4. C. Philibert, *Solar Energy Perspectives*. (Organisation for Economic Co-operation and Development (OECD)/International Energy Agency (IEA)/IEA Publications/Imprimerie Centrale Printers, Luxembourg, 2011), pp. 1–228. 978-92-64-12457-8
5. Global, B. P., *BP Energy Outlook 2017* (2017), pp. 1–103/103 pages, <https://www.bp.com/content/dam/bp/pdf/energy-economics/energy-outlook-2017/bp-energy-outlook-2017.pdf>
6. Burger, Willeke, Philipps et al., Research Projects. Fraunhofer Institute for Solar Energy Systems, ISE (2016), <https://www.ise.fraunhofer.de/en/research-projects.html>
7. GTMR, US Solar Market Insight, *GTM Research* (2017), <https://www.greentechmedia.com/research>
8. P. Mints, Insights & Experience. Next Generation Solar PV, Navigant Consulting (2017), <https://www.navigantresearch.com/reports/next-generation-solar-pv>
9. R. Pravalie, G. Bandoc, Nuclear energy: between global electricity demand, worldwide decarbonization imperativeness, and planetary environmental implications. *J. Environ. Manag.* 209, 81–92 (2018)
10. C. Breyer, D. Bogdanov, A. Aghahosseini, A. Gulagi, M. Child, A.S. Oyewo, P. Vainikka, Solar photovoltaics demand for the global energy transition in the power sector, in *Progress in Photovoltaics: Research and Applications* (2017), pp. 505–523/693 pages
11. X. Lu, M.B. McElroy, J. Kiviluoma, Global potential for wind-generated electricity, in *Proceedings of the National Academy of Sciences*, 106(27), 10933–10938 (National Academy of Sciences, Washington DC, USA)
12. A. Méjean, C. Guivarch, J. Lefèvre, M. Hamdi-Cherif, The transition in energy demand sectors to limit global warming to 1.5 °C. *Energy Effic.*, 12(2), 441–462, Springer Nature (Switzerland, AG) (2019)
13. M.J. Lynch, Peak oil, Chapter 2.17, in *Companion to Environmental Studies*. Routledge in association with GSE Research, Vol. 228, No. 231, ed. by N. Castree, M. Hulme, J. D. Proctor. (Taylor and Francis Group, Oxon, 2018), pp. 228–231/848. ISBN: 978-1-138-19220-1
14. M.Z. Jacobson, M.A. Delucchi, Z.A. Bauer, S.C. Goodman, W.E. Chapman, M.A. Cameron, J.R. Erwin, 100% clean and renewable wind, water, and sunlight all-sector energy roadmaps for 139 countries of the world. *Joule* 1(1), 108–121 (2017)
15. C.J. Rhodes, Biofuel from algae: salvation from peak oil?, in *Seaweeds and Their Role in Globally Changing Environments* (Springer, Dordrecht, 2010), pp. 229–248/480 pages
16. A. Pérez-Tomás, E. Chikoidze, M. R. Jennings, S. A. Russell, F. H. Teherani, P. Bove, ... & D. J. Rogers, Wide and ultra-wide bandgap oxides: where paradigm-shift photovoltaics meets transparent power electronics, in *Oxide-based Materials and Devices IX*, vol 10533, (International Society for Optics and Photonics, 2018), p. 105331Q
17. G. Gaither, U.S. Patent Application No. 10/017,053, 2018
18. B.P. Jelle, C. Breivik, H.D. Røkenes, Building integrated photovoltaic products: a state-of-the-art review and future research opportunities. *Sol. Energy Mater. Sol. Cells* 100, 69–96 (2012)
19. ASTM, *G173-03 Standard Tables for Reference Solar Spectral Irradiances: Direct Normal and Hemispherical on 37° Tilted Surface* (ASTM International, West Conshohocken, 2012), pp. 1–3/20 pages, <https://www.astm.org/Standards/G173.htm>
20. B. Leckner, The spectral distribution of solar radiation at the earth's surface – elements of a model. *Sol. Energy* 20(2), 143–150 (1978)

21. L.M. Perliski, S. Solomon, On the evaluation of air mass factors for atmospheric near-ultraviolet and visible absorption spectroscopy. *J. Geophys. Res. Atmos.* **98**(D6), 10363–10374 (1993)
22. L.C. Marquard, T. Wagner, U. Platt, Improved air mass factor concepts for scattered radiation differential optical absorption spectroscopy of atmospheric species. *J. Geophys. Res. Atmos.* **105**(D1), 1315–1327 (2000)
23. C.A. Gueymard, Parameterized transmittance model for direct beam and circumsolar spectral irradiance. *Sol. Energy* **71**(5), 325–346 (2001)
24. K.R. Lang, *Astrophysical data: Planets and stars*. (Springer, New York, 2012), pp. 3–78/937. 978-1-4684-0642-9
25. R. Russell, *The Multispectral Sun*. (Windows to the Universe.Org., 2017), https://www.windows2universe.org/sun/spectrum/multispectral_sun_overview.html
26. COMET, *Solar Radiation* (2018), <http://www.comet.ucar.edu/>
27. N. Li, M. Karin, Ionizing radiation and short wavelength UV activate NF-kB through two distinct mechanisms. *Proc. Natl. Acad. Sci.* **95**(22), 13012–13017 (1998)
28. N.S. Kapany, U.S. Patent No. 3,985,116. U.S. Patent and Trademark Office, Washington, DC, 1976
29. J. Zimmer, M. DiLabio, U.S. Patent Application No. 29/066,097, 1998
30. V.E. Cenusă, G. Darie, D. Tutica, M. Norisor, F.N. Alexe, C.M. Musat, Energetic and exergetic analysis of Rankine cycles for solar power plants with a parabolic trough and thermal storage. *Renew. Energy Environ. Sustain.* **1**, 10 (2016)
31. EIA, *Levelized Cost and Levelized Avoided Cost of New Generation Resources in the Annual Energy Outlook 2018* (US Energy Information Administration, 2018), pp. 1–20/20 pages, https://www.eia.gov/outlooks/aeo/pdf/electricity_generation.pdf
32. T. Tsoutsos, N. Frantzeskaki, V. Gekas, Environmental impacts of solar energy technologies. *Energy Policy* **33**(3), 289–296 (2005)
33. J. Peng, L. Lu, H. Yang, Review on life cycle assessment of energy payback and greenhouse gas emission of solar photovoltaic systems. *Renew. Sust. Energ. Rev.* **19**, 255–274 (2013)
34. D. Nugent, B.K. Sovacool, Assessing the lifecycle greenhouse gas emissions from solar PV and wind energy: a critical meta-survey. *Energy Policy* **65**, 229–244 (2014)
35. A. Goetzberger, C. Hebling, H.W. Schock, Photovoltaic materials, history, status, and outlook. *Mater. Sci. Eng. R. Rep.* **40**(1), 1–46 (2003)
36. H.W. Schock, Thin film photovoltaics. *Appl. Surf. Sci.* **92**, 606–616 (1996)
37. R.W. Miles, K.M. Hynes, I. Forbes, Photovoltaic solar cells: an overview of state-of-the-art cell development and environmental issues. *Prog. Cryst. Growth Charact. Mater.* **51**(1–3), 1–42 (2005)
38. M.E. Levinshtein, S.L. Rumyantsev, M.S. Shur (eds.), *Properties of Advanced Semiconductor Materials: GaN, AlN, InN, BN, SiC, SiGe* (Wiley, 2001), pp. 1–24, 31–44, 49–65, 67–91, 93–143 and 146–186/216 pages
39. ElProCus, *Basic Structure of a Silicon Solar Cell* (ElProCus, 2018), <https://elprocus.wordpress.com/2013/08/02/basic-structure-of-a-silicon-solar-cell/>
40. M.A. Green, *Solar Cells: Operating Principles, Technology, and System Applications* (Prentice-Hall, Englewood Cliffs, 1982), pp. 1–9, 2–37, 4–59, 85–101 and 103–119/274 pages
41. L. El Chaar, N. El Zein, Review of photovoltaic technologies. *Renew. Sust. Energ. Rev.* **15**(5), 2165–2175 (2011)
42. C. Liu, J. Fan, H. Li, C. Zhang, Y. Mai, Highly efficient perovskite solar cells with substantial reduction of lead content. *Sci. Rep.* **6**, 35705 (2016)
43. M. Cardona, Y.Y. Peter, *Fundamentals of Semiconductors* (Springer, Berlin/Heidelberg, 2005), pp. 1–15, 17–105, 159–202 and 203–241/639 pages
44. A.G. Aberle, Thin-film solar cells. *Thin Solid Films* **517**(17), 4706–4710 (2009)
45. T.M. Razykov, C.S. Ferekides, D. Morel, E. Stefanakos, H.S. Ullal, H.M. Upadhyaya, Solar photovoltaic electricity: current status and future prospects. *Sol. Energy* **85**(8), 1580–1608 (2011)

46. N.G. Dhere, Present status and future prospects of CIGSS thin film solar cells. *Sol. Energy Mater. Sol. Cells* **90**(15), 2181–2190 (2006)
47. H. Spanggaard, F.C. Krebs, A brief history of the development of organic and polymeric photovoltaics. *Sol. Energy Mater. Sol. Cells* **83**(2–3), 125–146 (2004)
48. T.L. Benanti, D. Venkataraman, Organic solar cells: an overview focusing on active layer morphology. *Photosynth. Res.* **87**(1), 73–81 (2006)
49. V.V. Tyagi, N.A. Rahim, N.A. Rahim, A. Jeyraj, L. Selvaraj, Progress in solar PV technology: research and achievement. *Renew. Sust. Energ. Rev.* **20**, 443–461 (2013)
50. Q. Liu, Z. Liu, X. Zhang, N. Zhang, L. Yang, S. Yin, Y. Chen, Organic photovoltaic cells based on an acceptor of soluble graphene. *Appl. Phys. Lett.* **92**(22), 195 (2008)
51. B. O'regan, M. Grätzel, A low-cost, high-efficiency solar cell based on dye-sensitized colloidal TiO₂ films. *Nature* **353**(6346), 737 (1991)
52. U. Bach, D. Lupo, P. Comte, J.E. Moser, F. Weissörtel, J. Salbeck, M. Grätzel, Solid-state dye-sensitized mesoporous TiO₂ solar cells with high photon-to-electron conversion efficiencies. *Nature* **395**(6702), 583 (1998)
53. N.G. Park, Perovskite solar cells: an emerging photovoltaic technology. *Mater. Today* **18**(2), 65–72 (2015)
54. T. Horiuchi, H. Miura, K. Sumioka, S. Uchida, A high efficiency of dye-sensitized solar cells based on metal-free indoline dyes. *J. Am. Chem. Soc.* **126**(39), 12218–12219 (2004)
55. M.A. Green, K. Emery, Y. Hishikawa, W. Warta, E.D. Dunlop, Solar cell efficiency tables (version 47). *Prog. Photovolt. Res. Appl.* **24**(1), 3–11 (2015)
56. C.I. Ferreira, D.S. Kim, Techno-economic review of solar cooling technologies based on location-specific data. *Int. J. Refrig.* **39**, 23–37 (2014)
57. W. Shockley, H.J. Queisser, Detailed balance limit of efficiency of p-n junction solar cells. *J. Appl. Phys.* **32**(3), 510–519 (1961)
58. T. Tiedje, E. Yablonovitch, G.D. Cody, B.G. Brooks, Limiting efficiency of silicon solar cells. *IEEE Trans. Electron Devices* **31**(5), 711–716 (1984)
59. C. Downs, T.E. Vandervelde, Progress in infrared photodetectors since 2000. *Sensors* **13**(4), 5054–5098 (2013)
60. J.C. Shin, M. D'Souza, J. Kirch, L.J. Mawst, D. Botez, I. Vurgaftman, J.R. Meyer, Low temperature sensitive, deep-well 4.8 μm emitting quantum cascade semiconductor lasers, in *Lasers and Electro-Optics, 2009 and 2009 Conference on Quantum Electronics and Laser Science Conference, CLEO/QELS 2009*. Conference on, IEEE, June 2009, pp. 1–2
61. A. Martí, A. Datas, J.R. González, C. Baur, Limiting efficiencies of novel solar cell concepts in space, in *E3S Web of Conferences*, vol. 16 (EDP Sciences, 2017), p. 03004
62. J. Wilson, Thermal issues in GaAs analog RF devices. *Electron. Cooling* **8**, 14–21 (2002)
63. M. Wagner, Simulation of thermoelectric devices. (Matr. Nr. 9925860) Eingereicht An Der (*Technischen Universität Wien*) (Fakultät Für Elektrotechnik Und Informationstechnik von, Bad Mitterndorf, 2007), <http://www.iue.tuwien.ac.at/phd/mwagner/diss.html>
64. Ioffe, *Silicon Electronic Properties* (Ioffe, 2018), <http://www.ioffe.ru/SVA/NSM/Semicond/Si/electric.html>
65. G.J. Snyder, E.S. Toberer, Complex thermoelectric materials, in *Materials for Sustainable Energy* (2011), V. Dusastre (Ed.), ISBN: 978-981-4317-66-5. World Scientific Publishing Co Pte Ltd (London, UK), pp. 101–110/360
66. Z.M. Gibbs, H.S. Kim, H. Wang, G.J. Snyder, Bandgap estimation from temperature dependent Seebeck measurement-deviations from the $2e|S|_{\max} T_{\max}$ relation. *Appl. Phys. Lett.* **106** (2), 022112 (2015)
67. Y.H. Kuo, Germanium-Silicon electroabsorption modulators, Doctoral dissertation, Stanford University, 2006, p. 20/107 pages, <http://snowweb.stanford.edu/thesis/Kuo.pdf>
68. Solar Cell Central, *Solar Efficiency Limits* (2018), http://solarcellcentral.com/limits_page.html
69. G.J. Snyder, T.S. Ursell, Thermoelectric efficiency and compatibility. *Phys. Rev. Lett.* **91**(14), 148301 (2003)
70. U.M. Gosele, Fast diffusion in semiconductors. *Annu. Rev. Mater. Sci.* **18**(1), 257–282 (1988)

71. PV Education, *Open-Circuit Voltage* (PV Education, 2018), <https://www.pveducation.org/pvcdrom/open-circuit-voltage>
72. V.K. Khanna, *Extreme-Temperature and Harsh-Environment Electronics*; Physics, technology and applications (2017), pp. 77–109/488. ISBN: 978-0-7503-1156-4. IOP Publishing, (Bristol, UK) IOP
73. P.N. Cheremisinoff, W.C. Dickinson (eds.), *Solar Energy Technology Handbook*, Part A (Marcel Dekker/Taylor and Francis Group, New York, 1980), pp. 483–499 and 500–515/882. ISBN: 0824768728
74. S. Kuravi, J. Trahan, D.Y. Goswami, M.M. Rahman, E.K. Stefanakos, Thermal energy storage technologies and systems for concentrating solar power plants. *Prog. Energy Combust. Sci.* **39** (4), 285–319 (2013)
75. J. Dostál, J. Pšencík, D. Zigmantas, In situ mapping of the energy flow through the entire photosynthetic apparatus. *Nat. Chem.* **8**(7), 705 (2016)
76. E. Singh, K.S. Kim, G.Y. Yeom, H.S. Nalwa, Atomically thin-layered molybdenum disulfide (MoS₂) for bulk-heterojunction solar cells. *ACS Appl. Mater. Interfaces* **9**(4), 3223–3245 (2017)
77. H. Kim, H.S. Kim, J. Ha, N.G. Park, S. Yoo, Empowering semi-transparent solar cells with thermal-mirror functionality. *Adv. Energy Mater.* **6**(14), 1502466 (2016)
78. A. Kojima, K. Teshima, Y. Shirai, T. Miyasaka, Organometal halide perovskites as visible-light sensitizers for photovoltaic cells. *J. Am. Chem. Soc.* **131**(17), 6050–6051 (2009)
79. X. Jiang, Z. Yu, Y. Zhang, J. Lai, J. Li, G.G. Gurzadyan, L. Sun, High-performance regular perovskite solar cells employing low-cost poly (ethylenedioxythiophene) as a hole-transporting material. *Sci. Rep.* **7**, 42564 (2017)
80. M. Chirumamilla, A.S. Roberts, F. Ding, D. Wang, P.K. Kristensen, S.I. Bozhevolnyi, K. Pedersen, Multilayer tungsten-alumina-based broadband light absorbers for high-temperature applications. *Opt. Mater. Express* **6**(8), 2704–2714 (2016)
81. M. Khalili, M. Abedi, H.S. Amoli, S.A. Mozaffari, Comparison of chitosan and chitosan nanoparticles on the performance and charge recombination of water-based gel electrolyte in dye-sensitized solar cells. *Carbohydr. Polym.* **175**, 1–6 (2017)
82. M. Freitag, J. Teuscher, Y. Saygili, X. Zhang, F. Giordano, P. Liska, A. Hagfeldt, Dye-sensitized solar cells for efficient power generation under ambient lighting. *Nat. Photonics* **11**(6), 372 (2017)
83. C. Winneker, *Global Market Outlook for Photovoltaics 2013–2017* (Construction21 International, 2013), <http://www.construction21.org/articles/h/report-global-market-outlook-for-photovoltaics-2013-2017.html>
84. X. Pan, I. Medina-Ramirez, R. Mernaugh, J. Liu, Nanocharacterization and bactericidal performance of silver modified titania photocatalyst. *Colloids Surf. B: Biointerfaces* **77**(1), 82–89 (2010)
85. Mindat, *Rutile Mineral Data* (Mindat, 2018), <https://www.mindat.org/min-3486.html>
86. W.S. Cho, B.C. Kang, J.K. Lee, J. Jeong, J.H. Che, S.H. Seok, Comparative absorption, distribution, and excretion of titanium dioxide and zinc oxide nanoparticles after repeated oral administration. *Part. Fibre Toxicol.* **10**(1), 9 (2013)
87. Mindat, *Anatase Mineral Data* (Mindat, 2018), <https://www.mindat.org/min-213.html>
88. Mindat, *Brookite Mineral Data* (Mindat, 2018), <https://www.mindat.org/min-787.html>
89. R. Kägi, A. Ulrich, B. Sinnet, R. Vonbank, A. Wichser, S. Zuleeg, M. Boller, Synthetic TiO₂ nanoparticle emission from exterior facades into the aquatic environment. *Environ. Pollut.* **156** (2), 233–239 (2008)
90. S. Dalai, S. Pakrashi, M.J. Nirmala, A. Chaudhri, N. Chandrasekaran, A.B. Mandal, A. Mukherjee, Cytotoxicity of TiO₂ nanoparticles and their detoxification in a freshwater system. *Aquat. Toxicol.* **138**, 1–11 (2013)
91. S. Pakrashi, S. Dalai, T.C. Prathna, S. Trivedi, R. Myneni, A.M. Raichur, A. Mukherjee, Cytotoxicity of aluminum oxide nanoparticles towards freshwater algal isolates at low exposure concentrations. *Aquat. Toxicol.* **132**, 34–45 (2013)

92. B.J. Cardinale, R. Bier, C. Kwan, Effects of TiO₂ nanoparticles on the growth and metabolism of three species of freshwater algae. *J. Nanopart. Res.* **14**(8), 913 (2012)
93. J. Ji, Z. Long, D. Lin, Toxicity of oxide nanoparticles to the green algae *Chlorella* sp. *Chem. Eng. J.* **170**(2–3), 525–530 (2011)
94. V.P. Utgikar, N. Chaudhary, A. Koeniger, H.H. Tabak, J.R. Haines, R. Govind, Toxicity of metals and metal mixtures: analysis of concentration and time dependence for zinc and copper. *Water Res.* **38**(17), 3651–3658 (2004)
95. X. Zou, J. Shi, H. Zhang, Coexistence of silver and titanium dioxide nanoparticles: enhancing or reducing environmental risks? *Aquat. Toxicol.* **154**, 168–175 (2014)
96. V. Iswarya, M. Bhuvaneshwari, S.A. Alex, S. Iyer, G. Chaudhuri, P.T. Chandrasekaran, A. Mukherjee, Combined toxicity of two crystalline phases (anatase and rutile) of Titania nanoparticles towards freshwater microalgae: *Chlorella* sp. *Aquat. Toxicol.* **161**, 154–169 (2015)
97. A. Hassen, N. Saidi, M. Cherif, A. Boudabous, The resistance of environmental bacteria to heavy metals. *Bioresour. Technol.* **64**(1), 7–15 (1998)
98. S. Ramamoorthy, D.J. Kushner, Binding of mercuric and other heavy metal ions by microbial growth media. *Microb. Ecol.* **2**(2), 162–176 (1975)
99. A. Yamamoto, R. Honma, M. Sumita, Cytotoxicity evaluation of 43 metal salts using murine fibroblasts and osteoblastic cells. *J. Biomed. Mater. Res.* **39**(2), 331–340 (1998)
100. F. Heidenau, W. Mittelmeier, R. Detsch, M. Haenle, F. Stenzel, G. Ziegler, H. Gollwitzer, A novel antibacterial titania coating: metal ion toxicity and in vitro surface colonization. *J. Mater. Sci. Mater. Med.* **16**(10), 883–888 (2005)
101. A. Panas, C. Marquardt, O. Nalcaci, H. Bockhorn, W. Baumann, H.R. Paur, C. Weiss, Screening of different metal oxide nanoparticles reveals selective toxicity and inflammatory potential of silica nanoparticles in lung epithelial cells and macrophages. *Nanotoxicology* **7**(3), 259–273 (2012)
102. W. Lin, Y.W. Huang, X.D. Zhou, Y. Ma, In vitro toxicity of silica nanoparticles in human lung cancer cells. *Toxicol. Appl. Pharmacol.* **217**(3), 252–259 (2006)
103. J.L. Kang, C. Moon, H.S. Lee, H.W. Lee, E.M. Park, H.S. Kim, V. Castranova, Comparison of the biological activity between ultrafine and fine titanium dioxide particles in RAW 264.7 cells associated with oxidative stress. *J. Toxic. Environ. Health A* **71**(8), 478–485 (2008)
104. H.L. Karlsson, P. Cronholm, J. Gustafsson, L. Moller, Copper oxide nanoparticles are highly toxic: a comparison between metal oxide nanoparticles and carbon nanotubes. *Chem. Res. Toxicol.* **21**(9), 1726–1732 (2008)
105. C.M. Sayes, R. Wahi, P.A. Kurian, Y. Liu, J.L. West, K.D. Ausman, V.L. Colvin, Correlating nanoscale titania structure with toxicity: a cytotoxicity and inflammatory response study with human dermal fibroblasts and human lung epithelial cells. *Toxicol. Sci.* **92**(1), 174–185 (2006)
106. A. Simon-Deckers, B. Gouget, M. Mayne-L'Hermite, N. Herlin-Boime, C. Reynaud, M. Carriere, In vitro investigation of oxide nanoparticle and carbon nanotube toxicity and intracellular accumulation in A549 human pneumocytes. *Toxicology* **253**(1–3), 137–146 (2008)
107. S. Mayor, R.E. Pagano, Pathways of clathrin-independent endocytosis. *Nat. Rev. Mol. Cell Biol.* **8**(8), 603 (2007)
108. J. Kasper, M.I. Hermans, C. Bantz, M. Maskos, R. Stauber, C. Pohl, J.C. Kirkpatrick, Inflammatory and cytotoxic responses of an alveolar-capillary coculture model to silica nanoparticles: comparison with conventional monocultures. *Part. Fibre Toxicol.* **8**(1), 6 (2011)
109. K.M. Waters, L.M. Masiello, R.C. Zangar, B.J. Tarasevich, N.J. Karin, R.D. Quesenberry, B.D. Thrall, Macrophage responses to silica nanoparticles are highly conserved across particle sizes. *Toxicol. Sci.* **107**(2), 553–569 (2008)
110. T. Morishige, Y. Yoshioka, H. Inakura, A. Tanabe, X. Yao, S. Narimatsu, Y. Mukai, The effect of surface modification of amorphous silica particles on NLRP3 inflammasome-mediated IL-1 β production, ROS production, and endosomal rupture. *Biomaterials* **31**(26), 6833–6842 (2010)

111. M. Winter, H.D. Beer, V. Hornung, U. Krämer, R.P. Schins, I. Förster, Activation of the inflammasome by amorphous silica and TiO₂ nanoparticles in murine dendritic cells. *Nanotoxicology* **5**(3), 326–340 (2011)
112. G.A. Orr, W.B. Chrisler, K.J. Cassens, R. Tan, B.J. Tarasevich, L.M. Markillie, B.D. Thrall, Cellular recognition and trafficking of amorphous silica nanoparticles by macrophage scavenger receptor A. *Nanotoxicology* **5**(3), 296–311 (2011)
113. H. Ruh, B. Kühn, G. Brenner-Weiss, C. Hopf, S. Diabaté, C. Weiss, Identification of serum proteins bound to industrial nanomaterials. *Toxicol. Lett.* **208**(1), 41–50 (2012)
114. C.M. Sayes, J.D. Fortner, W. Guo, D. Lyon, A.M. Boyd, K.D. Ausman, J.L. West, The differential cytotoxicity of water-soluble fullerenes. *Nano Lett.* **4**(10), 1881–1887 (2004)
115. A. Selloni, A. Vittadini, M. Grätzel, The adsorption of small molecules on the TiO₂ anatase (101) surface by first-principles molecular dynamics. *Surf. Sci.* **402**, 219–222 (1998)
116. A. Vittadini, A. Selloni, F.P. Rotzinger, M. Grätzel, Structure and energetics of water adsorbed at TiO₂ anatase(101) and(001) surfaces. *Phys. Rev. Lett.* **81**(14), 2954 (1998)
117. C.M. Sayes, A.M. Gobin, K.D. Ausman, J. Mendez, J.L. West, V.L. Colvin, Nano-C60 cytotoxicity is due to lipid peroxidation. *Biomaterials* **26**(36), 7587–7759 (2005)
118. C. Ouverney, V.E. Zavala, *Microbiology Laboratory # 9. Images of Common Microorganism, Grown on Nutrient Agar.* (San Jose State University, San Jose, 2018).



First-Principles Simulations for CuInGaSe_2 (CIGS) Solar Cells

2

Yu-Wen Cheng, Hong-Tao Xue, Fu-Ling Tang, and Jingbo Louise Liu

Contents

2.1	Introduction	46
2.2	Methods	48
2.2.1	First-Principles Calculation and the Software VASP	48
2.2.2	Cluster Expansion and Monte Carlo (MC) Simulations	48
2.3	Simulation Results	49
2.3.1	Solar Cell Materials under High Pressure and Phase Transformation	49
2.3.2	Solar Cell Materials upon Doping	52

Author Contribution

Y.-W. Cheng did the DOS calculation on the CIS, while H.-T. Xue did the DOS on the CGS system. F.-L. Tang extended the LDOS and generated some of the figures and supervised the calculations, and J. L. Liu edited the manuscript and assisted with the PBE analyses.

Cheng summarized this chapter from the results of Tang's group, and Xue took part in all the works. The authors further acknowledge that there is no financial relationship with the editors or publisher and have contributed original work in this chapter, other than what acknowledged or appropriately cited with copyright permission.

Y.-W. Cheng · H.-T. Xue

Department of Materials Science and Engineering, Lanzhou University of Technology, Lanzhou, China

e-mail: 1109551346@qq.com; xueht987@163.com

F.-L. Tang (✉)

Department of Materials Science and Engineering, Lanzhou University of Technology, Lanzhou, China

Department of Chemistry, Texas A&M University, Kingsville, TX, USA

e-mail: tfl@lut.cn

J. L. Liu

Department of Chemistry, Texas A&M University-Kingsville, Kingsville, TX, USA

Department of Chemistry, Texas A&M University (TAMU), College Station, TX, USA

e-mail: Jingbo.Liu@tamuk.edu

2.3.3	Atomistic Distribution in Solar Cell Materials	56
2.3.4	Interfaces in Solar Cells	66
2.4	Conclusions	71
	References	72

Abstract

In this chapter, simulations for CuInGaSe₂ (CIGS) solar cell materials are illustrated from the viewpoint of first-principles calculations. The solar cell materials under high pressure, upon doping, the atomistic distribution in solar cell materials, and the interface in solar cells were studied. Their lattice structure and mechanics, optical, and electrical properties were studied. Our purpose is to obtain quantitative atomic and electronic structure information in the battery material, and then to understand the relationship among composition, structure, and performance. This will help to design element composition and to determine the technical process parameters. Our study may provide theoretical guidance and help to reduce the usage of highly toxic and scarce elements, reduce battery manufacturing costs, and mitigate potential environmental pollution. In addition, interface states in CuInGaSe₂ thin-film solar cell always do harm to its overall performance by reducing both open-circuit voltage and photoelectric conversion efficiency. In order to maximally weaken the negative impacts of interface states, we used the first-principles calculation to systematically study the local structures and electronic properties of the interfaces. The aim of these simulations was to deeply understand the relationship among the local structures of the interfaces, interface states, and CuInGaSe₂ thin-film solar cell performances, and to reveal the micro-mechanism of photoelectric changes introduced by interface states. As theoretical guides, quantitative results at atomic scale will be helpful to design the chemical components of the cell's materials and those at the interfaces, to modify the interface structures, to manipulate the interface properties, to take advantage of so-called interface engineering, and then to improve the cell's performances.

2.1 Introduction

Simulations are powerful tools for researching on solar cell materials, which are important compensation for experimental research. Homogeneous and single-phase CuInGaSe₂ (CIGS) films are considered to be suitable for materials for high-efficiency CIGS-based solar cells. But as has been found in many previous investigations, the existence of the phase separation of phase (Copper, Cu; Indium, In; Gallium, Ga; and Sulfur, S) CuInGaS₂ (CIS) and CGS (or In-rich CIGS and Ga-rich CIGS) in CIGS alloys resulting in the inhomogeneous distribution of elemental Ga. Ludwig et al. found that CIGS alloys tend to phase-separating into In-rich and Ga-rich CIGS phases in thermal equilibrium below the room temperature [23]. Tinoco et al. obtained the T(x) phase diagram of CuIn_{1-x}Ga_xSe₂ (Selenium, Se) alloys at a temperature above 1073 K by using x-ray diffraction and differential thermal analysis [34]. Yan et al. [47] observed the alloy inhomogeneity associated

with the spatial fluctuation in In and Ga concentrations in CIGS films [47]. Huang et al. have calculated the phase diagram (the binodal curve) of CIGS as a function of Ga concentration and have separately found that the critical temperature (T_c) in CIGS is 420 K [14]. All of these theoretical studies showed that CIGS has a tendency to phase separating at low temperature. The existence of phase-separation of CuInSe₂ (or Se-rich CISS) and CuInS₂ (or S-rich CISS) in CISS alloys resulting in the inhomogeneous distribution of Se-S atoms. Engelmann et al. have produced graded CISS alloy films by reacting CuInSe₂ films in a flowing hydrogen sulfide/argon (H₂S/Ar) atmosphere [10]. Sheppard et al. have found that it is a typical reaction that the two distinct and stable ternary phases CuInSe₂ and CuInS₂ form in CISS alloys during the selenization and sulfurization of CuIn metallic alloys [30]. A direct consequence of the inhomogeneous distribution of Se-S atoms is that the band gap of the CISS absorber films is not uniform. The performances of devices produced from these phase-separation absorber films are inferior, such as causing to having open-circuit voltages and fill factors due to the limited band gap value of absorber films [29, 31]. Werner et al. have shown that even small fluctuations in the composition is un-favored [39], due to the phase separation, which can affect the electronic and optical properties of CIGS. It has been proved that Cu(In_{1-x}Ga_x)Se₂ (CIGS) alloys have the phase-separation behavior [18, 34] and inhomogeneity [3]. Recent first-principles study of phase equilibrium of similar pseudobinary alloys, CuInSe₂-CuGaSe₂ [41, 45] and CuInSe₂-CuAlSe₂ [32, 40], (Aluminum, Al), has predicted the miscibility gap and upper critical solution temperature (UCST) or consolute temperature of these alloys [33, 46], though the available phase diagrams show complete miscibility in the solid state [19, 23]. All of these literatures mean that the knowledge of the alloy phase equilibrium and homogeneity is essential for effective designing of the CISS alloy.

The photoelectric properties of CIGS cells depend not only on the composition and properties of the materials each layer but also on the composition, the structure, and the properties of the interface between the adjacent layers; this is because of the abrupt change of structure at the interface between adjacent layers will lead to the appearance of the interface states and change the band structure of the semiconductor and will have a serious negative impact on the battery performance. Therefore, it is important to study the structure of the interface and eliminate the interface states. Sandino et al. used high-resolution transmission electron microscopy (HRTEM) to analyze the cross-sectional of Mo/CIS interface (Molybdenum, Mo), and observed the formation of a very thin MoS₂ layer (~15–25 nm) among the Mo/CIS interface [28]. Tomić et al. used a hybrid density functional theory to study the electronic structure of the wurtzite CuInS₂ material [36]. Dong et al. studied the band alignment at the interface of cadmium sulfide/zinc oxide (CdS/ZnO) heterojunction and suggested that the interface of CdS/ZnO possesses type-II alignment [9]. Derkaoui et al. studied ZnO/CdS/CdTe (cadmium telluride, CdTe) multilayer coatings' optical characteristics by using first-principles calculations and found that ZnO(300 nm)/CdS(10 nm)/CdTe (1000 nm) configuration solar absorption efficiency was larger than 80% in the visible region [8]. Hong et al. studied bond characteristics and interfacial energetic and electronic structure of Mo/MoSi₂ (001) interface by the first-principles calculation [12]. Liu et al. deposited a ZnO

intermediate layer on the $\text{Cu}_2\text{ZnSnS}_4$ (CZTS) (Tin, Sn) absorber and Mo back contact interface [21]. Yang et al. used X-ray photoelectron spectroscopy (XPS) combined with first-principles calculations to study the band alignments of the CZTS/ZnO heterojunction and suggested that ZnO can be an attractive Cd-free buffer layers candidate for CZTS-based solar cells [48]. Bao et al. studied the valence band offsets in the CZTS/ZnO heterointerface by calculating the local density of states of each atom in the supercell and found that the CZTS/ZnO interface is of type I heterojunction [1]. For passivation interface states, fluorine (F), hydrogen (H), and chlorine (Cl) are the common passivation elements for they easily get electrons from other elements when they formed compound, and researchers have studied F and H [20] and Cl [38] passivation for silicon carbide/silica oxide (SiC/SiO_2) and gallium dioxide/gallium arsenide (HfO_2/GaAs) interfaces, respectively, by the first-principles calculations. These results showed that the interface states can be reduced by F, H, and Cl atoms.

In this chapter, we illustrate the first-principles simulations on solar cell materials. Their lattice structures and electronic and photonic properties are provided. We study their lattice structure and mechanics, optical, and electrical properties. Our purpose is to obtain quantitative atomic and electronic structure information in about the battery material, and then to understand the relationship among the composition, the structure, and the performances.

2.2 Methods

2.2.1 First-Principles Calculation and the Software VASP

In this chapter, most of the calculation works were carried out within the Vienna ab initio simulation package (VASP) [15, 16] based on first-principles density functional theory (DFT) with the Perdew-Burke-Ernzerhof (PBE) version [25] of the generalized gradient approximation (GGA). The projector augmented wave (PAW) method [17] was applied to describe the pseudopotential. The electronic configurations are $[\text{Ar}] 3d^{10}4s^1$, $[\text{Kr}] 5s^25p^1$, $[\text{Ar}] 4s^24p^1$, $[\text{Ar}] 4s^24p^4$, $[\text{Ar}] 3d^{10}4s^2$, $[\text{Kr}] 4d^{10}5s^25p^2$, $[\text{Kr}] 3d^{10}5s^2$, $[\text{Ne}] 3s^23p^1$, $[\text{Ne}] 3s^23p^4$, $2s^22p^4$, $1s^1$ for copper, indium, gallium, selenium, zinc, tin, cadmium, aluminum, sulfur, oxygen, hydrogen, respectively. The conjugate gradient (CG) [50] method was used to optimize the lattice structure. The tetrahedron method with Bloch corrections [2] was used for calculating the interface binding energy, the band structure, and the density of states (DOS) in all systems. Meanwhile, our theoretical approach is based on the GGA with on-site Coulomb interaction parameter (GGA + U method) (taking account of the Hubbard correction) [13].

2.2.2 Cluster Expansion and Monte Carlo (MC) Simulations

As the Monte Carlo (MC) simulation of an $A_{1-x}B_x$ binary alloy involves comparing the energy of many different atomic configurations, it requires calculation of the total

energy for each of these configurations of placing atoms A and B on n sites of the underlying Bravais lattice. But in fact, it would be infeasible to calculate the total energy of all these configurations from first principles because the number of these configurations 2^n becomes enormous even for a modest number of sites n . Therefore, in this work we first employed the cluster expansion (CE) method, which is a well-established method and has been extensively and successfully used in many alloys [27, 37, 42–44], to obtain the effective cluster interactions (ECIs) that define a computationally efficient Hamiltonian for the configurational energy of an alloy. And then the ECIs were used as the main input parameters to performing MC simulations. The CE enables prediction of the energy of any configuration from the energies of a small number of configurations (typically between 30 and 50), thus making the procedure amenable to using of first-principles calculations [37].

In an $A_{1-x}B_x$ binary alloy, the CE is defined by first specifying occupation variables s_i to each of the n atomic sites ($i = 1, 2, 3, \dots, n$). The occupation variables s_i take the value +1 or -1 depending on the A atom or the B atom occupying the site. Each of the arrangements of these occupation variables on the atomic sites is called a configuration and is represented by a vector s which contains the value of the occupation variable for each atomic site in the $A_{1-x}B_x$ binary alloy. This approach is known as the structure inversion method (SIM) or the Collony-Williams method [7]. Once the cluster expansion has been constructed, i.e., the ECIs have been obtained, the energy of any configuration can be calculated by using Eq. 2.1 at a very small computational cost. Therefore, the aim of the CE method is to determine a limited set of ECIs such that the expansion can be truncated and computational expense is minimized while the predictive power is maximized.

2.3 Simulation Results

2.3.1 Solar Cell Materials under High Pressure and Phase Transformation

2.3.1.1 Phase Diagram of CuGaSe₂

The total energy of per CuGaSe₂ unit, lattice constants, bulk modulus, and pressure derivative of the bulk modulus for the three phases under zero-pressure were obtained by fitting the *Energy-Volume* ($E-V$) data points to the Murnaghan equation of state (EOS) [24]. The calculated total energy of per CuGaSe₂ unit as a function of volume for three structures are shown in Fig. 2.1. From these *Energy-Volume* ($E-V$) curves, it is clear find that the zero-pressure equilibrium structure of the $I\bar{4}2d$ phase has the lowest energy, which is the most stable structure. As the pressure increasing, the lattice volume decreases: the $Fm\bar{3}m$ structure and then $Cmcm$ structure has the lowest energy sequentially. The inset of Fig. 2.1 shows the variation of the Gibbs free energy (G , kJ/mol) of the three phases as a function of pressure (P , Pa). The $G-P$ curves can predict the possibility of the pressure-induced transformations between the three phases as well as the stability of the three phases under high pressure. As can be seen in Figure 2.1, when the pressure is below 11.87 GPa, the $I\bar{4}2d$ phase has a lower Gibbs free energy than that of the $Fm\bar{3}m$ phase, which indicates that the $I\bar{4}2d$

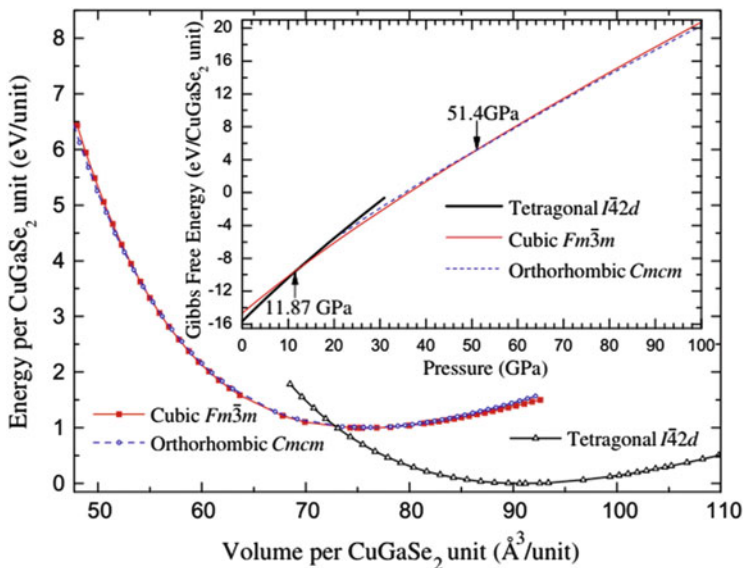


Fig. 2.1 Energy-volume curves and Gibbs free energy (inset) of CGS phase transition. The energy of *I*42d phase at zero pressure is set as 0 eV

phase is thermodynamically more stable than that of the *Fm*3̄m phase below 11.87 GPa, vice versa. Therefore, the point of intersections of curves corresponding to two phases gives us the pressure and the Gibbs free energy (at 0 K) for the phase transformation. Such a CGS *I*42d to *Fm*3̄m phase transition pressure 11.87 GPa from *G-P* curves is in good agreement with the previous experimental result (13 GPa). For the *Cmc* phase, at pressures above 51.4 GPa, it is thermodynamically more stable than the *Fm*3̄m phase due to its lower Gibbs free energy. While below this pressure, it is less stable than the latter one. Hence, our calculations indicate that it is possible for CGS (CuGaSe₂) to transform from the cubic *Fm*3̄m structure to an orthorhombic *Cmc* structure at about 51 GPa. The results imply that the structure of CGS is more harder than that of CIS (CuInGaS₂).

Figure 2.2 shows the volume versus the pressure relation. This relation provides the information on about the volume decrease (per CuGaSe₂ unit), $-\Delta V/V_0$, at each phase transitions. It can be found that the volume decrease at the *I*42d to *Fm*3̄m transition is 13.3%. And the calculated lattice parameter of the *Fm*3̄m structure at 16.21 GPa is $a = 5.057(5)$ Å. The corresponding volume decrease at the *Fm*3̄m to *Cmc* transition is 0.49%. The calculated unit cell of the orthorhombic *Cmc* structure at 54.91 GPa is $a = 4.726(3)$ Å, $b = 4.869(7)$ Å, and $c = 4.644(4)$ Å. The atomic position of the *Cmc* structure (0, y , 1/4) at this pressure with y (Cu/Ga) = 0.690(6) and y (Se) = 0.195(2) is obtained. The transition pressures and the volume reductions are summarized and compared with the experimental data as shown in Fig. 2.3. It is readily seen that the calculations give a good description of the experimental result [35]. It should be noted that the calculations' results are obtained at 0 K, while the experimental results were always obtained at

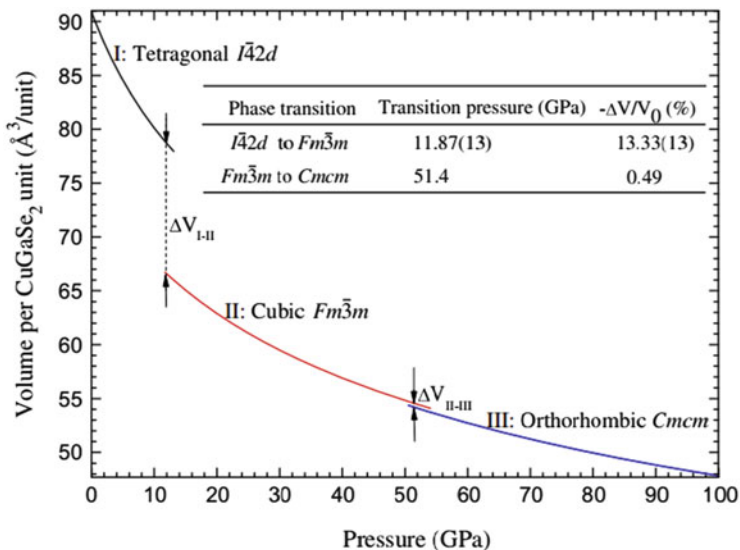


Fig. 2.2 Volume-pressure curves of CGS phase transition upon pressure between 0 and 100 GPa. The internal table shows the transition pressure and volume reduction. The internal table shows the transition pressure and the volume reduction, compared with the existing experimental data [35] in parentheses

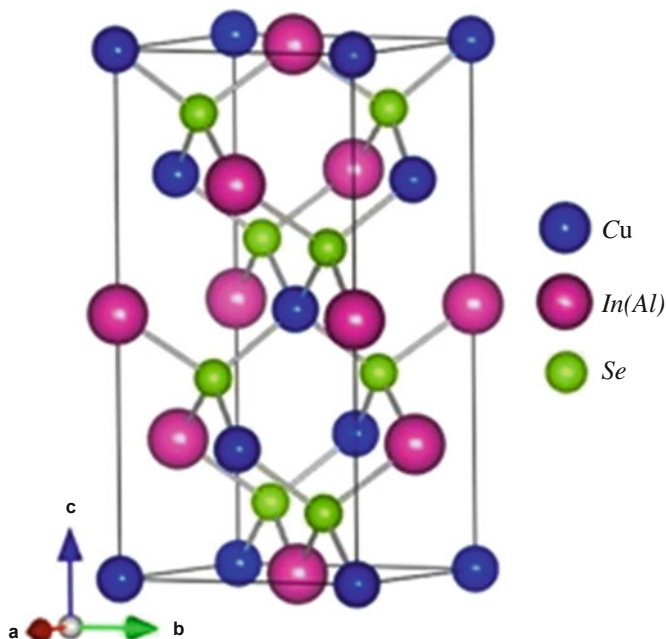


Fig. 2.3 Simulated unit cell diagram for the chalcopyrite system $\text{CuIn}_{1-x}\text{Al}_x\text{Se}_2$

ambient temperature. The possible inaccuracy of total-energy calculation results is amplified of the computation of the transition pressures. For example, in case of the phase transition of $I\bar{4}2d$ to $Fm\bar{3}m$, an error of 0.1 eV in the total-energy computation would lead to an error of ~ 0.43 GPa in the pressure calculation. Therefore the calculated results of the CGS $Fm\bar{3}m$ - $Cmcm$ phase transition need experimental verification.

2.3.2 Solar Cell Materials upon Doping

2.3.2.1 Al-Doped CuInSe_2 : $\text{CuIn}_{1-x}\text{Al}_x\text{Se}_2$ Structural, Electronic, and Optical Properties

Structural Properties

$\text{CuIn}_{1-x}\text{Al}_x\text{Se}_2$ crystallizes in the chalcopyrite structure, which is shown in Fig. 2.3. The chalcopyrite structure can be obtained from the cubic zinc blende structure, which contains only one type of cation. However, the presence of two different cations in the chalcopyrite structure ordered in the half tetrahedral sites yields a doubling of the zincblende unit cell along the c direction. In general, the bond lengths of I–VI and III–VI (denoted by d_{I-VI} and d_{III-VI} , respectively) are not equal, which can lead to a tetragonal distortion. Two structural parameters $\eta = c/a$ and $\mu = 0.25 + \left(d_{I-VI}^2 - d_{III-VI}^2 \right) / a^2$, where a is the lattice constant (\AA) in the x or y direction and c is in the z direction, are employed to characterize this tetragonal distortion. The structural parameter η describes a deformation of the unit cell to a length c (\AA) which is generally different from $2a$ and μ describes a repositioning of the anions in the x - y plane (\AA).

Electronic Properties

The calculated energy gaps are 0.31 and 1.21 eV, respectively, for CuInSe_2 and CuAlSe_2 (see Fig. 2.4), both of them are smaller than their experimental values 1.04 and 2.67 eV [26], respectively. This is because of the correlation between the valence electrons is underestimated in the GGA, and the DFT method is known to underestimate the energy gap value and overestimate the lattice constants. However, the energy gap tends to increase with the increase of Al content, which is basically the same as the experimental result (see Fig. 2.4). The compositional dependence of the band gap can be fit by Eq. (2.1)

$$E_g(x) = E_g(0) + (E_g(1) - E_g(0))x + bx(x - 1), \quad (2.1)$$

here b is the optical bowing parameter (eV), which describes the band gap variation of a composite semiconductor alloy. It is known to be related to the electronic structure and the lattice deformation in the semiconductor alloys. The least squares fit shown in Fig. 2.4 gives a value of $b = 0.49$.

Optical (Absorption) Properties of $\text{CuIn}_{1-x}\text{Al}_x\text{Se}_2$

The absorption coefficient indicates that the fraction of energy lost by the wave when it passes through a unit thickness of the material. The absorption spectra of

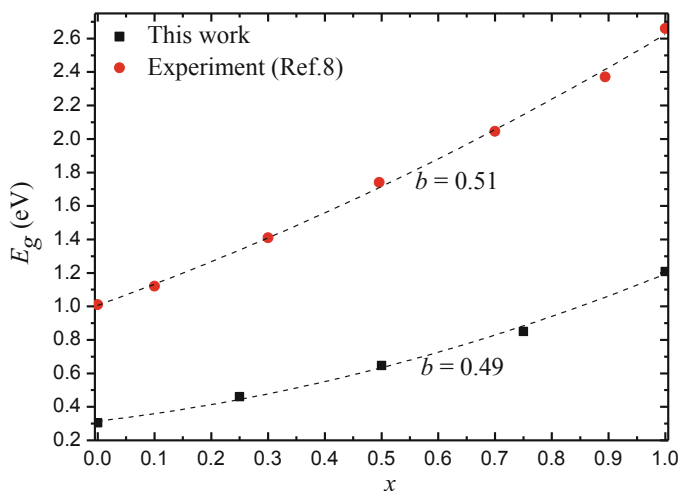


Fig. 2.4 Variation of the band energy gap of CuIn_{1-x}Al_xSe₂ with Al content

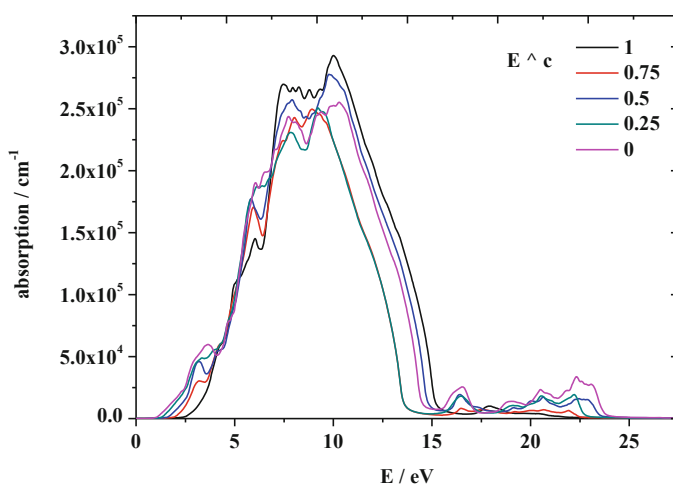


Fig. 2.5 The absorption of CuIn_{1-x}Al_xSe₂ in the ordinary polarization

CuIn_{1-x}Al_xSe₂ with five doping densities are given in Fig. 2.5. From the absorption spectra, the band gap can also be obtained. It can be found that Al reduces when the band gap is less than 4 eV, and the transparent region increases up to 2.4 eV or more than 25 eV. When the photon energy is less than 4 eV, the absorption decreases with x from 0 to 1 (cm³). When x is 0.25 and 0.75, the absorption of CuIn_{1-x}Al_xSe₂ in the high energy region is almost the same, and their absorption peak is the lowest, while the pure CuAlSe₂ has the highest peak.

2.3.2.2 Generalized Stacking Fault Energies and Cleavage Energies of Cu(Al/Ga/In)Se₂ and CuGa(S/Se/Te)₂

Generalized Stacking Fault Energies

Generalized stacking fault (GSF) energies $\gamma(u)$ in CuXSe₂ and CuGaY₂ compounds for fault vectors u along the directions of $\langle 110 \rangle(001)$, $\langle 100 \rangle(001)$, and $\langle \bar{1}10 \rangle(112)$ are displayed in Fig. 2.6. As can be seen in Fig. 2.6, all the γ -curves exhibit a maximum value at $u/b = 0.25$ and a minimum value at $u/b = 0.5$, where b is the Burgers vector. These maximum and minimum values define the unstable stacking fault energies γ_{us} and the intrinsic stacking fault energies γ_{isf} of these compounds, respectively.

Values of γ_{us} along the $\langle 110 \rangle(001)$ direction for five compounds is lower than that of along the $\langle 100 \rangle(001)$ direction, which indicates that it is easier to slip along the $\langle 110 \rangle$ direction on the (001) plane. The values of γ_{us} along the $\langle \bar{1}10 \rangle(112)$ direction are even lower than that value along the $\langle 110 \rangle(001)$ direction. Therefore, it is easiest for these compounds to slip along the $\langle \bar{1}10 \rangle(112)$ direction among the three slip systems considered here.

γ_{isf} of CuInSe₂ (~ 0.24 J/m²) is about an order of magnitude higher than that of the other four compounds along the $\langle 110 \rangle(001)$ direction. The value of γ_{isf} characterizes the possibility of a full dislocation splits into partial dislocations

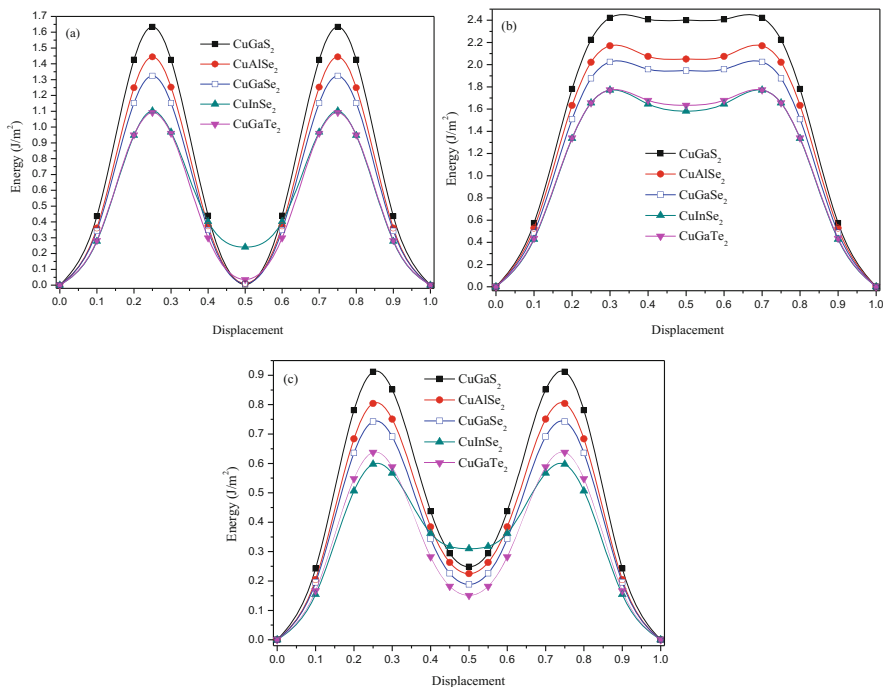


Fig. 2.6 γ -curves of CuGaS₂, CuAlSe₂, CuGaSe₂, CuInSe₂, and CuGaTe₂ for displacement along the directions: (a) $\langle 110 \rangle(001)$, (b) $\langle 100 \rangle(001)$, (c) $\langle \bar{1}10 \rangle(112)$

joined by a stacking fault defect. The distance between the partial dislocations is closer to the width of the dislocation core as γ_{isf} becomes larger. When γ_{isf} is large enough, the full dislocation will not split, and the motion of the full dislocation will be impeded. The values of γ_{isf} along the $\langle 100 \rangle (001)$ direction for five compounds is much larger than that value along the $\langle 110 \rangle (001)$ direction. Hence, the full dislocation $\langle 100 \rangle (001)$ probably has a compact core, and the tendency of the $\langle 100 \rangle (001)$ dislocation to split into partials is smaller than that of the $\langle 110 \rangle (001)$ dislocation.

γ_{isf} along the $\langle 110 \rangle (001)$ and $\langle \bar{1}10 \rangle (112)$ directions can also be called antiphase boundary (APB) energies, E_{APB} . This is because of along the two slip directions antiphase boundary defects can be formed in the sheared lattice configurations at $u/b = 0.5$. And in the configuration with an antiphase boundary defect, the copper sites at and above the slip plane are taken by group-III atoms and vice versa, while sites of a group-VI atom are not changed. γ_{isf} along the $\langle 100 \rangle (001)$ direction are not E_{APB} , as there are no antisites in the sheared lattice configurations at $u/b = 0.5$. Values of γ_{isf} along the $\langle 110 \rangle (001)$ and $\langle \bar{1}10 \rangle (112)$ directions also represent the possibility of formation of antiphase boundary defect in the five compounds. The low APB energies ($\sim 0.004 \text{ J/m}^2$ to $\sim 0.31 \text{ J/m}^2$) in these compounds imply that the formation of the stable antiphase boundary defects along the $\langle 110 \rangle (001)$ and $\langle \bar{1}10 \rangle (112)$ directions are quite probable.

Both γ_{us} and γ_{isf} on the γ -curve are the key factors of influencing the plastic deformation of materials. As suggested by Gornostyrev [11], there is a critical stress intensity factor for the nucleation of a leading partial dislocation on the slip plane near the crack tip. And the critical stress intensity factor is proportional to the value of $\sqrt{\gamma_{\text{us}}}$. When the leading partial dislocation moves away from the crack, it leaves behind a stacking fault. The stacking fault facilitates to the nucleation of a trailing partial dislocation, but the leading partial always impedes the nucleation. So, there is also a critical stress intensity factor which is proportional to the value of $\sqrt{\gamma_{\text{us}} - \gamma_{\text{isf}}}$ for the nucleation of the trailing partial dislocation [11, 37]. Along the $\langle \bar{1}10 \rangle (112)$ direction, γ_{us} of CuInSe₂ ($\sim 0.6 \text{ J/m}^2$) is the lowest among the five compounds, while its γ_{isf} ($\sim 0.31 \text{ J/m}^2$) is the highest. So $\gamma_{\text{us}} - \gamma_{\text{isf}}$ of CuInSe₂ ($\sim 0.29 \text{ J/m}^2$) should be the lowest. It means that along the $\langle \bar{1}10 \rangle (112)$ slip direction the critical stress intensity factors of CuInSe₂ for the nucleation of the leading and trailing partial dislocations are the lowest among these compounds. Hence, along with the $\langle \bar{1}10 \rangle (112)$ slip direction the nucleation of the leading and trailing partial dislocations is the easiest for CuInSe₂ among the five compounds. As a result, it is most possible for CuInSe₂ to undergo a dislocation-nucleation-induced plastic deformation along the $\langle \bar{1}10 \rangle (112)$ slip direction among the five compounds.

Cleavage Energies γ_{cl}

The cleavage energy γ_{cl} is the energy required for creating two surfaces. The cleavage energy for (112) plane of CuInSe₂ should be no larger than 1.28 J/m^2 and for (001) plane of CuGaSe₂ should be about 1.9 J/m^2 . As can be seen in Fig. 2.7, the

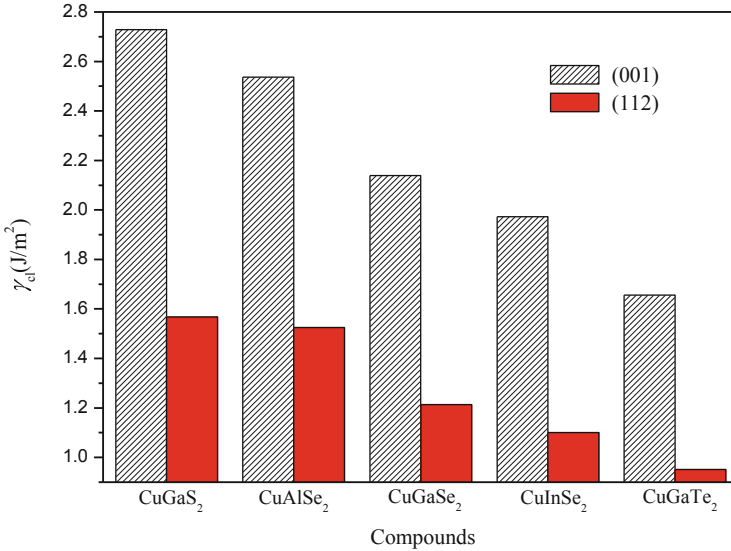


Fig. 2.7 Cleavage energies of (001) and (112) planes in CuGaS₂, CuAlSe₂, CuGaSe₂, CuInSe₂, and CuGaTe₂

results show that the cleavage energy for (112) plane of CuInSe₂ and for (001) plane of CuGaSe₂ is 1.1 J/m² and 2.14 J/m², respectively. In Fig. 2.6, it is obvious that γ_{cl} of (112) plane is lower than that of (001) plane for any of the five compounds. Therefore, (112) plane is the preferable plane for fracture in these compounds. And from Fig. 2.7, one can see that γ_{cl} of (001) and (112) planes decrease with increasing atomic radius in the CuXSe₂ compounds (X: Al ! Ga ! In) and in the CuGaY₂ compounds (Y: S → Se → Te) (Tellurium, Te).

2.3.3 Atomistic Distribution in Solar Cell Materials

2.3.3.1 Temperature Effects on Distribution and Inhomogeneous Degree of In-Ga Atoms in CuIn_{1-x}Ga_xSe₂ Alloys

In Fig. 2.8, to make the observation easier, Cu and Se atoms are not displayed in the snapshots. It is seen that there is a segregation of In and Ga atoms in CIGS alloys when the temperature is low, while the In-Ga distributions become homogeneous at the high temperature. The clustering of Ga or In atoms in CIGS alloys with different Ga contents exists in a spherical, rod-like, lamellar or a massive structure at the low temperature. It is very possible to prepare CIGS-based quantum dots (QDs) at low temperatures via the phase-separation found here because the growth of QDs by phase-separation has already been established for the similar material InGaAs.

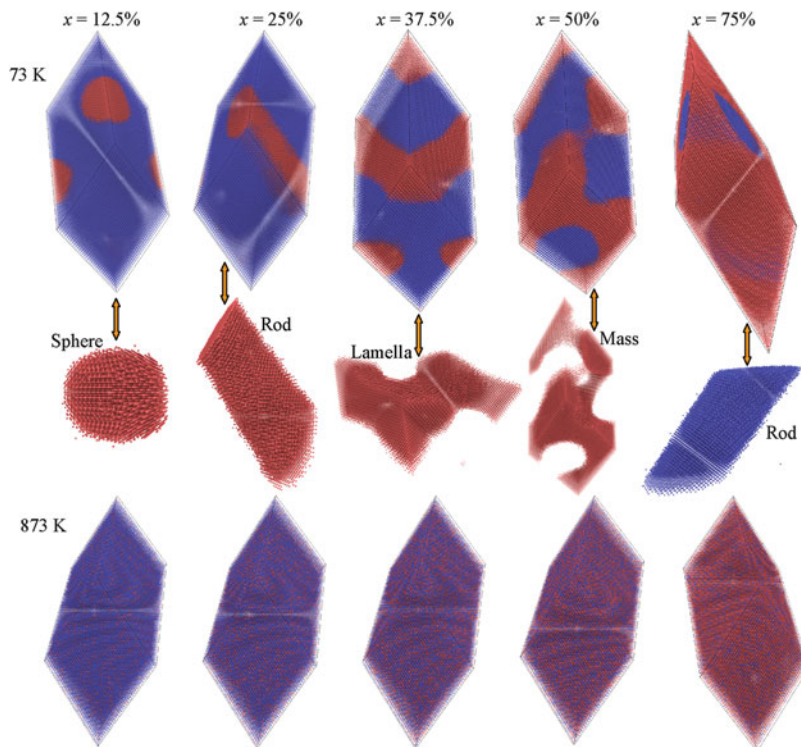


Fig. 2.8 Snapshots of the In-Ga distributions in $\text{CuIn}_{1-x}\text{Ga}_x\text{Se}_2$ alloys at 73 K (upper row) and 873 K (lower row). Blue and red balls represent the In and Ga atoms, respectively. The middle row shows the morphologies of Ga(In) clustering in corresponding CIGS supercells at 73 K. (For interpretation of the references to color in this figure legend, the reader is referred to the web version of this article)

2.3.3.2 Effect of Temperature on Atomic Distribution and Inhomogeneity in $\text{CuIn}(\text{Se}_{1-x}\text{S}_x)_2$ Alloys

The Distribution Morphologies of Se-S Atoms in $\text{CuIn}(\text{Se}_{1-x}\text{S}_x)_2$ Alloys

Figure 2.9 shows the distribution morphologies of Se-S atoms in $\text{CuIn}(\text{Se}_{1-x}\text{S}_x)_2$ (CISS) alloys at the typical temperatures of 48 K, 110 K (low temperatures), and 773 K (high temperature), respectively, because of the distribution morphologies of Se-S atoms in CIGS alloys are similar at low or high temperatures. To make the observation easier, both Cu and In atoms are not displayed in the snapshots, and the distribution morphologies of simplex S(Se) atoms in CISS alloys are further shown by deleting all Se(S) atoms. From Fig. 2.9, it can be observed that there is a segregation of S and Se atoms in CISS alloys both at 48 K and 110 K, which means that there is a phase separation of CuInSe_2 (or Se-rich CISS) and CuInS_2 (or S-rich CISS) in CISS alloys at low temperatures. This result agrees well with the phase diagram of CISS alloys (Xue et al. 2014) calculated by us. When the temperature

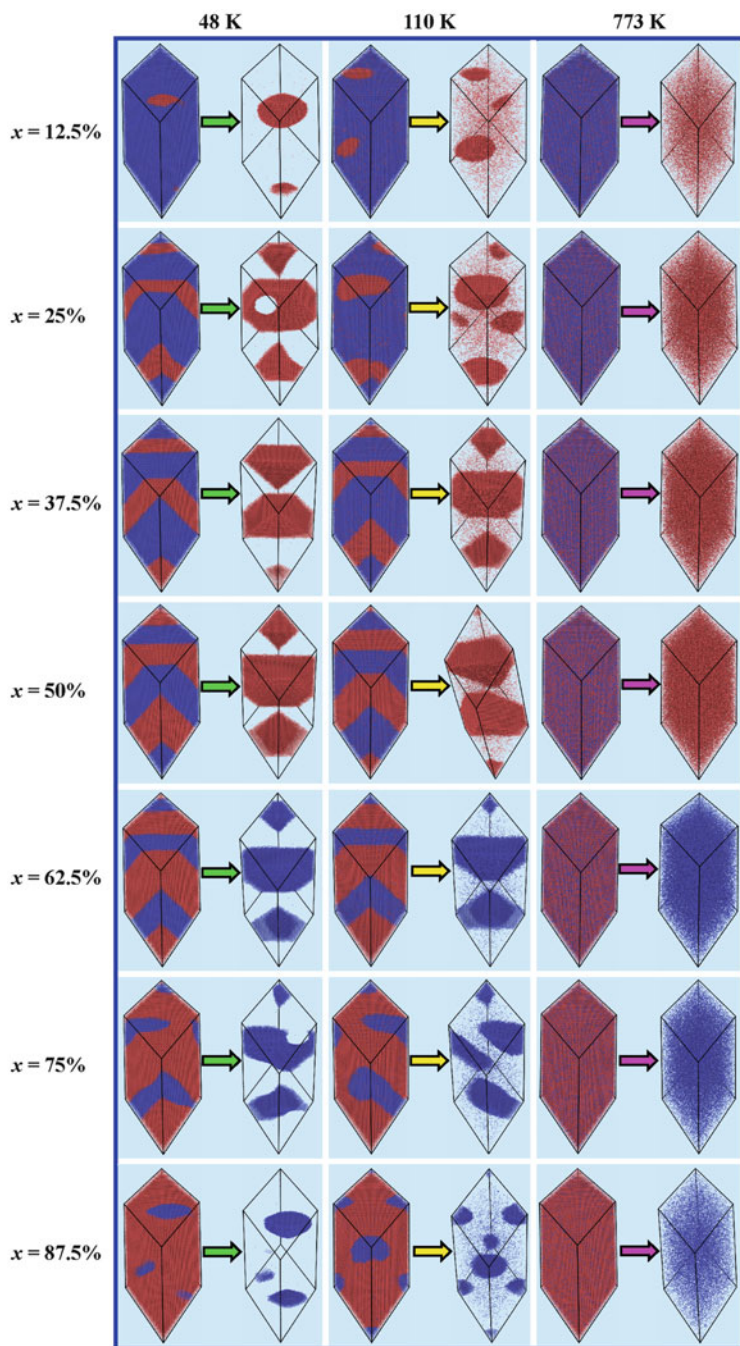


Fig. 2.9 Snapshots of the Se-S distributions in $\text{CuIn}(\text{Se}_{1-x}\text{S}_x)_2$ alloys with $x = 12.5\%$, 25% , 37.5% , 50% , 62.5% , 75% , and 87.5% at the temperatures of 48 K, 110 K, and 773 K are shown on the left side of the green, yellow, and magenta arrows, respectively. Red and blue balls represent S

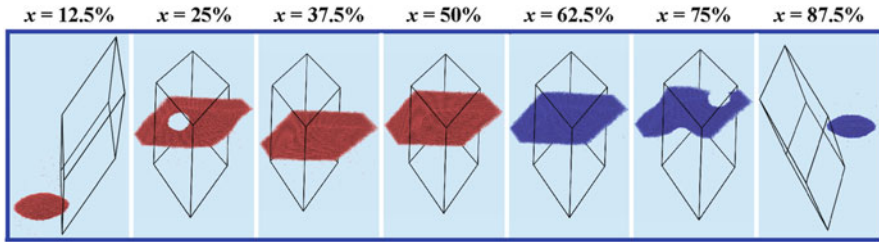


Fig. 2.10 The distribution morphologies of S(Se) atoms in $\text{CuIn}(\text{Se}_{1-x}\text{S}_x)_2$ alloys with $x = 12.5, 25, 37.5, 50, 62.5, 75,$ and 87.5% respectively at 48 K, which can be obtained by translating the S (Se) atoms shown on the right side of the green arrows in the column of 48 K of Fig. 2.3 according to the periodicity. Red and blue balls represent S and Se atoms, respectively

rises from 48 K to 110 K, more S(Se) atoms are scattered around. And the Se-S distributions seem to be homogeneous when the temperature is 773 K. As a result, the Se-S distribution in CISS alloys becomes more and more homogeneous as the temperature is raised from the low temperature to relatively high temperature.

As shown in Fig. 2.10, to better observing the distribution morphologies of S (Se) atoms in CISS alloys at 48 K, the S(Se) atoms in supercells were translated periodically. The distribution morphologies are shown in Fig. 2.10, which are equivalent to that shown on the right side of the green arrows in the column of 48 K of Fig. 2.9. It is seen that the clustering of S(Se) atoms in CISS alloys exists in an ellipsoidal or a lamellar structure at 73 K. When the concentration of S(Se) atoms is less than 12.5%, the S(Se) atoms in CISS alloys should cluster in a form of ellipsoids or spheres. As the concentration of S(Se) atoms increases from 12.5% to 25%, the clustering of S(Se) atoms in CISS alloys changes from ellipsoids to lamellas with holes which should be filled with Se(S) atoms. The clustering of S (Se) atoms keeps lamellar as the concentration of S(Se) atoms increases from 25% to 50%, meanwhile the thickness of the lamellas increases. Therefore, for CISS alloys with $x = 25, 37.5, 50, 62.5,$ and 75% respectively, the microstructures will appear in periodic patterns consisted of alternate S-rich and Se-rich CISS lamellas at low temperatures, which is a characteristic feature of the phase separation.

2.3.3.3 Phase Diagram of the CuInSe_2 - CuGaSe_2 Pseudobinary System

Figure 2.11 shows the calculated dependence of the total energy E against volume V for $\text{CuIn}_{1-x}\text{Ga}_x\text{Se}_2$. By fitting the E - V data points to the Birch-Murnaghan EOS one can obtain the equilibrium volume V_0 and the equilibrium total energy E_0 of CIGS for a different fraction of Ga. In view of the complexity of the SQSSs of CIGS, the dependence of V_0 on the composition instead of the lattice constant was plotted, as shown in Fig. 2.12. And the equilibrium volumes of CIGS we calculated are

←
Fig. 2.9 (continued) and Se atoms, respectively. The distribution morphologies of S(Se) atoms in CISS alloys at 48 K, 110 K, and 773 K are shown on the right side of the green, yellow, and magenta arrows, respectively

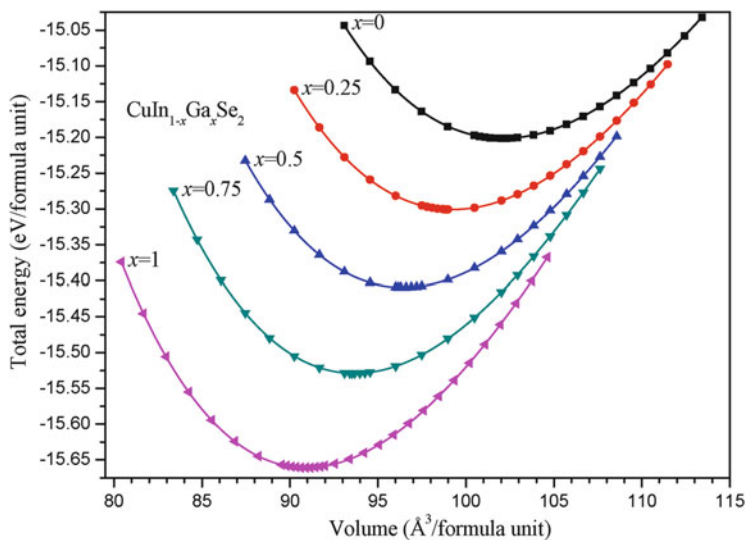


Fig. 2.11 The dependence of the total energy on volume for the $\text{CuIn}_{1-x}\text{Ga}_x\text{Se}_2$ alloys

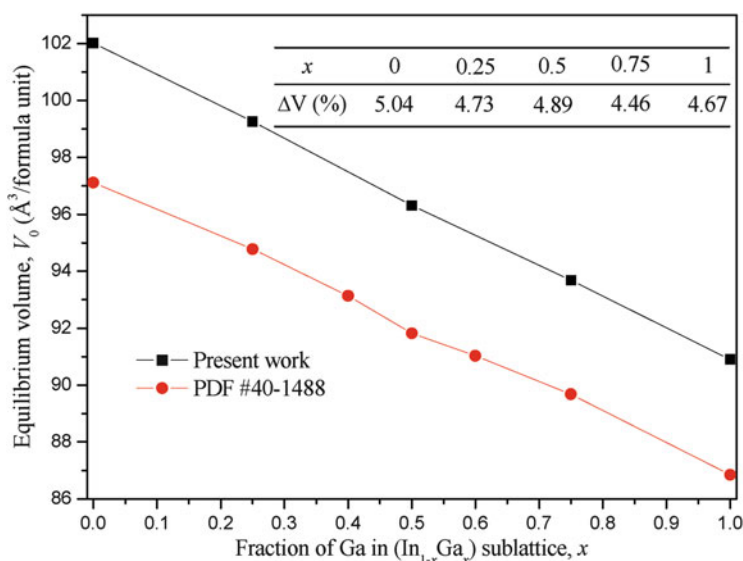


Fig. 2.12 The calculated equilibrium volume of $\text{CuIn}_{1-x}\text{Ga}_x\text{Se}_2$ as a function of the Ga fraction x : a comparison with the powder diffraction file (PDF) 40-1488. The inserted table shows the volume error percentages for a different fraction of Ga

overestimated compared with those of experimental data (PDF #40-1488). The errors, $\Delta V = (V_0 - V_{\text{Experiment}})/V_{\text{Experiment}}$, are no larger than 5.04%; all of these are within the errors usually obtained by DFT-PBE calculations.

In order to determine the Gibbs free energy of mixing of the CuIn_{1-x}Ga_xSe₂ solid solution with respect to the isostructural terminal phases, we have to calculate the interaction parameter $\Omega(x)$ first. The isostructural CIS and CGS were chosen as the terminal phases for CIGS. The interaction parameter $\Omega(x)$ can be obtained from Eqs. (2.2) and (2.3), that is,

$$\begin{aligned} E(\text{CuIn}_{1-x}\text{Ga}_x\text{Se}_2) - [(1-x)E(\text{CuInSe}_2) + xE(\text{CuGaSe}_2)] \\ = x(1-x)\Omega(x). \end{aligned} \quad (2.2)$$

$$\Omega(x) = \alpha x^2 + \beta x + \gamma. \quad (2.3)$$

Figure 2.13a shows the Gibbs free energy (kJ/mol) of mixing of CuIn_{1-x}Ga_xSe₂, ΔG_{mix} , as a function of x at a given absolute temperature of 360 K. Figure 2.13b shows the temperature-composition phase diagram derived from the curves of Gibbs free energy of mixing. The binodal curve denotes the equilibrium solubility limits of the solid solution and is defined by the condition at the chemical of all solution components is equal in each phase. In general, the binodal can be determined at a given temperature by drawing a common tangent line to the curve of Gibbs free energy of mixing, as shown in Fig. 2.13a for $T = 360$ K. The spinodal is the limit of stability of the solution and can be determined as the curve of the second derivative of Gibbs free energy of mixing with respect to the Ga fraction is zero, that is, $\partial^2(\Delta G_{\text{mix}})/\partial x^2 = 0$ (see Fig. 2.13a). Inside the spinodal curve, where $\partial^2(\Delta G_{\text{mix}})/\partial x^2 < 0$, the thermodynamically driving phase segregation occurs without any activation; therefore, the mixture of two phases of CuInSe₂ and CuGaSe₂ (or In-rich CIGS and Ga-rich CIGS) is stable in this region. Between the spinodal and binodal curves, where $\partial^2(\Delta G_{\text{mix}})/\partial x^2 > 0$, the phase segregation occurs by activated nucleation and growth, and this region is also known as the metastable phase region. Outside the binodal curve, the single-phase CIGS is stable.

From Fig. 2.13b one can see that the CIS-CGS pseudobinary system exhibits the phase separation at low temperature. The binodal curve gives the consolute temperature T_c (the critical temperature above which the components of a mixture are miscible in all proportions) of 485 K for CIGS alloys, and the Ga concentration associated with T_c , x_c , is about 0.804 (mole fraction). Our result shows that it is possible to obtain the homogeneous CIGS phase in the whole Ga concentration range at relatively low temperature under equilibrium growth conditions. Here, one should also note that in practice to overcome the energy barrier for the diffusing of atom and shortening the time of atom growth time, it is usually required to increase the growth temperature intentionally for most of the growth conditions.

In Fig. 2.13b, it is important to note that both the binodal and spinodal curves are significantly asymmetric, and on both curves, there is an unusual local between maximum and minimum. This phenomenon occurs at temperatures lower than 500 K, the regime where data are difficult to obtain experimentally due to slow kinetics. As shown in Fig. 2.13b, the temperature of both the equilibrium solubility limit and the stability limit for CuIn_{0.25}Ga_{0.75}Se₂ is higher than that of for CuIn_{0.75}Ga_{0.25}Se₂. It means that the temperature range where two phases may

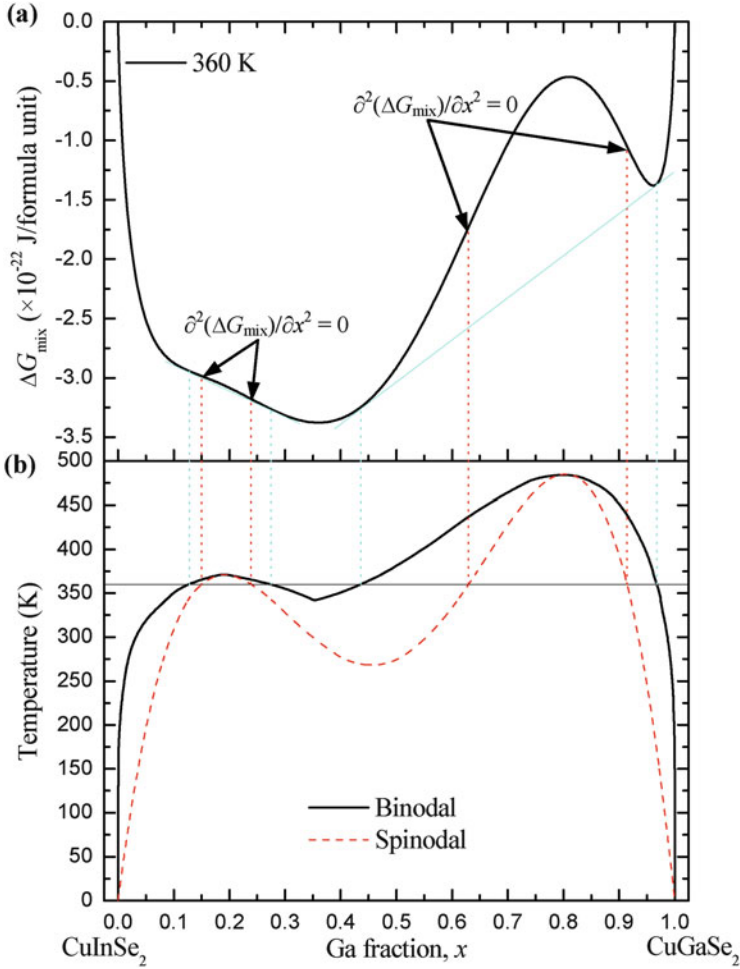


Fig. 2.13 (a) Gibbs free energy of mixing of the $\text{CuIn}_{1-x}\text{Ga}_x\text{Se}_2$ solid solution as a function of Ga fraction, x , at $T = 360$ K. (b) Calculated temperature-composition phase diagram for $\text{CuIn}_{1-x}\text{Ga}_x\text{Se}_2$ with CuInSe_2 and CuGaSe_2 chosen as reference states. The binodal (solid line) is defined by the points at which a common tangent line touches the curve of Gibbs free energy of mixing, and the spinodal (dashed line) is determined as the curve of which the second derivative of Gibbs free energy of mixing with respect to the Ga fraction is zero

coexist in thermal equilibrium (i.e., the inhomogeneous region) for the former is wider than that for the latter. In a particular case where the temperature is 400 K, the $\text{CuIn}_{0.75}\text{Ga}_{0.25}\text{Se}_2$ has been homogeneous as it is outside the binodal curve, and $\text{CuIn}_{0.25}\text{Ga}_{0.75}\text{Se}_2$ is still inhomogeneous as it is located in the spinodal curve. Therefore, it is understandable that the inhomogeneous degree of $\text{CuIn}_{0.25}\text{Ga}_{0.75}\text{Se}_2$ is larger than that of $\text{CuIn}_{0.75}\text{Ga}_{0.25}\text{Se}_2$ when compared them at the same temperature.

One should keep in mind that the phase diagram shown in Fig. 2.13b is calculated with the temperature-independent interaction parameter. And it does not consider the short-range order existing in the solid solution as well as the phonon contribution to the free energy. Any improvement such as using larger unit cells, a temperature-dependent interaction parameter, a more accurate treatment of the entropy of mixing, a self-consistent determination of the short-range order, and so on can make the calculating phase diagram more accurate.

2.3.3.4 Phase Equilibrium of a CuInSe_2 - CuInS_2 Pseudobinary System

The calculated phase diagram of $\text{CuIn}(\text{Se}_{1-x}\text{S}_x)_2$ alloys is shown in Fig. 2.14, where the miscibility gaps (binodal curves) correspond to the coexistence of two stable phases. Inside the miscibility gaps, the phase separation occurs, and the mixture of two phases of CuInSe_2 and CuInS_2 is stable. Outside the miscibility gaps, single-phase homogeneous $\text{CuIn}(\text{Se}_{1-x}\text{S}_x)_2$ is stable. In this study, the consolute temperature (the critical temperature, above which the components of a mixture are miscible in all proportions), T_C predicted by the conventional cluster expansion without vibrational contribution is 170 K, and the corresponding concentration associated with T_C , X_C is about 0.61 (mole fraction). The miscibility gap is asymmetric. And the result also shows that the CISS alloys can exhibit the phase separation at low temperature; the tendency to phase separation can cause alloy inhomogeneity to some extent. To confirm the calculation method and result, the phase diagram of $\text{Cu}(\text{In}_{1-x}\text{Al}_x)\text{Se}_2$ alloys, in the same way, is calculated and compared with available data reported, as shown in the inset of Fig. 2.14.

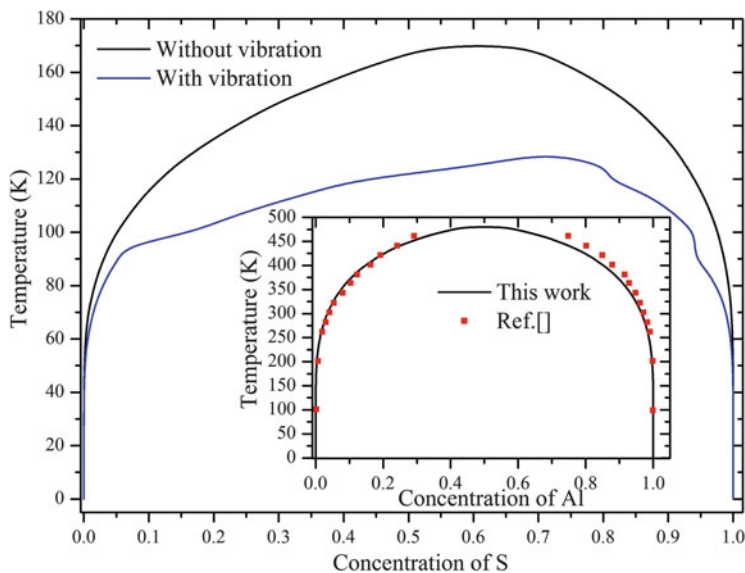


Fig. 2.14 The calculated phase diagrams of $\text{CuIn}(\text{Se}_{1-x}\text{S}_x)_2$ and $\text{Cu}(\text{In}_{1-x}\text{Al}_x)\text{Se}_2$ (inset) alloys

From the inset of Fig. 2.14, one can see that the binodal curve of $\text{Cu}(\text{In}_{1-x}\text{Al}_x)\text{Se}_2$ calculated is in close agreement with the data calculated by Kumagai et al. [18]. And the consolute temperature of $\text{Cu}(\text{In}_{1-x}\text{Al}_x)\text{Se}_2$ alloys is 480 K, only of 20 K higher than the result (460 K) obtained by Kumagai et al. [18]. This indicates that the calculation method is reasonable and the calculated phase diagram of CISS alloys should be reliable. Moreover, the consolute temperature is 170 K for CuInSe_2 - CuInS_2 system, suggesting that CISS alloys are stable at typical growth temperatures. It should be noted that the low temperature of the miscibility gap can partly contribute to the accuracy of the cluster expansion. Because the effective cluster interactions (ECIs) can be modified by considering structures with more atoms, this is likely to influence the calculated phase boundary. However, as the slow atomic diffusion at low temperatures often prevents the direct observation of phase separation, the miscibility gap predicted by first-principles calculations is very likely to be overlooked in the experiments due to low temperature and slow kinetics.

2.3.3.5 Sulfur-Selenium Segregation in $\text{ZnSe}_{1-x}\text{S}_x$: The Role of Lattice Vibration

Phase Diagram of $\text{ZnSe}_{1-x}\text{S}_x$

The phase diagrams of $\text{ZnSe}_{1-x}\text{S}_x$ alloys computed with and without lattice vibration effects are shown in Fig. 2.15, where the miscibility gaps (binodal curves) correspond to the coexistence of two stable phases. Inside the miscibility gaps, the phase separation occurs, and the mixture of two phases of zinc selenide (ZnSe) and zinc sulfide (ZnS) is stable. Outside the miscibility gaps, single-phase homogeneous

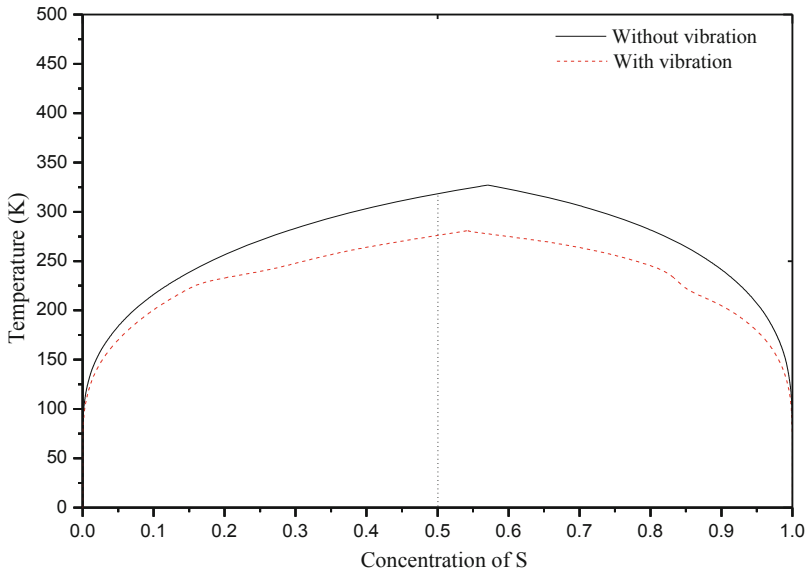


Fig. 2.15 The calculated phase diagram of $\text{ZnSe}_{1-x}\text{S}_x$ alloys

ZnSe_{1-x}S_x is stable. As shown in Fig. 2.15, the consolute temperature T_c predicted without vibrational contribution is 327 K ($x_c = 0.571$ mole fraction). The ZnSe_{1-x}S_x system exhibits slight asymmetry, with maximum closer to the end member ZnS. The result also shows that the ZnSe_{1-x}S_x alloys can exhibit the phase separation at low temperature; the tendency to phase separation can cause alloy inhomogeneity to a certain extent.

Figure 2.15 also explains that the contribution of lattice vibrations reduces the consolute temperature to 281 K ($x_c \approx 0.543$). And the miscibility gap is also asymmetric. The x_c with the vibrational effect (0.543) is smaller than that without the vibrational effect (0.571). The miscibility gap with considering the effect of vibration exhibits subtle increase symmetry than that without considering the effect of vibration. Such results about the critical temperatures are in agreement with the few available experimental findings on the coexistence curves of such alloys and indicate the complete miscibility of the ZnSe_{1-x}S_x system.

Distribution of S and Se Atoms in ZnSe_{1-x}S_x Alloys

As shown in Fig. 2.16, at low temperature, for example, at 250 K, obvious phase separation between ZnS and ZnSe can be observed in ZnSe_{0.5}S_{0.5} alloy, which means that there are two phases in ZnSe_{0.5}S_{0.5} alloy: a rich-S and a poor-Se ZnSe_{1-x}S_x phase. As temperature increasing, ZnSe_{0.5}S_{0.5} becomes more homogeneous especially over 300 K. Similar observation can also be found in the right part of the Fig. 2.16 which shows the spatial distribution of S and Se atoms in ZnSe_{0.5}S_{0.5} alloy with lattice vibration effects.

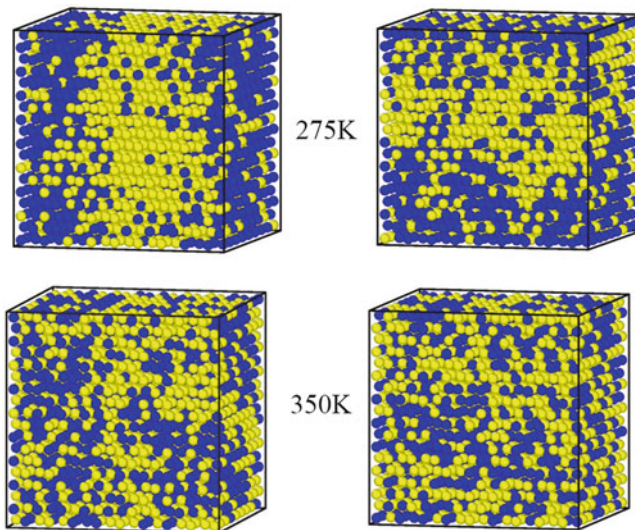


Fig. 2.16 Snapshot of the ZnSe_{0.5}S_{0.5} with (on the right) and without (on the left) lattice vibration effects at the temperature of 275 K and 350 K. Yellow and blue spheres represent S and Se atoms, respectively

2.3.4 Interfaces in Solar Cells

2.3.4.1 $\text{Cu}_2\text{ZnSnS}_4/\text{WZ-ZnO}$ Interface

Interface Structural and Electronic Properties

Figure 2.17a shows the copper zinc tin sulfur/Wurtzite structure zinc oxide ($\text{Cu}_2\text{ZnSnS}_4/\text{WZ-ZnO}$) interface model. The optimized parameters of CZTS/WZ-ZnO interface model are $a = 10.66 \text{ \AA}$, $b = 5.56 \text{ \AA}$, $c = 57.53 \text{ \AA}$. This interface has two possible bonding types (see Fig. 2.1b–c, A1 to B1 or A2 to B2) called model A. The interface distance can be obtained by adopting single point energy calculation method. When the interlayer distance is 2.044 \AA and 2.099 \AA , the model A and the model B interface has the lowest interface total energy, respectively. The binding energy for model A and model B interface system is -0.21 J/m^2 and -0.19 J/m^2 , respectively. The result indicates that model A interface system is slightly more stable than model B interface.

Figure 2.18a shows the total density of states (TDOS) of CZTS (1 0 2)/WZ-ZnO (1 1 0) interface. New electronic states appear near the Fermi level, and these are so-called interface states. Further analysis indicates that the local density of states (LDOS) of CZTS layer 1 and WZ-ZnO layer 1 are contributed to the interface states from 0.5 eV to 0.9 eV . In addition, compared to the LDOS of WZ-ZnO layer 5, the LDOS of WZ-ZnO layer 1 also has a density peak at about -0.7 eV to -0.2 eV .

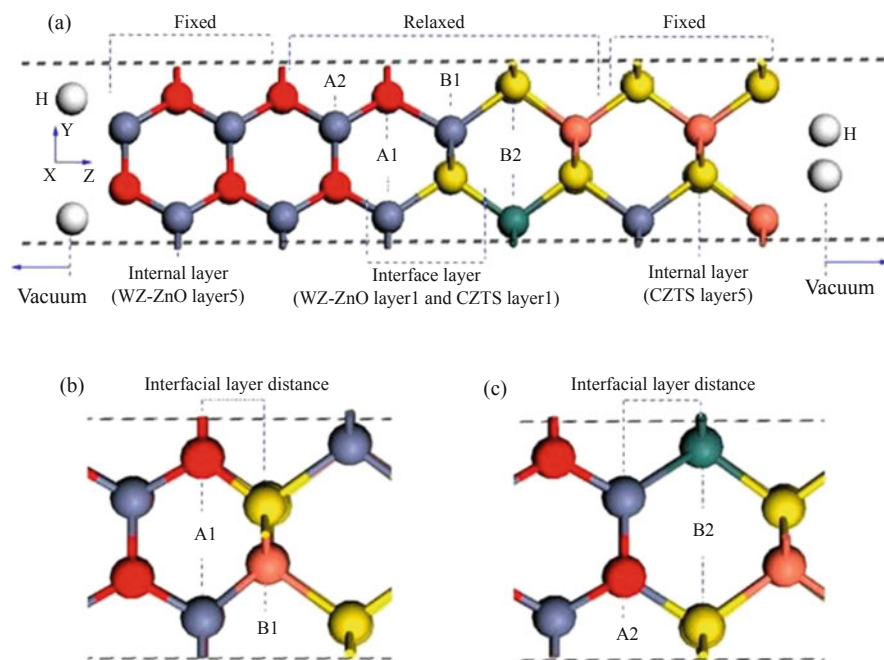


Fig. 2.17 Schematic diagram of CZTS (1 0 2)/WZ-ZnO (1 1 0) interface model (a), the interface bonding style of model A (b) and bonding style of model B (c)

Figure 2.18f–k are the partial density of states (PDOS) of Cu, Zn, Sn, S atoms on CZTS layer 1, respectively. The PDOS of Zn and O atoms on WZ-ZnO layer 1 are shown in Fig. 2.18j and k. There are some hybridizations of Cu-3*d* orbital with S-3*p* orbital from -4.1 eV to -0.2 eV, S-3*p* with Sn-5*s* orbital at about 0.5 eV to 0.9 eV through comparing Fig. 2.18f with i. By comparing Fig. 2.18j with k, we see that Zn-4*s* also has hybridization with O-2*p* from -4.8 eV to -1.5 eV.

Figure 2.19a is the general charge transfer in the interface system. Figure 2.19b is the partially enlarged charge transfer view on the interface. Figures 2.20a and 2.4b is the cross-section difference density charge of CZTS layer1 and WZ-ZnO layer 1 at the interface. The yellow color represents positive (means electron gain), and the mint green color represents negative (means electron loss). The electrons are redistributed on the interface atoms (in Fig. 2.19b), while atoms far away from the interface have less electron transfer than those on the interface (Fig. 2.19a).

Origins of the Interface States

Electron numbers are marked of each atom at the interface after relaxation, as shown in Figs. 2.19b and 2.20a and b. For the bulk CZTS, the S atoms gain about $0.81 e$,

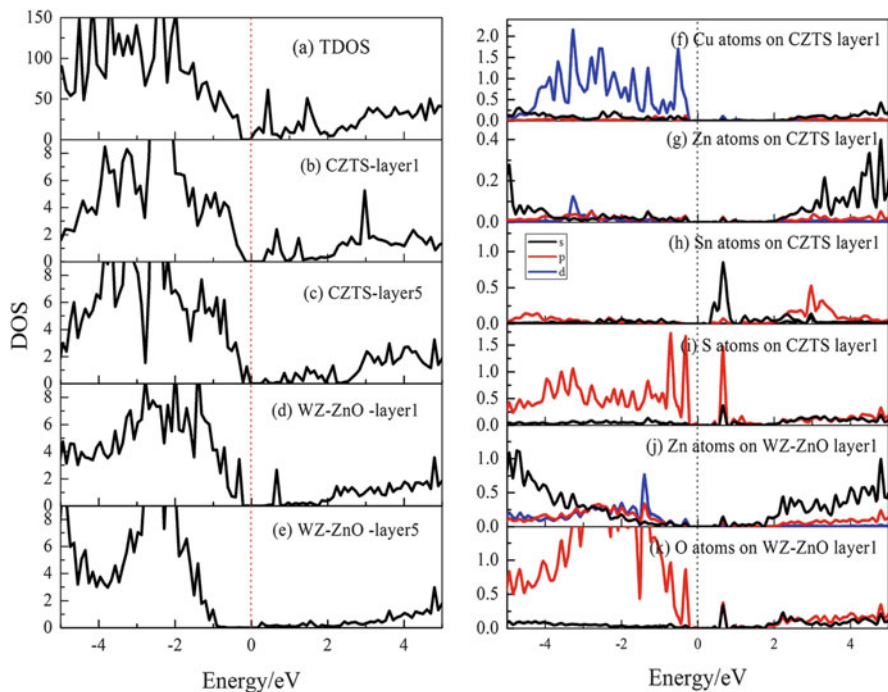


Fig. 2.18 The total density of states of CZTS (1 0 2)/WZ-ZnO (1 1 0) model A interface; local density of states on CZTS layer5 (b) and layer1 (c); local density of states on WZ-ZnO layer 1 (d) and layer 5 (e); partial density of states of Cu (f), Zn (g), Sn (h), S (i) atoms on CZTS layer 1; partial density of states of Zn(j) and O (k) atoms on WZ-ZnO layer1

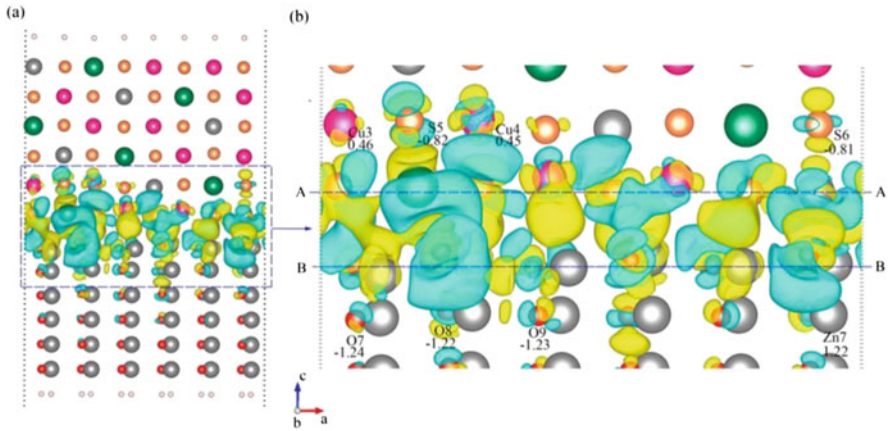


Fig. 2.19 The difference density charge (a); the partial enlarged view of CZTS (1 0 2)/WZ-ZnO (1 1 0) interface (b)

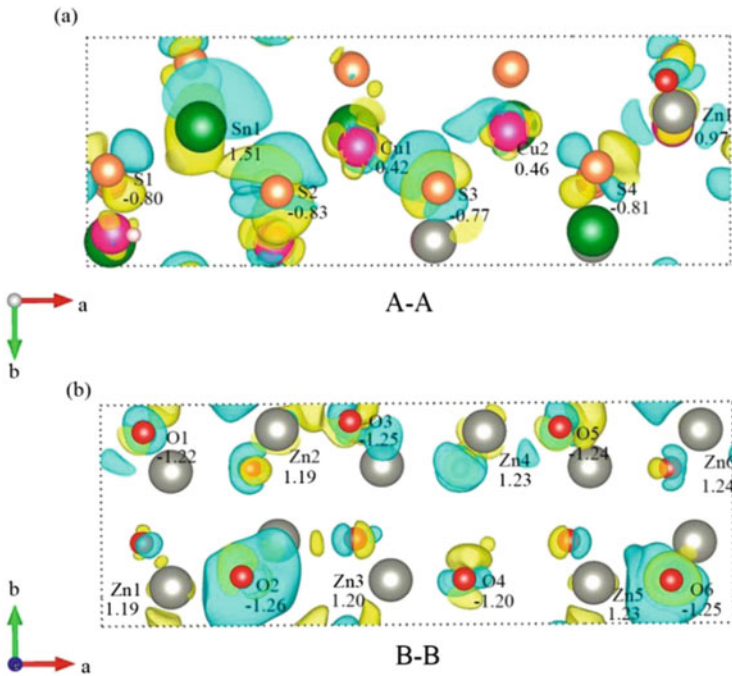


Fig. 2.20 The cross-section difference density charge of CZTS layer1 (a) and WZ-ZnO layer1 (b) at the interface

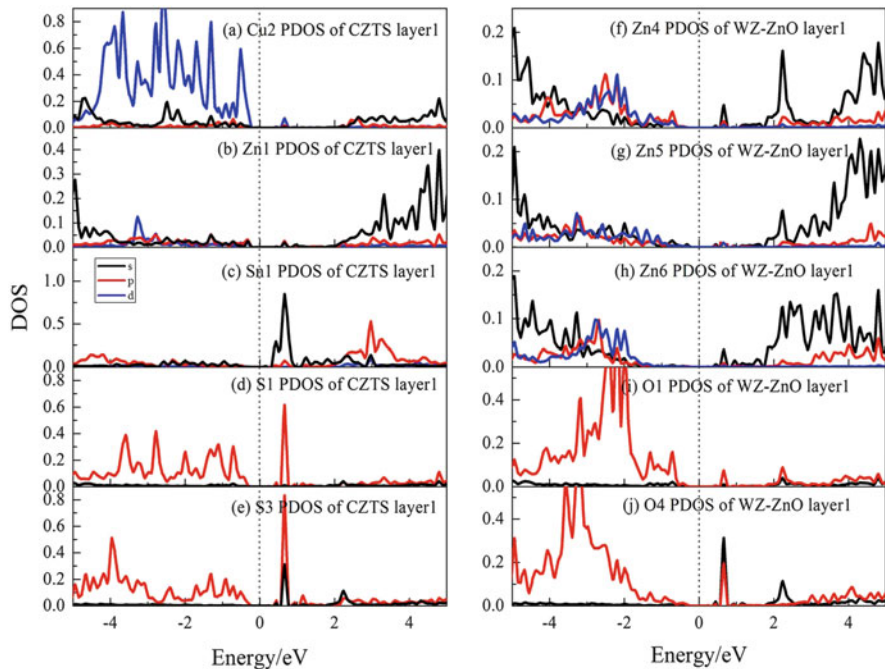


Fig. 2.21 The partial density of states of Cu2 (a), Zn1 (b), Sn1 (c), S1 (d), S3 (e) atom on the CZTS layer1 and O1 (f), O4 (g), Zn4 (h), Zn5 (i), Zn6 (j) atoms on the WZ-ZnO layer1

and Cu, Zn, and Sn atoms lose about 0.45, 0.88, and 1.47 e , respectively. These results indicate that the electron number transferred from Sn atoms to S atoms and from Zn atoms to S atoms is larger than that of Cu atoms to S atoms. Hence, Sn-S and Zn-S bonds are more ionic than Cu-S bonds. In bulk WZ-ZnO, Zn atoms and O atoms lose and gain about 1.23 e , respectively.

From CZTS layer1, Cu, Zn, and Sn atoms lose about 0.42 (or 0.46), 0.97, and 1.51 e , respectively. The S atoms gain about 0.77, 0.80, 0.83, and 0.81 e . These results indicate that the Cu atoms on the CZTS layer 1 lose fewer electrons compared with the corresponds values in the bulk. The Zn atoms on the CZTS layer 1 lose more electrons compared with the corresponds values in the bulk. Most of S atoms on the CZTS layer 1 gain fewer electrons compared with the corresponds values in the bulk. These results show that the Cu-S bonds tend to be more covalent and the Zn-S and Sn-S bonds tend to be more ionic than those in the bulk. Zn and O atoms in the WZ-ZnO layer 1 have almost same Bader's atomic charges as them in the WZ-ZnO bulk. That is to say, the bonding behavior of Zn-O is same as that in WZ-ZnO bulk.

Figure 2.21a–j show the PDOS of Cu2, Zn, Sn, S1, S3, O1, O4, Zn4, Zn5, and Zn6 atoms at the interface. From Fig. 2.21a–e, we can see that on the CZTS layer 1 the interface states are derived from 3d-orbital of Cu2 atom, 5s-orbital of Sn atom,

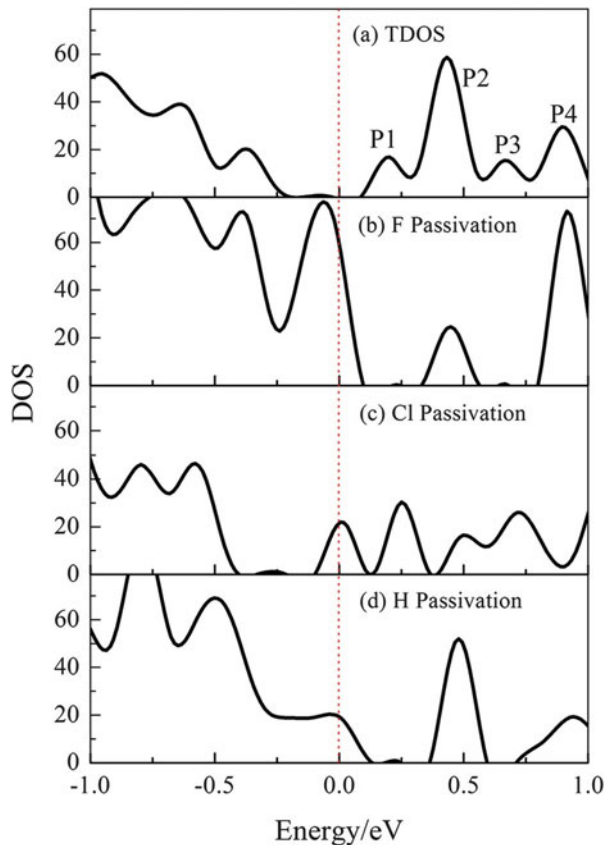
3s-orbital of S1 atom, and 3s- and 3p-orbital of S3 atom, respectively. On the WZ-ZnO side (see Fig. 2.21f–j), the interface states are caused by 4s-orbital of Zn4 and Zn6 atoms, 3d-orbital of Zn5 atom, 2s-orbital of O1 atom, and 2s- and 2p-orbital of O4 atom, respectively.

As discussed above, the model A interface has high-density interface states near the Fermi level. The interface bonding (-0.21 J/m^2) and electron transfers are lower than previous values in Mo/MoSe₂ (-1.2 J/m^2) [49], CuInS₂/MoS₂ (-0.65 J/m^2) [22], and WZ-ZnO/CdS (-0.61 J/m^2) [4, 5] interfaces. From the values of interface bonding energies, the CZTS/WZ-ZnO interface is relatively less stable. The atoms near the interface are not fully bonded with each other. All of these factors lead to CZTS/WZ-ZnO to a poor quality interface for high-efficiency solar cells.

2.3.4.2 Cu₂ZnSnS₄/WZ-ZnO Interface States Passivation Mechanism

Figure 2.22a shows the total density of states (TDOS) of CZTS/WZ-ZnO interface. At the interface, there are four interfacial peaks at about 0.1–1.0 eV, labeled as P1, P2, P3, and P4. These four peaks are mainly derived from Sn and a few from O and S

Fig. 2.22 The total density of states (TDOS) of CZTS/WZ-ZnO interface without passivation (a), and with F (b), Cl (c), and H (d) passivation



atoms on the CZTS first layer. The biggest peak P2 is derived from $5s$ -orbital of Sn atom and $3p$ -orbital of S atom.

Figure 2.22b is the TDOS after F passivation Sn atom on CZTS first layer. It is found that P1 and P3 are removed, and P2 is reduced. However, P4 becomes stronger than that without F passivation. For Cl passivation, it is found that just P2 becomes lower than that without Cl passivation, while P1, P3, and P4 are identical (in Fig. 2.22c). When H atom passivates the interface, P1 and P3 peaks are eliminated, and P2 and P4 peaks are also reduced (in Fig. 2.22d). The results suggest that interfacial density state peaks can be reduced by F, Cl, and H atom passivation. Comparing Figs. 2.22b and d with Fig. 2.22c, we know that the P1 and P3 peaks are removed; the P2 peak is reduced by F and H atoms passivation. While the P1 and P3 peaks are identical, just P2 peak reduced by Cl atom passivation. So, one can make a conclusion that H and F may have a more effective passivation effect than Cl atoms.

The Bader atomic charge and charge density difference are calculated to explore the electron transferring with and without F, Cl, and H passivation. Figure 2.23a shows that the electrons are redistributed on the interface atoms. The Sn atoms lose electrons (mint green color). The Bader atomic charge of Sn atom is 1.47 and 1.51 electrons (e) in bulk CZTS and in CZTS first layer, respectively. After F, Cl, and H passivation, the Bader atomic charge of Sn is 1.59, 1.51, and 1.44 e , respectively. The Bader atomic charge of Sn changes slightly compared with that in the bulk of the interface. The Bader atomic charge of F, Cl, and H atoms are -0.74 , -0.33 , $-0.32 e$, respectively. The results show that F, Cl, and H atoms get about 0.74, 0.33, and 0.32 e after passivation, respectively. The total electrons of the interface are kept unchanging, while the passivation atoms (F, Cl, H) get electrons. Combining the results of Fig. 2.22a–d and Fig. 2.23a–d, it is known that F, Cl, and H can get the electrons of Sn which may lead to interface states. So the interface states can be passivated by F, Cl, and H atoms. The three atoms cannot fully remove the interface states for the new states not only deriving from Sn, but they also from the S and O atoms on CZTS layer 1.

2.4 Conclusions

This chapter summarized some simulations by first-principles calculations for CuInGaSe_2 (CIGS) solar cell materials. Under high pressure, upon doping, the lattice structure and mechanics, the optical, and the electrical properties were provided. In addition, interface states in CuInGaSe_2 thin-film solar cell were investigated to maximally weaken the negative impacts of interface states. The local structures and electronic properties of the interfaces were calculated. These simulations are helpful to understand the relationship between the local structures and the local atomic distribution in the solar cell materials and near the interfaces and are also useful to reveal the micro-mechanism of photoelectric changes introduced by interface states. These chapter indicates that the theoretical calculation becomes a powerful tool to understanding and to improving the CuInGaSe_2 solar cell's performances.

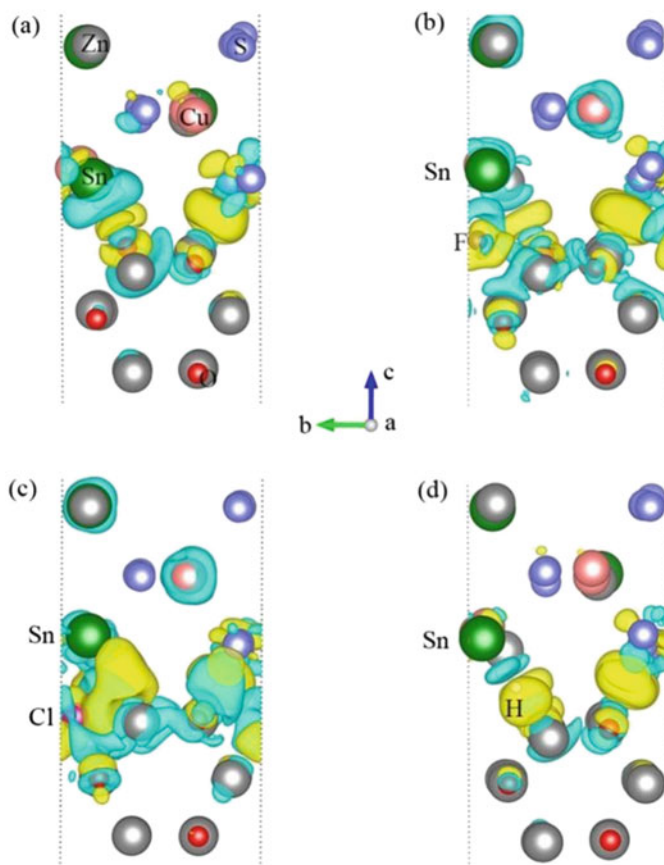


Fig. 2.23 The charge density difference for an interface without passivation (a) and with F (b), Cl (c), and H (d) passivation

Acknowledgments This work was financially supported by the National Natural Science Foundation of China (10964003, 11164014, and 11364025), the Petroleum Research Fund of the American Chemical Society (53827-UR10), and the Robert Welch Foundation (Departmental Grant, AC-0006).

The work in this chapter was performed in the Gansu Supercomputer Center. F.-L. Tang was financially supported by the Chinese Scholarship Council (201408625041). The authors thank the editors in allowing us to extend our previously published works as in the references.

References

1. W. Bao, M. Ichimura, Band offsets at the ZnO/Cu₂ZnSnS₄ interface based on the first principles calculation. *Jpn. J. Appl. Phys.* **52**, 061203 (2013)
2. P.E. Blöchl, O. Jepsen, O.K. Andersen, Improved tetrahedron method for Brillouin-zone integrations. *Phys. Rev. B* **49**, 16223 (1994)
3. I.V. Bodnar, I.N. Tsyrelchuk, I.A. Victorov, Preparation and analysis of the CuAl_xIn_{1-x}Se₂ solid solutions. *J. Mater. Sci. Lett.* **13**, 762–764 (1994)

4. Y.W. Cheng, F.L. Tang, H.T. Xue, et al., Bonding and electronic properties of the $\text{Cu}_2\text{ZnSnS}_4/\text{WZ-ZnO}$ interface from first-principles calculations. *J. Phys. D. Appl. Phys.* **49**, 285107 (2016)
5. Y.W. Cheng, F.L. Tang, H.T. Xue, et al., First-principles study on electronic properties and lattice structures of WZ-ZnO/CdS interface. *Mater. Sci. Semicond. Process.* **45**, 9–16 (2016)
6. Y.W. Cheng, F.L. Tang, H.T. Xue, et al., Passivation for $\text{Cu}_2\text{ZnSnS}_4/\text{WZ-ZnO}$ interface states: from the first principles calculations. *Appl. Surf. Sci.* **394**, 58–62 (2017)
7. J.W.D. Connolly, A.R. Williams, Density-functional theory applied to phase transformations in transition-metal alloys. *Phys. Rev. B* **27**, 5169 (1983)
8. Z. Derkaoui, Z. Kebbab, R. Miloua, et al., Theoretical study of optical characteristics of multilayer coatings ZnO/CdS/CdTe using first-principles calculations. *Solid State Commun.* **149**, 1231–1235 (2009)
9. Z.Y. Dong, Y.F. Li, B. Yao, et al., An experimental and first-principles study on band alignments at interfaces of $\text{Cu}_2\text{ZnSnS}_4/\text{CdS/ZnO}$ heterojunctions. *J. Phys. D. Appl. Phys.* **47**, 075304 (2014)
10. M. Engelmann, B.E. McCandless, R.W. Birkmire, Formation and analysis of graded $\text{CuIn}(\text{Se}_{1-y}\text{S}_y)_2$ films. *Thin Solid Films* **387**, 14–17 (2001)
11. Y.N. Gornostyrev, M.I. Katsnelson, N.I. Medvedeva, et al., Peculiarities of defect structure and mechanical properties of iridium: results of ab initio electronic structure calculations. *Phys. Rev. B* **62**, 7802 (2000)
12. T. Hong, J.R. Smith, D.J. Srolovitz, Adhesion at a heterophase interface: first-principles study of $\text{Mo}(001)/\text{MoSi}_2(001)$. *Interface Sci.* **1**, 223–235 (1994)
13. G.Y. Huang, C.Y. Wang, J.T. Wang, Detailed check of the LDA+U and GGA+U corrected method for defect calculations in wurtzite ZnO . *Comput. Phys. Commun.* **183**, 1749–1752 (2012)
14. B. Huang, S. Chen, H.X. Deng, et al., Origin of reduced efficiency in Cu(In, Ga)Se_2 solar cells with high Ga concentration: alloy solubility versus intrinsic Defects. *IEEE J. Photovoltaics* **4**, 477–482 (2014)
15. G. Kresse, J. Furthmüller, Efficiency of ab-initio total energy calculations for metals and semiconductors using a plane-wave basis set. *Comput. Mater. Sci.* **6**, 15–50 (1996)
16. G. Kresse, J. Furthmüller, Efficient iterative schemes for ab initio total-energy calculations using a plane-wave basis set. *Phys. Rev. B* **54**, 11169 (1996)
17. G. Kresse, D. Joubert, From ultrasoft pseudopotentials to the projector augmented-wave method. *Phys. Rev. B* **59**, 1758 (1999)
18. Y. Kumagai, Y. Soda, F. Oba, et al., First-principles calculations of the phase diagrams and band gaps in $\text{CuInSe}_2\text{-CuGaSe}_2$ and $\text{CuInSe}_2\text{-CuAlSe}_2$ pseudobinary systems. *Phys. Rev. B* **85**, 033203 (2012)
19. X.K. Li, H.T. Xue, F.L. Tang, et al., First-principles calculation of sulfur-selenium segregation in $\text{ZnSe}_{1-x}\text{S}_x$: the role of lattice vibration. *Mater. Sci. Semicond. Process.* **39**, 96–102 (2015)
20. Y. Liu, M.R. Halfmoon, C.A. Rittenhouse, et al., Passivation effects of fluorine and hydrogen at the SiC-SiO_2 interface. *Appl. Phys. Lett.* **97**, 242111 (2010)
21. X. Liu, H. Cui, W. Li, et al., Improving $\text{Cu}_2\text{ZnSnS}_4$ (CZTS) solar cell performance by an ultrathin ZnO intermediate layer between CZTS absorber and Mo back contact. *Phys. Status Solidi (RRL)-Rapid Res. Lett.* **8**, 966–970 (2014)
22. H.X. Liu, F.L. Tang, H.T. Xue, et al., Lattice structures and electronic properties of $\text{WZ-CuInS}_2/\text{MoS}_2$ interface from first-principles calculations. *Appl. Surf. Sci.* **351**, 382–391 (2015)
23. C.D.R. Ludwig, T. Gruhn, C. Felser, et al., Indium-Gallium Segregation in $\text{CuIn}_x\text{Ga}_{1-x}\text{Se}_2$: an ab initio-based Monte Carlo study. *Phys. Rev. Lett.* **105**, 025702 (2010)
24. F.D. Murnaghan, The compressibility of media under extreme pressures. *Proc. Natl. Acad. Sci.* **30**, 244–247 (1944)
25. J.P. Perdew, K. Burke, M. Ernzerhof, Generalized gradient approximation made simple. *Phys. Rev. Lett.* **77**, 3865 (1996)
26. J. Pohl, K. Albe, Thermodynamics and kinetics of the copper vacancy in CuInSe_2 , CuGaSe_2 , CuInS_2 , and CuGaS_2 from screened-exchange hybrid density functional theory. *J. Appl. Phys.* **108**, 023509 (2010)
27. B. Puchala, A. Van der Ven, Thermodynamics of the Zr-O system from first-principles calculations. *Phys. Rev. B* **88**, 094108 (2013)

28. J. Sandino, E. Romero, J.S. Oyola, et al., Study of the Mo/CuInS₂/ZnS system by TEM. *Sol. Energy Mater. Sol. Cells* **95**, 2006–2009 (2011)
29. C.J. Sheppard, V. Alberts, Deposition of single-phase CuIn(Se, S)₂ thin films from the sulfurization of selenized CuIn alloys. *J. Phys. D. Appl. Phys.* **39**, 3760 (2006)
30. C.J. Sheppard, V. Alberts, W.J. Bekker, Deposition of CuIn(Se, S)₂ thin films by sulfurization of selenized Cu/In alloys. *Phys. Status Solidi B* **201**, 2234–2238 (2004)
31. C.J. Sheppard, V. Alberts, J.R. Botha, Structural and optical characterization of single-phase CuIn(Se, S)₂ thin films deposited using a two-step process. *Phys. Status Solidi C* **5**, 641–644 (2008)
32. F.L. Tang, Z.X. Zhu, H.T. Xue, et al., Optical properties of Al-doped CuInSe₂ from the first principle calculation. *Physica B* **407**, 4814–4818 (2012)
33. Y. Tani, K. Sato, H. Katayama-Yoshida, Materials design of spinodal nanodecomposition in CuIn_{1-x}Ga_xSe₂ for high-efficiency solar energy conversion. *Appl. Phys. Express* **3**, 101201 (2010)
34. T. Tinoco, C. Rincón, M. Quintero, et al., Phase diagram and optical energy gaps for CuIn_yGa_{1-y}Se₂ alloys. *Phys. Status Solidi A* **124**, 427–434 (1991)
35. T. Tinoco, J.P. Itié, A. Polian, et al., Combined x-ray absorption and x-ray diffraction studies of CuGaS₂, CuGaSe₂, CuFeS₂ and CuFeSe₂ under high pressure. *J. Phys. IV* **4**, 151–154 (1994)
36. S. Tomić, L. Bernasconi, B.G. Searle, et al., Electronic and optical structure of wurtzite CuInS₂. *J. Phys. Chem. C* **118**, 14478–14484 (2014)
37. A. Van De Walle, M. Asta, G. Ceder, The alloy theoretic automated toolkit: a user guide. *Calphad* **26**, 539–553 (2002)
38. W. Wang, K. Xiong, G. Lee, et al., Origin of HfO₂/GaAs interface states and interface passivation: a first-principles study. *Appl. Surf. Sci.* **256**, 6569–6573 (2010)
39. J.H. Werner, J. Mattheis, U. Rau, Efficiency limitations of polycrystalline thin film solar cells: case of Cu(In, Ga)Se₂. *Thin Solid Films* **480**, 399–409 (2005)
40. H.T. Xue, W.J. Lu, Z.X. Zhu, et al., Al-doped CuInSe₂: an ab initio study of structural and electronic properties of photovoltaic material. *Adv. Mater. Res.* **512**, 1543–1547 (2012)
41. H.T. Xue, F.L. Tang, W.J. Lu, et al., First-principles investigation of structural phase transitions and electronic properties of CuGaSe₂ up to 100GPa. *Comput. Mater. Sci.* **67**, 21–26 (2013)
42. H.T. Xue, W.J. Lu, F.L. Tang, et al., Phase diagram of the CuInSe₂-CuGaSe₂ pseudobinary system studied by combined *ab initio* density functional theory and thermodynamic calculation. *J. Appl. Phys.* **116**, 053512 (2014)
43. H.T. Xue, F.L. Tang, T. Gruhn, et al., Generalized stacking fault energies, cleavage energies, ionicity and brittleness of Cu(Al/Ga/In)Se₂ and CuGa(S/Se/Te)₂. *Model. Simul. Mater. Sci. Eng.* **22**, 035002 (2014)
44. H.T. Xue, F.L. Tang, X.K. Li, et al., Phase equilibrium of a CuInSe₂-CuInS₂ pseudobinary system studied by combined first-principles calculations and cluster expansion Monte Carlo simulations. *Mater. Sci. Semicond. Process.* **25**, 251–257 (2014)
45. H.T. Xue, F.L. Tang, F.Z. Zhang, et al., Effect of temperature on the distribution and inhomogeneity degree of Se-S atoms in CuIn(Se_{1-x}S_x)₂ alloys. *J. Phys. D. Appl. Phys.* **49**, 025101 (2016)
46. H.T. Xue, F.L. Tang, F.Z. Zhang, et al., Temperature effects on distribution and inhomogeneous degree of In-Ga atoms in CuIn_{1-x}Ga_xSe₂ alloys. *Mater. Lett.* **164**, 169–171 (2016)
47. Y. Yan, R. Noufi, K.M. Jones, et al., Chemical fluctuation-induced nanodomains in Cu(In, Ga)Se₂ films. *Appl. Phys. Lett.* **87**, 121904 (2005)
48. G. Yang, Y.F. Li, B. Yao, et al., Band alignments at the interface of Cu₂ZnSnS₄/ZnO heterojunction: an X-ray photoelectron spectroscopy and first-principles study. *J. Alloys Compd.* **628**, 293–297 (2015)
49. Y. Zhang, F.L. Tang, H.T. Xue, et al., Lattice structures and electronic properties of Mo/MoSe₂ interface from first-principles calculations. *Phys. E.* **66**, 342–349 (2015)
50. J.G. Zhou, D.M. Causon, C.G. Mingham, et al., The surface gradient method for the treatment of source terms in the shallow-water equations. *J. Comput. Phys.* **168**, 1–25 (2001)



Design of Photovoltaics-Based Manufacturing System Using Computer-Aided Design

3

José Ezequiel Santibañez-Aguilar, Sergio Castellanos, Benjamin B. Shapiro, Douglas M. Powell, Ian M. Peters, Tonio Buonassisi, Daniel M. Kammen, and Antonio Flores-Tlacuahuac

Contents

3.1	Introduction	76
3.2	Photovoltaic (PV) Manufacturing System Design	77
3.3	The Mathematical Formulation for the PV Manufacturing System Design	79
3.4	Uncertainty in PV Manufacturing Systems Design	82
3.5	Adjust of Important Functions for the PV Manufacturing System	83
3.6	Influence of Tariff Level in the PV Manufacturing System Topology	85
3.7	Conclusions	87
	References	88

Author Contribution

The first draft was written by Santibañez-Aguilar J. E. and subsequently reviewed by Castellanos S. The final draft was reviewed by the remaining authors.

J. E. Santibañez-Aguilar (✉) · A. Flores-Tlacuahuac
School of Engineering and Science, Tecnológico de Monterrey, Monterrey, Mexico
e-mail: santibanez.ezequiel@tec.mx

S. Castellanos · D. M. Kammen
Energy and Resources Group and Berkeley Energy and Climate Institute, University of California, Berkeley, USA

B. B. Shapiro
E3 Consulting, San Francisco, CA, USA

D. M. Powell
Golman School of Public Policy, University of California, Berkeley, CA, USA

I. M. Peters
MIT Photovoltaic Research Laboratory, Cambridge, MA, USA

T. Buonassisi
Massachusetts Institute of Technology, Massachusetts Avenue, Cambridge, MA, USA

Abstract

Carbon dioxide has increased drastically in the last decades due to energy production, exacerbating the global warming problem. To address this issue, researchers have focused on developing energy production technologies from renewable sources. From the renewable energy sources, solar has shown great promise chiefly due to its high availability. The conversion of solar energy into electricity (photovoltaics) requires specialized equipment such as solar cells, and a coordinated supply chain to be able to manufacture this technology in a sustainable way and at low cost. Therefore, this chapter proposes an approach based on mathematical programming for the optimal design of a solar photovoltaics manufacturing system considering diverse criteria linked to economic and environmental variables such as minimum sustainable price, transportation costs, and technical limits. In addition, the dependence of the minimum sustainable price over inflation, electricity price, and weighted average capital cost is analyzed, showing that a variation of minimum sustainable price could significantly change the manufacturing supply chain topology.

3.1 Introduction

Due to an increase in worldwide energy demand and high associated emissions, solar energy has become an attractive low-emission alternative to satisfy electricity demands, due in part to its high availability and null operational emissions. In fact, Michael et al. [1] stated that the total energy consumed in 1 year is lower than 1 h of solar energy. In addition, solar energy has been used mainly by photovoltaic (PV) generation systems [2], with the PV having increased around 40% in recent years as was mentioned by Razykov et al. [3] and Maycock [4]. Furthermore, Loomis et al. [5] reported an increase of 39% between 2013 and 2014 in the United States; nevertheless, other countries, such as China, have increased their PV installations even at higher rates.

Historically, one of the main barriers for solar PV deployment has been its relative high costs. However, significant cost reductions have been recently achieved; for instance, cost for first generation of solar cells rounded \$US 3.50/W, and recently this cost has reached \$US 0.50/W [6]. This cost reduction has been caused by a global expansion of the solar energy industry [7]. Such global expansion in deployment and manufacturing consists of optimally producing in a country, while obtaining the different input materials from within, or abroad, and selling the goods also either locally or abroad. In this sense, manufacturing costs and tariffs imposed by countries play a crucial role in the design of the manufacturing supply chain system design. Several studies have proposed different approaches to address the PV manufacturing systems design to satisfy the present and future requirements for the PV industry. For instance, Powell et al. [8] developed a model to obtain the minimum sustainable price (MSP) of a virtually integrated manufacturing company considering the factory capital expenditure, internal rate of return, and weighted

average capital cost (WACC), among other variables, in a given PV manufacturing system. Loomis and Aldeman [5] considered different PV systems under several production capacities to examine the number of jobs and the economic impact associated with the manufacturing system. Kim and Jeong [2] developed two models to help PV system establish supply chain planning to choose recycling policies under several circumstances. Nevertheless, most of the previous approaches do not consider the interactions between different countries which ought to include tariffs, typically used to protect small or local industries.

There are some works that have considered the interaction between different countries in PV manufacturing system. For example, Castellanos et al. [9] developed a techno-economic tool and strategy for the PV manufacturing system design considering the diverse value of tariff and transportation cost. Such approach allows for the evaluation of different tariff values between several countries, but important factors such as inflation or electricity price are considered constant. Under some situations, however, the deterministic solutions could be infeasible or suboptimal; hence, uncertainty analysis should be accounted for in supply chain analysis and design. Furthermore, uncertainty in economic parameters could seriously affect the manufacturing system performance since economic parameters are subject to variations due to both global and domestic issues (see [10] and [11]).

Regarding uncertainty in a PV manufacturing system, Dehghani et al. [12] developed an approach for the planning of PV supply chains considering uncertainty in the demand of annual solar energy, where uncertainty was taken into account via the generation of different scenarios. Similarly, Dehghani et al. [13] took into account diverse economic terms as uncertain parameters. Some of these uncertain parameters were the unit manufacturing cost and the unit inventory cost. However, no explicit consideration of the tariff between different countries was implemented [12, 13], which might be a drawback of the paper because the tariff level could affect strongly the final supply chain topology, as seen in Castellanos et al. [9].

As seen, works that have analyzed the PV manufacturing system design through mathematical models have considered diverse aspects such as tariff levels, manufacturing costs, and MSP computing, the interaction between different countries, and uncertainty in economic parameters. Most of them have used tools based on mathematical programming and other tools to evaluate important contributions in the PV manufacturing system design area. Therefore, this chapter presents a part of the model by Castellanos et al. [9] as well as alternatives to consider the uncertainty in that model through diverse computational tools.

3.2 Photovoltaic (PV) Manufacturing System Design

A solar PV module is composed of diverse components, such as the raw material (silicon) which is transformed into wafers, processed afterwards into cells, and assembled into the modules. All these processes are parts of a manufacturing system, which is affected by global and domestic factors.

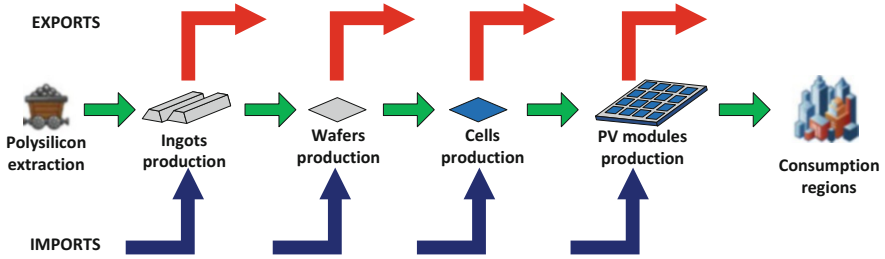


Fig. 3.1 General representation of the proposed PV manufacturing system

This chapter shows a mathematical programming model for analyzing the manufacturing design of PV modules considering external factors such as tariff due to exports and imports, inflation and electricity price, as well as internal factors such as transportation cost, manufacturing cost, and product and raw material prices, akin to that developed in Castellanos et al. [9], and expanded to incorporate uncertainty in a variety of values. Figure 3.1 shows a general representation of the proposed PV manufacturing system. The proposed photovoltaic manufacturing system takes into account silicon extraction and processing, ingots, wafers, solar cells, and PV modules production. The manufacturing system considers the interaction between local and global markets through exports and imports for all products (silicon, ingots, wafers, cells, and PV modules).

Once the PV manufacturing system is defined, the design problem can be stated as follows:

Given:

- Potential locations (global and local) for the manufacturing system's facilities
- Data for lower and upper bounds for electricity cost expected inflation and was a factor
- Distance between the potential manufacturing system nodes
- Transportation cost data for final and intermediate products
- Minimum sustainable price (MSP) dependence over processing capacity for each processing activity
- Data for demand regarding each product

Subject to:

- Constraints based on material balances for each manufacturing system node
- Limits for processing, transportation, exports, and imports in order to promote local production
- Constraints to define if exports are permitted

It is possible to obtain:

- The optimal manufacturing system topology (optimal selection for supply chain locations nodes)
- Production capacity value (W) for the different selected processing nodes
- Capacities (W) of manufactured goods to transport, export and import

It should be noted that the manufacturing system design can be obtained by optimizing one or several objective functions at once. These objective functions can be defined and selected depending on the focus to improve upon: whether economic, environmental, social, or technical performance.

3.3 The Mathematical Formulation for the PV Manufacturing System Design

The mathematical formulation for the PV manufacturing system requires a formulation of the mass balances at each node of the manufacturing system (i.e., polysilicon extraction and processing, ingots, wafers, cells, and PV modules manufacturing).

Equation (3.1) describes the balance in polysilicon extraction nodes with an inventory level at time t equal to previous inventory level, plus the amount of extracted polysilicon, minus the total polysilicon distributed to the international and domestic ingot producer nodes.

$$M_{n0,t}^{\text{inventory}} = M_{n0,t-1}^{\text{inventory}} + \left(- \sum_{n1 \in N1} M_{n0,n1,t}^{\text{outlet-local}} - \sum_{e1 \in E1} M_{j,e1,t}^{\text{export-international}} \right), \quad \forall n0 \in N0, t \in T \quad (3.1)$$

Besides, Eq. (3.2) can be generalized for the ingot, wafer, cell, and PV modules production nodes. In this case, the nodes receive raw material from previous nodes, which can be sent to processing to obtain the good in which the nodes are specialized (ingots, wafers, cells, and PV modules)

$$G_{j,t}^{\text{inventory}} = G_{j,t-1}^{\text{inventory}} + \left(\sum_{i \in \text{PREVIOUS}} G_{i,j,t}^{\text{inlet-local}} + \sum_{ei \in \text{EXPREVIOUS}} G_{ei,j,t}^{\text{import-international}} - G_{j,t}^{\text{toprocessing-local}} \right), \quad \forall_{t \in T}^{j \in \text{NODE}} \quad (3.2)$$

Alike, Eq. (3.3) is used to model the production of ingots, wafer, cell, and PV modules production nodes. In this sense, the nodes can produce a given good, which can be distributed to international nodes or used for domestic production.

$$G_{j,t}^{\text{inventory}} = G_{j,t-1}^{\text{inventory}} + \left(- \sum_{k \in \text{NEXT}} G_{j,k,t}^{\text{outlet-local}} - \sum_{ek \in \text{EXTNEXT}} G_{j,ek,t}^{\text{export-international}} - G_{j,t}^{\text{produced-local}} \right), \forall_{\substack{j \in \text{NODE} \\ t \in T}} \quad (3.3)$$

As shown in Eq. (3.4), other constraints are focused in including constraints that limit transportation, production, and imports and exports. Constraints in exports limit the amount of exported good and is equal to zero when the good's MSP, plus the imposed tariff and unit transportation cost for the locally produced good, is greater than the good's price plus the imposed tariff and unit transportation cost for the externally produced good. Otherwise, the amount of exported goods could take values between zero and a maximum limit.

$$\left[\begin{array}{c} Y_{j,ek}^{\text{exported-good}} \\ \frac{MSP_{j,ek}^{\text{exported-good}} \cdot (1 + \text{Tariff}_{j,ek}^{\text{exported-good}}) + TC_{j,ek}^{\text{exported-good}} \cdot d_{j,ek}}{\sum_{ej} \frac{MSP_{ej,ek}^{\text{global-good}} \cdot (1 + \text{Tariff}_{ej,ek}^{\text{global-good}}) + TC_{ej,ek}^{\text{global-good}} \cdot d_{ej,ek}}{\text{Total global nodes } EJ}} \\ G_{j,ek,t}^{\text{exported-good}} \leq \text{Max } G_{j,ek,t}^{\text{exported-good}} \end{array} \right] \quad \forall \begin{array}{l} j \in \text{Node} \\ \forall ek \in \text{Node} - \text{to} - \text{Export} \\ t \in T \end{array}$$

$$\vee$$

$$\left[\begin{array}{c} \neg Y_{j,ek}^{\text{exported-good}} \\ \frac{MSP_{j,ek}^{\text{exported-good}} \cdot (1 + \text{Tariff}_{j,ek}^{\text{exported-good}}) + TC_{j,ek}^{\text{exported-good}} \cdot d_{j,ek}}{\sum_{ej} \frac{MSP_{ej,ek}^{\text{global-good}} \cdot (1 + \text{Tariff}_{ej,ek}^{\text{global-good}}) + TC_{ej,ek}^{\text{global-good}} \cdot d_{ej,ek}}{\text{Total global nodes } EJ}} \\ G_{j,ek,t}^{\text{exported-good}} = 0 \end{array} \right] \quad (3.4)$$

In Eqs. (3.1), (3.2), (3.3), and (3.4), index j represents supply chain nodes in which the balance is carried out. Indexes i and ei represent the processing stage previous to stage j . Indexes k and ek represent the following processing stage in the PV manufacturing system.

Further equations ought to be considered in the mathematical model to introduce decision variables or objective functions for the PV manufacturing system.

Equation (3.5) depicts the global MSP, which takes into account the MSP for each node in the manufacturing system. Note that global MSP considers only the terms with a real contribution to the PV manufacturing system, such that if a processing

node is not used, then that processing node does not contribute to the global MSP calculated.

$$MSP^{global} = \sum_{n0} MSP_{n0}^{Step0} + \sum_{n1} MSP_{n1}^{Step1} + \sum_{n2} MSP_{n2}^{Step2} + \sum_{n3} MSP_{n3}^{Step3} + \sum_{n4} MSP_{n4}^{Step4} \quad (3.5)$$

Equation (3.6) states the transportation cost to markets considering the unit transportation cost from local and international processing plants to their end markets, considering the distance and the amount of transported goods.

$$TC^{Markets} = \sum_{n4} \sum_{n5} TP_{n4,n5}^{local-PV} \cdot d_{n4,n5}^{local} \cdot TC^{local-markets} + \sum_{e4} \sum_{n5} TP_{e4,n5}^{international-PV} \cdot d_{e4,n5}^{international} \cdot TC^{international-markets} \quad (3.6)$$

Total local production, given in Eq. (3.7), is considered because the local manufacturing system can manufacture in each processing stage.

$$P^{Local} = P^{Local-Si} + P^{Local-ingot} + P^{Local-wafer} + P^{Local-cells} + P^{Local-PV} \quad (3.7)$$

In addition, export costs account for the transportation costs caused by exporting goods (ingots, silicon, wafers, or cells) and the associated tariff, as described in Eq. (3.8).

$$TC^{Exports} = \sum_{n0} \sum_{e1} TC_{n0,e1}^{Export-Si} + \sum_{n1} \sum_{e2} TC_{n1,e2}^{Export-ingot} + \sum_{n2} \sum_{e3} TC_{n2,e3}^{Export-wafer} + \sum_{n3} \sum_{e4} TC_{n3,e4}^{Export-cells} \quad (3.8)$$

Furthermore, the PV manufacturing system considers import costs along with the transportation costs for imported materials (ingots, silicon, wafers, or cells), and paid tariffs due to the amount and type of exported materials, as shown in Eq. (3.9).

$$TC^{Imports} = \sum_{e0} \sum_{n1} TC_{e0,n1}^{Imports-Si} + \sum_{e1} \sum_{n2} TC_{e1,n2}^{Imports-ingot} + \sum_{e2} \sum_{n3} TC_{e2,n3}^{Imports-wafer} + \sum_{e3} \sum_{n4} TC_{e3,n4}^{Imports-cells} \quad (3.9)$$

Equation (3.10) states that total local transportation costs are equal to the sum of transportation costs between internal nodes which consists of a unitary transportation cost multiplied by the distance between involved nodes and the transported amount of material.

$$\begin{aligned}
TC^{Local} = & \sum_{n0} \sum_{n1} TP_{n0,n1}^{Local-Si} \cdot d1_{n0,n1}^{Local} \cdot TC_{n0,n1}^{Local-Si} \\
& + \sum_{n1} \sum_{n2} TP_{n1,n2}^{Local-ingot} \cdot d2_{n1,n2}^{Local} \cdot TC_{n1,n2}^{Local-ingot} \\
& + \sum_{n2} \sum_{n3} TP_{n2,n3}^{Local-wafer} \cdot d3_{n2,n3}^{Local} \cdot TC_{n2,n3}^{Local-wafer} \\
& + \sum_{n3} \sum_{n4} TP_{n3,n4}^{Local-cells} \cdot d4_{n3,n4}^{Local} \cdot TC_{n3,n4}^{Local-cells}
\end{aligned} \tag{3.10}$$

The decision variable could be grouped in a single objective function to get the optimal PV manufacturing system topology. Each of the decision variables can be included in a compromise function considering different priorities between them. A compromise function has been formulated for different problems with several objectives in works such as those by Castellanos et al. [9], Sanchez-Bautista et al. [14], and Fuentes-Cortes et al. [15]. Taking into account the decision variables presented in Eqs. (3.5), (3.6), (3.7), (3.8), (3.9), and (3.10), the compromise function is given in Eq. (3.11) as follows:

$$\begin{aligned}
OF^{composed} = & +\omega_{MSP} \cdot \frac{Upper\ MSP^{global} - MSP^{global}}{Upper\ MSP^{global} - Lower\ MSP^{global}} \\
& + \omega_{TCM} \cdot \frac{Upper\ TC^{Markets} - TC^{Markets}}{Upper\ TC^{Markets} - Lower\ TC^{Markets}} \\
& + \omega_{LP} \cdot \frac{P^{Local} - Lower\ P^{Local}}{Upper\ P^{Local} - Lower\ P^{Local}} \\
& + \omega_{TCE} \cdot \frac{Upper\ TC^{Exports} - TC^{Exports}}{Upper\ TC^{Exports} - Lower\ TC^{Exports}} \\
& + \omega_{TCI} \cdot \frac{Lower\ TC^{Imports} - TC^{Imports}}{Upper\ TC^{Imports} - Lower\ TC^{Imports}} \\
& + \omega_{LTC} \cdot \frac{Upper\ TC^{Local} - TC^{Local}}{Upper\ TC^{Local} - Lower\ TC^{Local}}
\end{aligned} \tag{3.11}$$

Equation (3.11) considers the normalized terms to limit the values of the objective function; in this way, if the target value for all decision variables is obtained, then the compromise solution tends toward 1, otherwise the value of the compromise solution would be near to zero 0.

3.4 Uncertainty in PV Manufacturing Systems Design

Works such as Dehghani et al. [12, 13] have considered uncertainty in diverse parameters when designing PV manufacturing systems. These works included uncertainty through diverse scenarios for economic terms as well as solar energy demand. Nevertheless, the uncertainty element could also be considered in other important parameters such as

Table 3.1 Upper and lower bounds for inflation, WACC, and electricity price

	Upper bound	Lower bound	Units
Inflation	0.07	0.02	%
WACC	0.16	0.08	Dimensionless
Electricity price	0.20	0.02	\$US/kWh

inflation, electricity price, and WACC, since these parameters directly (and indirectly) affect manufacturing cost, raw material prices, MSP, and other economic terms.

Therefore, a methodology based on mathematical programming could consider the generation of several scenarios such as weighted-average cost of capital (WACC), inflation, and electricity price. These scenarios could be generated via a probability density function or Latin hypercube sampling, considering a uniform distribution as well as lower and upper limits as shown in Santibañez-Aguilar et al. [16]. This scenario generation can generate a representative uncertain space for all uncertain parameters, and it could be useful whether there is not a specific probability density function for them.

In order to show how the inflation, WACC, and electricity price could be related, we assumed a case study for Mexico to establish limits for inflation, WACC, and electricity price to generate random values, which should be between these two limits. It is worth noting that random values are generated per each location for the case of electricity price and WACC because these parameters could be different depending on each location. In addition, inflation is assumed to equal for all locations since PV manufacturing system is supposed for domestic production. Table 3.1 presents the upper and lower bound for inflation, WACC, and electricity price for the proposed case study.

In addition, Fig. 3.2a shows the relationship between inflation and WACC for each scenario and one of the supply chain nodes (e.g., 1 cells producer), while Fig. 3.2b illustrates the same relationship for all supply chain nodes (i.e., all cells producers). In this case, there are 32 manufacturing nodes where we assume one per state in Mexico. A virtually full uncertain space is met as seen in Fig. 3.2b, which indicates that scenarios are a good representation of the full uncertain space.

Figure 3.3a shows the inflation and WACC behavior regarding each of the modeled scenarios. Figure 3.3b elucidates how a scenario can have either high or low inflation values and yet have both high and low WACC values across different states in the same scenario. This behavior indicates that there is not a direct correlation between these parameters, and also a manufacturing system could be adjusted by taking into account the locations with different WACC values to improve its performance.

3.5 Adjust of Important Functions for the PV Manufacturing System

Another important stage in a model formulation is computing important functions in the PV manufacturing system such as that of MSP as a function of capacity. MSP is the price at which the net present value for a manufacturing process is equal to zero [17].

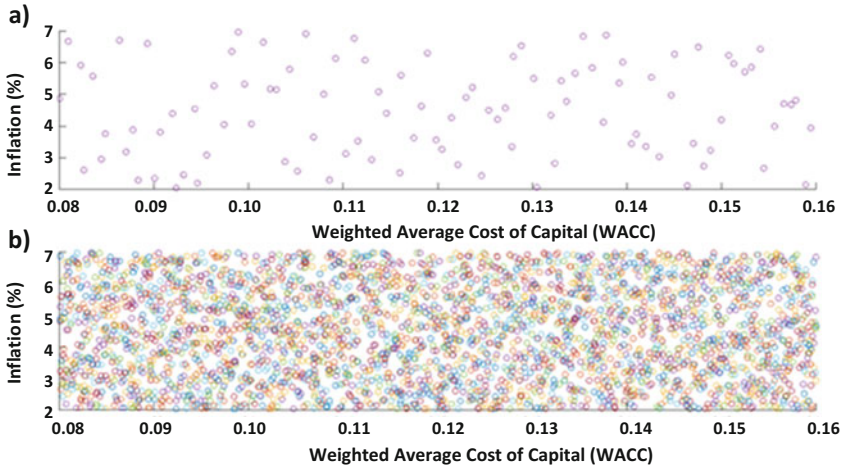


Fig. 3.2 A relationship between inflation and WACC for each scenario. (a) The case for one of the manufacturing system nodes, and (b) the case for all manufacturing system nodes (32 nodes)

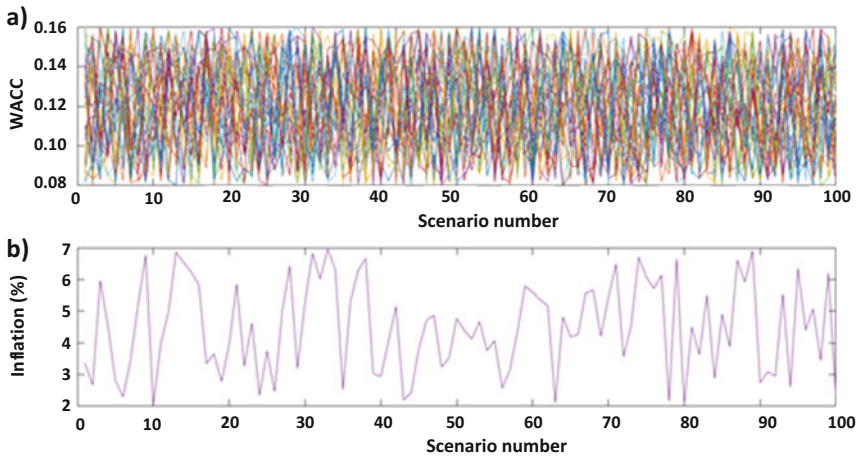


Fig. 3.3 The behavior of inflation and WACC values for each modeled scenario. (a) WACC values for different manufacturing system nodes at each scenario, (b) inflation values for the entire system at each scenario

This variable could be used to evaluate the performance of a manufacturing system by computing it according to a model presented by Powell et al. [8, 17] for a set of inflation, electricity prices, and WACC. This MSP model could be extended to obtain different MSP values for different inflation, electricity price, and WACC values, which can be useful for PV manufacturing system design under uncertainty. However, the MSP depends on production capacity which is a strongly nonlinear and no convex function, and its values should be first fit to be used in a mathematical programming approach.

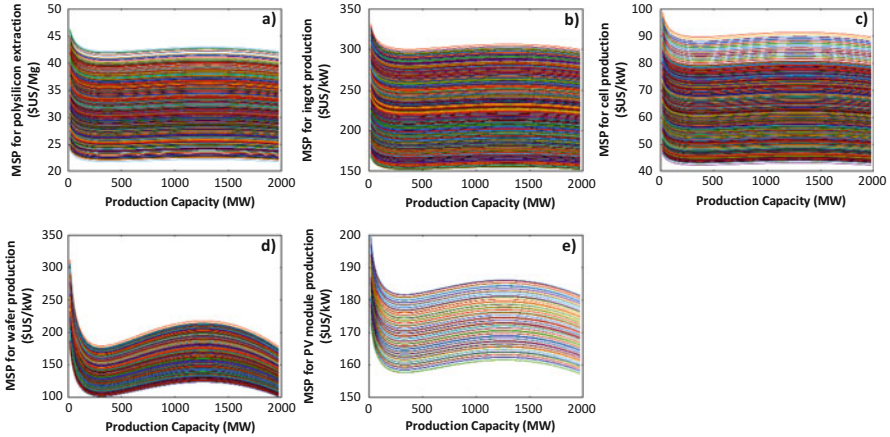


Fig. 3.4 MSP versus production capacity for the manufacturing system nodes under different sets of inflation, WACC, and electricity price values. Each line represents a different modeled scenario. (a) Polysilicon extraction and processing, (b) ingot production, (c) wafers production, (d) cells production, and (e) PV modules production

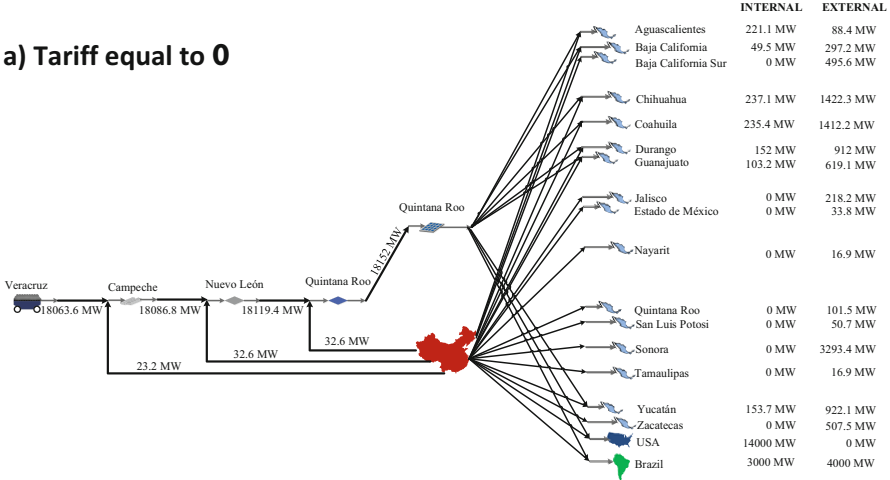
The MSP curve is recreated from Powell et al. [8] for several capacity values and processes, and curves are then segmented to find functions to be fit to. Castellanos et al. [9] carried out linear fits for functions of MSP versus capacity. Nevertheless, a linear adjust could be unrealistic in some cases. To address that potential shortcoming, a base function is obtained for MSP versus capacity, the data is then fit using a specialized software to obtain mathematical relationships with an acceptable correlation factor [18].

Figure 3.4 shows MSP versus capacity functions for different process stages in a PV manufacturing system, taking into account multiple values for inflation, WACC, and electricity prices. These variables have important effects in the MSP function. For instance, the MSP for polysilicon production changes from \$US 25 to \$US 47 per ton of extracted and processed silicon (based on 20 MW), which represents an 88% deviation from the lower bound. MSP value for PV modules could reach values of \$US 0.180 and up to \$US 0.200 per Watt, being 11% away from the lower limit. It is important to mention that the data fit could be deemed acceptable as the reported fit average errors varied between 2% and 7%.

3.6 Influence of Tariff Level in the PV Manufacturing System Topology

Regarding the tariff level in a PV manufacturing system, most of the previous works have not taken into account the interactions between different countries since that assumption could imply to introduce a tariff value for different combinations of goods and countries. Nevertheless, tariffs are shown to significantly alter PV system topology [9]. Castellanos et al. [9] proposed a TIT-4-TAT model, which considered

a) Tariff equal to 0



b) High tariff case

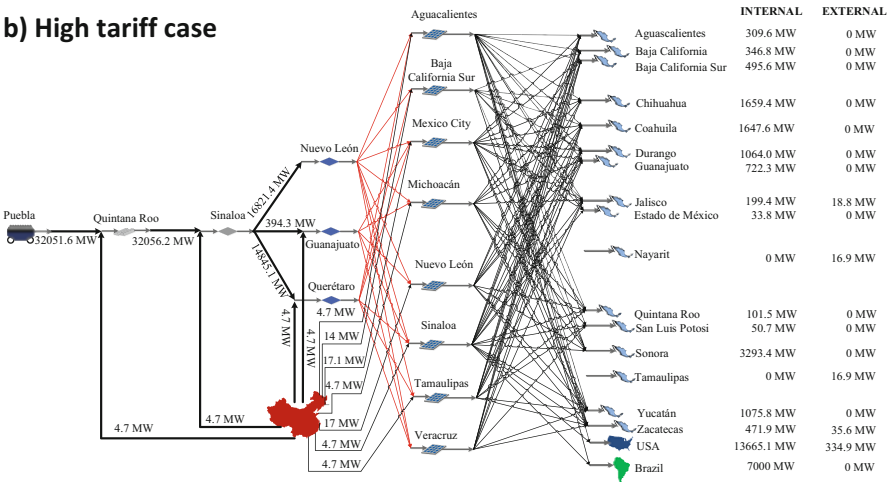


Fig. 3.5 PV manufacturing system topology under different tariff levels. (a) A case with no tariffs imposed between the countries China, the USA, Brazil, and Mexico. (b) The case where high tariffs are imposed between the same countries, and they retaliate in response with the same tariff level. (Figure based on Castellanos et al. [9])

two case studies with different assumptions in tariff levels for evaluation: a case where all tariffs were supposed to be zero and a case where different tariff levels were introduced for Mexico, Brazil, the USA, and China.

Figure 3.5 illustrates how a PV manufacturing system under the same considerations and different values for tariffs can be drastically affected. Figure 3.5a shows the supply chain configuration when the tariff was assumed equal to zero for all

goods and countries, whereas Fig. 3.5b depicts the PV manufacturing system topology when a case with high tariff between countries was considered.

The comparison between no tariff and high tariff cases allows for the impact assessment of protectionist measures in the global PV supply chain. For instance, the high tariff case shows that imported and exported goods are reduced, but the number of PV modules producers increase from one to eight. Moreover, the interconnections between consumption regions are significantly increased, which similarly increases transportation costs. Also, the PV solar modules demand is almost met by domestic production. Lastly, the effect of tariffs is crucial to a system topology because if a tariff war were to occur, the final products would be more expensive for the consumers due to the imposed tariff values, transportation costs, and forced sub-optimal local manufacturing.

3.7 Conclusions

As discussed, there are different stages and aspects to consider in the PV manufacturing system design problem. These aspects could be addressed separately in different approaches such as Castellanos et al. [9] involved different tariff level, Powell et al. [8] proposed a model to compute the MSP, or Dehghani et al. [12] included uncertain parameters and interactions between different countries. However, a methodology able to consider all these aspects simultaneously could help us to introduce the PV energy to the global market more quickly.

In addition, different presented sections show that a combination of diverse aspects such as computing of MSP over inflation and electricity price, adjusting of MSP versus capacity function, or the optimal planning through a mathematical programming model could be accomplished in a sequential manner since some of these are unrelated to each other.

Furthermore, forecast projections need to be altered if market conditions are changed since presented mathematical model in current chapter and Castellanos et al. [9] is deterministic. These modifications could be the new tariff for steel and glass between the USA and China. In this case, a stochastic formulation could be useful to determine the supply chain able to support the variations.

Lastly, local and global PV manufacturing system designs depend on the specific objectives or decision variables being considered; nevertheless, some of the most important ones due to their influence in the supply chain were presented in the this chapter.

Acknowledgments The authors wish to thank the support from Mexican government agencies (ProMexico, SENER) with general data. Castellanos, S. thanks support from Tecnológico de Monterrey fellowship. Santibañez-Aguilar, J.E., and Flores-Tlacuahuac, A., appreciate the financial support provided by the Mexican National Council for Science and Technology (CONACYT), Secretaría de Energía-Conacyt through the Binational Energy Laboratory grant. Also, Santibañez-Aguilar, J.E., Flores-Tlacuahuac, A., and Castellanos, S., thank the Energy and Climatic Change Research Group at Tecnológico de Monterrey, Monterrey, Mexico.

References

1. J.J. Michael, I. Selvarasan, R. Goic, Fabrication, experimental study, and testing of a novel photovoltaic module for photovoltaic thermal applications. *Renew. Energy* **90**, 95–104 (2016)
2. S. Kim, B. Jeong, Closed-loop supply chain planning model for a photovoltaic system manufacturer with internal and external recycling. *Sustainability* **8**(7), 596 (2016)
3. T.M. Razykov, C.S. Ferekides, D. Morel, E. Stefanakos, H.S. Ullal, H.M. Upadhyaya, Solar photovoltaic electricity: current status and future prospects. *Sol. Energy* **85**(8), 1580–1608 (2011)
4. P.D. Maycock, PV news. *PV Energy Syst.* **29**, 108–119 (2010)
5. D.G. Loomis, J.H. Jo, M.R. Aldeman, Economic impact potential of solar photovoltaics in Illinois. *Renew. Energy* **87**, 253–258 (2016)
6. P. Díaz, R. Peña, J. Muñoz, C.A. Arias, D. Sandoval, Field analysis of solar PV-based collective systems for rural electrification. *Energy* **36**(5), 2509–2516 (2011)
7. A.C. Goodrich, D.M. Powell, T.L. James, M. Woodhouse, T. Buonassisi, Assessing the drivers of regional trends in solar photovoltaic manufacturing. *Energy Environ. Sci.* **6**(10), 2811–2821 (2013)
8. D.M. Powell, R. Fu, K. Horowitz, P.A. Basore, M. Woodhouse, T. Buonassisi, The capital intensity of photovoltaics manufacturing: a barrier to scale and opportunity for innovation. *Energy Environ. Sci.* **8**(12), 3395–3408 (2015)
9. S. Castellanos, J.E. Santibañez-Aguilar, B.B. Shapiro, D.M. Powell, I.M. Peters, T. Buonassisi, . . . , A. Flores-Tlacuahuac, Sustainable silicon photovoltaics manufacturing in a global market: a techno-economic, tariff, and transportation framework. *Appl. Energy* **212**, 704–719 (2018)
10. C. Norberto, C.N. Gonzalez-Brambila, Y. Matsumoto, Systematic analysis of factors affecting solar PV deployment. *J. Energy Storage* **6**, 163–172 (2016)
11. E.R. Shouman, E.T. El Shenawy, N.M. Khattab, Market financial analysis and cost performance for photovoltaic technology through international and national perspective with a case study for Egypt. *Renew. Sust. Energ. Rev.* **57**, 540–549 (2016)
12. E. Dehghani, M.S. Jabalameli, A. Jabbarzadeh, Robust design and optimization of the solar photovoltaic supply chain in an uncertain environment. *Energy* **142**, 139–156 (2018a)
13. E. Dehghani, M.S. Jabalameli, A. Jabbarzadeh, M.S. Pishvaei, Resilient solar photovoltaic supply chain network design under business-as-usual and hazard uncertainties. *Comput. Chem. Eng.* **111**, 288–310 (2018b)
14. A.F. Sánchez-Bautista, J.E. Santibañez-Aguilar, L.F. Fuentes-Cortés, A. Flores-Tlacuahuac, J.M. Ponce-Ortega, A multi-stakeholder approach for the optimal planning of sustainable energy systems. *ACS Sustain. Chem. Eng.* **6**, 9451–9460 (2018)
15. L.F. Fuentes-Cortés, Y. Ma, J.M. Ponce-Ortega, G. Ruiz-Mercado, V.M. Zavala, Valuation of water and emissions in energy systems. *Appl. Energy* **210**, 518–528 (2018)
16. J.E. Santibañez-Aguilar, G. Guillen-Gosálbez, R. Morales-Rodríguez, L. Jiménez-Esteller, A.J. Castro-Montoya, J.M. Ponce-Ortega, Financial risk assessment and optimal planning of biofuels supply chains under uncertainty. *Bioenergy Res.* **9**(4), 1053–1069 (2016)
17. D.M. Powell, M.T. Winkler, A. Goodrich, T. Buonassisi, Modeling the cost and minimum sustainable price of crystalline silicon photovoltaic manufacturing in the United States. *IEEE J. Photovoltaics* **3**(2), 662–668 (2013)
18. ALAMO, ALAMO software (2018), <https://minlp.com/alamo>. Accessed Feb 2019



Solar Energy Harvesting by Perfect Absorbers Made of Natural Hyperbolic Material

Zhaolong Wang and Ping Cheng

Contents

4.1	Introduction	90
4.2	Dielectric Tensor of Bi_2Te_3 and underlying Mechanisms for Perfect Absorption	92
4.2.1	Slow-Light Effect	92
4.2.2	Gradient Index Effect	94
4.3	Results and Discussion of the Simulated Results	95
4.3.1	Broadband Perfect Absorber for Solar Energy Harvesting	96
4.3.2	Effects of the Nano-Pyramids' Geometry Parameters	98
4.3.3	Effects of the Substrate Material and Thickness	100
4.3.4	Optical Properties of Bi_2Te_3 with Different Roughness	101
4.4	Sample Fabrication and Characterization	102
4.4.1	Sample Fabrication	102
4.4.2	Characteristics of the Sample	104
4.4.3	Results and Discussion	105
4.5	Concluding Remarks	107
	References	108

Author Contribution

The research work was carried out by the first author (ZLW) and supervised by the second author (PC). The paper was drafted by ZLW and edited by PC.

Z. Wang

College of Mechanical and Vehicle Engineering, Hunan University, Changsha, China

e-mail: zhaolong.wang0207@gmail.com

P. Cheng (✉)

MOE Key Laboratory for Power Machinery and Engineering, School of Mechanical and Power Engineering, Shanghai Jiao Tong University, Shanghai, China

e-mail: pingcheng@sjtu.edu.cn

Abstract

A perfect absorber, with pyramidal nanostructures made of a natural hyperbolic material, for solar energy harvesting is proposed in this chapter. A numerical investigation is first carried out for regularly arranged bismuth telluride (Bi_2Te_3 , an anisotropic and natural hyperbolic material) pyramidal nanostructures placed on top of a Ag substrate, and the metamaterial is submerged in water. The calculated results show that the absorptance of the absorber exceeds 99.9% in the wavelength range of 300–2400 nm. The underlying mechanisms are revealed by the electric field and power dissipation density distribution in the absorber. It is found that the slow light effect in the type-II hyperbolic region (300–1000 nm) and the gradient index effect in the long wavelength range (1000–2400 nm) contribute to the perfect absorption of the solar energy for the proposed absorber. Effects of geometry parameters of nano-pyramids and the substrate on optical properties of the proposed absorber are illustrated. In addition, a rough surface with sharp nanostructures made of Bi_2Te_3 is also numerically studied. Based on simulation results of rough Bi_2Te_3 surface, samples with nanostructures made of Bi_2Te_3 are experimentally manufactured and optical properties of the samples are measured by using an integrating sphere with a grating monochromator. The absorptance of the samples can be as high as 97.5%, and the lowest absorptance of the sample is still higher than 94% in the wavelength range of 380–1800 nm. Moreover, other samples are also fabricated and studied to validate underlying mechanisms of the perfect absorption of solar energy. The results of the present study open a new revenue for effectively harvesting solar energy by using metamaterials with nanostructures made of natural hyperbolic materials submerged in water.

4.1 Introduction

It is known that there are four ways for utilization of solar energy: (i) photovoltaic process such as a solar cell to generate electricity [1], (ii) photobiology process such as photosynthesis [8], (iii) photochemistry process such as photocatalysis [1], and (iv) photothermal process for vapor generation [10, 29, 30, 37]. Total absorption of solar energy is the key factor for utilization of such kind of abundant clean and renewable energy, which has attracted a great deal of interests in the past few decades [26]. In order to soak up all the incident solar energy, many methods have been proposed and investigated, such as change of different material [14], coating [33], employing nanostructures [31, 39, 53], etc. Among them, the use of nanostructures is one of the most promising ways for harvesting solar energy because of their ability to enhance the absorptance [is the flux ratio of the object, and absorbance is the log value of the intensity ratio] to 100%, sustain high temperature, and so on. In addition, there are other special characteristics for specially designed nanostructures by adding some functional groups to the surface of nanostructures, such as sterilization [40]. However, almost all

materials that enhance the absorption properties of solar energy are isotropic, and anisotropic materials have seldom been used in solar energy absorbers.

Anisotropic materials have shown quite unique optical properties because of the combination of different dielectric functions in one nanostructure. The anisotropic polarization of such materials is either because of their shapes, such as nano-tubes and nano-rods [22, 23, 27, 36], or because of their optical constants such as in bismuth telluride (Bi_2Te_3), hierarchical boron nitride (hBN), graphene [51], and so on. For example, nanorods have a longitudinal mode and a transverse mode of plasmon resonance along the long axis and the short axis of the rod, respectively. However, enhanced absorption mechanisms of light in nanostructures made of anisotropic material are totally different. For example, spherical Bi_2Te_3 nanoparticles (NPs) have both electric dipole and magnetic dipole resonances because of anisotropic dielectric functions in different crystal axes, leading to a broad absorption band with at least four absorption peaks in the solar spectrum [43]. The metamaterials made from these materials, which have completely different dielectric functions (metallic and dielectric media) in two orthogonal directions, show strong slow-light effect. And the slow-light effect can trap light with different wavelengths in a nanostructure with increasing cross-sectional area [12, 17, 21, 51, 52], leading to a broad absorption band. Recently, metamaterials made of anisotropic materials are attracting more and more attention because of their potential applications in broadband absorption [5, 17, 46], thermal radiation [2, 18, 32, 38], superlenses [6, 9, 16, 48], subwavelength light concentrators in nanolithography [19, 42, 47], and so on.

However, it should be noted that it is very challenging to manufacture metamaterials made from anisotropic media, although there are so many merits of metamaterials made from anisotropic materials [7, 28]. For example, the sawtooth anisotropic metamaterial proposed by Cui et al. [5] consisting of 20 pairs of alternating layers of flat metal and dielectric plates with gold plates of 15 nm thick and germanium dielectric plates of 35 nm thick. But optical properties of such kind of absorber depend strongly on the geometry of the layer, and precise control of their shapes during the nanofabrication process is still impossible with current technology. It should be noted that dielectric functions of natural anisotropic materials in solar energy spectrum were measured only recently [7, 28], and the discovery of natural anisotropic material (hyperbolic materials) opens a gate for fabrication of metamaterials with anisotropic response to the incident light in different crystal axes.

In this chapter, a perfect absorber made from a natural anisotropic material, bismuth telluride (Bi_2Te_3), for solar energy harvesting is proposed. Mechanisms of perfect absorption of solar energy are studied numerically and theoretically. A rough surface with sharp nanostructures made of Bi_2Te_3 , which can replace the regularly arranged nanostructures, is studied numerically and is fabricated for experimental investigation. The absorptance of these samples is measured and analyzed in detail. It is demonstrated that the perfect absorber made of a natural anisotropic material submerged in water can be used as effectively as a heat source for vapor generation under sunlight.

4.2 Dielectric Tensor of Bi_2Te_3 and underlying Mechanisms for Perfect Absorption

The proposed absorber has two layers as shown in Fig. 4.1. A two-dimensional (2D) periodic array (with a period Λ) of pyramidal nanostructures made of Bi_2Te_3 is arranged regularly on the top of a substrate. The geometric parameters of the nano-pyramid are defined as follows: w_1 is top width, w_2 is bottom width, H is the height, and h is the thickness of the substrate. As shown in Fig. 4.1a, the light is incident in the positive z -direction, which is also in parallel to the axis of the nano-pyramid, while the electric field vibrates in x -direction. Because of the specially designed structures and optical constants of Bi_2Te_3 , two key mechanisms that give rise to the perfect absorption to the solar energy are the slow-light effect of the hyperbolic material in the type-II hyperbolic region and the gradient index effect of tapered nanostructures in the long wavelength region, which will be analyzed in detail below.

4.2.1 Slow-Light Effect

The dielectric function of Bi_2Te_3 (a uniaxial medium) is a tensor, which can be expressed as [3, 7]:

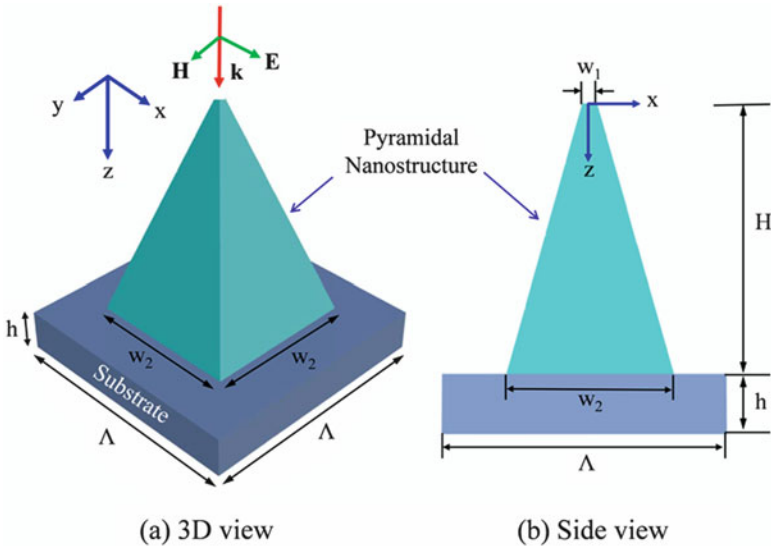


Fig. 4.1 Schematic of a unit cell of the perfect absorber. Periodic Bi_2Te_3 nano-pyramids are regularly arranged above a thin substrate, and the absorber is submerged in water: (a) 3D view and (b) side view. The wave vector \mathbf{k} indicates the direction of the incident light, which is also the positive z -direction, while electric field vibrates in the x -direction. Other geometric parameters are also indicated. (From Ref. [44])

$$\varepsilon = \begin{pmatrix} \varepsilon_x & 0 & 0 \\ 0 & \varepsilon_x & 0 \\ 0 & 0 & \varepsilon_z \end{pmatrix} \quad (4.1)$$

It can be observed from both Eq. (4.1) and Figs. 4.2a, b that dielectric functions in x and y -direction (ε_x) are the same, while the dielectric function in z -direction (ε_z) is different. The real and imaginary parts of the dielectric functions for Bi_2Te_3 were measured by Esslinger et al. [7], which are replotted in Figs. 4.2a, b, respectively. The refractive index n and extinction coefficient k of Bi_2Te_3 in different directions can be calculated respectively by using the complex dielectric function of ε_x and ε_z given by $\varepsilon = (n + ik)^2$. According to the real part of the dielectric functions of Bi_2Te_3 (Fig. 4.2a), the wavelength range of 300–2400 nm can be divided into two parts. In the wavelength

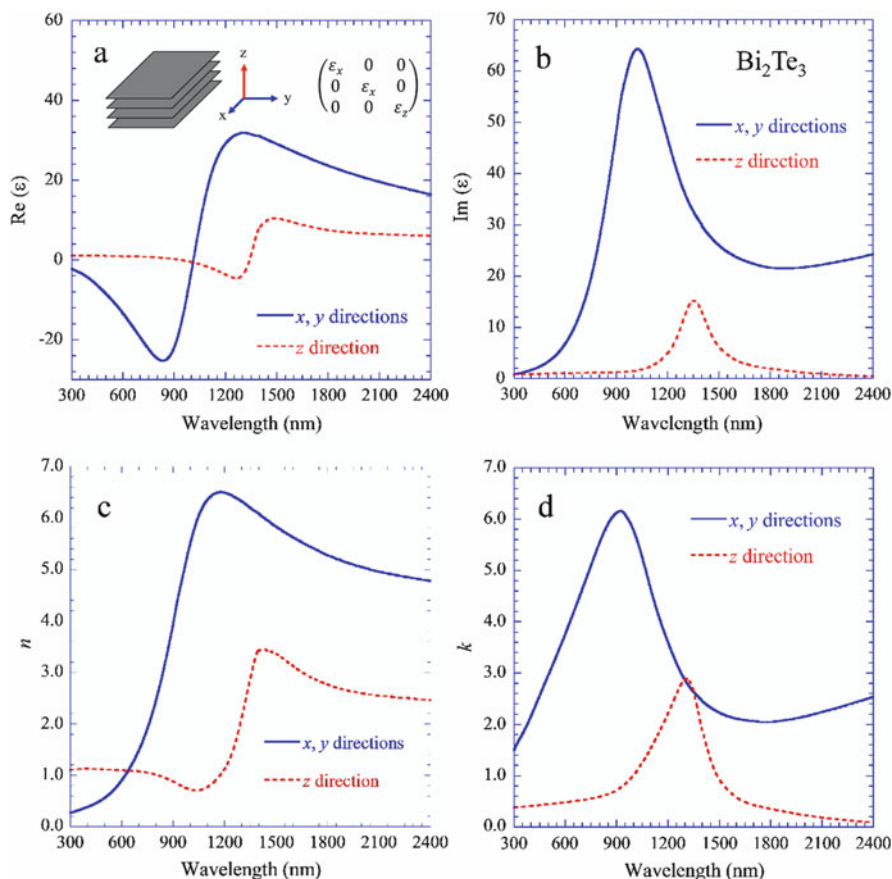


Fig. 4.2 The dielectric function tensor and a complex refractive index of Bi_2Te_3 , where the insert in (a) is the crystalline structure and dielectric tensor. (a, b) Real and imaginary parts of the dielectric functions in different directions; (c, d) the dielectric constants in different directions, which are refractive indices n and the extinction coefficients k , respectively. (From Ref. [44])

region of 300–1000 nm, $\text{Re}(\epsilon_x) < 0$ and $\text{Re}(\epsilon_z) > 0$, where the former indicates that the material exhibits metallic behavior in x and y directions, while the latter indicates dielectric behavior in z -direction. This wavelength region is the type-II hyperbolic region, which exhibits a slow-light effect because of the hyperbolic shape of iso-frequency contour [51]. The wavelength of 1000–2400 nm will be discussed later.

The slow-light effect can also be calculated by the dispersion relation of hyperbolic phonon polaritons (HPPs) on a thin film made of hyperbolic material with a thickness d [17, 51].

$$\frac{k_{x,2}\epsilon_z}{k_{x,1}\epsilon} = \tan\left(k_{x,1}\frac{w}{2}\right) \quad (4.2)$$

with $k_{x,2} = \sqrt{\zeta^2 - \epsilon k_0^2}$, $k_{x,1} = \sqrt{\epsilon_z k_0^2 - (\epsilon_z/\epsilon_x)\zeta^2}$, where ϵ_z is the dielectric function of the hyperbolic material in the z -direction, ϵ is the dielectric function of the surrounding medium. ζ is the wavevector in the z -direction, and w is the width of the nanostructure considered. Furthermore, multiple orders of HPPs are allowed if the width of the nanostructure increases gradually.

4.2.2 Gradient Index Effect

As shown in Fig. 4.1, the cross section of nano-pyramids increases gradually in the positive z -direction. When nano-pyramids are submerged in water, the mixture of nano-pyramids and water can be treated as a stratified effective homogeneous medium, even though it is an inhomogeneous medium [3, 24, 49]. According to the effective medium theory of electric field in the x - y plane, the effective dielectric function of the stratified effective homogeneous medium at each layer is expressed as follows:

$$\frac{1}{\epsilon_{\text{eff}}} = \frac{f}{\epsilon_x} + \frac{1-f}{\epsilon_{\text{water}}} \quad (4.3)$$

where ϵ_{eff} and ϵ_{water} are dielectric functions of effective medium and water, respectively, and f is the ratio of a cross section of the nanostructure and the distance between two nanostructures. As shown in Fig. 4.1a, the value of f increases in the positive z -direction, which is also the direction from the top to the bottom in a pyramidal nanostructure. In addition, the effective refractive index n_{eff} and extinction coefficients k_{eff} in x - or z -direction can be calculated ϵ_{eff} according to the following relation.

$$\epsilon_{\text{eff}} = (n_{\text{eff}} + ik_{\text{eff}})^2 \quad (4.4)$$

It can be seen from Eq. (4.3) that the effective dielectric function increases from the dielectric function of water at the top to the dielectric function of Bi_2Te_3 at the

bottom. Accordingly, based on Eq. (4.4) the effective refractive index n_{eff} of the proposed absorber gradually increases from 1.33 for water to a larger value for Bi_2Te_3 in the positive z directions. The reflection of light at the interface of two materials with different refractive indices only depends on the contrast of the refractive indices and becomes smaller for smaller contrast. This is the reason that the pyramidal nanostructure is chosen to create an effective index profile that gradually increases in the positive z -direction, as shown in Fig. 4.1. Consequently, the reflection at the interface of each cross section will be suppressed. However, the effective medium theory is valid only when the wavelength is much longer than the grating period. Therefore, the rigorous coupled-wave analysis (RCWA) method was used to calculate the electric field and power dissipation density distribution in the metamaterial to reveal the underlying mechanisms, and finite-difference time-domain (FDTD) method was used to calculate the absorption spectrum of the proposed absorber. The effective medium theory together with the gradient index concept provide qualitative insights to help intuitively understand the underlying physical mechanisms of perfect absorption to the solar energy by the metamaterials shown in Fig. 4.1.

In order to validate the slow-light and reflection suppression effects, the local power dissipation density distribution in the x - z plane at $y = 0$ within the nano-pyramids is calculated as follows [50]:

$$q = \frac{1}{2} \varepsilon_0 \omega \varepsilon_x'' (|E_x|^2 + |E_y|^2) + \frac{1}{2} \varepsilon_0 \omega \varepsilon_z'' |E_z|^2 \quad (4.5a)$$

where ε_0 is the vacuum permittivity, ω is the angular frequency, and ε_x'' and ε_z'' are the imaginary parts of the dielectric functions of Bi_2Te_3 in x and z directions, respectively. Since isotropic material is used for the substrate, consequently, Eq. (4.5a) reduces to

$$q = \frac{1}{2} \varepsilon_0 \omega \varepsilon'' |E|^2 \quad (4.5b)$$

where ε'' is the imaginary part of the dielectric function of the isotropic substrate and the magnitude of the electric field is $|E| = \sqrt{E_x^2 + E_y^2 + E_z^2}$.

4.3 Results and Discussion of the Simulated Results

Two different methods are used to calculate the transmittance (T) and reflectance (R) of the proposed absorber, the electric field, and the power dissipation density distribution within the nano-pyramids. Specifically, the transmittance and reflectance of the absorber are calculated by the FDTD method to solve Maxwell's equations, while local power dissipation density is calculated by RCWA method for nano-structures made of anisotropic material [13, 51]. The absorptance is obtained by $A = 1 - T - R$. The dielectric function of gold was taken from the data from Olmon et al.

[34], while dielectric functions of remaining materials are taken from the data compiled by Palik [35]. The proposed absorber is submerged in water, whose refractive index is 1.33.

4.3.1 Broadband Perfect Absorber for Solar Energy Harvesting

In order to investigate the absorptance of the proposed absorber for solar energy harvesting, calculations are carried out in a broad wavelength range from 300 to 2400 nm. After computing many cases to find out suitable ranges of parameters for perfect absorption for solar energy, the geometry parameters of a representative absorber are chosen to be: $w_1 = 4$ nm, $w_2 = 200$ nm, $H = 3000$ nm, and $\Lambda = 200$ nm; the thickness of an Ag substrate is 100 nm ($h = 100$ nm). It should be noted that these parameters are taken as default values for the sake of demonstration and comparison unless otherwise indicated in the following. Figure 4.3 shows the absorption spectrum of the proposed absorber with an array of regularly arranged nano-pyramids made from Bi_2Te_3 on an Ag substrate. It can be seen that the absorptance of the absorber is higher than 99.9% in the range of 300–2400 nm with most of the absorptance equals to 1. It follows that the proposed absorber can totally harvest the solar energy incidents on its surface in the wavelength range of 300–2400 nm when submerged in water.

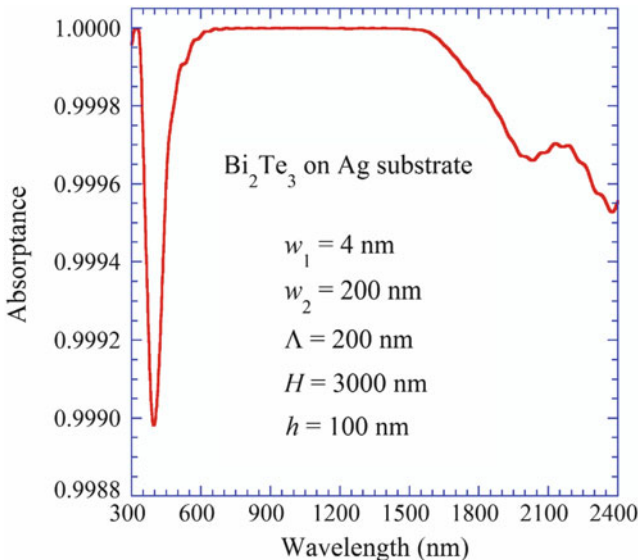


Fig. 4.3 The absorptance of the proposed absorber with Bi_2Te_3 pyramidal nanostructures, the geometry parameters are as follows: $H = 3000$ nm, $w_1 = 4$ nm, and $w_2 = 200$ nm, $\Lambda = 200$ nm on an Ag layer with $h = 100$ nm. (From Ref. [44])

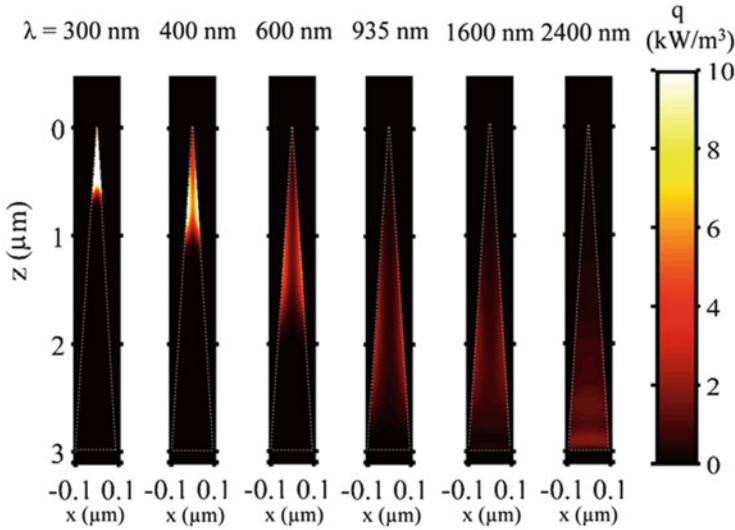
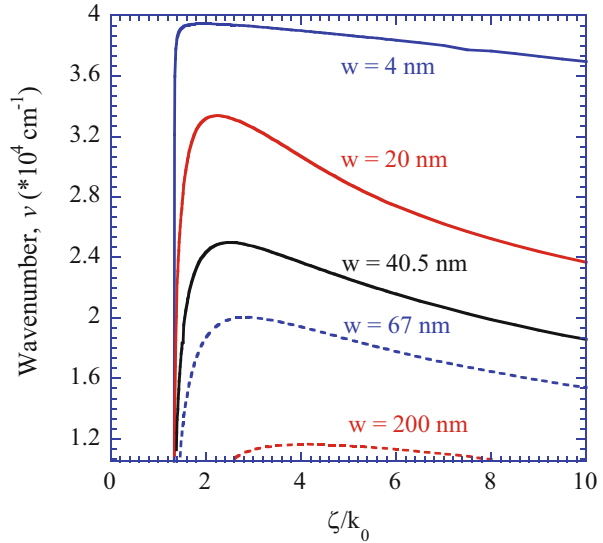


Fig. 4.4 Power dissipation density distributions at six different wavelengths within the Bi_2Te_3 nano-pyramid with the default geometry parameters. (From Ref. [44])

The underlying mechanisms for perfect absorption in such a broad wavelength range are explained next. Figure 4.4 shows the heat dissipation density distribution at different wavelengths. It can be seen from the left four figures (with wavelengths from 300 to 935 nm) that the energy is trapped in different parts of the nano-pyramid with a gradually increasing cross section in the positive z -direction, and the cross section of the location of total absorption of incident light increases with the increase of the wavelength. The slow-light effect in type-II hyperbolic region dominates perfect absorption of the light in 300–1000 nm. For the proposed absorber, cross sections of the nano-pyramids on the surface gradually increase in the z -direction. The impedance matching at the interface between the incident medium and the top of the absorber can suppress its reflection on the top, while the effective refractive index gradually increasing from water to that of Bi_2Te_3 on the substrate suppress the light to be reflected at each cross section of the nano-pyramid. The reflection suppression from the gradient index effect can be observed from the two right-hand figures in Fig. 4.4. In the long wavelength region, which is 1000–2400 nm in the present study, the power of the light is suppressed at the bottom of the nano-pyramid. It should be noted that the gradient index effect also makes a difference in the type-II hyperbolic region, though it is not the key factor for perfect absorption in the region of 300–1000 nm. The substrate is also important for reflecting the light back into the nano-pyramid to be reabsorbed again, which will be explained next.

The dispersion relation of the HPPs waveguide can also be used to explain the perfect absorption in the type-II hyperbolic region. Based on Eq. (4.2), the dispersion relations of the HPPs waveguide at different cross sections of nano-pyramid are plotted in Fig. 4.5. The horizontal coordinate is the angular velocity of the incident

Fig. 4.5 The dispersion relation of a waveguide for Bi_2Te_3 nano-pyramids in the type-II hyperbolic region. (From Ref. [44])



light, while the vertical coordinate represents the wave number. The gradient of the curve is the velocity of the power of the light, which is also known as the group velocity of electromagnetic waves. It can be seen from Fig. 4.5 that the velocity of the power decreases to 0 for different electromagnetic waves at different width of the nano-pyramid. Specifically, the velocity of the power decreases to 0 for light with a wavelength of 300 nm for the width of the nano-pyramid equals to 20 nm, while the wavelengths at where the velocity of the power decreases to 0 increase with the increase of the width of the portion of the nanostructures. The results predicted by the dispersion relation of Eq. (4.2) also indicate that the slow-light effect in type-II hyperbolic region dominates the perfect absorption of the absorber to the incident light in the wavelength region of 300–1000 nm.

4.3.2 Effects of the Nano-Pyramids' Geometry Parameters

Effects of the geometry of nano-pyramids (w_1 , w_2 , H , and Λ) are studied numerically and results are presented in Fig. 4.6. The thickness of the Ag substrate is fixed at 100 nm. As shown in Fig. 4.6a, changing the top width (w_1) of nano-pyramids makes no difference in the absorption spectrum of the absorber if it is smaller than 20 nm. That is because the suitable width of the nano-pyramid for the total absorption of the light of 300 nm is 20 nm according to Eq. (4.2), and a larger width at the top will affect the slow-light effect, which can be seen from the blue dashed line for a top width of 60 nm, where the absorptance is drastically reduced at a wavelength below 1000 nm. As shown in Fig. 4.6b, the change of the width at the bottom (fixing $\Lambda = w_2$) affects the absorption property of the absorber as well, though there is a tolerable range. Again, it can be calculated from Eq. (4.2) that the width for perfect

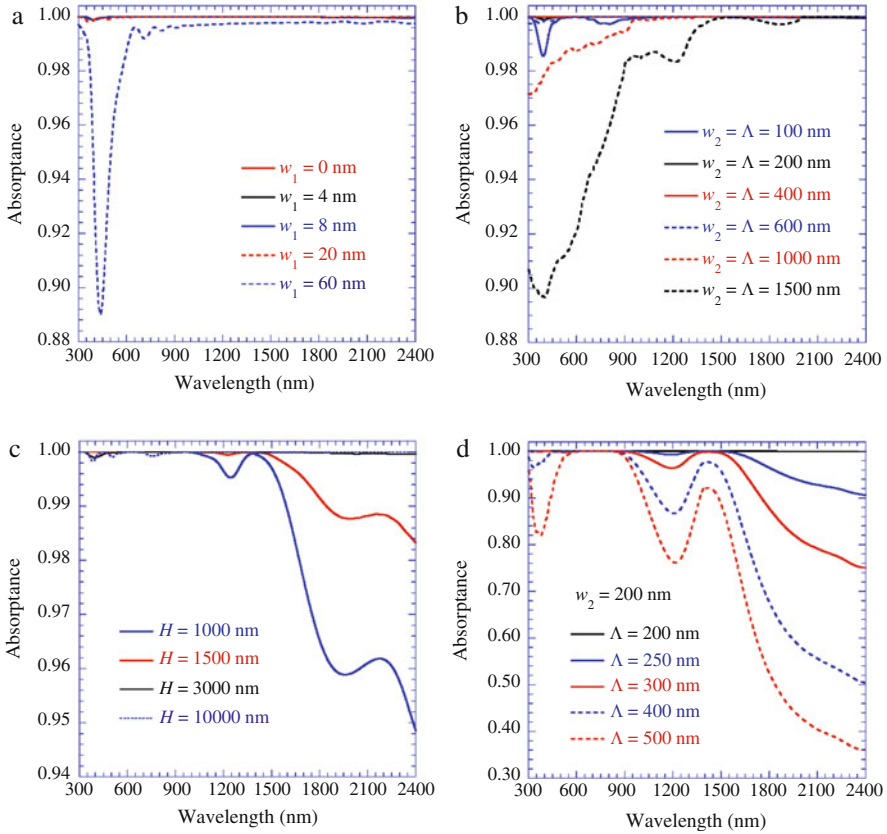


Fig. 4.6 Effects of geometry parameters of Bi₂Te₃ nano-pyramids on the absorption spectrum of the proposed absorber with an Ag layer: (a) top width w_1 ; (b) bottom width w_2 and period Λ ; (c) height H ; and (d) period at $w_2 = 200$ nm. Except as indicated, geometric parameters are fixed to default values. (From Ref. [44])

absorption of light at 1000 nm is around 200 nm, so a width at the bottom smaller than 200 nm will lower the absorbance of the absorber, which can be seen from the blue solid line for a bottom width of 100 nm, as shown in Fig. 4.6b. However, a very large bottom width will confine the slow-light effect in a very narrow depth along the z -direction, which will weaken the slow-light effect. This can be seen from the cases with a bottom width larger than 600 nm in Fig. 4.6b, as indicated by blue, red, and black dashed lines for a bottom width of 600, 1000, and 1500 nm, respectively.

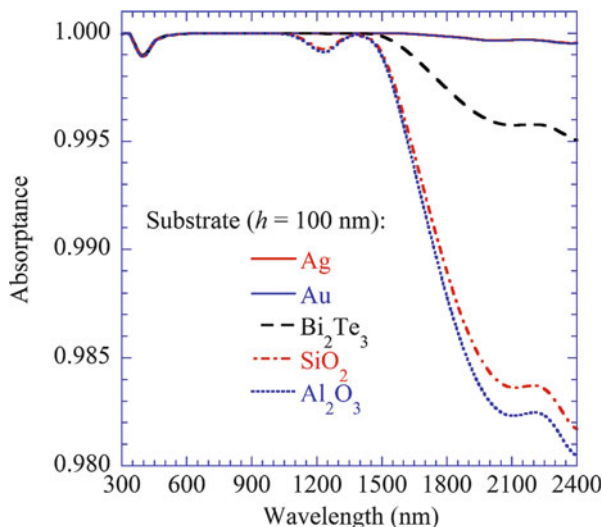
Figure 4.6c shows the effect of the height H of nano-pyramids on the absorbance of the absorber. It can be seen that the absorbance of the absorber in the long wavelength region will be lowered if the height of the nano-pyramid is smaller than 3000 nm. The reason is that the increasing rate of the effective refractive index increases with the decreasing height of the nano-pyramid, and the gradient index effect will be weakened if the increasing rate of the effective index is too large. On

the other hand, changing the distance between two nano-pyramids with a fixed bottom width (fixing $w_2 = 200$ nm) of the nano-pyramid will change the effective refractive index at the bottom of the nano-pyramid. The gradient index effect is affected by a smaller effective refractive index at the bottom of the nano-pyramid. The results shown in Fig. 4.6d illustrate that changing the distance between nano-pyramids lowers the absorptance of the absorber because of the gradient index effect, though there is also a tolerable range.

4.3.3 Effects of the Substrate Material and Thickness

Although the substrate absorbs only a small portion of the energy of electromagnetic waves directly, its purpose is to reflect the unabsorbed incident light passing through the nano-pyramids back to be reabsorbed again, which is particularly important in the long wavelength region. Figure 4.7 shows the effect of the substrate's material on the absorptance. We examine both metallic materials (gold, Au; silver, Ag) and dielectric materials (alumina, Al_2O_3 ; silica, SiO_2). In addition, a substrate made from Bi_2Te_3 is also included for comparison. We can see from Fig. 4.7 that the absorptance is nearly 100% in the type-II hyperbolic region regardless of the material of the substrate. This is because the energy is trapped in nano-pyramids before reaching the substrate. However, the incident light is suppressed at the bottom of the nano-pyramids in the long wavelength region because of the gradient index effect. Consequently, long wavelength light is blocked by the substrate. Since the penetration depth of metallic materials is smaller than that of dielectric materials, a substrate made of metallic materials is much better than a dielectric substrate. Note that Bi_2Te_3 combines both the merits of metal and dielectric materials, as indicated by black

Fig. 4.7 Effects of the material of the substrate on the absorption spectrum of the proposed absorber with a fixed thickness of 100 nm. All other parameters are the same as the default. (From Ref. [44])



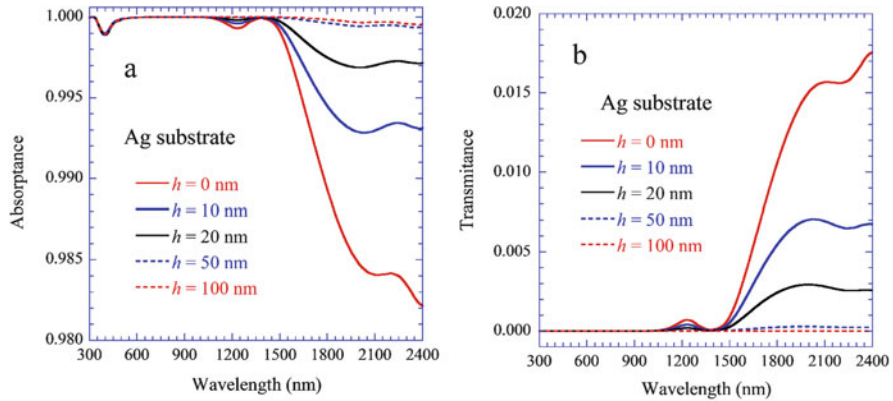


Fig. 4.8 Effects of substrate thickness on the absorption spectrum of the proposed absorber with an Ag substrate. All other parameters are the same as the default. (From Ref. [44])

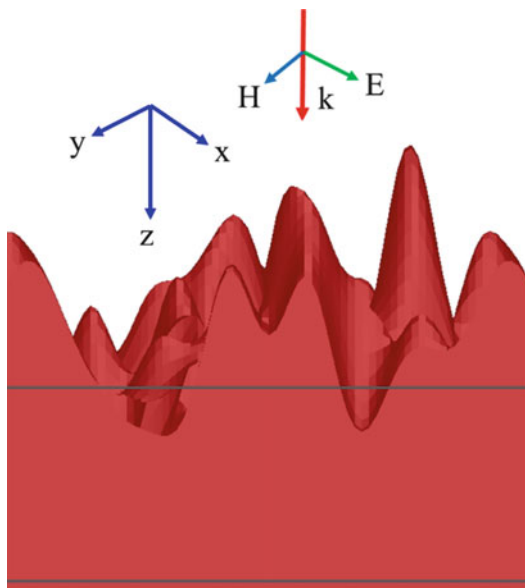
dashed lines in Fig. 4.7. Thus, a substrate made of Bi_2Te_3 is also a good choice for the absorber, although it is slightly worse than a metallic substrate.

Figures 4.8a, b show the effects of Ag substrate thickness on the absorptance and transmittance of the proposed absorber. Again, the short waves can be totally absorbed before reaching the substrate, and the thickness of the substrate makes no difference in the absorption property in the type-II hyperbolic region. However, it can be seen from red solid lines in Figs. 4.8a, b that a thinner substrate lowers the absorptance of the absorber by enhancing the transmittance of the long electromagnetic waves. A thick Ag substrate will sufficiently block the light and reflect the light back into the nano-pyramids to be reabsorbed when lines with the same color in both Figs. 4.8a, b are compared. Since the Ag substrate is very thin, the whole absorber can be placed on a smooth surface (such as a glass or a polished metallic surface) during the fabrication process.

4.3.4 Optical Properties of Bi_2Te_3 with Different Roughness

It remains to be a very challenging task to fabricate nanostructures with very large length/width ratio even though nanofabrication technology has been developed for a long time. The height/width ratio of the nano-pyramid shown in Fig. 4.1 is about 15, which is impossible to manufacture with the current technology. So, rough surfaces with sharp nanostructures made of Bi_2Te_3 are studied numerically to replace the nano-pyramids shown in Fig. 4.1. The proposed absorber structure is shown in Fig. 4.9, and the FDTD method is used for the calculation. The plane wave incidents in the positive z -direction, while electric field \mathbf{E} vibrates in the x -direction. In the calculation, the dielectric function of Bi_2Te_3 in the z -direction is different from those in x and y directions. As demonstrated in Sect. 4.3.3, a thick metallic substrate can block all the electromagnetic waves from a transmission, so a silver (Ag) substrate with a thickness of 500 nm is used in the calculated model.

Fig. 4.9 Schematic of the rough Bi_2Te_3 surface used in the calculation. The \mathbf{k} indicates the direction of the incident light, pointing to the positive z -direction, while electric field vibrates in x -direction. (From Ref. [45])



Calculations are carried out for four surfaces made of Bi_2Te_3 with the roughness of 0, 100, 800, and 1500 nm, and the results are presented in Fig. 4.10. It can be seen from Fig. 4.10 that the absorptance of the smooth Bi_2Te_3 surface (the red dashed line) is very low, although it has a broad absorption spectrum. The absorptance of the rough Bi_2Te_3 surface increases with the increasing roughness of the surface. The rough Bi_2Te_3 surface with a roughness of 800 nm is almost a perfect absorber in the solar spectrum. The results shown in Fig. 4.10 indicate that the nano-pyramids studied in Fig. 4.1 can be well replaced by a rough Bi_2Te_3 surface with sharp nanostructures, and such a rough surface is easy to be fabricated than a regularly arranged array of nano-pyramids.

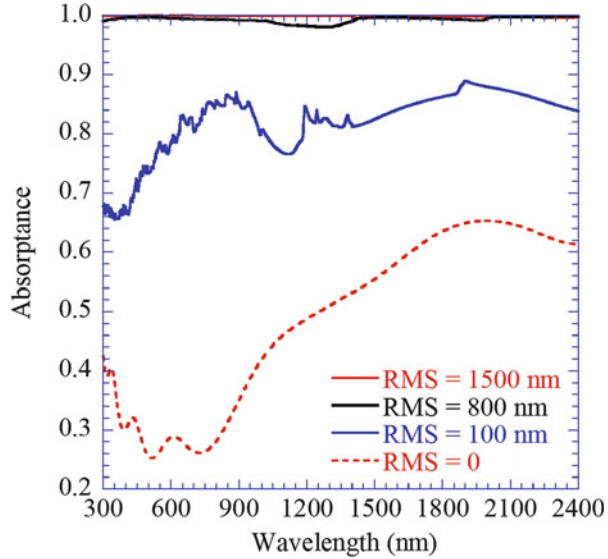
4.4 Sample Fabrication and Characterization

Encouraged by the simulated results shown in Fig. 4.10, a Bi_2Te_3 surface with roughness around 800 nm is manufactured.

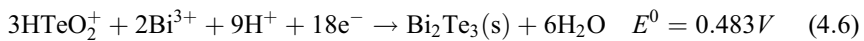
4.4.1 Sample Fabrication

As one of the promising materials for a thermoelectric device, the fabrication of a film made of Bi_2Te_3 has been well studied. However, previous investigations are

Fig. 4.10 The absorption spectra of the proposed absorbers with different roughnesses. (From Ref. [45])



focused on how to minimize the roughness of the Bi_2Te_3 film to reduce the thermal and electrical contact resistance at the interface between the nanostructured alloy and the metallic electrodes [11]. Manufacturing a Bi_2Te_3 film with large roughness is still a challenging task with the present technology. It has been reported that the Bi_2Te_3 films can be elaborated by a variety of deposition techniques, such as electrochemical deposition [25], molecular beam epitaxy (MBE) [15], evaporation [20], and metal organic chemical vapor deposition (MOEVD) [4]. Among them, the electrochemical deposition method is very popular for its advantages of relative ease in modulating film composition, cost-effectiveness, controlling Bi_2Te_3 film thickness and roughness, as well as large-area coverage. The deposition mechanism of the electrochemical deposition method is well understood, which can be expressed by the following chemical formula [25].



It has been demonstrated that thickness and roughness of Bi_2Te_3 films are affected by the time of the reaction, potential of the electrodes, as well as the temperature of the reaction. In the present study, a stainless steel sheet (around $2.5\text{ cm} \times 2.5\text{ cm}$) was polished and used as the substrate, while the fabrication was carried out at room temperature via electrochemical deposition method by using a conventional three-electrode cell configuration. The potential applied during deposition was -80 mV and the deposition time was 30 min for manufacturing a Bi_2Te_3 film with roughness around 800 nm. Other samples with different roughnesses were fabricated by varying the potential and deposition time of the reaction to control the morphology of the nanostructures forming the rough Bi_2Te_3 surface.

4.4.2 Characteristics of the Sample

Figure 4.11 shows characteristics of the fabricated sample made of Bi_2Te_3 , which includes the scanning electron microscopy (SEM) derived figure and roughness analysis. The SEM figure is shown in Fig. 4.11a which was taken by using a scanning electron microscope (Tescan Mira3 field emission scanning electron microscopy, FESEM). It can be seen from this figure that there are a lot of nanostructures in the sample. In addition, the nanostructures have sharp tips and a gradually changing cross section, which can also be found from the confocal microscope image shown in Fig. 4.11b. The roughness measured by an Olympus LEXT OLS4000 3D laser confocal microscope and the roughness of the surface was around 794 nm when neglecting the texture of the stainless steel. However, it should be noted that even though the metallic substrate had been polished, there were still some ridges and valleys on the surface in microscale, which can be seen in Figs. 4.11b, c. The sharp nanostructures and the large roughness of the sample meet in Sect. 4.3.1. However, the Bi_2Te_3 nanostructures of the fabricated sample are slightly different from those in the simulation model, which is shown in Fig. 4.9.

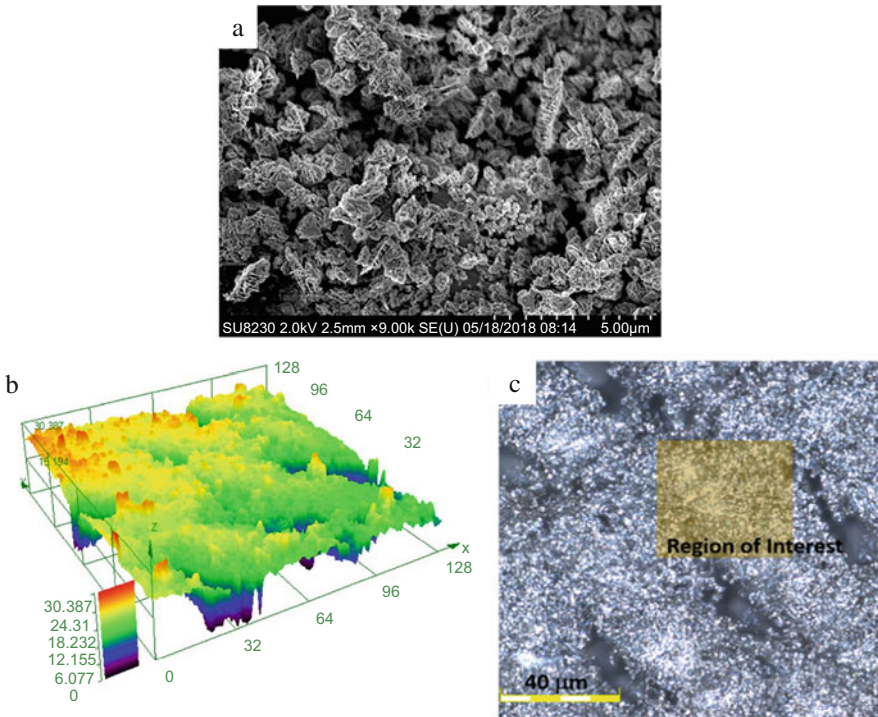


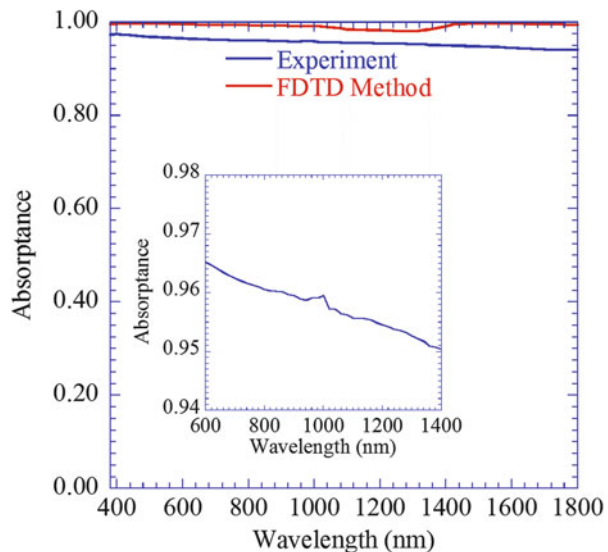
Fig. 4.11 The SEM image and sample roughness measurement from a confocal microscope. (a) SEM image; (b) roughness analysis; (c) interested region. (From Ref. [45])

4.4.3 Results and Discussion

Figure 4.12 shows the comparison of the absorptance of the sample made of a rough Bi_2Te_3 surface with a roughness of 800 nm, where the measured value is indicated by a blue solid line and the calculated absorptance is plotted as a solid red line. An integrating sphere with a grating monochromator was used to measure the spectral, directional-hemispherical reflectance of the sample. Due to the limitation of the tungsten-halogen lamp of the setup, the measurement was carried out only in the wavelength range of 380–1800 nm with an increment of 20 nm. It can be seen from Fig. 4.12 that the maximum absorptance of the sample is 0.975 at 400 nm with a minimum of around 0.94 from the measurement. In addition, there is a jump at the wavelength around 1000 nm in the inserted figure, validating that the underlying mechanisms derived from the simulation, which are slow-light effect for 300–1000 nm, and gradient index effect for wavelength longer than 1000 nm. However, there is a slight difference (which is smaller than 5%) between the absorptance of simulation and measurements. The difference comes from different nanostructures used in the simulation model and those obtained from fabrication. The roughness of the surface can be precisely controlled in the fabrication process, but further work is required to control the morphology of the nanostructures to get a rougher surface as shown in Fig. 4.9 to achieve total absorption of solar energy.

Another three samples with different nanostructures and roughnesses were fabricated by varying the potential of the electrodes and reaction time of the electrochemical deposition method. The SEM figures of all four samples are presented in Fig. 4.13, in which Sample 1 is the one shown in Fig. 4.11a. As can be seen from Fig. 4.13, the nanostructures of Sample 2 is much smaller than those of Sample 1, while there are micro-sized structures in both Sample 3 and Sample 4. However, the microstructures in

Fig. 4.12 The absorptance of the manufactured Bi_2Te_3 sample, the calculated results are also plotted in the same figure. (From Ref. [45])



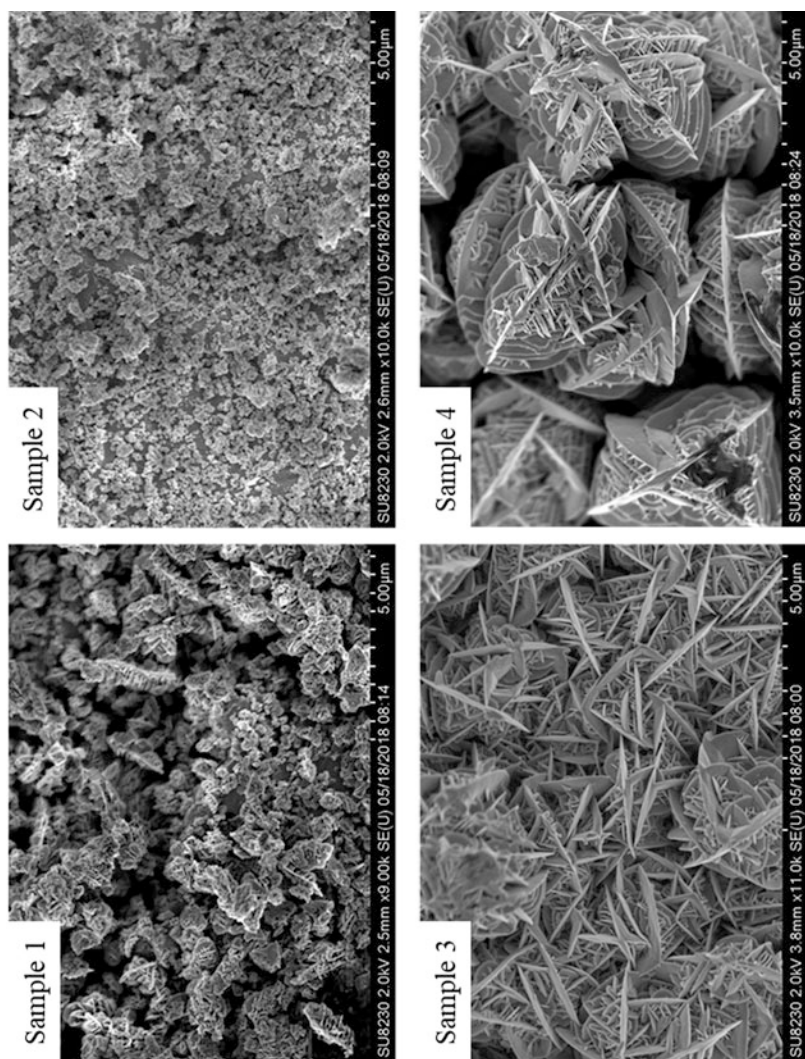
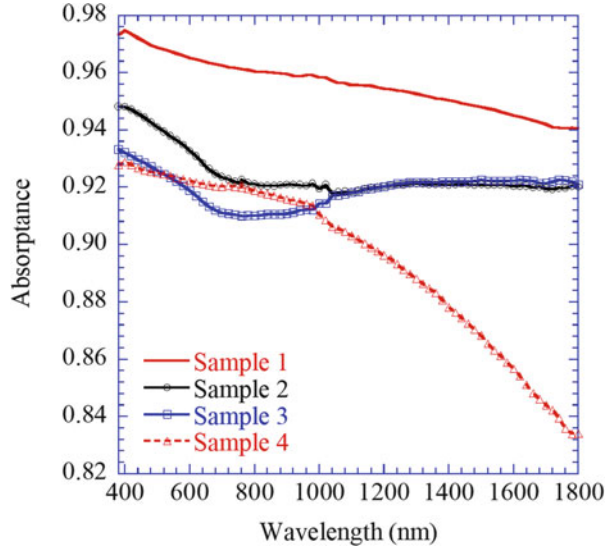


Fig. 4.13 SEM of the four Bi₂Te₃ samples with different roughnesses. (From Ref. [45])

Fig. 4.14 Absorption spectra of the four samples in the spectral regions from 380 to 1800 nm. (From Ref. [45])



Sample 4 are larger than those of Sample 3 with a larger distance between the microstructures in Sample 4. The absorption spectra of the four samples are presented in Fig. 4.14. By comparing the red solid line for Sample 1 and black solid line with circles of Sample 2, it can be seen that the roughness greatly affects the absorbance of the rough surface. A Bi_2Te_3 surface with a roughness smaller than 800 nm has lower absorbance in the wavelength range of 380–1800 nm. On the other hand, the distance between Bi_2Te_3 structures affects the absorption property in long wavelength range, which is the region of 1000–1800 nm, and this conclusion can be drawn from the comparison of blue solid line with squares and red dashed line with triangles, which are for the absorbance of Sample 3 and Sample 4, respectively.

4.5 Concluding Remarks

A perfect absorber made of a natural hyperbolic, anisotropic material (Bi_2Te_3) for solar energy harvesting is proposed. Numerical studies have been carried out for regularly arranged Bi_2Te_3 nano-pyramids on a thin substrate submerged in water. In addition, four samples made of Bi_2Te_3 with different roughness have also been fabricated, and the absorbance of these samples was measured. The results from simulations and experiments can be summarized as follows:

- I. The surface with regularly arranged Bi_2Te_3 nano-pyramids has a perfect absorption to the solar energy. The slow-light effect in type-II hyperbolic region and gradient index effect in long wavelength region are the main underlying mechanisms, respectively. These two mechanisms should be respectively considered to realize perfect absorption of solar energy in practice.

- II. The absorption properties of the absorber greatly depend on the geometry of the Bi_2Te_3 nano-pyramids, the material, and thickness of the substrate, even though there is a tolerable range about those parameters. The top and bottom widths of the nano-pyramids mainly affect the absorption in the region of 300–1000 nm, while the height of the nano-pyramids and the distance between them affect the absorptance of the absorber in the region of 1000–2400 nm. In addition, the substrate mainly reflects the light back to the nanostructures to be reabsorbed.
- III. Rough Bi_2Te_3 surface with sharp nanostructures can well replace the ideal metamaterial with nano-pyramids in the simulation to totally absorb the solar energy. The absorptance of such Bi_2Te_3 absorber with a roughness larger than 800 nm will be a perfect absorber in the calculation, while the fabricated sample with a roughness of 794 nm reaches 97.5% with a minimum of 94% in the wavelength range of 380–1800 nm. The analysis of four samples clearly validates the underlying mechanisms derived from theoretical investigations.

The present study opens a gate for perfect absorption of solar energy by using natural hyperbolic materials, and proposed absorbers have promising applications in the photothermal conversion of solar energy in water or aqueous solutions.

Acknowledgments This work was supported by the National Natural Science Foundation of China through Grant No. 51420105009.

References

1. R. Asahi, T. Morikawa, T. Ohwaki, K. Aoki, Y. Taga, Visible-light photocatalysis in nitrogen-doped titanium oxides. *Science* **293**, 269–271 (2001)
2. S. Biehs, M. Tschikin, P. Ben-Abdallah, Hyperbolic metamaterials as an analog of a blackbody in the near field. *Phys. Rev. Lett.* **109**, 104301 (2012)
3. C. Bohren, D. Huffman, *Absorption and Scattering of Light by Small Particles* (Wiley, New York, 1983)
4. A. Boulouze, A. Giani, F. Pascal-Delannoy, M. Boulouze, A. Foucaran, A. Boyer, Preparation and characterization of MOCVD bismuth telluride thin films. *J. Cryst. Growth* **194**, 336 (1998)
5. Y. Cui, K. Fung, J. Xu, H. Ma, Y. Jin, S. He, N. Fang, Ultrabroadband light absorption by a sawtooth anisotropic metamaterial slab. *Nano Lett.* **12**, 1443–1447 (2012)
6. S. Dai, Q. Ma, T. Andersen, A. Mcleod, Z. Fei, M. Liu, M. Wagner, K. Watanabe, T. Taniguchi, M. Thiemens, F. Keilmann, P. Jarillo-Herrero, M. Fogler, D. Basov, Subdiffraction focusing and guiding of polaritonic rays in a natural hyperbolic material. *Nat. Commun.* **6**, 6963 (2015)
7. M. Esslinger, R. Vogelgesang, N. Talebi, W. Khunsin, P. Gehring, S. Zuani, B. Gompf, K. Kern, Tetradymites as natural hyperbolic materials for the near-infrared to visible. *ACS Photon.* **1**, 1285–1289 (2014)
8. P. Falkowski, J. Raven, *Aquatic Photosynthesis* (Princeton University Press, Princeton, 2013)
9. A. Fang, T. Koschny, C. Soukoulis, Optical anisotropic metamaterials: negative refraction and focusing. *Phys. Rev. B* **79**, 245127 (2009)
10. Z. Fang, Y. Zhen, O. Neumann, A. Polman, F. Javier García de Abajo, P. Nordlander, N. Halas, Evolution of light-induced vapor generation at a liquid-immersed metallic nanoparticle. *Nano Lett.* **13**, 1736–1742 (2013)

11. H. Feng, B. Yu, S. Chen, K. Collins, C. He, Z. Ren, G. Chen, Studies on surface preparation and smoothness of nanostructured Bi₂Te₃-based alloys by electrochemical and mechanical methods. *Electrochim. Acta* **56**(8), 3079–3084 (2011)
12. L. Ferrari, C. Wu, D. Lepage, X. Zhang, Z. Liu, Hyperbolic metamaterials and their applications. *Prog. Quantum Electron.* **40**, 1–40 (2015)
13. E. Glytsis, T. Gaylord, Three-dimensional (vector) rigorous coupled-wave analysis of anisotropic grating diffraction. *J. Opt. Soc. Am. A* **7**(8), 1399–1420 (1990)
14. C. Granqvist, Solar energy materials. *Adv. Mater.* **15**(21), 1789–1803 (2003)
15. S. Harrison, S. Li, Y. Huo, B. Zhou, Y. Chen, J. Harris, Two-step growth of high quality Bi₂Te₃ thin films on Al₂O₃ by molecular beam epitaxy. *Appl. Phys. Lett.* **102**, 171906 (2013)
16. A. Hoffman, L. Alekseyev, S. Howard, K. Franz, D. Wasserman, V. Podolskiy, E. Narimanov, D. Sivco, C. Gmachl, Negative refraction in semiconductor metamaterials. *Nat. Mater.* **6**, 946–950 (2007)
17. H. Hu, D. Ji, X. Zeng, K. Liu, Q. Gan, Rainbow trapping in hyperbolic metamaterial waveguide. *Sci. Rep.* **3**, 1249 (2013)
18. S. Igor, C. Simovski, Giant radiation heat transfer through micron gaps. *Phys. Rev. B* **84**, 195459 (2011)
19. S. Ishii, A. Kildishev, E. Narimanov, V. Shalaev, V. Drachev, Subwavelength interference pattern from volume plasmon polaritons in a hyperbolic medium laser. *Laser Photonics Rev.* **7**, 265–271 (2013)
20. L. Jyun-Min, C. Ying-Chung, L. Chi-Pi, Annealing effect on the thermoelectric properties of Bi₂Te₃ thin films prepared by a thermal evaporation method. *J. Nanomater.* **2013**, 1 (2013)
21. H. Krishnamoorthy, Z. Jacob, E. Narimanov, I. Kretzschmar, V. Menon, Topological transitions in metamaterials. *Science* **336**, 205–209 (2012)
22. M. Kyoung, M. Lee, Nonlinear absorption and refractive index measurements of silver nanorods by the Z-scan technique. *Opt. Commun.* **171**(1–3), 145–148 (1999)
23. J. Li, S. Liu, Y. Liu, F. Zhou, Z. Li, Anisotropic and enhanced absorptive nonlinearities in a macroscopic film induced by aligned gold rods. *Appl. Phys. Lett.* **96**(26), 263103 (2010)
24. X. Liu, L. Wang, Z. Zhang, Wideband tunable omnidirectional infrared absorbers based on doped-silicon nanowire arrays. *J. Heat Transf.* **135**, 061602 (2013)
25. Y. Ma, A. Johansson, E. Ahlberg, A. Palmqvista, A mechanistic study of electrodeposition of bismuth telluride on stainless steel substrates. *Electrochim. Acta* **55**, 4610–4617 (2010)
26. A. Meier, N. Gremaud, A. Steinfeld, Economic evaluation of the industrial solar production of lime. *Energy Convers. Manag.* **46**, 905–926 (2005)
27. S. Mohan, J. Lange, H. Graener, G. Seifert, Surface plasmon assisted optical nonlinearities of uniformly oriented metal nano-ellipsoids in the glass. *Opt. Express* **20**, 28655–28663 (2012)
28. E. Narimanov, A. Kildishev, Metamaterials: naturally hyperbolic. *Nat. Photonics* **9**, 214–216 (2015)
29. O. Neumann, A. Urban, J. Day, S. Lal, P. Nordlander, N. Halas, Solar vapor generation enabled by nanoparticles. *ACS Nano* **7**, 42–49 (2012)
30. O. Neumann, C. Feronti, A. Neumann, A. Dong, K. Schell, B. Lu, E. Kim, M. Quinn, S. Thompson, N. Grady, P. Nordlander, M. Oden, N. Halas, Compact solar autoclave based on steam generation using broadband light-harvesting nanoparticles. *Proc. Natl. Acad. Sci.* **110**, 11677–11681 (2013)
31. G. Ni, G. Li, S. Boriskina, H. Li, W. Yang, T. Zhang, G. Chen, The steam generation under one sun enabled by a floating structure with thermal concentration. *Nat. Energy* **1**, 16126 (2016)
32. A. Nikitin, E. Yoxall, M. Schnell, S. Velez, I. Dolado, P. Alonso-Gonzalez, F. Casanova, L. Hueso, R. Hillenbrand, Nanofocusing of hyperbolic phonon polaritons in a tapered boron nitride slab. *ACS Photon.* **3**, 924–929 (2016)
33. N. Nwachukwu, W. Okonkwo, Effect of an absorptive coating on solar energy storage in a Trombe wall system. *Energ. Buildings* **40**(3), 371–374 (2008)
34. R. Olmon, B. Slovick, T. Johnson, D. Shelton, S. Oh, G. Boreman, M. Raschke, Optical dielectric function of gold. *Phys. Rev. B* **86**, 235147 (2012)

35. E. Palik, *Handbook of Optical Constants of Solids* (Academic, San Diego, 1998)
36. V. Perebeinos, J. Tersoff, P. Avouris, Effect of exciton-phonon coupling in the calculated optical absorption of carbon nanotubes. *Phys. Rev. Lett.* **94**, 027402 (2005)
37. A. Polman, Solar steam nanobubbles. *ACS Nano* **7**, 15–18 (2013)
38. C. Simovski, S. Maslovski, I. Nefedov, S. Tretyakov, Optimization of radiative heat transfer in hyperbolic metamaterials for thermophotovoltaic applications. *Opt. Express* **21**, 14988–15013 (2013)
39. T. Soga, *Nanostructured Materials for Solar Energy Conversion* (Elsevier, Amsterdam, 2006)
40. P. Tao, G. Ni, C. Song, W. Shang, J. Wu, J. Zhu, G. Chen, T. Deng, Solar-driven interfacial evaporation. *Nat. Energy* **3**, 1031–1041 (2018)
41. T. Todorov, K. Reuter, D. Mitzi, High-efficiency solar cell with earth-abundant liquid-processed absorber. *Adv. Mater.* **22**, E156–E159 (2010)
42. L. Verslegers, P. Catrysse, Z. Yu, S. Fan, Deep-subwavelength focusing and steering of light in an aperiodic metallic waveguide array. *Phys. Rev. Lett.* **103**, 033902 (2009)
43. Z. Wang, Z. Zhang, P. Cheng, Natural anisotropic nanoparticles with a broad absorption spectrum for solar energy harvesting. *Int. Commun. Heat Mass Transf.* **96**, 109–113 (2018a)
44. Z. Wang, Z. Zhang, X. Quan, P. Cheng, A perfect absorber design using a natural hyperbolic material for harvesting. *Sol. Energy* **159**, 329–336 (2018b)
45. Wang, Z, Yang, P, Qi, G, Zhang, Z, and Cheng, P (2019). Measurements of the Absorptance of an Absorber Made of a Natural Hyperbolic Material for Harvesting Solar Energy
46. J. Wu, Broadband light absorption by tapered metal-dielectric multilayered grating structures. *Opt. Commun.* **365**, 93–98 (2016)
47. Y. Xiong, Z. Liu, X. Zhang, Projecting deep-subwavelength patterns from diffraction-limited masks using metal-dielectric multilayers. *Appl. Phys. Lett.* **93**, 111116 (2008)
48. J. Yao, Z. Liu, Y. Liu, Y. Wang, C. Sun, G. Bartal, A. Stacy, X. Zhang, Optical negative refraction in bulk metamaterials of nanowires. *Science* **21**, 930–930 (2008)
49. Z. Zhang, *Nano/Microscale Heat Transfer* (McGraw-Hill, New York, 2007)
50. J. Zhao, Z. Zhang, Electromagnetic energy storage and power dissipation in nanostructures. *J. Quant. Spectrosc. Radiat. Transf.* **151**, 49–57 (2015)
51. B. Zhao, Z. Zhang, Perfect absorption with trapezoidal gratings made of natural hyperbolic materials. *Nanoscale Microscale Thermophys. Eng.* **21**(3), 123–133 (2017)
52. J. Zhou, A. Kaplan, L. Chen, L. Guo, Experiment and theory of the broadband absorption by a tapered hyperbolic metamaterial array. *ACS Photon.* **1**, 618–624 (2014)
53. L. Zhou, Y. Tan, D. Ji, B. Zhu, P. Zhang, J. Xu, Q. Gan, Z. Yu, J. Zhu, Self-assembly of highly efficient, broadband plasmonic absorbers for solar steam generation. *Sci. Adv.* **2**(4), e1501227 (2016)



Strategies for Improving Solar Energy Conversion: Nanostructured Materials and Processing Techniques

5

Monica C. So, Sung Won Yoon, and Nicole D. Mackie

Contents

5.1	Introduction	112
5.1.1	The Current Dilemma with Solar Energy Conversion	112
5.1.2	Chapter Direction and Outline	113
5.2	Enhancing Light Absorption	113
5.2.1	Perovskites and Light Harvesting	113
5.2.2	Single Organic Cation Perovskites	114
5.2.3	Mixed Organic Cation Perovskites	114
5.2.4	Metal-Organic Frameworks (MOFs) and Sensitization	115
5.2.5	Molecular Chromophores as Sensitizers	115
5.2.6	Chromophores Integrated as MOF Building Blocks	116
5.2.7	MOFs as Sensitizers	116
5.3	Enhancing Exciton Splitting	116
5.3.1	Energy Transfer Mechanisms in MOFs	116
5.3.2	Metalloporphyrins Facilitating Förster Energy Transfer	117
5.3.3	Perylene Diimides Facilitating Förster Energy Transfer	120
5.4	Enhancing Charge Separation and Collection	121
5.4.1	Importance of Processing Techniques to Improve Morphology	121
5.4.2	Liquid-Solid Interface Methods	121
5.4.3	Liquid-Liquid Interface Methods	123
5.4.4	Air-Liquid Interface Methods	127
5.5	Conclusions	131
	References	132

Author Contribution

S. Yoon and N. Mackie wrote and edited the first draft based on research and review data. M.C. So wrote, revised, and submitted the manuscript to the publishers.

M. C. So (✉) · S. W. Yoon · N. D. Mackie

Department of Chemistry and Biochemistry, California State University, Chico, Chico, CA, USA

e-mail: mso@csuchico.edu

Abstract

Organic photovoltaics, the technology to convert sunlight into electricity by employing thin films of organic semiconductors, has received increased interest due to innovations in nanomaterials and processing methods. These technological improvements have the potential to advance a new generation of low-cost, solar-powered products with small form factors. Here, we review the photophysical and chemical concepts of organic photovoltaics and discuss some recent synthesis and fabrication results as well as future challenges.

5.1 Introduction

5.1.1 The Current Dilemma with Solar Energy Conversion

To meet future demands, we must maximize our use of renewable resources while minimizing our dependence on fossil fuels. Fossil fuels collectively represent over 80% of our total energy supply, while renewable sources only account for 10%. While there are many sources of renewable energy, solar energy is one of the most abundant. In fact, the sun delivers up to 67 terawatts per year of power, which exceeds the projected global energy demand of 30 terawatts per year by 2050. Organic photovoltaics (OPVs) show promise for light-to-electrical energy conversion with the cells having power conversion efficiencies of 13.2%, but the theoretical maximum is at 32%. If efficiencies can be increased to even a fraction of the way to ca. 16%, OPVs would be more cost-competitive with their inorganic counterparts.

However, there are four major challenges in improving OPV performance. These include (a) poor light harvesting, (b) inefficient exciton splitting into holes and electrons, (c) increased recombination of separated charges at the donor/acceptor interface and (d) inefficient collection of charges at the active layer/electrode interface. The problem related to (a) results in a limited range of absorbance of visible light. The problem for (b) originates from the limited diffusion length of the exciton, typically ca. 10 nm. The problem for (c) results in the problem (d), such as partial electrical shorting. OPVs constructed from conventional materials and architectures involve conflicting design requirements, which make it difficult to address all four problems simultaneously.

The aim of this chapter is to provide an overview of nanomaterials and thin film processing techniques. Specifically, this chapter discusses nanomaterials and thin film processing techniques, which have the potential to overcome the challenges associated with conventional OPV cells. To address the problem (a), we incorporate two novel nanomaterials (perovskites and metal-organic frameworks) to expand the light collection in the near-infrared region of light. To address the problem (b), we can precisely align the chromophores in a metal-organic framework platform. To address problems (c) and (d), we can optimize optical path length and crystal-thickness by using thin film deposition techniques. These approaches can potentially lead to much higher efficiencies, based on the simultaneous resolution of the four challenges hindering OPV performance.

5.1.2 Chapter Direction and Outline

Nanomaterials and thin film processing techniques are critical to resolving the current dilemma hindering OPV efficiency. Nanomaterials consist of interchangeable components, allowing for synthetic and chemical tunability on the nanoscale. Thin film processing techniques interface nanomaterials to industrially relevant supports, which are critical for manufacturing photovoltaics.

Section 5.2 presents a chemical approach to expanding light harvesting using two new classes of materials. These classes of materials include lead-halide perovskites and metal-organic frameworks (MOFs). Lead-iodide perovskites (APbI_3 , A = monovalent cation) can be modified to improve light absorption in the near-infrared region. Since MOFs are composed of both metal cations and organic linkers, their framework can be synthetically or chemically modified to improve light harvesting in deficient regions of the solar spectrum. Both modular nanomaterials provide promise in enhancing the light collection ability of solar energy conversion schemes.

Section 5.3 provides another chemical route to enhance exciton splitting by mimicking energy transport phenomena in plants. Given that energy migration in natural photosynthesis occurs, in part, through highly ordered porphyrin-like pigments (chlorophylls), crystalline MOFs assembled from photoactive components may exhibit the same behavior. To do so, organic linkers have been used to build and modify MOFs to study long-range Förster resonance energy transfer (FRET) mechanisms. By exploiting long-range, rather than short-range, energy transport in nanostructures, the lifetime of excitons will increase.

Section 5.4 highlights several thin film processing techniques which allow for deposition of nanomaterials. These techniques must produce ultrathin, low roughness, and homogeneous coatings on industrially relevant substrates, such as silicon. We discuss solid-liquid interface methods, such as layer-by-layer deposition, a stepwise, automated liquid phase process for depositing nanomaterials into thin coatings. Liquid-liquid interface methods will also be discussed. Air-liquid interface methods are other facile approaches which produce films of subnanometer roughness. An example is the Langmuir-Blodgett method, which assembles thin films by dipping hydrophobic or hydrophilic components into a liquid subphase. These are time-efficient and cost-effective processing techniques for deposition of nanomaterials, which are important for the fabrication of solar energy conversion devices.

Section 5.5 discusses the future outlook of these materials and techniques in enhancing OPV performance.

5.2 Enhancing Light Absorption

5.2.1 Perovskites and Light Harvesting

Perovskites conform to the structure ABX_3 , in which the A and B cations are coordinated with the X anions. The cations and anions of the perovskite structure are modular. Since different monovalent cations (A^+) can be used to construct

perovskites, a range of optical properties can be obtained. This underscores the versatility of perovskites to be integrated with high performing solar cells, enabling a diversity of approaches for light-to-electricity conversion.

5.2.2 Single Organic Cation Perovskites

The most common perovskites solar cells contain methylammonium lead iodide ($\text{CH}_3\text{NH}_3\text{PbI}_3$). Though they contain methylammonium cation (MA^+ , $\text{H}_3\text{CN}^+(\text{H}_3)$), formamidinium (FA^+ , $^+\text{NH}_2 = \text{C}(\text{H})\text{-NH}_2 \dots \text{I}^-$) can replace the MA^+ . Consequently, a redshifting of the absorbance occurs, attributed to the larger size and stability of the FA^+ compared to MA^+ (Fig. 5.1) [1, 2]. This suggests that a broader spectrum of visible light can potentially be converted from light to electricity in a solar cell. The challenge with using formamidinium iodide (FA^+ precursor) is that it is more hygroscopic than methylammonium iodide (MA^+ precursor), so the former should be stored in an inert atmosphere.

5.2.3 Mixed Organic Cation Perovskites

Another modification to the perovskite structure is to include mixed cations. Pellet et al. [3] reported such an approach by studying the optical properties of mixed cation lead-based halide perovskites. Compared to unmixed cation perovskite, such as methylammonium lead iodide (CH_3NH_3) PbI_3 , the mixed-cation lead iodide perovskite (CH_3NH_3) $_{0.8}$ (HNCHNH_3) $_{0.2}$ PbI_3 exhibits a 20 nm red shift of the absorbance onset upon addition of only 20 mol % of formamidinium iodide (FAI) into the structure. As the FA^+ concentration was increased, three effects were observed: (1) the absorbance onset shifted to shorter wavelengths, (2) the absorbance of the film decreased, and (3) no change in the band gap was detected. Pellet and

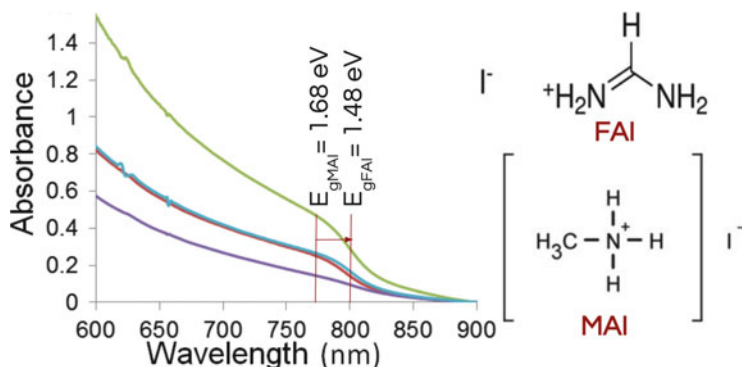
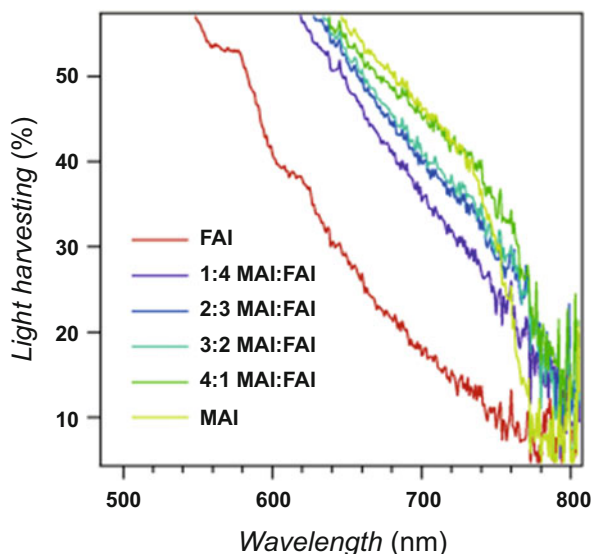


Fig. 5.1 UV-visible spectra of FAPbI_3 films are redshifted from that of MAPbI_3 , due to differences in cation structure

Fig. 5.2 Light-harvesting spectra of perovskite films show that optimized 4:1 MAI:FAI concentration redshifts the absorbance onset by 20 nm relative to the MAI sample. (Reproduced from Ref. [3] with permission from Wiley VCH)



coworkers optimized the MAI:FAI ratio of 4:1 or 3:2 (c/c) in the 2-propanol bath solution for maximizing light absorption of the perovskite into the red while maintaining the high absorption coefficient of $(\text{CH}_3\text{NH}_3)\text{PbI}_3$. Another benefit of formamidinium lead iodide is that it scatters light less strongly than methylammonium lead iodide. Therefore, the former serves as a promising organic cation to utilize in perovskite solar cells (Fig. 5.2).

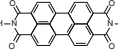
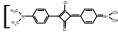
5.2.4 Metal-Organic Frameworks (MOFs) and Sensitization

Since MOFs can be assembled from a plethora of organic and inorganic building blocks, the MOFs can exhibit a diverse range of optoelectronic properties. Consequently, they can be integrated into a variety of energy conversion nanomaterials and systems [4–10].

There are examples of MOFs serving as (a) the sensitizer agent, which transfers energy to a neighboring material [11–13], and (b) the material to be sensitized. Note for the latter case, MOFs are generally synthesized with molecular chromophores (struts) to optimize exciton migration. However, the more challenging issue is to include struts that exhibit ideal absorption characteristics which overlap with the solar spectrum. Therefore, ideal MOFs for functional harvesting of solar energy must not only exhibit efficient exciton migration but also optimize solar absorption.

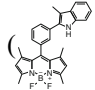
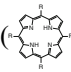
5.2.5 Molecular Chromophores as Sensitizers

To develop materials suitable for solar light absorption, MOF chemists have generally incorporated porphyrin struts [3, 14, 15]. These struts have demonstrated

directional exciton migration over several tens of struts after the initial strut has been excited. However, other than the Soret band region, porphyrins do not absorb strongly in the regions aligned with the remainder of the solar spectrum. Therefore, secondary chromophores, such as perylene diimides [] and squaraine derivatives [] must be installed into MOFs to account for the deficiency in solar light absorption.

5.2.6 Chromophores Integrated as MOF Building Blocks

An alternative strategy to sensitizing porphyrin MOFs is to build the MOF with an additional strut that absorbs in complementary regions of the solar spectrum. Lee and coworkers reported such an approach by building an MOF with both boron

dipyrromethene () and porphyrin struts ( ZnTCPP) [13]. The

bodipy absorbs in the green spectral region where the porphyrin absorbs only marginally. Additionally, this study showed that energy absorbed by the bodipy struts was efficiently (i.e., essentially quantitatively) transferred to the porphyrin struts. Thus, under green illumination, strong emission from the porphyrin was observed, even though the irradiation directly excited only bodipy. However, the longer length of the bodipy struts in the vertical direction creates a larger spacing between porphyrins in the MOF. This results in diminished lateral dipolar coupling between the porphyrins, decreasing the efficiency of exciton migration.

5.2.7 MOFs as Sensitizers

To compensate for the loss in exciton migration efficiency, an alternative approach is to mimic light-harvesting complexes in plants, such as carotenoids and reaction centers. In other words, molecules of higher exciton energy can transfer energy to those with lower exciton energy in an MOF structure [16].

5.3 Enhancing Exciton Splitting

5.3.1 Energy Transfer Mechanisms in MOFs

Since MOFs can self-assemble into ordered structures containing both donor (D) and acceptor (A) chromophores (i.e., metalloporphyrins), MOFs serve as promising platforms for monitoring the energy transport. For supramolecular systems containing weakly coupled chromophores, the Förster and Dexter energy transfer mechanisms best model the transfer of energy.

In the Förster energy transfer mechanism (Eq. 5.1) [17], the rate of intermolecular energy transfer (k_{EnT}) between a fixed pair of molecules depends on the overlap integral (OI) between the normalized emission spectrum of D and the normalized absorption spectrum of A, and the exciton coupling constant (J , cm^{-1}) between D and A (arbitrary units).

$$k_{EnT} = \frac{2\pi}{\hbar} J^2(OI) \quad (5.1)$$

The magnitude of J is related to the magnitude of the oscillator strength for excitation to the lowest singlet excited state, the fluorescence quantum yield, the separation distance (R , m) between the D and A moieties ($J^2 \propto \frac{1}{r^6}$ for point dipoles), and the angle between their transition dipoles.

Unlike Förster energy transfer which only applies to allowed transitions, the Dexter energy transfer can occur when the spin state is not conserved. Another difference is that Dexter transfer dominates over very short distances relative to those for Förster transfer. Since Dexter energy transfer depends on electronic coupling and orbital overlap of D and A, the rate of Dexter energy transfer tapers off with increased R (Eq. 5.2) [18]:

$$k_{EnT} = \frac{2\pi}{\hbar} K^2 e^{-2R/L}(OI) \quad (5.2)$$

In Eq. 5.2, L is the sum of the van der Waals radius (Å), and K is related to the degree of electronic coupling at close contact between D and A. Others have extensively observed Dexter transfer in ruthenium-based MOFs [1, 3, 5, 6, 19–29], but we highlight only MOFs exhibiting Förster energy transfer in this chapter. There are two main changes that have been demonstrated in the literature involving Förster energy transfer: (a) electronic structure of organic linkers or (b) spatial variations in the supramolecular structure.

5.3.2 Metalloporphyrins Facilitating Förster Energy Transfer

Commonly incorporated into MOFs, metalloporphyrins share structural and chromophoric features of plant chlorophylls. Since metalloporphyrin linkers are synthetically tunable, they can exhibit a wide range of light harvesting and energy transfer capabilities [30–32].

Lee and colleagues utilized a metalloporphyrin-based MOF of the pillared paddlewheel motif for one of the earliest energy transfer studies [13]. Built from dinuclear zinc clusters as nodes, bodipy as the pillar, and zinc-based tetracarboxyphenyl porphyrin (TCPP) as the paddlewheel linker, the BOP MOF emitted fluorescence upon excitation by red, blue, and green photons. Consequently, the authors observed efficient energy transfer from the antenna pillar to the primary chromophore linker (Fig. 5.3.). Despite the geometric orthogonality of its linkers,

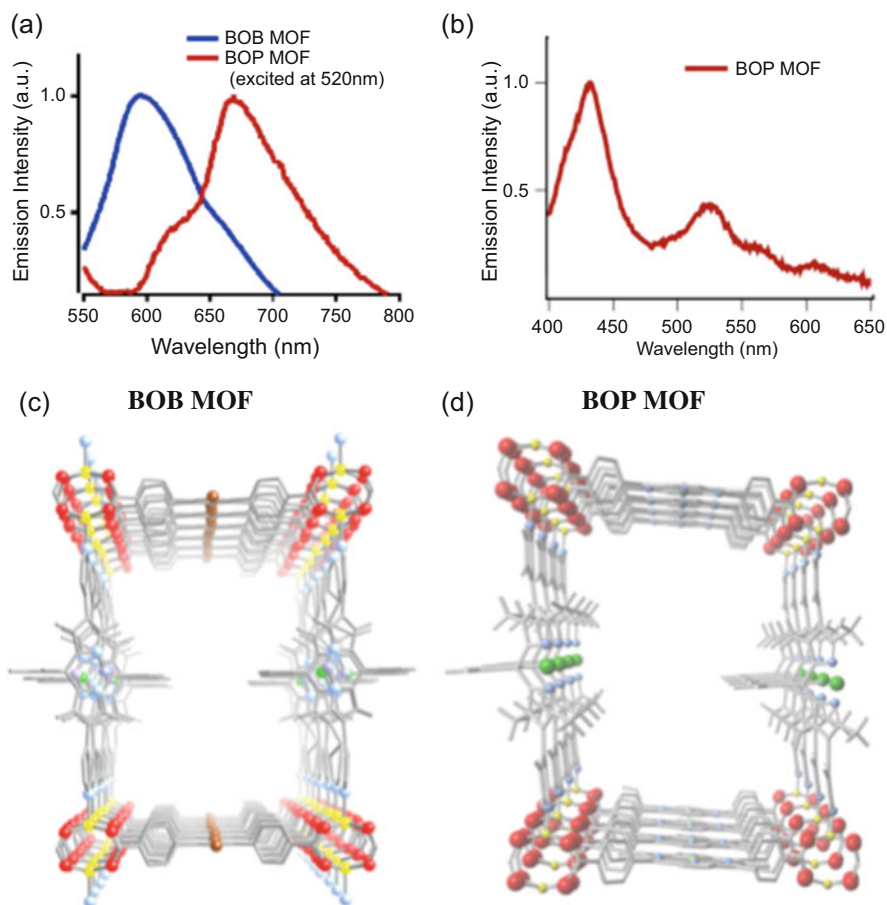


Fig. 5.3 (a) Emission spectra of BOB and BOP MOFs took at 520 nm excitation. (b) Excitation spectra of BOP and pyridine-treated BOP MOF monitored at 667 nm. Crystallographic illustration of (c) BOB MOF and (d) BOP MOF. O = red spheres, Zn = yellow spheres, C = gray segment, N = blue spheres, B = green spheres, F = white segment. (Reproduced from Ref. [33] with permission from the American Chemical Society)

energy transfer occurred due to the slight deviation of their root-mean-square value of the angle from 90° . To avoid ligand-to-metal charge transfer and resulting quenching of struts, the authors incorporated Zn(II) as metal nodes. This seminal work established that metalloporphyrin-based MOFs can be used as platforms for studying energy transfer behavior.

Given that the criteria for energy transfer directionality were vaguely defined in a metalloporphyrin-based MOF (DA-MOF), Patwardhan et al. [16] set out to investigate. He increased the anisotropy of energy transfer by replacing the TCPP linkers with a

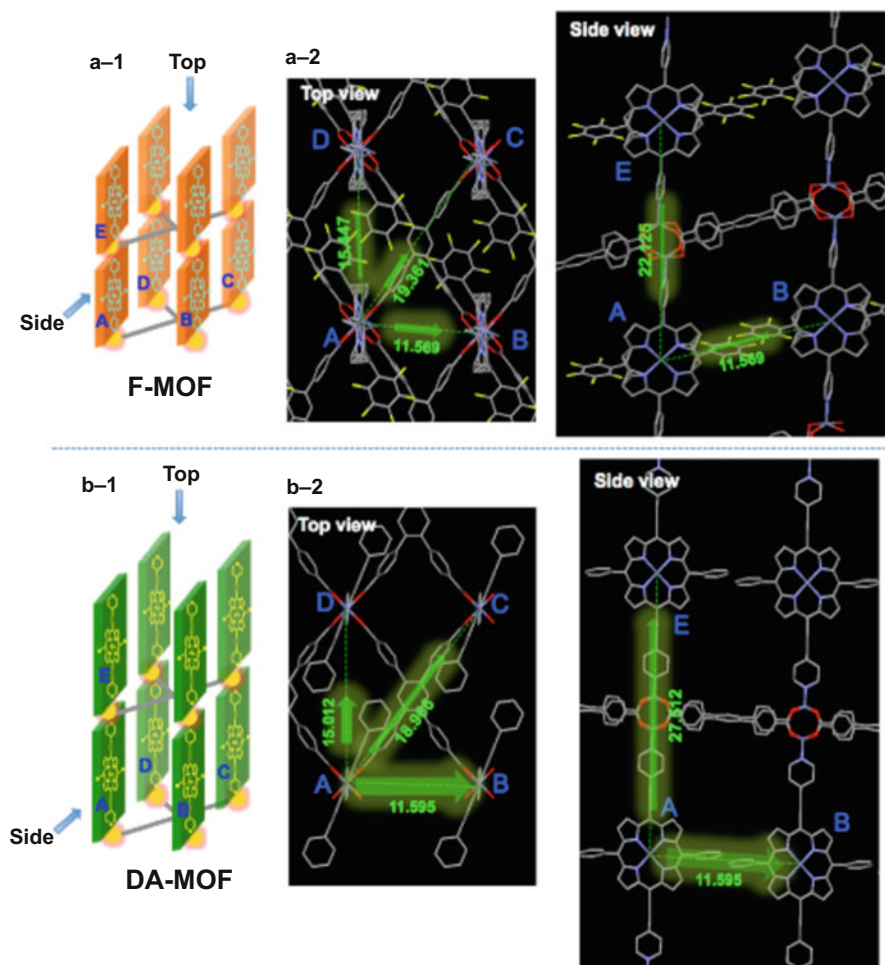


Fig. 5.4 Capped stick representations of the crystal structure of F-MOF (a-2) and DA-MOF (b-2) with arrows indicating the four energy transfer directions from A to B, C, D, and E between nearest neighboring porphyrin blocks. (Reproduced from Ref. [34] with permission from the American Chemical Society)

longer pyrene-based linker (TA-Py). This small modification increased lengths in the AB-, AC-, and AD-directions but not the AE-direction (Fig. 5.4) of the MOF. Importantly, the exciton transfer rates reduce by 60% in the AB-direction but remain the same in the AE direction when TA-Py is utilized. By spatial modifying the MOF, the anisotropy of energy transfer increased. This improves transport of excitons in planar structures, relevant for solar energy conversion devices.

5.3.3 Perylene Diimides Facilitating Förster Energy Transfer

Compounds built from perylene diimides (PDI) have been prominent acceptor components in solar energy conversion applications. This is partly attributed to their large electron affinities and high electron mobilities [35, 36]. By simply altering substituents at the perylene bay position (Fig. 5.5), the electronic and optical properties change [33, 37].

Since the linkers in MOFs are readily tunable, they can be optimized for long-range energy transfer. Having high spectral overlap between the emission of the donor and the absorption of the acceptor, the exciton can migrate efficiently from the bluest to the reddest absorber. This results in exclusive emission from the red absorbing organic linker in the MOF. By positioning chromophores within a distance that matches the exciton propagation length, complete energy transfer occurs. In other words, if the exciton needs to hop a farther distance, inefficient energy transfer occurs. Therefore, MOFs are viable candidates for investigating the nuances of long-range energy transfer.

Park, So, and colleagues [38] demonstrated that long-range energy transfer can occur in MOFs built from linkers arranged in an energy cascade manner. These structures were assembled from three chromophores: two PDI derivatives and one redder absorbing dye (S1). By synthetically modifying the PDIs, they produced chromophores with wide visible light absorption from 350 to 750 nm. Importantly, the synthetic changes of the PDIs resulted in high spectral overlap and directional energy transfer through energy cascade among the three chromophores. When the two PDIs and S1 were incorporated into thin films, the authors achieved film thicknesses on the order of the Förster radius and observed anisotropic energy transfer from a blue to a red absorber in the multicomponent MOF films. These findings are critical for not only enhancing light harvesting but exciton migration of MOF-based solar energy conversion applications.

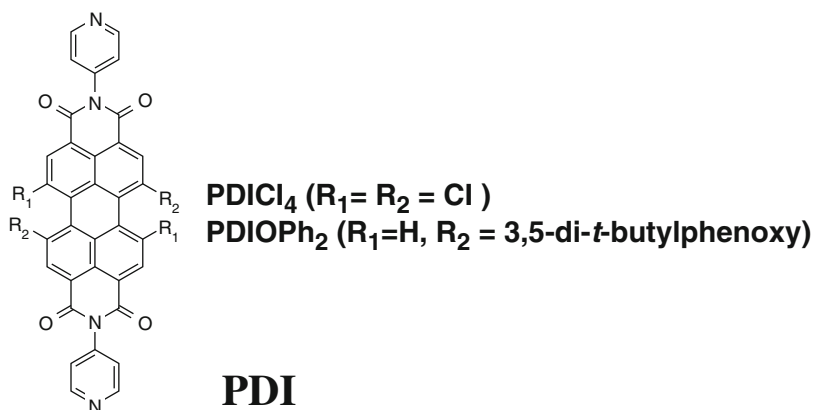


Fig. 5.5 Bay positions denoted by R in PDI molecules

5.4 Enhancing Charge Separation and Collection

5.4.1 Importance of Processing Techniques to Improve Morphology

The morphology (e.g., grain size, crystal density, uniformity, thickness) of thin film layers is intimately correlated to the charge separation and collection of energy conversion devices. Ultimately, the efficiency of the resulting solar cell device is affected. To facilitate the formation of thin film layers, one must consider suitable processing techniques. Among the most promising deposition techniques for controlling the film thickness and uniformity are liquid-solid interface methods, liquid-liquid methods, air-liquid interface methods.

5.4.2 Liquid-Solid Interface Methods

The liquid-solid interface methods hold much potential for film formation. One such method is called the layer-by-layer (LBL) method, which affords control over film thicknesses with molecular layer precision [39, 40]. Briefly, the LBL method involves a step-by-step growth method that consists of sequentially flowing solutions of the metal precursor (M^{2+}) and organic linker over a solid substrate with solvent washing steps between cycles (Fig. 5.6). During the deposition process, linkers exchange at the interface between the solid and liquid phases, allowing the metal ions to bind to linker groups at the surface and vice versa.

However, the growth mechanism of the layer-by-layer method is poorly understood. One way to elucidate its growth process is to quantify each growth step using an accurate time-resolved tool, such as a quartz crystal microbalance (QCM). In QCM, a mechanical shear oscillation can be induced by an alternating electric field. Therefore, as molecules adsorb onto the electrodes (e.g., metals, metal oxides), the oscillation frequency of the quartz crystal decreases, allowing in situ monitoring of the deposition kinetics. For rigid films, the Sauerbrey equation is often used to correlate the observed frequency shifts to deposited mass:

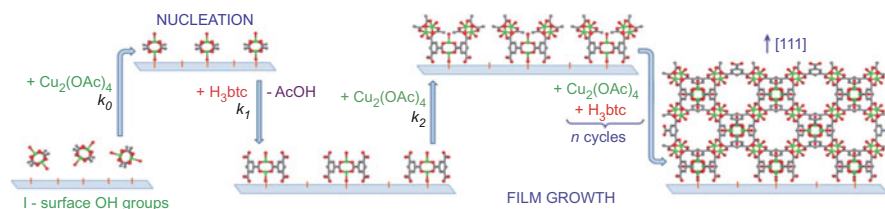


Fig. 5.6 Proposed model for stepwise growth of MOF membranes via nucleation and growth on oxide surfaces. The atoms are shown as follows: Cu = green, O = red, and C = gray. (Reproduced with permission from Ref. [39] from the Royal Society of Chemistry)

$$\Delta m = \frac{A\sqrt{\rho G}}{-2f_0^2} \Delta f$$

where Δm is the change in mass (g), A is the surface area of the resonator (cm^2), ρ and G are the density (g/cm^3) and shear modulus (Pa) of quartz, f_0 is the resonance frequency of the unloaded resonator (Hz), and Δf is the change in resonance frequency (Hz). The QCM can monitor mass changes corresponding to submonolayer film thicknesses up to several microns, so QCM can be coupled to the layer-by-layer system (Fig. 5.7) to monitor nanomaterial growth in situ [40]. Sources of error will be minimized by strict temperature control, paying careful attention to the QCM crystal surface functionalization, growing relatively thin coatings of rigid films, and optimizing the flow rates used during deposition to minimize instrument noise.

To fully harness the potential of the layer-by-layer method, the reaction conditions for each MOF film need to be carefully selected. Automating the layer-by-layer method enables scientists to test a variety of concentrations of metal and linker solutions and reaction timing of each deposition step. Further, a range of different pre-treatments of the substrate (e.g., self-assembled monolayers, pre-soaking in precursor solution) can be tested to determine optimal growth of MOF film. To process MOFs into films, conditions cannot be generalized and must be determined on a case-by-case basis.

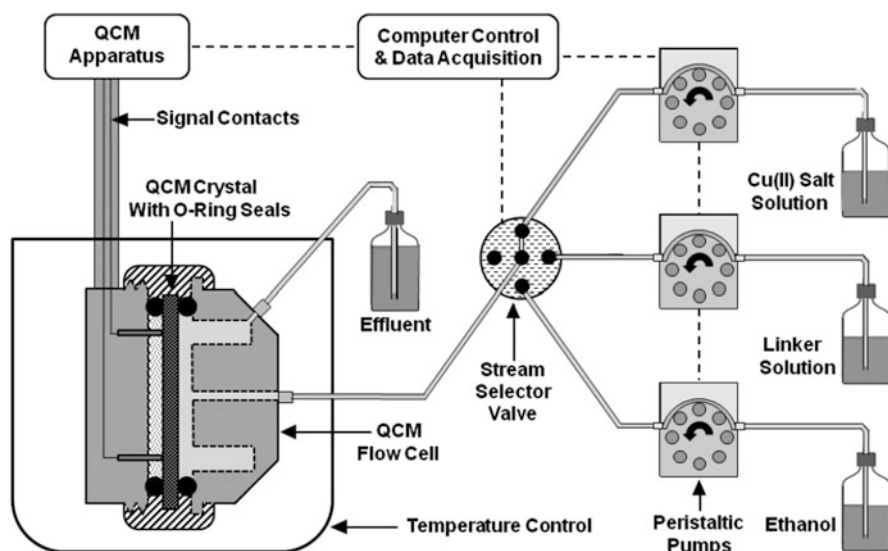


Fig. 5.7 Schematic diagram for QCM setup interfaced with layer-by-layer (LBL) deposition system. Computers control the motion of peristaltic pumps, which controls the introduction of each metal and linker precursor in a step-by-step process to form the thin membranes in a flow cell. Rinsing steps separate each deposition step to remove unreacted precursors from the flow cell, located inside the temperature-controlled QCM. (Reproduced from Ref. [39] with permission from the Royal Society of Chemistry)

5.4.3 Liquid-Liquid Interface Methods

Liquid-liquid interface method is another way to fabricate a film between two interfaces. Langmuir-Blodgett (LB) technique is one example of a liquid-liquid interface method. Sathaye and colleagues applied the LB technique to fabricate cadmium sulfide film using a 10^{-5} M cadmium carbonate solution in double-distilled water, an aqueous subphase, and a 10^{-6} M solution of carbon disulfide (or other sources of sulfide ion) in carbon tetrachloride to form a thin membrane interface (Fig. 5.8) [41]. Though LB technique and other liquid-liquid interface methods appear to be straightforward, there are a few criteria that need to be considered, such as changes in the concentration of reagents, reaction temperature and time. Several studies have found that these factors can contribute to the type of products, particle size, thickness, and film coverage.

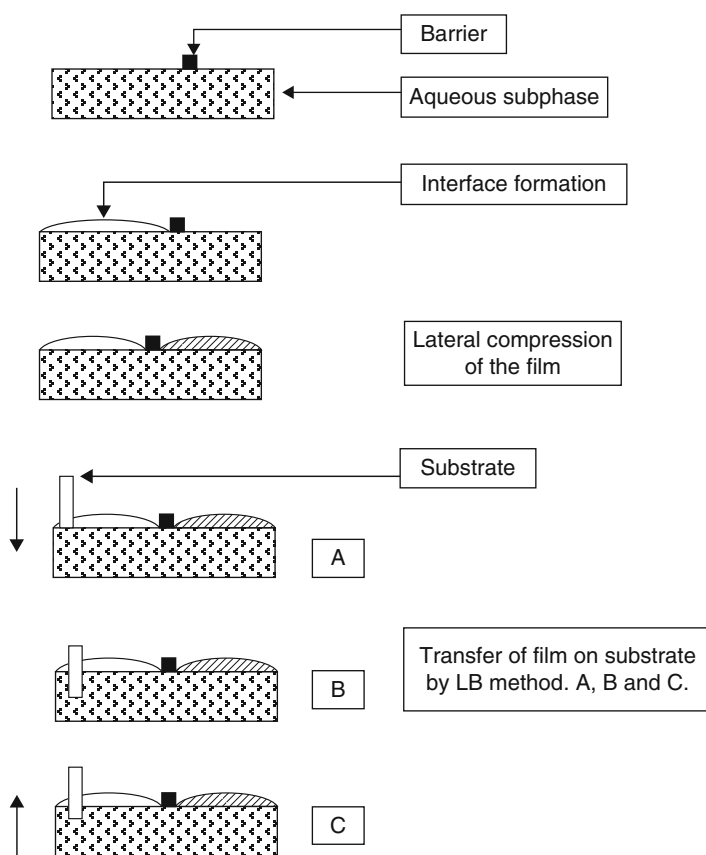


Fig. 5.8 Schematic of the LB technique. (Reproduced from Ref. [42] with permission from the American Chemical Society)

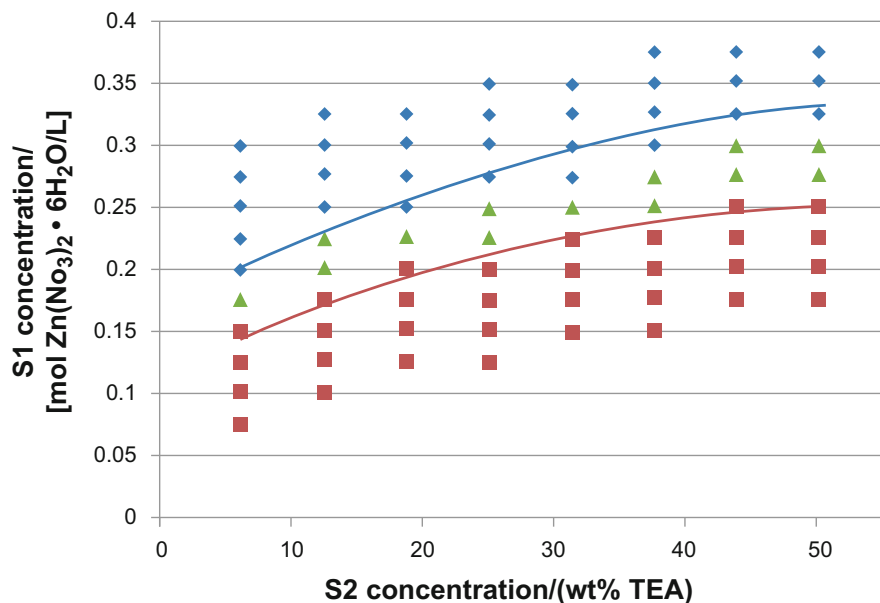


Fig. 5.9 Three different types of formation of the product depending on the concentration of two liquids; only membrane formation (diamonds), only particles formation (squares), both membrane and particles (triangles). (Reproduced from Ref. [41] with permission from the American Chemical Society)

The effect of concentrations on the form of the product can be seen in the research from Zhu and colleagues. They investigated 16 different precursor concentrations ranging from 0.025 to 0.4 mol/L with 0.025 mol/L increment and 8 different catalyst solution concentrations ranging from 6.25 to 50 wt% triethylamine (TEA, C₆H₁₅N) in hexane (C₆H₁₄) with 6.25% increment. Figure 5.9 shows three different shapes, diamond, triangle, and square, which represent the types of the products [41]. The concentration of metal precursor and the reducing agent is also found in the research conducted by Rao and colleagues. As the concentration of the metal precursor increased, they observed the increase in the number of the particles in nanocrystalline films as well as the thickness of the films [44]. On the other hand, when the concentration of the reducing agent was increased, less uniform films were fabricated (Fig. 5.10). The metal precursor and reducing agent are chloro(tri-phenylphosphine)gold(I) [Au(PPh₃)Cl] in toluene (C₇H₈) and tetrakis-hydroxymethyl phosphonium chloride (THPC, [P(CH₂OH)₄]Cl) in sodium hydroxide (NaOH), respectively. The transmission electron micrographs (TEM) in Fig. 5.11 show more uniform films since they had lower concentrations of reducing agent [45].

Reaction temperatures are another significant factor for film morphology. Figure 5.11 shows TEM of nanocrystalline Au films fabricated at four different reaction temperatures. The increase in temperature results in the increase of the mean

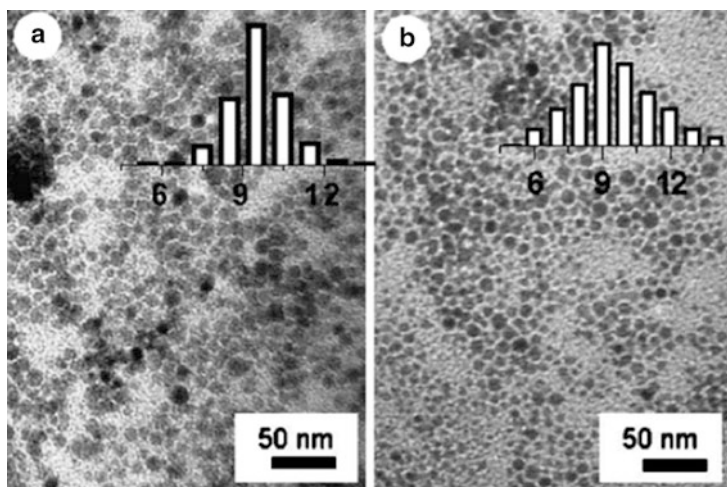


Fig. 5.10 TEM images of Au films when the concentration of reducing agent, THPC, was increased from 330 μL to (a) 660 and (b) 1200 μL . Bar graphs indicate the particle size distribution. (Reproduced from Ref. [43] with permission from the American Chemical Society)

diameters of the nanocrystals while the interparticle separation is nearly consistent. In addition, X-ray diffraction (XRD) patterns showed the growth of (111) peak, which suggests the increase in the particle size (Fig. 5.12) [44]. The effect of changing the temperature on film morphology was observed through scanning electron micrographs (SEM) as well. As Fig. 5.13 shows, the films fabricated at 30 $^{\circ}\text{C}$ had more holes and cracks, compared to those fabricated at 60 $^{\circ}\text{C}$ [45].

Reaction times can also contribute to the morphology of films. Rao and colleagues observed the increase in the film coverage with longer reaction time. Figure 5.14 shows that films made after 3, 6, and 9 h of contact time can be compared to films in Fig. 5.11, which reacted for 24 h [45]. In fact, a reaction time also contributes to the change in the diameter and thickness of the [cadmium sulfide] CdS films. Stansfield and colleagues found that the reaction time played an important role in diameter. The trend showed the growth of a diameter with the increase in the time. It showed a significant change with reaction time up to 5.2 h and a slight change up to 15 h. After 15 h, there were no changes observed [46]. The effect of reaction time on a thickness of the films is shown in Fig. 5.15b. The trend showed that a thickness of the films grew with an increase of the reaction time. It showed an even sharper change in the range from 4.5 to 5.0 h [46].

Varying these factors result in different configurations of nanocrystalline films. Changes in concentration can form three types of products: only membrane, only particles, and both membrane and particles. It also influenced the thickness of the films. In addition, changes in reaction temperature can differ the particle size of the film. Changes in reaction time made a difference in the film coverage, diameter, and thickness of the films.

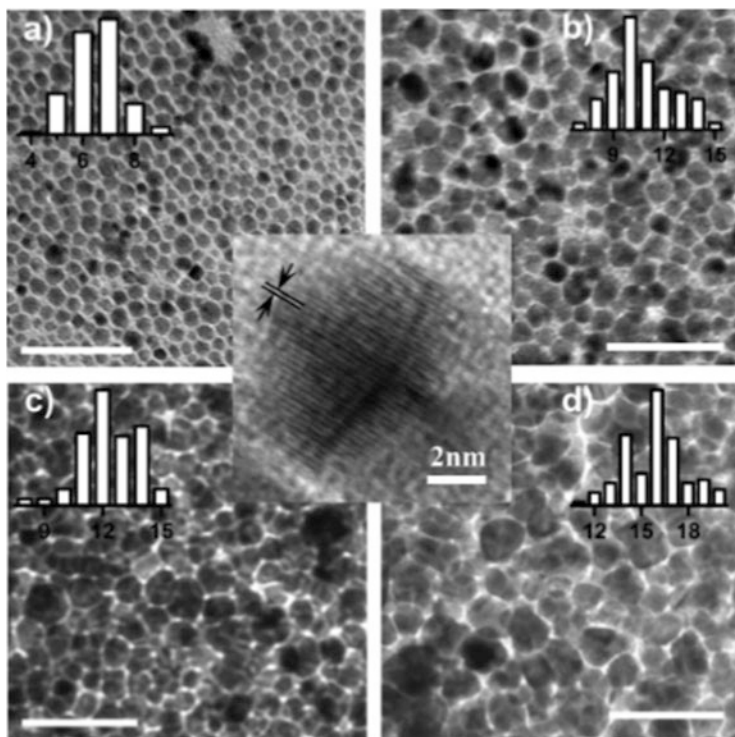
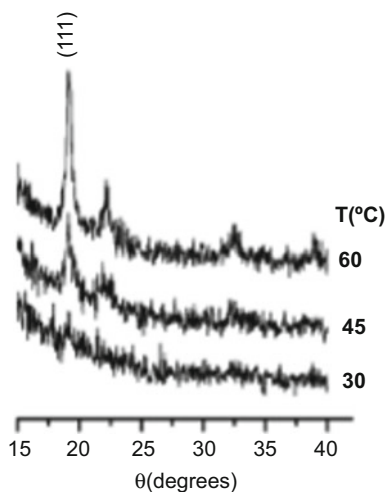


Fig. 5.11 TEM of nanocrystalline Au films with four different reaction temperatures: (a) 30, (b) 45, (c) 60, and (d) 75 °C. Bar graphs indicate the particle size distribution. The scale bars are 50 nm. The image in the middle shows an individual particle. (Reproduced from Ref. [43] with permission from the American Chemical Society)

Fig. 5.12 XRD patterns of nanocrystalline Au films with different reaction temperatures. (Reproduced from Ref. [44] with permission from the American Chemical Society)



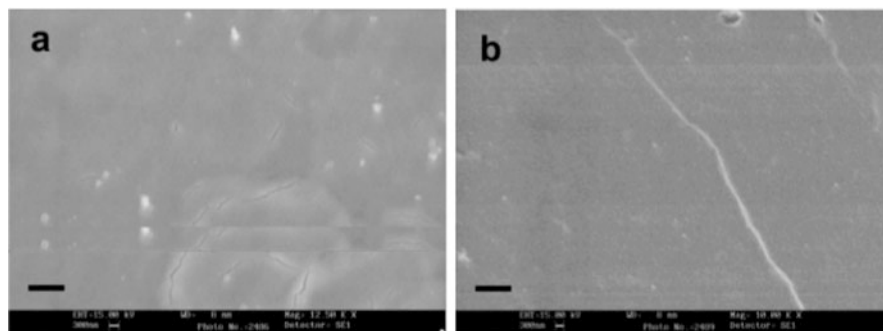


Fig. 5.13 SEM images of nanocrystalline Au films at two different temperature: (a) 30 and (b) 60 °C. (Reproduced from Ref. [45] with permission from the American Chemical Society)

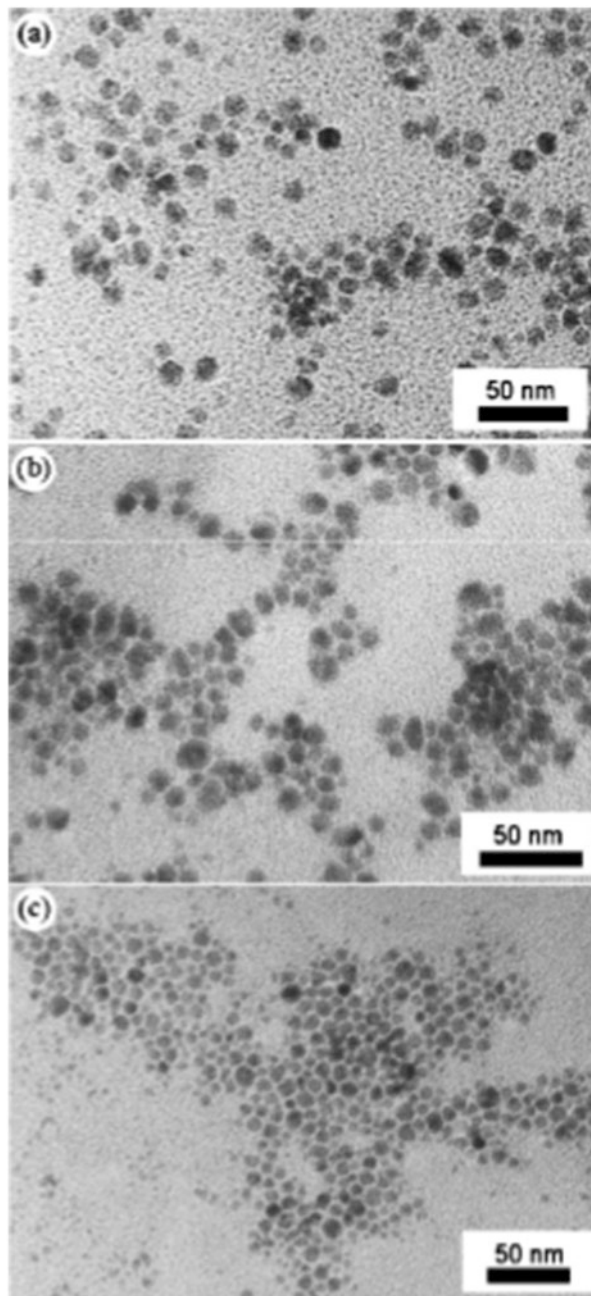
5.4.4 Air-Liquid Interface Methods

For materials to be utilized in energy conversions devices, they must be processed into thin films. Ideally, these materials should share structural and electrical similarities to that of graphene. Several MOFs have been synthesized and exhibit desirable graphene-like properties. One MOF in particular, $\text{Ni}_3(2,3,6,7,10,11\text{-hexa-iminotriphenylenesemiquinonate})_2$ or $\text{Ni}_3(\text{HITP})_2$ (Fig. 5.16a), is an attractive candidate, due to its fully conjugated pi-system. This results in a high conductivity and low thermal conductivity, which are attractive for use in electronic devices. Sheberla and colleagues synthesized identified $\text{Ni}_3(\text{HITP})_2$ as one of the most conductive MOFs. In fact, its film yields 40 S/cm – the highest conductivities achieved for this class of materials (Fig. 5.16b) [47].

Although Sheberla and colleagues were successful in depositing a film, the material was far too rough and thick for more efficient solar cell applications. Wu et al. successfully deposited $\text{Ni}_3(\text{HITP})_2$ MOF into a film, via growth at an air-liquid interface (Fig. 5.17). The procedure entails mixing the metal and organic reactants together in a beaker until thin films form at the air-liquid interface. At that point, a stamp with a substrate lifts the membrane from the interface. The MOF membrane was composed of thin and ultra-smooth nanolayers, as observed by the scanning electron microscopy (SEM) images in Fig. 5.18. This procedure allowed the MOF to be incorporated and tested as a field effect transistor (FET). Like the sample prepared by Sheberla, the film had a conductivity of 40 S/cm at room temperature [50].

However, the deposition of the film using these stamping techniques is not straightforward and complicated by experimental conditions. These include the base used to deprotonate the linker, the concentration of species, and the timing to start and end stamping [51]. For instance, Wu and his colleagues used the base in excess to catalyze the reaction. The base deprotonates the nitrogen and makes it more nucleophilic for the reaction with the Ni^{2+} cation. In unpublished work, So and colleagues studied the effects of replacing the original base (ethylamine, $\text{C}_2\text{H}_7\text{N}$) with butylamine ($\text{C}_4\text{H}_{11}\text{N}$) and octylamine ($\text{C}_8\text{H}_{19}\text{N}$). Just like ethylamine,

Fig. 5.14 TEM images of Au films with different reaction time; (a) 3, (b) 6, and (c) 9 h. (Reproduced from Ref. [45] with permission from the American Chemical Society)



butylamine was able to form the $\text{Ni}_3(\text{HITP})_2$ MOF films at 60°C , but octylamine had a very little reaction with the linker. The pK_a values of triethyl- $[-(\text{CH}_2\text{CH}_3)_3]$, tributyl- $[\text{CH}_3(\text{CH}_2)_3\text{O}]_3$, and triethylamine $[\text{C}_6\text{H}_{15}\text{N}]$ are 10.78, 10.89, and 10.08, respectively. Although it is not substantial, octylamine is less nucleophilic than the

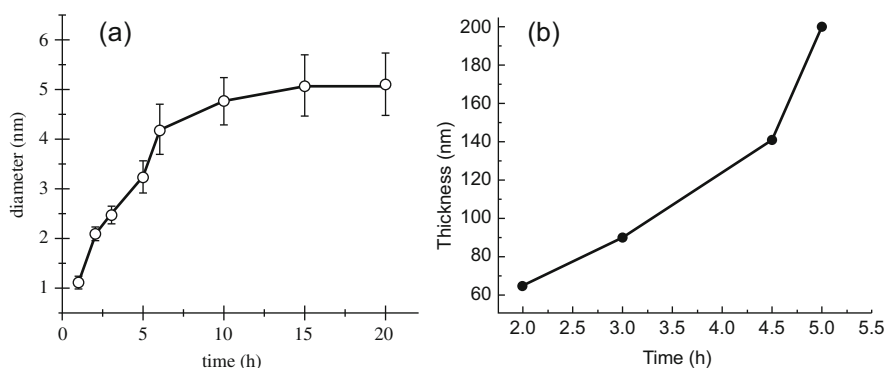


Fig. 5.15 The influence of reaction time in (a) diameter and (b) thickness of particles in CdS films. (Reproduced from Ref. [46] with permission from the American Chemical Society)

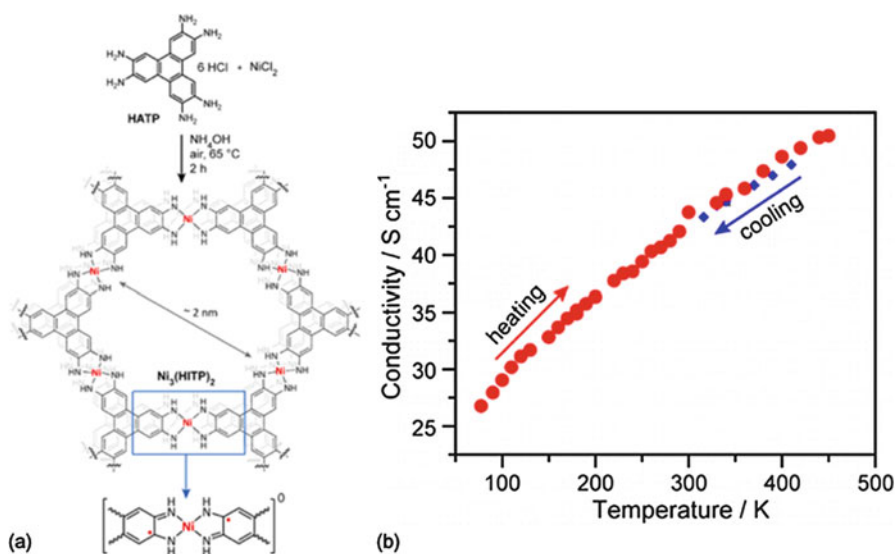


Fig. 5.16 (a) The conjugated structure of the Ni₃(HITP)₂ endows the MOF material with high conductivities. (b) Resulting MOF shows that conductivity increases with temperature. (Reproduced from Ref. [47] with permission from the American Chemical Society)

other two amines and far more sterically hindered. This makes the lone pair of electrons less readily available to react as compared to the other two amines.

The concentration of the reactants – nickel cation and organic linker – must also be sufficient to react with one another to form the desired MOF. If concentrations are too low, the reactants do not react in a timely manner to form a film at the surface. At higher concentrations, a thicker, more viscous film forms at the air-liquid interface. In a work by Rao, increasing the concentration of the gold metal increased the number of crystals and film thickness of the film [45]. This concentration is key for the synthesis of Ni₃(HITP)₂ films, since controlling the concentration to favor the

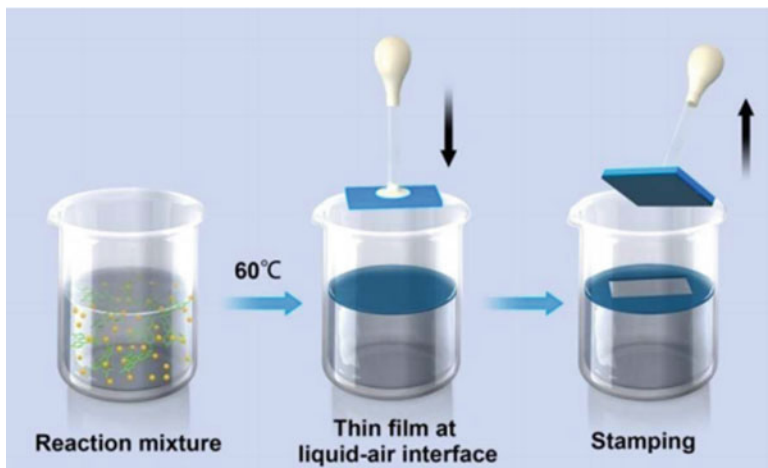


Fig. 5.17 Stamping method for film formation on a silicon substrate. (Reproduced from Ref. [49] with permission from the American Chemical Society)

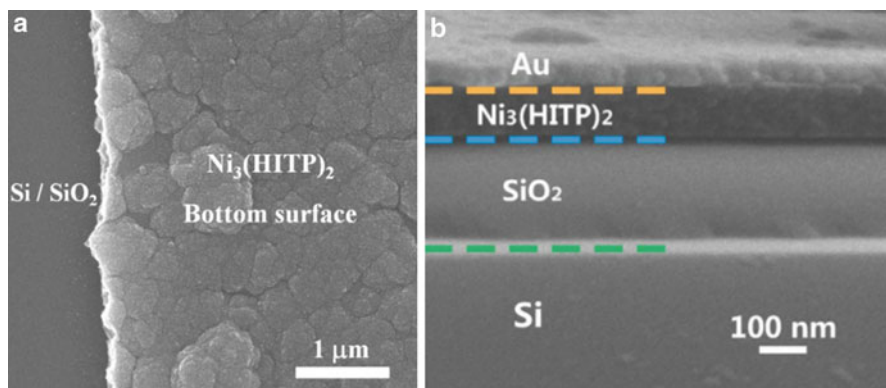


Fig. 5.18 SEM images of (a) bottom-surface of freestanding $\text{Ni}_3(\text{HITP})_2$ membrane, showing highly uniform surface and the (b) cross section of $\text{Ni}_3(\text{HITP})_2$ -based FET. (Reproduced from Ref. [49] with permission from the American Chemical Society)

formation of ultrathin films is essential for the transistor to function without causing device problems, such as short-circuiting. Another paper by Lu et al. found consistent results during the synthesis of zinc-based films via a liquid-liquid interface. When the reactants are in relatively low concentrations during the reaction, the material does not form a film and instead sinks to the bottom of the reaction vessel. At high concentrations, the resulting film is thicker and more viscous, which, as seen in work by Wu, is not ideal for an ultrathin film for FET applications [49]. The conditions necessary for liquid-liquid interface methods should be similar to that of

the air-liquid interface methods. The concentration must be optimized and be able to form a film within a reasonable amount of time that exhibits the desired thickness.

The temperature must also be regulated for proper film growth and suitable reaction time. The temperature must be high enough to quickly form the MOF. If the reaction proceeds too quickly, however, the film is disrupted by the formation of clumps before the stamping can occur. Therefore, an ultra smooth film will not be deposited on the substrate. The temperature must also be low enough to allow time for stamping and ideal film deposition onto the substrate. In contrast, if the temperature is too low, the MOF is unable to form a sufficient film at the air-liquid interface and is less likely to physisorbed to the surface of the substrate. Rao and colleagues demonstrated that the liquid-liquid interface growth of Au film depends on the temperature during synthesis. In fact, the temperature influences the diameter of the nanocrystals. Furthermore, temperatures of 30, 45, 60, and 75 °C formed nanocrystals with diameters of 7, 10, 12, and 15 nm, respectively [45]. When applied to the $\text{Ni}_3(\text{HITP})_2$ material, it is important to control the crystal size to ensure that the films possess a smooth and uniform surface. This limits grain boundaries, which optimizes conductivity.

To improve reproducibility of films, automating the process will minimize the multiple sources of error. Wu et al. observed that the thickness of the film can be determined by reaction time, but human error in timing may cause irreproducibility under the same reaction conditions [49]. Automation of the process, such as in the layer-by-layer synthesis method, can improve such efforts. The optimization of $\text{Ni}_3(\text{HITP})_2$ MOF synthesis via air-liquid interfacial film growth can be transferrable to other MOFs. Ultimately, we can construct a more generalized synthetic procedure and allow for more direct comparisons among other MOF film candidates.

5.5 Conclusions

Enhancing the performance of photovoltaics by incorporating novel materials and processing techniques presents different sets of challenges. Perovskites and MOFs have drawbacks that must be overcome before incorporating them into conversion schemes. Solid-liquid, liquid-liquid, and air-liquid interface methods still need to be optimized to make ultrathin, homogeneous, and low roughness coatings.

To resolve issues involving the first step (light harvesting), we can improve the absorption features of perovskites and MOFs to better align with that of the solar spectrum. For perovskites, varying single and mixed cations and their ratios can dramatically redshift their absorption features into the near-infrared region. For MOFs, modifying chromophoric linkers to absorb more of visible light and near-infrared regions will be critical. Alternatively, this can be done by sensitizing MOFs with secondary chromophores or quantum dots. However, a monolayer or less of sensitizer materials on the planar surface of an MOF does not have enough extinction to produce a significant increase in solar absorption efficiency. To overcome this issue, we can embed additional chromophores into the pores of MOFs without

impacting electronic coupling between the struts that support exciton flow. For either perovskites or MOFs, if the thickness of the materials exceeds the exciton transport length, some excitons will not be captured and the quantum efficiency of the perovskites or MOF in a solar cell device will suffer.

To resolve the challenges of the second step (exciton separation), we need to optimize the parameters of the Förster energy transfer rate. This includes but is not limited to chromophore and framework symmetry, fluorescence quantum yield, chromophore oscillator strength, and others. Since exciton transport is diffusive, we would require the construction of chromophore cascades to improve directionality of exciton transport. This must all be done without compensating for the structural integrity and increasing defect site density within MOFs.

To resolve problems related to the third (charge transport) and fourth (charge collection) steps, we need to improve film processing techniques. Ideally, once an exciton has reached its intended destination, they should participate in interfacial electron or hole transfer to a proximal electrode. However, holes or electrons often recombine, reducing charge collection efficiency, due to the presence of defects in the bulk film. Additional investigations are required to elucidate crystal growth dependence on temperature, annealing times, and annealing temperatures [51]. For MOF materials to be sandwiched between electrodes, the MOF orientation must be optimized to facilitate the anisotropic flow of energy and charges to the electrodes. Further, interfacial charge transfer will need to be understood and optimized. The ties between the diversity of fabrication approaches and resulting film morphology and optoelectronic and performance properties must be simultaneously understood and optimized before we can make advancements.

Acknowledgments We acknowledge the release time for M.C.S from Office of Research and Sponsored Programs at California State University, Chico (CSUC), and CSU Council on Ocean Affairs, Science & Technology. We also thank the faculty members from the Faculty Learning Communities of Office of Faculty Development at CSUC for their helpful comments and suggestions on this book chapter.

References

1. N. Ahn, S.M. Kang, J.W. Lee, M. Choi, N.G. Park, Thermodynamic regulation of $\text{CH}_3\text{NH}_3\text{PbI}_3$ crystal growth and its effect on the photovoltaic performance of perovskite solar cells. *J. Mater. Chem. A* **3**, 19901–19906 (2015)
2. J.L. Barnett, V.L. Cherette, C.J. Hutcherson, M.C. So, Effects of solution-based fabrication conditions on morphology of lead halide perovskite thin film solar cells. *Adv. Mater. Sci. Eng.* (2016). <https://doi.org/10.1155/2016/4126163>
3. N.P. Pellet, P. Gao, P. Gregori, T.Y. Yang, M.K. Nazeeruddin, J. Maier, M. Grätzel, Mixed-organic-cation perovskite photovoltaics for enhanced solar-light harvesting. *Angew. Chem. Int. Ed.* **53**(12), 3151–3157 (2014)
4. S. Jin, H.J. Son, O.K. Farha, G.P. Wiederrecht, Energy transfer from quantum dots to metal-organic frameworks for enhanced light harvesting. *J. Am. Chem. Soc.* **135**(3), 955–958 (2013)
5. G. Lu, S. Li, Z. Guo, et al., Imparting functionality to a metal-organic framework material by controlled nanoparticle encapsulation. *Nat. Chem.* **4**, 310 (2010)

6. J. Lin, X. Hu, P. Zhang, et al., Triplet excitation energy dynamics in metal-organic frameworks. *J. Phys. Chem. C* **117**, 22250 (2013)
7. C.A. Kent, D. Liu, A. Ito, et al., Rapid energy transfer in non-porous metal-organic frameworks with caged Ru(bpy)₃²⁺ chromophores: Oxygen trapping and luminescence quenching. *J. Mater. Chem. A* **1**, 14982–14989 (2013)
8. W.A. Maza, S.R. Ahrenholtz, C.C. Epley, C.S. Day, A.J. Morris, Solvothermal growth and photophysical characterization of a ruthenium(II) tris-(2,2'-bipyridine)-doped zirconium UiO-67 metal-organic framework thin film. *J. Phys. Chem. C* **118**, 14200–14210 (2014)
9. W.A. Maza, A.J. Morris, Photophysical characterization of a ruthenium(II) tris-(2,2'-bipyridine)-doped zirconium UiO-67 metal-organic framework. *J. Phys. Chem. C* **118**, 8803–8817 (2014)
10. D.E. Williams, J.A. Rietman, J.M. Maier, et al., Energy transfer on demand: photoswitch-directed behavior of metal-porphyrin frameworks. *J. Am. Chem. Soc.* **136**, 11886–11889 (2014)
11. J.T. Joyce, F.R. Laffir, C. Silien, Layer-by-layer growth and photocurrent generation in metal-organic coordination films. *J. Phys. Chem. C* **117**, 12502–12509 (2013)
12. D.Y. Lee, D.V. Shinde, S.J. Yoon, et al., Cu-based metal-organic frameworks for photovoltaic application. *J. Phys. Chem. C* **118**, 16328–16334 (2014)
13. K. Leong, M.E. Foster, B.M. Wong, et al., Energy and charge transfer by donor-acceptor pairs confined in a metal-organic framework: a spectroscopic and computational investigation. *J. Mater. Chem. A* **2**, 3389–3398 (2014)
14. C.Y. Lee, O.K. Farha, B.J. Hong, et al., Light-harvesting metal-organic frameworks (MOFs): efficient strut-to-strut energy transfer in bodipy and porphyrin-based MOFs. *J. Am. Chem. Soc.* **133**, 15858 (2011)
15. M.C. So, S. Jin, H.J. Son, et al., Layer-by-layer fabrication of an oriented thin film based on a porphyrin-containing metal-organic framework. *J. Am. Chem. Soc.* **135**, 15698 (2013)
16. G. McDermott, S. Prince, A. Freer, et al., Crystal structure of an integral membrane light-harvesting complex from photosynthetic bacteria. *Nature* **374**, 517 (1995)
17. S. Patwardhan, S. Jin, H.J. Son, G.C. Schatz, Ultrafast energy migration in porphyrin-based metal-organic frameworks (MOFs). *MRS Online Proc. Libr.* **1539**, Mrss13-1539-d06-06 (2013)
18. C.B. Murphy, Y. Zhang, T. Troxler, et al., Probing Förster and Dexter energy-transfer mechanisms in fluorescent conjugated polymer chemosensors. *J. Phys. Chem. B* **108**, 1537 (2004)
19. J. Brey, C. Kratzer, H. Yersin, Crystal engineering as a tool for directed radiationless energy transfer in layered $\{\Delta\text{-[Ru(bpy)}_3\text{]}\Delta\text{-[Os(bpy)}_3\text{]}\}$ (PF6)₄. *J. Am. Chem. Soc.* **122**, 2548 (2000)
20. M. Devenney, L.A. Worl, S. Gould, et al., Excited state interactions in electropolymerized thin films of RuII, OsII, and ZnII polypyridyl complexes. *J. Phys. Chem. A* **101**, 4535 (1997)
21. C.N. Fleming, P. Jang, T.J. Meyer, J.M. Papanikolas, Energy migration dynamics in a Ru (II)- and Os (II)-based antenna polymer embedded in a disordered, rigid medium. *J. Phys. Chem. B* **108**, 2205 (2004)
22. C.N. Fleming, K.A. Maxwell, J.M. DeSimone, T.J. Meyer, J.M. Papanikolas, Ultrafast excited-state energy migration dynamics in an efficient light-harvesting antenna polymer based on Ru (II) and Os (II) polypyridyl complexes. *J. Am. Chem. Soc.* **123**, 10336 (2001)
23. N. Ikeda, A. Yoshimura, M. Tsushima, T. Ohno, Hopping and annihilation of 3MLCT in the crystalline solid of [Ru (bpy)₃]²⁺X₂ (X = Cl⁻, ClO₄⁻ and PF₆⁻). *J. Phys. Chem. A* **104**, 6158 (2000)
24. C.A. Kent, D. Liu, L. Ma, J.M. Papanikolas, T.J. Meyer, W. Lin, Light harvesting in microscale metal-organic frameworks by energy migration and interfacial electron transfer quenching. *J. Am. Chem. Soc.* **133**, 12940 (2011)
25. C.A. Kent, D. Liu, T.J. Meyer, W. Lin, Amplified luminescence quenching of phosphorescent metal-organic frameworks. *J. Am. Chem. Soc.* **134**, 3991 (2012)
26. C.A. Kent, B.P. Mehl, L. Ma, et al., Energy transfer dynamics in metal-organic frameworks. *J. Am. Chem. Soc.* **132**, 12767 (2010)
27. S.A. Trammell, J. Yang, M. Sykora, et al., Molecular energy transfer across oxide surfaces. *J. Phys. Chem. B* **105**, 8895 (2001)

28. M. Tsushima, N. Ikeda, A. Yoshimura, K. Nozaki, T. Ohno, Solid-state photochemistry: energy-transfer and electron-transfer of 3CT in crystals of $[\text{Os}_x\text{Ru}_{1-x}(\text{bpy})_3]\text{X}_2$ ($x = 0-0.23$). *Coord. Chem. Rev.* **208**, 299 (2000)
29. M.D. Ward, F. Barigelletti, Control of photoinduced energy transfer between metal-polypyridyl luminophores across rigid covalent, flexible covalent, or hydrogen-bonded bridges. *Coord. Chem. Rev.* **216**, 127 (2001)
30. B. Abrahams, B. Hoskins, D. Michail, R. Robson, Assembly of porphyrin building blocks into network structures with large channels. *Nature* **369**, 727 (1994)
31. O.K. Farha, A.M. Shultz, A.A. Sarjeant, S.T. Nguyen, J.T. Hupp, Active-site-accessible, porphyrinic metal-organic framework materials. *J. Am. Chem. Soc.* **133**, 5652 (2011)
32. A.M. Shultz, A.A. Sarjeant, O.K. Farha, J.T. Hupp, S.T. Nguyen, Post-synthesis modification of a metal-organic framework to form metallosalen-containing MOF materials. *J. Am. Chem. Soc.* **133**, 13252 (2011)
33. S. Becker, A. Böhm, K. Müllen, New thermotropic dyes based on amino-substituted perylene-dicarboximides. *Chem. Eur. J.* **6**, 3984 (2000)
34. H.J. Son, S. Jin, et al., Light-harvesting and ultrafast energy migration in porphyrin-based metal-organic frameworks. *J. Am. Chem. Soc.* **135**, 862 (2013)
35. B.A. Gregg, R.A. Cormier, Doping molecular semiconductors: n-type doping of a liquid crystal perylene diimide. *J. Am. Chem. Soc.* **123**, 7959 (2001)
36. A. Breeze, A. Salomon, D. Ginley, Polymer – perylene diimide heterojunction solar cells. *Appl. Phys. Lett.* **81**, 3085 (2002)
37. H. Langhals, O. Krotz, K. Polborn, P. Mayer, A novel fluorescent dye with strong, anisotropic solid-state fluorescence, small stokes shift, and high photostability. *Angew. Chem. Int. Ed.* **44**, 2427 (2005)
38. H.J. Park, M.C. So, et al., Layer-by-layer assembled films of perylene diimide-and squaraine-containing metal-organic framework-like materials: solar energy capture and directional energy transfer. *ACS Appl. Mater. Interfaces* **8**(38), 24983–24988 (2016)
39. V. Stavila, J. Volponi, A.M. Katzenmeyer, M.C. Dixon, M.D. Allendorf, Kinetics and mechanism of metal-organic framework thin film growth: systematic investigation of HKUST-1 deposition on QCM electrodes. *Chem. Sci.* **3**(5), 1531–1540 (2012)
40. M.C. So, S. Jin, H.J. Son, G.P. Wiederrecht, O.K. Farha, J.T. Hupp, Layer-by-layer fabrication of oriented porous thin films based on porphyrin-containing metal-organic frameworks. *J. Am. Chem. Soc.* **135**(42), 15698–15701 (2013)
41. H. Lu, S. Zu, Interfacial synthesis of free-standing metal-organic framework membranes. *Eur. J. Inorg. Chem.*, **8**, 1294–1300 (2013)
42. S.D. Sathaye, K.R. Patil, D.V. Paranjape, et al., Preparation of Q-cadmium sulfide ultrathin films by a new liquid-liquid interface reaction technique (LLIRT). *Langmuir* **16**, 3487–3490 (2000)
43. C.N.R. Rao, G.U. Kulkarni, V.V. Agrawal, U.K. Gautam, M. Ghosh, U. Tumkurkar, Use of the liquid-liquid interface for generating ultrathin nanocrystalline films of metals, chalcogenides, and oxides. *J. Colloid Interface Sci.* **289**(2), 305–318 (2005)
44. C.N.R. Rao, K.P. Kalyanikutty, The liquid-liquid interface as a medium to generate nanocrystalline films of inorganic materials. *Acc. Chem. Res.* **41**(4), 489–499 (2008)
45. V.V. Agrawal, G.U. Kulkarni, C.N.R. Rao, Nature and properties of ultrathin nanocrystalline gold films formed at the organic-aqueous interface. *J. Phys. Chem.* **109**(15), 7300–7305 (2005)
46. G.L.e.a. Stansfield, Growth of nanocrystals and thin films at the water-oil interface. *Phil. Trans. R. Soc. A* **368**, 4313–4330 (2010)
47. D. Sheberla, L. Sun, M. Blood-Forsythe, et al., High electrical conductivity in $\text{Ni}_3(2,3,6,7,10,11\text{-hexaiminotriphenylene})_2$ a semiconducting metal organic graphene analog. *J. Am. Chem. Soc.* **136**, 8859–8862 (2014)

48. D. Fan, P.J. Thomas, P. O'Brien, Deposition of CdS and ZnS thin films at the water/toluene interface. *J. Mater. Chem.* **17**, 1381–1386 (2007)
49. G. Wu, J. Huang, Y. Zang, et al., Porous field-effect transistor based on a semiconducting metal-organic framework. *J. Am. Chem. Soc.* **139**, 1360–1363 (2017)
50. J. Berry, T. Buonassisi, D.A. Egger, et al., Hybrid organic-inorganic perovskites (HOIPs): opportunities and challenges. *Adv. Mater.* **27**(35), 5102–5112 (2015)
51. H.S. Kim, N.G. Park, Parameters affecting I-V hysteresis of CH₃NH₃PbI₃ perovskite solar cells: effects of perovskite crystal size and mesoporous TiO₂ layer. *J. Phys. Chem. Lett.* **5**(17), 2927–2934 (2014)



The Recent Research and Growth in Energy Efficiency in $\text{Cu}_2\text{ZnSnS}_4$ (CZTS) Solar Cells

6

R. J. Deokate

Contents

6.1	Introduction	138
6.1.1	Seeking the Ideal Material	140
6.2	The Sun: An Energy Source	141
6.3	Solar Energy Conservation	142
6.4	$\text{Cu}_2\text{ZnSnS}_4$ (CZTS) as an Absorber Material	144
6.5	Topical Research and Development in the CZTS Thin Film in the Application of Solar Cells	145
6.5.1	Pretreatment and Synthesis	147
6.5.2	Crystal Defect Study	151
6.5.3	Post-Sulfurization/Selenization	152
6.5.4	Buffer Layer and Interfaces	156
6.6	Conclusion	157
	References	158

Abstract

Currently the energy harvesting by photoelectric conversion has been efficiently used in energy economics and renewable energy area. The development of solar cell technology is started from the first-generation silicon solar cell to the emerging fourth-generation “inorganics-in-organic” solar cell. Various solar absorber compounds have been used for solar cell manufacturing such as

Author Contribution

R.J. Deokate wrote the entire manuscript based on public domain information.

R. J. Deokate (✉)

Vidya Pratishthan's Arts Science and Commerce College, Baramati, India

e-mail: deokate2000@yahoo.co.in

cadmium telluride (CdTe), copper indium gallium selenide ($\text{Cu}_2\text{InGaS}_4$, CIGS), copper indium gallium sulfur selenide (CIGSSe), copper zinc tin sulfide kesterite ($\text{Cu}_2\text{ZnSnS}_4$, CZTS), and copper zinc tin sulfide selenide (CZTSSe). These compounds have conversion efficiencies with some advantages and drawbacks. To overcome the drawbacks and achieve higher conversion efficiency, the efforts have been devoted. With some physical and chemical parametric changes, researchers have got better results in the last 10 years. In the present chapter, research and development on the $\text{Cu}_2\text{ZnSnS}_4$ thin film in the request of high-efficiency solar cells is discussed. The effect of various structural and compositional changes in the CZTS; different buffer layers such as cadmium sulfide (CdS), copper sulfide (CuS), zinc sulfide (ZnS), Indium(III) sulfide (In_2S_3), hybrid Indium(III) sulfide/cadmium sulfide ($\text{In}_2\text{S}_3/\text{CdS}$), etc. with interfaces doping into the host material of silver (Ag), sodium (Na), antimony (Sb), etc.; partial substitution of the elements from the host by cadmium (Cd) and selenium (Se); different synthesis; and post-treatments are thoroughly studied. Further, some challenges regarding improving the conversion efficiency of copper zinc tin sulfide (CZTS) solar cells and the future of the solar cell application are discussed.

6.1 Introduction

Global demand for energy is increasing by the hour as developing countries move toward industrialization. Experts estimate that by the year 2050, worldwide demand for electricity may reach 30 terawatts (TW). Today solar energy provides only about 1% of the world's electricity. Electricity is the best flexible and suitable form of energy. But, electricity is not the primary stage of energy. It can be generated by other energy sources like coal, oil, natural gases, hydrodynamical, geothermal, solar, wind, ocean-tidal, biomass, nuclear, fuel cells, etc. The critical challenge is making it less expensive to convert photo-energy into usable electrical energy. The electricity requirement of the world is greater than 10^{12} KWh every year. As shown in the Fig. 6.1 [1], the energy demand is rising every day as there are industrialization and civilization.

Currently it is very essential to discover the materials that absorb sunlight and convert into electricity efficiently should available abundant and cost-effective in environment to fabricate into solar devices. Researchers from around the world are working to develop solar cell technologies that are efficient and affordable. As per our energy necessity, amount of energy must be produced every year by all the possible ways and complete the need. Out of the total generated electrical energy, about 75% of energy is generated every year by the nonrenewable energy sources, Fig. 6.2 [2].

The goal is to bring the installation cost of solar electricity below a certain limit per watt. Several companies and universities are investigating ways to make thin-film solar cells using materials that are abundant in nature and nontoxic. To develop

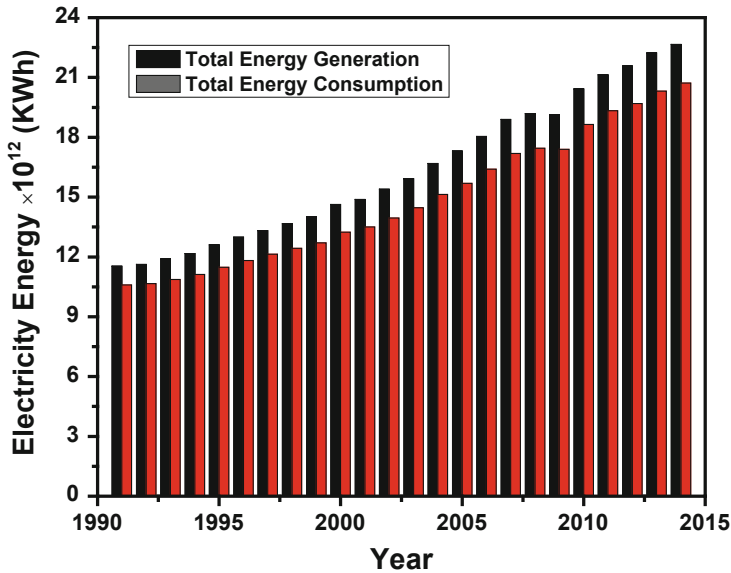


Fig. 6.1 Simple bar representation of energy generation and utilization in every year [2]

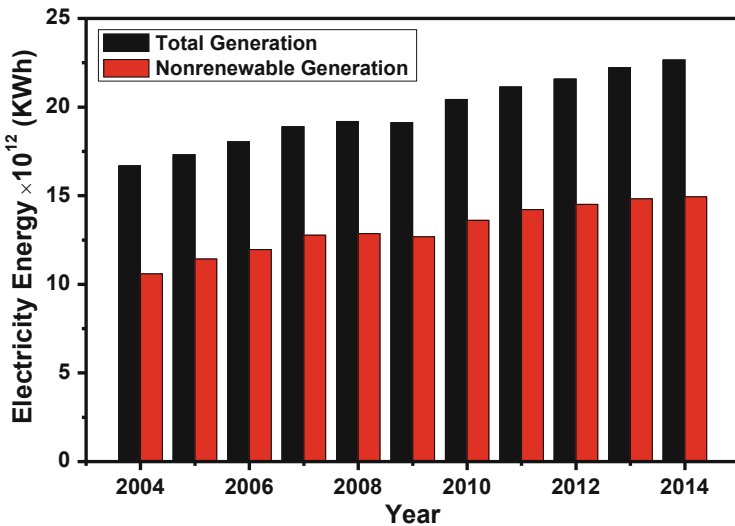


Fig. 6.2 Nonrenewable energy generation out of total energy generation per year [3]

solar cells that are reliable, highly efficient at converting sunlight to electricity, and inexpensive to manufacture, researchers have identified two materials that have great potential as solar absorbers: pyrite, better known as fool’s gold because of its metallic luster, and copper-zinc-tin-sulfide (CZTS).

6.1.1 Seeking the Ideal Material

Today's commercial solar cells are made from one of three materials: silicon (Si), cadmium telluride (CdTe), and copper-indium-gallium-selenide (CIGS). Each has strengths and weaknesses. Silicon solar cells are highly efficient, theoretically converting up to 48% of the sunlight that falls on them into electricity, and very durable. The theoretical efficiencies versus band gap are plotted in Fig. 6.3 [3]. As expected, efficiencies are low for high band gaps since few electron-hole pairs are created and decrease with lower band gaps due to wasted excess photon energy. Also indicated in Fig. 6.3 is the location of several different materials on the efficiency curve, providing a basis for comparison between different photovoltaic candidates.

Silicon solar cells – often referred to as first-generation solar cells – are used in the panels that have become familiar sights on rooftops. Thin film solar cells are made by putting a thin layer of solar absorbent material over a substrate, such as glass or plastic, which typically are flexible and less expensive than crystalline solar cells made from silicon. It is not possible to coat crystalline silicon on a flexible substrate, so we need a different material to use as a solar absorber. Although thin-film solar technology is improving rapidly, some of the materials in today's thin film solar cells are scarce or hazardous. For example, the cadmium in CdTe is highly toxic to all living things and is known to cause cancer in humans. Cadmium telluride can separate into cadmium and tellurium at high temperatures (e.g., in a laboratory or house fire), posing a serious inhalation risk.

Copper-zinc-tin-sulfide (CZTS) thin film solar cell is a reliable option because they are nontoxic and very inexpensive. CZTS costs about 0.005 cents per watt, and pyrite costs a mere 0.000002 cents per watt (<https://www.weforum.org/agenda/2016/05/a-cheaper-future-for-solar-cell-technology>). They also are among the most abundant

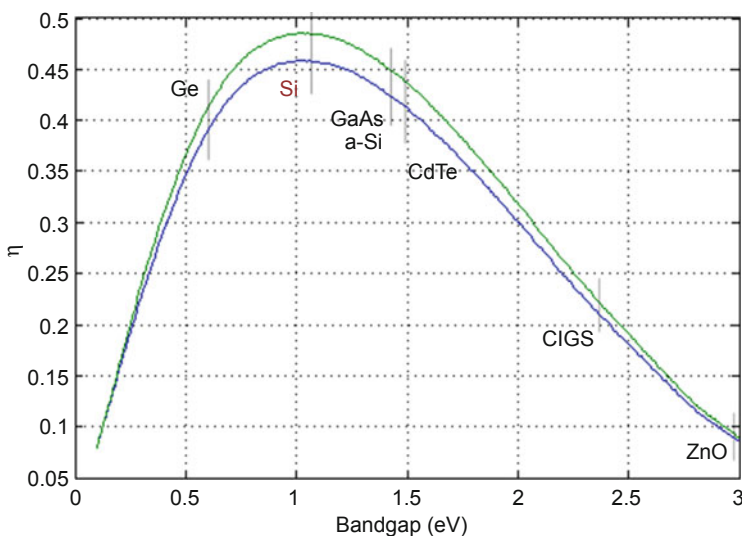


Fig. 6.3 Maximum efficiency versus band gap. Select materials indicated [3]

materials in the Earth's crust and absorb the visible spectrum of sunlight efficiently. These films can be as thin as 1/1000th of a millimeter. So far, however, CZTS solar cells are relatively inefficient: they convert less than 13% of the sunlight that falls upon them to electricity, compared to 20% for more expensive CIGS solar cells. The CZTS solar cells have the potential to be 30% efficient. The main challenges are (1) synthesizing high-quality CZTS thin film without any traces of impurities and (2) finding a suitable material for the "buffer" layer underneath it, which helps to collect the electric charges that sunlight creates in the absorber layer. Our lab has produced a CZTS thin film with 7% efficiency; we hope to approach 15% efficiency soon by synthesizing high-quality CZTS layers and finding suitable buffer layers.

6.2 The Sun: An Energy Source

The distribution of solar radiation as a function of the wavelength is called the solar spectrum, which consists of an uninterrupted emission with some superimposed line structures shown in Fig. 6.4 [4, 5]. From the figure, it is cleared that the measured spectrum does not exactly follow the blackbody curve. The solar spectrum at the top of the atmosphere (yellow colored spectra) is approximately equivalent to the blackbody emission spectrum at 5250 °C (Blackline spectra).

There is close fitting of the solar radiation with the blackbody radiation at 5250 °C in the visible and infrared regions, but in terms of the equivalent blackbody temperature of the Sun, the ultraviolet (UV) region (<400 nm) of solar radiation deviates greatly from the visible and infrared regions. The amount of solar energy received by the Earth in 1 h is more than the yearly world energy consumption and interruption distribution is nonuniform [6–8]. The numbers of

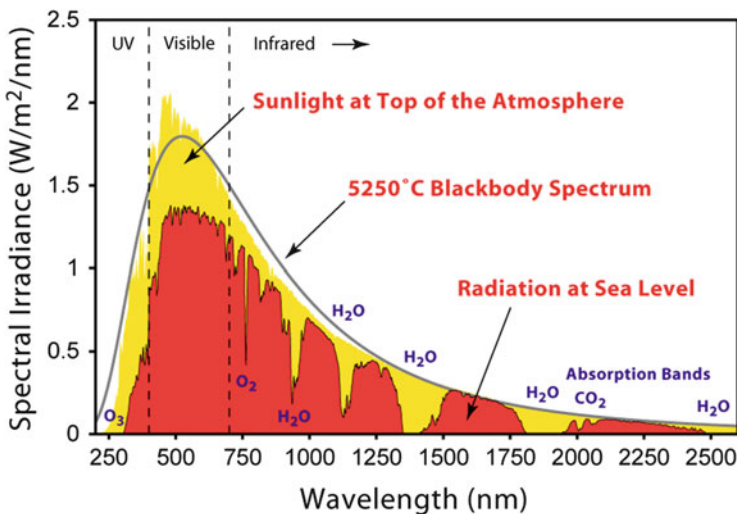


Fig. 6.4 The solar spectrum [4, 5]

deviations or breaks in the solar radiation are observed on the Earth at sea level, Fig. 6.2 (red colored spectra). These deviations or breaks are mainly due to the absorption of the radiations by various molecules in the atmosphere such as water vapor (H_2O), carbon dioxide (CO_2), laughing gas (nitrogen dioxide, NO_2), methane (CH_4), fluorinated hydrocarbons, as well as dust (carbon clusters), oxygen (O_2), ozone (O_3), etc. [9]. Also, the atmospheric scattering plays a vital role in removing higher frequencies from direct sunlight and scattering about the sky [10]. Absorption is rising with the length of the route over the atmosphere and therefore with the mass of the air through which the radiation permits. The path length (l) through the atmosphere and solar radiations strikes at an angle (α) relative to the normal to the earth's surface is given by [11]:

$$l = \frac{l_0}{\cos\alpha} \quad (6.1)$$

where l_0 is the thickness of the atmosphere and the ratio l/l_0 is called the air-mass coefficient. The spectrum outside the atmosphere is nominated by AM0 and that on the surface of the Earth for normal incidence by AM1. A typical spectrum for moderate weathers is AM1.5, which corresponds to an angle of incidence of solar radiation of 48° relative to the surface normal. While in summer AM number for mid-latitudes during midday is less than 1.5, larger numbers apply to the morning and evening and at other times of the year. Therefore, AM1.5 ($\sim 1000 \text{ W/m}^2$) is useful to characterize the complete annual average for mid-latitudes [11].

6.3 Solar Energy Conservation

Solar energy can be directly or indirectly transformed into electricity by resources of numerous techniques [4–12], of which, concentrated solar power (CSP) with its many arrangements and solar photovoltaic (PV) with a diversity of materials can harvest significant amounts of electricity. A photovoltaic cell is an electrical device that changes the energy of sunlight directly into electricity by the photovoltaic effect, which is a physical and chemical phenomenon and whose electrical characteristics, such as current, voltage, or resistance, vary when exposed to light. Numerous techniques have been inspected for the transformation of light into electrical energy, with the semiconductors that absorb light in the visible region being the most effective when exposed to photons with energies beyond optical band gap. Depending upon the progress in the technology, solar cells are classified into four generations [13]. Originally, the solar cells are divided on the basis of cost and conversion efficiency as high cost/high efficiency (first generation), low cost/low efficiency (second generation), low cost/high efficiency (third generation) and The fourth generation (4G) which combines the low cost/flexibility of polymer thin films with the stability of novel inorganic nanostructure materials used as shown by M. A. Green, Fig. 6.5 [13].

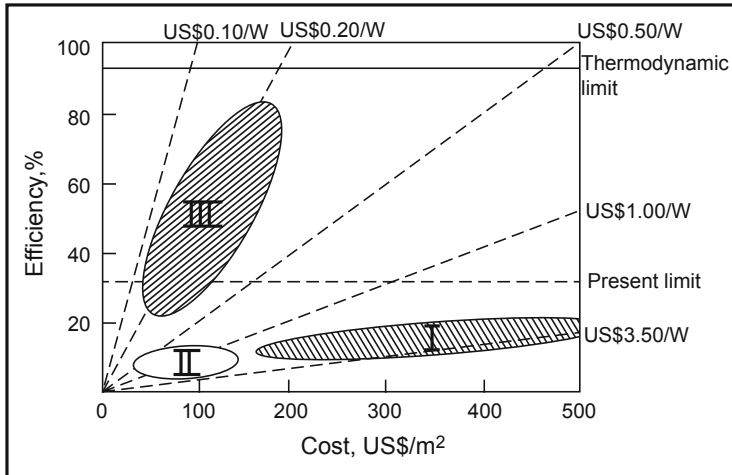


Fig. 6.5 Efficiency and cost projections for first (I), second (II), and third (III) generation photovoltaic technologies (wafers, thin-films, and advanced thin-films, respectively). (Copy@ Elsevier 2019)

As we know, silicon-based solar cells such as monocrystalline silicon (m-Si), polycrystalline silicon (p-Si), amorphous silicon (a-Si) solar cells, etc. have better photoelectric energy conversion efficiency and moderate stability. But as far as the cost of production is concerned, silicon-based solar cells are very costly; so the power conversion per unit currency is low. Also, the earlier discovered tandem solar cells (TSC), dye-sensitized solar cells (DSSC), organic solar cells, quantum dot solar cells (QDSC), etc. are comparatively cost effective and have moderate conversion efficiency, but those solar cells have sealing problems and degrade due to temperature, ultraviolet light, humidity, etc. Thus, silicon-based solar cells and the third-generation solar cells such as tandem solar cells (TSC), dye-sensitized solar cells (DSSC), organic solar cells, quantum dot solar cells (QDSC), etc. are not suitable to use these days. Thin film solar cells from second generation have the promising advantage of low cost and quite low but moderately better energy conversion efficiency. Some of the thin film solar cells contain toxic and rare elements like cadmium, indium, tellurium, gallium, etc., which are costly and harmful. Copper-zinc-tin-sulfide (CZTS) is one of the effective compounds that contain earth abundant and economically low-cost materials with high stability [14]. The reports on the progress inefficiencies of the solar cells are tabulated [15]. Maximum energy conversion efficiency (12.6%) of the CZTS thin film solar cell was recorded by the International Business Machine (IBM) group on 0.42 cm^2 substrate in 2013 with partial replacement of sulfur by selenium [16]. The University of New South Wales (UNSW) research group recently achieved a 7.6% photoelectric conversion efficiency for 1 cm^2 CZTS thin film solar cell [17].

6.4 $\text{Cu}_2\text{ZnSnS}_4$ (CZTS) as an Absorber Material

Copper zinc tin sulfide ($\text{Cu}_2\text{ZnSnS}_4$, CZTS) is a four-material compound that contains copper, zinc, tin, and sulfur. Basically, it has two crystallographic phases: one is stannite and the other is kesterite. Stannite is Zn-poor or zinc replaced by iron also called as ferrokesterite or stannite. Stannite is from the space group $I^- 42 m$ with tetragonal crystal system. Kesterite structured CZTS (space group $I^- 4$) is Zn-rich and involves of a cubic close-packed (CCP) array of sulfur atoms, with metal atoms occupying one-half of the tetrahedral sites. Figure 6.6 gives a clear view of the kesterite crystal structures. Schäfer and Nitsche in 1974 synthesized, studied, and showed that the CZTS had a sphalerite-like crystal structure with c/a (ratio of lattice parameter) being close to 2 ($a = 5.43 \text{ \AA}$, $c = 10.83 \text{ \AA}$), used frequently to determine CZTS phase in the literature [18]. Study, computation, and simulation of disorders and defects of the quaternary compounds are quite difficult. A consequence of the many components of the material is an increase in the number of possible lattice defects, with concern for cation disorder [19].

During the deposition of CZTS, vacancies – V_{Cu} , V_{Zn} , V_{Sn} , and V_{S} ; antisite defects – Cu_{Zn} , Zn_{Cu} , Cu_{Sn} , Sn_{Cu} , Zn_{Sn} , and tin-zinc (SnZn); and intrinsic defects – Cu_i , Zn_i , and Sn_i – are possible. Kesterite copper zinc tin sulfide ($\text{Cu}_2\text{ZnSnS}_4$) semiconductor is the p-type due to the copper atoms occupies the locations of zinc atoms, which are from the CuZn antisite defect. The computational mapping of disordered CZTS using first principles quantum mechanics joint with Monte Carlo simulations of Cu and Zn chemical potentials by Yu et al. [20, 21]. Singh et al. studied the shape-controlled transformation from meta-stable wurtzite copper zinc tin sulfide selenium (CZTSSe) nanocrystals into highly stable zincblende phases which was achieved through a solution treatment, while conversion from wurtzite nanocrystals into kesterite grains was accomplished by direct annealing [22]. Single-phase CZTS crystals can be formed in a very restricted region in the equilibrium diagram of Cu_2S - ZnS - SnS_2 system shown in Fig. 6.7 [23]. In the other regions of the

Fig. 6.6 The stannite and kesterite crystal structures single crystal [18]. (Copy@ Elsevier 2019)

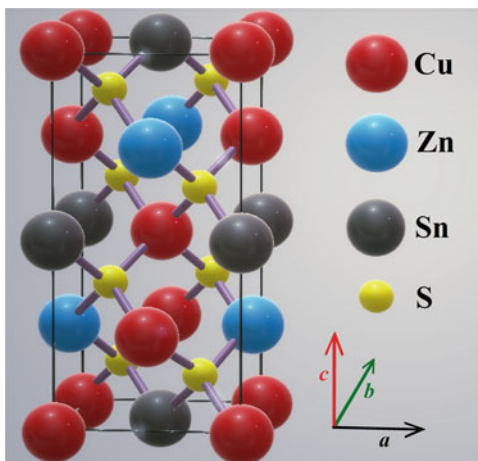
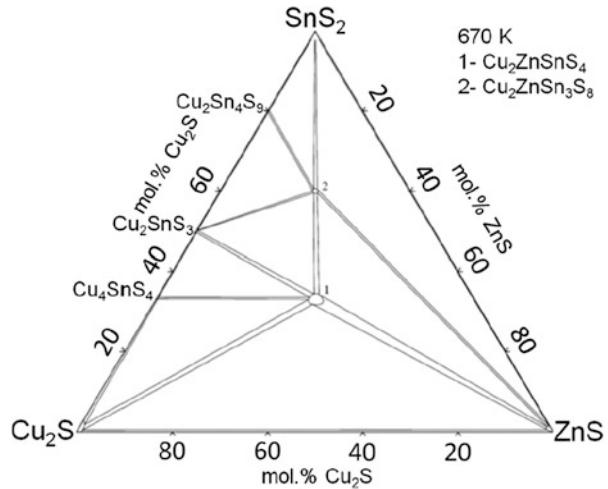


Fig. 6.7 Equilibrium diagram of Cu_2S - ZnS - SnS_2 [23]. (Copy@ Elsevier 2019)



same diagram, the secondary phases, like binary, ternary, and quaternary for copper / tin sulfides with or without zinc such as Cu_2S , CuS_2 , SnS , SnS_2 , Sn_2S_3 , Cu_xSn_y , Cu_2SnS_3 , $\text{Cu}_2\text{ZnSn}_3\text{S}_8$ [24–31]. Malebra et al. investigated the blistering of the CZTS thin films synthesized via co-sputtering by sputtering parameters [32]. The delimitation occurred at the CZTS/substrate interface after the annealing as shown in Fig. 6.8.

The blistering occurred mainly due to the relief of compressive stressor on the formation of over-pressurized trapped gas bubbles. The analysis shows that increasing the sputtering pressure decreases both compressive stress in precursors and blistering extent in the CZTS film. A theoretically determined optical band gap of stoichiometric kesterite structured CZTS is 1.50 eV [33]. Experimentally, the band gap of CZTS varies from 1.4 to 1.5 eV by deposition parameters and method to method [34–37].

Absorption coefficient is a very important parameter of the solar cell, and absorption coefficient of CZTS is more than 10^4 cm^{-1} [38–40]. Wei et al. experimentally controlled the band gap of CZTS nanocrystals' incorporation of selenium, and it is also theoretically proved [41] revealing a parabolic nature as shown in Fig. 6.9.

The band gap initially decreased with the increase in $\text{Se}/(\text{S} + \text{Se})$ ratio up to 0.55 (eV) and then increased with the increase in $\text{Se}/(\text{S} + \text{Se})$ ratio. They found a band gap of CZTS nanocrystal.

6.5 Topical Research and Development in the CZTS Thin Film in the Application of Solar Cells

Every year, scanty research papers are published on the CZTS material, and several techniques are used to synthesize CZTS thin films such as chemical vapor deposition, chemical bath deposition, chemical spray pyrolysis, electrochemical deposition,

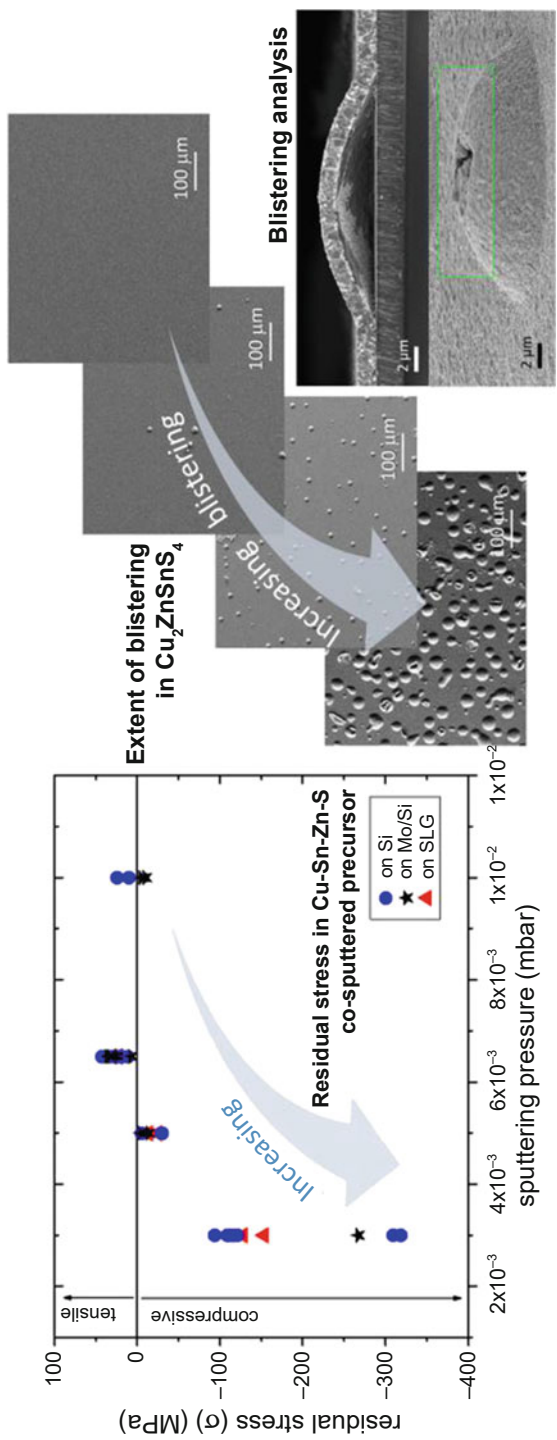


Fig. 6.8 The delamination occurred at the CZTS/substrate interface after the annealing [32]. (Copy@ Elsevier 2019)

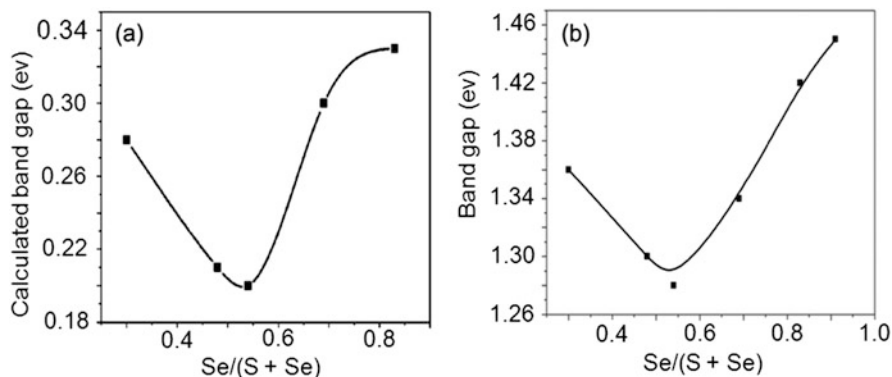


Fig. 6.9 Theoretical (a) and practical (b) band gap variation of $\text{Cu}_2\text{ZnSnS}_{4x}\text{Se}_{4(1-x)}$ nanocrystals by the variation of $\text{Se}/(\text{S} + \text{Se})$ ratio [41]. (Copy@ Elsevier 2019)

hydrothermal, spin coating, solvothermal, hot injection, solution route, doctor blading, combustion, deep coating, sol-gel, successive ionic layer adsorption and reaction (SILAR), sputtering, co-evaporation, pulsed laser deposition, vacuum thermal evaporation, etc. [42–57]. Each technique has a specialty in grain size growth, adhesion, porosity, stoichiometry, thickness sustainability, purity, etc. In a solar cell, the output current is associated with the period of the movement of charge carriers through the bulk material. They can reach the depletion region only if life expectancy is long enough to complete the journey [58]. Here, we review some of the best articles published in recent years on the $\text{Cu}_2\text{ZnSnS}_4$ thin film as an absorber material for solar cell. Some basic and applied concepts related to material synthesis, structure, and processing and their use in the application are important to study. By keeping the enhancement of conversion efficiency in mind, efforts have been made in different ways. Typical and beneficial ways to improve the efficiency of CZTS thin film-based solar cells are as follows: (i) preprocessing and synthesis, (2) crystal defect study and its purity, (3) post-processing – annealing and sulfurization/selenization, and (4) buffer layer and interfaces. These four application parameters play important roles in the enhancement of the efficiency of CZTS solar cell. The continuing works on these application parameters are discussed below in brief. Fan et al. also suggested a three-step process for the crystal quality of the absorber layer [59].

6.5.1 Pretreatment and Synthesis

Yang et al. used a facile water-based approach to fabricate CZTSSe solar cells; the crystalline quality of the CZTSSe thin film was improved by the sodium (Na) doping and the highest power conversion efficiency (PCE) of 6.96% was obtained at 4% Na-doping concentration as shown in Fig. 6.10 [60]. Also, 6.0% conversion efficiency was recorded by Na doping and tin sulfide (SnS) powder incorporation in the sulfurization process [61–65]. To achieve better efficiency, Na was incorporated on

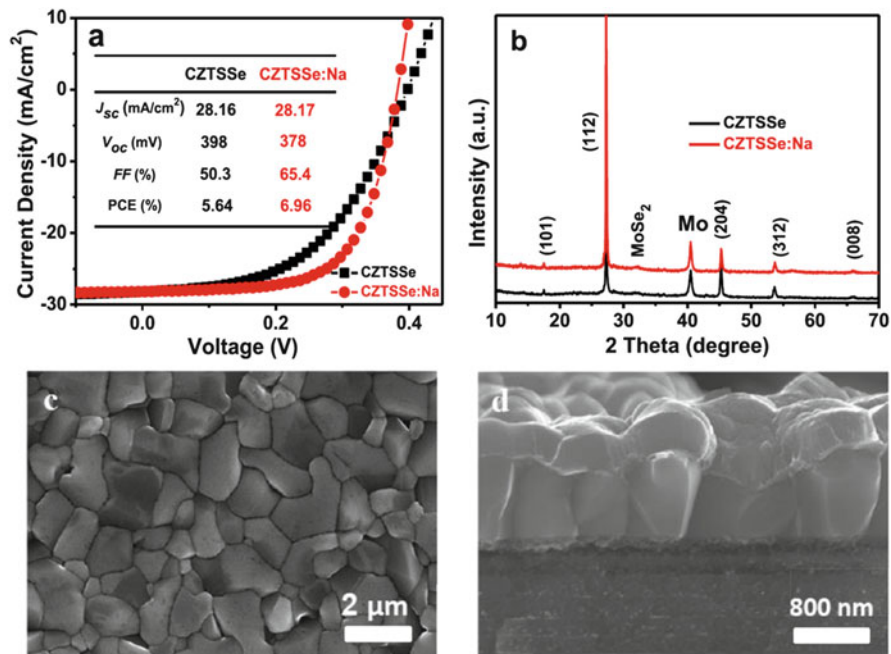


Fig. 6.10 (a) The comparison of J-V curves for the CZTSSe device and Na-doped CZTSSe device. (b) X-ray powder diffraction (XRD) patterns of CZTSSe thin film and Na-doped CZTSSe thin film under the identical selenization condition. (c) The top-view scanning electron microscope (SEM) image of Na-doped CZTSSe thin film. (d) The cross-sectional SEM image of Na-doped CZTSSe device [60]. (Copy@ Elsevier 2019)

the surface of CZTS thin film by sodium sulfide (Na_2S), but Na_2S reduces the cadmium sulfide (CdS)-buffer layer grain growth.

To overcome deficiency of Sulphur, two routes were discovered: first is the oxidation of Na_2S by annealing the CZTS film to form sodium sulfite (Na_2SO_3) and sodium sulfate (Na_2SO_4) and the second is using water deep process instead of potassium cyanide (KCN) etching and achieves 6.5% efficiency. The hydrogen peroxide (H_2O_2) processing on the CZTS thin films was studied [66, 67]. While co-doping antimony (Sb) and Na in the solution based chemical route deposited CZTS thin films, 5.7% cell efficiency was observed by simulating under AM 1.5 illumination [68, 69]. Ritscher et al. successfully synthesized kesterite copper zinc tin sulfide (CZTS) nanoparticles by mechanochemical route method. Average neutron scattering length method was used to analyze cation distribution and revealed a partial disorder of copper and zinc on the (2c) and (2d) sites [70]. Li et al. prepared copper zinc tin sulfide selenide (CZTSSe) by co-sputtering on molybdenum (Mo)-coated substrates based on three-layer precursors with Cu-poor and Zn-rich in the top and bottom layer while stoichiometric in middle layer [71]. The improvement in conversion efficiency of CZTSSe solar cell was from 0.97% to 4.51% with the utilization of a three-layer precursor. Physics of ordered defects and grain boundary in CZTS were

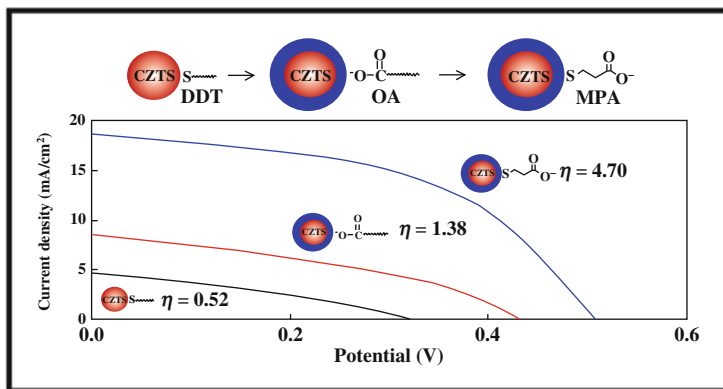


Fig. 6.11 Current density-voltage (J-V) characteristics of quantum dot solar cell (QDSC) of copper zinc tin sulfide (CZTS) with different capping [73]. (Copy@ Elsevier 2019). The effect of iodine pressure on the properties of CZTS thin films deposited by close spaced vapor transport (CSVT) was studied [75]. Iodine pressure cannot affect the compositional and electrical properties of the film but increased crystallite size and the band gap

studied by Samji et al. [72]. They studied X-ray photoelectron spectroscopy (XPS) of CZTS to define the position of valence band edge and reported the development of ordered vacancy compounds along with absorption studies.

A quantum dot (QD)-sensitized solar cell (QDSC) of the quaternary $\text{Cu}_2\text{ZnSnS}_4$ (CZTS) quantum dots synthesized via hydrolysis approach by capping these QDs with 3-mercaptopropionic acid (MPA) results in 4.70% conversion efficiency by the water-soluble treatment of CZTS/CdSe cell shown in Fig. 6.11 [73]. The defect on the grain growth and the defect passivation of the sodium diffusion from soda lime glass at high-temperature annealing of chalcogenide/kesterite solar cells were reported by Singh et al. [74]. They concluded the improvement in the grain growth and declination in the optical band gap with sodium diffusion.

A partial replacement of zinc (Zn^{+2}) cation by cadmium (Cd^{+2}) cation into the host lattice of CZTSSe can affect the band gap, crystal growth, space-charge density, depletion width, and photoelectric conversion efficiency of CZTSSe cells. Similarly, the effect of Li in substitution with copper (Cu) in CZTS was experimentally and theoretically investigated [76]. The device efficiency of 7.2% was achieved by partial incorporation of silver in partial replacement of copper by solution processable method. A very small amount of silver (< 7 mol % of Cu content) enhances grain size and depletion width and reduces antisite defect concentration states [77]. Using heat-up method, CZTS nanocrystals were synthesized in a novel formamide solvent, and the effect of different sulfide precursors was studied and the study reported that the sulfide precursors affect the nucleation and growth characteristics of the nanocrystals and not the transformation of the phase [78]. Williams et al. studied the occurrence of carbon [79] and examined whether the carbon exhibits a more complex and significant role in enhancing the grain growth abnormally during annealing. The dithiocarbamate $[\text{CH}_2\text{NS}_2]$ -based copper zinc tin sulfide

($\text{Cu}_2\text{ZnSnS}_4$, CZTS) precursor solutions were prepared using various amino groups, such as methylamine [H_3CNH_2], ethylamine [$\text{C}_2\text{H}_7\text{N}$], propylamine [$\text{C}_3\text{H}_9\text{N}$], butylamine [$\text{C}_4\text{H}_{11}\text{N}$], amylamine [$\text{C}_5\text{H}_{13}\text{N}$], hexylamine [$\text{C}_6\text{H}_{15}\text{N}$], octylamine [$\text{C}_8\text{H}_{19}\text{N}$], and ethanolamine [$\text{C}_2\text{H}_7\text{NO}$], and spin coated followed by annealing to fabricate CZTS thin films. The ethanoldithiocarbamate [$\text{C}_5\text{H}_{10}\text{NS}_2^-$]-based $\text{Cu}_2\text{ZnSn}(\text{S},\text{Se})_4$ solar cell achieved the best power conversion efficiency of 7.66% under 1.5 AM illumination [80–82].

The effects of cadmium (Cd) alloying and mechanism supporting the performance enhancement have been investigated. The introduction of Cd can considerably decrease the band tailing subject, which is confirmed by the drop in the distinction between the photoluminescence peak and optical band gap (E_g), as well as decrease the Urbach energy, and an 11% efficiency was achieved by Cd-alloyed zinc tin sulfide (CZCTS) solar cell. Figure 6.12a and b gives the current density-

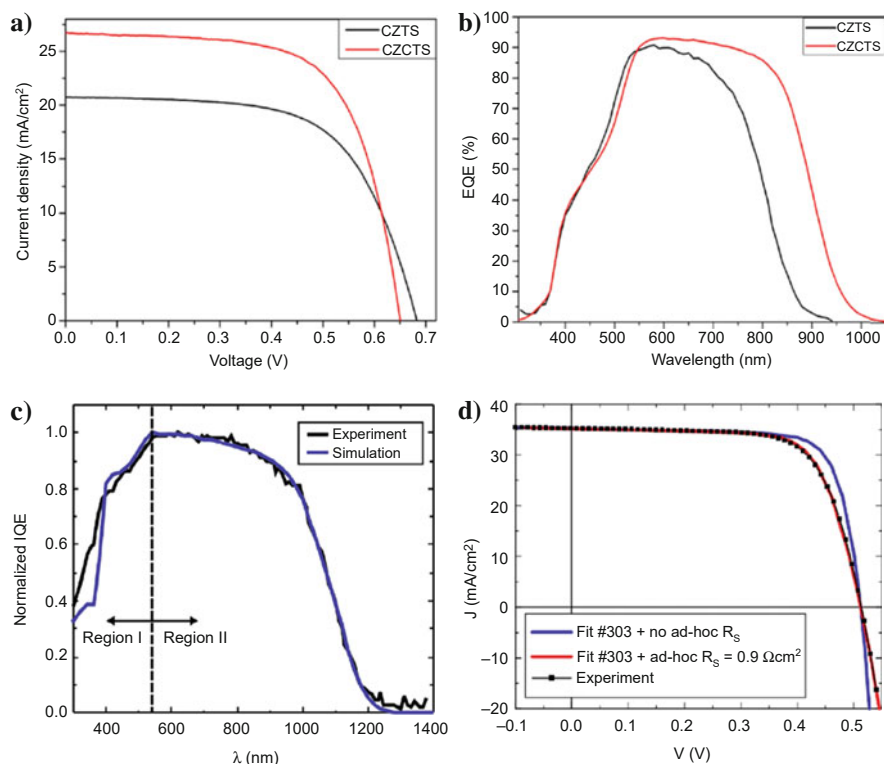


Fig. 6.12 (a) Current density-voltage ($J - V$) curves and (b) external quantum efficiency (EQE) curves of copper zinc tin sulfide (CZTS) and champion copper zinc cadmium tin sulfide (CZCTS) devices [83]. (Copy@ Elsevier 2019). (c) Comparison of normalized internal quantum efficiency (IQE) for the 12.6% efficient copper zinc tin sulfide selenide (CZTSSe) solar cell and the simulated data and (d) Comparison of current-voltage (I-V) data for the 12.6% efficient copper zinc tin sulfide selenide (CZTSSe) solar cell and the simulated data for the device with and without the added series resistance [91]. (Copy@ Elsevier 2019)

Table 6.1 Device characteristics of the CZTS and CZCTS solar cells [83]

Absorber	V_{oc} (mV)	J_{sc} (mA/cm ²)	FF (%)	Eff. (%)	$E_g/q-V_{oc}$ (mV)	$R_{s, L}$ (Ω cm ²)	$G_{s, L}$ (mS/cm ²)	A	J_0 (A/cm ²)
CZTS	683	20.7	62.5	8.8	847	0.96	0.67	3.3	8.1×10^{-6}
CZCTS	650	26.7	66.1	11.5	730	0.45	1.0	2.5	1.2×10^{-6}

voltage (J-V) curve and external quantum efficiency for zinc tin sulfide (CZTS) and kesterite material copper zinc cadmium tin sulfide (CZCTS) device. The device characteristics are given in Table 6.1 [83].

The tin sulfide (SnS) and zinc sulfide (ZnS) as a secondary phase tend to segregate at both the surface and the back side of annealed CZTS films with copper (Cu)-poor and zinc (Zn)-rich composition. When tin sulfide (SnS) segregates on the CZTS rear, it is beneficial to the solar cell but harmful when on the surface of the CZTS.

6.5.2 Crystal Defect Study

Highly ordered layers of CZTS nanorods are synthesized in three dimension (3D) using either discrete one-dimensional (1D) rods or two-dimensional (2D) monolayer super crystals rods as the building blocks. The assembly approaches are dependent on tunable properties of the rods such as charge (ligand state) and dipole moment (composition and aspect ratio); the approach is generally applicable across any nanorod system. The intermediate self-assembly step can be eliminated by carrying out a judicious ligand exchange, allowing selectivity for dimensional control of layer formation from nanorod building blocks in one, two, and three dimensions [84, 89]. A successful increase in the conversion efficiency from 5.41 to 8.11% was achieved by introducing the additional element in the copper zinc tin sulfide selenide (CZTSSe) [85, 90]. To overcome this problem, the lack of in-depth understanding of the kinetics of the dynamic phase formation process at the time of annealing treatment, the in situ Raman monitored-annealing was applied to study the phase formation kinetics of nano-crystalline kesterite from a precursor deposited on titania (TiO₂) mesoscopic scaffold [86, 91]. The nucleation of primary kesterite crystallites starts at a temperature (~170 °C) significantly lower than previous ex situ study [87, 92]. The real-time temperature dependence of Raman peak intensity improvement shifts and broadening for CZTS provides a valuable reference in CZTS research. Wang et al. synthesized the crack-free and high-quality CZTSSe films having good crystallinity using novel nontoxic hybrid ink method for solar cell application with 6.39% conversion efficiency [88, 93]. The photovoltaic conversion efficiencies varied from about 4% in the case of more ordered materials up to nearly 8% after the disordering treatment [89, 94].

Coupled optical and electrical modeling and simulations of different CZTS solar cell nanostructures are studied for taking full advantage of the absorption, carrier generation, carrier collection, and efficiency in CZTS solar cells [90, 91, 95, 96].

Figure 6.12c and d gives the simulated and experimental data having good correspondence over the complete wavelength range and whole current-voltage (I-V) curve for the simulated data with an additional resistance (R_s) of $0.9 \Omega\text{cm}^2$ for the experimentally measured I-V curve. The projected data showed that the nanotube CZTS/CdS provided the highest generation rate of charge carriers as well as the highest efficiency (7.91%). Modeling achieved good agreement compared to previous reports.

Xiao et al. theoretically investigated the density-functional theory to determine atom structures and electronic structures for the CdS/CZTS heterointerfaces in the CZTS-based solar cells [92]. The cadmium sulfide (CdS) favors to epitaxially grow on the copper-zinc (Cu-Zn) plane of copper zinc tin sulfide (CZTS) along the direction of (100); hence, the effect of wrong bonds at the interfaces can be reduced and charge carrier recombination barrier enhanced. The studies of zinc (Zn) segregation at the buffer/absorber interface conclude that the Zn segregation enhances the stabilization of heterointerfaces but wrongly affects the solar cell property. The temperature dependence of the order/disorder behavior of Cu/Zn-sites was investigated by neutron powder diffraction measurement technique on the CZTS samples annealed at 200–350 °C temperature range [93, 94]. In the whole temperature range, Cu completely occupies the 2a and Sn the 2b position. For Zn and the remaining Cu on sites 2d and 2c, a clear change from ordered to disordered kesterite structure was found. Secondary phase's tin sulfide (SnS), zinc sulfide (ZnS), and copper tin sulfide (Cu_2SnS_3) are observed and considered an important role in high efficiency [95]. Spin-coated copper (Cu), zinc (Zn), tin (Sn), and sulfur (S) precursors on molybdenum (Mo)-coated glass substrates followed by selenization formed CZTSSe films. The device consisting of aluminum/aluminum-doped zinc oxide/zinc oxide/cadmium sulfide/copper zinc tin sulfide selenide/molybdenum [Al/AZO/ZnO/CdS/CZTSSe/Mo]-glass and studied under AM1.5G illumination gives 9.08% conversion efficiency [96]. The spatial grain growth and composition evolution during the sulfurization of wurtzite nanocrystal coatings were systematically investigated by classifying samples into temperature and time series [97]. The reversible migration of Cu and Zn species on the surface results in the continuous growth of kesterite CZTS. At higher temperature, the phase transformation from wurtzite to kesterite was observed away from the surface. The cell of pure-sulfide $\text{Cu}_2\text{ZnSnS}_4$ absorber from wurtzite nanocrystal-based coatings shows 6.0% efficiency without an antireflection coating.

6.5.3 Post-Sulfurization/Selenization

Ma et al. studied comparatively the properties of CZTS and CZTSSe synthesized nano-crystalline ink of CZTS by a solid-phase reaction, doctor-bladed on Mo-coated substrates followed by selenization [98]. The study of X-ray powder diffraction (XRD), Raman spectroscopy, X-ray photoelectron spectroscopy (XPS), field emission scanning electron microscopy (FESEM), ultraviolet (UV-vis) spectroscopy, and

electrochemical of copper sulfide (CuS), zinc (Zn), and tin (Sn) targets followed by a rapid annealing process.

The band gap found from Tauc plots was $E_g = 1.57 \pm 0.02$ eV, and the absorption coefficients were found to be a few 10^4 cm^{-1} . The sub-band-gap k-value was found to be $k \sim 0.05$ or less, considerably moderate band tail was present. The annealing effect on $\text{Cu}_2\text{ZnSn}(\text{SSe})_4$ was studied by Li et al. [99], and 2.8% and 5.3% device efficiency were observed for the samples having thickness 500 and 800 nm, respectively, also the photoluminescence behavior was observed [100–105]. After CZTS nano-crystalline annealing treatment, field emission scanning electron microscopy (FESEM) images (Fig. 6.13a and b) show a packed patty structure with middle structures of CuO, also observed by Inamdar et al. [106]. As shown in Fig. 6.13c, for thin film solar cell application, both CZTS nano-crystalline and selenized CZTSSe film demonstrated suitable properties and also 7.48% efficiency was found by selenizing the CZTSSe films [107]. Li et al. synthesized CZTS films on soda-lime glass (SLG) substrates and molybdenum (Mo)-coated SLG by direct current (DC) magnetron co-sputtering in argon (Ar) and hydrogen sulfide (H_2S) atmosphere of copper sulfide (CuS), zinc (Zn), and tin (Sn) targets followed by a

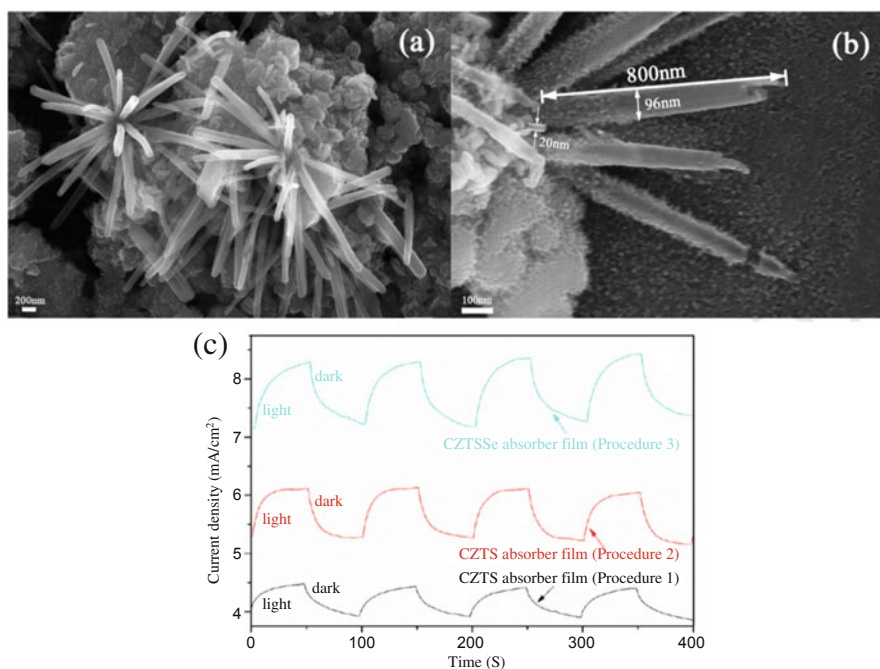


Fig. 6.13 Plane-view field emission scanning electron microscopy (FESEM) images of (a) the annealed CZTS nano-crystalline covered with needle structure of copper oxide (CuO), (b) an enlarged view of the needle structure, and (c) photocurrent-time (j-t) responses of CZTS and CZTSSe absorber films on Mo-coated substrates in a 0.25 M sodium sulfide/sodium sulfite ($\text{Na}_2\text{S}/0.35$ M Na_2SO_3) solution under AM1.5G irradiation [106]. (Copy@ Elsevier 2019)

rapid annealing process. The spectroscopic ellipsometry analysis were exploited to build a multilayer stack optical model and to develop the dielectric functions with refractive indices.

To investigate the distribution of zinc sulfide (ZnS) in CZTS films prepared at different annealing temperatures, Nam et al. carried out depth-resolved Raman spectroscopy. A strong relationship between solar cell efficiency and the distribution of ZnS was observed, and the highest conversion efficiency of 7.5% for 570 °C sulfurization temperature was reported [108]. Dimitrievska et al. studied the Raman spectroscopy and first principle analysis of kesterite CZTS [109]. Rana et al. deposited CZTS thin films using chemical bath deposition (CBD) method by stacking the layers of CuS, ZnS, and SnS on soda-lime glass (SLG) and by post-sulfurization [110]. The problem of the peeling-off films was resolved while stacking the layers by adjusting the pH of the solution. Kesterite structure, large grain size, and optical band gap energy in the range from 1.48 to 1.51 eV were observed after sulfurization, which is mandatory for the solar cell application. Li et al. reported the results on the CZTS by chemical bath deposition-annealing route by stacking the layers and compared Cu sources as Cu and CuS in the fabrication of $\text{Cu}_2\text{ZnSnS}_4$ thin films and solar cells with stacked layers of SnS/Cu(S)/ZnS. The stacking layer of SnS/Cu/ZnS is more suitable for the high performance of $\text{Cu}_2\text{ZnSnS}_4$ thin film solar cells with a high-quality morphology and phase purity. The improved conversion efficiency of 3.79% was recorded using the stacking layer SnS/Cu/ZnS rather than SnS/CuS/ZnS stacking layer. Rawat et al. synthesized CZTS nanoparticles by a wet chemical method and studied the effect of assistance of polyethylene glycol (PEG) on CZTS nanoparticle film [111]. Copper zinc tin sulfide (CZTS) nanoparticles showed tetragonal kesterite structure with a crystallite size of 2.33 nm. A result of PEG changes the morphology from spherical to nanoflake and nanorod. Huang et al. prepared CZTS thin films on fluorine-doped tin oxide (FTO) substrates by a solvothermal method using PEG and found p-type CZTS nanoworm film with the band gap of 1.62 eV [112].

The effects of the deposition parameters such as the annealing temperature, the annealing time, and the ratios of Cu/(Zn + Sn) and Zn/Sn on structural and optical properties are studied using the Taguchi L9 (3^4) orthogonal array for the $\text{Cu}_2\text{ZnSnS}_4$ (CZTS) thin films without sulfurization synthesized using the sol-gel method associated to spin coating [113]. The signal to noise (S/N) ratio and analysis of variance (ANOVA) results from statistical analysis show that the near finest combination of factor levels leads to the optimal band gap of 1.5 eV. The Zn/Sn ratio and the annealing temperature were observed as the dominant parameters of the CZTS thin films. Espindola-Rodriguez et al. deposited $\text{Cu}_2\text{ZnSnS}_4$ thin films under an argon atmosphere by pneumatic spray pyrolysis technique by a selenization process with the variation of annealing temperature and selenium weight, finding that the films results to be Se-rich but not S-free with efficiencies up to 2.1% [114, 119].

The high conversion efficiency was achieved for the CZTSSe films synthesized by the novel-aqueous-ink method and analyzed by various techniques to investigate phase, crystallinity and composition, Fig. 6.14 [115–117].

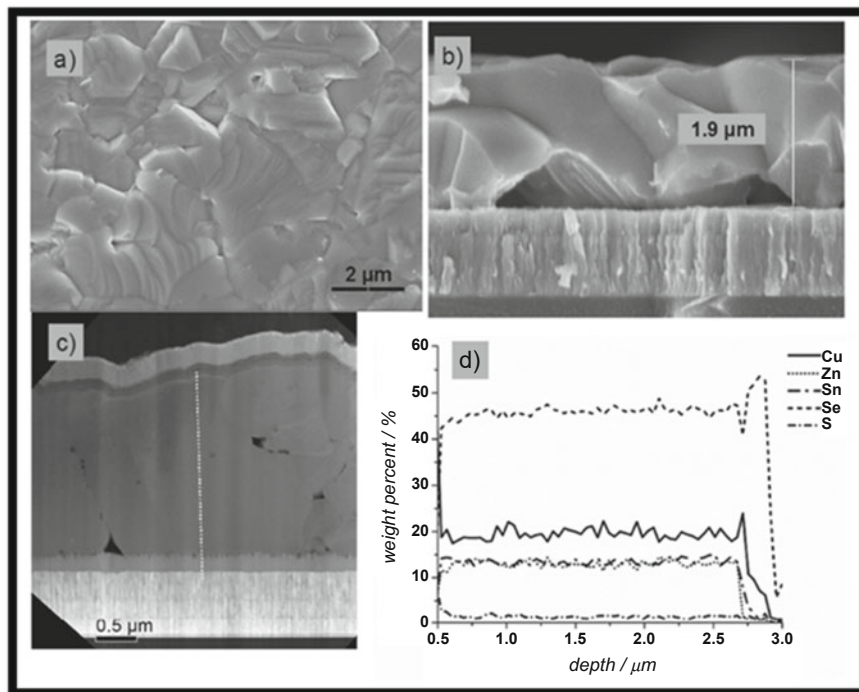


Fig. 6.14 (a) Scanning electron microscope (SEM) images of the surface, (b) cross-section of a CZTSSe film on molybdenum (Mo)-coated glass, (c) transmission electron microscope (TEM) image of champion completed device film with (d) corresponding energy-dispersive X-ray spectroscopy (EDX) scan taken along the dotted line [117]. (Copy@ Elsevier 2019)

A comparative study of dynamic-annealing and static-annealing processes of the sulfurization on CZTS thin films was prepared by spin-coating of sol-gel precursor [118]. The conversion efficiency 6.68% was observed for the thin films sulfurized with a static-annealing approach by etching ZnS from the surface using hydrochloric acid. Synthesis of wurtzite CZTS nanocrystals using top-down strategy was done by green hydrothermal method without any organic ligands [119]. In dye-sensitized solar cells, using CZTS/carbon cloth composite structure as a flexible counter electrode based on a facile electrodeposition method and mild solvothermal treatment shows power conversion efficiency of 7.53% with long-operation life performance, high catalytic activity, good conductive framework, effective photo-generated electron migration, and high iodide species diffusion rate of the composite CE [120]. Copper zinc tin sulfide ($\text{Cu}_2\text{ZnSnS}_4$) nanoparticles sensitized metal-organic frameworks (MOFs) derived mesoporous TiO_2 photoanodes synthesized by a facile hot injection and hydrothermal method [Copper zinc tin sulfide (CZTS)/metal-organic frameworks (MOFs)-derived (titania) TiO_2 photoanodes] can achieve the conversion performance of 8.10% [121]. Improvement in the conversion efficiency from 2.1 to 7.5% of copper zinc tin (CZT) alloy in CZTSSe thin films is

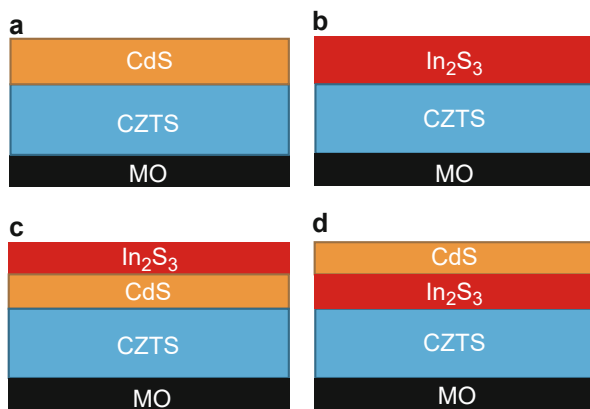
carried out by sulfurization-after selenization (SAS) in hydrogen sulfide (H_2S) and hydrogen selenide (H_2Se) atmosphere synthesized by direct current (DC)-magnetron sputtering [122].

6.5.4 Buffer Layer and Interfaces

The complete design of the CZTS/CZTSSe solar cell is shown in Fig. 6.15. The CZTS-based absorber exhibits lower current characteristics than the copper indium gallium selenium (CIGSe) and copper indium gallium sulfur selenium (CIGSSe) absorber layer [123, 124] in terms of the band gap alignment and electron-hole recombination at the cadmium sulfide (CdS)-absorber interface [125, 130]. The conduction band offset between CdS and CZTS/CZTSSe does not imply any major limitation on device performance [126–128]. The effects of the self-constituent buffer layer (CuS, SnS, and ZnS) on the CZTS thin films material properties and phase purity, crystallinity, and elementary distribution were studied by Chen et al. [129]. Chen et al. deposited 20 nm thick layers of metallic Cu, Sn, and Zn individually on the Mo substrates by sputtering, and these samples were sulfurized at 300 °C, 300 °C, and 250 °C temperatures respectively for 1 h to become CuS, SnS, and ZnS as a buffer layer.

On these buffer layers, sequentially Cu-Sn-Zn (CZT) metal precursors were sputtered and sulfurized in a tube furnace for 2 h at 550 °C to form CZTS. The samples Mo/CZTS, Mo/ZnS/CZTS, Mo/SnS/CZTS, and Mo/CuS/CZTS were tested for phase purity, crystallinity, and stoichiometry. A comparative study concluded that the sample having an insertion of SnS buffer layer shows defectless, secondary phaseless and stoichiometric CZTS. To study the solar cell property of the CZTS absorber layer in the presence of different buffer layers, Yan et al. synthesized CZTS layer by co-sputtering Cu/ZnS/SnS precursors on Mo-coated soda lime glass and buffer layers of In_2S_3 and/or CdS on top of the CZTS layer by CBD [130]. In the best

Fig. 6.15 Schematic solar cell device structure with approximate thicknesses. (Copy@ Elsevier 2019)



devices, it has been shown that the back contact with Mo is Ohmic in nature [131]. A considerable improvement in the V_{oc} , or decrease in the V_{oc} debit, can be accomplished using In_2S_3 and In_2S_3/CdS hybrid buffers. When a hybrid In_2S_3/CdS buffer is utilized, higher efficiency (6.6%) pure sulfide CZTS solar cells can be achieved. Rapid post-heat treatment to the Cd-free buffer layer of In_2S_3 stacked with electro-deposited Cu_2ZnSnS_4 layer gives conversion efficiency of 6.9% due to an increase in acceptor density of CZTS layer close to the In_2S_3 -CZTS heterointerface [132–135]. The energy difference between the conduction band minimum of In_2S_3 and that of Cu_2ZnSnS_4 at the In_2S_3/Cu_2ZnSnS_4 heterointerface was determined to be a slightly positive value of 0.11 eV, indicating the formation of a “notch-type” conduction band offset for efficient suppression of the interface recombination.

The Cu_2ZnSnS_4 (CZTS) films were prepared on n-type GaN substrate by an e-beam evaporation technique. The Au/CZTS/n-GaN heterojunction (HJ) demonstrated an exceptional rectifying property with low-leakage current (3.033×10^{-8} A) and high barrier height (0.82 eV) compared to the Schottky junction (SJ) (3.575×10^{-6} A and 0.69 eV). The extracted interface state density (NSS) was found to be less for the HJ compared with the SJ. These results confirmed that the occurrence of CZTS interlayer is effective in modifying the potential barrier and interface state of SJ [136]. Ren et al. demonstrated that the sulfur partial pressure P_{S_2} can be monitored by investigating the Sn-S phase transformation. They showed that sulfur partial pressure P_{S_2} drops considerably over the annealing time, causing gradual alterations in CZTS: (i) a change in defect type; (ii) evolution of ZnS and Sn_xS_y phases. Solar cells with nonoptimal CdS buffer can be repeatedly achieved when CZTS is prepared under sufficiently high P_{S_2} [137].

6.6 Conclusion

The present understanding of the research and development in the Cu_2ZnSnS_4 thin film for the application of high-efficiency solar cells, presented the world's energy economics, energy resources (renewable and nonrenewable) and energy consumption. The vital energy source, the sun, and energy collection types are discussed in brief, and the solar cell technology development from the first-generation silicon solar cell to the emerging fourth generation “inorganics-in-organic” solar cell is presented. A number of research articles on the absorber layer CZTS, its structure, phases, defects and minimization, different morphologies using different synthesis techniques, buffer layers and interface mechanism, impurities due to doping and effect on the efficiency and device performances are presented here for the maximum efficiency.

Acknowledgments Author is very thankful to Springer Nature for the invitation to contribute a chapter in the book *Nanostructured Materials for Next-Generation Energy Storage and Conversion Vol 4: Photovoltaic and Solar Energy*.

References

1. T.G. Gutowski, S.B. Gershwin, T. Bounassisi, *Proceedings of the IEEE International Symposium on Sustainable Systems and Technology*, Washington, DC, 2010
2. BP Energy Economics, Energy consumption. www.bp.com. Accessed Feb 2017
3. Independent Statistics and Analysis, U.S. Energy Information Administration www.eia.gov. Accessed Feb 2017
4. R.T. Pierrehumbert, Concept warming the world. *Nature* **432**, 677–677 (2004)
5. J. Tyndall, *On Radiation: The 'Rede' Lecture, Delivered in the Senate-House Before the University of Cambridge on Tuesday, May 16, 1865* (D. Appleton, New York, 1865)
6. H. Balat, C. Öz, Technical and economic aspects of carbon capture and storage – a review. *Energy Explorer. Exploit.* **25**, 357–392 (2007)
7. U. S. DOE (2001). <http://earthobservatory.nasa.gov/Features/CarbonCycle/>
8. M. Aresta, A. Dibenedetto, Utilisation of CO₂ as a chemical feedstock: opportunities and challenges. *Dalton Trans.* **28**, 2975–2992 (2007)
9. K. Li, X. An, K.H. Park, M. Khraisheh, J. Tang, A critical review of CO₂ photoconversion: catalysts and reactors. *Catal. Today* **224**, 3–12 (2014)
10. H. Khatib, IEA world energy outlook 2011 – a comment. *Energy Policy* **48**, 737–743 (2012)
11. N. Armaroli, V. Balzani, Towards an electricity-powered world. *Energy Environ. Sci.* **4**, 3193–3222 (2011)
12. N. Armaroli, V. Balzani, *Energy for a Sustainable World. From the Oil Age to a Sun-Powered Future* (Wiley-VCH, Weinheim, 2011)
13. BP Energy Economics, Statistical Review of World Energy. www.bp.com/statisticalreview. Accessed Feb 2017
14. Reference Solar Spectral Irradiance: Air Mass 1.5. <http://rredc.nrel.gov/solar/spectra/am1.5/>. Accessed June 2014
15. J. Duffie, W. Beckman, *Solar Engineering of Thermal Processes* (Wiley, Hoboken, 2006)
16. N.S. Lewis, D.G. Nocera, Powering the planet: chemical challenges in solar energy utilization. *Proc. Natl. Acad. Sci.* **103**, 15729–15735 (2006)
17. *World Energy Assessment Report: Energy and the Challenge of Sustainability* (U. N. D. Program, United Nations, New York, 2003)
18. World Map of Global Horizontal irradiation. http://solargis.info/doc/_pics/freemaps/1000px/ghi/SolarGIS-Solar-map-World-map-en.png. Accessed June 2014
19. M. Iqbal, *An Introduction to Solar Radiation* (Academic, Toronto, 1983)
20. F. Kasten, A.T. Young, Revised optical air mass tables and approximation formula. *Appl. Opt.* **28**, 4735–4738 (1989)
21. P. Würfel, *Physics of Solar Cells: From Principles to New Concepts* (Wiley-VCH Verlag GmbH & Co. KGaA, Weinheim, 2005). ISSN 3-527-40428-7
22. H.B. Gray, Powering the planet with solar fuel. *Nat. Chem.* **1**, 7 (2009)
23. K.D.G.I. Jayawardena, L.J. Rozanski, C.A. Mills, M.J. Beliatas, N.A. Nismy, S.R.P. Silva, 'Inorganics – in – organics': recent developments and outlook for 4G polymer solar cells. *Nanoscale* **5**, 8411–8427 (2013)
24. M.A. Green, Third generation photovoltaics: ultra-high conversion efficiency at low cost. *Prog. Photovolt. Res. Appl.* **9**, 123–135 (2001)
25. W. Wang, M.T. Winkler, O. Gunawan, T. Gokmen, T.K. Todorov, Y. Zhu, D.B. Mitzi, Device characteristics of CZTSSe thin-film solar cells with 12.6% efficiency. *Adv. Energy Mater.* **4**(7), 1301465 (1–5) (2013)
26. UNSW Newsroom, UNSW takes lead in the race for non-toxic, thin-film solar cells. <http://newsroom.unsw.edu.au/news/science-tech/unsw-takes-lead-race-non-toxic-thin-film-solar-cells>. Accessed Mar 2017
27. W. Schäfer, R. Nitsche, Tetrahedral quaternary chalcogenides of the type Cu₂II-IV-S₄(Se₄). *Mater. Res. Bull.* **9**, 645–654 (1974)

28. L.L. Baranowski, P. Zawadzki, S. Lany, E.S. Toberer, A. Zakutayev, A review of defects and disorder in multinarytetrahedrally bonded semiconductors. *Semicond. Sci. Technol.* **31**, 123004–123019 (2016)
29. K. Yu, E.A. Carter, Determining and controlling the stoichiometry of $\text{Cu}_2\text{ZnSnS}_4$ photovoltaics: the physics and its implications. *Chem. Mater.* **28**(12), 4415–4420 (2016)
30. S.Y. Chen, J.-H.H. Yang, X.G. Gong, A. Walsh, S.-H.H. Wei, Intrinsic point defects and complexes in the quaternary kesterite semiconductor $\text{Cu}_2\text{ZnSnS}_4$. *Phys. Rev. B: Condens. Matter Mater. Phys.* **81**, 245204-1–245204-13 (2010)
31. S. Singh, M. Brandon, P. Liu, F. Laffir, W. Redington, K.M. Ryan, Selective phase transformation of wurtzite Cu_2ZnSn (SSe)₄ nanocrystals into zinc blende and kesterite by solution and solid state transformations. *Chem. Mater.* **28**(14), 5055–5062 (2016)
32. I.D. Oleksyuk, I.V. Dudchar, L.V. Piskach, Phase equilibria in the Cu_2S – ZnS – SnS_2 system. *J. Alloys Compd.* **368**, 135–143 (2004)
33. M.I. Khalil, O. Atici, A. Lucotti, S. Binetti, A.L. Donne, L. Magagnin, CZTS absorber layer for thin film solar cells from electrodeposited metallic stacked precursors (Zn/Cu - Sn). *Appl. Surf. Sci.* **379**, 91–97 (2016)
34. K.V. Gurav, S.M. Pawar, S.W. Shin, M.P. Suryawanshi, G.L. Agawane, P.S. Patil, J.-H. Moon, J.H. Yun, J.H. Kim, Electrosynthesis of CZTS films by sulfurization of CZT precursor: effect of soft annealing treatment. *Appl. Surf. Sci.* **283**, 74–80 (2013)
35. C.-Y. Su, C.-Y. Chiu, J.-M. Ting, $\text{Cu}_2\text{ZnSnS}_4$ absorption layers with controlled phase purity. *Sci. Rep.* **5**, 9291-1–9291-8 (2015)
36. J.J. Scragg, P.J. Dale, L.M. Peter, Towards sustainable materials for solar energy conversion: preparation and photoelectrochemical characterization of $\text{Cu}_2\text{ZnSnS}_4$. *Electrochem. Commun.* **10**, 639–642 (2008)
37. T. Shiyani, D. Raval, M.K. Patel, I. Mukhopadhyay, A. Ray, Effect of initial bath condition and post-annealing on co-electrodeposition of $\text{Cu}_2\text{ZnSnS}_4$. *Mater. Chem. Phys.* **171**, 63–72 (2016)
38. J. Tao, J. Liu, J. He, K. Zhang, J. Jiang, L. Sun, P. Yang, J. Chu, Synthesis and characterization of $\text{Cu}_2\text{ZnSnS}_4$ thin films by the sulfurization of co-electrodeposited Cu – Zn – Sn – S precursor layers for solar cell applications. *RSC Adv.* **4**, 23977–23984 (2014)
39. S. Kermadi, S. Sali, F.A. Ameur, L. Zougar, M. Boumaour, A. Toumiat, N.N. Melnik, D.W. Hewak, A. Duta, Effect of copper content and sulfurization process on optical, structural and electrical properties of ultrasonic spray pyrolyzed $\text{Cu}_2\text{ZnSnS}_4$ thin films. *Mater. Chem. Phys.* **169**, 96–104 (2015)
40. A.A. Barragan, H. Malekpour, S. Exarhos, A.A. Balandin, L. Mangolini, Grain-to-grain compositional variations and phase segregation in CZTS films. *ACS Appl. Mater. Interfaces* **8**(35), 22971–22976 (2016)
41. C. Malerba, M. Valentini, C.L. Azanza Ricardo, A. Rinaldi, E. Cappelletto, P. Scardi, A. Mittiga, Blistering in $\text{Cu}_2\text{ZnSnS}_4$ thin films: correlation with residual stresses. *Mater. Des.* **108**, 725–735 (2016)
42. H. Katagiri, K. Jimbo, W.S. Maw, K. Oishi, M. Yamazaki, H. Araki, A. Takeuchi, Development of CZTS-based thin film solar cells. *Thin Solid Films* **517**, 2455–2460 (2009)
43. A. Wangperawong, J.S. King, S.M. Herron, B.P. Tran, K.P. Okimoto, S.F. Bent, Aqueous bath process for deposition of $\text{Cu}_2\text{ZnSnS}_4$ photovoltaic absorbers. *Thin Solid Films* **519**, 2488–2492 (2011)
44. J. He, L. Sun, K. Zhang, W. Wang, J. Jiang, Y. Chen, P. Yang, J. Chu, Effect of post-sulfurization on the composition, structure and optical properties of $\text{Cu}_2\text{ZnSnS}_4$ thin films deposited by sputtering from a single quaternary target. *Appl. Surf. Sci.* **264**, 133–138 (2013)
45. H. Araki, Y. Kubo, K. Jimbo, W.S. Maw, H. Katagiri, M. Yamazaki, K. Oishi, A. Takeuchi, Preparation of $\text{Cu}_2\text{ZnSnS}_4$ thin films by sulfurization of co-electroplated Cu - Zn - Sn precursors. *Phys. Status Solidi* **6**, 1266–1268 (2009)
46. H. Katagiri, K. Saitoh, T. Washio, H. Shinohara, T. Kurumadani, S. Miyajima, Development of thin film solar cell based on $\text{Cu}_2\text{ZnSnS}_4$ thin films. *Sol. Energy Mater. Sol. Cells* **65**, 141–148 (2001)

47. G. Larramona, S. Bourdais, A. Jacob, C. Chone, T. Muto, Y. Cuccaro, B. Delatouche, C. Moisan, D. Pere, G. Dennler, 8.6% efficient CZTS_{Se} solar cells sprayed from water-ethanol CZTS colloidal solutions. *J. Phys. Chem. Lett.* **5**, 3763–3767 (2014)
48. T.H. Nguyen, W. Septina, S. Fujikawa, F. Jiang, T. Harada, S. Ikeda, Cu₂ZnSnS₄ thin film solar cells with 5.8% conversion efficiency obtained by a facile spray pyrolysis technique. *RSC Adv.* **5**, 77565–77571 (2015)
49. X. Lin, J. Kavalakkatt, K. Kornhuber, S. Levchenko, M.C.L. Steiner, A. Ennaoui, Structural and optical properties of Cu₂ZnSnS₄ thin film absorbers from ZnS and Cu₃SnS₄ nanoparticle precursors. *Thin Solid Films* **535**, 10–13 (2013)
50. H. Wei, Z. Ye, M. Li, Y. Su, Z. Yang, Y. Zhang, Tunable band gap Cu₂ZnSnS₄_xSe_{4(1-x)} nanocrystals: experimental and first-principles calculations. *CrystEngComm* **13**, 2222–2226 (2011)
51. T. Washio, T. Shinji, S. Tajima, T. Fukano, T. Motohiro, K. Jimbo, H. Katagiri, 6% efficiency Cu₂ZnSnS₄-based thin film solar cells using oxide precursors by open atmosphere type CVD. *J. Mater. Chem.* **22**, 4021–4024 (2012)
52. C. Gao, T. Schnabel, T. Abzieher, C. Krämmer, M. Powalla, H. Kalt, M. Hetterich, Cu₂ZnSn(S, Se)₄ solar cells based on chemical bath deposited precursors. *Thin Solid Films* **562**, 621–624 (2014)
53. M. Patel, I. Mukhopadhyay, A. Ray, Structural, optical and electrical properties of spray-deposited CZTS thin films under a non-equilibrium growth condition. *J. Phys. D. Appl. Phys.* **45**, 445103–445113 (2012)
54. S.A. Khalate, R.S. Kate, J.H. Kim, S.M. Pawar, R.J. Deokate, Effect of deposition temperature on the properties of Cu₂ZnSnS₄ (CZTS) thin films. *Superlattice. Microst.* **103**, 335–342 (2017)
55. M. Courel, J.A. Andrade-Arvizu, A. Guillén-Cervantes, M.M. Nicolás-Marín, F.A. Pulgarín-Agudelo, O. Vigil-Galán, Optimization of physical properties of spray-deposited Cu₂ZnSnS₄ thin films for solar cell applications. *Mater. Des.* **114**, 515–520 (2017)
56. J. Tao, J. Liu, L. Chen, H. Cao, X. Meng, Y. Zhang, Z. Chuanjun, L. Sun, P. Yang, J. Chu, 7.1% efficiency co-electroplated Cu₂ZnSnS₄ thin film solar cells with sputtered CdS buffer layers. *Green Chem.* **18**, 550–557 (2016)
57. V.T. Tiong, Y. Zhang, J. Bell, H. Wang, Phase-selective hydrothermal synthesis of Cu₂ZnSnS₄ nanocrystals: the effect of the sulfur precursor. *CrystEngComm* **16**, 4306–4313 (2014)
58. J.W. Cho, A. Ismail, S.J. Park, W. Kim, S. Yoon, B.K. Min, Synthesis of Cu₂ZnSnS₄ thin films by a precursor solution paste for thin film solar cell applications. *ACS Appl. Mater. Interfaces* **5**, 4162–4165 (2013)
59. W.C. Chen, V. Tunuguntla, M.-H. Chiu, L.-J. Li, I. Shown, C.-H. Lee, J.-S. Hwang, L.-C. Chen, K.-H. Chen, Co-solvent effect on microwave-assisted Cu₂ZnSnS₄ nanoparticles synthesis for thin film solar cell. *Sol. Energy Mater. Sol. Cells* **161**, 416–423 (2017)
60. X. Zhai, H. Jia, Y. Zhang, Y. Lei, J. Wei, Y. Gao, J. Chu, W. He, J.-J. Yin, Z. Zheng, In situ fabrication of Cu₂ZnSnS₄ nanoflake thin films on both rigid and flexible substrates. *CrystEngComm* **16**, 6244–6249 (2014)
61. S.C. Riha, S.J. Fredrick, J.B. Sambur, Y. Liu, A.L. Prieto, B.A. Parkinson, Photoelectrochemical characterization of nanocrystalline thin-film Cu₂ZnSnS₄ photocathodes. *ACS Appl. Mater. Interfaces* **3**(1), 58–66 (2011)
62. X. Jin, J. Li, G. Chen, C. Xue, W. Liu, C. Zhu, Preparation of Cu₂ZnSnS₄-based thin film solar cells by a combustion method. *Sol. Energy Mater. Sol. Cells* **146**, 16–24 (2016)
63. Y. Sun, Y. Zhang, H. Wang, M. Xie, K. Zong, H. Zheng, Y. Shu, J. Liu, H. Yan, M. Zhu, W.M. Lau, Novel non-hydrazine solution processing of earth-abundant Cu₂ZnSn(S, Se)₄ absorbers for thin-film solar cells. *J. Mater. Chem. A* **1**, 6880–6887 (2013)
64. M.P. Suryawanshi, P.S. Patil, S.W. Shin, K.V. Gurav, G.L. Agawane, M.G. Gang, J.H. Kim, A.V. Moholkar, The synergistic influence of anionic bath immersion time on the photoelectrochemical performance of CZTS thin films prepared by a modified SILAR sequence. *RSC Adv.* **4**, 18537–18540 (2014)

65. Y. Feng, B. Yu, G. Cheng, T. Lau, Z. Li, L. Yin, Q. Song, C. Yang, X. Xiao, Searching for a fabrication route of efficient $\text{Cu}_2\text{ZnSnS}_4$ solar cells by post-sulfuration of co-sputtered Sn-enriched precursors. *J. Mater. Chem. C* **3**, 9650–9656 (2015)
66. A. Cazzaniga, A. Crovetto, C. Yan, K. Sun, X. Hao, J.R. Estelrich, S. Canulescu, E. Stamate, N. Pryds, O. Hansen, J. Schou, Ultra-thin $\text{Cu}_2\text{ZnSnS}_4$ solar cell by pulsed laser deposition. *Sol. Energy Mater. Sol. Cells* **166**, 91–99 (2017)
67. S. Wozny, K. Wang, Weillie Zhou, $\text{Cu}_2\text{ZnSnS}_4$ nanoplate arrays synthesized by pulsed laser deposition with high catalytic activity as counter electrodes for dye-sensitized solar cell applications. *J. Mater. Chem. A* **1**, 15517–15523 (2013)
68. E. Garcia-Llamas, J.M. Merino, R. Gunder, K. Neldner, D. Greiner, A. Steigert, S. Giraldo, V. Izquierdo-Roca, E. Saucedo, M. León, S. Schorr, R. Caballero, $\text{Cu}_2\text{ZnSnS}_4$ thin film solar cells grown by fast thermal evaporation and thermal treatment. *Sol. Energy* **141**, 236–241 (2017)
69. Z.R. Mohammad, Modeling minority carrier's recombination lifetime of the a-Si solar cell. *Int. J. Renew. Energy Res.* **2**, 117–122 (2012)
70. Y. Yang, X. Kang, L. Huang, S. Wei, D. Pan, A general water-based precursor solution approach to deposit earth abundant $\text{Cu}_2\text{ZnSn(S, Se)}_4$ thin film solar cells. *J. Power Sources* **313**, 15–20 (2016)
71. K. Sun, F. Liu, C. Yan, F. Zhou, J. Huang, Y. Shen, R. Liu, X. Hao, Influence of sodium incorporation on kesterite $\text{Cu}_2\text{ZnSnS}_4$ solar cells fabricated on stainless steel substrates. *Sol. Energy Mater. Sol. Cells* **157**, 565–571 (2016)
72. X. Liu, J. Huang, F. Zhou, F. Liu, K. Sun, C. Yan, J.A. Stride, X. Hao, Understanding the key factors of enhancing phase and compositional controllability for 6% efficient pure-sulfide $\text{Cu}_2\text{ZnSnS}_4$ solar cells prepared from quaternary wurtzite nanocrystals. *Chem. Mater.* **28**(11), 3649–3658 (2016)
73. Y. Zhang, J. Han, C. Liao, Investigation on the role of sodium in $\text{Cu}_2\text{ZnSnS}_4$ film and the resulting phase evolution during sulfurization. *Cryst. Eng. Comm.* **18**, 9026–9032 (2016)
74. J. Kim, G.Y. Kim, W. Jo, K.-J. Yang, J.-H. Sim, D.-H. Kim, J.-K. Kang, Effects of Mo back-contact annealing on surface potential and carrier transport in $\text{Cu}_2\text{ZnSnS}_4$ thin film solar cells. *RSC Adv.* **6**, 103337–103345 (2016)
75. O.P. Singh, A. Sharma, K.S. Gour, S. Husale, V.N. Singh, Fast switching response of Na-doped CZTS photodetector from visible to NIR range. *Sol. Energy Mater. Sol. Cells* **157**, 28–34 (2016)
76. Y. Ren, J.J. Scragg, M. Edoff, J.K. Larsen, C. Platzer-Björkman, Evolution of Na-S(O) compounds on the $\text{Cu}_2\text{ZnSnS}_4$ absorber surface and their effects on CdS thin film growth. *ACS Appl. Mater. Interfaces* **8**, 18600–18607 (2016)
77. D. Tiwari, T. Koehler, X. Lin, R. Hamman, I. Griffiths, L. Wang, D. Cherns, R. Klenk, D.J. Fermin, $\text{Cu}_2\text{ZnSnS}_4$ thin-films generated from a single solution-based precursor: the effect of Na and Sb doping. *Chem. Mater.* **28**(14), 4991–4997 (2016)
78. X. Zhang, M. Han, Z. Zeng, Y. Duan, The role of Sb in solar cell material $\text{Cu}_2\text{ZnSnS}_4$. *J. Mater. Chem. A* **5**, 6606–6612 (2017)
79. A. Ritscher, J. Just, O. Dolotko, S. Schorr, M. Lerch, A mechanochemical route to single phase $\text{Cu}_2\text{ZnSnS}_4$ powder. *J. Alloys Compd.* **670**, 289–296 (2016)
80. J. Li, H. Shen, W. Wang, J. Chen, H. Shang, Y. Li, Z. Zhai, Improvement of CZTSSe thin film solar cell by introducing a three-layer structure precursor. *Mater. Lett.* **172**, 90–93 (2016)
81. S.K. Samji, R. Maanam, M.S.R. Rao, Do defects get ordered in $\text{Cu}_2\text{ZnSnS}_4$? *Scr. Mater.* **117**, 11–15 (2016)
82. B. Bai, D. Kou, W. Zhou, Z. Zhou, Q. Tian, Y. Meng, S. Wu, Quaternary $\text{Cu}_2\text{ZnSnS}_4$ quantum dot-sensitized solar cells: synthesis, passivation and ligand exchange. *J. Power Sources* **318**, 35–40 (2016)
83. O.P. Singh, K.S. Gour, R. Parmar, V.N. Singh, Sodium induced grain growth, defect passivation and enhancement in the photovoltaic properties of $\text{Cu}_2\text{ZnSnS}_4$ thin film solar cell. *Mater. Chem. Phys.* **177**, 293–298 (2016)

84. A. Sagna, K. Djessas, C. Sene, K. Medjnoun, S. Grillo, Close spaced vapor transport deposition of $\text{Cu}_2\text{ZnSnS}_4$ thin films: effect of iodine pressure. *J. Alloys Compd.* **685**, 699–704 (2016)
85. A. Lafond, C. Guillot-Deudon, J. Vidal, M. Paris, C. La, S. Jobic, Substitution of Li for Cu in $\text{Cu}_2\text{ZnSnS}_4$: toward wide band gap absorbers with low cation disorder for thin film solar cells. *Inorg. Chem.* **56**(5), 2712–2721 (2017)
86. A. Guchhait, Z. Su, Y.F. Tay, S. Shukla, W. Li, S.W. Leow, J.M.R. Tan, S. Lie, O. Gunawan, L.H. Wong, Enhancement of open circuit voltage of solution-processed $\text{Cu}_2\text{ZnSnS}_4$ solar cell with 7.2% efficiency by incorporation of silver. *ACS Energy Lett.* **1**(6), 1256–1261 (2016)
87. T.J. Huang, R.L. Guang-Ren, X. Yin, C. Tang, G. Qi, H. Gong, Effect of sulfide precursor selection on the nucleation, growth, and elemental composition of $\text{Cu}_2\text{ZnSnS}_4$ nanocrystals. *Cryst. Growth Des.* **17**(1), 73–79 (2017)
88. B.A. Williams, M.A. Smeaton, N.D. Trejo, L.F. Francis, E.S. Aydil, Effect of nanocrystal size and carbon on grain growth during annealing of copper zinc tin sulfide nanocrystal coatings. *Chem. Mater.* **29**(4), 1676–1683 (2017)
89. K. Liu, B. Yao, Y. Li, Z. Ding, H. Sun, Y. Jiang, G. Wang, D. Pan, A versatile strategy for fabricating various $\text{Cu}_2\text{ZnSnS}_4$ precursor solutions. *J. Mater. Chem. C* **5**, 3035–3041 (2017)
90. R.M. Valls, T.S. Lyubenova, I.C. Roures, L. Oliveira, D.F. Chiva, J.B.C. Castelló, Easy and low-cost aqueous precipitation method to obtain Cu_2ZnSn (S, Se)₄ thin layers. *Sol. Energy Mater. Sol. Cells* **161**, 432–438 (2017)
91. Y.-P. Lin, T.-E. Hsieh, Y.-C. Chen, K.-P. Huang, Characteristics of Cu_2ZnSn (SxSe_{1-x})₄ thin-film solar cells prepared by sputtering deposition using single quaternary $\text{Cu}_2\text{ZnSnS}_4$ target followed by selenization/sulfurization treatment. *Sol. Energy Mater. Sol. Cells* **162**, 55–61 (2017)
92. C. Yan, K. Sun, J. Huang, S. Johnston, F. Liu, B.P. Veettil, K. Sun, A. Pu, F. Zhou, J.A. Stride, M.A. Green, X. Hao, Beyond 11% efficient sulfide kesterite $\text{Cu}_2\text{ZnxCd}_{1-x}\text{SnS}_4$ solar cell: effects of cadmium alloying. *ACS Energy Lett.* **2**, 930–936 (2017)
93. Y. Ren, M. Richter, J. Keller, A. Redinger, T. Unold, O. Donzel-Gargand, J.J. Scragg, C.P. Björkman, Investigation of the $\text{SnS}/\text{Cu}_2\text{ZnSnS}_4$ interfaces in kesterite thin-film solar cells. *ACS Energy Lett.* **2**, 976–981 (2017)
94. M.H. Sayed, J. Schoneberg, J. Parisi, L. Gütay, Improvement of the structural and electronic properties of CZTSSe solar cells from spray pyrolysis by a CuGe seed layer. *RSC Adv.* **7**, 20406–20411 (2017)
95. M. Courel, E. Valencia-Resendiz, J.A. Andrade-Arvizu, E. Saucedo, O. Vigil-Galán, Towards understanding poor performances in spray-deposited $\text{Cu}_2\text{ZnSnS}_4$ thin film solar cells. *Sol. Energy Mater. Sol. Cells* **159**, 151–158 (2017)
96. T.M. Ng, M.T. Weller, G.P. Kissling, L.M. Peter, P. Dale, F. Babbe, J. de Wild, B. Wenger, H.J. Snaith, D. Lane, Optoelectronic and spectroscopic characterization of vapour-transport grown $\text{Cu}_2\text{ZnSnS}_4$ single crystals. *J. Mater. Chem. A* **5**, 1192–1200 (2017)
97. P. Liu, S. Singh, G. Bree, K.M. Ryan, Complete assembly of $\text{Cu}_2\text{ZnSnS}_4$ (CZTS) nanorods at substrate interfaces using a combination of self and directed organisation. *Chem. Commun.* **52**, 11587–11590 (2016)
98. J. Fu, Q. Tian, Z.-J. Zhou, D. Kou, Y. Meng, W.-H. Zhou, S. Wu, Improving the performance of solution-processed Cu_2ZnSn (S, Se)₄ photovoltaic materials by Cd^{2+} substitution. *Chem. Mater.* **28**(16), 5821–5828 (2016)
99. Z. Wang, S. Elouatik, G.P. Demopoulos, Understanding the phase formation kinetics of nanocrystalline kesterite deposited on mesoscopic scaffold via in-situ multi-wavelength Raman-monitored annealing. *Phys. Chem. Chem. Phys.* **18**, 29435–29446 (2016)
100. A. Fairbrother, X. Fontané, V. Izquierdo-Roca, M. Espíndola-Rodríguez, S. López-Marino, M. Placidi, L. Calvo-Barrio, A. Pérez-Rodríguez, E. Saucedo, On the formation mechanisms of Zn-rich $\text{Cu}_2\text{ZnSnS}_4$ films prepared by sulfurization of metallic stacks. *Sol. Energy Mater. Sol. Cells* **112**, 97–105 (2013)
101. W. Wang, H. Shen, L.H. Wong, H. Yao, Z. Su, Y. Li, Preparation of high-efficiency Cu_2ZnSn (S, Se)₄ solar cells from novel non-toxic hybrid ink. *J. Power Sources* **335**, 84–90 (2016)

102. O.A.M. Abdelraouf, N.K. Allam, Nanostructuring for enhanced absorption and carrier collection in CZTS based solar cells: coupled optical and electrical modeling. *Opt. Mater.* **54**, 84–88 (2016)
103. W. Xiao, J.N. Wang, J.W. Wang, G.J. Huang, L. Cheng, L.J. Jiang, L.G. Wang, Structural and electronic properties of the heterointerfaces for $\text{Cu}_2\text{ZnSnS}_4$ photovoltaic cells: a density-functional theory study. *Phys. Chem. Chem. Phys.* **18**, 12029–12034 (2016)
104. A. Ritscher, M. Hoelzel, M. Lerch, The order-disorder transition in $\text{Cu}_2\text{ZnSnS}_4$ – a neutron scattering investigation. *J. Solid-State Chem.* **238**, 68–73 (2016)
105. A. Irkhina, S. Levchenko, V. Hinrichs, P. Plate, T. Unold, Metal acetate-based synthesis of small-sized $\text{Cu}_2\text{ZnSnS}_4$ nanocrystals: effect of injection temperature and synthesis time. *RSC Adv.* **7**, 11752–11760 (2017)
106. H.R. Jung, S.W. Shin, M.P. Suryawanshi, S.J. Yeo, J.H. Yun, J.H. Moon, J.H. Kim, Phase evolution pathways of kesterite $\text{Cu}_2\text{ZnSnS}_4$ and $\text{Cu}_2\text{ZnSnSe}_4$ thin films during the annealing of sputtered Cu-Sn-Zn metallic precursors. *Sol. Energy* **145**, 2–12 (2017)
107. K.-J. Kim, C. Pan, S. Bansal, R. Malhotra, D.-H. Kim, C.-H. Chang, Scalably synthesized environmentally benign, aqueous-based binary nanoparticle inks for $\text{Cu}_2\text{ZnSn}(\text{S}, \text{Se})_4$ photovoltaic cells achieving over 9% efficient. *Sustain. Energy Fuels* **1**, 267–274 (2017)
108. X. Liu, J. Huang, F. Zhou, F. Liu, J.A. Stride, X. Hao, Spatial grain growth and composition evolution during sulfurizing metastable wurtzite $\text{Cu}_2\text{ZnSnS}_4$ nanocrystal-based coatings. *Chem. Mater.* **29**(5), 2110–2121 (2017)
109. R. Ma, F. Yang, S. Li, X. Zhang, X. Li, S. Cheng, Z. Liu, Fabrication of $\text{Cu}_2\text{ZnSn}(\text{S}, \text{Se})_4$ (CZTSSe) absorber films based on solid-phase synthesis and blade coating processes. *Appl. Surf. Sci.* **368**, 8–15 (2016)
110. A.I. Inamdar, S. Lee, K.-Y. Jeon, C.H. Lee, S.M. Pawar, R.S. Kalubarme, C.J. Park, H. Im, W. Jung, H. Kim, Optimized fabrication of sputter deposited $\text{Cu}_2\text{ZnSnS}_4$ (CZTS) thin films. *Sol. Energy* **91**, 196–203 (2013)
111. Z. Xiao, B. Yao, Y. Li, Z. Ding, Z.-M. Gao, H. Zhao, L. Zhang, Z. Zhang, Y. Sui, G. Wang, Influencing mechanism of the selenization temperature and time on the power conversion efficiency of $\text{Cu}_2\text{ZnSn}(\text{S}, \text{Se})_4$ -based solar cells. *ACS Appl. Mater. Interfaces* **8**(27), 17334–17342 (2016)
112. C. Li, B. Yao, Y. Li, Z. Ding, H. Zhao, L. Zhang, Z. Zhang, Impact of sequential annealing step on the performance of $\text{Cu}_2\text{ZnSn}(\text{S}, \text{Se})_4$ thin film solar cells. *Superlattice. Microst.* **95**, 149–158 (2016)
113. S.-Y. Li, C. Häggglund, Y. Ren, J.J. Scragg, J.K. Larsen, C. Frisk, K. Rudisch, S. Englund, C. Platzer-Björkman, Optical properties of reactively sputtered $\text{Cu}_2\text{ZnSnS}_4$ solar absorbers determined by spectroscopic ellipsometry and spectrophotometry. *Sol. Energy Mater. Sol. Cells* **149**, 170–178 (2016)
114. S. Gupta, T.J. Whittles, Y. Batra, V. Satsangi, S. Krishnamurthy, V.R. Dhanak, B.R. Mehta, A low-cost, sulfurization free approach to control optical and electronic properties of $\text{Cu}_2\text{ZnSnS}_4$ via precursor variation. *Sol. Energy Mater. Sol. Cells* **157**, 820–830 (2016)
115. D. Nam, S. Cho, J.-H. Sim, K.-J. Yang, D.-H. Son, D.-H. Kim, J.-K. Kang, M.-S. Kwon, C.-W. Jeon, H. Cheong, Solar conversion efficiency and distribution of ZnS secondary phase in $\text{Cu}_2\text{ZnSnS}_4$ solar cells. *Sol. Energy Mater. Sol. Cells* **149**, 226–231 (2016)
116. M. Dimitrievska, F. Boero, A.P. Litvinchuk, S. Delsante, G. Borzone, A.P. Rodriguez, V. Izquierdo-Roca, Structural polymorphism in “kesterite” $\text{Cu}_2\text{ZnSnS}_4$: Raman spectroscopy and first-principles calculations analysis. *Inorg. Chem.* **56**(6), 3467–3474 (2017)
117. T.R. Rana, N.M. Shinde, J.H. Kim, Novel chemical route for chemical bath deposition of $\text{Cu}_2\text{ZnSnS}_4$ (CZTS) thin films with stacked precursor thin films. *Mater. Lett.* **162**, 40–43 (2016)
118. K. Rawat, H.-J. Kim, P.K. Shishodia, Synthesis of $\text{Cu}_2\text{ZnSnS}_4$ nanoparticles and controlling the morphology with polyethylene glycol. *Mater. Res. Bull.* **77**, 84–90 (2016)
119. Y. Huang, G. Li, Q. Fan, M. Zhang, Q. Lan, X. Fan, Z. Zhou, C. Zhang, Facile solution deposition of $\text{Cu}_2\text{ZnSnS}_4$ (CZTS) nano-worm films on FTO substrates and its photo-electrochemical property. *Appl. Surf. Sci.* **28**, 148–155 (2016)

120. J.H.N. Tchognia, B. Hartiti, A. Ridah, J.-M. Ndjaka, P. Thevenin, Application of Taguchi approach to optimize the sol-gel process of the quaternary $\text{Cu}_2\text{ZnSnS}_4$ with good optical properties. *Opt. Mater.* **57**, 85–92 (2016)
121. M. Espindola-Rodriguez, Y. Sanchez, S. L'opez-Marino, D. Sylla, M. Placidi, M. Neuschitzer, H. Xie, V. Izquierdo-Roca, O. Vigil-Galan, E. Saucedo, Selenization of $\text{Cu}_2\text{ZnSnS}_4$ thin films obtained by pneumatic spray pyrolysis. *J. Anal. Appl. Pyrolysis* **120**, 45–51 (2016)
122. S.Y. Wei, Y.C. Liao, C.-H. Hsu, C.-H. Cai, W.-C. Huang, M.-C. Huang, C.-H. Lai, Achieving high-efficiency $\text{Cu}_2\text{ZnSn(S, Se)}_4$ solar cells by non-toxic aqueous ink: defect analysis and electrical modeling. *Nano Energy* **26**, 74–82 (2016)
123. R. Liu, M. Tan, L. Xu, X. Zhang, J. Chen, X. Tang, Preparation of high-quality $\text{Cu}_2\text{ZnSnS}_4$ thin films for solar cells via the improvement of sulfur partial pressure using a static annealing sulfurization approach. *Sol. Energy Mater. Sol. Cells* **157**, 221–228 (2016)
124. Y. Sun, Z. Hu, J. Zhang, L. Wang, C. Wu, J. Xu, A top-down strategy to synthesize wurtzite $\text{Cu}_2\text{ZnSnS}_4$ nanocrystals by green chemistry. *Chem. Commun.* **52**, 9821–9824 (2016)
125. S.-L. Chen, J. Tao, H.-J. Tao, Y.-Z. Shen, T. Wang, L. Pan, High-performance and low-cost dye-sensitized solar cells based on kesterite $\text{Cu}_2\text{ZnSnS}_4$ nanoplate arrays on a flexible carbon cloth cathode. *J. Power Sources* **330**, 28–36 (2016)
126. R. Tang, Z. Xie, S. Zhou, Y. Zhang, Z. Yuan, L. Zhang, L. Yin, $\text{Cu}_2\text{ZnSnS}_4$ nanoparticle sensitized metal-organic framework derived mesoporous TiO_2 as photoanodes for high-performance dye-sensitized solar cells. *ACS Appl. Mater. Interfaces* **8**(34), 22201–22212 (2016)
127. K.-C. Wang, H.-R. Hsu, H.-S. Chen, Study of surface sulfurization of $\text{Cu}_2\text{ZnSn(S, Se)}_4$ thin film solar cell by sequential H_2Se -selenization/ H_2S -sulfurization. *Sol. Energy Mater. Sol. Cells* **163**, 31–37 (2017)
128. K.J. Yang, J.H. Sim, D.-H. Son, D.-H. Jeon, D.K. Hwang, D. Nam, H. Cheong, S.Y. Kim, J.H. Kim, D.-H. Kim, J.-K. Kang, Comparison of chalcopyrite and kesterite thin-film solar cells. *J. Ind. Eng. Chem.* **45**, 78–84 (2017)
129. T. Gershon, T. Gokmen, O. Gunawan, R. Haight, S. Guha, B. Shin, Understanding the relationship between $\text{Cu}_2\text{ZnSn(S, Se)}_4$ material properties and device performance. *MRS Commun.* **4**, 159–170 (2014)
130. H.J. Chen, S.-W. Fu, S.-H. Wu, H.-T. Wu, C.-F. Shih, Comparative study of self-constituent buffer layers (CuS, SnS, ZnS) for synthesis $\text{Cu}_2\text{ZnSnS}_4$ thin films. *Mater. Lett.* **169**, 126–130 (2016)
131. C. Yan, F. Liu, K. Sun, N. Song, J.A. Stride, F. Zhou, X. Hao, M. Green, Boosting the efficiency of pure sulfide CZTS solar cells using the In/Cd-based hybrid buffers. *Sol. Energy Mater. Sol. Cells* **144**, 700–706 (2016)
132. O. Gunawan, T. Gokmen, D.B. Mitzi, Suns- V_{oc} characteristics of high-performance kesterite solar cells. *J. Appl. Phys.* **116**, 084504-1–084504-9 (2014)
133. F. Jiang, C. Ozaki, Gunawan, T. Harada, Z. Tang, T. Minemoto, Y. Nose, S. Ikeda, Effect of indium doping on surface optoelectrical properties of $\text{Cu}_2\text{ZnSnS}_4$ photoabsorber and interfacial/photovoltaic performance of cadmium free $\text{In}_2\text{S}_3/\text{Cu}_2\text{ZnSnS}_4$ heterojunction thin film solar cell. *Chem. Mater.* **28**(10), 3283–3291 (2016)
134. V.R. Reddy, V. Janardhanam, J. Won, C.-J. Choi, Microstructural, electrical and frequency-dependent properties of Au/p- $\text{Cu}_2\text{ZnSnS}_4$ /n-GaN heterojunction. *J. Colloid Interface Sci.* **499**, 180–188 (2017)
135. Y. Ren, N. Ross, J.K. Larsen, K. Rudisch, J.J.S. Scragg, C. Platzer-Björkman, Evolution of $\text{Cu}_2\text{ZnSnS}_4$ during non-equilibrium annealing with quasi-in-situ monitoring of sulfur partial pressure. *Chem. Mater.* **29**(8), 3713–3722 (2017)
136. X. Liu, Y. Feng, H. Cui, F. Liu, X. Hao, G. Conibeer, D.B. Mitzi, M. Green, The current status and future prospects of kesterite solar cells: a brief review. *Prog. Photovolt.* **24**, 879–898 (2016)
137. S.K. Wallace, D.B. Mitzi, A. Walsh, The steady rise of kesterite solar cells. *ACS Energy Lett.* **2**, 776–779 (2017)



Counter Electrode Materials for Organic-Inorganic Perovskite Solar Cells

7

Zonghao Liu and Hongshan He

Contents

7.1	Introduction	166
7.1.1	Overview	166
7.1.2	Perovskite Solar Cells	167
7.1.3	Challenges Facing PSCs	168
7.1.4	Counter Electrode for Perovskite Solar Cells	169
7.1.5	Metal Electrodes	170
7.1.6	Metal Thin-Film Electrodes	170
7.1.7	Metal Nano-Structured Electrode	180
7.2	Carbon Materials-Based Electrodes	188
7.2.1	Graphene Electrodes	188
7.2.2	Carbon Nanotube Electrode	191
7.2.3	Conductive Carbon Electrode	194
7.2.4	Conductive Metal Oxides Electrode	203
7.2.5	Conductive Polymers Electrode	208
7.3	Perspectives	212
	References	213

Author Contribution

Z. Liu wrote the first draft of the review and H. He edited and checked the PCEs.

Z. Liu

Wuhan National Laboratory for Optoelectronics, School of Optical and Electronic Information, Huazhong University of Science and Technology, Wuhan, P. R. China

H. He (✉)

Department of Chemistry and Biochemistry, Eastern Illinois University, Charleston, IL, USA
e-mail: hhe@eiu.edu

Abstract

Perovskite solar cells (PSCs) are arising as strong candidates for the next generation of thin-film photovoltaic techniques due to their high efficiency, low-cost, and simple manufacture process. A PSC usually is consisted of several components including in conductive bottom substrate, electron or hole transport layer, perovskite layer, and a counter electrode. However, PSCs are facing issues such as inaccurate evaluation of power conversion efficiency due to hysteresis, poor long-term stability, an inability for continuous manufacturing large area cells, and the use of noble metal as counter electrodes. In fact, a counter electrode is one of the key factors that govern the charge collection, long-term stability, and total cost of PSCs. Despite its importance, less attention has been paid to the exploration of counter electrode materials for PSCs. Here, we provided a summary of the recent development of counter electrode for PSCs, including metal thin-film electrode, super-thin metal thin-film electrode, nanostructured metal electrode, graphene electrode, carbon nanotube electrode, carbon black/graphite electrode, conductive oxide electrode, and polymer electrode. We highlighted findings of novel counter electrode materials towards low cost and stable PSCs as well as some drawbacks with an aim to provide readers a concise overview of the field for developing new counter electrode materials.

7.1 Introduction

7.1.1 Overview

With the rapid development of the global economy, the demand for energy is increased dramatically. The limited fossil energy resource leads scientists to explore novel clean energy technology, such as solar energy, wind power, tidal energy, geothermal energy, and biomass energy to fulfill the energy demand of human being. Among those, converting solar energy to thermal energy, chemical energy, or electric energy is one of the effective ways to provide clean energy to a human being. Specifically, the conversion of solar energy to electricity is foreseen as an effective way of utilization of solar energy. In fact, since the first practical solar cell demonstrated in 1954 at Bell Laboratories, several generations of solar cells have been developed to realize this process. The first generation of solar cells is based on single- and multi-crystal silicon, whose efficiencies have reached 25.3% and 21.9%, respectively. These types of solar cells show good performance as well as high stability and dominate the current photovoltaic market. However, they are rigid, bulky, and require a lot of energy in production, especially in the process of high-purity silicon wafers. The second-generation solar cells are based on amorphous silicon (a-Si), cadmium tellurium (CdTe), and copper indium gallium selenide (CIGS), whose efficiencies have reached 14.0%, 22.1%, and 22.6%, respectively [1]. However, the energy consumption of second-generation solar cells is still large due to the use of vacuum processes and high-temperature treatments. Furthermore,

the scarce and toxic elements used in the cells are another adverse factor against mass production. The third-generation solar cells are based on nanomaterials or organic materials. They are solutions that are processable, cost- and energy-effective, suitable for flexible substrates, and can be easily integrated. These cells include organic solar cells, dye-sensitized solar cells, quantum dot solar cells, and perovskite solar cells (PSCs). The newly developing photovoltaics are based on perovskites. The cells are quite efficient; however, there are some major concerns for practical applications including expensive counter electrode materials. In this chapter, the emerging counter electrode materials for PSCs will be discussed.

7.1.2 Perovskite Solar Cells

Perovskite material has a structural formula of ABX_3 , where the A can be an organic ion such as methylammonium ($CH_3NH_3^+$, MA^+), formamidinium ($CH_3(NH_2)_2^+$, FA^+), or an inorganic cation such as cesium; B is a divalent metal cation (e.g., Pb^{2+} , Sn^{2+} , Ge^{2+}); and X is a halide anion (e.g., Cl^- , Br^- , I^-). Perovskite was used in 2009 by Kojima et al. [2] as a light absorber in dye-sensitized solar cells for the first time with power conversion efficiency (PCE) of 3.8%. In 2012, Kim et al. [3] developed all-solid-state solar cells by replacing the liquid electrolyte with N^2 , N^2 , $N^{2'}$, $N^{2'}$, N^7 , N^7 , $N^{7'}$, $N^{7'}$ -octakis(4-methoxyphenyl)-9,9'-spirobi[9H-fluorene]-2,2',7,7'-tetramine (spiro-OMeTAD) as hole transport material with an impressive PCE of 9.7%. The perovskite used has a composition of methylammonium lead halide ($CH_3NH_3PbI_3$) and its crystal structure is shown in Fig. 7.1a. The thin layer of this material on the mesoporous titania (TiO_2) surface is shown in Fig. 7.1b. The cell has a mesoscopic configuration with only several micrometers to 0.6 μm thick as shown in Fig. 7.1c. Further study by Heo et al. [4] for a mesoscopic PSC with a configuration of fluorine-doped tin oxide/compact titanium dioxide/mesoporous titanium dioxide (methylammonium lead iodide)/poly (triarylamine)/gold [FTO/c- TiO_2 /m- TiO_2 ($CH_3NH_3PbI_3$)/PTAA/Au] pushed the efficiency up to 12.0%. The seminal work by Lee et al. in 2012 revealed the ambipolar nature of perovskite [5]. They reported the PCE of 10.9% in an all-solid-state device with a configuration of fluorine-doped tin oxide/compact TiO_2 /mesoporous Al_2O_3 (methylammonium lead iodide)/poly(triarylamine)/spiro-OMeTAD/gold [FTO/c- TiO_2 /m- Al_2O_3 ($CH_3NH_3PbI_3(Cl)$)/spiro-OMeTAD/Au]. The findings indicated that both electrons and holes can transport within the perovskite film with a long charge diffusion length [6, 7]. In 2013, Liu et al. [8] reported a planar device structure with a configuration of FTO/c- TiO_2 / $CH_3NH_3PbI_3(Cl)$ /spiro-OMeTAD/Au. The device produced a PCE over 15%. Excellent ambipolar nature of perovskite enables efficient charge transfer process. Hole transport material free PSCs with Au [9, 10] or carbon [11] as a counter electrode were also developed, which highlighted the excellent charge transport properties of perovskite. Various perovskite deposition methods including one [3, 5] or two [12] step solution process, low-temperature vapor-assisted solution process [13], and vacuum-evaporation deposition [8] were also developed. In 2014, Jeon et al. [14] reported a certified PCE of 16.2% for a $CH_3NH_3PbI_3$ ($MAPbI_3$)

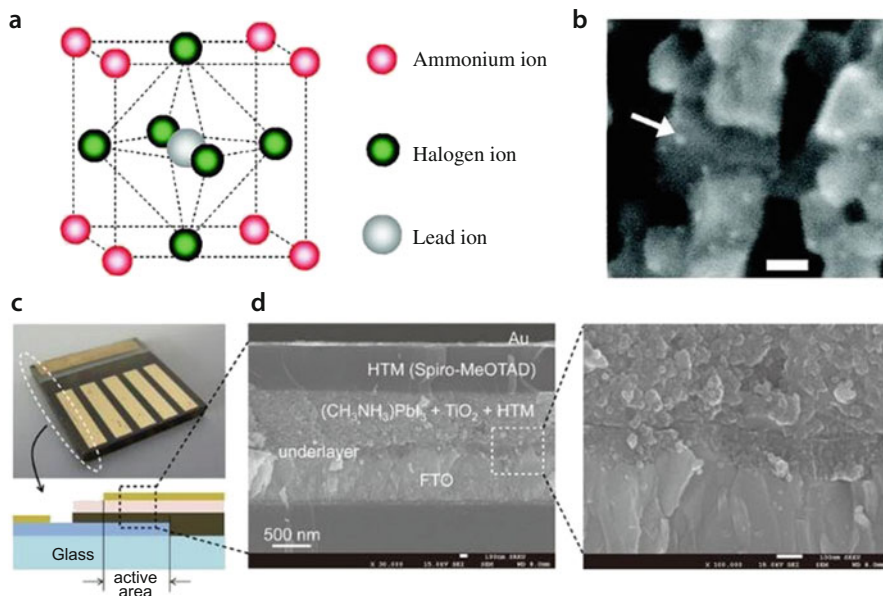


Fig. 7.1 (a) Crystal structures of perovskite compounds. (b) Scanning electron microscopy (SEM) image of particles of nanocrystalline $\text{CH}_3\text{NH}_3\text{PbBr}_3$ deposited on the TiO_2 surface in sensitized solar cells. The arrow indicates a particle, and the scale bar shows 10 nm. (Reproduced with permission from Ref. [2]. Copyright (2009) American Chemical Society). (c) Schematic of device architecture of solid-state perovskite-based solar cells. (d) A cross-sectional structure of the device and cross-sectional SEM image of the device and the active layer-underlayer-FTO interfacial junction structure. (Reproduced with permission from Ref. [3]. Copyright (2012) Nature Publishing Group)

based normal structure (n-i-p) mesoscopic device. In 2017, the same group pushed the efficiency of PSCs up to 22.1% by careful control of the perovskite film quality.

7.1.3 Challenges Facing PSCs

PSCs have gained high efficiency comparable with commercialized silicon solar cells; however, this novel PV technology still faces challenges towards commercialization [15, 16]. Firstly, it is still quite challenging to fabricate PSCs with long lifetimes (>25 years) for out-door application [17–27]. The $\text{CH}_3\text{NH}_3\text{PbI}_3$, a key component of the PSC, degrades into lead iodide (PbI_2) and methylammonium Iodide ($\text{CH}_3\text{NH}_3\text{I}$) due to the moisture, which significantly affects the stability of PSCs [28–32]. Meanwhile, the existence of oxygen also affects the stability of $\text{CH}_3\text{NH}_3\text{PbI}_3$ [33, 34, 35–38]. Recently, it was found that $\text{CH}_3\text{NH}_3\text{PbI}_3$ also degrades under continuous light illumination [39], especially when the ultraviolet (UV) light are not filtered [40]. Secondly, the hysteresis is problematic.

Hysteresis phenomena observed in current density-voltage measurements, where the measured PCE highly depends on scan rate/direction and preconditions [41]. The origin of hysteretic effects is still unclear [42, 43], ferroelectric polarization of perovskites [44, 45], ion migration within perovskites [46–52], charge trapping and de-trapping of charge carriers [57, 58], capacitive effects [53, 54] could be the cause of this phenomena. Several strategies including immobilizing ion transport and/or reducing interfacial traps [55, 56], surface passivation of perovskite films [57, 58], and interface modification of charge transport layers [57] have been investigated to alleviate hysteresis. Thirdly, the use of lead (Pb) is of great concern. The lead is quite toxic to the environment [58]. Even though strict encapsulation can decrease the risk of releasing toxic compounds into the environment [59], it is desirable to develop lead-free PSCs [58, 60, 61]. Fourthly, upscaling is quite challenging. The current champion cells are made in a very small cell ($\sim 0.09 \text{ cm}^2$). For practical applications, it is imperative to develop technology for large scale, energy-efficient, high-throughput, low-cost manufacturing commercialized perovskite photovoltaics (PV) using doctors blade [62–76], inkjet printing [77–80], slot-die printing [81–85], screen printing [11], spray coating [75, 86–95], roll to roll [81, 96–99], etc. Lastly, the most used noble metal counter electrode materials and their deposition cost take up a large part of the cost of PSCs. The use of the noble metal counter electrode in large scale PSCs will largely increase the cost. The noble metal thin-film electrodes also suffer from long-term stability concern. In addition, metal thin-film electrodes usually require high vacuum thermal evaporation system, which is highly energy consuming and complicated, thereby limiting its mass production for large-scale PSCs. Therefore, it is urgent to develop low-cost and stable counter electrode materials, such as metal nanostructured materials, carbon materials electrode, and conductive polymer electrode, etc., to replace expensive noble metal thin-film electrode.

7.1.4 Counter Electrode for Perovskite Solar Cells

Although the PSCs are evolved from dye-sensitized solar cells, the catalytic activity for electrolyte regeneration is no longer required for counter electrode materials. Ideally, a counter electrode in PSCs should possess high conductivity, good mechanical properties, robust physical and chemical stability, easy deposition, low cost, and eco-friendly qualities. Besides the high efficiency, PSCs are also appealing for the constructing of tandem solar cells to overcome the Shockley-Queisser limit of single junction solar cells. In addition, PSCs are promising for building integrated photovoltaics, especially if made semitransparent and used as solar windows. For tandem or transparent solar cells, incident light is required to penetrate through the counter electrode before reaching the absorber in transparent solar cells or tandem solar cells, a good optical transmittance is also a critical property for counter electrode.

7.1.5 Metal Electrodes

In PSC, metal electrodes are the most common materials for counter electrode due to their high conductivity, good reflectivity, and also easy integration process. Although different metals have different work function, it has been demonstrated that the device performance of PSCs is mainly determined by an intrinsic quasi-Fermi level splitting of perovskite and the interaction with electron and hole transport materials. The work function of the bottom and top conductive electrode may be not that much essential [62]. This is due to the fact that perovskite exhibits low exciton binding energy and superior carrier conductivity, the anode-cathode work function difference appears not that important for the separation and collection of photogenerated carriers [62]. Thus, different metals can be employed as counter electrode materials in PSCs.

7.1.6 Metal Thin-Film Electrodes

Metal thin film is usually deposited through vacuum thermal evaporation, in which metal source is heated at high temperature to form evaporated metal vapor in a vacuum with a typical pressure of 10^{-4} ~ 10^{-5} Pa and the vapor travel directly to the target substrate (PSCs without electrode) and condense to a solid thin film using a shadow mask to pattern the electrodes. Sometimes, the metal thin-film electrode can be also etched via simple scrape or laser etching to form the desired pattern such as interconnections for modules. However, noble metal thin-film electrode is not an ideal counter electrode for commercialization of PSCs due to the high cost of the high purity metal source, high vacuum requirement during electrode deposition, and also the low production efficiency of electrode disposition. Besides, the reaction of the metal thin films with the ambient environment and also the bottom active layers raise a long-term stability concern regarding the metal thin-film electrode for commercialization of PSCs.

Gold (Au) is one of the most common counter electrode materials in PSCs because of its resistance to corrosion, electrical conductivity (4.5×10^7 S/m), excellent ductility, and lack of toxicity. To date, most of the high efficiency normal structured PSCs were equipped with vacuum evaporated gold thin-film (80~100 nm) as a counter electrode to collect charge carriers, including the PSCs with record PCEs of 22.1% [100]. Gold electrodes also have some drawbacks. It has been demonstrated that the diffusion of Au across the hole transport layer after storage can lead to degradation of device performance, which will be discussed in the following part. In addition, Au is an expensive metal (Price is 39.78 US dollar/g from London Gold Fix, 2017, July) that closely related with global economics, which hampers its large-scale applications as an electrode in solar cells.

Alternatively, silver (Ag) has also been used as a counter electrode in both normal [101, 102] and inverted [103–105] structured high-efficiency PSCs. The electrical conductivity of silver is the greatest of all metals (6.2×10^7 S/m). The price of Ag is 0.52 dollar/g from London Gold Fix (2017, July) much cheaper than that of

Au. However, Ag is very active in the existence of halide, resulting in corrosion or contamination of the Ag electrode. It has been reported that the Ag electrode-based PSCs degrade after being kept under humidity air.

Aluminum (Al) is the most widely used nonferrous metal in human activity; its production exceeded that of any other metal except iron. Al is much cheaper than Ag, but it exhibits high conductivity (3.5×10^7 S/m). In inverted structured PSCs, Al is commonly employed as a top electrode [106, 107]. In particular, Shao et al. [108] reported high efficiency of 19.4% for inverted structured planar PSCs with Al counter electrode. However, Al has been reported to be associated with issues such as air-exposure-induced oxidation and interdiffusion of Al atoms into the organic layer, which hampers its application in PSCs [109].

Copper (Cu) is used mostly as a pure metal, which has been widely used in electrical wire, roofing and plumbing, and industrial machinery. Cu is also a cheap metal, but it exhibits comparable conductivity (5.96×10^7 S/m) to Al. However, Cu has been rarely used as the top electrode in PSCs. When Cu was first used as a top electrode in flexible inverted structured planar PSCs with additional chromium(III) oxide/chromium ($\text{Cr}_2\text{O}_3/\text{Cr}$) interlayer, increased device stability under ambient conditions was observed [110]. Huang's group first demonstrated the employment of pure Cu thin film as a top electrode in inverted structured planar PSCs and highlight the good stability of Cu electrode [62, 111, 112]. They used vacuum thermal evaporated Cu, Al, and Au as counter electrode in planar inverted PSCs with doctor-blade coated mixed cation perovskite ($\text{FA}_x\text{MA}_{1-x}\text{PbI}_3$), and methylammonium lead iodide (MAPbI_3) as light absorber and the devices with Cu cathode gave champion PCE of 18.3% ($\text{FA}_x\text{MA}_{1-x}\text{PbI}_3$), which is higher than that of Al and Au due to less reaction of perovskite with Cu than Al [62]. Recently, the same group reported a certified PCE of 20.59% for Cu electrode-based inverted structured planar PSCs via defects passivation [112]. This group also demonstrated the employment of commercial conductive Cu tape as a counter electrode of planar inverted PSCs, obtaining PCE of 12.7% and good stability. The Cu tape was transferred on the charge transport layer via a vacuum-free low-temperature lamination technique, which significantly reduces the cost of device fabrication [113]. Their work suggested that Cu may be a better choice for the counter electrode material in PSCs than other widely used electrode materials, and also Cu ink or pate might be potential for scalable manufacturing of PSCs [111].

Chromium (Cr) is usually used in the form of metal alloys in the chemical, refractory, and foundry industries. Pure Cr exhibits relatively high conductivity (7.9×10^6 S/m). So far, Cr has been rarely used as the top electrode in PSCs. When used in PSCs, Cr_2O_3 were observed at the charge transport layer/Cr interface, which can act as a protective layer and improve the long term stability [110, 114].

Nickel (Ni) has a work function of ~ 5.04 eV, very close to that of gold (~ 5.1 eV), but with a unit price less than 0.03% of that of gold. A sputtering-coated nickel film was first used as the counter electrode in a normal-structured mesoscopic PSCs and obtained PCE of 10.4% [115]. Later, a sputter deposited nickel oxide/nickel [NiO_x/Ni] double layer was also reported as a hole transport material (HTM)/contact couple in normal architecture of PSC with PCE of 7.28% [116]. Without using vacuum

thermal or electron-beam evaporation, Ku et al. [117] used a printable mesoporous nickel film as the counter electrode in printable PSCs, giving a PCE of 13.6%. Their printable Ni electrode has a thickness of 2 μm with favorable conductivity, which can offer robust protection of underlayer to improve the device's long-term stability. This low-cost, printable Ni electrode is promising for low-cost, fully-printable solar cells with high efficiency and long service life. Moreover, they demonstrated a reuse process of the mesoporous Ni electrode-based PSCs by washing and reloading perovskite for fresh devices and obtained an efficiency of 12.1% for reused devices. The reusable mesoporous metal-cathode based PSC provides a promising approach towards low-cost PSC with a long service life [117].

Molybdenum (Mo) is also one of the metals possessing a high work function and also high electrical conductivity, enabling this metal to be a candidate material for low-cost and highly efficient PSCs. In addition, Mo is chemically more stable against reactions with halides and oxidation in the air compared to Ag and Al, respectively. Jeong et al. [118] first employed a thermal evaporated Mo as a counter electrode of PSCs. By optimizing the thickness of Mo electrode and combination with high-quality perovskite layer, their PSCs exhibited the best PCE of 15.06% with small hysteresis. Moreover, the Mo electrode was demonstrated to have superior resistance and restoration capability against external scratch or deformation compared to the Au electrode.

Super thin-film metal electrodes with a thickness of several nanometers can be also used as a counter electrode, especially in semitransparent PSCs. Such devices are promising for application in building integrated photovoltaics such as solar window due to their decent efficiency and good transparency. However, because of the trade-off of the conductivity and transparency of the semitransparent electrode, it is important to optimize the electrode to achieve both high conductivity and high transparency. Eperon et al. [119] used a thin (~ 10 nm) layer of gold as the counter electrode in semi-transparent PSCs featuring configuration of FTO/TiO₂/CH₃NH₃PbI_{3-x}Cl_x/spiro-OMeTAD/Au, as shown in Fig. 7.2. The devices are reasonably transparent; however, the gold electrode is a major source of transmittance loss. Their devices with PCE about 8% showed average visible transmittance (AVT) of 7%. Such low PCE and AVT is attributed to the large electrode resistance and low transparency, respectively. Thus, more transparent electrodes as well as with high conductivity are necessary, specifically the counter electrode, for fully optimized semitransparent PSCs [119]. A semitransparent PSCs based on Au thin (~ 40 nm) layer and perovskite grid also demonstrate 20–70% transparency with a PCE of 5% at 20% transparency [120]. A pure Ag thin (~ 20 nm) layer was also used as transparency electrode for PSCs featuring configuration of indium tin oxide/copper(I) thiocyanate/methylammonium lead iodide/[6,6]-phenyl C61 butyric acid methyl ester/silver [ITO/CuSCN/CH₃NH₃PbI₃/PC61BM/Ag], realizing a PCE of 10% and AVT of 25% [121]. A thinner Ag (~ 10 nm) layer was also used as transparency electrode for PSCs featuring configuration of indium tin oxide/(poly(3,4-ethylenedioxythiophene) polystyrene sulfonate)/methylammonium lead iodide/[6,6]-Phenyl C71 butyric acid methyl ester/fullerene/11-amino-1-undecanethiol hydrochloride/silver [ITO/PEDOT:PSS/CH₃NH₃PbI₃/

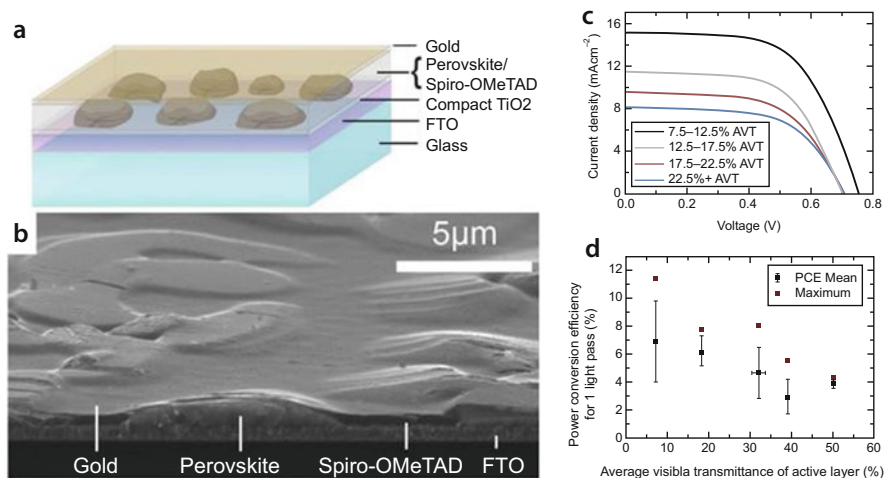


Fig. 7.2 Diagram showing the architecture of the semitransparent PSC, (b) tilted cross-sectional SEM image of a full semitransparent solar cell, (c) Average current density-voltage ($J-V$) characteristics for the cells, and (d) power conversion efficiency plotted as a function of active layer AVT. (Reproduced with permission from Ref. [119]. Copyright (2014) American Chemical Society)

PC71BM/C60/AUH/Ag], realizing a PCE of 8.2% and AVT of 34% [122]. Besides the top transparent electrode, a super thin metal electrode can be also acting as series connection transparent layer in a tandem solar cell. Liu et al. [123] demonstrated a series connection of a ~ 90 nm thick perovskite front sub-cell and a ~ 100 nm thick polymer: fullerene blend back sub-cell that benefits from an efficient graded recombination layer containing a zwitterionic fullerene, Ag, and molybdenum trioxide (MoO_3). The resultant tandem perovskite/polymer solar cell gave a PCE of 16.0%, with low hysteresis.

The transparency of super-thin metal film can be enhanced by applying a protective layer due to the anti-reflective and optical interference. Roldán-Carmona et al. [124] used super thin Au layer as a transparent counter electrode in a PSCs featuring configuration of fluorine-doped tin oxide/(poly(3,4-ethylenedioxythiophene) polystyrene sulfonate)/methylammonium lead iodide/[6,6]-Phenyl-C61-butyric acid methyl ester/gold/lithium fluoride [FTO/PEDOT:PSS/ $\text{CH}_3\text{NH}_3\text{PbI}_3$ /PCBM/Au/LiF] as shown in Fig. 7.3a. They reduced the thickness of Au layer to 6 nm, and another LiF capping layer with a thickness of 100 nm was used to protect the Au layer and reduce the energy lost by the specular reflection of the device while enabling more transparency and keeping a high short-circuit current density (J_{sc}). As shown in Fig. 7.3b, their semitransparent PSCs with PCE of 6.4% showed an AVT of 30%. An electrode consists of a thin Ag top layer (10 nm) capped with MoO_3 (20 nm) layer was also used as a top electrode in inverted PSCs; the resultant device showed PCEs of 11.0 and 8.7% for the front and back incidence, respectively [125].

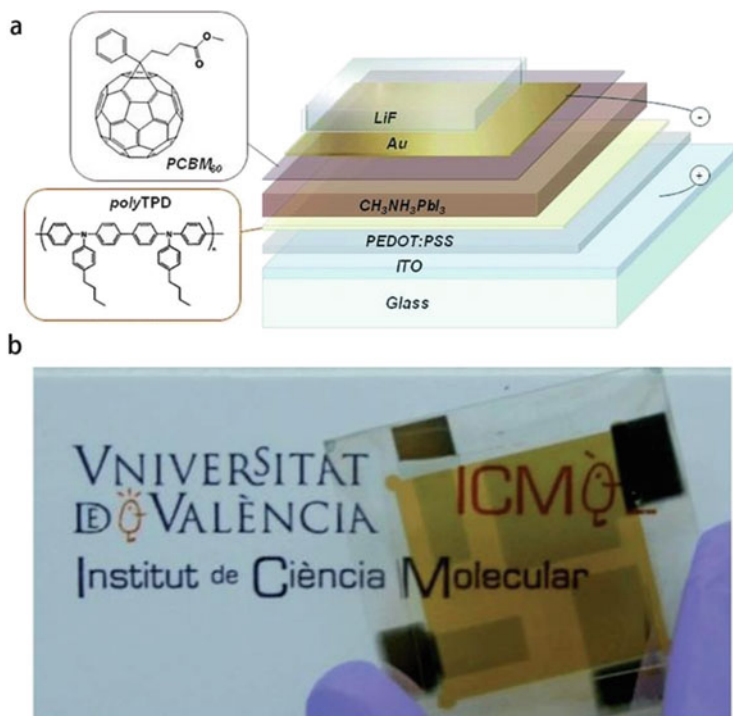


Fig. 7.3 (a) Diagram showing the architecture of the semitransparent PSC and chemical structures of the organic hole and electron transport materials. (b) Photograph of the semitransparent PSC with an AVT \sim 30% and a PCE of 6.4%. (Reproduced with permission from Ref. [124]. Copyright (2014), Royal Society of Chemistry)

Different from the above transparent electrode with single super thin-film metal layer, a dielectric–metal–dielectric (DMD) multilayer relying on interference effects provided by the two dielectric layers, exhibits good light transmission and also decent conductivity [126]. DMD electrode has been widely adopted as visible-transparent and infrared (IR)-reflective coatings [126, 127], and as transparent electrode for various optoelectronic devices, including organic solar cells [128–131], organic light emitting diodes [132–135], and transparent field effect transistors [136]. A critical factor to their success as semi-transparent windows is the precise selection and thickness optimization of the individual dielectric and metal films, where the metal layer stacking in-between the dielectric materials determines the trade-off between the transparency and the conductivity of the entire top electrode [137].

Gaspera et al. [137] first employed DMD transparent electrode composed of a MoO_3 –Au (10 nm)– MoO_3 stack in PSCs as shown in Fig. 7.4, where MoO_3 enable efficient hole injection properties and a good nucleation surface for Au deposition (Fig. 7.4e and f); Au provide good conductivity and stability towards air oxidation.

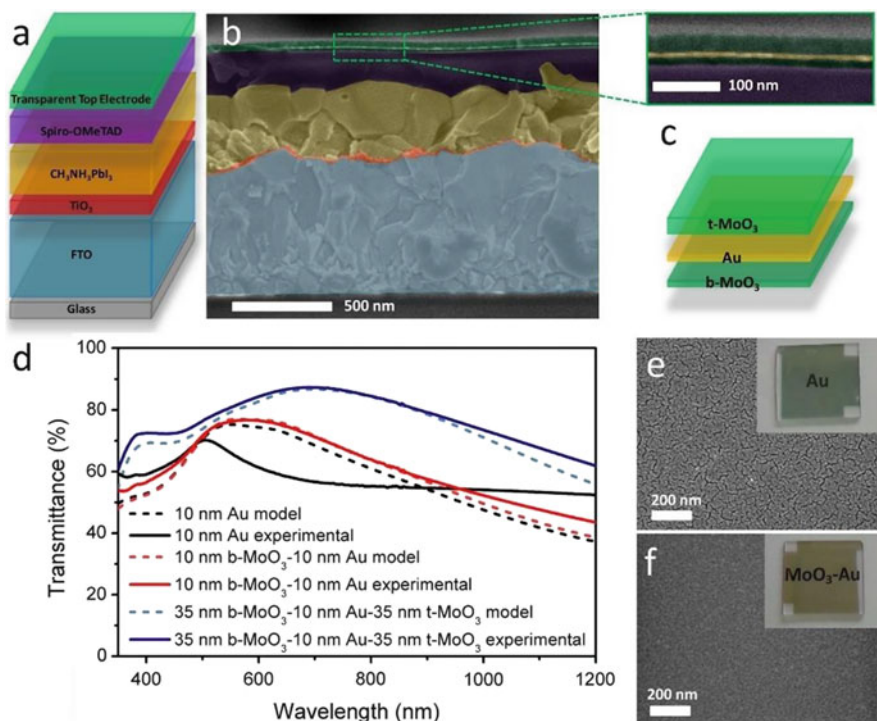


Fig. 7.4 (a) Schematic illustration (not to scale) of the PSC. (b) Cross-sectional SEM image of PSC. (c) An enlarged view of the multilayer top electrode and schematic of the DMD structure. (d) Simulations (shaded dashed lines) and experimental data (solid lines) showing the transmittance of Au (black), b-MoO₃/Au (red), and b-MoO₃/Au-t-MoO₃ (blue). (e) SEM image of Au film. (f) SEM image of b-MoO₃/Au film. The insets show photos of the two samples. Reproduced with permission from Ref. [137]. (Copyright (2015) Elsevier)

By combining gas-quenching deposited thin CH₃NH₃PbI₃ layer, their device with PCEs between 5.5% and 13.6% delivered AVT values of 31% and 7%, respectively.

A DMD of MoO_x/Ag (12, 18, 24 nm)/zinc sulfide (ZnS) electrode was also designed to achieve excellent thermal-mirror functionality for a semi-transparent PSCs [138]. By selectively maximizing electrode transmission at visible and reflectance at NIR region, heat-blocking and “cool-to-touch” operation with near-infrared surface-enhanced Raman spectroscopy (near infra-red surface enhanced resonance, NIR-SER) as high as 85.5% was demonstrated with no sacrifice in average visible-light transmittance and luminous transmittance using an electrode structure that incorporates a thick Ag layer in conjunction with ZnS as a high-index capping layer. They demonstrated efficient semitransparent solar cells with ideal heat management capability, which can greatly enhance the viability in various practical applications of PSCs. An efficient DMD electrode of polyethylenimine (PEIE) silver/ Molybdenum n-oxide [PEIE/Ag/MoO_x] was also developed for planar inverted PSCs [139].

The high transparency of the DMD electrode also enables the tandem solar cells. Yang et al. [140] constructed a four terminal tandem solar cell employing solution processed CIGS and PSCs integrated with a DMD top electrode. For the DMD electrode, they introduced an ultrathin gold seed layer (~ 1 nm) beneath a silver film to improve the adhesion. It was found that the seed layer induced continuous film formation [141]. As shown in Fig. 7.5a–c, the silver film without a gold seed layer is not continuous at 11 nm, presenting isolated metal islands, and the film is highly

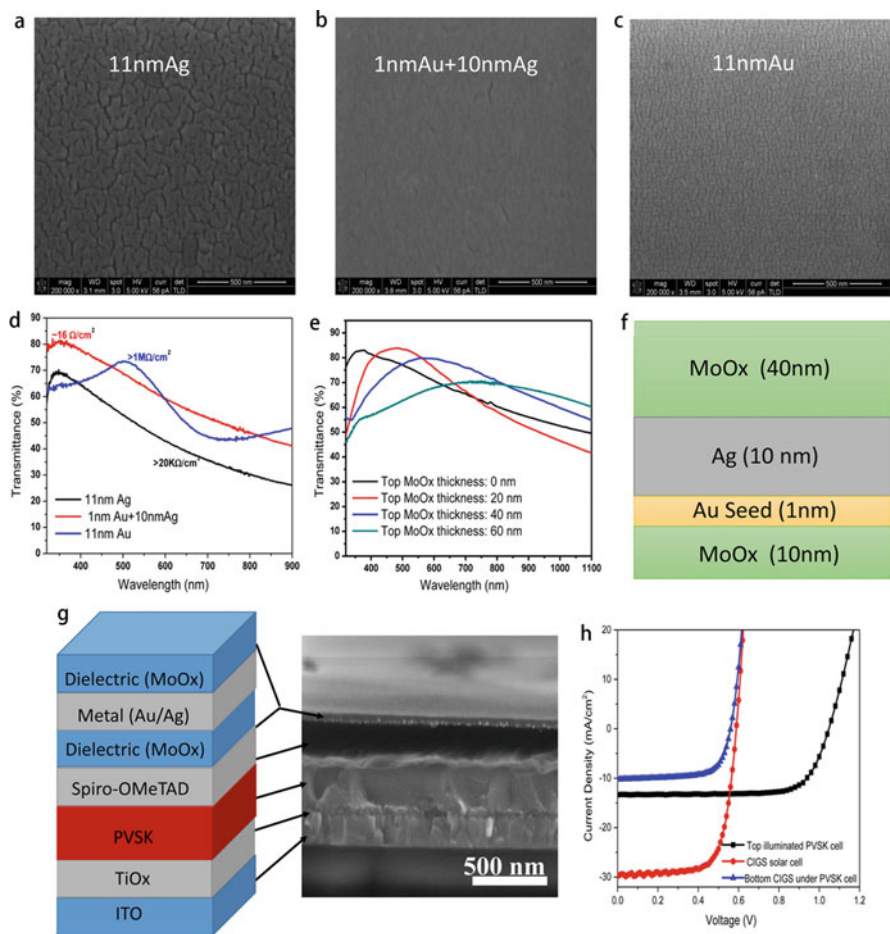


Fig. 7.5 The film morphology of pristine silver (a), gold seeded silver (b), and pristine gold (c) layer with same metal thickness. (d) The transparency and conductivity of pristine silver, gold seeded silver, and pristine gold film. (e) The transparency of the multilayer electrode with different MoO_x topping layer thickness. (f) The optimized parameters for the DMD transparent electrode. (g) The schematic and SEM cross-sectional image of the semitransparent PSC. (h) The J–V curves of top illuminated PSC, CIGS, and CIGS cell under the PSC. (Reproduced with permission from Ref. [140]. Copyright (2015) American Chemical Society)

resistive. With the same metal film thickness, the silver film with 1 nm gold seed layer becomes continuous across the entire film as shown in Fig. 7.5b. As a result, the conductivity of the corresponding silver film improves several orders of magnitude from $20 \text{ K}\Omega \text{ sq}^{-1}$ (11 nm Ag) to around $16 \Omega \text{ sq}^{-1}$ (1 nm Au + 10 nm Ag). In terms of conductivity and transparency, the gold-seeded silver film (1 nm Au + 10 nm Ag) shown in Fig. 7.5f is also superior to pure gold film, where the same thickness of gold is very resistive and exhibits low transmittance in the visible region due to the strong plasmonic scattering effect of the gold nano-domains. With improved conductivity and transparency, their semitransparent PSCs illuminated from DMD top electrode gave a PCE of 11.5%, and the resultant tandem cell gave a PCE of 15.5% (Fig. 7.5h) [140]. Device modeling has shown that the optical spectrum matching of the top sub-cell and bottom sub-cell is critical to realize high-efficiency tandem solar cell. The excellent bandgap tunability of perovskites provides a platform for optimizing both wide bandgap top sub-cell (1.7–1.9 eV) or low bandgap bottom sub-cell (0.9–1.2 eV) [142, 143]. Zhao et al. [144] demonstrated an efficient low-bandgap ($\sim 1.25 \text{ eV}$) with the composition of $(\text{FASnI}_3)_{0.6}(\text{MAPbI}_3)_{0.4}$ and achieved a maximum PCE of 17.6% and a certified efficiency of 17.01% by optimizing perovskite thin-film thickness and film quality. When mechanically stacked with a 1.58 eV, bandgap perovskite top cell featuring a configuration of glass/FTO/($\text{SnO}_2/\text{C60-SAM}/\text{FA}_{0.3}\text{MA}_{0.7}\text{PbI}_3/\text{Spiro-OMeTAD}/\text{MoO}_x$ (10 nm)/Au (8.5 nm)/ MoO_x (10 nm), their all-perovskite four-terminal tandem cell delivered a steady-state efficiency of 21%. These results highlight that DMD electrode is promising for the transparent counter electrode in PSC-based tandem solar cells.

Super thin metal electrode has been used as a bottom transparent electrode for a flexible solar cell. An electrode with photoresist containing an average of eight epoxy units per polymeric unit SU-8/ MoO_3/Au structure was developed for inverted planar PSCs with vapor-deposited perovskite film, giving PCE of 9.05% [145]. The PCE maintained 74% of the initial value after 2000 bending cycles with a bending radius of 3.5 mm. An ITO-free semitransparent inverted PSC with a super thin Au film as a bottom electrode and DMD multilayer with structure of MoO_3 (3 nm)/Au (1 nm)/Ag (7 nm)/ MoO_3 (5 nm)/tris-8-hydroxyquinoline aluminum (Alq3) (50 nm) as the top electrode was also reported [146]. The PSC achieved a PCE of 8.67% with AVT of 15.94%. Moreover, the flexible device maintains 88% of its initial PCE after 1000 bending cycles with a bending radius of 3.9 mm. The authors further introduced another MoO_3 layer between Norland Optical Adhesive 63 (NOA63) and Au [147]. The resultant PSC achieved a PCE of 6.96% with AVT of 18.16%. Moreover, the flexible device maintains 71% of its initial PCE after 1000 bending cycles with a bending radius of 4 mm.

PSCs with metal thin-film counter electrode still suffer from issues. In PSCs, a metal thin film was deposited on the top of the device, the stability issues related to the counter electrode may rely on the contact interface between the metal contact electrode and charge transporting layer under the ambient condition. Zafer et al. [148] observed the presence of pinholes in a spiro-OMeTAD layer with an average diameter of $\sim 135 \text{ nm}$ and a density of $\sim 3.72 \text{ holes}/\mu\text{m}^2$ by atomic force microscopy and large pinholes with diameters in the range of 1–20 μm and a density of

~ 289 holes/ mm^2 by optical microscopy and Fourier transform infrared microscopy. Such pinholes increase the possibility of contact between perovskite and metal electrode. These pinholes provide a quick migration pathway for the outward diffusion of the halide compounds towards metal electrode and facilitate the potential inward migration of metal to the perovskite layer. It has been observed that PSCs operating devices employing a spiro-OMeTAD and Au electrode at temperatures exceeding 70°C causes irreversible performance loss [149]. This is speculated to be due to the migration of Au across the spiro-OMeTAD into the perovskite layer, which has been confirmed by time of flight secondary ion mass spectroscopy elemental depth profiling and inductively coupled plasma mass spectrometry [149]. The formation of gold precipitates at the interface between spiro-OMeTAD and perovskite and of bigger clusters within the perovskite active layer and the mesoporous TiO_2 layer was also observed that further suggest the migration of Au [150]. Au diffusing inside the perovskite can produce shunts across the device and create deep trap states causing nonradiative recombination and consequentially results in device performance deterioration. Continuous light illumination was also observed to cause photo-induced degradation of PSCs, correlated with the chemical contact breaking and inefficient charge collection at hole transport material/Au electrode interface [151]. Different from the instability of perovskite under humidity condition, even strict encapsulation cannot avoid the migration of Au and the degradation at hole transport material/Au electrode interface under light illumination. Ag is much more active than Au, which makes Ag easily react with halide compound resulting degradation. However, Ag can become corroded when it is in contact with the perovskite or the halide compounds origin from perovskite degradation [40, 152, 153]. Kato et al. [109] proposed as a mechanism that the $\text{CH}_3\text{NH}_3\text{PbI}_3$ layer first decomposes into mobile methylammonium iodide ($\text{CH}_3\text{NH}_3\text{I}$) and hydrogen iodide (HI), which is accelerated with the presence of water or oxygen in ambient conditions. These iodide compounds then migrate through spiro-OMeTAD layer towards Ag electrode, aided by pinholes. For Al electrode, air-exposure can induce fast oxidation of the electrode and the interdiffusion of Al atoms into the organic layer. Thus, Al is considered as an unstable electrode for PSCs. Furthermore, it is reported that Al can rapidly reduce Pb^{2+} to Pb^0 , converting $\text{CH}_3\text{NH}_3\text{PbI}_3$ first to $(\text{CH}_3\text{NH}_3)_4\text{PbI}_6 \cdot 2\text{H}_2\text{O}$ and then to $\text{CH}_3\text{NH}_3\text{I}$ [154].

An interlayer has been introduced into PSCs to block the interaction of electrode and bottom vivacious chemical source. In general, oxide and organic materials are the most common interlayer materials used in PSCs. For example, the employment of titanium-niobium n-oxide (TiNbO_x) as an interlayer beneath Ag can significantly enhance device stability by inhibiting Ag migration into the bottom layer and penetration of humidity [104]. An efficient zinc oxide (ZnO) electron transport layer also exhibited the outstanding capability of inhibiting Al migration superior to PCBM, the resultant devices showed good stability [155]. Sanehira et al. [156] found that devices with MoO_x/Al electrodes are more stable than devices with more conventional, and more costly, Au and Ag electrodes, when they investigated the stability of unencapsulated PSCs with Au, Ag, MoO_x/Au , MoO_x/Ag , and MoO_x/Al

electrode under constant illumination and constant load conditions. Other kinds of interlayers have also been reported. For example, stable Cr metal interlayer was deposited between the hole transport layer (HTL) and a gold electrode to reduce high-temperature-induced irreversible long-term losses [149]. In addition, graphene was also demonstrated to be a useful buffer layer that blocks the diffusion of air and Au into the perovskite layer [157]. A thiol-functionalized cationic surfactant (11-mercapto undecyl)trimethylammonium bromide (MUTAB) has also been used as interlayer to exert multi-positive effects for the enhancement of Ag stability, including decrease of contact resistance between the active layer and Ag electrode, improvement of ambient and thermal stability, and reduction of the percolation threshold of ultrathin Ag film [158]. Apart from the penetration of the metal across charge transport layer towards perovskite, the mobile iodide compound come from the perovskite may also diffuse outward to corrode the metal contact. Kwanghee Lee et al. [159] introduced an amine-mediated titanium suboxide as a chemical inhibition layer between the PCBM and Ag contact electrode to inhibit the corrosion of Ag by halide compounds (Fig. 7.6). The relevant PSCs maintained almost 80% of their initial PCEs after 1 year (9000 h) storage in nitrogen and 80% of the initial PCEs after 200 h in ambient conditions without any encapsulation.

Another promising strategy to solve the issues regarding the noble metal electrode is to replace them with other low cost and stable metal electrode materials, such as Cu [62, 111, 112], Cr [114], Mo [118], Ni [115, 117], or carbon [11, 160], etc. Taking Cu, for example, Huang et al. [111] have reported that Cu is stable even in direct contact with MAPbI₃ in the encapsulated device, and it is predicted to be

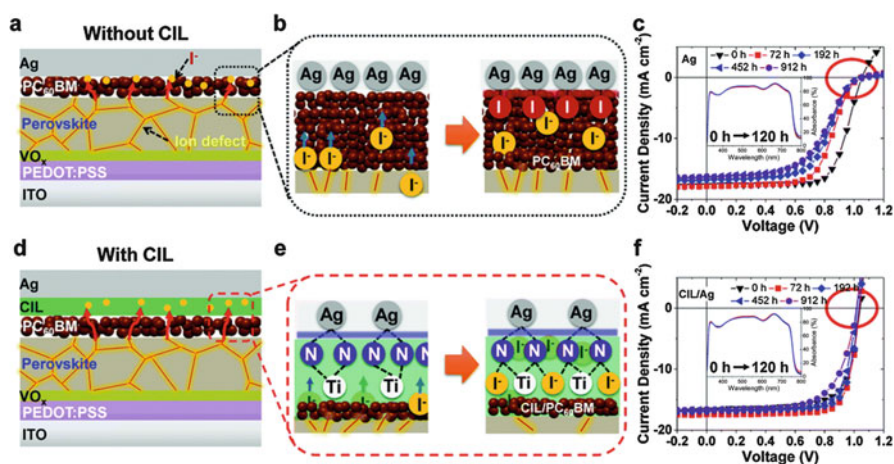


Fig. 7.6 Schematic diagram and J–V characteristics with fast degradation by ionic defects in PSC. (a–c) The reference structure of p–i–n planar PSC and the counter electrode degradation process with J–V characteristics and absorption spectra (inset). (d–f) The p–i–n devices with a CIL buffer layer and the counter electrode protection process with J–V characteristics and absorption spectra (inset). (Reproduced with permission from Ref. [159]. Copyright (2016), Royal Society of Chemistry)

stable for almost 170 years at room temperatures and 22 years under operation at 40 °C. Their devices with a Cu electrode exhibited a PCE above 20% and retained 98% of the initial efficiency after 816 h storage in an ambient environment without encapsulation. Mo is also chemically more stable against reaction with halides, ambient condition, and also superior mechanical and scratch-resistance properties, which enable this material to be a promising candidate for a stable counter electrode for PSCs [118]. In addition, the metal alloy is also a promising candidate for a noble metal electrode. For example, silver aluminum (AgAl) alloy electrode has been demonstrated to be more stable than Ag and Al, which is due to the formation of alumina n-oxide (AlO_x), acting as an interlayer layer to inhibit not only the diffusion of Ag atoms into bottom layer but also the penetration of moisture encroachment [161, 162].

Fabrication of metal thin-film electrode is challenging. The expensive raw electrode materials and the complicate vacuum deposition system for metal thin-film electrode largely increase the cost of manufacturing PSCs. They are not applicable for large-scale production due to the limitation of vacuum thermal evaporation. The high vacuum thermal evaporation process is also highly energy consuming and complicated, thereby limiting its mass production. Therefore, it is desirable to exploit substitution of these metal electrodes to improve stability, simplify the cost of device fabrication, and recognize large-scale fabrication for scalable PSCs (cf. Table 7.1).

7.1.7 Metal Nano-Structured Electrode

Metal nanostructures in the form of nanogrids, nanowires, or continuous nanofibers as efficient transparent and conductive electrodes are promising candidates of counter electrode materials in PSCs due to their low-cost, high conductivity, easy deposition, solution processability, excellent transparency, and flexibility. In general, these metal nanostructures possess larger thickness than that of the metal thin film, which makes their conductivity is close to the metal thin film. Moreover, the metal nanostructures can form conductive networks that enable high conductivity. In addition, the interspace of the metal nanostructures can provide excellent light transmittance, which makes metal nanostructures to be a promising candidate as an efficient transparent conductive electrode in semitransparent PSCs. Besides, metal nanostructures such as nanowires can be easily dispersed in a solvent or mixed with the polymer to form a paste, which makes it possible to deposit these materials via simple processing methods, such as spin coating, spray coating, screen printing or roll to roll printing, etc.

Metal nanowires (NWs) are one-dimension metallic nanomaterials, with widths of a few tens of nanometers and lengths on the micrometer scale, which are widely used as a conductive electrode. A variety of metal including Ag, Cu, Au, and Ni have been explored with quite diverse photovoltaic performance in the PSC as summarized in Table 7.2 [163–167]. NWs usually are solution processable and can be deposited via different processing methods, such as spin coating, doctor blading,

Table 7.1 Summary of the device performance of perovskite solar cells with a super thin-metal electrode

Perovskites	Bottom electrode	Counter electrode	Structure	ATV (%)	V _{oc} (V)	J _{sc} (mA/cm ²)	FF	PCE (%)	Ref.
MAPb(I _{1-x} Cl _x) ₃	FTO	Au (10 nm)	Normal planar	7.2	0.88	10.1	0.68	7.0	[119]
				18.3	0.80	14.8	0.56	6.2	
				32.1	0.75	13.3	0.53	4.6	
				39.2	0.72	9.7	0.47	2.9	
				50.3	0.76	9.7	0.60	3.9	
MAPbI ₃	FTO	Au (40 nm)	Normal mesoscopic (TiO ₂)	19	0.68	14.87	0.49	4.98	[120]
				25	0.71	10.5	0.51	3.79	
				38	0.53	4.32	0.45	1.04	
				46	0.49	3.14	0.53	0.83	
				67	0.61	1.31	0.48	0.38	
MAPbI ₃	ITO	Ag (20 nm)	Inverted planar	37.5	1.07	9.15	0.75	7.53	[121]
				25.7	1.07	12.2	0.76	10.22	
				13.0	1.06	13.0	0.73	10.73	
MAPbI ₃	ITO	Ag (10 nm)	Inverted planar	12	0.94	18.3	0.73	12.6	[122]
				16	0.94	16.4	0.72	11.1	
				24	0.94	14.4	0.69	9.3	
				29	0.94	13.8	0.67	8.7	
				34	0.94	11.7	0.67	7.4	
				47	0.87	7.5	0.59	3.8	
MAPbI ₃	ITO	Ag	Polymer/PSC two terminal tandem		1.63	13.1	0.751	16.0	[123]
MAPbI ₃	ITO	Au (6 nm)/LiF (100 nm)	Inverted planar	35.4	1.037	5.66	0.577	3.39	[124]
				29	1.074	10.30	0.579	6.41	

(continued)

Table 7.1 (continued)

Perovskites	Bottom electrode	Counter electrode	Structure	ATV (%)	V _{OC} (V)	J _{SC} (mA/cm ²)	FF	PCE (%)	Ref.
				22	1.037	13.43	0.525	7.31	
MAPbI ₃	ITO	Ag (10 nm)/MoO ₃ (20 nm)	Inverted planar	10	1.052	15.88	0.46	7.73	
					1.02	16.6	0.64	10.66	[125]
					1.01	12.03	0.58	7.18 ^a	
					0.98	11.08	0.61	6.87	
					0.98	8.84	0.57	5.13 ^a	
MAPbI ₃	FTO	MoO ₃ (5 nm)-Au (10 nm)-MoO ₃ (35 nm)	Normal planar	31	0.718	9.7	0.66	4.6	[137]
				19	0.941	13.7	0.63	8.1	
				16	0.950	14.7	0.65	9.3	
				7	0.988	20.4	0.58	11.7	
MAPbI ₃	ITO	MoO _x (7 nm)/Ag (12 nm)/ZnS (30 nm)	Normal planar	7.29	1.01	17.3	0.663	11.9	[138]
		MoO _x (7 nm)/Ag (18 nm)/ZnS (30 nm)		6.70	1.02	18.5	0.673	13.1	
		MoO _x (7 nm)/Ag (24 nm)/ZnS (30 nm)		7.93	1.01	18.8	0.673	13.3	
MAPbI ₃	ITO	Ag/MoO _x	Inverted planar		0.95	16.91	0.65	10.4	[139]
		Ag/MoO _x			0.92	10.40	0.69	6.54 ^a	
		PEIE/Ag/MoO _x			0.98	18.60	0.74	13.55	
		PEIE/Ag/MoO _x			0.94	11.52	0.78	8.41 ^a	
MAPbI ₃	ITO	MoO _x /Au (1 nm)/Ag (10 nm)/MoO _x	Normal planar		1.05	14.6	0.751	11.5	[140]

			CIGS cell		0.59	29.8	0.707	12.4
			CIGS cell under PSC		0.56	10.2	0.696	4.0
			Four terminal CIGS/PSC tandem cell					15.5
	ITO	MoO _x (10 nm)/Au (8.5 nm)/ MoO _x (10 nm)	Inverted planar		1.114	20.1	0.764	17.1 ^b
					1.141	20.1	0.800	18.3 ^c
(FA _{0.3} MA _{0.7} PbI ₃) _{0.6} (MAPbI ₃) _{0.4}	ITO	Ag	Inverted planar		0.857	28.7	0.713	17.5 ^b
					0.856	28.3	0.717	17.4 ^c
					0.800	4.8	0.763	2.9 ^b
					0.808	4.8	0.744	2.9 ^c
			Four terminal PSC/PSC tandem cell					20.0 ^b
								21.2 ^c

^aIlluminated from top counter electrode side

^bForward scan efficiency

^cReverse scan efficiency

[144]

Table 7.2 Summary of the device performance of perovskite solar cells with the metal nano-structured electrode

Perovskites	Bottom electrode	Counter electrode	Structure	ATV (%)	V _{oc} (V)	J _{sc} (mA/cm ²)	FF	PCE (%)	Ref.
MAPb (_{1-x} Cl _x) ₃	ITO	ZnO/AgNWs	Inverted planar	28.4	0.964	13.18	0.668	8.49	[169]
MAPb (_{1-x} Cl _x) ₃	ITO	ZnO/AgNWs	Inverted planar	44.3	1.03	5.40	0.656	3.6	[171]
				15.6	1.03	6.08	0.656	4.1	
				4.9	1.03	5.96	0.656	4.0	
				9.6	1.03	6.33	0.656	4.3	
				31.4	1.03	6.23	0.656	4.2	
MAPbI ₃	ITO	CuNWs	Normal planar	37.5	0.95	19.10	0.5457	9.88	[172]
MAPbI ₃	Ti	AgNWs	Normal mesoscopic (TiO ₂)	35.4	0.918	16.48	0.49	7.45	[173]
MAPbI ₃	FTO	PEDOT:PSS/Ni mesh (PET)	Normal mesoscopic (Al ₂ O ₃)		0.95	20.7	0.636	13.3	[177]
					0.93	13.9	0.677	9.8 ^a	
MAPbI ₃	ITO/glass	Ag ink	Normal planar		0.84	12.5	0.51	5.2	[81]
	ITO/PET	Ag ink	Normal planar		0.88	7.9	0.49	3.4	
	ITO/glass	Ag ink	Inverted planar		0.87	8.8	0.58	4.4	
	ITO/PET	Ag ink	Inverted planar		0.87	9.2	0.59	4.7	
	ITO/PET	Ag ink	Inverted planar		0.69	4.6	0.47	1.6	

^aIlluminated from top counter electrode side

spray coating, and lamination, which allows easy translating from lab-scale to industrial-scale fabrication [168]. In general, metal NWs electrodes exhibit high conductivity, excellent transparency, and robust flexibility, making them a promising candidate to replace not only metal thin-film electrode for the top counter electrode but also the traditional indium tin oxide bottom electrode as the next-generation transparent and flexible electrode [168]. Guo et al. [169] used silver nanowires (AgNWs) as top electrodes in inverted structured planar PSCs featuring configuration of ITO/PEDOT:PSS/CH₃NH₃PbI_{3-x}Cl_x/PCBM/ZnO/AgNWs by spraying isopropanol diluted AgNWs on the top of PCBM/ZnO layer, where zinc oxide nanoparticles is introduced between the AgNWs and PCBM to ensure Ohmic contact and protect underlying perovskite as shown in Fig. 7.7. As a result, their device gave a fill factor (FF) of 66.8%, open circuit voltage (V_{oc}) = 0.964 V, J_{sc} = 13.18 mA cm⁻², and PCE of 8.49% with a transmittance of 28.4%. The high transmittance is attributed to the excellent transmittance of the AgNWs and also the inverted structure of the device without using transmittance regressive charge transport materials. The device

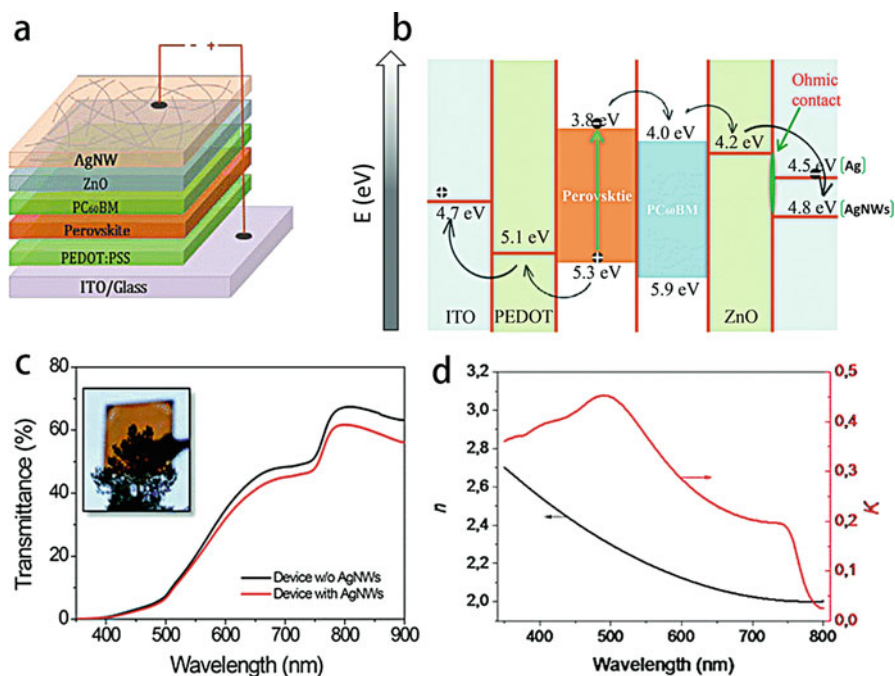


Fig. 7.7 (a) Schematic structure of PSC with solution-processed AgNWs as a counter electrode. (b) Energy diagram of the devices with a ZnO layer between PC60BM and Ag (or AgNWs). (c) Transmittance spectra of the PSC without and with AgNW top electrodes, which were measured before and after AgNWs deposition. The inset shows the photo of a complete semitransparent PSC. (d) Optical constants (n and k) of the CH₃NH₃PbI_{3-x}Cl_x thin film as determined from reflection and transmission measurements. (Reproduced with permission from Ref. [169]. Copyright (2014), Royal Society of Chemistry)

performance can also be improved by the introduction of a robust ZnO layer [158, 170]. Interestingly, when the AgNWs counter electrode-based PSCs were combined with dielectric mirrors to tailor the device appearance to almost any desired color and simultaneously offers additional light harvesting for the solar cell, a PCE of 4.2% and an AVT of 31% were demonstrated for cells showing a colored aesthetic appeal [171]. Copper nanowires (CuNWs) has also been reported as a top electrode in PSCs, yielding a PCE of 9.88% with much better stability [172].

One unique property of metal NWs as an electrode is their ability to make flexible PSCs. Compared to commonly used indium tin oxide (ITO) or fluorine-doped tin oxide (FTO) glass, the metal nanowires exhibited excellent flexibility. Lee et al. [173] recently reported a flexible normal structured PSC using Ti substrate as a bottom conductive electrode and spray-coated AgNWs as a top conductive electrode. As the Ti substrate is opaque, in their devices, the incident light is penetrated into the device through the AgNWs electrode. By carefully control of the AgNWs deposition, their device showed a PCE of 7.45%, with V_{oc} of 0.918 V, J_{sc} of 16.48 mA cm⁻², and FF of 49%. The PCE of the device remained 97.4% of the initial value after 100 bending cycles with a bending radius of 10 mm, which supports the high potential of AgNWs as materials for top electrodes in flexible perovskite devices. Metal NWs also shows application potential in fiber-like PSCs. For example, Li et al. [174] reported a fiber-like PSCs featuring configuration of CNT/[mesoporous titania] m-TiO₂/CH₃NH₃PbI_{3-x}Cl₃/P₃HT-SWNT [poly(3-hexylthiophene-2,5-diyl)-modified single-walled nanotubes]/AgNWs from the inner core to the outer surface. The best PCE of 3.03% was obtained for the twisted PSCs with V_{oc} of 0.615 V, J_{sc} of 8.75 mA cm⁻², FF of 56.4%, and the PCE remained 89% of initial value after a 1000 cycles bending test after in ambient conditions.

Nanogrids have also been used for PSCs [175]. It was found that nanogrid can be easily controlled by varying the grid width, spacing, and thickness, which are beneficial to the manufacturer [167, 175]. These grids can be used as a conductive electrode as both bottom [176] and top [177–180] conductive electrode. For example, a Ni grid/conductive polymer combined electrode as shown in Fig. 7.8 was used as a top conductive electrode for semitransparent PSCs via lamination fabrication method [177]. In this combined electrode, a metal grid embedded in a polymer film provides x–y conduction with large area lateral conductivity of ca 1.2 Ω sq.⁻¹ and the organic conductor, i.e., PEDOT: PSS, provides z conduction to the grid. An average PCE of 13.3% was obtained for the transparent PSCs with V_{oc} of 0.95 V, J_{sc} of 20.7 mA cm⁻², and FF of 63.6% when illuminated from FTO side, and an average PCE of 9.8% was obtained with V_{oc} of 0.93 V, J_{sc} of 13.9 mA cm⁻², and FF of 67.7% when illuminated from metal grids side. These results suggest that metal grids electrode is a promising alternative of electrode materials for PSCs.

It should be mentioned that metal nanoparticles could also be an option for acting as a metal electrode for PSC due to their compatibility with high conductivity and low-temperature processing technique as observed in numerous printed electronics [181]. Schmidt et al. [81] first employed screen printed Ag electrode in a fully printable PSCs. However, a given ink can adversely affect underlying layers and if

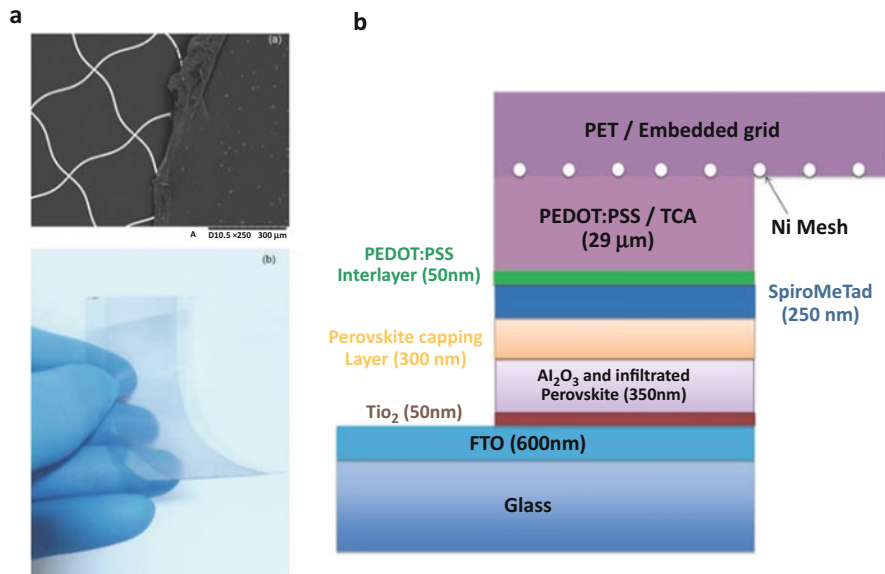


Fig. 7.8 (a) SEM micrograph of transparent conducting adhesive applied to an embedded Ni grid on PET substrate (top) and a photo of the TCA-Laminate transparent counter electrode incorporating the metal mesh (bottom). (b) Schematic of PSC with Ni mesh counter electrode. (Reproduced with permission from Ref. [177]. Copyright (2014), Wiley)

the ink contains incompatible solvent. Thus, it is challenging to find a suitable ink system for stable perovskite.

Metal nanostructures-based electrodes also suffer from several drawbacks, which block their practical application in PSCs. One drawback of metal nanostructures is poor stability due to degradation. AgNWs was found to be covered with nodules, which were iodine-containing compound further confirmed by energy-dispersive X-ray spectroscopy (EDX) data when directly deposited on the top of the perovskite/HTM active layer as a top electrode in PSCs as shown in Fig. 7.9 [182]. The degradation mechanism is same as above described decomposition of Ag thin film, in which the mobile halide source, such as CH₃NH₃I and HI from decomposed perovskite, migrate through the pinhole of the HTM layer and encounter Ag electrode results in the formation of silver iodide (AgI) [109]. To improve the stability, an interlayer, such as oxide [169] and inert metal [182], were usually introduced between the HTM and AgNWs electrode acting as a protective layer to block the interaction of electrode and bottom vivacious chemical source. Another drawback is the strong polar solvent in the metal nanostructures dispersion ink, which may dissolve the bottom active layer and consequentially destroy the device. Besides, a thermal treatment of deposited nanostructured metal electrodes can significantly enhance their conductivity. However, the active layer, especially the perovskite layer, is sensitive to high temperature. A high-temperature treatment may lead to decomposition of perovskite. Given this

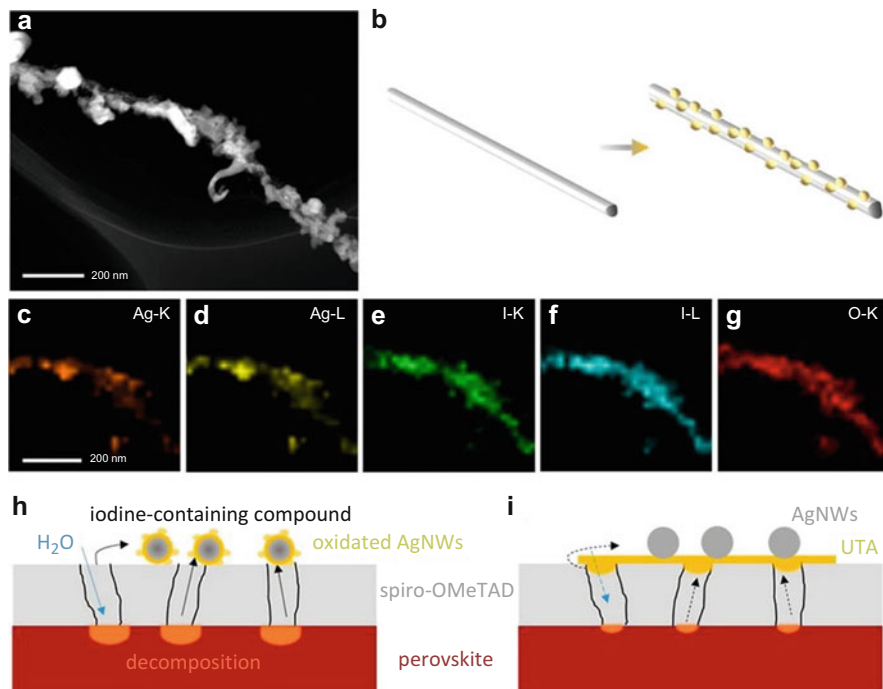


Fig. 7.9 (a) TEM image (b) schematic illustration of the degrading mechanism of Ag and elemental mapping of (c) Ag-K, (d) Ag-L, (e) I-K, (f) I-L, and (g) O-K. Mechanism of halide migration (h) without ultrathin transparent Au layer (i) with ultrathin transparent Au layer. (Reproduced with permission from Ref. [182]. Copyright (2016) American Chemical Society)

problem, a pre-high temperature treatment and a followed transfer method is an effective strategy to resolve this issue. In addition, a plasmonic welding method is also a potential strategy [183].

7.2 Carbon Materials-Based Electrodes

Earth-abundant carbon materials such as graphene, carbon nanotubes, and carbon black/graphite electrode have been used as counter electrode materials due to their good conductivity, chemical inertness, excellent stability, and low cost. These electrodes unlock the enormous potential for low-cost, easy fabrication, and stable PSCs.

7.2.1 Graphene Electrodes

Graphene is a monolayer of sp^2 -hybridized carbon atoms that arranged in a honeycomb structure, which enable charge carriers to behave as Dirac fermions within this

semimetal material [184]. This unique material possesses outstanding properties, such as high conductivity, excellent optical transmittance, good thermal and chemical stability, and remarkable mechanical properties, which make graphene useful in applications ranging from electronic devices to energy storage devices [185]. Its large π conjugated chemical structure make graphene exhibit ultrahigh carrier mobility, which is predicted to be $10^6 \text{ cm}^2 \text{ V}^{-1} \cdot \text{s}$ accompanied with an intrinsic charge carrier concentration of 10^{12} cm^{-2} [186]. Consequently, graphene seems to be a suitable candidate as a conductive electrode in devices such as organic light-emitting diode [187], solar cells [188–190], and an electronic device. Peng et al. [191] first employed chemical vapor deposited graphene transparent electrodes as a counter electrode for semitransparent perovskite solar cells via lamination method. An intrinsic single-layer graphene film normally has a high sheet resistance of about $1050 \pm 150 \Omega \text{ sq}^{-1}$. By introducing another PEDOT: PSS layer, the sheet resistance can be reduced to $260 \pm 40 \Omega \text{ sq}^{-1}$. The sheet resistance can be further reduced when multilayer graphene and d-sorbitol modified PEDOT: PSS were used. Their devices with double-layer graphene electrodes show the maximum PCEs of $12.02\% \pm 0.32\%$ and $11.65\% \pm 0.35\%$ from the FTO and graphene sides, respectively. The good transparency of graphene also enabled their application as a transparent electrode for tandem solar cells. Lang et al. [192] used large-area graphene grown by chemical vapor deposition (CVD) as a highly transparent electrode in PSCs and achieved a PCE of 13.2% for a four-terminal tandem solar cell with [amorphous silica] a-Si: H/[crystalline silica] c-Si solar cell as bottom cell and graphene-based semitransparent PSC as a top cell (cf. Table 7.3).

Graphene can be also directly deposited on the glass as a bottom conductive semitransparent electrode for PSCs. Sun et al. [193] used a chemical vapor deposited graphene transparent as a bottom conductive electrode for inverted PSCs. By adding a MoO_3 layer, wettability and work function of the graphene electrode were tuned to enable a PCE of 17.1%. Consider the excellent flexibility of graphene, they also fabricated flexible inverted PSCs with graphene/polyethylene naphthalate (PEN) substrate, giving a PCE of 16.8% [194]. In addition, their flexible devices maintain 85% of their initial PCE even after bending 5000 times at a bending radius of 2 mm. A flexible polyethylene terephthalate (PET)/graphene as a bottom electrode for PSCs has also been demonstrated, achieving a PCE of 11.5%, high bending durability, and power output per weight (specific weight) of about 5 W/g [195].

However, the massive use of graphene electrode still faces major problems for scale-up production, quality issues, and inconveniences transfer stage [196]. In general, most of the high-quality graphene films are produced by CVD. While CVD is not suitable to obtain abundant high-quality graphene [196]. In addition, graphene usually is deposited on an insulator substrate, which makes it complicated to transfer graphene for actual application [196]. Batmunkh et al. [197] used solution-processed graphene as a bottom conductive electrode for PSCs. However, due to the poor quality of the graphene, a PCE of 0.62% was obtained. Thus, it still appealing for developing low cost and simple high-quality graphene production method and application method [198]. For example, Yan et al. [199] employed chemically cleaved, multilayered graphene oxide as a counter electrode in an

Table 7.3 Summary of the device performance of perovskite solar cells with graphene counter electrode

Perovskites	Bottom electrode	Counter electrode	Structure	V _{OC} (V)	J _{SC} (mA/cm ²)	FF	PCE (%)	Ref.
MAPb(I _{1-x} Cl _x) ₃	FTO	PEDOT:PSS/graphene (1 L)	Normal planar	0.910	17.46	0.578	9.18	[191]
		PEDOT:PSS/graphene (2 L)		0.905	16.35	0.5907	8.74 ^a	
		PEDOT:PSS/graphene (3 L)		0.945	17.75	0.7172	12.03 ^a	
		PEDOT:PSS/graphene (4 L)		0.940	18.54	0.6570	11.45	
				0.950	17.04	0.6758	10.94 ^a	
				0.950	18.05	0.6572	11.27	
MAPbI ₃	FTO	Graphene back reflector	Normal planar	0.930	16.01	0.6837	10.18 ^a	
		Graphene		0.99	14.75	0.566	8.3	[191]
			Si unfiltered	0.90	12.56	0.550	6.2	
			Si filtered	0.71	36.1	0.721	18.5	
			Si/PSC four terminal tandem	0.67	14.0	0.738	7.0	
MAPbI ₃	FTO	Single-layered graphene	Normal mesoscopic (TiO ₂) HTM-free	0.878	14.2	0.54	6.7	[199]
		Multilayered graphene		0.943	16.7	0.73	11.5	

^aIlluminated from top counter electrode side

HTM-free PSCs. They demonstrated that multilayered graphene is a better hole extraction material for PSC, due to the as-formed Schottky barrier. Their graphene electrode-based device gave a PCE of 11.5% (cf. Table 7.3).

7.2.2 Carbon Nanotube Electrode

Carbon nanotubes (CNTs) are allotropes of carbon with a cylindrical nanostructure. Due to their unique π -electron system, CNTs possess excellent conductivity along the tubular axis. Due to their high length-to-diameter ratio ($1.32 \times 10^8:1$), CNTs can be considered as conducting nanowires. The high carrier mobility, great chemical stability, unique nanostructure makes CNTs to be promising carbon materials for a conductive electrode [200]. In addition, CNTs exhibit excellent flexibility and optical transparency. Moreover, CNTs can be also used as hole transport materials in PSCs due to the inherent p-type nature with a work function in the range of 4.7–5.1 eV [200, 201]. In general, CNTs are synthesized by arc discharge, laser ablation, CVD, and high-pressure carbon monoxide disproportionation, which usually require a vacuum or process with gases. However, the repeatability is a major problem with CVD growth due to the batch by batch process. In addition, the tendency to agglomerate, high cost, and low production yield of CNTs make it difficult to process for mass applications.

Carbon nanotubes have been successfully used in PSCs in various applications. Li et al. [202] first used CNTs network as both HTMs and counter electrode in PSCs via lamination technique. Their HTM-free device with the configuration of FTO/[compact]c-TiO₂/[mesoporous] m-TiO₂/CH₃NH₃PbI₃/CNTs gave a PCE of 6.87%. The comparatively low efficiency may be due to the relatively high resistance of the CNT film and a lack of charge-selectivity. By adding spiro-OMeTAD beneath the CNTs network, the PCE of the devices were improved to 9.90% due to the enhanced hole extraction and reduced recombination in solar cells. The good transparency of the CNTs network also allows the device to be illuminated from both sides, as shown in Fig. 7.10, which makes the solar cells promising in building integrated photovoltaic applications, such as solar cell windows.

Wei et al. [203] compared three types of HTM-free mesoscopic devices with multi-walled CNTs, carbon black, and graphite as a counter electrode as shown in Fig. 7.11. They demonstrated that CNTs-based devices have high FF and hysteresis-free performance, which was attributed to two major factors: one is better electric contact and a suitable Schottky junction enable efficient charge transfer from CH₃NH₃PbI₃ to CNTs, and the other one is higher conductivity enable faster charge transport in CNTs electrode. After optimization, their CNTs-based devices gave a PCE of 12.67%.

Qiu et al. [204] also attached an aligned CNT sheet on the top of perovskite as a counter electrode in flexible PSCs and achieved PCE of 9.49%. Their flexible PSCs maintained 93% of initial PCE after bending for 500 cycles at a bending curvature radius of 7.5 mm. Luo et al. [205] used cross-stacked super-aligned CNTs with excellent conductivity, porosity, and flexibility as a low-cost counter electrode for

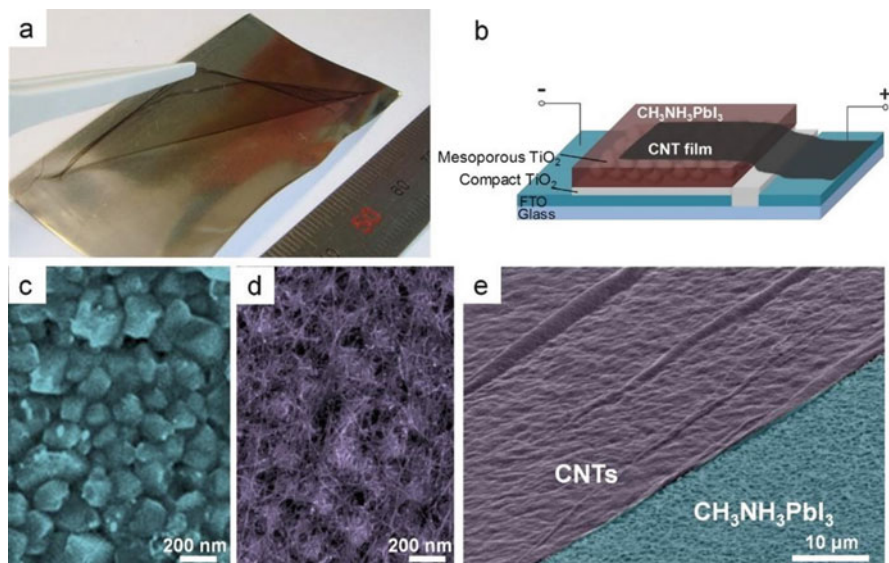


Fig. 7.10 (a) Photo of freestanding CNT film lifting by tweezers to transfer onto other substrates. (b) Schematic of $\text{CH}_3\text{NH}_3\text{PbI}_3$ PSC with laminated CNT counter electrode. (c) Top view SEM images of $\text{CH}_3\text{NH}_3\text{PbI}_3$ perovskite substrate before and (d) after CNT transfer. (e) Tilted SEM image of $\text{CH}_3\text{NH}_3\text{PbI}_3$ perovskite substrate (blue) partly covered by CNT film (purple). (Reproduced with permission from Ref. [202]. Copyright (2014) American Chemical Society)

HTM-free mesoscopic PSCs with the configuration of FTO/c-TiO₂/m-TiO₂/Al₂O₃/CNT(CH₃NH₃PbI₃). In the device, the CNTs electrode was transferred on to Al₂O₃ before depositing perovskite, and perovskite was filled in all of the mesoporous layers. By doping the CNTs with iodine to enhance electrode conductivity and optimizing the thickness of CNTs electrode to increase grain size and improve crystallinity of perovskite, the efficiency of their device can be increased to 10.54% due to the significant improvement in the FF and J_{sc}. Additionally, their PSCs encapsulated with PMMA show outstanding stability in the dark and prolonged light soaking. A solid-state, flexible PSC with Ti foil as the bottom electrode and laminated CNTs film as the top transparent electrode was also been demonstrated [206]. In the device, incident light was illuminated from the transparent conductive CNT network. The flexible device gave a PCE of 8.31% and show little performance deterioration after 100 mechanical bending cycles. These results suggested that both Ti foil and carbon nanotube have great potential for applications in PSCs. CNTs can be also mixed with other materials to modify the electrode. For example, Zheng et al. [207] used poly(3-hexylthiophene) (P3HT) modified CNTs as counter electrode in HTM-free PSCs. The thin P3HT modifier acted as an electron blocker to inhibit electron transfer from perovskite to CNTs and also as a binder to tightly cross-link the CNTs to enhance the conductivity of the electrode and stability of the device, giving a PCE of 13.43%. Recently, the same authors modified CNTs by boron doping for the counter electrode in HTM-free PSCs [208]. The boron

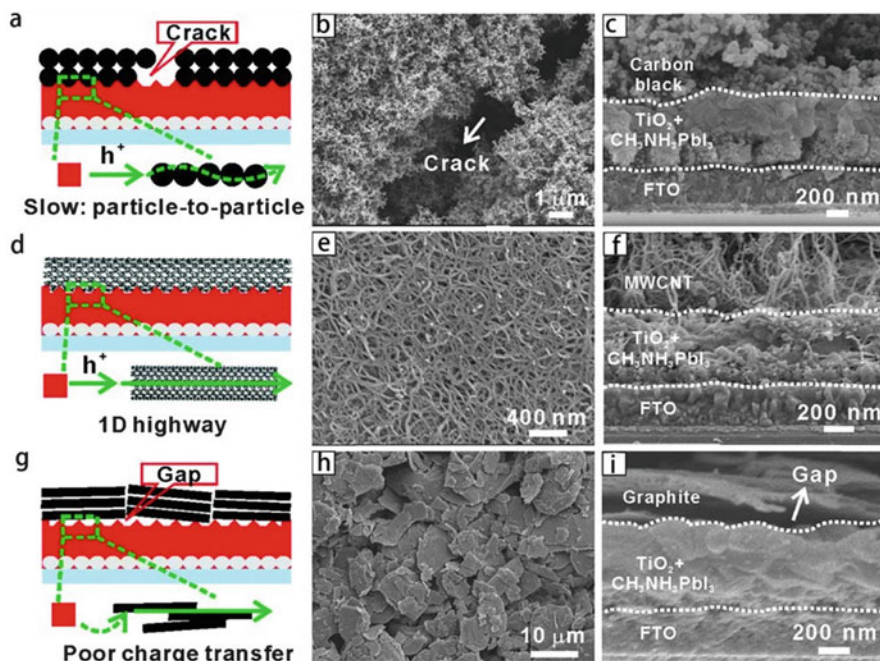


Fig. 7.11 Schematic diagram of device architecture and the hole extraction process of three carbon-based PSCs fabricated with different carbon materials: (a) carbon black, (d) MWCNT, and (g) graphite flake (the green and solid arrows indicate effective and fast transport, while the green and dashed arrows denote poor pathways). (b, e, and h) Top view and (c, f, and i) cross-sectional SEM images of the carbon black, MWCNT, and graphite-based PSC. The dashed lines in c, f, and i represent the interface of FTO/TiO₂ and CH₃NH₃PbI₃/C, respectively. (Reproduced with permission from Ref. [203]. Copyright (2015), Royal Society of Chemistry)

doping was demonstrated to enable enhanced hole extraction and transport by increasing work function, carrier concentration, and conductivity of CNTs, improving the PCE from 10.70% to 14.60%. By further introducing a thin layer of insulating Al₂O₃ on the mesoporous TiO₂ film as a physical barrier to substantially reduce the charge losses, the PCE was further pushed to 15.23%, and the resultant device also showed good long-term stability.

Carbon nanotubes can also be made to paste ink, which can be deposited with a printing technique to avoid energy-consuming vacuum deposition. Gopi et al. [209] first employed a doctor blading coated CNTs electrode as a counter electrode for HTM-free mesoscopic normal structured PSCs. By optimizing the processing method to improve the charge collection, their devices gave a PCE of 7.83%. Their high-vacuum-free deposition process in air simplifies the processing and lowers the threshold of both scientific research and industrial production of PSCs. Besides, CNTs can be also used as a counter electrode in a flexible fiber structure PSCs. For example, Qiu et al. [210] fabricated flexible fiber structured PSCs by continuously winding an aligned multi-walled CNTs sheet electrode onto a fiber

electrode and obtained PCE of 3.3%. Their fiber-like PSCs remained 95% of initial PCE after 50 cycles bending. By controlling perovskite deposition and optimizing charge transport layer, they further improved the PCE of fiber-like PSCs to 7.1% [211]. They also demonstrated PSCs fibers and fabrics twisted in three dimensions without obvious damage to the structure [212]. Their results indicated that fiber-like PSCs may be woven into electronic textiles for large-scale application by well-developed textile technologies (cf. Table 7.4).

7.2.3 Conductive Carbon Electrode

Carbon black can be easily obtained by burning carbonaceous materials such as coal, natural gas, and petroleum oil. Graphite can be obtained from natural graphite. Comparing with graphene CNTs, carbon black and graphite are abundantly available, very low-cost electrode materials. In general, carbon black is existed in the form of nanoparticles with large surface area, enabling good electrochemical properties. In graphite, the layered planar structure with honeycomb lattice is bonded in sp^2 configuration with only three of the four potential binding sites of each carbon atom. The fourth electron is free to migrate in the plane, making graphite electrically conductive. In general, carbon black and graphite are mixed together with polymer or other additives to form conductive paste or ink, in which the graphite, typically tens of microns in length, provides excellent lateral conductivity, the carbon black particles with side of a few tens of nanometers act as conducting bridges between graphite, and the polymer or additive are used as bonder. This carbon black/graphite composite provides an excellent conductive matrix for high conductivity and excellent electric-chemical properties. Moreover, this kind of electrode can be deposited by a simple printing method, including doctor blading, screen printing, and roll to roll printing, which makes it possible to fabricate fully printable PSCs. In addition, chemical inertness, excellent stability, and hydrophobicity of carbon black and graphite make this kind of electrode to be promising for stable PSCs.

In 1996, Kay et al. [213, 214] firstly reported a new monolithic dye-sensitized solar cells based on cheap graphite/carbon black electrode, in which graphite was used to increase the lateral conductivity and carbon black was used to enhance the electrolyte regeneration and electric contact, and sometimes little amount of oxide, such as ZrO_2 , a binder to enhance the mechanical property of the electrode. Such electrode usually requires high-temperature annealing (400~500 °C) to remove the organic compounds, such as hydroxypropyl cellulose, and create mesoporous pores for the filling of an absorber. Here we denote such a carbon electrode as a high-temperature carbon electrode. Based on the above monolithic structure, Ku et al. [11] first reported printable carbon black/graphite electrode-based PSCs with configuration of FTO/c-TiO₂/-TiO₂/m-ZrO₂/m-carbon (CH₃NH₃PbI₃), where triple mesoporous layers were deposited by screen printing method, and the perovskite were filled in the mesoporous scaffold by drop casting perovskite precursor on the top of carbon layer. In this HTM-free device, the insulated ZrO₂ layer cannot transport charge and acted as a spacer to separate TiO₂ and carbon to prevent short circuit, and

Table 7.4 Summary of the device performance of perovskite solar cells with carbon nanotubes counter electrode

Perovskites	Bottom electrode	Counter electrode	Structure	V _{OC} (V)	J _{SC} (mA/cm ²)	FF	PCE (%)	Ref
MAPb (I _{1-x} Cl _x) ₃	FTO	CNTs	Normal mesoscopic (TiO ₂) HTM-free	0.86	16.7	0.44	6.29	[202]
			Normal mesoscopic (TiO ₂)	1.00	18.1	0.55	9.90	
MAPbI ₃	FTO	CNTs	Normal mesoscopic (TiO ₂) HTM-free	0.88	18.80	0.80	12.67	[203]
MAPbI ₃	PEN/ITO	CNTs	Normal mesoscopic (TiO ₂) HTM-free	0.91	15.9	0.656	9.49	[204]
MAPbI ₃	FTO	CNTs	Normal mesoscopic (TiO ₂ /Al ₂ O ₃) HTM-free	0.849	14.91	0.67	8.65	[205]
		Iodine modified CNTs		0.853	17.22	0.71	10.54	
MAPbI ₃	Ti	CNTs+spiro-OMeTAD	Normal mesoscopic (TiO ₂ nano tubes)	0.99	14.36	0.68	8.31 ^a	[206]
MAPbI ₃	FTO	CNTs	Normal mesoscopic (TiO ₂), HTM-free	0.82	20.49	0.63	10.59	[207]
		CNTs@P3HT	Normal mesoscopic (TiO ₂)	0.91	22.70	0.65	13.43	
MAPbI ₃	FTO	CNTs	Normal mesoscopic (TiO ₂), HTM-free	0.84	17.94	0.71	10.70	[208]
MAPbI ₃	FTO	Boron doping CNTs	Normal mesoscopic (TiO ₂), HTM-free	0.90	21.35	0.76	14.60	
MAPbI ₃	FTO	Noron doping CNTs	Normal mesoscopic (TiO ₂)	0.92	21.50	0.77	15.23	
MAPbI ₃	FTO	CNTs	Normal	0.703	18.54	0.600	7.83	[209]

(continued)

Table 7.4 (continued)

Perovskites	Bottom electrode	Counter electrode	Structure	V_{OC} (V)	J_{SC} (mA/cm ²)	FF	PCE (%)	Ref
			Mesoscopic (TiO ₂)					
MAPbI ₃	Stainless	CNTs sheet	Normal	0.644	10.2	0.487	3.3	[210]
	Steel		Mesoscopic (TiO ₂), fiber-like cell					
MAPbI ₃	Titanium	CNTs	Normal	0.874	14.5	0.56	7.1	[211]
	Wire	Sheet/silver	Mesoscopic (TiO ₂), fiber-like cell					

^aIlluminated from top counter electrode side

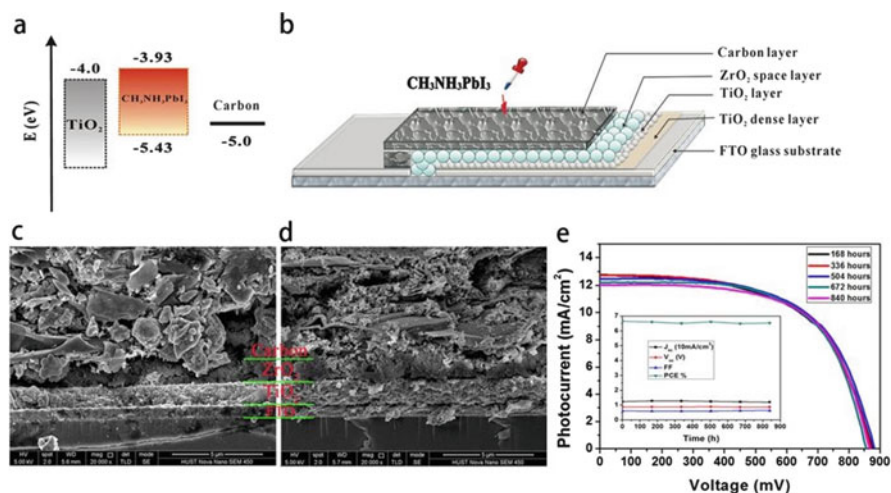


Fig. 7.12 (a) Energy levels and (b) schematic structure of printable carbon electrode-based HTM-free PSC. (c) Spheroidal graphite and (d) flaky graphite-based printable carbon electrode-based HTM-free PSC. (e) Long-term stability at room temperature in the dark printable carbon electrode-based HTM-free PSC. Inset: the changing characters of the device in 840 h after been fabricated. (Reproduced with permission from Ref. [11]. Copyright (2013) Nature Publishing Group)

perovskite itself in the mesoporous pores acted as conductor to transport photo-generated charge, the carbon with a work function of 5.0 eV can exact holes from perovskite as shown in Fig. 7.12. They compared two carbon electrodes with carbon black/flaky graphite and carbon black/spheroidal graphite composites, respectively. Since the carbon counter electrode is the pathway for the infiltration of perovskite precursors, its structure plays an important role in the device performance in such carbon electrode-based PSCs. The loose structure and better conductivity of

spheroidal graphite is favor of pore-filling of perovskite in the mesoporous layers. A better device performance (PCE of 6.64%) was obtained for the carbon black/spheroidal graphite device. Most encouragingly, this kind of device maintained PCE of 6.5% after 840 h storage in dry air at room temperature without encapsulation, which suggests the superior stability of carbon electrode PSCs. The same group also reported the employment of highly ordered mesoporous carbon with well-connected frameworks as a counter electrode in such HTM-free PSCs [215]. With lower charge resistance, the highly ordered mesoporous carbon-based device obtained a PCE of 7.02%. Besides, the thickness of mesoporous carbon electrode will affect the crystallization of perovskite; an over-thick carbon layer will restrict the diffusion perovskite precursor from the top carbon layer to the bottom layers, resulting in incomplete pore filling, while an over-thin carbon layer will decrease the FF of the device owing to the decrease of conductivity [216]. By optimizing the thickness of carbon electrode, device with an about 9 μm carbon layer gave the highest PCE of 11.64% [216]. The authors also investigated the influence of graphite diameters on device performance and found that 8 μm graphite-based carbon layer had a larger average pore size, a smaller square resistance, and a higher PCE [216]. Later, ultrathin graphite was also being incorporated into the high-temperature carbon electrode to increase the specific surface area of the carbon layer without sacrificing the conductivity [217]. The large specific surface area facilitated the hole collection from the perovskite to carbon layer, as well as the penetration of perovskite precursor solution in the carbon layer, resulting in improvement PCE from 12.63% to 14.07%. The charge collection at the counter electrode interface of the HTM-free device can significantly affect final device performance. Li et al. [218] found that the charge lifetime at the counter electrode interface is in the range of microsecond, which is much faster than that of titania/methylammonium lead iodide ($\text{TiO}_2/\text{CH}_3\text{NH}_3\text{PbI}_3$) interface with recombination lifetime at millisecond scale for the counter electrode-based HTM-free PSCs. Thus, the counter electrode interface dominates the charge recombination in such a device. By introducing single-walled carbon nanotube to tune the work function of the carbon layer, the charge collection was significantly enhanced, and charge recombination was suppressed, delivering a promising PCE of 14.7% [218]. In addition, the binder also plays an important role in such high-temperature electrode. Xu et al. [219] used TiO_2 nanoparticles as binders in a highly conductive carbon electrode for HTM-free PSCs. They found that carbon films were condensed by a dehydration reaction between surface hydroxyls from both TiO_2 nanoparticles and carbon particles, which is beneficial for adhesion ability and conductivity of carbon film, and the formation and filling properties of perovskite. The sheet resistance can be reduced from 10 to 2.74 $\Omega \text{sq.}^{-1}$ when annealed at a relatively lower temperature of 350 $^\circ\text{C}$, resulting in an improvement of averaged PCEs from 5.40 (± 1.32) % to 9.21(± 1.04) % and 11.07% (champion).

Apart from optimizing the counter electrode, the device performance of the high-temperature carbon electrode-based HTM-free PSCs can be also optimized by tuning TiO_2 layer [220–223] or spacer layer [224, 225], TiO_2 /perovskite interfacial engineering [226], solvent engineering to improve perovskite quality

[227, 228], and composition engineering to enhance device performance [224, 229–233], respectively. An impressive breakthrough in device stability for the counter electrode-based HTM-free PSCs was achieved by incorporating 5-ammoniumvaleric acid (5-AVA) into methylammonium lead iodide ($\text{CH}_3\text{NH}_3\text{PbI}_3$), which significantly improved pore-filling and perovskite quality [234]. Such device achieved a certified PCE of 12.8% with over 1000 h stability in ambient air under full sunlight [234] and also excellent stability in the hot desert climate and indoor long-term light soaking as well as heat exposure during three months at 80–85 °C [235]. Besides of the excellent stability and compatibility of a fully printable method of such carbon electrode-based HTM-free PSCs, the demonstration of automation perovskite deposition method [78, 236] and solar modules [237, 238] suggest the promising potential for commercializing of such devices.

The carbon electrode usually does not exhibit good charge selectivity, the TiO_2 /methylammonium lead iodide ($\text{TiO}_2/\text{CH}_3\text{NH}_3\text{PbI}_3$) heterojunction is the only efficient charge separation interface in HTM-free PSCs, the inefficient charge collection at the counter electrode interface leads to serious charge recombination. To solve this problem, Liu et al. introduced a nickel(II) oxide (NiO) layer as hole transport materials into high temperature carbon electrode-based PSCs and exploited two device structures with configuration of fluorine-doped tin oxide/compact- TiO_2 /mesoporous TiO_2 /mesoporous nickel(II) oxide/mesoporous carbon methylammonium lead iodide [FTO/c- TiO_2 /m- TiO_2 /m-NiO/m-carbon($\text{CH}_3\text{NH}_3\text{PbI}_3$)] ([n-type/p-type] n/p structure, as shown in Fig. 7.13c) [239] and fluorine-doped tin oxide/compact- TiO_2 /mesoporous TiO_2 /mesoporous zirconium/nickel(II) oxide/mesoporous carbon methylammonium lead iodide [FTO/c- TiO_2 /m- TiO_2 /m- ZrO_2 /m-NiO/m-carbon($\text{CH}_3\text{NH}_3\text{PbI}_3$)] [240, 241] ([n-type/undoped intrinsic/p-type semiconductor] n/i/p structure, as shown in Fig. 7.13d). They proved that the introduction of NiO can facilitate hole extraction at the counter electrode interface and prolong the charge recombination time, obtained much improved V_{oc} and a PCE of 11% for n/p device [239]. With an additional zirconium(IV) oxide (ZrO_2) layer between the TiO_2 layer and NiO layer, the charge recombination can be further suppressed, leading to much-improved PCE to 14.9% [240]. Similarly, carbon electrode-based [negative-type/positive-type semiconductor] n/p and [n-type/undoped intrinsic semiconductor/p-type semiconductor] n/i/p PSCs also exhibited good stability due to the thick active layer and also the hydrophobicity of carbon electrode as above HTM-free device.

Although high-temperature carbon electrode-based PSCs have shown excellent device stability and promising device performance, all the mesoporous layers require high energy consuming high-temperature annealing, which may significantly increase the energy pay-back time of the PSCs and also make this kind of device not compatible with the flexible substrate. To solve this problem, a high-temperature carbon electrode can be replaced by a low-temperature carbon electrode, while the processing is different from the high-temperature device. Similar to regular PSCs, carbon electrode can be also deposited as top counter electrode after formation of perovskite. In this case, the high temperature is no longer needed, and the carbon used is denoted as low-temperature carbon.

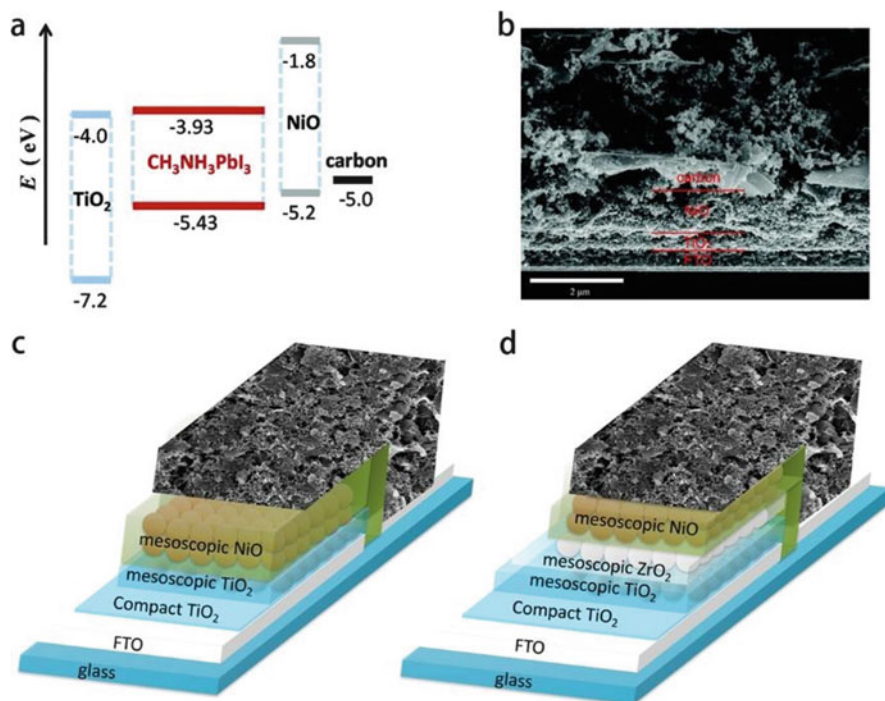


Fig. 7.13 (a) Energy levels, (b) cross-sectional SEM image, and (c) schematic structure of the TiO₂/NiO/carbon(CH₃NH₃PbI₃) PSC. (d) Schematic structure of the TiO₂/ZrO₂/NiO/carbon (CH₃NH₃PbI₃) PSC. (Reproduced with permission from Ref. [239]. Copyright (2014), Royal Society of Chemistry)

Zhang et al. [242] and Zhou et al. [243] reported doctor blading coated low-temperature commercial carbon as a counter electrode for HTM-free PSCs with the configuration of FTO/c-TiO₂/m-TiO₂/CH₃NH₃PbI₃/carbon as shown in Fig. 7.14 and achieved PCE of 8.31% and 9.08%, respectively. In their device, perovskite was deposited on the TiO₂ layer and carbon was deposited after the formation of perovskite. High-temperature annealing of the carbon is no longer needed, but the carbon ink should not contain a component that can destroy the perovskite layer. Thus, Zhou et al. [243] removed the solvent in the commercial carbon ink and used chlorobenzene as a dispersing agent to enable the coating process. Besides, the perovskite layer should be compact enough to act as a spacer layer to separate the carbon layer and TiO₂ layer to avoid short circuit.

As shown in Fig. 7.15, Wei et al. [244] used candle soot as a carbon source to fabricated carbon electrode for HTM-free PSCs. In their devices, a predeposited PbI₂ layer acted as a spacer layer to separate the TiO₂ and the carbon layer and the PbI₂ layer transformed to the perovskite layer at a later stage via a two-step method. They found that the candle soot-based carbon electrode exhibited good hole extraction and electron blocking properties by forming a Schottky junction as shown in Fig. 7.15c.

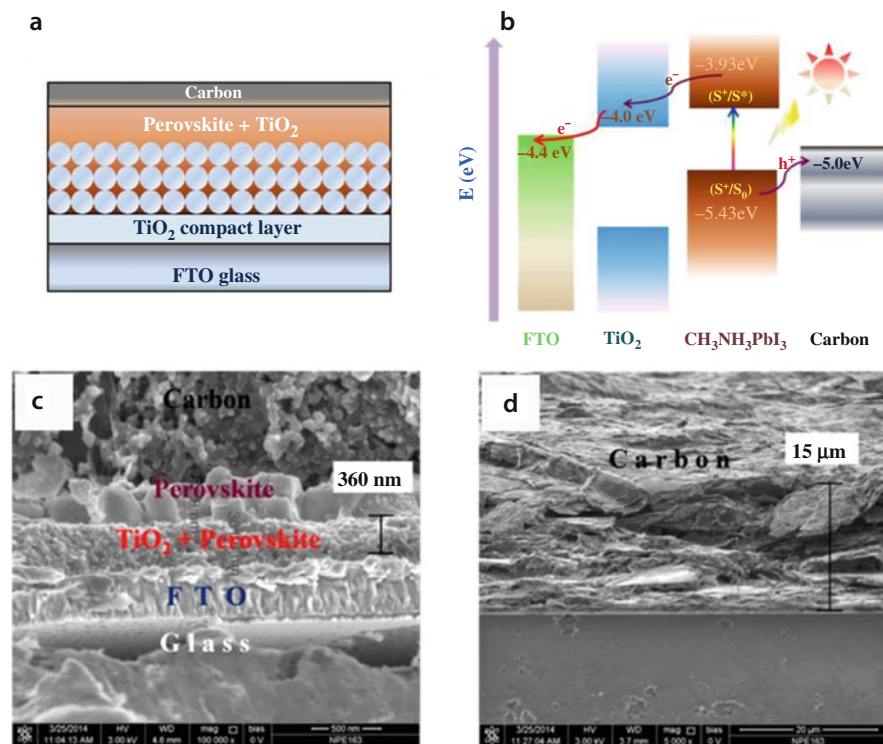


Fig. 7.14 (a) Device architecture and (b) energy level diagram of low-temperature carbon electrode-based HTM-free PSC. (c) and (d) Cross-section image of the whole device. (Reproduced with permission from Ref. [242]. Copyright (2014) American Chemical Society)

By optimizing the fabrication process, the interface contact of $\text{CH}_3\text{NH}_3\text{PbI}_3$ /carbon can be significantly enhanced as shown in Fig. 7.15d and e. As a result, their roll coated carbon electrode-based HTM-free PSCs gave a PCE of 11.02%. Also, optimizing carbon electrode to improve charge transport in the carbon and tuning the perovskite/carbon interface to improve charge extraction from perovskite to carbon were carried out to further improve device performance.

Yang et al. [245] reported an all-carbon flexible counter electrode consisting of a mesoscopic carbon layer and another highly conductive industrial flexible graphite sheet as a second extraction layer for HTM-free PSCs. By optimizing the size and morphology of carbon materials to enable good electrical contact at the $\text{CH}_3\text{NH}_3\text{PbI}_3$ /carbon interface, their devices gave a PCE of 10.2%. Wei et al. [77] demonstrated an inkjet-printed carbon electrode-based planar PSC. To achieve a good electric contact at the $\text{CH}_3\text{NH}_3\text{PbI}_3$ /carbon interface, they developed an inkjet printing technique to deposit carbon black + $\text{CH}_3\text{NH}_3\text{I}$ ink on the top of predeposited lead (II) iodide (PbI_2) to transform PbI_2 to methylammonium lead iodide ($\text{CH}_3\text{NH}_3\text{PbI}_3$) in situ and created an interpenetrating interface between $\text{CH}_3\text{NH}_3\text{PbI}_3$ and carbon electrode to suppress charge recombination and enhance

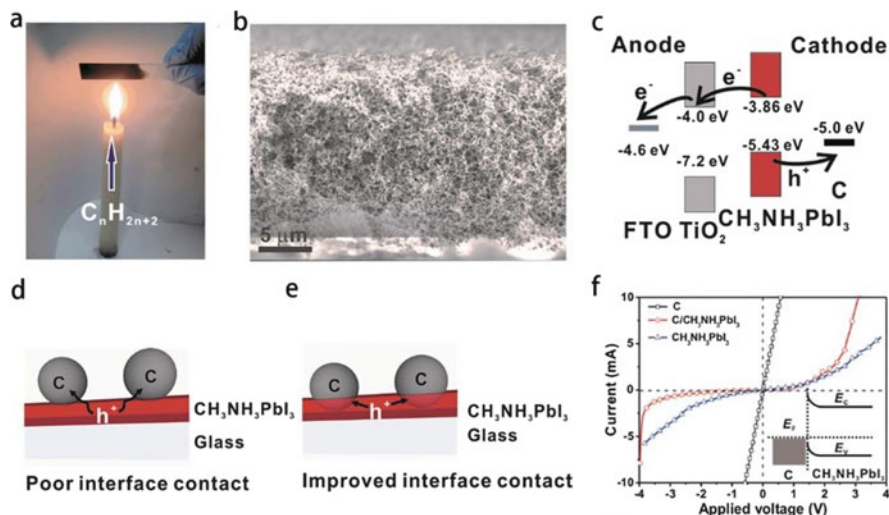


Fig. 7.15 (a) A digital photograph portraying the flame deposition of candle soot. (b) Cross-sectional SEM image of the sponge-like candle soot film. (c) Energy band diagram of candle soot electrode-based HTM-free PSC. Schematic structure of the counter electrode with poor (d) and improved (e) interface contact of carbon and CH₃NH₃PbI₃. (f) J–V curves of FTO/Carbon/FTO, FTO/CH₃NH₃PbI₃/FTO, and FTO/Carbon/CH₃NH₃PbI₃/FTO clamping devices (the inset is a schematic equilibrium energy diagram of the Schottky junction of Carbon/CH₃NH₃PbI₃). (Reproduced with permission from Ref. [244]. Copyright (2014), Royal Society of Chemistry)

charge collection. The waterproof properties of the counter electrode are beneficial for the long-term stability of PSCs. Wei et al. [246] also reported an HTM-free PSC based on a carbon + epoxy/Ag electrode and obtained a PCE of 10.99%. In their device, the epoxy was introduced into a commercialized carbon ink to achieve better waterproof properties and interface electrical contact. An additional hydrophobic silver (Ag) paste layer was deposited on the top blade coated carbon layer via brush coating to further enhance the waterproof property and conductivity of the counter electrode. As a result, their device can be directly immersed in water and no performance degradation occurred at the first 80 min. Moreover, nearly no device performance degradation was observed under high humidity and 50 °C thermal stressing condition for 250 h. Yue et al. [247] also optimized the ratio of carbon black particles and graphite flakes in low-temperature carbon electrode to modulate the connection of carbon black and graphite flakes, and also the contact between the counter electrode and perovskite layer, achieving a PCE of 7.29%. Liu et al. [248] also reported a low-temperature carbon electrode to consist of graphite flakes, carbon black powder, and nano-graphite powder for HTM-free PSCs. The size and ration of carbon material also were found to affect the conductivity of the carbon electrode and electric contact at the CH₃NH₃PbI₃/carbon interface. Their relevant devices gave a PCE of 6.88% and excellent stability. Chen et al. [249] used boron and phosphorus co-doped carbon with different work function and

conductivity as the counter electrode in HTM-free PSCs, delivering a PCE of 6.78%, which is higher than those of pristine carbon (3.72%), phosphorus-doped carbon (5.39%), and boron-doped carbon (5.20%)-based PSCs. Cheng et al. [250] introduced multi-walled CNTs into the perovskite layer to enhance the electric contact of perovskite and carbon electrode in carbon electrode based HTM-free PSCs. They proved that CNTs can act as charge transport high way between individual perovskite nanoparticles and facilitate charge collection at the counter electrode interface, leading to a $\sim 15\%$ improvement of averaged PCE (11.6%). Yu et al. [251] reported a bi-layer back contact consisting of a carbon/ $\text{CH}_3\text{NH}_3\text{I}$ composite layer and a compact hydrophobic carbon layer as a counter electrode for HTM-free PSCs. The cell showed a final PCE of 13.6% from an initial PCE of 11.3% after thermal stress, and the encapsulated cell retained 90% of the initial PCE after water exposure and under thermal stress at 150 °C for half an hour.

Besides above described low-temperature carbon electrode processed with blade coating or other printing methods, low-temperature carbon electrode can be also processed with a transfer method. A free-standing thermoplastic carbon film with good flexibility and conductivity was also being developed and hot pressed onto the perovskite layer as a counter electrode for HTM-free PSCs [252]. By optimizing the composition of carbon films and hot-pressing pressure, a PCE of 13.53% was achieved. Low-cost carbon cloth was applied in PSCs with a configuration of FTO/c-TiO₂/m-TiO₂/perovskite/spiro-OMeTAD/carbon, giving champion stabilized PCE of 14.8% (PCE of 15.29% from J-V curve) and good stability [253]. Apart from optimizing the counter electrode, the device performance and stability of low-temperature carbon electrode-based PSCs can be also optimized by tuning TiO₂ layer [254–258], improving perovskite quality [259–263], and composition engineering [264–266], respectively. Furthermore, the introduction of a hole transport layer between perovskite and carbon electrode can also improve the device performance and enhance device stability of low-temperature carbon electrode-based PSCs [267–269].

The carbon materials electrode-based PSCs has attracted much attention due to their outstanding advantages such as low-cost, vacuum-free, long-term stability, easy fabrication process, compatibility, etc. However, some issues are still associated with carbon materials electrode-based PSCs. The first issue is their lower efficiency when compared with high-efficiency metal thin-film electrode-based PSC. This is because of that most of the carbon electrode-based PSCs adopt a HTM-free device structure, which leads to different working mechanism from a regular p-i-n structure. In PSCs, the V_{oc} is determined by the difference of electron quasi-Fermi levels (E_{fn}) and the hole quasi-Fermi levels (E_{fp}) [160]. In the p-i-n device, E_{fn} is determined by the interaction of electron transport medium (ETM) and perovskite, and E_{fp} is determined by the interaction of HTM [160]. Both perovskite/ETM interface and the perovskite/HTM interface exhibit good charge selectivity for efficient charge separation, which leads to V_{oc} range from 1.0 to 1.2 V. However, in HTM-free device, the absence of HTM leads to inefficient charge separation at the counter electrode interface, resulting in fast charge recombination at this interface with nearly three orders of magnitude reduction in charge recombination lifetime [218], and lower V_{oc}

range from 0.8 to 1.0 V [160]. In terms of counter electrode, the inferior electric contact at the counter electrode interface in carbon electrode PSCs can also result in serious charge recombination and low V_{oc} . Thus, it is necessary to modulate the counter electrode interface of carbon electrode-based PSCs to improve the V_{oc} aiming at high efficiency. So far, several strategies have been made to improve the V_{oc} of carbon electrode-based PSCs, including in developing p-i-n like structure device by introducing another HTM layer [239, 241, 269], using carbon material with lower Fermi level [218, 270], optimizing the electric contact at the counter electrode interface [250]. In terms of the J_{sc} , regular PSCs device with metal electrode usually gave a J_{sc} at the range of 21–23 mA/cm². However, the J_{sc} of carbon electrode-based PSCs is at the range 17–20 mA/cm². This is due to the fact that the mirror-like metal electrode can reflect the light enable a secondary absorption of the light by perovskite with a thickness of 400–600 nm [271]. While the carbon electrode cannot reflect light, a thicker perovskite with thickness over 1 μ m is required for complete light absorption [160]. Thus, it requires efficient charge transportation and collection within the carbon-based PSCs with such thick perovskite layer. Furthermore, the relative lower conductivity of the carbon electrode and inferior electric contact at the counter electrode interface result in lower FF at range from 0.6 to 0.7, when compared with metal electrode PSCs possessing FF at range from 0.75 to 0.8. When comes to large area PSCs module, the conductivity of the electrode significantly affects the total sheet resistance (cf. Table 7.5). Therefore, it is desirable to develop a carbon electrode with higher conductivity combining good electric contact with the bottom layer to improve FF.

In view of processing, high-temperature carbon electrode-based PSCs require high energy consuming high-temperature annealing, which may significantly increase the energy pay-back time of the PSCs and also make this kind of device not compatible with the flexible substrate. For low-temperature carbon electrode PSCs, the low-temperature carbon ink may damage the bottom layer during the deposition process. Thus, a polar solvent in commercial carbon ink should be removed before the deposition [243], and binder and additive should also be carefully selected to avoid the possibility of damaging the bottom layer.

7.2.4 Conductive Metal Oxides Electrode

Transparent conducting oxides (TCOs) are the most commonly used materials for a bottom transparent conductive electrode in an electronic device and photovoltaic device due to their excellent transparency and conductivity. TCOs materials can be also used as a top counter electrode, especially in transparent solar cells or tandem solar cell. When used as a top electrode, the TCOs such as indium tin oxide (ITO) is usually deposited by magnetron sputtering. However, the high-energy sputtered particles and high temperatures during deposition and post-annealing may damage the perovskite layer and the organic charge transport layers. To solve this problem, Löper et al. [272] first reported a four-terminal crystalline silicon (c-Si)/PSC tandem solar cells with molybdenum n-oxide/ indium tin oxide (MoO_x /ITO) electrode

Table 7.5 Summary of the device performance of perovskite solar cells with conductive carbon counter electrode

Perovskites	Bottom electrode	Counter electrode	Structure	V _{OC} (V)	J _{SC} (mA/cm ²)	FF	PCE (%)	Ref.
MAPbI ₃	FTO	High-temperature carbon black/graphite	Normal mesoscopic (TiO ₂ /ZrO ₂ /carbon HTM-free)	0.878	12.4	0.61	6.64	[11]
MAPbI ₃	FTO	High-temperature carbon black/graphite/carbon nano tube	Normal mesoscopic (TiO ₂ /Al ₂ O ₃ /carbon HTM-free)	1.01	21.26	0.69	14.70	[218]
(5-AVA) _x (MA) _{1-x} PbI ₃	FTO	High-temperature carbon black/graphite	Normal mesoscopic (TiO ₂ /ZrO ₂ /carbon HTM-free)	0.858	22.8	0.66	12.84*	[234]
MAPbI ₃	FTO	High-temperature carbon black/graphite	Normal mesoscopic (TiO ₂ /ZrO ₂ /carbon HTM-free)	0.818	16.4	0.60	8.2	[239]
			Normal mesoscopic (TiO ₂ /NiO/carbon p/n)	0.890	18.2	0.71	11.4	
MAPbI ₃	FTO	High-temperature carbon black/graphite	Normal mesoscopic (TiO ₂ /ZrO ₂ /NiO/carbon p/i/n)	0.917	21.36	0.76	14.9	[240]
MAPbI ₃	FTO	Low-temperature carbon	Normal mesoscopic (TiO ₂ , HTM-free)	0.90	16.78	0.55	8.31	[242]
MAPbI ₃	FTO	Low-temperature carbon	Normal mesoscopic (TiO ₂ , HTM-free)	0.80	21.02	0.54	9.08	[243]
MAPbI ₃	FTO	Sponge-like candle soot	Normal mesoscopic (TiO ₂ , HTM-free)	0.88	17.00	0.72	11.02	[244]
MAPbI ₃	FTO	Low-temperature carbon	Normal mesoscopic (TiO ₂ , HTM-free)	0.9107	18.15	0.649	10.73	[245]
MAPbI ₃	FTO	Low-temperature carbon +MAI	Normal mesoscopic (TiO ₂ , HTM-free)	0.95	17.20	0.71	11.60	[77]

(continued)

Table 7.5 (continued)

Perovskites	Bottom electrode	Counter electrode	Structure	V _{OC} (V)	J _{SC} (mA/cm ²)	FF	PCE (%)	Ref.
MAPbI ₃	FTO	Low-temperature carbon +epoxy/Ag	Normal mesoscopic (TiO ₂ , HTM-free)	0.97	19.20	0.59	10.99	[246]
MAPbI ₃	FTO	Free-standing carbon + Al foil	Normal mesoscopic (TiO ₂ , HTM-free)	1.002	21.30	0.634	13.53	[252]
Cs _{0.05} (MA _{0.17} F A _{0.83}) _{0.95} Pb(I _{0.83} Br _{0.17}) ₃	FTO	Carbon cloth	Normal mesoscopic (TiO ₂)	1.12	20.42	0.670	15.29	[253]

^aCertified efficiency

possessing a series resistance of 19.6 Ω sq.⁻¹ as top transparent electrode for the normal structured mesoscopic PSCs top cell as shown in Fig. 7.16a, where the MoO_x layer not only acted as a buffer layer to protect the bottom spiro-OMeTAD layer but also a hole extraction layer to help the hole collection at the counter electrode interface. Their top PSCs with ITO counter electrode gave a PCE of 6.2%, and the final tandem solar cells gave a PCE of 13.4%.

Several studies on metal oxide as an electrode for PSCs have been reported. Bush et al. [273] demonstrated the use of solution-processed aluminum-doped zinc oxide (AZO) nanoparticles as a buffer layer with both efficient hole-blocking properties and bottom PCBM protective capability beneath the sputtered ITO layer for transparent inverted planar PSC. Their ITO layer with a thickness of 500 nm on the top of the AZO films achieved a sheet resistance of 9.9 Ω sq.⁻¹ after annealing at 100 °C. Their four-terminal [crystalline] c-Si/PSC tandem solar cells achieved PCE of 18.0%. An ITO counter electrode-based semitransparent PSC with an efficiency of 12% and near-infrared transmittance of >80% was demonstrated by Duong et al. [274] Their four-terminal perovskite/silicon tandem solar cells have an efficiency of 20.1%. Another promising conductive electrode is indium zinc oxide (IZO). An IZO top transparent electrode-based four-terminal c-Si/PSC tandem solar cells with or without MoO_x buffer layer as shown in Figs. 7.16b and c exhibited nearly identical efficiency approaching 18.2% [275]. To minimize damage to the underlying layers during the TCO deposition, a soft zinc oxide/aluminum (ZnO: Al) sputter process was developed by Kranz et al. [276] for copper indium gallium selenide (CIGS)/perovskite solar cell (PSC) four terminal tandem solar cells. The semitransparent PSCs achieved PCE of 12.1% and an AVT of 71% at a wavelength range from 800 and 1000 nm and the CIGS/PSC four terminal tandem solar cells achieved PCE of 19.5% [142]. McMeekin et al. [277] developed a wide band gap perovskite formamidinium (FA) cesium-methyl ammonium mixed-cation lead iodide/bromide [FA_{0.83}Cs_{0.17}Pb(I_{0.6}Br_{0.4})₃] (~1.74 eV) with the solution-processed indium tin oxide (ITO) nanoparticles as a buffer between the spiro-OMeTAD and the ITO. A PCE of 15.1% and a stabilized PCE of 12.5% were obtained. Yang et al. [278] used a MAPbI₃-based cell with configuration of indium tin oxide/nickel(II) oxide/methylammonium lead iodide [6,6]-Phenyl-C61-butyric acid methyl

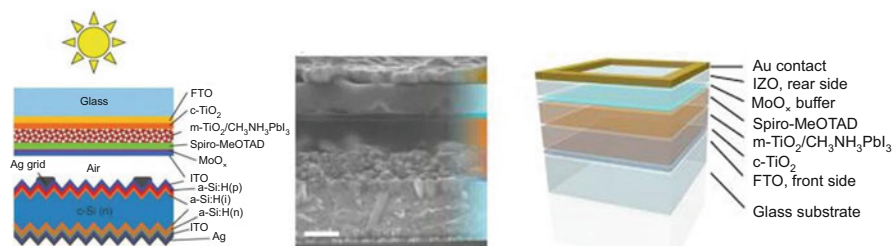


Fig. 7.16 (a) Schematic of the mechanically stacked four-terminal tandem consist of an a-Si: H/c-Si bottom cell and a PSC top cell with a metal-free MoO_x/ITO transparent electrode. (Reproduced with permission from Ref. [272]. Copyright (2014), Royal Society of Chemistry). (b) SEM cross-sectional image (scale bar is 250 nm) and (c) schematic illustration of a PSC with an IZO-based transparent counter electrode and Au contact. (Reproduced with permission from Ref. [275]. Copyright (2015), Elsevier)

ester/fullerene/indium tin oxide [ITO/NiO_x/MAPbI₃/PCBM/C60/ITO] as top cell and a low-bandgap (1.33 eV) methylammonium /formamidinium/lead /tin iodide [MA_{0.5}FA_{0.5}Pb_{0.75}Sn_{0.25}I₃]-based cell with configuration of indium tin oxide/poly(3,4-ethylenedioxythiophene)/polystyrene sulfonate/methylammonium/formamidinium/lead/tin iodide/[6,6]-Phenyl-C61-butyric acid methyl ester/fullerene/silver [ITO/PEDOT:PSS/MA_{0.5}FA_{0.5}Pb_{0.75}Sn_{0.25}I₃/PCBM/C60/Ag] as bottom cell. Their resultant four-terminal all-perovskite tandem solar cell achieved efficiency of 19.08%. By carefully light-harvesting management, Eperon et al. [279] also stacked an infrared-absorbing FA_{0.75}Cs_{0.25}Sn_{0.5}Pb_{0.5}I₃ perovskite (1.2 eV)-based cell with configuration of ITO/PEDOT:PSS/perovskite/C60/[2,9-dimethyl-4,7-diphenyl-1,10-phenanthroline] BCP/Ag and a wider-band gap FA_{0.83}Cs_{0.17}Pb(I_{0.83}Br_{0.17})₃ perovskite (1.6 eV)-based semitransparent cell with configuration of ITO/NiO_x/perovskite/PCBM/SnO₂/ZnO/ITO to form a four terminal perovskite/perovskite tandem solar cell, and achieved stabilized efficiency of 20.3%. Fan et al. [280] deposited an hydrogen-doped indium oxide (In₂O₃: H) layer with a thickness of 149 nm via a room-temperature radio-frequency magnetron sputtering; the resultant electrode without post-annealing can deliver a reasonably high mobility of 51.3 cm² V⁻¹ s⁻¹ and a sheet resistance of 25.7 Ω sq.⁻¹. When used as transparent electrodes for a semitransparent PSC featuring, configuration of FTO/ZnO/PCBM/CH₃NH₃PbI₃/spiro-OMeTAD/MoO₃/In₂O₃: H, the relevant device gave a steady-state efficiency of 14.2% along with 72% AVT in the near-infrared region. Moreover, they stacked the semitransparent PSC with a low-bandgap CIGS cell to construct a four-terminal tandem solar cell and demonstrated an efficiency of 20.5%.

Transparent conducting oxides (TCOs) are widely used as the top transparent electrode in monolithic, two-terminal tandem solar cells. Albrecht et al. [281] reported a two-terminal silicon/perovskite tandem solar cell with a planar perovskite top cell and a (p,i)a-Si:H/(n)c-Si heterojunction bottom cell, featuring a configuration of LiF/ITO/MoO₃/spiro-OMeTAD/perovskite/SnO₂/ITO/a-Si:H(p⁺)/a-Si:H(i)/c-Si/a-Si:H(i)/a-Si:H(n⁺)/AZO/Ag as shown in Figs. 7.17a and b. “The incident” light was illuminated from the top ITO side, achieving a backward scanned PCE of 19.9%, backward scanned PCE of 19.1%, and a stabilized PCE of 18.1%. Werner

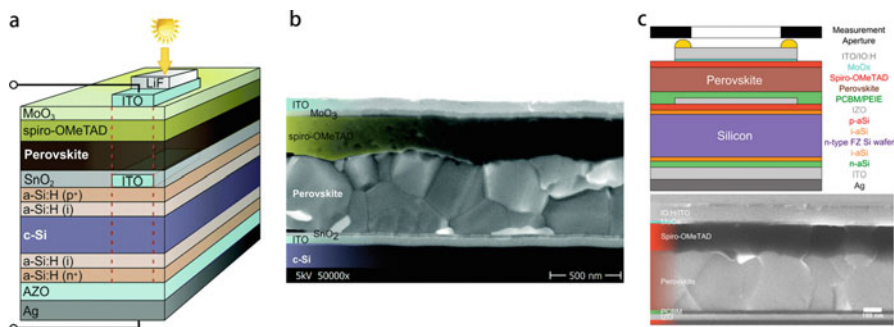


Fig. 7.17 (a) Schematic of the two terminal Si/PSC tandem solar cell with MoO_x/ITO top electrode. The red dashed line indicates the active area. (b) Cross-sectional SEM image of a Si/PSC tandem solar cell with MoO_x/ITO top electrode. (Reproduced with permission from Ref. [281]. Copyright (2015), Royal Society of Chemistry). (c) Schematic and cross-sectional SEM image of the Si/PSC heterojunction tandem solar cell with ITO/IO: H/MoO_x top electrode. (Reproduced with permission from Ref. [282]. Copyright (2016) American Chemical Society)

et al. [282] also reported a two-terminal silicon/perovskite tandem solar cell with a planar perovskite top cell and a (p,i)a-Si:H/(n)c-Si heterojunction bottom cell, featuring a configuration of ITO/[hydrogen-doped iodide oxide] IO:H/MoO_x/spiro-OMeTAD/perovskite/PCBM/PEIE/IZO/a-Si:H(p⁺)/a-Si:H(i)/c-Si/a-Si:H(i)/a-Si:H(n⁺)/AZO/Ag as shown in Fig. 7.17c.

Their tandem cells gave stabilized efficiencies of up to 19.2% with an active size of 1.22 cm² and of up to 21.2% on smaller cells with an active size of 0.17 cm². Perovskite/perovskite tandem solar cells can be also fabricated in a two-terminal tandem cell form. Different from an above-described device fabricated with layer by layer process, Heo et al. [283] laminated an FTO/[thick dense blocking] bi-TiO₂/MAPbBr₃/wet [poly (3-hexylthiophene-2,5-diyl)] P3HT or [poly(triarylamine)] PTAA sub-cell and the PCBM/MAPbI₃/PEDOT: PSS/ITO sub-cell by pressurizing with double clip and subsequent drying. By optimizing the tunnel junction, their tandem solar cells gave a PCE of 10.4%. In the work of Eperon et al. [279] described above, they also fabricated a two terminal perovskite/perovskite tandem solar cell featuring a configuration of ITO/NiO_x/FA_{0.75}Cs_{0.25}Sn_{0.5}Pb_{0.5}I₃/PCBM/SnO₂/ZnO/ITO/PEDOT: PSS/FA_{0.75}Cs_{0.25}Sn_{0.5}Pb_{0.5}I₃/C₆₀/BCP/Ag with FA_{0.75}Cs_{0.25}Sn_{0.5}Pb_{0.5}I₃ perovskite (1.2 eV) and FA_{0.75}Cs_{0.25}Sn_{0.5}Pb_{0.5}I₃ perovskite (1.8 eV), and achieved efficiency of 17.0% with a V_{oc} of 1.65 V.

Although TCOs-based PSC or tandem solar cell gained remarkable achievement, they are also facing some challenges for future large-scale use. Taking ITO for example, the limitation of global indium resources and the high cost of indium is one of the greatest concerns for the boosted demand of ITO for PV device. The high vacuum-based deposition techniques and low ITO resource utilization rate also add to the cost of ITO. In addition, the high-temperature deposition process and the brittle nature of ITO hamper its applications in a flexible device. Aside from the high cost of raw materials and deposition processes, the high-energy processing condition also damages the underlying organic materials without a buffer. Although the

employment of buffer can relieve the damage of underlying organic materials, this can increase the complexity of the processing and cost of the process. Thus, it is desirable to develop an alternative for conductive metal oxides (cf. Table 7.6).

7.2.5 Conductive Polymers Electrode

Conductive polymers are organic polymers that conduct electricity through a large number of delocalized π system. The conductivity and absorption of the polymers can be tuned by modifying their chemical structure, which makes it possible to achieve good conductivity and suitable optical bandgap. When the bandgap is large enough, the conductive polymer is a good candidate for a transparent electrode. The organic nature of the conductive polymer also makes this kind of materials to be of low cost. In addition, conductive polymers can be dispersed in a solvent, which makes them processable with a simple deposition method, such as spin coating, spray coating, etc. PEDOT is one of the most used conductive polymers for a transparent conductive layer in the form of PEDOT: PSS dispersions. Furthermore, PEDOT:PSS also showed very good flexibility, which is suitable for a flexible device. PEDOT: PSS have been used for both the bottom conductive electrode and the top counter electrode. Sun et al. [284] deposited PEDOT: PSS films on rigid glass or flexible PET substrate as a conductive electrode for inverted planar PSCs, and achieved efficiency of 11% for the rigid PSCs and efficiency of 8.6% for the flexible PSCs. Transparent top PEDOT: PSS electrode could be a good candidate for the above-described metal thin film or TCOs counter electrode due to their easy fabrication, high transmittance, and high conductivity and low cost.

Conducting polymers have been used as a counter electrode for PSCs. Jiang et al. [285] first reported PEDOT: PSS as the top electrode of PSCs with the structure of FTO/c-TiO₂/m-TiO₂/CH₃NH₃PbI₃/spiro-OMeTAD/PEDOT:PSS via a transfer-lamination technique. Their device fabricated in gave a PCE of 11.29%, which suggested their method was a simple method to lowers the threshold of both scientific research and industrial production of PSCs. Bu et al. [286] deposited a PEDOT: PSS on commercial plastic wrap to form a thin film to avoid using PDMS substrate, and then the PEDOT; PSS electrode was laminated on the top of hole transport layer as the transparent counter electrode as shown in Fig. 7.18. Their semitransparent PSCs gave a PCE of 10.1% with an active area of 0.06 cm², 2.9% with an active area of 1 cm², and AVT of 7.3%. By replacing the Ag electrode with the PEDOT: PSS transparent electrode, Xiao et al. [287] also reported a PCE of 8.21% with AVT of 23% at a wavelength range from 390 to 700 nm. The good transmittance of semi-transparent PEDOT: PSS enables the use as light penetration side electrode for an opaque bottom substrate-based PSCs. Xiao et al. [288] employed PEDOT: PSS as a counter electrode for a Ti foil-based PSCs. Another ITO/PEN laminated on the top of PEDOT: PSS was used to improve the charge separation and transportation. As a result, the Ti foil-based PSC achieved efficiency of 13.07% with an active area of 1.00 cm². Their promising results highlighted the potential application of the PEDOT and Ti foil in cost-effective, large-area, and flexible PSCs [288].

Table 7.6 Summary of the device performance of perovskite solar cells with conductive metal oxide counter electrode

Perovskites	Bottom electrode	Counter electrode	Structure	V_{oc} (V)	J_{sc} mA/cm ²	FF	PCE (%)	Ref
MAPbI ₃	FTO	MoO _x /ITO	Normal mesoscopic (TiO ₂)	0.821	14.5	51.9	6.2	[272]
			Silicon SHJ bottom	0.689	13.7	0.767	7.2	
MAPbI ₃	ITO	Al:ZnO/ITO/MgF ₂	PSC/Si four terminal tandem				13.4	
			Inverted planar	0.952	16.5	0.77	12.3	[273]
			Silicon	0.597	38.3	0.754	17.0	
			Filtered silicon	0.562	13.3	0.762	5.7	
			Silicon/PSC four terminal tandem cell				18.0	
MAPbI ₃	ITO	MoO _x /ITO/Au/Pt	Normal mesoscopic (TiO ₂)	0.95	18.8	0.69	12.4	[274]
				0.66	39.1	0.76	19.6	
				0.64	16.9	0.73	7.9	
							20.1	
MAPbI ₃	ITO	MoO _x /IZO	Silicon unfiltered	0.715	35.94	0.7548	19.38	[275]
			Normal mesoscopic (TiO ₂)	0.870	17.5	0.68	10.36	
			Silicon filtered	0.690	14.6	0.776	7.82	
			Silicon/PSC four terminal tandem cell				18.18	
MAPbI ₃	ITO	IZO	Normal mesoscopic (TiO ₂)					
MAPbI ₃	ITO	MoO _x /ITO/Au/Pt mesoscopic (TiO ₂)	Normal					
MAPbI ₃	ITO	MoO _x /IZO	Normal mesoscopic (TiO ₂)	0.938	17.36	0.596	9.70	

(continued)

Table 7.6 (continued)

Perovskites	Bottom electrode	Counter electrode	Structure	V_{OC} (V)	J_{SC} mA/cm ²	FF	PCE (%)	Ref
			Silicon filtered	0.693	15.81	0.7744	8.48	
			Silicon/PSC four terminal tandem cell				18.19	
MAPbI ₃	FTO	MoO ₃ /ZnO:Al/MgF ₂	Normal mesoscopic(TiO ₂)	1.034	16.7	0.703	12.1	[276]
			CIGS unfiltered	0.689	34.1	0.784	18.4	
			CIGS filtered	0.661	14.4	0.774	7.4	
			PSC/CIGS four terminal tandem cell				19.5	
FA _{0.83} Cs _{0.17} Pb(I _{0.6} Br _{0.4}) ₃	FTO	ITO	Normal planar	1.1	19.9	0.707	15.1	[277]
							(12.5)	
			Silicon unfiltered	0.72	37.2	0.721	19.2	
			Silicon filtered	0.69	13.9	0.764	7.3	
			PSC/silicon four terminal tandem cell				19.8	
MAPbI ₃	ITO	ITO	Inverted planar	1.08	16.69	0.75	13.52	[278]
MA _{0.5} FA _{0.5} Pb _{0.75} Sn _{0.25} I ₃	ITO	Ag	Inverted planar	0.78	23.03	0.79	14.19	
MA _{0.5} FA _{0.5} Pb _{0.75} Sn _{0.25} I ₃	ITO	Ag	Inverted planar, filtered	0.76	9.14	0.80	9.14	
			PSC/PSC four terminal tandem cell				19.08	
FA _{0.83} Cs _{0.17} Pb(I _{0.83} Br _{0.17}) ₃	ITO	ITO	Inverted planar, 1.6 eV cell	0.97	20.3	0.79	15.8	[279]
FA _{0.75} Cs _{0.25} Sn _{0.5} Pb _{0.5} I ₃	ITO	Ag	Inverted planar	0.74	26.7	0.71	14.8	
MA _{0.5} FA _{0.5} Pb _{0.75} Sn _{0.25} I ₃	ITO	Ag	Inverted planar, filtered	0.74	7.9	0.73	4.5	
			PSC/PSC four terminal tandem cell				20.3	

$\text{FA}_{0.83}\text{Cs}_{0.17}\text{Pb}(\text{I}_{0.5}\text{Br}_{0.5})_3$				Inverted planar, 1.8 eV	1.12	15.1	0.58	9.8
$\text{FA}_{0.83}\text{Cs}_{0.17}\text{Pb}(\text{I}_{0.5}\text{Br}_{0.5})_3/$ $\text{MA}_{0.5}\text{FA}_{0.5}\text{Pb}_{0.75}\text{Sn}_{0.25}\text{I}_3$	ITO	Ag		PSC/PSC two terminal tandem cell	1.66	14.5	0.70	17.0
MAPbI ₃	FTO	$\text{MoO}_3/\text{In}_2\text{O}_3:\text{H}$		Inverted planar	1.104	17.4	0.736	14.1 [280]
				CIGS unfiltered	0.6986	34.1	0.767	18.3
				CIGS filtered	0.6674	12.7	0.749	6.3
				PSC/CIGS four terminal tandem cell				20.5
$\text{FA}_{0.83}\text{MA}_{0.17}\text{Pb}_{1.08}\text{I}_{2.67}\text{Br}_{0.5}$	AZO/Ag	LiF/ITO/MoO ₃		PSC/silicon two terminal tandem cell	1.785	14.0	0.795	19.9 (18.1) [281]
MAPbI ₃	AZO/A	ITO/IO:H/MoO _x		PSC/silicon two terminal tandem cell, 0.17 cm ²	1.692	15.8	0.799	21.4 (21.2) [282]
				PSC/silicon two terminal tandem cell, 1.22 cm ²	1.703	16.1	0.709	19.5 (19.2)
MAPbBr ₃ /MAPbI ₃	FTO	ITO		PSC/PSC two terminal	1.95	8.4	0.66	10.8 [283]

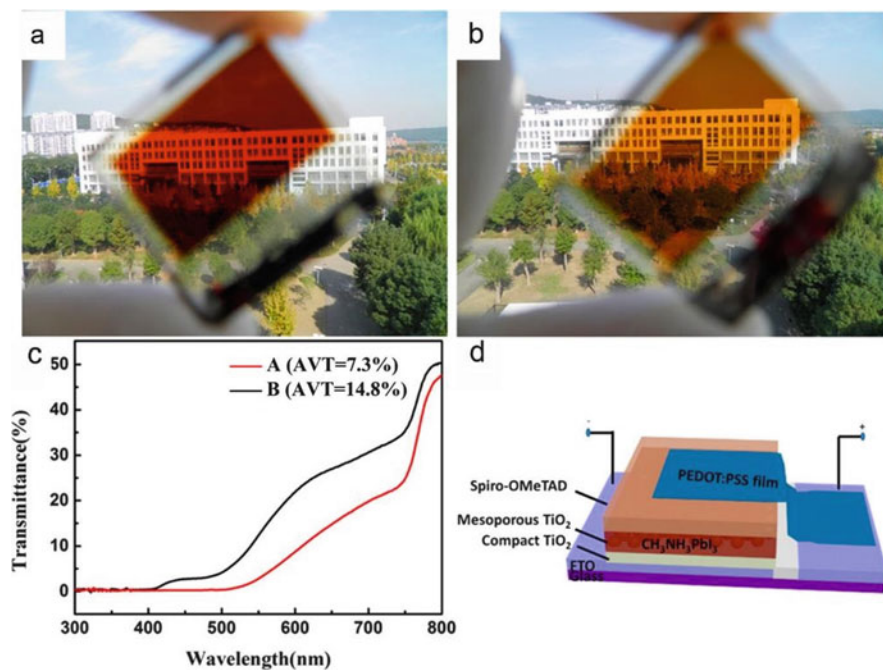


Fig. 7.18 Pictures of the semitransparent PSCs with a configuration of (FTO/*c*-TiO₂/*m*-TiO₂/CH₃NH₃PbI₃/HTM/PEDOT:PSS): (a) the cell with 240 nm *m*-TiO₂ thickness (cell A), (b) the cell with 140 nm *m*-TiO₂ (cell B). (c) The transmittance of the two semitransparent solar cells. (d) The device structure of semitransparent PSCs with PEDOT:PSS counter electrode. (Reproduced with permission from Ref. [286]. Copyright (2015) American Chemical Society)

Although, the employment of PEDOT:PSS as counter electrode have been successfully demonstrated. PEDOT:PSS also suffer from some drawbacks which hamper their application in PSCs. One major disadvantage is the acidic and aqueous nature of PEDOT:PSS, which causes cell degradation when used in PSCs. In general, some additives were used to modify the PEDOT:PSS to increase the conductivity. However, PEDOT:PSS film prepared from the dispersion also showed relatively low conductivity than that of metal or ITO, which may increase the sheet resistance of the device. Besides, the poor stability of the conductive polymer itself is another concern for the application in PSCs. Thus, it is desirable to develop stable conductive polymer materials for the conductive electrode application (cf. Table 7.7).

7.3 Perspectives

In this chapter, we have reviewed recent progress on the counter electrode materials for PSCs, including metal thin-film electrode, super-thin metal thin-film electrode, nanostructured metal electrode, graphene electrode, carbon nanotube electrode,

Table 7.7 Summary of the device performance of perovskite solar cells with PEDOT: PSS counter electrode

Perovskites	Bottom electrode	Counter electrode	Structure	ATV %	V _{OC} (V)	J _{SC} mA/cm ²	FF	PCE	Ref.
MAPbI ₃	FTO	PEDOT: PSS	Normal mesoscopic (TiO ₂)		1.02			11.29	[285]
MAPbI ₃	FTO	PEDOT: PSS	Normal mesoscopic (TiO ₂)	7.3	0.966	16.0	0.654	10.1	[286]
				14.8	0.959	9.2	0.633	5.6	
MAPbI ₃	FTO	PEDOT: PSS	Normal planar	23	1.02	12.2	0.66	8.21	[287]
MAPbI ₃	Ti	PEDOT: PSS/ITO/PEN	Normal planar		0.940	21.72	0.64	13.07	[288]

carbon black/graphite electrode, conductive oxide electrode, and polymer electrode. Although there are a variety of electrode materials and electrode structures suitable for counter electrode of PSCs, to find a suitable counter electrode for PSCs, several important factors such as the function of the counter electrode, the cost of the materials, and relevant deposition technique should be carefully considered to achieve efficient charge collection and expected photovoltaic application. Furthermore, the counter electrode also plays an important role in the long-term stability of the PSCs. Thus, it is appealing to develop novel electrode materials and also suitable integrating process for counter electrode in PSCs towards future commercialized photovoltaic.

Acknowledgments HH thanks Department of Chemistry & Biochemistry, Eastern Illinois University, for the support of this work. ZL thanks Wuhan National Laboratory for Optoelectronics, School of Optical and Electronic Information, Huazhong University of Science and Technology for the support of this work.

References

1. Y.-B. Cheng, A. Pascoe, F. Huang, Y. Peng, Print flexible solar cells. *Nature* **539**, 488–489 (2016)
2. A. Kojima, K. Teshima, Y. Shirai, T. Miyasaka, Organometal halide perovskites as visible-light sensitizers for photovoltaic cells. *J. Am. Chem. Soc.* **131**, 6050–6051 (2009)
3. H.-S. Kim et al., Lead iodide perovskite sensitized all-solid-state submicron thin film mesoscopic solar cell with efficiency exceeding 9%. *Sci. Rep.* **2**, 591 (2012)
4. J.H. Heo et al., Efficient inorganic-organic hybrid heterojunction solar cells containing perovskite compound and polymeric hole conductors. *Nat. Photon.* **7**, 486–491 (2013)
5. M.M. Lee, J. Teuscher, T. Miyasaka, T.N. Murakami, H.J. Snaith, Efficient hybrid solar cells based on meso-superstructured organometal halide perovskites. *Science* **338**, 643–647 (2012)
6. G. Xing et al., Long-range balanced electron- and hole-transport lengths in organic-inorganic CH₃NH₃PbI₃. *Science* **342**, 344–347 (2013)

7. S.D. Stranks et al., Electron-hole diffusion lengths exceeding 1 micrometer in an organometal trihalide perovskite absorber. *Science* **342**, 341–344 (2013)
8. M. Liu, M.B. Johnston, H.J. Snaith, Efficient planar heterojunction perovskite solar cells by vapor deposition. *Nature* **501**, 395–398 (2013)
9. L. Etgar et al., Mesoscopic $\text{CH}_3\text{NH}_3\text{PbI}_3/\text{TiO}_2$ heterojunction solar cells. *J. Am. Chem. Soc.* **134**, 17396–17399 (2012)
10. W.A. Laban, L. Etgar, Depleted hole conductor-free lead halide iodide heterojunction solar cells. *Energy Environ. Sci.* **6**, 3249–3253 (2013)
11. Z. Ku, Y. Rong, M. Xu, T. Liu, H. Han, Full printable processed mesoscopic $\text{CH}_3\text{NH}_3\text{PbI}_3/\text{TiO}_2$ heterojunction solar cells with carbon counter electrode. *Sci. Rep.* **3**, 3132 (2013)
12. J. Burschka et al., Sequential deposition as a route to high-performance perovskite-sensitized solar cells. *Nature* **499**, 316–319 (2013)
13. Q. Chen et al., Planar heterojunction perovskite solar cells via vapor-assisted solution process. *J. Am. Chem. Soc.* **136**, 622–625 (2014)
14. N.J. Jeon et al., Solvent engineering for high-performance inorganic-organic hybrid perovskite solar cells. *Nat. Mater.* **13**, 897–903 (2014)
15. N.-G. Park, M. Grätzel, T. Miyasaka, K. Zhu, K. Emery, Towards stable and commercially available perovskite solar cells. *Nat. Energy* **1**, 16152 (2016)
16. A.B., Djurišić et al., Perovskite solar cells – an overview of critical issues. *Prog. Quantum Electron.* **53**, 1–37 (2017)
17. T. Leijtens et al., Stability of metal halide perovskite solar cells. *Adv. Energy Mater.* **5**, 1500963 (2015)
18. K. Leo, Perovskite photovoltaics: signs of stability. *Nat. Nano* **10**, 574–575 (2015)
19. G. Niu, X. Guo, L. Wang, Review of recent progress in chemical stability of perovskite solar cells. *J. Mater. Chem. A* **3**, 8970–8980 (2015)
20. X. Zhao, N.-G. Park, Stability issues on perovskite solar cells. *Photo-Dermatology* **2**, 1139 (2015)
21. N.H. Tiep, Z. Ku, H.J. Fan, Recent advances in improving the stability of perovskite solar cells. *Adv. Energy Mater.* **6**, 1501420 (2015)
22. T.A. Berhe et al., Organometal halide perovskite solar cells: degradation and stability. *Energy Environ. Sci.* **9**, 323–356 (2016)
23. P. Docampo, T. Bein, A long-term view on perovskite optoelectronics. *Acc. Chem. Res.* **49**, 339–346 (2016)
24. M. Shahbazi, H. Wang, Progress in research on the stability of organometal perovskite solar cells. *Sol. Energy* **123**, 74–87 (2016)
25. D. Wang, M. Wright, N.K. Elumalai, A. Uddin, Stability of perovskite solar cells. *Sol. Energy Mater. Sol. Cells* **147**, 255–275 (2016)
26. Z. Wang, Z. Shi, T. Li, Y. Chen, W. Huang, Stability of perovskite solar cells: a perspective on the substitution of the a cation and X anion. *Angew. Chem. Int. Ed.* **56**, 1190–1212 (2016)
27. M.I. Asghar, J. Zhang, H. Wang, P.D. Lund, Device stability of perovskite solar cells – a review. *Renew. Sust. Energ. Rev.* **77**, 131–146 (2017)
28. G. Niu et al., Study on the stability of $\text{CH}_3\text{NH}_3\text{PbI}_3$ films and the effect of post-modification by aluminum oxide in all-solid-state hybrid solar cells. *J. Mater. Chem. A* **2**, 705–710 (2014)
29. G. Grancini et al., $\text{CH}_3\text{NH}_3\text{PbI}_3$ perovskite single crystals: surface photophysics and their interaction with the environment. *Chem. Sci.* **6**, 7305–7310 (2015)
30. C. Müller et al., Water infiltration in methylammonium lead iodide perovskite: Fast and inconspicuous. *Chem. Mater.* **27**, 7835–7841 (2015)
31. Z. Zhu et al., Interaction of organic cation with water molecule in perovskite MAPbI_3 : from dynamic orientational disorder to hydrogen bonding. *Chem. Mater.* **28**, 7385–7393 (2016)
32. E. Mosconi, J.M. Aspiroz, F. De Angelis, Ab initio molecular dynamics simulations of methylammonium lead iodide perovskite degradation by water. *Chem. Mater.* **27**, 4885–4892 (2015)

33. N. Aristidou et al., Fast oxygen diffusion and iodide defects mediate oxygen-induced degradation of perovskite solar cells. *Nat. Commun.* **8**, 15218 (2017)
34. D. Bryant et al., Light, and oxygen-induced degradation limits the operational stability of methylammonium lead triiodide perovskite solar cells. *Energy Environ. Sci.* **9**, 1655–1660 (2016)
35. Y. Rong, L. Liu, A. Mei, X. Li, H. Han, Beyond efficiency: the challenge of stability in mesoscopic perovskite solar cells. *Adv. Energy Mater.* **5**, 1501066 (2015)
36. E.J. Juarez-Perez, Z. Hawash, S.R. Raga, L.K. Ono, Y. Qi, Thermal degradation of $\text{CH}_3\text{NH}_3\text{PbI}_3$ perovskite into NH_3 and CH_3I gases observed by coupled thermogravimetry-mass spectrometry analysis. *Energy Environ. Sci.* **9**, 3406–3410 (2016)
37. E. Tenuta, C. Zheng, O. Rubel, Thermodynamic origin of instability in hybrid halide perovskites. *Sci. Rep.* **6**, 37654 (2016)
38. G. Divitini et al., In situ observation of heat-induced degradation of perovskite solar cells. *Nat. Energy* **1**, 15012 (2016)
39. R.K. Misra et al., Temperature- and component-dependent degradation of perovskite photovoltaic materials under concentrated sunlight. *J. Phys. Chem. Lett.* **6**, 326–330 (2015)
40. T. Leijtens et al., Overcoming ultraviolet light instability of sensitized TiO_2 with meso-superstructure organometal tri-halide perovskite solar cells. *Nat. Commun.* **4**, 2885 (2013)
41. H.J. Snath et al., Anomalous hysteresis in perovskite solar cells. *J. Phys. Chem. Lett.* **5**, 1511–1515 (2014)
42. B. Chen, M. Yang, S. Priya, K. Zhu, Origin of J–V hysteresis in perovskite solar cells. *J. Phys. Chem. Lett.* **7**, 905–917 (2016)
43. N.K. Elumalai, A. Uddin, Hysteresis in organic-inorganic hybrid perovskite solar cells. *Sol. Energy Mater. Sol. Cells* **157**, 476–509 (2016)
44. J.M. Frost, K.T. Butler, A. Walsh, Molecular ferroelectric contributions to anomalous hysteresis in hybrid perovskite solar cells. *APL Mater.* **2**, 081506 (2014)
45. J. Wei et al., Hysteresis analysis based on the ferroelectric effect in hybrid perovskite solar cells. *J. Phys. Chem. Lett.* **5**, 3937–3945 (2014)
46. Y. Yuan, J. Huang, Ion migration in organometal trihalide perovskite and its impact on photovoltaic efficiency and stability. *Acc. Chem. Res.* **49**, 286–293 (2016)
47. S. Chen et al., Mobile ion induced slow carrier dynamics in organic-inorganic perovskite $\text{CH}_3\text{NH}_3\text{PbBr}_3$. *ACS Appl. Mater. Interfaces* **8**, 5351–5357 (2016)
48. P. Calado et al., Evidence for ion migration in hybrid perovskite solar cells with minimal hysteresis. *Nat. Commun.* **7**, 13831 (2016)
49. X. Xu, M. Wang, Photocurrent hysteresis related to ion motion in metal-organic perovskites. *Sci. China Chem.*, **60**, 1–9 (2016)
50. G. Richardson et al., Can slow-moving ions explain hysteresis in the current-voltage curves of perovskite solar cells? *Energy Environ. Sci.* **9**, 1476–1485 (2016)
51. D.A. Egger, L. Kronik, A.M. Rappe, Theory of hydrogen migration in organic-inorganic halide perovskites. *Angew. Chem. Int. Ed.* **54**, 12437–12441 (2015)
52. M. De Bastiani et al., Ion migration and the role of preconditioning cycles in the stabilization of the J–V characteristics of inverted hybrid perovskite solar cells. *Adv. Energy Mater.* **6**, 1501453 (2016)
53. H.-S. Kim, N.-G. Park, Parameters affecting I–V hysteresis of $\text{CH}_3\text{NH}_3\text{PbI}_3$ perovskite solar cells: effects of perovskite crystal size and mesoporous TiO_2 layer. *J. Phys. Chem. Lett.* **5**, 2927–2934 (2014)
54. H.-S. Kim et al., Control of I–V hysteresis in $\text{CH}_3\text{NH}_3\text{PbI}_3$ perovskite solar cell. *J. Phys. Chem. Lett.* **6**, 4633–4639 (2015)
55. Y. Shao, Z. Xiao, C. Bi, Y. Yuan, J. Huang, Origin and elimination of photocurrent hysteresis by fullerene passivation in $\text{CH}_3\text{NH}_3\text{PbI}_3$ planar heterojunction solar cells. *Nat. Commun.* **5**, 5784 (2014)
56. J. Xu et al., Perovskite-fullerene hybrid materials suppress hysteresis in planar diodes. *Nat. Commun.* **6**, 7081 (2015)

57. K. Wojciechowski et al., Heterojunction modification for highly efficient organic-inorganic perovskite solar cells. *ACS Nano* **8**, 12701–12709 (2014)
58. A. Babayigit, A. Ethirajan, M. Muller, B. Conings, Toxicity of organometal halide perovskite solar cells. *Nat. Mater.* **15**, 247–251 (2016)
59. S.T. Williams, A. Rajagopal, C.-C. Chueh, A.K.Y. Jen, Current challenges and prospective research for upscaling hybrid perovskite photovoltaics. *J. Phys. Chem. Lett.* **7**, 811–819 (2016)
60. H. Hu, B. Dong, W. Zhang, Low-toxic metal halide perovskites: opportunities and future challenges. *J. Mater. Chem. A* **5**, 11436–11449 (2017)
61. M. Lyu, J.-H. Yun, P. Chen, M. Hao, L. Wang, Addressing toxicity of lead: progress and applications of low-toxic metal halide perovskites and their derivatives. *Adv. Energy Mater.* **7**, 1602512 (2017)
62. Y. Deng, Q. Dong, C. Bi, Y. Yuan, J. Huang, Air-stable, efficient mixed-cation perovskite solar cells with Cu electrode by scalable fabrication of active layer. *Adv. Energy Mater.* **6**, 1600372 (2016)
63. J.H. Kim, S.T. Williams, N. Cho, C.-C. Chueh, A.K.Y. Jen, Enhanced environmental stability of planar heterojunction perovskite solar cells based on blade-coating. *Adv. Energy Mater.* **5**, 1401229 (2015)
64. J. Lee et al., A printable organic electron transport layer for low-temperature-processed, hysteresis-free, and stable planar perovskite solar cells. *Adv. Energy Mater.* **7**, 1700226 (2017)
65. Z. Yang et al., High-performance fully printable perovskite solar cells via blade-coating technique under the ambient condition. *Adv. Energy Mater.* **5**, 1500328 (2015)
66. A.T. Mallajosyula et al., Large-area hysteresis-free perovskite solar cells via temperature controlled doctor blading under ambient environment. *Appl. Mater. Today* **3**, 96–102 (2016)
67. Y. Deng et al., Scalable fabrication of efficient organolead trihalide perovskite solar cells with doctor-bladed active layers. *Energy Environ. Sci.* **8**, 1544–1550 (2015)
68. S. Razza et al., Perovskite solar cells and large area modules (100 cm²) based on an air flow-assisted PbI₂ blade coating deposition process. *J. Power Sources* **277**, 286–291 (2015)
69. M. Yang et al., Perovskite ink with a wide processing window for scalable high-efficiency solar cells. *Nat. Energy* **2**, 17038 (2017)
70. S. Li et al., High-performance formamidinium-based perovskite photodetectors fabricated via doctor-blading deposition in ambient condition. *Org. Electron.* **47**, 102–107 (2017)
71. H. Wu et al., Efficient planar heterojunction perovskite solar cells fabricated by in-situ thermal-annealing doctor blading in ambient condition. *Org. Electron.* **45**, 302–307 (2017)
72. H. Back et al., Interfacial modification of hole transport layers for efficient large-area perovskite solar cells achieved via blade-coating. *Sol. Energy Mater. Sol. Cells* **144**, 309–315 (2016)
73. M. Bag et al., Rapid combinatorial screening of inkjet-printed alkyl-ammonium cations in perovskite solar cells. *Mater. Lett.* **164**, 472–475 (2016)
74. H. Huang et al., Two-step ultrasonic spray deposition of CH₃NH₃PbI₃ for efficient and large-area perovskite solar cell. *Nano Energy* **27**, 352–358 (2016)
75. W.-C. Chang, D.-H. Lan, K.-M. Lee, X.-F. Wang, C.-L. Liu, Controlled deposition and performance optimization of perovskite solar cells using ultrasonic spray-coating of photo-active layers. *ChemSusChem* **10**, 1405–1412 (2017)
76. M. Remeika, S.R. Raga, S. Zhang, Y. Qi, Transferrable optimization of spray-coated PbI₂ films for perovskite solar cell fabrication. *J. Mater. Chem. A* **5**, 5709–5718 (2017)
77. Z. Wei, H. Chen, K. Yan, S. Yang, Inkjet printing and instant chemical transformation of a CH₃NH₃PbI₃/Nanocarbon electrode and interface for planar perovskite solar cells. *Angew. Chem. Int. Ed.* **53**, 13239–13243 (2014)
78. S.G. Hashmi et al., Long term stability of air processed inkjet infiltrated carbon-based printed perovskite solar cells under intense ultra-violet light soaking. *J. Mater. Chem. A* **5**, 4797–4802 (2017)
79. S.-G. Li et al., Inkjet printing of CH₃NH₃PbI₃ on a mesoscopic TiO₂ film for highly efficient perovskite solar cells. *J. Mater. Chem. A* **3**, 9092–9097 (2015)

80. F. Mathies et al., Multipass inkjet printed planar methylammonium lead iodide perovskite solar cells. *J. Mater. Chem. A* **4**, 19207–19213 (2016)
81. T.M. Schmidt, T.T. Larsen-Olsen, J.E. Carlé, D. Angmo, F.C. Krebs, Upscaling of perovskite solar cells: fully ambient roll processing of flexible perovskite solar cells with printed Back electrodes. *Adv. Energy Mater.* **5**, 1500569 (2015)
82. D. Vak et al., 3D printer based slot-die coater as a lab-to-fab translation tool for solution-processed solar cells. *Adv. Energy Mater.* **5**, 1401539 (2015)
83. T. Qin et al., Amorphous hole-transporting layer in slot-die coated perovskite solar cells. *Nano Energy* **31**, 210–217 (2017)
84. J. Ciro, M.A. Mejía-Escobar, F. Jaramillo, Slot-die processing of flexible perovskite solar cells in ambient conditions. *Sol. Energy* **150**, 570–576 (2017)
85. G. Cotella et al., One-step deposition by a slot-die coating of mixed lead halide perovskite for photovoltaic applications. *Sol. Energy Mater. Sol. Cells* **159**, 362–369 (2017)
86. A.T. Barrows et al., Efficient planar heterojunction mixed-halide perovskite solar cells deposited via spray-deposition. *Energy Environ. Sci.* **7**, 2944–2950 (2014)
87. S. Das et al., High-performance flexible perovskite solar cells by using a combination of ultrasonic spray-coating and low thermal budget photonic curing. *ACS Photon.* **2**, 680–686 (2015)
88. M.-C. Kim et al., Electro-spray deposition of a mesoporous TiO₂ charge collection layer: toward large scale and continuous production of high-efficiency perovskite solar cells. *Nanoscale* **7**, 20725–20733 (2015)
89. Z. Liang et al., A large grain size perovskite thin film with a dense structure for planar heterojunction solar cells via spray deposition under ambient conditions. *RSC Adv.* **5**, 60562–60569 (2015)
90. J.H. Heo, M.H. Lee, M.H. Jang, S.H. Im, Highly efficient CH₃NH₃PbI_{3-x}Cl_x mixed halide perovskite solar cells prepared by re-dissolution and crystal grain growth via spray coating. *J. Mater. Chem. A* **4**, 17636–17642 (2016)
91. Y.-S. Jung et al., Differentially pumped spray deposition as a rapid screening tool for organic and perovskite solar cells. *Sci. Rep.* **6**, 20357 (2016)
92. D.K. Mohamad, J. Griffin, C. Bracher, A.T. Barrows, D.G. Lidzey, Spray-cast multilayer organometal perovskite solar cells fabricated in air. *Adv. Energy Mater.* **6**, 1600994 (2016)
93. Z. Bi et al., Fast preparation of uniform large grain size perovskite thin film in air condition via spray deposition method for high efficient planar solar cells. *Sol. Energy Mater. Sol. Cells* **162**, 13–12 (2017)
94. S.C. Hong et al., Precise morphology control and continuous fabrication of perovskite solar cells using droplet-controllable electrospray coating system. *ACS Appl. Mater. Interfaces* **9**, 7879–7884 (2017)
95. S. Kavadiya, D.M. Niedzwiedzki, S. Huang, P. Biswas, Electrospray-assisted fabrication of moisture-resistant and highly stable perovskite solar cells at ambient conditions. *Adv. Energy Mater.* **7**, 1700210 (2017)
96. Z. Gu et al., Interfacial engineering of self-assembled monolayer modified semi-roll-to-roll planar heterojunction perovskite solar cells on flexible substrates. *J. Mater. Chem. A* **3**, 24254–24260 (2015)
97. K. Hwang et al., Toward large scale roll-to-roll production of fully printed perovskite solar cells. *Adv. Mater.* **27**, 1241–1247 (2015)
98. Q. Hu et al., Large-area perovskite nanowire arrays fabricated by large-scale roll-to-roll microgravure printing and doctor blading. *Nanoscale* **8**, 5350–5355 (2016)
99. L.H. Rossander et al., In situ X-ray scattering of perovskite solar cell, active layers roll-to-roll coated on flexible substrates. *CrystEngComm* **18**, 5083–5088 (2016)
100. W.S. Yang et al., Iodide management in formamidinium-lead-halide-based perovskite layers for efficient solar cells. *Science* **356**, 1376–1379 (2017)

101. N. Ahn et al., Highly reproducible perovskite solar cells with average efficiency of 18.3% and best efficiency of 19.7% fabricated via Lewis base adduct of lead(II) iodide. *J. Am. Chem. Soc.* **137**, 8696–8699 (2015)
102. D.-Y. Son et al., Self-formed grain boundary healing layer for highly efficient $\text{CH}_3\text{NH}_3\text{PbI}_3$ perovskite solar cells. *Nat. Energy* **1**, 16081 (2016)
103. Y. Wu et al., Perovskite solar cells with 18.21% efficiency and area over 1 cm^2 fabricated by heterojunction engineering. *Nat. Energy* **1**, 16148 (2016)
104. W. Chen et al., Efficient and stable large-area perovskite solar cells with inorganic charge extraction layers. *Science* **350**, 944–948 (2015)
105. Y. Wu et al., Thermally stable MAPbI_3 perovskite solar cells with efficiency of 19.19% and area over 1 cm^2 achieved by additive engineering. *Adv. Mater.*, **29**, 1701073 (2017)
106. J.-Y. Jeng et al., $\text{CH}_3\text{NH}_3\text{PbI}_3$ perovskite/fullerene planar-heterojunction hybrid solar cells. *Adv. Mater.* **25**, 3727–3732 (2013)
107. L. Meng, J. Yu, T.-F. Guo, Y. Yang, Recent advances in the inverted planar structure of perovskite solar cells. *Acc. Chem. Res.* **49**, 155–165 (2015)
108. Y. Shao, Y. Yuan, J. Huang, Correlation of energy disorder and open-circuit voltage in hybrid perovskite solar cells. *Nat. Energy* **1**, 15001 (2016)
109. Y. Kato et al., Silver iodide formation in methyl ammonium Lead iodide perovskite solar cells with silver top electrodes. *Adv. Mater. Interfaces* **2**, 1500195 (2015)
110. M. Kaltenbrunner et al., Flexible high power-per-weight perovskite solar cells with chromium oxide-metal contacts for improved stability in air. *Nat. Mater.* **14**, 1032–1039 (2015)
111. J. Zhao et al., Are Cu a stable electrode material in hybrid perovskite solar cells for a 30-year lifetime? *Energy Environ. Sci.* **9**, 3650–3656 (2016)
112. X. Zheng et al., Defect passivation in hybrid perovskite solar cells using quaternary ammonium halide anions and cations. *Nat. Energy* **2**, 17102 (2017)
113. Y. Shao, Q. Wang, Q. Dong, Y. Yuan, J. Huang, Vacuum-free laminated top electrode with conductive tapes for scalable manufacturing of efficient perovskite solar cells. *Nano Energy* **16**, 47–53 (2015)
114. A. Guerrero et al., Interfacial degradation of planar lead halide perovskite solar cells. *ACS Nano* **10**, 218–224 (2015)
115. Q. Jiang, X. Sheng, B. Shi, X. Feng, T. Xu, Nickel-cathode perovskite solar cells. *J. Phys. Chem. C* **118**, 25878–25883 (2014)
116. B. Abdollahi Nejad, V. Ahmadi, H.R. Shahverdi, New physical deposition approach for low-cost inorganic hole transport layer in Normal architecture of durable perovskite solar cells. *ACS Appl. Mater. Interfaces* **7**, 21807–21818 (2015)
117. Z. Ku, X. Xia, H. Shen, N.H. Tiep, H.J. Fan, A mesoporous nickel counter electrode for printable and reusable perovskite solar cells. *Nanoscale* **7**, 13363–13368 (2015)
118. I. Jeong et al., Highly efficient perovskite solar cells based on mechanically durable molybdenum cathode. *Nano Energy* **17**, 131–139 (2015)
119. G.E. Eperon, V.M. Burlakov, A. Goriely, H.J. Snaith, Neutral color semitransparent microstructured perovskite solar cells. *ACS Nano* **8**, 591–598 (2014)
120. S. Aharon et al., Self-assembly of perovskite for fabrication of semitransparent perovskite solar cells. *Adv. Mater. Interfaces* **2**, 1500118 (2015)
121. J.W. Jung, C.-C. Chueh, A.K.Y. Jen, High-performance semitransparent perovskite solar cells with 10% power conversion efficiency and 25% average visible transmittance based on transparent CuSCN as the hole-transporting material. *Adv. Energy Mater.* **5**, 1500486 (2015)
122. S. Bag, M.F. Durstock, Efficient semi-transparent planar perovskite solar cells using a ‘molecular glue’. *Nano Energy* **30**, 542–548 (2016)
123. Y. Liu et al., High-efficiency tandem thin-perovskite/polymer solar cells with a graded recombination layer. *ACS Appl. Mater. Interfaces* **8**, 7070–7076 (2016)
124. C. Roldan-Carmona et al., High efficiency single-junction semitransparent perovskite solar cells. *Energy Environ. Sci.* **7**, 2968–2973 (2014)

125. G.M. Kim, T. Tatsuma, Semitransparent solar cells with ultrasmooth and low-scattering perovskite thin films. *J. Phys. Chem. C* **120**, 28933–28938 (2016)
126. J.A. Pracchia, J.M. Simon, Transparent heat mirrors: influence of the materials on the optical characteristics. *Appl. Opt.* **20**, 251–2583 (1981)
127. C.G. Granqvist, Radiative heating and cooling with spectrally selective surfaces. *Appl. Opt.* **20**, 2606–26153 (1981)
128. H. Jin et al., Efficient, large area ITO-and-PEDOT-free organic solar cell sub-modules. *Adv. Mater.* **24**, 2572–25773 (2012)
129. W. Cao et al., Flexible organic solar cells using an oxide/metal/oxide trilayer as a transparent electrode. *Org. Electron.* **13**, 2221–22283 (2012)
130. L. Cattin, J.C. Bernède, M. Morsli, Toward indium-free optoelectronic devices: dielectric/metal/dielectric alternative transparent conductive electrode in organic photovoltaic cells. *Phys. Status Solidi A* **210**, 1047–10613 (2013)
131. N.P. Sergeant et al., Design of transparent anodes for resonant cavity enhanced light harvesting in organic solar cells. *Adv. Mater.* **24**, 728–7323 (2012)
132. T. Schwab et al., Highly efficient color stable inverted white top-emitting OLEDs with ultrathin wetting layer top electrodes. *Adv. Opt. Mater.* **1**, 707–7133 (2013)
133. H. Cho, C. Yun, S. Yoo, Multilayer transparent electrode for organic light-emitting diodes: tuning its optical characteristics. *Opt. Express* **18**, 3404–3414 (2010)
134. H. Cho, J.-M. Choi, S. Yoo, Highly transparent organic light-emitting diodes with a metallic top electrode: the dual role of a Cs_2CO_3 layer. *Opt. Express* **19**, 1113–1121 (2011)
135. H. Cho, C. Yun, J.-W. Park, S. Yoo, Highly flexible organic light-emitting diodes based on $\text{ZnS}/\text{Ag}/\text{WO}_3$ multilayer transparent electrodes. *Org. Electron.* **10**, 1163–1169 (2009)
136. H. Moon, H. Cho, M. Kim, K. Takimiya, S. Yoo, Towards colorless transparent organic transistors: potential of Benzothieno[3,2- b]benzothiophene-based wide-gap semiconductors. *Adv. Mater.* **26**, 3105–3110 (2014)
137. E. Della Gaspera et al., Ultra-thin high-efficiency semitransparent perovskite solar cells. *Nano Energy* **13**, 249–257 (2015)
138. H. Kim, H.-S. Kim, J. Ha, N.-G. Park, S. Yoo, Empowering semi-transparent solar cells with thermal-mirror functionality. *Adv. Energy Mater.* **6**, 1502466 (2016)
139. S. Pang et al., Efficient bifacial semitransparent perovskite solar cells with silver thin film electrode. *Sol. Energy Mater. Sol. Cells* **170**, 278–286 (2017)
140. Y. Yang et al., Multilayer transparent top electrode for solution-processed perovskite/Cu(In, Ga)(Se, S)₂ four terminal tandem solar cells. *ACS Nano* **9**, 7714–7721 (2015)
141. S. Schubert, J. Meiss, L. Müller-Muschamp, K. Leo, Improvement of transparent metal top electrodes for organic solar cells by introducing a high surface energy seed layer. *Adv. Energy Mater.* **3**, 438–443 (2013)
142. B. Chen, X. Zheng, Y. Bai, N.P. Padture, J. Huang, Progress in tandem solar cells based on hybrid organic-inorganic perovskites. *Adv. Energy Mater.*, **7**, 1602400 (2017)
143. J. Hu, Q. Cheng, R. Fan, H. Zhou, Recent development of organic-inorganic perovskite-based tandem solar cells. *Solar RRL* **1**, 1700045 (2017)
144. D. Zhao et al., Low-bandgap mixed tin-lead iodide perovskite absorbers with long carrier lifetimes for all-perovskite tandem solar cells. *Nat. Energy* **2**, 17018 (2017)
145. M. Xu et al., Flexible perovskite solar cells with ultrathin Au anode and vapor-deposited perovskite film. *Sol. Energy Mater. Sol. Cells* **169**, 8–12 (2017)
146. X.-L. Ou, M. Xu, J. Feng, H.-B. Sun, Flexible and efficient ITO-free semitransparent perovskite solar cells. *Sol. Energy Mater. Sol. Cells* **157**, 660–665 (2016)
147. X.-L. Ou, J. Feng, M. Xu, H.-B. Sun, Semitransparent and flexible perovskite solar cell with high visible transmittance based on ultrathin metallic electrodes. *Opt. Lett.* **42**, 1958–1961 (2017)
148. Z. Hawash, L.K. Ono, S.R. Raga, M.V. Lee, Y. Qi, Air-exposure induced dopant redistribution and energy level shifts in spin-coated Spiro-MeOTAD films. *Chem. Mater.* **27**, 562–569 (2015)

149. K. Domanski et al., Not all that glitters is gold: metal-migration-induced degradation in perovskite solar cells. *ACS Nano* **10**, 6306–6314 (2016)
150. S. Cacovich et al., Gold and iodine diffusion in large area perovskite solar cells under illumination. *Nanoscale* **9**, 4700–4706 (2017)
151. D. Wei et al., Photo-induced degradation of lead halide perovskite solar cells caused by the hole transport layer/metal electrode interface. *J. Mater. Chem. A* **4**, 1991–1998 (2016)
152. Y. Han et al., Degradation observations of encapsulated planar $\text{CH}_3\text{NH}_3\text{PbI}_3$ perovskite solar cells at high temperatures and humidity. *J. Mater. Chem. A* **3**, 8139–8147 (2015)
153. J. Li, Q. Dong, N. Li, L. Wang, Direct evidence of ion diffusion for the silver-electrode-induced thermal degradation of inverted perovskite solar cells. *Adv. Energy Mater.* **7**, 1602922 (2017)
154. L. Zhao et al., Redox chemistry dominate the degradation and decomposition of metal halide perovskite optoelectronic devices. *ACS Energy Lett.* **1**, 595–602 (2016)
155. J. You et al., Improved air stability of perovskite solar cells via solution-processed metal oxide transport layers. *Nat. Nano* **11**, 75–78 (2016)
156. E.M. Sanehira et al., Influence of electrode interfaces on the stability of perovskite solar cells: reduced degradation using MoO_x/Al for hole collection. *ACS Energy Lett.* **1**, 38–45 (2016)
157. C. Li, S. Pang, H. Xu, G. Cui, Methylamine gas based synthesis and healing process toward upscaling of perovskite solar cells: progress and perspective. *Solar RRL* **1**, 1700076 (2017)
158. C.-Y. Chang et al., Enhanced performance and stability of semitransparent perovskite solar cells using solution-processed thiol-functionalized cationic surfactant as cathode buffer layer. *Chem. Mater.* **27**, 7119–7127 (2015)
159. H. Back et al., Achieving long-term stable perovskite solar cells via ion neutralization. *Energy Environ. Sci.* **9**, 1258–1263 (2016)
160. H. Chen, S. Yang, Carbon-based perovskite solar cells without hole transport materials: the front runner to the market? *Adv. Mater.*, **29**, 1603994 (2017)
161. Z. Jiang et al., Amazing stable open-circuit voltage in perovskite solar cells using AgAl alloy electrode. *Sol. Energy Mater. Sol. Cells* **146**, 35–43 (2016)
162. Y. Luo et al., AgAl alloy electrode for efficient perovskite solar cells. *RSC Adv.* **5**, 56037–56044 (2015)
163. S. Ye, A.R. Rathmell, Z. Chen, I.E. Stewart, B.J. Wiley, Metal nanowire networks: the next generation of transparent conductors. *Adv. Mater.* **26**, 6670–6687 (2014)
164. T. Sannicolo et al., Metallic nanowire-based transparent electrodes for next generation flexible devices: a review. *Small* **12**, 6052–6075 (2016)
165. C.F. Guo, Z. Ren, Flexible transparent conductors based on metal nanowire networks. *Mater. Today* **18**, 143–154 (2015)
166. H. Lee, I. Kim, M. Kim, H. Lee, Moving beyond flexible to stretchable conductive electrodes using metal nanowires and graphenes. *Nanoscale* **8**, 1789–1822 (2016)
167. L. Hu, H. Wu, Y. Cui, Metal nanogrids, nanowires, and nanofibers for transparent electrodes. *MRS Bull.* **36**, 760–765 (2011)
168. J. Ahn, H. Hwang, S. Jeong, J. Moon, Metal-nanowire-electrode-based perovskite solar cells: challenging issues and new opportunities. *Adv. Energy Mater.*, **7**, 1602751 (2017)
169. F. Guo et al., High-performance semitransparent perovskite solar cells with solution-processed silver nanowires as top electrodes. *Nanoscale* **7**, 1642–1649 (2015)
170. C.O. Ramirez Quiroz et al., Pushing efficiency limits for semitransparent perovskite solar cells. *J. Mater. Chem. A* **3**, 24071–24081 (2015)
171. C.O. Ramirez Quiroz et al., Coloring semitransparent perovskite solar cells via dielectric mirrors. *ACS Nano* **10**, 5104–5112 (2016)
172. H. Hwang et al., Reducible-shell-derived pure-copper-nanowire network and its application to transparent conducting electrodes. *Adv. Funct. Mater.* **26**, 6545–6554 (2016)
173. M. Lee, Y. Ko, B.K. Min, Y. Jun, Silver nanowire top electrodes in flexible perovskite solar cells using titanium metal as substrate. *ChemSusChem* **9**, 31–35 (2016)

174. R. Li, X. Xiang, X. Tong, J. Zou, Q. Li, Wearable double-twisted fibrous perovskite solar cell. *Adv. Mater.* **27**, 3831–3835 (2015)
175. J.H. Park et al., Flexible and transparent metallic grid electrodes prepared by evaporative assembly. *ACS Appl. Mater. Interfaces* **6**, 12380–12387 (2014)
176. Y. Li et al., High-efficiency robust perovskite solar cells on ultrathin flexible substrates. *Nat. Commun.* **7**, 10214 (2016)
177. D. Bryant et al., A transparent conductive adhesive laminate electrode for high-efficiency organic-inorganic lead halide perovskite solar cells. *Adv. Mater.* **26**, 7499–7504 (2014)
178. M. Makha et al., A transparent, solvent-free laminated top electrode for perovskite solar cells. *Sci. Technol. Adv. Mater.* **17**, 260–266 (2016)
179. G.E. Eperon et al., Efficient, semitransparent neutral-colored solar cells based on microstructured formamidinium lead trihalide perovskite. *J. Phys. Chem. Lett.* **6**, 129–138 (2015)
180. M.T. Hörantner et al., Shunt-blocking layers for semitransparent perovskite solar cells. *Adv. Mater. Interfaces* **3**, 1500837 (2016)
181. R. Venkata Krishna Rao, K. Venkata Abhinav, P.S. Karthik, S.P. Singh, Conductive silver inks and their applications in printed and flexible electronics. *RSC Adv.* **5**, 77760–77790 (2015)
182. X. Dai et al., Working from both sides: composite metallic semitransparent top electrode for high-performance perovskite solar cells. *ACS Appl. Mater. Interfaces* **8**, 4523–4531 (2016)
183. E.C. Garnett et al., Self-limited plasmonic welding of silver nanowire junctions. *Nat. Mater.* **11**, 241–249 (2012)
184. K.S. Novoselov et al., Two-dimensional gas of massless Dirac fermions in graphene. *Nature* **438**, 197–200 (2005)
185. K. Rana, J. Singh, J.-H. Ahn, A graphene-based transparent electrode for use in flexible optoelectronic devices. *J. Mater. Chem. C* **2**, 2646–2656 (2014)
186. Y. Zhang, Y.-W. Tan, H.L. Stormer, P. Kim, Experimental observation of the quantum hall effect and Berry's phase in graphene. *Nature* **438**, 201–204 (2005)
187. J. Wu et al., Organic light-emitting diodes on solution-processed graphene transparent electrodes. *ACS Nano* **4**, 43–48 (2010)
188. P. Hyesung, A.R. Jill, K. Ki Kang, B. Vladimir, K. Jing, Doped graphene electrodes for organic solar cells. *Nanotechnology* **21**, 505204 (2010)
189. H. Park et al., Flexible graphene electrode-based organic photovoltaics with record-high efficiency. *Nano Lett.* **14**, 5148–5154 (2014)
190. J. Wu et al., Organic solar cells with solution-processed graphene transparent electrodes. *Appl. Phys. Lett.* **92**, 263302 (2008)
191. P. You, Z. Liu, Q. Tai, S. Liu, F. Yan, Efficient semitransparent perovskite solar cells with graphene electrodes. *Adv. Mater.* **27**, 3632–3638 (2015)
192. F. Lang et al., Perovskite solar cells with large-area CVD-graphene for tandem solar cells. *J. Phys. Chem. Lett.* **6**, 2745–2750 (2015)
193. H. Sung et al., Transparent conductive oxide-free graphene-based perovskite solar cells with over 17% efficiency. *Adv. Energy Mater.* **6**, 1501873 (2016)
194. J. Yoon et al., Super flexible, high-efficiency perovskite solar cells utilizing graphene electrodes: towards future foldable power sources. *Energy Environ. Sci.* **10**, 337–345 (2017)
195. Z. Liu, P. Yu, C. Xie, G. Tang, F. Yan, Ultrathin and flexible perovskite solar cells with graphene transparent electrodes. *Nano Energy* **28**, 151–157 (2016)
196. E. López-Naranjo et al., Transparent electrodes: a review of the use of carbon-based nanomaterials. *J. Nanomater.* **2016**, 12 (2016)
197. M. Batmunkh, C.J. Shearer, M.J. Biggs, J.G. Shapter, Solution processed graphene structures for perovskite solar cells. *J. Mater. Chem. A* **4**, 2605–2616 (2016)
198. Y. Song, W. Fang, R. Brenes, J. Kong, Challenges and opportunities for graphene as transparent conductors in optoelectronics. *Nano Today* **10**, 681–700 (2015)
199. K. Yan et al., High-performance graphene-based hole conductor-free perovskite solar cells: Schottky junction enhanced hole extraction and electron blocking. *Small* **11**, 2269–2274 (2015)

200. S.N. Habisreutinger, R.J. Nicholas, H.J. Snaith, Carbon nanotubes in perovskite solar cells. *Adv. Energy Mater.* **7**, 1601839 (2017)
201. S.N. Habisreutinger et al., Carbon nanotube/polymer composites as a highly stable hole collection layer in perovskite solar cells. *Nano Lett.* **14**, 5561–5568 (2014)
202. Z. Li et al., Laminated carbon nanotube networks for metal electrode-free efficient perovskite solar cells. *ACS Nano* **8**, 6797–6804 (2014)
203. Z. Wei, H. Chen, K. Yan, X. Zheng, S. Yang, Hysteresis-free multi-walled carbon nanotube-based perovskite solar cells with a high fill factor. *J. Mater. Chem. A* **3**, 24226–24231 (2015)
204. L. Qiu et al., An all-solid-state fiber-type solar cell achieving 9.49% efficiency. *J. Mater. Chem. A* **4**, 10105–10109 (2016)
205. Q. Luo et al., Cross-stacked super-aligned carbon nanotube electrodes for efficient hole conductor-free perovskite solar cells. *J. Mater. Chem. A* **4**, 5569–5577 (2016)
206. X. Wang et al., TiO₂ nanotube arrays based flexible perovskite solar cells with transparent carbon nanotube electrode. *Nano Energy* **11**, 728–735 (2015)
207. X. Zheng et al., High-performance, stable and low-cost mesoscopic perovskite (CH₃NH₃PbI₃) solar cells based on poly(3-hexylthiophene)-modified carbon nanotube cathodes. *Front. Optoelectron.* **9**, 71–80 (2016)
208. X. Zheng et al., Boron doping of multiwalled carbon nanotubes significantly enhances hole extraction in carbon-based perovskite solar cells. *Nano Lett.* **17**, 2496–2505 (2017)
209. C.V.V.M. Gopi, M. Venkata-Haritha, K. Prabhakar, H.-J. Kim, Low-temperature easy-processed carbon nanotube contact for high-performance metal- and hole-transporting layer-free perovskite solar cells. *J. Photochem. Photobiol. A Chem.* **332**, 265–272 (2017)
210. L. Qiu, J. Deng, X. Lu, Z. Yang, H. Peng, Integrating perovskite solar cells into a flexible fiber. *Angew. Chem. Int. Ed.* **53**, 10425–10428 (2014)
211. L. Qiu, S. He, J. Yang, J. Deng, H. Peng, Fiber-shaped perovskite solar cells with high power conversion efficiency. *Small* **12**, 2419–2424 (2016)
212. S. He et al., Radically grown obelisk-like ZnO arrays for perovskite solar cell fibers and fabrics through a mild solution process. *J. Mater. Chem. A* **3**, 9406–9410 (2015)
213. A. Kay, M. Grätzel, Low-cost photovoltaic modules based on dye sensitized nanocrystalline titanium dioxide and carbon powder. *Sol. Energy Mater. Sol. Cells* **44**, 99–117 (1996)
214. G. Liu et al., A mesoscopic platinized graphite/carbon black counter electrode for a highly efficient monolithic dye-sensitized solar cell. *Electrochim. Acta* **69**, 334–339 (2012)
215. M. Xu et al., Highly ordered mesoporous carbon for mesoscopic CH₃NH₃PbI₃/TiO₂ heterojunction solar cell. *J. Mater. Chem. A* **2**, 8607–8611 (2014)
216. L. Zhang et al., The effect of carbon counter electrodes on fully printable mesoscopic perovskite solar cells. *J. Mater. Chem. A* **3**, 9165–9170 (2015)
217. M. Duan et al., Efficient hole-conductor-free, fully printable mesoscopic perovskite solar cells with carbon electrode based on ultrathin graphite. *Carbon* **120**, 71–76 (2017)
218. H. Li et al., 14.7% efficient mesoscopic perovskite solar cells using single-walled carbon nanotubes/carbon composite counter electrodes. *Nanoscale* **8**, 6379–6385 (2016)
219. L. Xu et al., Stable monolithic hole-conductor-free perovskite solar cells using TiO₂ nanoparticle binding carbon films. *Org. Electron.* **45**, 131–138 (2017)
220. Y. Rong et al., Hole-conductor-free mesoscopic TiO₂/CH₃NH₃PbI₃ heterojunction solar cells based on anatase nanosheets and carbon counter electrodes. *J. Phys. Chem. Lett.* **5**, 2160–2164 (2014)
221. T. Liu et al., Critical parameters in TiO₂/ZrO₂/carbon-based mesoscopic perovskite solar cell. *J. Power Sources* **293**, 533–538 (2015)
222. Y. Yang et al., The size effect of TiO₂ nanoparticles on a printable mesoscopic perovskite solar cell. *J. Mater. Chem. A* **3**, 9103–9107 (2015)
223. X. Xu et al., Lead Methylammonium triiodide perovskite-based solar cells: an interfacial charge-transfer investigation. *ChemSusChem* **7**, 3088–3309 (2014)
224. K. Cao et al., MAPbI_{3-x}Br_x mixed halide perovskites for fully printable mesoscopic solar cells with enhanced efficiency and less hysteresis. *Nanoscale* **8**, 8839–8846 (2016)

225. T. Liu et al., Spacer improvement for efficient and fully printable mesoscopic perovskite solar cells. *RSC Adv.* **7**, 10118–10123 (2017)
226. L. Liu et al., Fully printable mesoscopic perovskite solar cells with organic silane self-assembled monolayer. *J. Am. Chem. Soc.* **137**, 1790–1793 (2015)
227. J. Chen et al., Solvent effect on the hole-conductor-free fully printable perovskite solar cells. *Nano Energy* **27**, 130–137 (2016)
228. C.-Y. Chan, Y. Wang, G.-W. Wu, E. Wei-Guang Diau, Solvent-extraction crystal growth for highly efficient carbon-based mesoscopic perovskite solar cells free of hole conductors. *J. Mater. Chem. A* **4**, 3872–3878 (2016)
229. J. Chen et al., Hole-conductor-free fully printable mesoscopic solar cell with mixed-anion perovskite $\text{CH}_3\text{NH}_3\text{PbI}_{(3-x)}(\text{BF}_4)_x$. *Adv. Energy Mater.* **6**, 1502009 (2015)
230. H. Zhang et al., SrCl_2 derived perovskite facilitating a high efficiency of 16% in hole-conductor-free fully printable mesoscopic perovskite solar cells. *Adv. Mater.* **29**, 1606608 (2017)
231. Y. Rong et al., Synergy of ammonium chloride and moisture on perovskite crystallization for efficient printable mesoscopic solar cells. *Nat. Commun.* **8**, 14555 (2017)
232. M. Hu et al., Efficient hole-conductor-free, fully printable mesoscopic perovskite solar cells with a broad light harvester $\text{NH}_2\text{CH}=\text{NH}_2\text{PbI}_3$. *J. Mater. Chem. A* **2**, 17115–17121 (2014)
233. K. Cao et al., Efficient mesoscopic perovskite solar cells based on the $\text{CH}_3\text{NH}_3\text{PbI}_2\text{Br}$ light absorber. *J. Mater. Chem. A* **3**, 9116–9122 (2015)
234. A. Mei et al., A hole-conductor-free, fully printable mesoscopic perovskite solar cell with high stability. *Science* **345**, 295–298 (2014)
235. X. Li et al., Outdoor performance and stability under elevated temperatures and long-term light soaking of triple-layer mesoporous perovskite photovoltaics. *Energ. Technol.* **3**, 551–555 (2015)
236. S.G. Hashmi et al., Air processed inkjet infiltrated carbon based printed perovskite solar cells with high stability and reproducibility. *Adv. Mater. Technol.* **2**, 1600183 (2017)
237. Y. Hu et al., Stable large-area ($10 \times 10 \text{ cm}^2$) printable mesoscopic perovskite module exceeding 10% efficiency. *Solar RRL* **1**, 1600019 (2017)
238. A. Priyadarshi et al., A large area (70 cm^2) monolithic perovskite solar module with high efficiency and stability. *Energy Environ. Sci.* **9**, 3687–3692 (2016)
239. Z. Liu et al., p-Type mesoscopic NiO as an active interfacial layer for carbon counter electrode based perovskite solar cells. *Dalton Trans.* **44**, 3967–3973 (2015)
240. X. Xu et al., Hole selective NiO contact for efficient perovskite solar cells with carbon electrode. *Nano Lett.* **15**, 2402–2408 (2015)
241. Z. Liu et al., NiO nanosheets as efficient top hole transporters for carbon counter electrode based perovskite solar cells. *J. Mater. Chem. A* **3**, 24121–24127 (2015)
242. F. Zhang et al., Structure engineering of hole-conductor free perovskite-based solar cells with low-temperature-processed commercial carbon paste as cathode. *ACS Appl. Mater. Interfaces* **6**, 16140–16146 (2014)
243. H. Zhou et al., Hole-conductor-free, metal-electrode-free $\text{TiO}_2/\text{CH}_3\text{NH}_3\text{PbI}_3$ heterojunction solar cells based on a low-temperature carbon electrode. *J. Phys. Chem. Lett.* **5**, 3241–3246 (2014)
244. Z. Wei et al., Cost-efficient clamping solar cells using candle soot for hole extraction from ambipolar perovskites. *Energy Environ. Sci.* **7**, 3326–3333 (2014)
245. Y. Yang et al., An all-carbon counter electrode for highly efficient hole-conductor-free organometal perovskite solar cells. *RSC Adv.* **4**, 52825–52830 (2014)
246. Z. Wei et al., A multifunctional C + epoxy/Ag-paint cathode enables efficient and stable operation of perovskite solar cells in watery environments. *J. Mater. Chem. A* **3**, 16430–16434 (2015)
247. G. Yue et al., Low-temperature prepared carbon electrodes for hole-conductor-free mesoscopic perovskite solar cells. *Electrochim. Acta* **218**, 84–90 (2016)

248. Z. Liu, T. Shi, Z. Tang, B. Sun, G. Liao, Using a low-temperature carbon electrode for preparing hole-conductor-free perovskite heterojunction solar cells under high relative humidity. *Nanoscale* **8**, 7017–7702 (2016)
249. M. Chen et al., Boron and phosphorus co-doped carbon counter electrode for efficient hole-conductor-free perovskite solar cell. *Chem. Eng. J.* **313**, 791–800 (2017)
250. N. Cheng et al., Multi-walled carbon nanotubes act as charge transport channel to boost the efficiency of hole transport material free perovskite solar cells. *J. Power Sources* **332**, 24–29 (2016)
251. Z. Yu et al., Stable organic-inorganic perovskite solar cells without hole-conductor layer achieved via cell structure design and contact engineering. *Adv. Funct. Mater.* **26**, 4866–4873 (2016)
252. H. Wei et al., Free-standing flexible carbon electrode for a highly efficient hole-conductor-free perovskite solar cells. *Carbon* **93**, 861–868 (2015)
253. S. Gholipour et al., Highly efficient and stable perovskite solar cells based on a low-cost carbon cloth. *Adv. Energy Mater.* **6**, 1601116 (2016)
254. X. Zheng et al., Designing nano bowl arrays of mesoporous TiO₂ as an alternative electron transporting layer for carbon cathode-based perovskite solar cells. *Nanoscale* **8**, 6393–6402 (2016)
255. X. Zheng et al., In-situ fabrication of dual porous titanium dioxide films as anode for carbon cathode based perovskite solar cell. *J. Energy Chem.* **24**, 736–743 (2015)
256. H. Hu et al., Atomic layer deposition of TiO₂ for a high-efficiency hole-blocking layer in hole-conductor-free perovskite solar cells processed in ambient air. *ACS Appl. Mater. Interfaces* **8**, 17999–18007 (2016)
257. Y. Xiao et al., W-doped TiO₂ mesoporous electron transport layer for efficient hole transport material free perovskite solar cells employing carbon counter electrodes. *J. Power Sources* **342**, 489–494 (2017)
258. Z. Yu et al., A composite nanostructured electron-transport layer for stable hole-conductor free perovskite solar cells: design and characterization. *Nanoscale* **8**, 5847–5851 (2016)
259. H. Chen et al., An amorphous precursor route to the conformable oriented crystallization of CH₃NH₃PbBr₃ in mesoporous scaffolds: toward efficient and thermally stable carbon-based perovskite solar cells. *J. Mater. Chem. A* **4**, 12897–12912 (2016)
260. H. Chen et al., Solvent engineering boosts the efficiency of paintable carbon-based perovskite solar cells to beyond 14%. *Adv. Energy Mater.* **6**, 1502087 (2016)
261. X. Chang et al., Colloidal precursor-induced growth of ultra-even CH₃NH₃PbI₃ for high-performance paintable carbon-based perovskite solar cells. *ACS Appl. Mater. Interfaces* **8**, 30184–30192 (2016)
262. N. Cheng et al., Enhanced performance in hole transport material free perovskite solar cells via morphology control of PbI₂ film by solvent treatment. *J. Power Sources* **319**, 111–115 (2016)
263. C. Zhang et al., Effective improvement of the photovoltaic performance of carbon-based perovskite solar cells by additional solvents. *Nano-Micro Lett.* **8**, 347–357 (2016)
264. S. Bai et al., Cubic: column composite structure (NH₂CH=NH₂)_x(CH₃NH₃)_{1-x}PbI₃ for efficient hole-transport material-free and insulation layer free perovskite solar cells with high stability. *Electrochim. Acta* **190**, 775–779 (2016)
265. X. Chang et al., Carbon-based CsPbBr₃ perovskite solar cells: all-ambient processes and high thermal stability. *ACS Appl. Mater. Interfaces* **8**, 33649–33655 (2016)
266. J. Liang et al., All-inorganic perovskite solar cells. *J. Am. Chem. Soc.* **138**, 15829–15832 (2016)
267. F. Zhang et al., Engineering of hole-selective contact for low temperature-processed carbon counter electrode-based perovskite solar cells. *J. Mater. Chem. A* **3**, 24272–24280 (2015)
268. X. Jiang et al., Interfacial engineering of perovskite solar cells by employing a hydrophobic copper phthalocyanine derivative as hole-transporting material with improved performance and stability. *ChemSusChem* **10**, 1838–1845 (2017)

269. F. Zhang, X. Yang, M. Cheng, W. Wang, L. Sun, Boosting the efficiency and the stability of low-cost perovskite solar cells by using CuPc nanorods as hole transport material and carbon as the counter electrode. *Nano Energy* **20**, 108–116 (2016)
270. S. Liu et al., Full printable perovskite solar cells based on mesoscopic TiO₂/Al₂O₃/NiO (carbon nanotubes) architecture. *Sol. Energy* **144**, 158–165 (2017)
271. Z. Liu et al., Chemical reduction of intrinsic defects in thicker heterojunction planar perovskite solar cells. *Adv. Mater.* **29**, 1606774 (2017)
272. P. Loper et al., Organic-inorganic halide perovskite/crystalline silicon four-terminal tandem solar cells. *Phys. Chem. Chem. Phys.* **17**, 1619–1629 (2015)
273. K.A. Bush et al., Thermal and environmental stability of semi-transparent perovskite solar cells for tandems enabled by a solution-processed nanoparticle buffer layer and sputtered ITO electrode. *Adv. Mater.* **28**, 3937–3943 (2016)
274. T. Duong et al., Semitransparent perovskite solar cell with sputtered front and rear electrodes for a four-terminal tandem. *IEEE J. Photovoltaics* **6**, 679–687 (2016)
275. J. Werner et al., Sputtered rear electrode with broadband transparency for perovskite solar cells. *Sol. Energy Mater. Sol. Cells* **141**, 407–413 (2015)
276. L. Kranz et al., High-efficiency polycrystalline thin-film tandem solar cells. *J. Phys. Chem. Lett.* **6**, 2676–2681 (2015)
277. D.P. McMeekin et al., A mixed-cation lead mixed-halide perovskite absorber for tandem solar cells. *Science* **351**, 151–155 (2016)
278. Z. Yang et al., Stable low-bandgap Pb–Sn binary perovskites for tandem solar cells. *Adv. Mater.* **28**, 8990–8997 (2016)
279. G.E. Eperon et al., Perovskite-perovskite tandem photovoltaics with optimized bandgaps. *Science* **354**, 861–865 (2016)
280. F. Fu et al., Low-temperature-processed efficient semi-transparent planar perovskite solar cells for bifacial and tandem applications. *Nat. Commun.* **6**, 8932 (2015)
281. S. Albrecht et al., Monolithic perovskite/silicon-heterojunction tandem solar cells processed at low temperature. *Energy Environ. Sci.* **9**, 81–88 (2016)
282. J. Werner et al., Efficient monolithic perovskite/silicon tandem solar cell with cell area >1 cm². *J. Phys. Chem. Lett.* **7**, 161–166 (2016)
283. J.H. Heo, S.H. Im, CH₃NH₃PbBr₃–CH₃NH₃PbI₃ perovskite–perovskite tandem solar cells with exceeding 2.2 V open circuit voltage. *Adv. Mater.* **28**, 5121–5125 (2015)
284. K. Sun, P. Li, Y. Xia, J. Chang, J. Ouyang, Transparent conductive oxide-free perovskite solar cells with PEDOT: PSS as transparent electrode. *ACS Appl. Mater. Interfaces* **7**, 15314–15320 (2015)
285. F. Jiang et al., Metal electrode-free perovskite solar cells with the transfer-laminated conducting polymer electrode. *Opt. Express* **23**, A83–A91 (2015)
286. L. Bu et al., Semitransparent fully air processed perovskite solar cells. *ACS Appl. Mater. Interfaces* **7**, 17776–17781 (2015)
287. S. Xiao et al., Hierarchical dual-scaffolds enhance charge separation and collection for high-efficiency semitransparent perovskite solar cells. *Adv. Mater. Interfaces* **3**, 1600484 (2016)
288. Y. Xiao, G. Han, H. Zhou, J. Wu, An efficient titanium foil based perovskite solar cell: using a titanium dioxide nanowire array anode and transparent poly(3,4-ethylenedioxythiophene) electrode. *RSC Adv.* **6**, 2778–2784 (2016)



Impact of Electron Transport Layers (ETLs) and Hole Transport Layer (HTLs) on Perovskite Solar Cells Performance

8

Shakhawan Ahmad Mhamad, Abdussamad Mukhtar Mohammed, Madzlan Aziz, and Farhana Aziz

Contents

8.1	Introduction	228
8.2	Electron Transport Layer (ETLs) in Perovskite Solar Cells	229
8.2.1	Titanium Oxide (TiO ₂) as ETLs	231
8.2.2	Zinc Oxide (ZnO) as ETLs	232
8.2.3	Tin Oxide (SnO ₂) as ETLs	233
8.3	Hole Transport Layers (HTLs) in Perovskite Solar Cells	234
8.3.1	Organic HTLs	235
8.3.2	Inorganic HTLs	235
8.3.3	Carbonaceous HTLs	239
8.4	Conclusions and Future Directions	239
	References	240

Author Contribution

The first draft was written by SA and AMM. The final draft was reviewed and edited by FA and MA.

S. A. Mhamad

Faculty of Sciences, UniversitiTeknologi Malaysia, Johor Bahru, Malaysia

Chemistry Department, Faculty of Education, University of Sulaimani, Kurdistan, Iraq

A. M. Mohammed

Faculty of Sciences, UniversitiTeknologi Malaysia, Johor Bahru, Malaysia

Department of Chemistry, Yobe State University, Damaturu, Yobe State, Nigeria

M. Aziz

Faculty of Sciences, UniversitiTeknologi Malaysia, Johor Bahru, Malaysia

F. Aziz (✉)

Advanced Membrane Technology Research Centre (AMTEC), School of Chemical and Energy Engineering, Faculty of Engineering, UniversitiTeknologi Malaysia, Johor Bahru, Malaysia

e-mail: farhana@petroleum.utm.my

Abstract

Perovskite solar cells (PSCs) have attracted more attention recently due to their high efficiency, low cost, and long charge carrier diffusion length. Generally, PSCs consist of three layers: the electron transport layer (ETL), the absorber layer (perovskite), and the hole transfer layer (HTL). To improve the device efficiency and enhance the cell stability of PSCs, great efforts toward developing novel and efficient electron and hole-transporting materials are needed. Due to its unique properties such as high efficiency, simple process and low-cost organic-inorganic halide perovskite solar cells (PSCs) provide great potential for the photovoltaics industry. Particularly, efficient interfacial layers are very important to enhance PSCs, as charge carriers need to have smooth transport pathway, and this can be achieved by manipulating the interfacial layers and by choosing suitable interfacial layers.

8.1 Introduction

Perovskite solar cells (PSCs) were regarded as the most promising photovoltaic technology due to its low production cost, easy fabrication, and high power conversion efficiency (PCE). The PCE leaping from 3.8% to a certified 22.7% in just a few years and the stability of the devices from seconds to thousand hours have been improved [1–6]. The typical device structure of PSCs consists of transparent conductive electrode (fluorine-doped tin oxide (FTO) or indium tin oxide (ITO))/electron transport layer (ETL)/perovskite absorption layer/hole-transport layer (HTL)/metal electrode. For the mesoporous structure, the ETL includes the condense layer and mesoporous layer. To remove the organic material in titania (TiO_2) paste and enhance TiO_2 crystallinity in TiO_2 mesoporous layer, high-temperature sintering is required. The mesoporous part can be removed in the planar structure of PSCs and only the condense layer was needed as ETL. Furthermore, all the layers in the planar structure of PSCs can be processed at low temperature. Planar structure is further divided into an *n-i-p* (regular) structure and *p-i-n* (inverted) structure based on the bottom charge transport layer near the conductive layer [7].

ETL and HTL should meet the following criteria in order to obtain efficient PSCs: (1) suitable energy-level alignment for efficient charge transfer and hole blocking, (2) high electron mobility to ensure fast electron transport within the ETL, (3) high transmittance to minimize the optical energy loss, (4) have high stability, and (5) easy processing and low cost [8–11]. In general, the interfacial layer materials can be classified as organic and inorganic ETL/HTLs. Graphene, fullerene, and their derivatives have been widely used as ETLs in PSCs [12]. Organic ETLs have some advantages such as solution process can be done easily and the devices display good performance, but at the same time have some drawbacks such as their environmental, thermal, and photostability is a great concern for the long-term stability of the devices. The most widely used inorganic metal oxide materials as ETL is TiO_2 . When the device with TiO_2 was illuminated by ultraviolet light, the oxygen could be absorbed and perovskite material could be decomposed [13]. In addition, the bulk electron mobility ($<1 \text{ cm}^2 \text{ V}^{-1} \text{ s}^{-1}$) is low, which makes the mobility of the TiO_2 film pretty low ($10^{-5} \text{ cm}^2 \text{ V}^{-1} \text{ s}^{-1}$) [14]. For achieving efficient charge transport

layer and developing suitable and reliable ETL, many attempts have been made to replace TiO_2 in ETLs. Many other low-temperature processed semiconductor metal oxides have been investigated as potential candidates to replace TiO_2 such as zinc oxide (ZnO) [7, 15]; ternary metal oxides (Zn_2SO_4 [16, 17], BaSnO_3 [18, 19], SrTiO_4 [20]); metal sulfide (CdS) [21]; and metal selenide (CdSe) [22].

In this chapter, we have critically summarized about the materials used so far in ETL and HTL for PSCs applications. Methods for enhancing ETL performance such as deposition methods and metal-doping are also discussed in detail. This review aims to give insights into the current state-of-the-art of ETLs and HTLs in perovskite solar cells applications.

8.2 Electron Transport Layer (ETLs) in Perovskite Solar Cells

One of the most important components in the PSCs for highly efficient performance which plays an essential role in extracting and transporting photogenerated electrons is the electron-transport layer (ETL). Electron transport layers serve as a hole-blocking layer to suppress carrier recombination. Figure 8.1 shows the schematic illustration of ETL roles in PSCs. The major characteristics which determine the device behavior and photovoltaic performance of PSCs are carrier mobility, energy band alignment, morphology, trap states, and related interfacial properties [4, 23]. To efficiently transport and collect electrons, relatively high electron mobility materials are needed, which increase short-circuit current density (I_{sc}) and fill factor (FF) [24–26]. Moreover, trap states in the ETLs play important roles in charge transport; hence, improving interface contact between ETLs and the perovskite layer is an efficient method to increase device performance and enhance charge transport [27].

In order to achieve better device performance, morphology of the ETL is modified to enhance its contact with the perovskite layer. Most frequently TiO_2 is used as ETLs in PSCs. The rate of electron injection between the TiO_2 ETLs and perovskite absorber is very fast, at the same time there is a probability of electron recombination

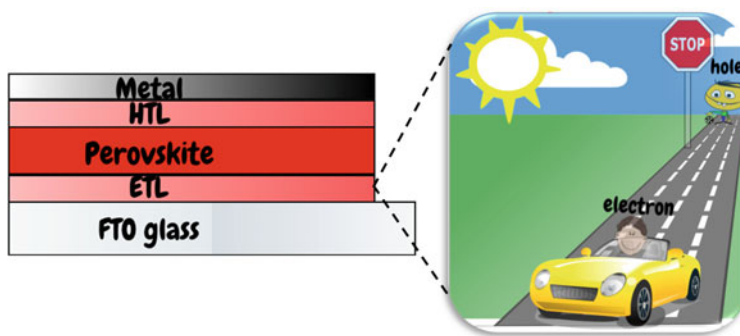


Fig. 8.1 A schematic illustration of ETL roles in perovskite solar cells

due to the low electron mobility and transport properties [28]. In addition, to get high-quality mesoscopic TiO_2 layer, a high-temperature process is required [4, 29, 30]. Therefore, to develop low-cost perovskite solar cells on various flexible substrates, the material characteristics may act as impediments to improve device performance and their application [31, 32]. In addition, a different type of zinc oxide (ZnO) morphologies has been found such as thin film, single-crystal, nanowire, and nanorod at low-temperature solution processes [33]. Additionally, ZnO has a similar energy level as TiO_2 but better electron mobility (bulk mobility: $200\text{--}300\text{ cm}^2/\text{V}\cdot\text{s}$ [33–35]) than TiO_2 , which makes it an ideal candidate for a low-temperature processed electron-selective contact for transparent electrodes, organic solar cell, thin-film transistors, light-emitting diodes, and perovskite solar cell. Liu and Kelly (2014) first used low-temperature processed thin compact ZnO layer to fabricate efficient planar PSC at room temperature and achieve efficiency up to 15.7% [15]. However, it was observed that the ZnO could easily react with perovskite if thermal annealing ($>100\text{ }^\circ\text{C}$) is carried out, which leads to the poor longtime stability of the devices [36]. To improve the device stability ZnO was combined with phenyl-C61-butric acid methyl ester (PCBM) to form PCBM/ZnO bilayer ETL, in which PCBM layer acts in charge extraction and the ZnO layer acts as a protecting layer to exclude oxygen and moisture, and also avoiding the metal electrode from diffusion [37]. To avoid a chemical reaction, zinc stannate (Zn_2SnO_4) with a good bulk electron mobility of $10\text{--}30\text{ cm}^2\text{ V}^{-1}\text{ s}^{-1}$ was investigated. Shin et al. used a quite tedious hydrothermal solution process ($<100\text{ }^\circ\text{C}$) to synthesize the ternary Zn_2SnO_4 as ETL for methylammonium iodide (MAPbI_3) perovskite solar cells (PSC), yielding a power conversion efficiency (PCE) of 15.3% [17]. Dai and coworkers first used lanthanum (La)-doped barium stannate (BaSnO_3 , LBSO) as ETL in PSCs and got device PCE of 15.1% [18]. Seok and coworkers prepared LBSO electrode below $300\text{ }^\circ\text{C}$ by using a superoxide colloidal solution route, combined with MAPbI_3 as perovskite layer, the device showed a stable output PCE of 21.2% and showed good long-time full-sun illumination stability [19]. In addition to metal oxide, several sulfides/selenides were also regarded as a replacement for TiO_2 . Mitzi and coworkers used chemical bath deposition (CBD) to deposit cadmium sulfide (CdS) and 15% stabilized efficiency were achieved. Somehow, the devices using this sulfide suffer from current losses in the ultraviolet (UV) range due to parasitic absorption caused by the rather low band gap of CdS film ($E_g = 2.4\text{ eV}$) [21, 22]. Cadmium sulfide has been used as ETL because of its high bulk electron mobility of $450\text{--}900\text{ cm}^2\text{ V}^{-1}\text{ s}^{-1}$ and it is easily obtained in low temperature. Using low-temperature solution processed CdSe nanocrystals have been prepared and a PCE of 12% have been achieved [38]. But the concern is the high toxicity of cadmium, which makes it necessary and critical to handle the liquid waste of cadmium-containing solutions. Although huge signs of progress have been obtained by replacing titania (TiO_2), as mentioned above, there are still some problems such as low device efficiency, poor chemical stability, or high-temperature processing. Recently, tin oxide (SnO_2) has attracted great attention as ETL for PSCs, and it is regarded as the most promising alternative to TiO_2 due to the following reasons: (a) SnO_2 owns good energy level and deep conduction band [39]. The excellent band

energy enhances electron extraction and hole blocking at ETL/perovskite interface. (b) Potentially it can improve the electron transport efficiency and reduce the recombination loss due to its high bulk electron mobility of up to $240 \text{ cm}^2 \text{ V}^{-1} \text{ s}^{-1}$ and high conductivity. (c) Due to its wide optical band gap (3.6–4.0 eV) and high transmittance over the whole visible spectra, SnO_2 will guarantee that most of light can come through and can be absorbed by the perovskite layer. (d) It is easily processed by low-temperature methods ($<200 \text{ }^\circ\text{C}$), which is compatible with flexible solar cells, tandem solar cells, and large-scale commercialization. (e) In comparison with TiO_2 or other ETLs, SnO_2 shows excellent chemical stability, ultraviolet (UV) resistance properties, and less photocatalytic activity which is helpful for overall device stability [40, 41].

8.2.1 Titanium Oxide (TiO_2) as ETLs

Titanium oxide is considered as the most used electron transport layer in perovskite solar cell as it owns proper electron mobility, high transparency, long electron lifetime, and favorable energy [42–44]. Generally, wide band gap of TiO_2 ($> 3.0 \text{ eV}$) can provide sufficient solar energy passing through it and maximize the absorption ability of perovskite active layer to light. The TiO_2 band gap associated with that of the perovskite layer should be compatible in order to produce superior electron transfer effect and hole blocking effect [45–49]. However, most of the TiO_2 ETLs are formed via high-temperature sintering ($> 450 \text{ }^\circ\text{C}$) with high crystallinity, which hampers the commercialization of flexible PSCs [50, 51]. This makes a number of researchers to focus more on the low-temperature PSCs that possess a simple device structure and low fabrication costs such as atomic layer deposition, electrodeposition, and chemical bath deposition method (CBD) [52–58].

Generally, it is observed that the band gap and trap states of metal oxide could be modified by doping with suitable metal elements into the lattice. Previous studies on TiO_2 doping as ETLs in PSCs are summarized in Table 8.1. Several elements have been inserted into TiO_2 such as magnesium, ruthenium, niobium, tantalum, yttrium,

Table 8.1 Doping effect on the power conversion efficiency of perovskite solar cell

Dopants	PCE (%)	References
Magnesium	12.8%	[59]
Ruthenium	15.7%	[60]
Niobium	16.3%	[61]
Tantalum	9.94%	[62]
Yttrium	16.5%	[8]
Lithium	17.1%	[63]
Indium	19.3%	[64]
Lanthanum	15.42%	[65]
Iron (III)	18.60%	[66]
Zinc	15.25%	[67]

lithium, lanthanum, iron (III), zinc, and indium in order to enhance the efficiency and stability of the corresponding devices [8, 59–67]. These results show that the semiconductive properties of TiO_2 modifying the TiO_2 conduction band minimum (CBM) and valence band maximum (VBM) level to increase the short-circuit current density (I_{sc}) or the open-circuit voltage (V_{oc}) of PSCs can be improved by elemental doping [61, 63–65, 68, 69]. However, the doping methods have some drawbacks including the complexity of the preparation procedure, high-temperature manufacturing, limited control of large-area spin-coating film quality, and expensive Ti/dopant organometal precursor; hence, investigating an efficient low-temperature method to obtain metal-doped TiO_2 layer is imminent. Introducing zinc ions into the compact TiO_2 lattice can result in better interfacial carrier extraction between ETL and perovskite. The experimental result shows that Zn doping can enhance carrier concentration of TiO_2 layer and passivate trap-state sites within TiO_2 , resulting in less carrier recombination and in turn improve the carrier transportation [70].

8.2.2 Zinc Oxide (ZnO) as ETLs

Zinc oxide (ZnO) is a II–VI semiconductor material with a band gap of 3.37 eV and a 60 meV exciton binding energy at room temperature [71, 72]. In comparison with TiO_2 , ZnO-based PSCs have some attractive advantages. For instance, ZnO is a wide band gap semiconductor; its band gap is similar to that of TiO_2 . Additionally, ZnO electron mobility is higher than TiO_2 , which makes it an ideal choice to replace TiO_2 [73, 74]. Furthermore, high crystalline ZnO can be achieved without sintering processes, which means that the ZnO thin films could give sufficient conductivity without a higher temperature sintering process [12, 75].

Studies found that deposition methods and morphological properties of ETLs are important factors in manipulating the performance of PSCs. Planar heterojunction devices have been fabricated by two-step deposition procedures, and the highest PCE of 15.7% was attained on rigid substrates [76]. In 2013, Kumar et al. used ZnO as ETL of PSCs; PCE of 8.90% were attained on rigid substrates [77]. In the same year, Bi et al. applied well-aligned ZnO nanorod arrays as ETLs; their results showed that the ZnO nanorod-based PSCs had good long-term stability of PSCs [78]. It was found that the ZnO nanorod length has a certain effect on electron transport time and lifetime. At the end of 2013, Liu and Kelly used thin compact ZnO ETL prepared by a co-precipitation method without any sintering steps to fabricate a highly efficient planar perovskite solar cell with a champion efficiency of 15.7% and an average efficiency of 13.7%, and the flexible ones yielded 10.2% [15]. Besides, solution-based co-precipitation ZnO ETLs prepared by Kim et al. in 2014 reported a sol-gel solution process to synthesize ZnO ETLs [79]. Moreover, for high-efficiency, PSCs' ZnO ETL has been prepared using vacuum process such as an atomic layer deposition (ALD) [80] or sputtering method [81].

On the other hand, the electrical characteristics of ZnO can be improved by extrinsically doping a small amount of aluminum [82, 83]. In the lattice point, aluminum (Al^{3+}) can replace zinc (Zn^{2+}) which acts as a donor and increase the

conductivity of ZnO [84, 85]; Al-doped ZnO thin film inhibits charge recombination at the ZnO/perovskite interface, resulting in better efficiency than pure ZnO devices [86]. Magnesium also can be used to suppress the charge recombination of ZnO-based device which refers to the conduction band offset at the interface between ZnO ETL and perovskite layer [87]. In addition, the electron extraction by the ETL in a perovskite cell depends on the work function of the ETL. An energy barrier mismatch (a Schottky barrier) between the work function of the ETL and the lowest unoccupied molecular orbital (LUMO) of perovskite absorber could lead to inefficient electron extraction, so matching the work function of ETL with the absorber could reduce a Schottky barrier or form an Ohmic contact to facilitate the electron injection or collection [88–90]. Another way to modify the ZnO ETL is the use of 3-aminopropanol acid [C_3H_9NO] monolayer which can enhance the interfacial energy level alignment by forming permanent dipole moments, which decrease the work function of ZnO from 4.17 to 3.52 eV, and hence obtain highly crystalline perovskite layer with reduced pin-hole and trap-state density [91]. The presence of oxygen vacancy of the lattice has a certain effect on the surface conductivity of ZnO. Zinc oxide film with more oxygen vacancies has higher surface conductivity. Furthermore, ZnO using pure Ar deposition has a lower work function of 4.33 eV than that using argon/oxygen (Ar/O_2) mixed gas deposition of 4.48 eV. Therefore, ZnO using pure argon (Ar) deposition lower conduction band level shift down than that using Ar/O_2 mixed gas deposition to increase the driven force of electron injection from ZnO/perovskite interface and lower valance edge can block the hole more efficiently [92]. In 2015, Yang et al. observed the thermal instability of PSCs prepared using ZnO as the ETLs [36]. Moreover, they showed that the basic nature of the ZnO surface leads to proton-transfer reactions at the zinc oxide/methylammonium lead halide ($ZnO/CH_3NH_3PbI_3$) interface, which results in decomposition of the perovskite film. Cheng et al. introduced a buffer layer between the zinc oxide nanoparticles (ZnO-NPs) and perovskite layers to minimize the decomposition. They found that [6, 6]-phenyl- C_{61} -butyric acid methyl ester can reduce it but not avoid completely. Furthermore, a polymeric buffer layer such as poly ethylenimine can effectively use to separate the ZnO-NPs and perovskite, which allows larger crystal formation with thermal annealing [93].

8.2.3 Tin Oxide (SnO_2) as ETLs

Recently, SnO_2 has attracted great attention as ETL for PSCs, and it is considered as the most promising alternative to TiO_2 due to following reasons: (1) SnO_2 owns deep conduction band and good energy level [39]. The excellent band energy at ETL/perovskite interface will enhance electron extraction and hole blocking. (2) SnO_2 owns high bulk electron mobility of up to $240 \text{ cm}^2 \cdot \text{V}^{-1} \cdot \text{s}^{-1}$ and high conductivity, which can potentially improve the electron transport efficiency and reduce the recombination loss. (3) SnO_2 has wide optical band gap (3.6–4.0 eV) and high transmittance over the whole visible spectra, which will guarantee that most of light can come through and can be absorbed by the perovskite layer. (4) SnO_2 is

easily processed by low-temperature methods ($<200\text{ }^{\circ}\text{C}$), which is compatible with flexible solar cells, tandem solar cells, and large-scale commercialization. (5) SnO_2 showed excellent chemical stability, UV-resistance properties, and less photocatalytic activity in comparison with TiO_2 or other ETLs, which is helpful for overall device stability [40, 41]. In 2015, several groups apart from each other applied SnO_2 in PSCs. Dai et al. using mesoporous SnO_2 nanoparticle films as ETL got an efficiency of 10.18% [94]. Ma et al. used SnO_2 combined with TiO_2 mesoporous layer as ETL and attained PCE of 7.43% [95]. Then, Kuang et al. prepared SnO_2 nanocolloidal film treated with titanium chloride (TiCl_4) as ETL and a PCE of 14.69% was achieved [96]. Although these considerable signs of progress in SnO_2 -based perovskite solar cells have been achieved, the performance of the device is still lower than the devices using TiO_2 as ETL. This could be referred to the existence of a large number of charge traps or recombination centers such as oxygen vacancies in the SnO_2 layer at high-temperature annealing. Low-temperature processed SnO_2 has been developed in order to prevent the defects induced by high-temperature processing. Tian et al. used SnO_2 thin films annealed at $200\text{ }^{\circ}\text{C}$ and a PCE of 13% was achieved [97]. Subsequently, Hagfeldt et al. prepared SnO_2 ETL using atomic layer deposition (ALD) process and a PCE of more than 18% was achieved [98]. The device's performance is still falling behind TiO_2 counterpart. You et al. reported high-quality SnO_2 nanocrystal colloidal as ETL, which annealed under moderate temperature and a PCE of 19.9% have been attained [14]. At the same time, Hagfeldt et al. using the chemical bath deposition (CBD) method prepared a double layer SnO_2 and a PCE of 20.7% was achieved [99].

8.3 Hole Transport Layers (HTLs) in Perovskite Solar Cells

The perovskite cell absorber layer is sandwiched between electron and hole transport layers (ETL and HTL). When the device is illuminated by the sun, the light is excited in the absorber layer when the excitons are extracted by the electron/hole transporting carrier layer, and finally, the charges are collected at the appropriate electrodes [100]. The basic function of the HTL is to transfer an electron from the HTL to the oxidized perovskite, but the holes should quickly move away from the interface to prevent the recombination of electrons from the metal oxide layer. The highest occupied molecular orbital (HOMO) of the HTL must lie above the highest occupied molecular orbital (HOMO) of the perovskite to provide a driving force for hole injection. Furthermore, the HTL must have good p-type conductivity and be compatible with the perovskite [101]. In order to achieve high performance in perovskite cells, HTLs have to possess: (1) suitable highest occupied molecular orbital (HOMO) energy levels for matching with the valence band energy (VBE) of perovskite materials, together with ensuring holes injection and transporting at each interfaces; (2) high hole mobility and photochemical stability; (3) suitable solubility in organic solvents and good film-forming ability for processing and device fabrication; (4) suitable light absorption in visible and near-IR region of the solar spectrum for high photocurrent [101, 102].

The stability and performance depend on the transporting layers used in the device architecture as they serve the various aspects in perovskite cells such as the following: (i) acting as a physical/energetic barrier between ETL and perovskite layer by blocking the electron transfer; (ii) improving the hole transporting efficiency due to its high hole mobility and its matching energy level with those of ETL/HTLs and electrode, (iii) avoiding the degradation and corrosion which can take place in the absence of an HTL at the metal-perovskite interface; (iv) suppressing charge recombination by fully separating the top contact from the bottom transport or contact layer leading to improved performance. Though we have a wide variety of device architectures available for achieving both stability and performance, the light-to-electricity conversion in PSCs can be further improved by using suitable HTMs with well-established device architecture [100, 103].

Insertion of suitable HTLs between perovskite layer and metal electrode can promote the separation of electrons and holes in the functional layer interface, and thus reduce charge recombination and improve the performance of solar cells. The HTLs with stable thermodynamic and optical properties would help to improve the stability of PSCs as well. Perovskite crystal can be easily decomposed in humid environments. Therefore, the quality of perovskite films can be mostly decided by the hydrophobicity of the hole-transporting layer. Those hydrophobic hole-transporting layers can protect perovskite materials from moisture and thus ensure perovskite materials to sustain crystals with larger grain size and fewer grain boundaries [102]. In general, HTLs can be classified as inorganic, organic, and carbonaceous HTLs.

8.3.1 Organic HTLs

Organic HTLs include long polymer-based HTLs and small molecule-based HTLs. The prominent ones used are 2,2', 7,7'-Tetrakis (N,N-di-p-methoxyphenylamino)-9,9'-spirobifluorene (spiro-OMeTAD, $C_{73}H_{52}N_4$), poly(3,4-ethylenedioxythiophene): polystyrene sulfonate $[(C_6H_4O_2S)_n:(C_8H_8O_3S)_n]$ (PEDOT:PSS), polytri-arylamine (PTAA, $[C_6H_4N(C_6H_2(CH_3)_3C_6H_4)]_n$), poly(3-hexylthiophene-2,5-diyl) (P3HT, $[C_{10}H_{14}S]_n$), crosslinked polymers, and other derivatives of smaller molecules like pyrene $[C_{16}H_{10}]$ derivatives, thiophene $[C_4H_4S]$ derivatives, porphyrin $[C_{34}H_{34}N_4O]$ derivatives, and carbazole $[C_{12}H_9N]$ derivatives. Figure 8.2 shows the molecular structures of organic HTLs. Till now a large number of reports on various organic HTLs such as spiro-OMeTAD, PEDOT:PSS, PTAA, and P3HT are available which have been used to provide higher open circuit voltage and achieve higher efficiencies, yet the industrial development and market potential of PSCs is restricted due to their high cost and instability in water, heat, and light [100–105].

8.3.2 Inorganic HTLs

Inorganic HTLs commonly used in perovskite solar cell can be classified into three namely: Nickel (Ni) and copper (Cu) based, a [positive] p-typed semiconductor

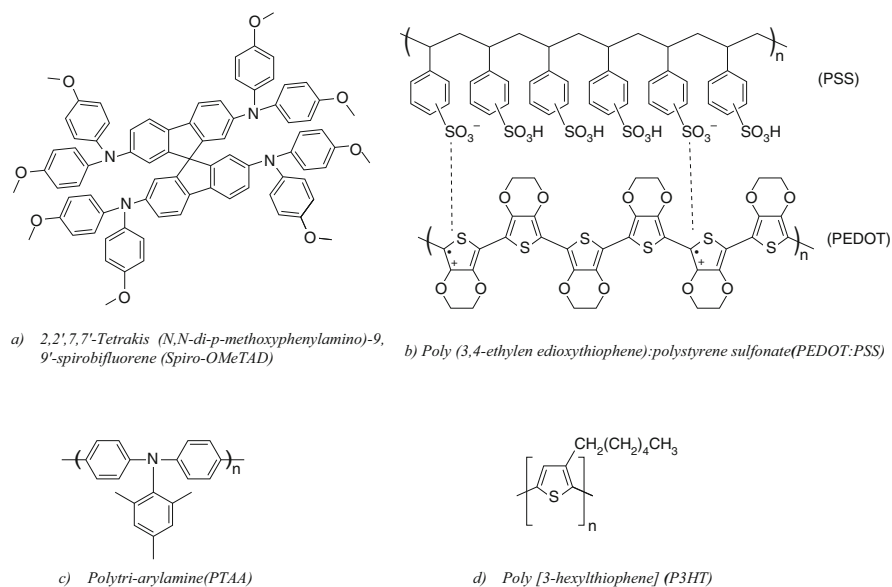


Fig. 8.2 Molecular structures of organic HTLs. **(a)** 2,2', 7,7'-Tetrakis (N,N-di-p-methoxyphenylamino)-9,9'-spirobifluorene (Spiro-OMeTAD). **(b)** Poly (3,4-ethylenedioxythiophene):polystyrene sulfonate (PEDOT:PSS). **(c)** Polytri-arylamine (PTAA). **(d)** Poly [3-hexylthiophene] (P3HT)

based, and transition metal oxide based. Nickel oxide (NiO), copper iodide (CuI), cupric oxide (CuO), cuprous oxide (Cu₂O), copper chromium oxide (CuCrO₂), and copper gallium oxide (CuGaO₂) are the examples of nickel- and copper-based HTLs used in perovskite, while copper(II) phthalocyanine (CuPc) and copper (I) thiocyanate (CuSCN) are the examples of p-typed semiconductor used. Likewise, molybdenum trioxide (MoO₃), vanadium(x) oxide (VO_x), and tungsten(x) oxide (WO_x) are the examples of transition metal oxide-based HTLs used in perovskite solar cell. To overcome the drawbacks of organic HTLs, alternate HTLs must be identified which are inexpensive and stable under all ambient conditions. This has led to the identification of effective inorganic hole transporters such as an interlayer which are inexpensive, abundant, nontoxic, and energy nonintensive. Many researchers have reported about the efficiency and stability of PSCs fabricated using various metal oxide HTLs. They have given an overview of both organic and inorganic HTLs and concluded that inorganic HTLs are better market competitors than organic HTLs [100, 101, 103, 105, 106]. Table 8.2 summarizes the examples of inorganic HTLs used in PSCs and its PCE.

8.3.2.1 Nickel Oxide

Nickel oxide (NiO) is one of the most promising HTLs with expected stability as it has good optical transparency, prevents electron leakage, and has appropriate energy levels. Nickel oxide (NiO) layer has a wide band gap and acts as a [positive] p-type transporting layer and acts as an electron blocking layer suppressing charge

Table 8.2 Examples of inorganic HTLs and its efficiency obtained so far

HTM	Thickness (nm)	PCE (%)	Ref.
Nickel oxide (NiO)	80–120	1.5–7.3	[107, 108]
Doped nickel oxide (NiO)	n/a	15.4	[109]
Copper iodide (CuI)	40–43	6.0–13.6	[110, 111]
Cuprous oxide (Cu ₂ O) and cupric oxide (CuO)	50–300	8.93–13.35	[112, 113]

recombination and enhances the hole extraction in solar cells since the performance of the solid-state PSC device mainly depends on the charge transport. Nickel oxide (NiO) as HTL also has the favorable deep-lying HOMO (valence band edge value) with work function from 5 eV to 5.6 eV. Nickel oxide (NiO) acts as a potential HTL with methylammonium lead iodide perovskite and exhibits good hole transfer characteristics and this leads to improved device performance. The inertness of NiO makes it noncorrosive toward ITO substrates, and its work function makes NiO a good HTL for PSCs. NiO is marked as a promising material for p-type or inverted PSCs. When Snaith's group used NiO layer as HTL, they found a photo-conversion efficiency of <0.1%, due to poor adhesion between perovskite and the NiO layer [100, 103, 108]. Docampo and his coworkers first reported a thin NiO layer as HTL using methyl ammonium lead iodide doped chloride [CH₃NH₃PbI₃-xCl_x] PSCs and noticed that a low coverage of perovskite surface leads to direct contact between the HTL (NiO) and the ETL (PCBM) resulting in low device performance PCE~0.1%. However, when mesoporous NiO is used as HTL in mesoscopic architecture compact layered-nickel oxide/nanoparticulate nickel oxide/methylammonium lead triiodate/phenyl-C61-butyric acid methyl ester/aluminum [CL-NiO/NP-NiO/CH₃NH₃PbI₃/PCBM/Al], they got a significant increase in PCE (~1.5%) by controlling the thickness of the bilayer nickel oxide (BL-NiO) and nanoparticulate nickel oxide (NP-NiO) to be 80 and 120 nm, respectively [103, 108, 114]. Similarly, Anand S. Subbiah et al. reported planar, inverse CH₃NH₃PbI₃ - xCl_x-based cells with inorganic hole conductors, using electro-deposited NiO as hole conductor, in which they are able to achieve a power conversion efficiency of 7.3% [107]. Likewise, Jong H. Kim et al. fabricated high-efficiency planar heterojunction perovskite solar cells based on solution-processed copper (Cu)-doped NiO_x(Cu:NiO_x) with impressive PCEs up to 15.40% and decent environmental stability; the doping significantly improved the performance [109].

8.3.2.2 Copper Iodide

Copper iodide (CuI) is a highly efficient, inexpensive, stable, wide band gap semiconductor with high conductivity and good material to use as an HTL in PSCs [108]. The first inorganic hole transport material which has been used in PSCs is CuI that resulted in a moderate PCE~6% with photovoltaic (PV) parameters ([saturation current density] J_{SC} ~17.8 mA cm⁻², [open circuit voltage] V_{OC}~0.55 V, [form factor] FF~0.62%) comparable to a spiro-OMeTAD based PSC (J_{SC}~16.1 mA cm⁻², V_{OC}~0.79 V, FF~0.61% yielding a PCE~7.9%). However, a lowering of ~300 mV in V_{OC} in CuI based PSCs was attributed to the

high recombination rate in CuI due to free iodine that could act as valence band trap and work as a recombination channel, as reported for solid state dye sensitized solar cells (s-DSSC) [110, 115]. High hole mobility of CuI which is five orders of magnitude greater than that of Spiro-OMeTAD still encourages its use in mesoscopic PSCs. Similarly, Chen et al. demonstrated that CuI as HTL in inverted planar PSCs showed PCE~13.6%, V_{OC} 1.04 V owing to its high transmittance and deep valence band (~5.1 eV), and J_{SC} 21.06 mA cm⁻² [111].

8.3.2.3 Copper Oxide and Cuprous Oxide

Cuprous oxide and cupric oxide are a typical p-type semiconductors with low valence band energy that can match very well with the perovskite (CH₃NH₃PbI₃), as well as they have high hole mobility of about 100 cm².v⁻¹.s⁻¹ and 0.129 cm².v⁻¹.s⁻¹, respectively and hence the good possibility for HTLs in PSCs [108]. CuOx-based solar cells were previously studied by creating a [positive-negative] p-n junction device structure. Cuprous oxide, with a band gap of 2.2–2.8 eV, is a promising and environmental friendly HTL for p-n junction solar. Moreover, very large hole mobility and charge diffusion length are reported for Cu₂O [113]. Considering the broad absorption of Cu₂O, as well as its close energy level alignment with the perovskite material, it could be an appropriate HTL candidate to boost the efficiency by extracting generated holes from the perovskite layer, and consequently reducing the production cost of perovskite solar cells with respect to cells employing Spiro-OMeTAD. It was shown through simulation that Cu₂O may be a strong HTL candidate in perovskite solar cells possibly reaching up to 13% efficiency conversion; however, the experimental fabrication of the proposed architecture was difficult owing to a large number of limitations related to the processing conditions [113].

Bahram Abdollahi Nejang et al. proposed a successful technique for the physical deposition for Cu₂O as a novel HTLs in perovskite solar cells. In the study, they introduced inorganic sandwiched perovskite solar cells with PCE values of up to 8.93%. Owing to the high sensitivity of Cu₂O to perovskite precursor solutions, reactive magnetron sputtering was used to deposit the Cu₂O on to the perovskite layer. The technique was used to achieve good coverage of the underlying perovskite layer and provide an effective junction between the perovskite and Cu₂O [113].

Similarly, there is a facile low-temperature method to prepare Cu₂O and CuO films and use them as HTMs in perovskite solar cells in which Cu₂O film was prepared via in situ conversion of CuI film in aqueous NaOH solution. CuO film was made by heating Cu₂O film in air. Compared with the cells using PEDOT:PSS, perovskite solar cells using Cu₂O and CuO as HTMs show significantly enhanced open-circuit voltage (V_{oc}), short-circuit current (J_{sc}), and PCE. PCEs of 13.35% and 12.16% were achieved for Cu₂O and CuO cells, respectively, which are close to the highest PCE of perovskite solar cells using inorganic HTMs. Furthermore, Cu₂O cells present improved stability.

Yan Wang et al. performed a device modeling study on planar perovskite solar cells with cuprous oxide (Cu₂O) hole transporting layers (HTLs) by using a solar cell simulation program, wxAMPS. The performance of a Cu₂O/perovskite solar cell

was correlated to the material properties of the Cu_2O HTL, such as thickness, carrier mobility, mid-gap defect, and doping concentrations. They also investigated the effect of interfacial defect densities on the solar cell performance. The simulation indicates that, with an optimized Cu_2O HTL, high-performance perovskite solar cells with efficiencies above 13% could be achieved, which shows the potential of using Cu_2O as an alternative HTL over other inorganic materials, such as NiOx and MoOx . Their study provides a theoretical breakthrough for developing perovskite solar cells with an inorganic hole transporting materials via a printing process [112].

8.3.3 Carbonaceous HTLs

Carbonaceous based HTLs involved hole-transport-free (carbon) based HTLs, graphene oxide, and reduced graphene oxide. Since efficiency and stability are both essential in photovoltaics, thus, carbon has also been identified as a potential HTL in terms of efficiency and long-term stability to some extent [100, 101, 103, 105, 106].

8.4 Conclusions and Future Directions

The major characteristics which determine the device behavior and photovoltaic performance of PSCs are carrier mobility, energy band alignment, morphology, trap states, and related interfacial properties. To efficiently transport and collect electrons, a relatively high electron mobility materials are needed, which increase short-circuit current density (I_{sc}) and fill factor (FF). Both ETLs and HTLs that are able to extract electrons and holes from the perovskite absorbing layers, respectively, are needed for the high-efficiency PSCs. Many other low-temperature processed semiconductor metal oxides have been investigated as potential candidates to substitute TiO_2 , such as ZnO , BaSnO_3 , SrTiO_4 , etc. Organic HTLs are found to be advantageous in terms of efficiency; however, it fails in ensuring long-term stability, while inorganic HTLs are found to be better when considering stability factor and relatively good efficiency. Copper and cuprous oxides can be said to be a better candidate than most of the inorganic HTLs, similarly copper iodide. Doping can significantly affect the efficiency of almost all the inorganic HTLs as can be seen in nickel oxide in which the efficiency was able to reach up to 15.40%. However, the high price of most dopant and the complexity of the doping process make it less economical. Thus, manipulating the properties of ETLs and HTLs such as varying the thickness of the interfacial layers in order to decrease the band gap of the respective material is seen as a good alternative for high performance and stable perovskite solar cells.

Acknowledgments The authors wish to thank the Ministry of Education (MOE) Malaysia [FRGS: R. J130000.7851.5F007] and Universiti Teknologi Malaysia (UTM) [GUP: Q.J130000.2513.20H63 and Q. J130000.2546.18H39] for funding.

References

1. A. Kojima, K. Teshima, Y. Shirai, T. Miyasaka, Organometal halide perovskites as visible-light sensitizers for photovoltaic cells. *J. Am. Chem. Soc.* **131**(17), 6050–6051 (2009)
2. J.H. Im, C.R. Lee, J.W. Lee, S.W. Park, N.G. Park, 6.5% efficient perovskite quantum-dot-sensitized solar cell. *Nanoscale* **3**(10), 4088–4093 (2011)
3. H.S. Kim, C.R. Lee, J.H. Im, K.B. Lee, T. Moehl, A. Marchioro, M. Grätzel, Lead iodide perovskite sensitized all-solid-state submicron thin film mesoscopic solar cell with efficiency exceeding 9%. *Sci. Rep.* **2**, 591 (2012)
4. W.S. Yang, J.H. Noh, N.J. Jeon, Y.C. Kim, S. Ryu, J. Seo, S.I. Seok, High-performance photovoltaic perovskite layers fabricated through intramolecular exchange. *Science* **348**(6240), 1234–1237 (2015)
5. W.S. Yang, B.W. Park, E.H. Jung, N.J. Jeon, Y.C. Kim, D.U. Lee, S.I. Seok, Iodide management in formamidinium-lead-halide-based perovskite layers for efficient solar cells. *Science* **356**(6345), 1376–1379 (2017)
6. NREL Best Research-Cell Efficiencies, <https://www.nrel.gov/pv/assets/images/efficiency-chart.png>. Accessed Apr 2018
7. J. You, L. Meng, T.B. Song, T.F. Guo, Y.M. Yang, W.H. Chang, Y. Liu, Improved air stability of perovskite solar cells via solution-processed metal oxide transport layers. *Nat. Nanotechnol.* **11**(1), 75 (2016)
8. H. Zhou, Q. Chen, G. Li, S. Luo, T.B. Song, H.S. Duan, Y. Yang, Interface engineering of highly efficient perovskite solar cells. *Science* **345**(6196), 542–546 (2014)
9. S.K. Pathak, A. Abate, P. Ruckdeschel, B. Roose, K.C. Gödel, Y. Vaynzof, A. Sepe, Performance and stability enhancement of dye-sensitized and perovskite solar cells by Al doping of TiO₂. *Adv. Funct. Mater.* **24**(38), 6046–6055 (2014)
10. H. Sun, J. Deng, L. Qiu, X. Fang, H. Peng, Recent progress in solar cells based on one-dimensional nanomaterials. *Energy Environ. Sci.* **8**(4), 1139–1159 (2015)
11. C.C. Chueh, C.Z. Li, A.K.Y. Jen, Recent progress and perspective in solution-processed interfacial materials for efficient and stable polymer and organometal perovskite solar cells. *Energy Environ. Sci.* **8**(4), 1160–1189 (2015)
12. J. You, Z. Hong, Y. Yang, Q. Chen, M. Cai, T.B. Song, Y. Yang, Low-temperature solution-processed perovskite solar cells with high efficiency and flexibility. *ACS Nano* **8**(2), 1674–1680 (2014)
13. T. Leijtens, G.E. Eperon, S. Pathak, A. Abate, M.M. Lee, H.J. Snaith, Overcoming ultraviolet light instability of sensitized TiO₂ with meso-superstructured organometal tri-halide perovskite solar cells. *Nat. Commun.* **4**, 2885 (2013)
14. Q. Jiang, L. Zhang, H. Wang, X. Yang, J. Meng, H. Liu, J. You, Enhanced electron extraction using SnO₂ for high-efficiency planar-structure HC(NH₂)₂PbI₃-based perovskite solar cells. *Nat. Energy* **2**(1), 16177 (2017)
15. D. Liu, T.L. Kelly, Perovskite solar cells with a planar heterojunction structure prepared using room-temperature solution processing techniques. *Nat. Photonics* **8**(2), 133 (2014)
16. S.S. Mali, C.S. Shim, C.K. Hong, Highly porous Zinc Stannate (Zn₂SnO₄) nanofibers scaffold photoelectrodes for efficient methyl ammonium halide perovskite solar cells. *Sci. Rep.* **5**, 11424 (2015)
17. S.S. Shin, W.S. Yang, J.H. Noh, J.H. Suk, N.J. Jeon, J.H. Park, S.I. Seok, High-performance flexible perovskite solar cells exploiting Zn₂SnO₄ prepared in solution below 100 C. *Nat. Commun.* **6**, 7410 (2015)
18. L. Zhu, J. Ye, X. Zhang, H. Zheng, G. Liu, X. Pan, S. Dai, Performance enhancement of perovskite solar cells using a La-doped BaSnO₃ electron transport layer. *J. Mater. Chem. A* **5**(7), 3675–3682 (2017)
19. S.S. Shin, E.J. Yeom, W.S. Yang, S. Hur, M.G. Kim, J. Im, S.I. Seok, Colloidally prepared La-doped BaSnO₃ electrodes for efficient, photostable perovskite solar cells. *Science* **356**(6334), 167–171 (2017)

20. A. Bera, K. Wu, A. Sheikh, E. Alarousu, O.F. Mohammed, T. Wu, Perovskite oxide SrTiO₃ as an efficient electron transporter for hybrid perovskite solar cells. *J. Phys. Chem. C* **118**(49), 28494–28501 (2014)
21. J. Liu, C. Gao, L. Luo, Q. Ye, X. He, L. Ouyang, W. Lau, Low-temperature, solution processed metal sulfide as an electron transport layer for efficient planar perovskite solar cells. *J. Mater. Chem. A* **3**(22), 11750–11755 (2015)
22. W.A. Dunlap-Shohl, R. Younts, B. Gautam, K. Gundogdu, D.B. Mitzi, Effects of Cd diffusion and doping in high-performance perovskite solar cells using CdS as electron transport layer. *J. Phys. Chem. C* **120**(30), 16437–16445 (2016)
23. G. Yang, H. Tao, P. Qin, W. Ke, G. Fang, Recent progress in electron transport layers for efficient perovskite solar cells. *J. Mater. Chem. A* **4**(11), 3970–3990 (2016)
24. S. Ryu, J.H. Noh, N.J. Jeon, Y.C. Kim, W.S. Yang, J. Seo, S.I. Seok, Voltage output of efficient perovskite solar cells with high open-circuit voltage and fill factor. *Energy Environ. Sci.* **7**(8), 2614–2618 (2014)
25. A.R.B.M. Yusoff, M.K. Nazeeruddin, Organohalide lead perovskites for photovoltaic applications. *J. Phys. Chem. Lett.* **7**(5), 851–866 (2016)
26. Y.F. Chiang, J.Y. Jeng, M.H. Lee, S.R. Peng, P. Chen, T.F. Guo, C.M. Hsu, High voltage and efficient bilayer heterojunction solar cells based on an organic–inorganic hybrid perovskite absorber with a low-cost flexible substrate. *Phys. Chem. Chem. Phys.* **16**(13), 6033–6040 (2014)
27. G.E. Eperon, V.M. Burlakov, P. Docampo, A. Goriely, H.J. Snaith, Morphological control for high performance, solution-processed planar heterojunction perovskite solar cells. *Adv. Funct. Mater.* **24**(1), 151–157 (2014)
28. S. Gubbala, V. Chakrapani, V. Kumar, M.K. Sunkara, Band-edge engineered hybrid structures for dye-sensitized solar cells based on SnO₂ nanowires. *Adv. Funct. Mater.* **18**(16), 2411–2418 (2008)
29. N.J. Jeon, J.H. Noh, W.S. Yang, Y.C. Kim, S. Ryu, J. Seo, S.I. Seok, Compositional engineering of perovskite materials for high performance solar cells. *Nature* **517**(7535), 476 (2015)
30. D. Bi, S.J. Moon, L. Häggman, G. Boschloo, L. Yang, E.M. Johansson, A. Hagfeldt, Using a two-step deposition technique to prepare perovskite (CH₃NH₃PbI₃) for thin film solar cells based on ZrO₂ and TiO₂ mesostructures. *RSC Adv.* **3**(41), 18762–18766 (2013)
31. Z.M. Beiley, M.D. McGehee, Modeling low cost hybrid tandem photovoltaics with the potential for efficiencies exceeding 20%. *Energy Environ. Sci.* **5**(11), 9173–9179 (2012)
32. C. Roldán-Carmona, O. Malinkiewicz, A. Soriano, G.M. Espallargas, A. Garcia, P. Reinecke, H.J. Bolink, Flexible high efficiency perovskite solar cells. *Energy Environ. Sci.* **7**(3), 994–997 (2014)
33. Ü. Özgür, Y.I. Alivov, C. Liu, A. Teke, M. Reshchikov, S. Doğan, H. Morkoç, A comprehensive review of ZnO materials and devices. *J. Appl. Phys.* **98**(4), 11 (2005)
34. H. Tang, K. Prasad, R. Sanjines, P.E. Schmid, F. Levy, Electrical and optical properties of TiO₂ anatase thin films. *J. Appl. Phys.* **75**(4), 2042–2047 (1994)
35. H.S. Bae, M.H. Yoon, J.H. Kim, S. Im, Photodetecting properties of ZnO-based thin-film transistors. *Appl. Phys. Lett.* **83**(25), 5313–5315 (2003)
36. J. Yang, B.D. Siempelkamp, E. Mosconi, F. De Angelis, T.L. Kelly, Origin of the thermal instability in CH₃NH₃PbI₃ thin films deposited on ZnO. *Chem. Mater.* **27**(12), 4229–4236 (2015)
37. L.Q. Zhang, X.W. Zhang, Z.G. Yin, Q. Jiang, X. Liu, J.H. Meng, H.L. Wang, Highly efficient and stable planar heterojunction perovskite solar cells via a low temperature solution process. *J. Mater. Chem. A* **3**(23), 12133–12138 (2015)
38. L. Wang, W. Fu, Z. Gu, C. Fan, X. Yang, H. Li, H. Chen, Low temperature solution processed planar heterojunction perovskite solar cells with a CdSe nanocrystal as an electron transport/extraction layer. *J. Mater. Chem. C* **2**(43), 9087–9090 (2014)
39. A.J. Nozik, R. Memming, Physical chemistry of semiconductor– liquid interfaces. *J. Phys. Chem.* **100**(31), 13061–13078 (1996)

40. B. Bob, T.B. Song, C.C. Chen, Z. Xu, Y. Yang, Nanoscale dispersions of gelled SnO₂: material properties and device applications. *Chem. Mater.* **25**(23), 4725–4730 (2013)
41. H.J. Snaith, C. Ducati, SnO₂-based dye-sensitized hybrid solar cells exhibiting near unity absorbed photon-to-electron conversion efficiency. *Nano Lett.* **10**(4), 1259–1265 (2010)
42. C. Liang, P. Li, Y. Zhang, H. Gu, Q. Cai, X. Liu, G. Shao, Mild solution-processed metal-doped TiO₂ compact layers for hysteresis-less and performance-enhanced perovskite solar cells. *J. Power Sources* **372**, 235–244 (2017)
43. P. Li, C. Liang, B. Bao, Y. Li, X. Hu, Y. Wang, Y. Song, Inkjet manipulated homogeneous large size perovskite grains for efficient and large-area perovskite solar cells. *Nano Energy* **46**, 203–211 (2018)
44. C. Liang, P. Li, H. Gu, Y. Zhang, F. Li, Y. Song, G. Xing, One-step inkjet printed perovskite in air for efficient light harvesting. *Solar RRL* **2**(2), 1700217 (2018)
45. C. Liang, Z. Wu, P. Li, J. Fan, Y. Zhang, G. Shao, Chemical bath deposited rutile TiO₂ compact layer toward efficient planar heterojunction perovskite solar cells. *Appl. Surf. Sci.* **391**, 337–344 (2017)
46. L. Wang, Z. Yuan, T.A. Egerton, Comparison of nano-particulate TiO₂ prepared from titanium tetrachloride and titanium tetraisopropoxide. *Mater. Chem. Phys.* **133**(1), 304–310 (2012)
47. J.H. Heo, M.S. You, M.H. Chang, W. Yin, T.K. Ahn, S.J. Lee, S.H. Im, Hysteresis-less mesoscopic CH₃NH₃PbI₃ perovskite hybrid solar cells by introduction of Li-treated TiO₂ electrode. *Nano Energy* **15**, 530–539 (2015)
48. D.O. Scanlon, C.W. Dunnill, J. Buckeridge, S.A. Shevlin, A.J. Logsdail, S.M. Woodley, G.W. Watson, Band alignment of rutile and anatase TiO₂. *Nat. Mater.* **12**(9), 798 (2013)
49. H. Tao, Z. Ma, G. Yang, H. Wang, H. Long, H. Zhao, G. Fang, Room-temperature processed tin oxide thin film as effective hole blocking layer for planar perovskite solar cells. *Appl. Surf. Sci.* **434**, 1336–1343 (2018)
50. Q. Yue, J. Duan, L. Zhu, K. Zhang, H. Wang, Effect of HCl etching on TiO₂ nanorod-based perovskite solar cells. *J. Mater. Sci.* **53**(21), 15257–15270 (2018)
51. D. Bi, C. Yi, J. Luo, J.D. Décoppet, F. Zhang, S.M. Zakeeruddin, M. Grätzel, Polymer-templated nucleation and crystal growth of perovskite films for solar cells with efficiency greater than 21%. *Nat. Energy* **1**(10), 16142 (2016)
52. M. Xiao, F. Huang, W. Huang, Y. Dkhissi, Y. Zhu, J. Etheridge, L. Spiccia, A fast deposition-crystallization procedure for highly efficient lead iodide perovskite thin-film solar cells. *Angew. Chem. Int. Ed.* **53**(37), 9898–9903 (2014)
53. Z. Xiao, C. Bi, Y. Shao, Q. Dong, Q. Wang, Y. Yuan, J. Huang, Efficient, high yield perovskite photovoltaic devices grown by interdiffusion of solution-processed precursor stacking layers. *Energy Environ. Sci.* **7**(8), 2619–2623 (2014)
54. Q. Cai, Y. Zhang, C. Liang, P. Li, H. Gu, X. Liu, G. Shao, Enhancing efficiency of planar structure perovskite solar cells using Sn-doped TiO₂ as electron transport layer at low temperature. *Electrochim. Acta* **261**, 227–235 (2018)
55. Y. Wu, F. Xie, H. Chen, X. Yang, H. Su, M. Cai, L. Han, Thermally stable MAPbI₃ perovskite solar cells with efficiency of 19.19% and area over 1 cm² achieved by additive engineering. *Adv. Mater.* **29**(28), 1701073 (2017)
56. F. Di Giacomo, V. Zardetto, A. D'Epifanio, S. Pescetelli, F. Matteocci, S. Razza, T.M. Brown, Flexible perovskite photovoltaic modules and solar cells based on atomic layer deposited compact layers and UV-irradiated TiO₂ scaffolds on plastic substrates. *Adv. Energy Mater.* **5**(8), 1401808 (2015)
57. D. Yang, R. Yang, J. Zhang, Z. Yang, S.F. Liu, C. Li, High efficiency flexible perovskite solar cells using superior low temperature TiO₂. *Energy Environ. Sci.* **8**(11), 3208–3214 (2015)
58. K. Wang, Y. Shi, Q. Dong, Y. Li, S. Wang, X. Yu, T. Ma, Low-temperature and solution-processed amorphous WO_x as electron-selective layer for perovskite solar cells. *J. Phys. Chem. Lett.* **6**(5), 755–759 (2015)

59. J. Wang, M. Qin, H. Tao, W. Ke, Z. Chen, J. Wan, G. Fang, Performance enhancement of perovskite solar cells with Mg-doped TiO₂ compact film as the hole-blocking layer. *Appl. Phys. Lett.* **106**(12), 121104 (2015)
60. Z. Xu, X. Yin, Y. Guo, Y. Pu, M. He, Ru-doping in TiO₂ electron transport layers of planar heterojunction perovskite solar cells for enhanced performance. *J. Mater. Chem. C* **6**(17), 4746–4752 (2018)
61. B.X. Chen, H.S. Rao, W.G. Li, Y.F. Xu, H.Y. Chen, D.B. Kuang, C.Y. Su, Achieving high-performance planar perovskite solar cell with Nb-doped TiO₂ compact layer by enhanced electron injection and efficient charge extraction. *J. Mater. Chem. A* **4**(15), 5647–5653 (2016)
62. R. Ranjan, A. Prakash, A. Singh, A. Singh, A. Garg, R.K. Gupta, Effect of tantalum doping in a TiO₂ compact layer on the performance of planar spiro-OMeTAD free perovskite solar cells. *J. Mater. Chem. A* **6**(3), 1037–1047 (2018)
63. D. Liu, S. Li, P. Zhang, Y. Wang, R. Zhang, H. Sarvari, Z.D. Chen, Efficient planar heterojunction perovskite solar cells with Li-doped compact TiO₂ layer. *Nano Energy* **31**, 462–468 (2017)
64. J. Peng, T. Duong, X. Zhou, H. Shen, Y. Wu, H.K. Mulmudi, K.J. Weber, Efficient indium-doped TiO_x electron transport layers for high-performance perovskite solar cells and perovskite-silicon tandems. *Adv. Energy Mater.* **7**(4), 1601768 (2017)
65. X.X. Gao, Q.Q. Ge, D.J. Xue, J. Ding, J.Y. Ma, Y.X. Chen, J.S. Hu, Tuning the fermi-level of TiO₂ mesoporous layer by lanthanum doping towards efficient perovskite solar cells. *Nanoscale* **8**(38), 16881–16885 (2016)
66. X. Gu, Y. Wang, T. Zhang, D. Liu, R. Zhang, P. Zhang, S. Li, Enhanced electronic transport in Fe³⁺-doped TiO₂ for high efficiency perovskite solar cells. *J. Mater. Chem. C* **5**(41), 10754–10760 (2017)
67. M. Lv, W. Lv, X. Fang, P. Sun, B. Lin, S. Zhang, N. Yuan, Performance enhancement of perovskite solar cells with a modified TiO₂ electron transport layer using Zn-based additives. *RSC Adv.* **6**(41), 35044–35050 (2016)
68. K. Wojciechowski, M. Saliba, T. Leijtens, A. Abate, H.J. Snaith, Sub-150 C processed meso-structured perovskite solar cells with enhanced efficiency. *Energy Environ. Sci.* **7**(3), 1142–1147 (2014)
69. J.T.W. Wang, J.M. Ball, E.M. Barea, A. Abate, J.A. Alexander-Webber, J. Huang, R.J. Nicholas, Low-temperature processed electron collection layers of graphene/TiO₂ nanocomposites in thin film perovskite solar cells. *Nano Lett.* **14**(2), 724–730 (2013)
70. M. Thambidurai, J.Y. Kim, Y. Ko, H.J. Song, H. Shin, J. Song, C. Lee, High-efficiency inverted organic solar cells with polyethylene oxide-modified Zn-doped TiO₂ as an interfacial electron transport layer. *Nanoscale* **6**(15), 8585–8589 (2014)
71. C.X. Xu, X.W. Sun, Z.L. Dong, G.P. Zhu, Y.P. Cui, Zinc oxide hexagram whiskers. *Appl. Phys. Lett.* **88**(9), 093101 (2006)
72. L. Wu, Y. Wu, X. Pan, F. Kong, Synthesis of ZnO nanorod and the annealing effect on its photoluminescence property. *Opt. Mater.* **28**(4), 418–422 (2006)
73. W. Ke, G. Fang, Q. Liu, L. Xiong, P. Qin, H. Tao, G. Yang, Low-temperature solution-processed tin oxide as an alternative electron transporting layer for efficient perovskite solar cells. *J. Am. Chem. Soc.* **137**(21), 6730–6733 (2015)
74. O. Malinkiewicz, A. Yella, Y.H. Lee, G.M. Espallargas, M. Graetzel, M.K. Nazeeruddin, H.J. Bolink, Perovskite solar cells employing organic charge-transport layers. *Nat. Photonics* **8**(2), 128 (2014)
75. Q. Wang, Y. Shao, Q. Dong, Z. Xiao, Y. Yuan, J. Huang, Large fill-factor bilayer iodine perovskite solar cells fabricated by a low-temperature solution-process. *Energy Environ. Sci.* **7**(7), 2359–2365 (2014)
76. J. Burschka, N. Pellet, S.J. Moon, R. Humphry-Baker, P. Gao, M.K. Nazeeruddin, M. Grätzel, Sequential deposition as a route to high-performance perovskite-sensitized solar cells. *Nature* **499**(7458), 316 (2013)

77. M.H. Kumar, N. Yantara, S. Dharani, M. Graetzel, S. Mhaisalkar, P.P. Boix, N. Mathews, Flexible, low-temperature, solution processed ZnO-based perovskite solid state solar cells. *Chem. Commun.* **49**(94), 11089–11091 (2013)
78. D. Bi, G. Boschloo, S. Schwarzmueller, L. Yang, E.M. Johansson, A. Hagfeldt, Efficient and stable $\text{CH}_3\text{NH}_3\text{PbI}_3$ -sensitized ZnO nanorod array solid-state solar cells. *Nanoscale* **5**(23), 11686–11691 (2013)
79. J. Kim, G. Kim, T.K. Kim, S. Kwon, H. Back, J. Lee, K. Lee, Efficient planar-heterojunction perovskite solar cells achieved via interfacial modification of a sol–gel ZnO electron collection layer. *J. Mater. Chem. A* **2**(41), 17291–17296 (2014)
80. X. Dong, H. Hu, B. Lin, J. Ding, N. Yuan, The effect of ALD-ZnO layers on the formation of $\text{CH}_3\text{NH}_3\text{PbI}_3$ with different perovskite precursors and sintering temperatures. *Chem. Commun.* **50**(92), 14405–14408 (2014)
81. L. Liang, Z. Huang, L. Cai, W. Chen, B. Wang, K. Chen, B. Fan, Magnetron sputtered zinc oxide nanorods as thickness-insensitive cathode interlayer for perovskite planar-heterojunction solar cells. *ACS Appl. Mater. Interfaces* **6**(23), 20585–20589 (2014)
82. K. Ellmer, Magnetron sputtering of transparent conductive zinc oxide: relation between the sputtering parameters and the electronic properties. *J. Phys. D: Appl. Phys.* **33**(4), R17 (2000)
83. Liu, Y., Li, Y., and Zeng, H. (2013). ZnO-based transparent conductive thin films: doping, performance, and processing. *J. Nanomater.*, 2013
84. J.A. Sans, J.F. Sánchez-Royo, A. Segura, G. Tobias, E. Canadell, Chemical effects on the optical band-gap of heavily doped ZnO: M III (M= Al, Ga, In): an investigation by means of photoelectron spectroscopy, optical measurements under pressure, and band structure calculations. *Phys. Rev. B* **79**(19), 195105 (2009)
85. J.L. Zhao, X.W. Sun, H. Ryu, Y.B. Moon, Thermally stable transparent conducting and highly infrared reflective Ga-doped ZnO thin films by metal organic chemical vapor deposition. *Opt. Mater.* **33**(6), 768–772 (2011)
86. K. Mahmood, B.S. Swain, H.S. Jung, Controlling the surface nanostructure of ZnO and Al-doped ZnO thin films using electrostatic spraying for their application in 12% efficient perovskite solar cells. *Nanoscale* **6**(15), 9127–9138 (2014)
87. J. Dong, J. Shi, D. Li, Y. Luo, Q. Meng, Controlling the conduction band offset for highly efficient ZnO nanorods based perovskite solar cell. *Appl. Phys. Lett.* **107**(7), 073507 (2015)
88. H. Kang, S. Hong, J. Lee, K. Lee, Electrostatically self-assembled nonconjugated polyelectrolytes as an ideal interfacial layer for inverted polymer solar cells. *Adv. Mater.* **24**(22), 3005–3009 (2012)
89. J.C. Yu, D.B. Kim, G. Baek, B.R. Lee, E.D. Jung, S. Lee, M.H. Song, High-performance planar perovskite optoelectronic devices: a morphological and interfacial control by polar solvent treatment. *Adv. Mater.* **27**(23), 3492–3500 (2015)
90. Y. Zhou, C. Fuentes-Hernandez, J. Shim, J. Meyer, A.J. Giordano, H. Li, M. Fenoll, A universal method to produce low-work function electrodes for organic electronics. *Science* **336**(6079), 327–332 (2012)
91. L. Zuo, Z. Gu, T. Ye, W. Fu, G. Wu, H. Li, H. Chen, Enhanced photovoltaic performance of $\text{CH}_3\text{NH}_3\text{PbI}_3$ perovskite solar cells through interfacial engineering using self-assembling monolayer. *J. Am. Chem. Soc.* **137**(7), 2674–2679 (2015)
92. Z.L. Tseng, C.H. Chiang, C.G. Wu, Surface engineering of ZnO thin film for high efficiency planar perovskite solar cells. *Sci. Rep.* **5**, 13211 (2015)
93. Y. Cheng, Q.D. Yang, J. Xiao, Q. Xue, H.W. Li, Z. Guan, S.W. Tsang, Decomposition of organometal halide perovskite films on zinc oxide nanoparticles. *ACS Appl. Mater. Interfaces* **7**(36), 19986–19993 (2015)
94. Y. Li, J. Zhu, Y. Huang, F. Liu, M. Lv, S. Chen, S. Dai, Mesoporous SnO_2 nanoparticle films as electron-transporting material in perovskite solar cells. *RSC Adv.* **5**(36), 28424–28429 (2015)
95. Q. Dong, Y. Shi, K. Wang, Y. Li, S. Wang, H. Zhang, T. Ma, Insight into perovskite solar cells based on SnO_2 compact electron-selective layer. *J. Phys. Chem. C* **119**(19), 10212–10217 (2015)

96. H.S. Rao, B.X. Chen, W.G. Li, Y.F. Xu, H.Y. Chen, D.B. Kuang, C.Y. Su, Improving the extraction of photogenerated electrons with SnO₂ nanocolloids for efficient planar perovskite solar cells. *Adv. Funct. Mater.* **25**(46), 7200–7207 (2015)
97. J. Song, E. Zheng, J. Bian, X.F. Wang, W. Tian, Y. Sanehira, T. Miyasaka, Low-temperature SnO₂-based electron selective contact for efficient and stable perovskite solar cells. *J. Mater. Chem. A* **3**(20), 10837–10844 (2015)
98. J.P.C. Baena, L. Steier, W. Tress, M. Saliba, S. Neutzner, T. Matsui, A. Petrozza, Highly efficient planar perovskite solar cells through band alignment engineering. *Energy Environ. Sci.* **8**(10), 2928–2934 (2015)
99. E.H. Anaraki, A. Kermanpur, L. Steier, K. Domanski, T. Matsui, W. Tress, J.P. Correa-Baena, Highly efficient and stable planar perovskite solar cells by solution-processed tin oxide. *Energy Environ. Sci.* **9**(10), 3128–3134 (2016)
100. S. Pitchaiya, M. Natarajan, A review on the classification of organic /inorganic /carbonaceous hole transporting materials for perovskite solar cell application. *Arab. J. Chem.*. King Saud University (2018). <https://doi.org/10.1016/j.arabjc.2018.06.006>
101. P. Dhingra, P. Singh, J.S. Rana, A. Garg, P. Kar, Hole-transporting materials for perovskite-sensitized solar cells. *Energy Technology.* **4**(8), 891–938 (2016). <https://doi.org/10.1002/ente.201500534>
102. X. Zhao, M. Wang, Organic hole-transporting materials for efficient perovskite solar cells. *Materials today energy.* **7**, 208–220 (2018). <https://doi.org/10.1016/j.mtener.2017.09.011>. Elsevier Ltd
103. Z.H. Bakr, Q. Wali, A. Fakhruddin, L. Schmidt-mende, T.M. Brown, R. Jose, Nano energy advances in hole transport materials engineering for stable and efficient perovskite solar cells. *Nano Energy.* **34**, 271–305 (2017). <https://doi.org/10.1016/j.nanoen.2017.02.025>. Nov 2016. Elsevier Ltd
104. D. Zhao, M. Sexton, H. Park, G. Baure, C.J. Nino, F. So, High-efficiency solution-processed planar perovskite solar cells with a polymer hole transport layer. *Advanced Energy Materials.* **5**(6), 1401855 (2015). <https://doi.org/10.1002/aenm.201401855>
105. L. Cali, S. Kazim, M. Gratzel, S. Ahmad, Hole-transport materials for perovskite solar cells. *Angewandte Chemie International Edition.* **55**(47), 14522–14545 (2016). <https://doi.org/10.1002/anie.201601757>
106. W. Yan, S. Ye, Y. Li, W. Sun, H. Rao, Z. Liu, Z. Bian, C. Hung, Hole-transporting materials in inverted planar perovskite solar cells. *Advanced Energy Materials.* **6**(17), 1600474 (2016). <https://doi.org/10.1002/aenm.201600474>
107. A.S. Subbiah, A. Halder, S. Ghosh, N. Mahuli, G. Hodes, S.K. Sarkar, inorganic hole conducting layers for perovskite-based solar cells. *J. Phys. Chem. Lett.* **5**(10), 1748–53 (2014).
108. R. Rajeswari, M. Mrinalini, S. Prasanthkumar, L. Giribabu, Emerging of inorganic hole transporting materials for perovskite solar cells, 1–20 (2017). <https://doi.org/10.1002/tcr.201600117>
109. J.H. Kim, P. Liang, S.T. Williams, N. Cho, C. Chueh, M.S. Glaz, D.S. Ginger, A.K.Y. Jen, High-performance and environmentally stable planar heterojunction perovskite solar cells based on a solution-processed copper-doped nickel oxide hole-transporting layer. *Advanced materials.* **27**(4), 695–701 (2014). <https://doi.org/10.1002/adma.201404189>
110. V.P.S. Perera, K. Tennakone, Recombination processes in dye-sensitized solid-state solar cells with CuI as the hole collector. *Solar Energy Materials and Solar Cells.* **79**(2), 249–255 (2003). [https://doi.org/10.1016/S0927-0248\(03\)00103-X](https://doi.org/10.1016/S0927-0248(03)00103-X)
111. W.Y. Chen, L.L. Deng, S.M. Dai, X. Wang, C.B. Tian, X.X. Zhan, S.Y. Xie, R.B. Huangb, L.S. Zheng, low-cost solution-processed copper iodide as an alternative to PEDOT: PSS hole transport layer for efficient and stable inverted planar heterojunction perovskite solar cells. *J. Mater. Chem. A.*, **3**(38), 19353–9 (2015). <https://doi.org/10.1039/C5TA05286F>
112. Y. Wang, Z. Xia, J. Liang, X. Wang, Y. Liu, C. Liu, S. Zhang, H. Zhou, Towards printed perovskite solar cells with cuprous oxide hole transporting layers : a theoretical design.

- Semicond. Sci. Technol. **30**(5), 54004 (2015). <https://doi.org/10.1088/0268-1242/30/5/054004>. IOP Publishing
113. B.A. Nejad, V. Ahmadi, S. Gharibzadeh, Cuprous oxide as a potential low-cost hole-transport material for stable perovskite solar cells. *Chem Sus Chem.* **9**(3), 302–313 (2016). <https://doi.org/10.1002/cssc.201501273>
114. P. Docampo, J.M. Ball, M. Darwich, G.E. Eperon, H.J. Snaith, Efficient organometal trihalide perovskite planar-heterojunction solar cells on flexible polymer substrates. *Nat. Commun.* **4**, 1–6 (2013). <https://doi.org/10.1038/ncomms3761>. Nature Publishing Group
115. J.A. Christians, R.C. Fung, P.V. Kamat, An inorganic hole conductor for organo-lead halide perovskite solar cells. Improved hole conductivity with copper iodide. *J. Am. Chem. Soc.* **136**(2), 758–64 (2013)<https://doi.org/10.1021/ja411014k>



Thermal Management Techniques for Concentrating Photovoltaic Modules

9

Xiaoru Zhuang, Xinhai Xu, and Jianpeng Cui

Contents

9.1	Introduction	248
9.2	Passive Cooling	249
9.2.1	Natural Convection Heat Sink Cooling	249
9.2.2	Heat Pipe Cooling	251
9.2.3	Phase Change Material (PCM) Cooling	254
9.3	Active Cooling	256
9.3.1	Jet Impingement Cooling	256
9.3.2	Liquid Immersion Cooling	257
9.3.3	Microchannel Heat Sink Cooling	262
9.4	Discussion and Conclusion Remarks	264
	References	276

Abstract

Concentrating photovoltaic technology is one of the most promising solar energy utilization technologies which can directly transform sunlight into electricity with high conversion efficiency up to 46%. Nevertheless, the concentrator brings a large amount of heat to the solar cell and temperature of the solar cell significantly affects its performance by reducing the efficiency and lifespan. Therefore, it is

X. Zhuang · J. Cui

School of Mechanical Engineering and Automation, Harbin Institute of Technology, Shenzhen, China

X. Xu (✉)

School of Mechanical Engineering and Automation, Harbin Institute of Technology, Shenzhen, China

Institute of Hydrogen and Fuel Cell, Harbin Institute of Technology, Shenzhen, China
e-mail: xuxinhai@hit.edu.cn

necessary to use proper cooling technology to dissipate the excess heat and maintain the solar cell temperature in an acceptable range. This work presents an overview of various cooling technologies available for concentrating photovoltaic systems in terms of passive and active methods. In passive cooling, natural convection heat sink cooling, heat pipe cooling, and phase change material cooling have been summarized. Inactive cooling, jet impingement cooling, liquid immersion cooling, and microchannel heat sink cooling have been evaluated. At last, discussions of these cooling techniques were reviewed.

9.1 Introduction

The photovoltaic (PV) cell is one of the most widespread renewable energy power generation technologies which can directly transform sunlight into electricity. The main challenge of PV cell commercialization is the high initial cost compared to conventional fossil sources-based power generation technologies [1, 2]. In order to increase the efficiency of PV power generation and make it more cost effective, concentrating photovoltaic (CPV) was proposed by using cheaper concentrating mirrors or lenses to capture the incident solar irradiance on a relatively large area and concentrate that energy onto small solar cell (SC) [3, 4]. The new world efficiency record of a CPV is up to 46% reported by Soitec and French Commission for Atomic Energy and Alternative Energies (CEA) – Laboratoire d'électronique des technologies de l'information (Leti), together with the Fraunhofer Institute for Solar Energy Systems (Fraunhofer ISE) and confirmed by Association for Iron & Steel Technology (AIST) in Japan [5], whereas non-concentrated photovoltaics (PVs), in general, have an efficiency of less than 25% [6]. According to the concentration ratio (CR) of a solar radiation incident, concentrating photovoltaic (CPV) systems can be classified under CR varying from 1 to 40 Suns [2.3 kW] for low, 40 to 300 Suns for medium, and 300 to 2000 Suns [100 kW] for high concentrating systems [7]. The ratio in “Suns” indicates the number of times the solar radiation is concentrated.

In a CPV system, only a fraction of incoming sunlight is converted into electricity, and the remaining solar energy is converted into heat [8]. The temperature of the PV cells can increase significantly without cooling. The cell efficiency is adversely influenced by the increasing temperature. Moreover, the high temperature can cause long-term degradation and irreversible structural damages to the cell such as deformation on the cell surface, delamination of the transparent layer, and development of micro-cracks on the cell [1, 9]. The temperature coefficient of conversion efficiency for most silicon SCs with a base temperature of 25 °C has been summarized by Skoplaki and Palyvos [10]. They reported that the average decrease in efficiency is around 0.45%/°C rise in operating temperature. Multi-junction (MJ) SCs are recently favored over single junction cells to be integrated into CPV systems as they are more efficient, have a better response to high concentration, and lower temperature coefficient [11]. Nashik et al. [12] reported the temperature coefficient of conversion

efficiency for [indium gallium phosphide/indium gallium arsenide/gallium] InGaP/In GaAs/Ge triple-junction SCs to be decreased by 0.248% at 1 Sun and 0.098% at 200 Suns for per degree rise in operating temperature. It is evident that thermal management of CPV systems plays a key role to improve the efficiency and life span of the SCs. Thus, it is necessary to introduce effective cooling technologies to dissipate heat, attain the higher performance, and prolong the lifetime of cells.

The following two sections will present and summarize current works in CPV cooling technologies in terms of passive cooling and active cooling. Passive cooling requires neither maintenance nor use of energy consuming devices such as pumps or fans, which are more reliable and cost-effective. In this section, natural convection heat sink cooling, heat pipe cooling, and phase change material (PCM) cooling methods will be summarized. Active cooling requires external energy to cool the SCs but is independent of the ambient conditions, so is usually easily controllable than passive cooling. In this section, it mainly evaluates the methods of jet impingement cooling, liquid immersion cooling, and microchannel heat sink cooling. Based on these efforts, discussions of those cooling techniques were reviewed for CPV cooling technologies.

9.2 Passive Cooling

9.2.1 Natural Convection Heat Sink Cooling

Heat sink with or without fins is one of the most common passive cooling solution applied in CPV systems [8]. It utilizes the effects of natural convection and radiation to dump waste heat for CPV by attaching the heat sink to the bottom of the cell (or cells). Araki et al. [13] conducted the outdoor experiments of a heat sink cooling for CPV systems at the concentration ratio of 500 Suns. They used an aluminum plate as the heat sink with a heat conductive epoxy and copper sheet between the SCs and metal plate. The results presented that the cell temperature only rose 18 °C under 500 Suns and 21 °C under 400 Suns to the ambient. Chou et al. [14] also numerically investigated the thermal performance of a high CPV system using an aluminum plate as the heat sink for cooling. The effects of the thickness of the heat sink, the thermal conductivity of the test board and solder paste of SCs assembly were discussed. The results showed that the thermal conductivity of the test board and solder paste had a slight effect to reduce cell temperature. However, the thickness of the heat sink played an important role in the thermal management of high CPV systems. The maximum cell temperature decreased as the aluminum thickness increased and became stable when the thickness was more than 20 mm. In order to predict the practical limits of flat plate cooling systems in natural convection for high CPV modules, Guladi et al. [15] proposed a thermal analytical model with the flat plate made of aluminum and a thickness of 3 mm. They found that flat plate systems cooled by natural convection of ambient air were sufficient to maintain the cell temperature below 80 °C up to CR of a few thousand Suns in the case of SCs side lengths of 2–4 mm and flat plate side lengths of 0–60 mm. Cui et al. [16] also

proposed a thermal model based on the energy conservation principle for CPV cells cooled by aluminum plates with a black coating as heat sinks. The heat sink area was 700 times larger than the area of SCs. According to the model, the cell temperature reduced as the heat sink area increased for a fixed CR. And for a certain fixed cell temperature, the heat sink area needed to increase linearly as a function of the concentration ratio. This model was verified by an outdoor experiment which measured the SCs temperature of 37 °C at the concentration ratio of 400 Suns.

Heat sink with fins can obviously increase the heat transfer surface area which remarkably enhances the thermal performance. Natarajan et al. [17] numerically studied the thermal performance of a CPV system cooling by a heat sink with and without fins. A two-dimensional (2-D) thermal model was developed to predict the SCs temperature. Based on the model, the SCs temperature with fins was significantly decreased compared to without fins. And they found that four uniform fins of 1 mm thickness and 5 mm height could effectively reduce the SCs temperature to 49.6 °C for CPV system at the concentration ratio of 10 Suns and ambient temperature of 20 °C. Aldossary et al. [11] also numerically investigated the feasibility of heat sink for passive cooling to maintain a single MJ PV cell surface temperature and electrical performance under high solar concentration in the harsh environment where ambient temperature could reach 50 °C. Two heat sink designs (shown in Fig. 9.1), namely, round pin heat sink (RPHS) and straight fins heat sink (SFHS), were simulated with the concentration ratio of 500 Suns. The results showed that SFHS had a better performance with the PV surface temperature of 21 °C lower than RPHS in ambient temperatures of 25–50 °C. The round pin heat sink was unable to keep the PV surface temperature below 80 °C at all test ambient temperatures and SFHS only could maintain the maximum PV surface temperature within the operating limit at an ambient temperature lower than 35 °C.

Micheli et al. [18] first used the least-material approach to design a heat sink for ultrahigh CPVs (concentration ratio over 2000 Suns). This method showed the potential to handle the thermal management of ultrahigh CPV systems, meanwhile limiting the costs and weight of the heat sink. The results showed that an 8-in × 11 cm wide × 6 cm high heat sink made of aluminum was able to keep a 3 mm × 3 mm MJ cell temperature below 80 °C at the concentration ratio of 4000

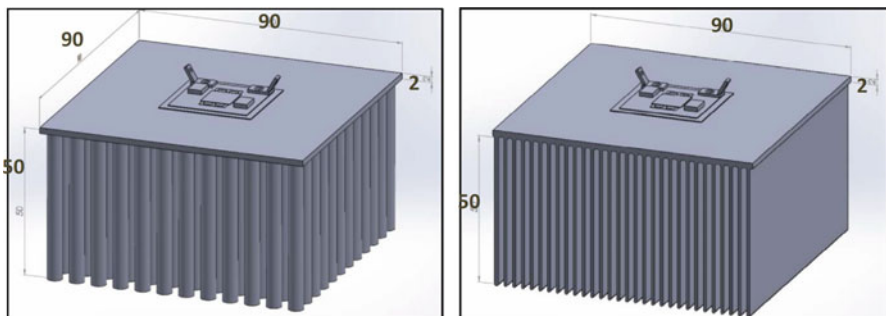


Fig. 9.1 Two heat sink structures investigated in Ref. [11], (a) RPHS, (b) SFHS

Suns. And it was concluded that the normalized cost of 0.1–0.18 \$/W_p was expected for production of optimized heat sinks for ultrahigh CPV systems at the concentration ratio from 1000 to 8000 Suns. Later, they optimized the least-material approach by reducing the heat sink baseplate extension and developed a 7-in × 9.6 cm wide × 5.62 cm high heat sink maintaining the cell temperature below 80 °C with a drop in weight and price of 61% [19]. Moreover, Micheli et al. [20] also investigated the feasibility of silicon micro-finned heat sinks for passive cooling of 500 Suns CPV systems by a simulation model. It was found that the SC temperature was lower than 80 °C by using a silicon wafer as a heat sink for both unfinned and finned conditions. And the fins performed better. The results showed that the application of micro-fins for passive cooling of CPV had the potential to reduce the material usage, the installation costs, and the tracker's energy consumptions, contributing to increasing the cost competitiveness of CPV in the renewable energy market.

For the purpose of estimating the thermal performance of a natural convective heat sink with fins for high CPV module cooling, Do et al. [21] proposed a general correlation based on extensive experimental data. And comparing with the previous studies [22, 23], the proposed correlation well predicted the effects of inclination angle and fin spacing on the thermal performance of the heat sink with plate-fins. They found that the optimal fin spacing strongly depended on the inclination angle and temperature difference for a specific geometry. The major problem related to the present natural convective heat sink cooling systems for heliostat concentrator photovoltaic (HCPV) is their heat dissipation efficiencies highly rely on the ambient temperature and wind speed. In order to solve this problem, Zou et al. [24] developed a novel passive air cooling device to provide enough cooling for SCs under the worst case scenario, i.e., high ambient temperature and no wind conditions (Fig. 9.2). The air could be automatically sucked into the channels of aluminum pipes heat sink and took away the waste heat of SCs. Then, the airflow leaving the pipes would be further heated inside the solar collector until it reached the bottom of the chimney, which was used to enhance the chimney effect. Numerical results showed that this novel cooling system could keep cell temperature under 75 °C even as the concentration ratio reached 700 Suns.

9.2.2 Heat Pipe Cooling

Heat pipes are hollow metal pipes consisting of a porous wick material and transport heat by two-phase flow of a working fluid. The liquid working fluid inside the wick is vaporized by the heat in the evaporator section and then flows toward the condenser section carrying the latent heat of vaporization in the tube. The vapor condenses and releases its latent heat in the condenser section, and then returns to the evaporator section through the wick structure by capillary effect. The phase change processes and two-phase flow circulation continue as long as the temperature difference between the evaporator and condenser sections are maintained. Because of the high thermal conductivity and heat transfer characteristics, heat pipe cooling has been used on CPV systems.

Fig. 9.2 Main components of the novel passive air cooling device in Ref. [24]

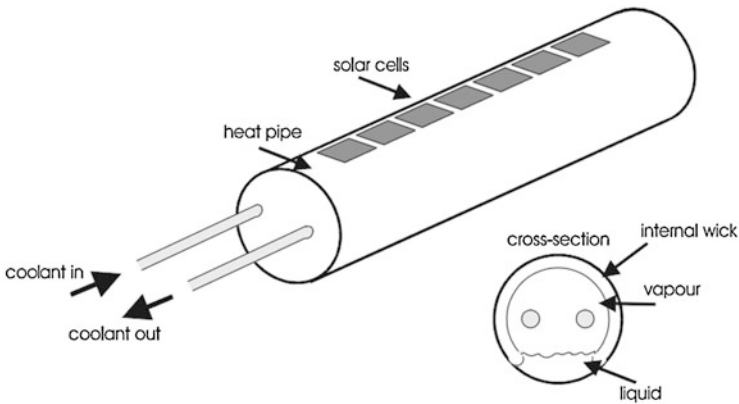
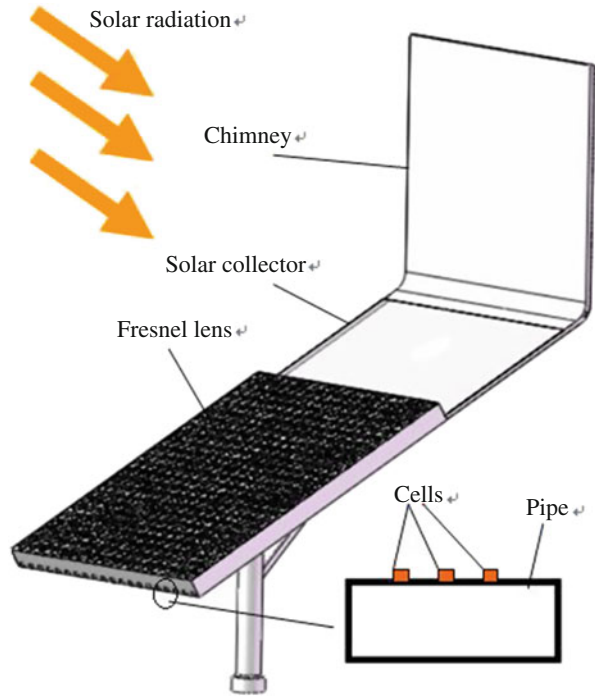


Fig. 9.3 Heat pipe cooling system proposed by Russell [25]

Russell [25] patented a heat pipe cooling system for CPV modules with linear Fresnel lenses. A string of cells mounted along the length of a heat pipe with an internal wick pulling the liquid up to the heated surface (Fig. 9.3). By ensuring a uniform temperature along the pipe, the heat was removed from the heat pipe by an internal coolant circuit. Akbarzadeh and Wadowski [26] experimentally investigated the performance of a heat pipe cooling method for CPV systems at the concentration ratio of

20 Suns. The cell was attached to the evaporator section of the heat pipe, and the upper condenser section extended by fins was exposed to natural convection air cooling. The cooling system was made of copper tube and charged with Freon R-11 [trichloromonofluoromethane, CCl_3F] as the working fluid. The CPV system was exposed to solar radiation for a period of 4 h and it was found that the cell surface temperature did not rise above 46°C . However, the cell surface temperature rose to 84°C and the output power dropped to 10.6 W instead of 20.6 W if the cooling system was not filled with any working fluid. Cheknane et al. [27] also conducted an experimental study regarding the role of heat pipe cooling on silicon-based CPV performance operating up to 500 Suns. The heat pipe cooling system was similar to that used in [26]. Water and acetone were employed as working fluids, and the heat pipe was made of a sealed copper cylinder with fins. The results showed that using acetone in heat pipe cooling improved the performance of SCs at high CR than water. Anderson et al. [28] designed a cooling system that uses a copper heat pipe with aluminum fins to cool a CPV cell by natural convection. They first compared five working fluids (water, ammonia, methanol, toluene, and pentane) for heat pipes and found that water heat pipe with three wraps of 150 mesh screen could carry more than six times heat energy compared to the other working fluids. Then, they determined the optimum fin size that minimized the temperature difference (ΔT , $^\circ\text{C}$) between the CPV cell and ambient air by computational fluid dynamics (CFD) simulation. A copper heater block with cartridge heaters was used to simulate the waste heat from the CPV cell in the experiments. The results showed that the heat pipe rejected the heat with a heat flux of 40 W/cm^2 to the environment with a ΔT rise of only 40°C . Huang et al. [29] proposed and evaluated the performance of a novel hybrid-structure flat plate heat pipe for a CPV (Fig. 9.4). The novel heat pipe was composed of a flattened copper pipe and a sintered wick structure supported by a coronary-stent-like rhombic copper mesh. Experiments presented that the novel heat pipe had less thermal resistance compared to a traditional copper heat pipe. The results also showed that the novel heat pipe provided better performance for a single SC, which could increase the photoelectric conversion efficiency by approximately 3.1%, compared to an aluminum substrate heat sink. Wang et al. [30] numerically and experimentally conducted a comprehensive investigation of the heat pipe cooling for CPV cell thermal management in a concentrator photovoltaics (CPV)/concentrated solar power (CSP) hybrid solar system. The heat transfer performance of three different designs of a

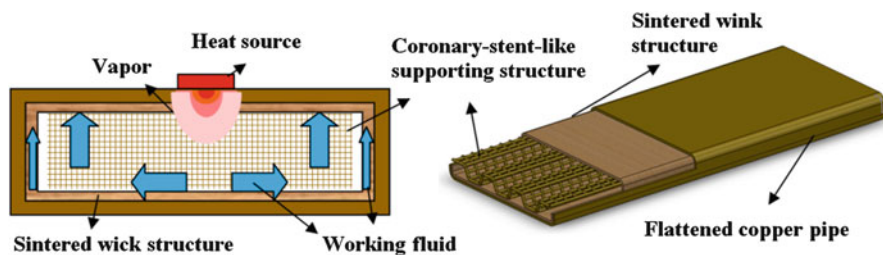


Fig. 9.4 (a) Working mechanism and (b) supporting structure of the novel hybrid-structure flat plate heat pipe in Ref. [29]

single heat pipe with radial fins, double heat pipes with radial fins, and double heat pipes with annular fins was evaluated under various heat rejection requirements. The results showed that heat pipes with radial fins presented narrow capability of dumping the heat, while heat pipes with annular fins had better performances under the same conditions. The double heat pipes with annular fins could bring most of the PV cells to the limited temperature or below under 50 W (13.0 W/cm²) or lower heat load.

9.2.3 Phase Change Material (PCM) Cooling

Phase change material (PCM) which absorb a significant amount of thermal energy as latent heat during the transition from solid to liquid phase are usually incorporated within PV systems for thermal regulation. Appropriately used PCMs can reduce the peak temperature which increases the electrical efficiency by preventing overheating of the system during the daytime. Numerous studies of PV thermal regulation using PCMs have been performed and comprehensively reviewed [31–35]. However, the investigations of CPV systems using PCM are limited.

Sharma et al. [36] presented an experimental investigation of PCM to enhance the thermal performance of very low-concentration building-integrated concentrated photovoltaic (BICPV) systems. The effect of PCM on electrical parameters of the BICPV systems was also discussed. An organic PCM of paraffin wax [(C_nH_{2n} + 2) based (RubiTherm) RT42 (melting temperature 38–43 °C, specific heat capacity 0.2 kJ/kg•K, heat conductivity 0.2 W/m•k] was used to fabricate PCM containment integrated with an in-house manufactured BICPV module. Indoor experiments were conducted with this BICPV-PCM system tested in naturally ventilated mode (without PCM) and then with PCM using highly collimated continuous light source at 1000 W/m². The results showed that stable BICPV temperature of 46.5 °C was achieved with an average temperature reduction of 3.8 °C at the BICPV module center and a relative electrical efficiency improvement of 7.7% with than without PCM. Later, they integrated the micro-fins with PCM and nanomaterial enhanced PCM (n-PCM) for cooling the BICPV systems [37]. In order to overcome PCM leakage, high manufacturing turnaround time, and associated costs, the PCM containment was fabricated using 3-D print technology in this paper. The experimental results showed that the average temperature in the center of the system was reduced by 10.7 °C (15.9%) using micro-fins with PCM and 12.5 °C (18.5%) using micro-fins with n-PCM as compared to using the micro-fins only. However, the n-PCM showed visual signs of agglomeration and deposition of [copper oxide] nano-CuO due to the difference in their densities after successive heating and melting cycles. Emam et al. [38] investigated the performance of an inclined CPV-PCM system using a comprehensive 2-D model comprising of the energy equations for CPV layers and a transient melting-solidification thermo-fluid model for PCM. The effects of inclination angle, concentration ratio, and PCM thickness on the thermal and electrical behaviors of the CPV-PCM system were studied. The results indicated that the system inclination angle had a significant effect on the time required to reach the complete melting state, the transient average solar cell temperature, and temperature

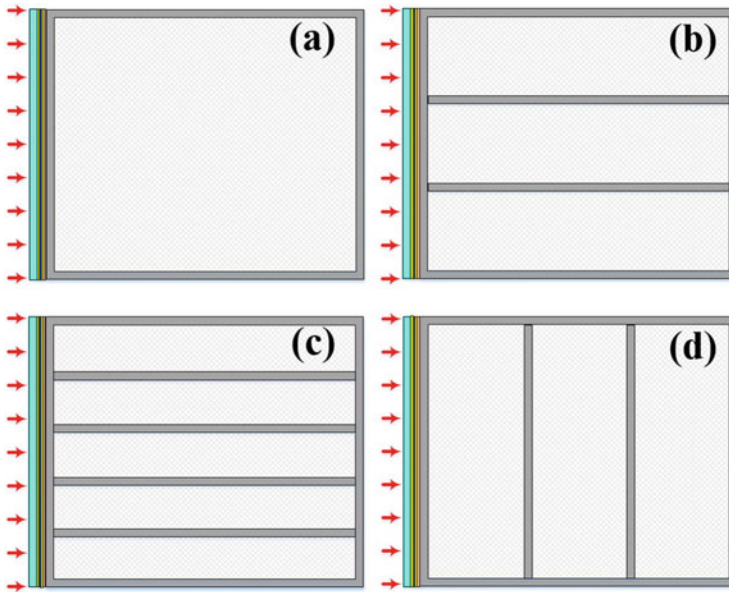


Fig. 9.5 Four different configurations of a PCM heat sink in Ref. [39], (a) a single cavity, (b) three-parallel cavity, (c) five-parallel cavity, and (d) three-series cavity

uniformity. The system at an inclination angle of 45° could reach the minimum average temperature with reasonable uniformity of local solar cell temperature which achieved the highest solar cell electrical efficiency and helped to prevent the hot spots in the solar cell. Later, they developed hybrid CPV-PCM systems to attain rapid thermal dissipation by enhancing the typically low thermal conductivity of PCM [39]. The systems included four different configurations of a PCM heat sink (shown in Fig. 9.5) and nine different pattern arrangements of three PCM materials (n-octadecane paraffin, $\text{CH}_{16}\text{CH}_3$; calcium chloride hexahydrate, $\text{CaCl}_2 \cdot 6\text{H}_2\text{O}$; and eutectic mixture of capric acid/palmitic acid, $\text{C}_{10}\text{H}_{20}\text{O}_2/\text{C}_{16}\text{H}_{32}\text{O}_2$). Using the similar 2-D model, the transient temperature variation at the concentration ratio of 10 and 20 Suns was numerically simulated. The results indicated that the SC temperature decreased with the increasing number of parallel cavities of the PCM heat sink. However, increasing the number of series cavities of PCM heat sink had an unfavorable effect on the SC temperature. Moreover, optimal patterning of PCMs would result in substantial enhancement of the thermal regulation of CPV-PCM systems. Su et al. [40] designed an encapsulated PCM (paraffin wax) spheres immersed in a water tank for a CPV/T system and performed the on-site experiments with a dish concentrator to measure solar irradiance, an output power of SCs and temperatures of the ambient air and water in the collector. The results showed that the average increases of the electrical, thermal, and overall efficiencies for the CPV/T system with PCM cooling were more than 10%, 5%, and 15%, respectively, compared to the CPV/T system with water cooling.

9.3 Active Cooling

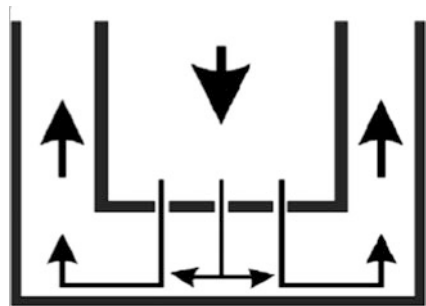
9.3.1 Jet Impingement Cooling

Jet impingement is an attractive cooling technique due to its very low thermal resistances (generally 10^{-5} – 10^{-6} $\text{K}\cdot\text{m}^2/\text{W}$) [41]. The liquid coolant is forced through a narrow hole or slot and impinged onto the heated surface in the normal direction. A very thin thermal boundary layer can be formed in the stagnation zone directly under the impingement and extends radially outward from the jet. As the heat transfer coefficient decreases rapidly with distance from the jet, an array of jets is usually used for cooling large surfaces [8].

Royne and Dey [42] proposed a jet impingement cooling technique for densely packed PV cells under high concentration ratio. Six different jet configurations under arrays of four and nine jets with side drainage normal to the impingement surface (Fig. 9.6) were tested. A model was developed to predict the pumping power required for a given average heat transfer coefficient for different device configurations and found that a higher number of nozzles per unit area improved the performance. They found that cell temperature decreased from 60 °C to 30 °C at the concentration ratio of 200 Suns and from 110 °C to 40 °C for 500 Suns at the maximum power point. Montorfano et al. [43] numerically and experimentally investigated the cells mean temperatures and pressure drop of an impingement water jet cooling system for a CPV cells module. The nozzle to plate distance, the number of jets, the nozzle pitch, and the distance between adjacent jets were optimized through literature and by means of accurate computational fluid dynamics (CFD) simulations. The results showed that the system experienced a pressure drop of 44.03 mbar and the temperature of the cell varied from a minimum of 48.3 °C to a maximum of 51.9 °C at a flow rate of 11 mL/s, a water inlet temperature of 27 °C, and constant incoming power of 150 W.

In order to reduce the temperature nonuniformity inherently induced by the jet impingement distribution, Barrau et al. [44, 45] designed a hybrid jet impingement/microchannel cooling device for densely packed PV cells under high concentration ratio. The device combined a slot jet impingement with a nonuniform distribution of microchannels (Fig. 9.7) and was evaluated by experimental measurements. The results showed that the hybrid device offered a minimum thermal resistance

Fig. 9.6 Schematic drawing of jet configuration with side drainage direction normal to the impingement surface [42]



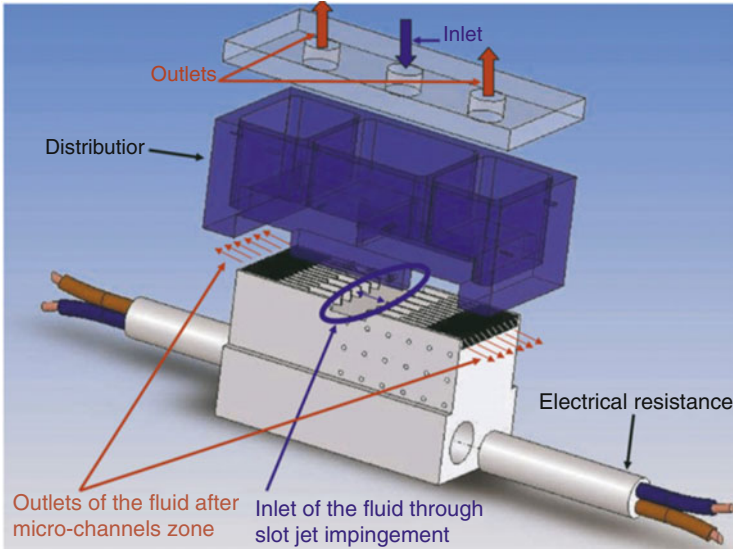


Fig. 9.7 3-D view of the experimental module in Refs. [44, 45]

coefficient of $2.18 \times 10^{-5} \text{ K}\cdot\text{m}^2/\text{W}$ with lower pressure drop and higher net PV output compared to only microchannel cooling. Later, they experimentally tested the efficiency of the hybrid device under real outdoor conditions [46]. A two-stage solar concentrator was used to provide a nonuniform illumination profile on a dummy cell. The results showed that the electrical output of the CPV receiver increased with the water flow rate and concentration ratio. It was indicated that the hybrid device could obtain a high-temperature uniformity of the whole PV receiver by modifying the internal geometry at the design stage to adapt the distribution of the local heat removal capacity.

9.3.2 Liquid Immersion Cooling

With liquid immersion cooling, SCs are directly immersed into the circulating liquid which reduces the contact thermal resistance. The contact thermal resistance is moved to the boundary layer between the bulk liquid and the CPV cell [47]. And the heat can be absorbed by the circulating liquid from both the top and bottom surfaces of the PV cells instead of just the bottom surface.

Zhu et al. [48] proposed a liquid immersion cooling method for densely packed SCs under high concentration ratio. The heat transfer and electrical performances were experimentally investigated under different concentration ratio, liquid temperatures, and flow velocities by using dimethyl-silicon oil as the dielectric fluid. The results showed that the module temperature could be cooled to lower than 45°C and the convective heat transfer coefficient could be higher than $3000 \text{ W}/(\text{m}^2\cdot\text{K})$. A

three-dimensional (3-D) simulation model was established to analyze the detailed velocity and temperature distributions surrounding the cell module. The numerical results indicated that the major heat transfer resistance was due to the laminar layers surrounding the cell and copper substrate. Liu et al. [49] also experimentally investigated the heat dissipation performance of a similar liquid immersion cooling system for SCs module under the conditions of irradiance of 50 and 70 kW/m². The dimethyl-silicon oil was used as the dielectric fluid. The results showed that the liquid inlet temperature had little effect on the module temperature distribution, but had a linear relationship with the average module temperature. The module temperature distribution in turbulent flow was found to be quite uniform, but with some degradation of the electrical performance.

Zhu et al. [50] applied deionized water immersion cooling to a dish high CPV system with a concentration ratio of 250 Suns. Time-dependent temperature distribution and electrical performance of the cell module were experimentally measured. The results showed that the module temperature was reduced to 45 °C at the direct normal irradiance (DNI) of 940 W/m² and 17 °C ambient temperature with 30 °C inlet water temperature. The overall convective heat transfer coefficient was approximately 6000 W/(m²·K). However, the electrical performance of the cell module obviously degraded after a long-time immersion in the deionized water even though its resistivity was kept constant. In order to understand the degradation mechanism, Han et al. [51] conducted the long-term deionized water immersion tests of bare cells, lead based-soldered tabbed cells, and epoxy tabbed cells, respectively. The results showed that the presence of lead oxides (PbO) and tin black oxides (SnO) on the lead based-soldered tabbed cells and red deposition on the epoxy [C₂₁H₂₅ClO₅] tabbed cells confirmed the occurrence of galvanic corrosion, which made the tabbed cells immeasurable finally. However, particular cleaning for the lead based-soldered tabbed cells could recover the (current-voltage) I-V performance toward its initial values, and partial recovery can be obtained for the epoxy tabbed cells, which indicated that the cells were not chemically damaged after long-time deionized water immersion. Xiang et al. [52] used the assembled solar receiver and CPV module prototype in [50] to establish a 3-D numerical simulation model for better understanding the mechanism of the direct-contact heat transfer process. The 3-D simulation model of the liquid-immersed solar receiver and the prototype of a CPV module are shown in Fig. 9.8. The heat transfer performance of the CPV module without and with fins under actual weather conditions was simulated and found that the finned module made the average temperature 8–10 °C lower than the bare one and reduced the temperature nonuniformity from 15 °C to below 10 °C. Sun et al. [53] designed a narrow rectangular channel receiver (Fig. 9.9) to reduce the liquid holdup at the concentration ratio of 9.1 Suns. The experimental results showed that the cell temperature was maintained in the range of 20–31 °C at a direct normal solar irradiance (DNI) of about 910 W/m², silicon oil inlet temperature of 15 °C, and Reynolds number (*Re*) ranging from 2720 to 13,602 (dimensionless). Long-term stability of silicon CPV cells immersed in dimethyl silicon oil was conducted under real climate conditions and found that the cells electrical performance had no obvious efficiency degradation for 270 days of operation.

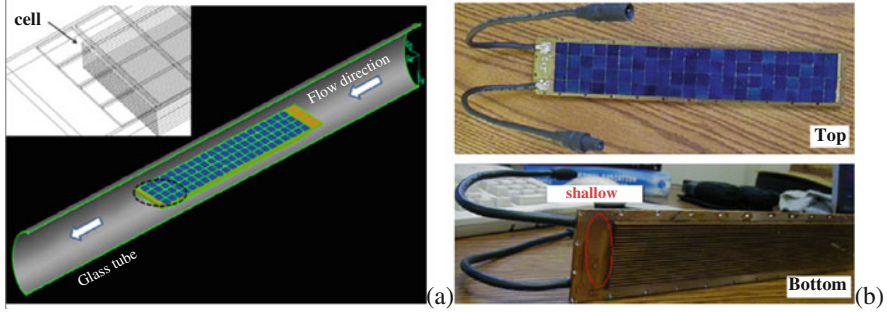


Fig. 9.8 (a) 3-D simulation model of the liquid-immersed solar receiver and (b) prototype of a CPV module in Ref. [52]

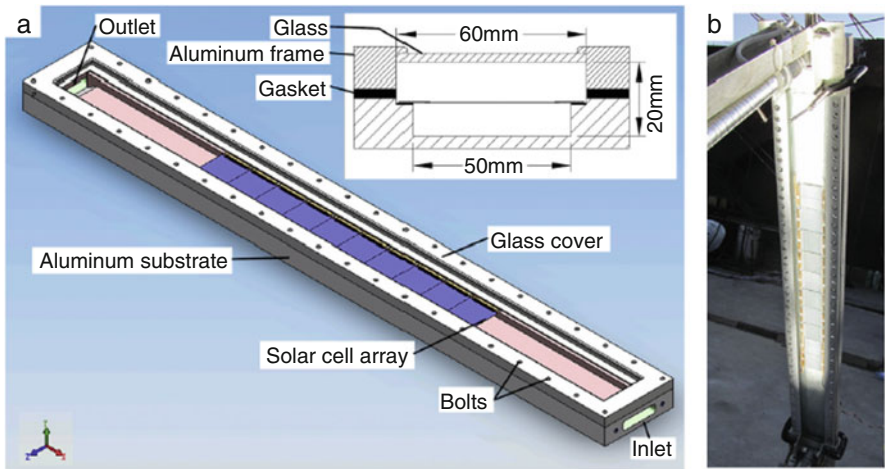


Fig. 9.9 (a) Section view and (b) photo of the narrow rectangular channel receiver in [53]

For purpose of selecting the appropriate dielectric liquid as immersion cooling liquid, Han et al. [47] conducted the optical transmittance measurements of deionized water, isopropyl alcohol, ethyl acetate, and dimethyl silicone oil and found that they all satisfied the optical requirements for silicon CPV applications as immersion coolants. Test cell samples were fabricated by encapsulating between two sheets of 100 mm × 100 mm and 3.3 mm thick Borofloat glass [81% silica, SiO₂; 13% boron oxide, B₂O₃; 4% sodium oxide/potassium oxide, Na₂O/K₂O; and 2% alumina, Al₂O₃], then sealing with silicone to provide a liquid cavity (Fig. 9.10). The electrical performance of silicon CPV cells immersed in those four dielectric liquids was experimental examined using the test cell samples with a constant voltage I-V flash tester. The results showed that the electrical performance of CPV cells improved in the candidate dielectric liquids at the concentration ratio of 10–30 Suns. The light reflection losses and cell surface recombination losses from surface

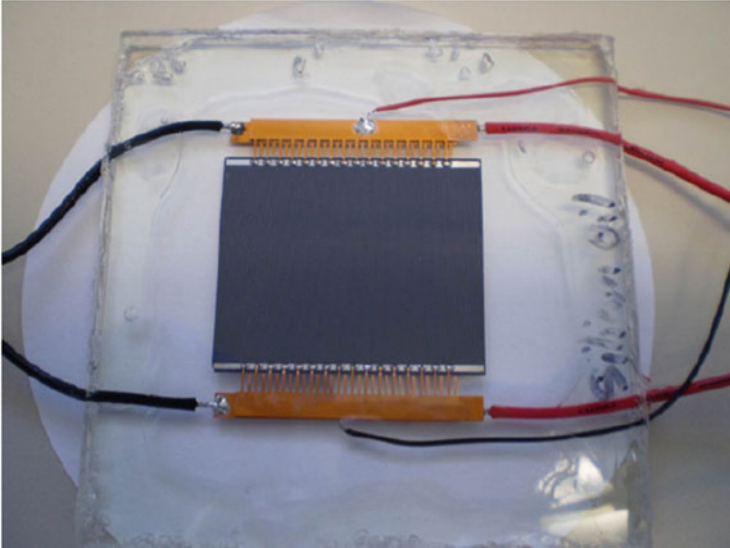


Fig. 9.10 Silicon CPV cell test sample immersed in dimethyl silicon oil used by [47]

adsorption of polar molecules were both reduced. Then, the thermal performance of a liquid immersion cooled solar receiver for a linear CPV system was investigated by numerical simulations and found that the fluid inlet velocity and flow mode, along with the fluid thermal properties, all had significant influences on the cell array temperature. Later, Han et al. [54] investigated the effect of the liquid layer thickness above the cell surface on the electrical performance of silicon CPV cells. The experimental results showed that an increase in the silicon SCs efficiency of 8.5–15.2% was achieved with 1.5 mm liquid thickness immersion, while the degree of the improvements to the efficiency decreased in 9 mm test due to more incident light was absorbed by the thicker liquid layer. And the optimum liquid thickness existed and depended on the liquid types. Long-term cell performance tests demonstrated that the reliable output of the silicon CPV cells was achieved when operated in isopropyl alcohol, ethyl acetate, and dimethyl silicone oil without silicone sealant involved, respectively. However, the stable electrical performance of the cell was difficult to be achieved when immersed in deionized water which was consistent with the report in Ref. [50].

Xin et al. [55] applied the liquid immersion cooling method for GaInP/GaInAs/Ge triple-junction SCs of high CPV systems. They presented that the silicone oil was quite transparent in the wavelength range of both GaInP sub-cell and GaInAs sub-cell, but the transmittances of silicon oil had slightly decreased in the wavelength range of Ge sub-cell. Flash testing showed that the silicon oil immersion could indeed improve the electrical performance of Ge-based MJ cell when the thickness was less than 6.3 mm under 500 Suns and 25 °C. Then, CFD simulation analysis showed that the silicon oil immersion thickness should not be less than 2.5 mm and the cell average temperature

was kept less than 67 °C when the silicon oil mass flow rate was not less than 20 kg/h. Han et al. [56] proposed a theoretical model for the direct liquid-immersed solar receiver with Ge-based MJ CPV cells to investigate the temperature of the receiver and the system electrical efficiency. The results showed that the CR, mass flow rate, and inlet liquid temperature had significant effects on the cell temperature and, by extension, system output power. The flow rate selection should match CR to maintain the cell temperature lower and increase the system electrical efficiency. Kang et al. [57] numerically investigated the heat transfer performance of silicon oil immersion cooling for the densely packed MJ SCs with fins at 500 Suns. The results showed that the cell temperature decreased and the heat transfer coefficient and pressure drop increased with the increasing inlet flow velocity. The cells average temperature was 63 °C, the heat transfer coefficient was 750 W/(m²·K), and the pressure drop was lower than 10 kPa/m when inlet flow velocity and temperature of silicon oil was 1 m/s and 25 °C under the optimized parameters of liquid immersion cooling receiver.

In all immersion cooling systems described above, a high flow rate is usually required to obtain a higher single-phase convective heat transfer due to the high CR and cells temperature, which results in higher parasitic energy consumption. In order to enhance the economic and heat transfer performances, Kang et al. [58] developed a direct-contact phase-change liquid immersion cooling method for dense-array SCs in high CPV system. Ethanol was used as a phase-change immersion cooling liquid. The cooling system could be self-regulating without consuming extra energy with ethanol mass flow rate of 158.3–180.6 kg/(m²·s) under the concentration ratio of 219.8–398.4 Suns. The experimental results showed that the electrical performance of MJ SCs could decline due to the light loss at the interface between ethanol and bubbles. Later, Wang et al. [59] optimized the liquid filling ratio of this cooling system and found that the optimal liquid filling ratio was 30% with the heat transfer coefficient of 9726.21 W/(m²·K).

As the phase-change liquid immersion cooling method generates bubbles which can reduce the cell efficiency and requires higher sealing quality, Wang et al. [60] firstly proposed a direct-contact liquid film cooling system for dense-array SCs in high CPV system. An electric heating plate was designed to simulate the dense-array SCs and water was used as a working fluid. The experimental results showed that the average temperature of simulated SCs and heat transfer coefficient of falling film vaporization both increased with the increasing concentration ratio. Higher water inlet flow rate was found to result in lower average temperature and higher heat transfer coefficient underwater inlet temperature of 30 °C. However, the water inlet flow rate had little impact on average temperature and heat transfer coefficient underwater inlet temperature of 75 °C, which implied that the latent heat transfer became the dominant way of heat transfer. Later, they derived a 2-D model of the direct-contact liquid film cooling system for dense-array SCs to present the temperature distribution on the SCs surface and flow characteristic of the liquid film [61]. The numerical results showed that inlet width had a significant effect on the liquid film thickness. And the subcooled boiling state was a necessary condition to ensure the cooling effect. The optimum inlet parameters at the concentration ratio of 500 Suns were inlet velocity of 1.06 m/s, inlet width of 0.75 mm, and inlet temperature of 75 °C.

9.3.3 Microchannel Heat Sink Cooling

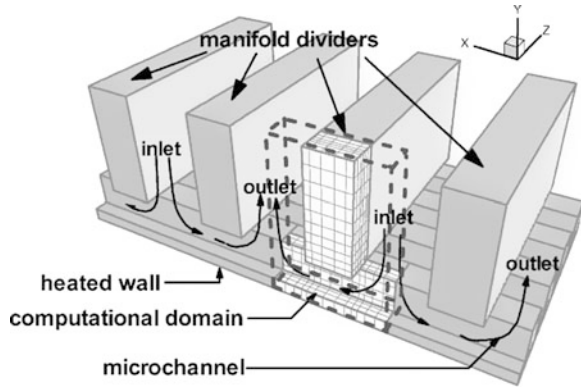
The application of a microchannel heat sink is a potential way to attain extremely high heat transfer rate because of the high surface-area-to-volume ratio of microchannels. Phillips et al. [62] indicated that the use of microchannel cooling system can dissipate heat load as high as 1000 W/cm^2 . Moreover, Royne et al. [8] presented that the microchannel heat sink was a particularly promising cooling technology for high CPV systems. A recent overview of the thermal and hydrodynamic analysis of microchannel heat sinks showed that laminar was the prevailing flow condition and the use of liquid coolants was preferable over gaseous coolants [63].

Ortegón et al. [64] analyzed a microchannel heat sink used for cooling a high CPV cell at the CR of 500 Suns by theoretical and numerical methods. The results indicated that microchannel heat sink cooling was an effective thermal management method for high CPV systems, which improved the cell efficiency to compensate for the higher pressure drop compared to a single rectangular channel heat sink. Capua et al. [65] integrated forward triangular ribs on the inner sidewalls of microchannels to enhance the cooling capability of microchannel heat sinks for a high CPV system. Two structures of aligned and offset distributions along the microchannel walls were considered and investigated in laminar flows by numerical analysis. The results showed that, compared to smooth microchannels, microchannels with aligned and offset rib distributions increased 1.8 and 1.6 times on average Nusselt number (Nu_L , dimensionless), respectively, as well as 3.9 and 2.3 times on average friction factors, respectively. As a relatively high pumping power demand, the microchannel heat sink with forwarding triangular ribs loses its advantage as an effective and efficient cooling system for high CPV application as Re increases, especially at $Re > 200$.

In the conventional microchannel heat sink, liquid coolant temperature can increase along the flow direction resulting in a temperature gradient between the inlet and outlet of the microchannels [66]. To minimize the temperature gradient, a higher coolant flow rate is necessary, which causes higher power consumption. Multi-layer microchannel heat sinks are considered to achieve more efficient cooling in terms of pumping power and heat removal capability [67]. Radwan and Ahmed [68] investigated the influence of microchannel heat sink configurations on the cooling performance of low CPV systems. The numerical results showed that the consumed pumping powers of the double-layer configurations were obviously lower than that of single-layer configurations and achieved a higher net power gain, especially for higher coolant mass flow rates. Siyabi et al. [69] used a 3-D incompressible laminar steady flow model to evaluate the performance of a multi-layer microchannel heat sink for cooling CPV cells. The numerical results showed that an increase in the number of microchannel layers exhibited a significant improvement in terms of SC temperature, the thermal resistance, and the fluid pumping power. Moreover, the channel height and width had no effect on the maximum SC temperature, while increasing channel height resulted in less fluid pumping power.

Another way to decrease the pressure drop and increase the uniformity of temperature distribution of microchannel heat sinks is to use manifold microchannel heat sinks. In a manifold microchannel, the fluid flows in an alternate way through

Fig. 9.11 Schematic of a manifold microchannel heat sink [70]



the direction perpendicular to the heat sink as depicted in Fig. 9.11. As the fluid has a shorter residence time in contact with the base, the uniform temperature distribution across the cooled surface can be obtained [70]. Kermani et al. [71] fabricated and tested a manifold microchannel heat sink for cooling CPV cells under CR of 1000 Suns and used water as the working fluid. The experimental results indicated that the manifold microchannel heat sink could provide high heat transfer coefficient with only moderate pressure drops. Yang and Zuo [72] designed a multi-layer manifold microchannel heat sink to effectively cool the cell surface temperature and improve the uniformity of surface temperature distribution for silicon SC module at CR lower than 100 Suns. The combined use of the multiple inlet/outlet manifolds and plenum chambers increased the fluid flow rate in the inlet area of the microchannels to produce the fluid turbulence which enhanced the heat transfer coefficient. The experimental results showed that the surface temperature difference of the CPV cells was below 6.3 °C. And the multi-layer manifold microchannel had a heat transfer coefficient up to 8235.84 W/(m²•K) and its pressure drop was lower than 3 kPa. Dong et al. [73] proposed a novel mini channel manifold heat sink for densely packed CPVs under CR of 500 Suns by numerical simulations. Two groups of T-shape minichannels were arranged in a manifold heat sink as shown in Fig. 9.12. It was found that the temperature of the maximum cell was lower than 80 °C and the difference between the maximum and minimum temperatures of 100 MJ cells was 26.49 °C when the water inlet velocity was 0.64 m/s.

In addition, two-phase coolants are considered to be used to enhance the cooling performance for microchannel heat sink by increasing the fluid thermal conductivity through using nanofluids or operated under forced convective boiling conditions. Radwan et al. [74] used aluminum oxide (Al₂O₃)-water and silicon carbide (SiC)-water nanofluids with different volume fractions as cooling mediums in a microchannel heat sink for cooling CPV systems. A comprehensive model was developed to estimate the electrical and thermal performances of the CPV systems which included a thermal model for the photovoltaic layers, coupled with thermo-fluid dynamics of two-phase flow model of the microchannel heat sink. The results showed that the use of nanofluids achieved a higher reduction in cell temperature

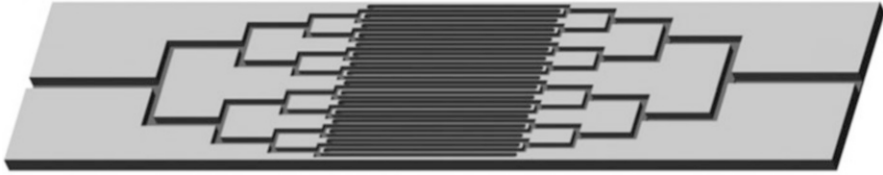


Fig. 9.12 T-shape manifold with a minichannels heat sink in Ref. [73]

and higher cell electrical efficiency than the use of water, particularly at lower Re and higher concentration ratio. The cell temperature decreased significantly with the increasing volume fraction of nanoparticles. Moreover, using SiC-water nanofluid with higher thermal conductivity had a relatively higher reduction in cell temperature than using Al_2O_3 -water. Later, they experimentally investigated a monolithic double-layer microchannel heat sink used for cooling CPV cells under forced convective boiling conditions [75]. Ethanol [C_2H_5OH] and acetone [C_3H_6O] with a boiling point of $78.4\text{ }^\circ C$ and $56\text{ }^\circ C$ were selected as the working fluids. The results showed that there was an excellent uniform temperature around the coolant boiling point over the entire heated wall in a wide range of flow rates. The temperature uniformities were below $1.6\text{ }^\circ C$ and $1.8\text{ }^\circ C$ for ethanol and acetone, respectively, under the counterflow operation of forced convective boiling at the CR of 11.5 Suns.

9.4 Discussion and Conclusion Remarks

A comprehensive summary of thermal management techniques for CPV systems has been presented above. As the parameters and performances are quite different for various cooling technologies, the six cooling methods were critically reviewed as listed in Tables 9.1, 9.2, 9.3, 9.4, 9.5, and 9.6.

It can be seen that natural convection heat sink cooling is an effective technique of passive cooling even for high CPV systems. The main drawback of this thermal management technique is that the heat sink area needed to maintain the cell temperature below the nominal operating value increases with the CR which makes the size and weight of CPV modules increase. In tracked CPV system, the weight of heat sink can sensibly affect the overall system performances. The heavier the system, the more the energy consumed by the tracker, and thus, the lower the system's efficiency [20]. Therefore, a large heat sink required to release heat from CPV systems would make the natural convection heat sink less realistic and attractive for cooling. Using fins on the flat plate can significantly improve the cooling capacity so that reduces the volume of a heat sink and also makes the system more compact. Another drawback of this thermal management technique is that ambient conditions such as air temperature and wind speed have major influences on the heat dissipation performance of cooling systems. Even using a very large heat sink, it cannot dissipate enough heat from the CPV module in high ambient temperature and no wind conditions.

Table 9.1 A detailed summary of natural convection heat sink cooling systems

Author (year)	Finned or unfinned	Heat sink dimensions L × W × H (mm ³)	CPV cell dimensions L × W (mm ²)	CPV cell type	The electrical efficiency of CPV cell	CR (Suns)	Cell temperature (°C)	Ambient temperature (°C)	Nature of work
Araki et al. (2002) [13]	Unfinned			Ge-based MJ cell	40%	400 and 500	18 and 21 more than ambient		Experimental
Chou et al. (2007) [14]	Unfinned	535 × 257 × 3	6.7 × 5.5	Ge-based MJ cell	20%	350	44.3	30.5	Numerical
Cui et al. (2009) [16]	Unfinned	700 times larger than SC area	3 × 3	Ge-based MJ cell	22.2%	400	37	27	Analytical
Guladi et al. (2013) [15]	Unfinned	0 × 0 × 3–60 × 60 × 3	2 × 2–10 × 10		40%	> 1000	80		Analytical
Natarajan et al. (2011) [16]	Finned	60 × 20 × 10		Silicon SC	18%	10	49.6	20	Numerical
Micheli et al. (2015) [18]	Finned	110 × 110 × 60	3 × 3	MJ cell	40%	4000	63.3	20	Analytical numerical
Micheli et al. (2015) [19]	Finned	84 × 84 × 56.2	3 × 3	MJ cell	40%	4000	79.3	27.5	Analytical numerical
Micheli et al. (2015) [20]	Finned	50 × 50 × 1.4	3 × 3	Ge-based MJ cell	42.5%	500	70.4	25	Numerical
Aldossary et al. (2016) [11]	Finned	90 × 90 × 52	10 × 10	Ge-based MJ cell	41.2%	500	118 (RPHS) 96 (SFHS)	50	Numerical
Zou et al. (2017) [24]	Unfinned	1400 × 200 × 100			25%	400–700	Under 75	30	Numerical

Table 9.2 A detailed summary of heat pipe cooling systems

Author (year)	Heat pipe structure	CPV cell dimensions $L \times W$ (mm ²)	CPV cell type	The electrical efficiency of CPV cell	CR (Suns)	Cell temperature (°C)	Heat flux for dissipation (W/cm ²)	Ambient temperature (°C)	Nature of work
Russell (1982) [25]	Pipe with the internal coolant circuit								
Akbarzadeh and Wadowski (1996) [26]	Copper pipe with fins	25 × 20	Polycrystalline SCs		20	46			Experimental
Cheknane et al. (2006) [27]	Copper pipe with fins	150	Silicon SC	17–18%	500				Experimental
Anderson et al. (2008) [28]	Copper pipe with aluminum fins	100	Simulated by heater			40 more than ambient	40		Experimental
Huang et al. (2012) [29]	The hybrid-structure flat heat pipe	10 × 10	Ge-based MJ cell	11.2%			40	35	Experimental
Wang et al. (2017) [30]	Copper pipe with fins	14 numbers of 5 × 5.5	Simulated by heater			80	13	35	Numerical experimental

Table 9.3 A detailed summary of CPV-PCM systems

Author (year)	PCM containment dimensions (mm ³)	PCM	CPV cell type	The electrical efficiency of CPV cell	CR (Suns)	Cell temperature (°C)	Ambient temperature (°C)	Nature of work
Sharma et al. (2016) [36]	170 × 160 × 42	RT42	Silicon SC			46.5		Experimental
Sharma et al. (2017) [37]	36 × 35 × 35	RT42 with 0.5% nano-CuO	Simulated by heater				25.6–27.7	Experimental
Emam et al. (2017) [38]	50 or 200 × 125 (2-D)	Calcium chloride hexahydrate CaCl ₂ ·6H ₂ O	Silicon SC	Around 17% for the inclination angles of 45°	5 and 20	Around 80 for the inclination angles of 45°	20	Numerical
Emam and Ahmed (2018) [39]	150 × 125(2-D)	N-octadecane paraffin, calcium chloride hexahydrate CaCl ₂ ·6H ₂ O, eutectic mixture of capric-palmitic acid	Silicon SC	Around 14% for the best	10 and 20	88 for the best	20	Numerical
Su et al. (2018) [40]		Paraffin wax	Silicon SC	Around 40%				Experimental

Table 9.4 A detailed summary of jet impingement cooling systems

Author (year)	CPV cell dimensions L×W (mm ²)	CPV cell type	The electrical efficiency of CPV cell	CR (Suns)	Cell temperature (°C)	Coolant inlet temperature (°C)	Coolant flow rate (L/min)	Thermal resistance (m ² ·K/W)	Nature of work
Roynce and Dey (2007) [42]		Simulated by heater		200 and 500	Around 30 for 200 suns, around 40 for 500 suns			$(3.57-3.7) \times 10^{-5}$ for 200 suns, $(2.63-2.7) \times 10^{-5}$ for 500 suns	Analytical experimental
Montorfano et al. (2014) [43]	5 numbers of 10×10	Ge-based MJ cell	37–40%	400–500	48.3–51.9	27	0.22–1.65	1.68×10^{-5}	Numerical
Barrau et al. (2010, 2011) [44, 45]	3600	Simulated by heater	30%	1905	Around 40	12.6	32.34	2.18×10^{-5}	Experimental
Barrau et al. (2014) [46]	29.75×29.75	Dummy cell	39.2%	603 and 861	Around 42 for 603 suns	17.5	1.31–2.94	6.2×10^{-5}	Experimental

Table 9.5 A detailed summary of liquid immersion cooling systems

Author (year)	Immersion liquid	CPV cell dimensions $L \times W$ (mm ²)	CPV cell type	The electrical efficiency of CPV cell	CR (Suns)	Cell temperature (°C)	Heat transfer coefficient (W/(m ² ·K))	Coolant inlet temperature (°C)	Coolant flow rate	Nature of work
Zhu et al. (2010) [48]	Dimethyl silicon oil	20 numbers of 5 × 5 in parallel	Silicon SC		160.8 and 202.9	37–57 for 160.8 suns, 40–60 for 202.9 suns	1800–2800 for 160.8 Suns, 2200–3400 for 202.9 Suns	17–28	2–2.8 m/s	Experimental numerical
Han et al. (2011) [47]	Deionized water, isopropyl alcohol, ethyl acetate, and dimethyl silicon oil	10 numbers of 40 × 50 in parallel	Silicon SC		37	31, 52, 41, and 74 for deionized water, isopropyl alcohol, ethyl acetate, and dimethyl silicon oil, respectively		25	4 m ³ /h	Numerical
Liu et al. (2011) [49]	Dimethyl silicon oil	20 numbers of 5 × 5 in parallel	Silicon SC		47.3 and 68.8	30 for 47.3 suns, 45 for 68.6 suns	About 1000 for $Re = 14,194$	17–46	$Re = 1999–14,194$	Experimental
Zhu et al. (2011) [50]	Deionized water	88 numbers of 10 × 10 in series	Silicon SC	24%	250	45	6000	30	2.22 m ³ /h	Experimental
Xiang et al. (2012) [52]	Deionized water	88 numbers of 11 × 11 in series with fins in the back	Silicon SC	24%	250	36.1		24.2	2.23 m ³ /h	Numerical

(continued)

Table 9.5 (continued)

Author (year)	Immersion liquid	CPV cell dimensions $L \times W$ (mm ²)	CPV cell type	The electrical efficiency of CPV cell	CR (Suns)	Cell temperature (°C)	Heat transfer coefficient (W/(m ² ·K))	Coolant inlet temperature (°C)	Coolant flow rate	Nature of work
Sun et al. (2014) [53]	Dimethyl silicone oil	10 numbers of 40×50 in parallel	Silicon SC	19%	9.1	20–31	$Nu = 0.154Re^{0.764}$	15	$Re = 2720-13,602$	Experimental
Xin et al. (2015) [55]	Dimethyl silicone oil	11.01×10.10	Ge-based MJ cell	About 38%	500	About 67		25	20 kg/h	Numerical
Han et al. (2015) [56]	Dimethyl silicone oil	25 numbers of 10×10 in five rows	Ge-based MJ cell	31–33%	100–600	32–97		20	1260–2160 kg/h	Analytical
Kang et al. (2016) [57]	Dimethyl silicone oil	64 numbers of 8×8 in series with fins in the back	Ge-based MJ cell	39.8%	500	63	750	25	1 m/s	Numerical
Kang et al. (2016) [58]	Ethanol	4 numbers of 40×10 in parallel	Simulated by heater	38%	219.8–398.4	87.3–88.5	23,490–46,980		0.245–0.215 m/s	Experimental
Wang et al. (2017) [59]	Deionized water	4 numbers of 40×10 in parallel	Simulated by heater	40%	300–600	65–110	4000–12,000	30–75	$0.1-0.3 \text{ m}^3/\text{h}$	Experimental

Table 9.6 A detailed summary of microchannel heat sink cooling systems

Author (year)	Microchannel heat sink structure	Coolant	CPV cell dimensions $L \times W$ (mm ²)	CPV cell type	The electrical efficiency of CPV cell	CR (Suns)	Cell temperature (°C)	Heat transfer coefficient (W/(m ² ·K))	Coolant inlet temperature (°C)	Coolant flow rate	Nature of work
Kermami et al. (2009) [71]	Multi-layer with manifold	Water		Simulated by heater	25%	1000		65,480		0.3–1.3 gr/s	Experimental
Yang and Zuo (2015) [72]	Multi-layer with manifold	Water	3 numbers of 17×17 in series	Silicon SC		23–98	20–45	1410–8235.84		5.35–37.7 g/s	Experimental
Radwan et al. (2016) [74]	Single layer	Al ₂ O ₃ -water and SiC-water nanofluids			17.5–20%	1–40	Lower than 60		30	$Re = 10–100$	Analytical
Ortegón et al. (2017) [64]	Single layer		10×10		40%	500	45.9		25	$330 \text{ kg}/(\text{m}^2 \cdot \text{K})$	Analytical numerical
Radwan and Ahmed (2017) [68]	Single and multi-layer	Water		Silicon SC	9–15%	5 and 20	80–150		30	$1.67–33.67 \text{ g/s}$	Analytical
Siyabi et al. (2017) [69]	Multi-layer	Water	10×10	Ge-based MJ cell	41.2%	500	Less than 65	Higher than 6000	25	2 g/s	Numerical

(continued)

Table 9.6 (continued)

Author (year)	Microchannel heat sink structure	Coolant	CPV cell dimensions $L \times W$ (mm ²)	CPV cell type	The electrical efficiency of CPV cell	CR (Suns)	Cell temperature (°C)	Heat transfer coefficient (W/(m ² ·K))	Coolant inlet temperature (°C)	Coolant flow rate	Nature of work
Mario Di Capua et al. (2018) [65]	Single layer integrated forward triangular ribs on the inner sidewalls	Water	3 × 3	Ge-based MJ cell	40%	1000	Lower than 28	Higher than 78,125	20	$Re = 100-400$	Numerical
Radwana et al. (2018) [75]	Multi-layer	Ethanol and acetone	13 × 40	Simulated by heater	20%	11.5	78.4 for ethanol, 56 for acetone			15–400 mL/h	Experimental
Dong et al. (2018) [73]	Single layer with manifold (minichannels)	Water	100 numbers of 10 × 10 in array	Ge-based MJ cell	39.2–40.6%	500	80	7692	34.8	0.64 m/s	Numerical

Heat pipe cooling is another effective passive cooling technique to move and reject heat from CPV modules, especially at low and medium concentration ratio levels. Many investigated works used fins on the heat pipe to improve the cooling capacity. Moreover, as heat pipe operates nearly isothermally, the portion of fins is more effective which needs a smaller volume of fins. Thus, a heat pipe is a good alternative to large natural convection heat sinks, especially when the available space for the cooling system is constrained. However, the use of that technique in terms of economic viability for high CPV systems needs further discussion.

In PCM cooling technology, it is evident from the literature that a limited amount of work has been done for CPV modules in contrast with most of the work done for non-concentrated PVs. The list of various PCMs and their thermal properties that have been used in PV systems is presented in Table 9.7. It can be seen that most PCMs have a low thermal conductivity, which slows their heat charging and discharging rate. The main advantage of using PCM is the ability to regulate temperature based on its latent heat which can result in uniform temperature cooling. Another advantage is its versatility in the choice of melting temperature, and the thickness of the PCM layer can determine the period of time that a relatively stable PV temperature can be maintained. Moreover, using fin designs and optimal patterning of multiple PCM components can also substantially enhance the thermal regulation of CPV-PCM systems. The limitations of using PCM include that some of them are toxic and corrosive, as well as the fire safety and disposal problem after the completion of the life cycle. Further investigations into the applicability of PCM in the thermal management of high CPV module should be conducted, especially in long-term operation.

Jet impingement cooling is an attractive active cooling technique due to its high extraction capability and low thermal resistance. However, as the distance from the jet increases, the heat transfer coefficient decreases rapidly leading to inherent nonuniform temperature distribution. An array of jets is usually used to partially alleviate this problem. But another problem of the disturbance arising from the interaction of the fountain of the jet to another jet can appear and has been shown to decrease the overall heat transfer drastically [76, 77]. The heat transfer characteristics of an array of impinging jets are highly dependent on a plate to nozzle pitch, a number of nozzles, diameter spacing, and fluid velocity which should be well optimized. Moreover, jet impingement with microchannels was shown to enhance the temperature uniformity and can regulate temperature depending upon the local heat removal capacity which makes it an attractive option for cooling CPV modules. Another challenge in the design of such systems is to minimize the pumping power consumption.

In the case of liquid immersion cooling technology, the heat transfer coefficient can go up to $47 \text{ kW}/(\text{m}^2 \cdot \text{K})$. The main applications for such type of cooling reported in the literature are used in densely packed CPV systems with the SCs working under medium and high concentration ratio levels. The common immersion liquid investigated in literature is dimethyl silicone oil, while deionized water was found to have better thermal properties of higher thermal conductivity, heat capacity, and lower viscosity. However, long-term stability tests of silicon CPV cells immersed in those

Table 9.7 List of various PCMs and their thermal properties that have been used in PV systems

PCM	Density (kg/m ³) Solid/ liquid	Specific heat capacity (kJ/(kg·K)) Solid/liquid	Thermal conductivity (W/(m·K)) Solid/liquid	Latent heat of fusion (kJ/kg)	Melting temperature (°C)	Thermal expansion coefficient (1/K)	References
RT18HC	880/770	2	0.2		17–19		[81]
RT20	880/750	1.4/1.7	0.2/0.18	134	21	0.001	[82]
RT25	785/749	1.8/2.4	0.19/0.18	232	26.6	0.001	[83]
RT27	880/760	1.78/2.37	0.2	184	25–28		[84]
RT28HC	880/770	2	0.2	245	28		[85]
RT30	870/760	1.8/2.4	0.2	222	28		[86]
RT35	880/760	1.8/2.4	0.2	157	35		[84]
RT42	800	0.2	0.2	174	38–43		[37]
RT42 with 0.5% nano-CuO	803	0.2	0.36	167–170.5	38.2–43.7		[37]
RT44HC	750	2	0.2	220	44		[87]
RT50	820	2	0.2	130	50		[87]
RT54HC	825	2	0.2	170	54		[87]
SP21E	1500/ 1400	2	0.6		22–23		[81]
SP22	1490/ 1440	1.4/1.95	0.6/0.4	150	23	0.0008	[82]
SP24E	1500/ 1400	2	0.6		24–35		[81]

GR40	710	1.5	0.15	82	43	Almost none	[83]
Waksol A	770/760	2.3/2.43	0.33/0.31	162	32–36		[84]
Calcium chloride hexahydrate $\text{CaCl}_2 \cdot 6\text{H}_2\text{O}$	1710/1560	1.4/2.1	1.08/0.56	191	29.8	0.0005	[38]
N-octadecane paraffin	865/770	1.93/2.16	0.36/0.15	243.5	28	0.00091	[39]
Eutectic mixture of capric-palmitic acid (C-P)	870/790	2/2.3	0.14	173	22.5	0.00078	[39]
Eutectic mixture of capric-lauric acid (C-L)	890/770	1.97/2.24	0.143/0.139	168	18.5	0.00067	[82]
Form-stable paraffin/expanded graphite composite	600		7.57	164.8	27.17		[88]
Pork fat	910/986	2.03/2.05	0.32–0.41	155–180	36–45		[89]

two dielectric fluids present that the electrical performance of the cell had no obvious degradation in dimethyl silicone oil, while obviously degraded in deionized water. But after particular cleaning, the cell could recover. The applications of liquid immersion cooling for Ge-based MJ cells in literature are mainly studied by numerical and analytical methods with none long-term electrical stability test of Ge-based MJ cells immersed in dielectric fluids. Furthermore, the phase-change liquid immersion cooling method was found to have the highest heat transfer coefficient, while the generating bubbles could reduce the cell electrical efficiency. The direct-contact liquid film cooling technology can solve this problem and has a relatively high heat transfer coefficient up to $12 \text{ kW}/(\text{m}^2 \cdot \text{K})$. Stable performance of liquid immersion cooling system for CPV cells under dielectric is a challenging task for future researchers. Moreover, long-term electrical stability tests of Ge-based MJ cells immersed in different dielectric fluids should be conducted to validate whether performance degradation exists or not. And further investigation employing methods such as conformal coating for minimizing the degradation of silicon SCs in deionized water could be conducted.

Microchannel heat sink cooling is also an effective active cooling technique to achieve low cells temperature and uniform temperature distribution of CPV systems. However, it also requires a huge amount of pumping power consumption because of a large pressure drop for the coolant to flow. The use of manifold in microchannel heat sink was reported to enhance cooling capability and minimize the pressure drop due to short microchannels length while allowing the redevelopment of the thermal boundary layer in each channel to obtain high heat transfer coefficients. Moreover, using nanofluid in microchannel heat sink can acquire a significant enhancement in the heat transfer coefficient due to the increase of the mixture of thermal conductivity and the existence of a relative slip/drift velocity between the two phases that eventually enhances the flow mixing [78]. By allowing the coolant fluid in microchannels to boil, a significantly huge heat flux can be dissipated by the latent heat capacity of the fluid and an almost isothermal surface can be obtained. However, the operation temperature of the systems can be slightly higher than the coolant saturation temperature corresponding to the operating pressure [79, 80]. Therefore, the type of coolant should be carefully selected to control the system operating temperature.

Acknowledgments Support from the National Natural Science Foundation of China (51706056) and China Postdoctoral Science Foundation (2018 M631927) is greatly acknowledged.

References

1. L. Micheli, N. Sarmah, X. Luo, K.S. Reddy, T.K. Mallick, Opportunities and challenges in micro-and nano-technologies for concentrating photovoltaic cooling: a review. *Renew. Sust. Energ. Rev.* **20**, 595–610 (2013)
2. S. Jakhar, M.S. Soni, N. Gakkhar, Historical and recent development of concentrating photovoltaic cooling technologies. *Renew. Sust. Energ. Rev.* **60**, 41–59 (2016)

3. K. Lovegrove, W. Stein, *Concentrating Solar Power Technology: Principles, Developments, and Applications* Woodhead Publishing Limited, Cambridge, UK (2012)
4. M. Soni, M. Padmini, Concentrating solar photovoltaic, in *IVth International Conference on Advances in Energy Research* Mumbai, India (2013)
5. I.S.E. Fraunhofer, The new world record for solar cell efficiency at 46% (2014). Press release, Fraunhofer ISE, December 1. Available at <https://www.ise.fraunhofer.de/en/press-media/pressreleases/2014/new-world-record-for-solar-cell-efficiency-at-46-percent.html>. 14 Sept 2017
6. M.A. Green, K. Emery, Y. Hishikawa, W. Warta, E.D. Dunlop, D.H. Levi, et al., Solar cell efficiency tables (version 49). *Prog. Photovolt. Res. Appl.* **25**, 565–572 (2010)
7. P. Pérez-Higueras, E. Muñoz, G. Almonacid, P.G. Vidal, High concentrator photovoltaics efficiencies: Present status and forecast. *Renew. Sustain. Energy Rev.* **15**(4), 1810–1815 (2011)
8. A. Royne, C.J. Dey, D.R. Mills, Cooling of photovoltaic cells under concentrated illumination: a critical review. *Sol. Energy Mater. Sol. Cells* **86**(4), 451–483 (2005)
9. Z. Ye, Q. Li, Q. Zhu, W. Pan, The cooling technology of solar cells under a concentrated system, in *Proceedings of the IEEE 6th International Power Electro and Motion Control Conference, IPEMC'09*, 3 Wuhan, China (2009), pp. 2193–2197
10. E. Skoplaki, J.A. Palyvos, On the temperature dependence of photovoltaic module electrical performance: a review of efficiency/power correlations. *Sol. Energy* **83**(5), 614–624 (2009)
11. A. Aldossary, S. Mahmoud, R. Al-Dadah, Technical feasibility study of passive and active cooling for concentrator PV in a harsh environment. *Appl. Therm. Eng.* **100**, 490–500 (2016)
12. K. Nashik, T. Takamoto, T. Agui, M. Kaneiwa, Y. Uraoka, T. Fuyuki, Annual output estimation of concentrator photovoltaic systems using high-efficiency gap/in GaAs/Ge triple-junction solar cells based on experimental solar cell's characteristics and field-test meteorological data. *Sol. Energy Mater. Sol. Cells* **90**(1), 57–67 (2006)
13. K. Araki, H. Uozumi, M. Yamaguchi, A simple passive cooling structure and its heat analysis for 500× concentrator PV module, in *Photovoltaic Specialists Conference, 2002. Conference Record of the Twenty-Ninth IEEE*, New Orleans, Los Angeles, USA, vol. 18 (IEEE, 2002), pp.1568–1571
14. T. L. Chou, Z. H. Shih, H. F. Hong, C. N. Han, Investigation of the thermal performance of high-concentration photovoltaic solar cell package, in *International Conference on Electronic Materials and Packaging Daejeon*, South Korea (IEEE, 2007), pp. 1–6
15. F. Gualdi, O. Arenas, A. Vossier, A. Dollet, V. Aimez, R. Arès, Determining passive cooling limits in CPV using an analytical thermal model, *9th International Conference on Concentrator Photovoltaic Systems*, Miyazaki, Japan, AIP Conference Proceeding. **1556**(48), 10–13 (2013)
16. M. Cui, N.F. Chen, X.L. Yang, Y. Wang, Y.N. Bai, X.W. Zhang, Thermal analysis and test for single concentrator solar cells. *J. Semicond.* **30**(4), 63–66 (2009)
17. S.K. Natarajan, T.K. Mallick, M. Katz, S. Weingaertner, Numerical investigations of solar cell temperature for photovoltaic concentrator system with and without passive cooling arrangements. *Int. J. Therm. Sci.* **50**(12), 2514–2521 (2011)
18. L. Micheli, E.F. Fernandez, F. Almonacid, K.S. Reddy, T.K. Mallick, *Enhancing Ultra-High CPV Passive Cooling Using Least-Material Finned Heat Sinks*, American Institute of Physics Conference Series, vol 1679 (AIP Publishing LLC, 2015), pp. 1810–001575
19. L. Micheli, E. F. Fernández, F. Almonacid, K. S. Reddy, T. K. Mallick, Optimization of the least-material approach for passive Ultra-High CPV cooling, in *Photovoltaic Specialist Conference*, New Orleans, Los Angeles, USA (IEEE, 2015), pp. 1–6
20. L. Micheli, S. Senthilarasu, K.S. Reddy, T.K. Mallick, Applicability of silicon micro-finned heat sinks for 500× concentrating photovoltaic systems. *J. Mater. Sci.* **50**(16), 5378–5388 (2015)
21. K.H. Do, T.H. Kim, Y.S. Han, B.I. Choi, M.B. Kim, A general correlation of a natural convective heat sink with plate-fins for high concentrating photovoltaic module cooling. *Sol. Energy* **86**(9), 2725–2734 (2012)
22. A. Bar-Cohen, M. Iyengar, A.D. Kraus, Design of optimum plate-fin natural convective heat sinks. *J. Electron. Packag.* **125**(2), 208–216 (2003)

23. A. Dayan, R. Kushnir, G. Mittelman, A. Ullmann, Laminar free convection underneath a downward facing hot fin array. *Int. J. Heat Mass Transfer* **47**(12), 2849–2860 (2004)
24. Z. Zou, H. Gong, J. Wang, S. Xie, Numerical investigation of solar enhanced passive air cooling system for concentration photovoltaic module heat dissipation. *J. Clean Energy Technol.* **5**(3) 206–211 (2017)
25. G. F. Russell, U.S. Patent No. 4,320,246, 1982. U.S. Patent and Trademark Office, Washington, DC
26. A. Akbarzadeh, T. Wadowski, Heat pipe-based cooling systems for photovoltaic cells under concentrated solar radiation. *Appl. Therm. Eng.* **16**(1), 81–87 (1996)
27. A. Chekane, B. Benyoucef, A. Chaker, Performance of concentrator solar cells with passive cooling. *Semicond. Sci. Technol.* **21**(2), 144 (2006)
28. W. G. Anderson, P. M. Dussinger, D. B. Sarraf, S. Tamanna, Heat pipe cooling of concentrating photovoltaic cells, in *Photovoltaic Specialists Conference*, 2008. PVSC'08. 33rd IEEE (IEEE, 2008, May), San Diego, California, USA, pp. 1–6
29. H.J. Huang, S.C. Shen, H.J. Shaw, Design and fabrication of a novel hybrid-structure heat pipe for a concentrator photovoltaic. *Energies* **5**(11), 4340–4349 (2012)
30. S. Wang, J. Shi, H. H. Chen, S. R. Schafer, M. Munir, G. Stecker, . . . , C. L. Chen, Cooling design and evaluation for photovoltaic cells within constrained space in a CPV/CSP hybrid solar system. *Appl. Therm. Eng.* **110**, 369–381 (2017)
31. M.C. Browne, B. Norton, S.J. McCormack, Phase change materials for photovoltaic thermal management. *Renew. Sust. Energ. Rev.* **47**, 762–782 (2015)
32. T. Ma, H. Yang, Y. Zhang, L. Lu, X. Wang, Using phase change materials in photovoltaic systems for thermal regulation and electrical efficiency improvement: a review and outlook. *Renew. Sust. Energ. Rev.* **43**, 1273–1284 (2015)
33. M.M. Islam, A.K. Pandey, M. Hasanuzzaman, N.A. Rahim, Recent signs of progress and achievements in photovoltaic-phase change material technology: a review with special treatment on photovoltaic thermal-phase change material systems. *Energy Convers. Manag.* **126**, 177–204 (2016)
34. S.S. Chandel, T. Agarwal, Review of cooling techniques using phase change materials for enhancing the efficiency of photovoltaic power systems. *Renew. Sust. Energ. Rev.* **73**, 1342–1351 (2017)
35. S. Preet, Water and phase change material based photovoltaic thermal management systems: a review. *Renew. Sust. Energ. Rev.* **82**, 791–807 (2018)
36. S. Sharma, A. Tahir, K.S. Reddy, T.K. Mallick, Performance enhancement of a building-integrated concentrating photovoltaic system using phase change material. *Sol. Energy Mater. Sol. Cells* **149**, 29–39 (2016)
37. S. Sharma, L. Micheli, W. Chang, A.A. Tahir, K.S. Reddy, T.K. Mallick, Nano-enhanced phase change material for thermal management of BICPV. *Appl. Energy* **208**, 719–733 (2017)
38. M. Emam, S. Ookawara, M. Ahmed, Performance study and analysis of an inclined concentrated photovoltaic-phase change material system. *Sol. Energy* **150**, 229–245 (2017)
39. M. Emam, M. Ahmed, Cooling concentrator photovoltaic systems using various configurations of phase-change material heat sinks. *Energy Convers. Manag.* **158**, 298–314 (2018)
40. Y. Su, Y. Zhang, L. Shu, Experimental study of using phase change material cooling in a solar tracking concentrated photovoltaic-thermal system. *Sol. Energy* **159**, 777–785 (2018)
41. W. M. Rohsenow, Y. I. Cho, in *Handbook of Heat Transfer*, ed. by J. P. Hartnett, vol. 3 (McGraw-Hill, New York, 1998)
42. A. Roynce, C.J. Dey, Design of a jet impingement cooling device for densely packed PV cells under high concentration. *Sol. Energy* **81**(8), 1014–1024 (2007)
43. D. Montorfano, A. Gaetano, M. C. Barbato, G. Ambrosetti, A. Pedretti, CPV cells cooling system based on submerged jet impingement: CFD modeling and experimental validation, in *AIP Conference Proceedings*, vol. 1616, No. 1 (AIP, 2014), Albuquerque, New Mexico, USA, pp. 135–139

44. J. Barrau, J. Rosell, M. Ibañez, Design of a hybrid jet impingement/microchannel cooling device for densely packed PV cells under high concentration, in *AIP Conference Proceedings*, vol. 1277, No. 1 (AIP, 2010), Freiburg, Germany, pp. 74–77
45. J. Barrau, J. Rosell, D. Chemisana, L. Tadriss, M. Ibañez, Effect of a hybrid jet impingement/micro-channel cooling device on the performance of densely packed PV cells under high concentration. *Sol. Energy* **85**(11), 2655–2665 (2011)
46. J. Barrau, A. Perona, A. Dollet, J. Rosell, Outdoor test of a hybrid jet impingement/micro-channel cooling device for densely packed concentrated photovoltaic cells. *Sol. Energy* **107**, 113–121 (2014)
47. X. Han, Y. Wang, L. Zhu, Electrical and thermal performance of silicon concentrator solar cells immersed in dielectric liquids. *Appl. Energy* **88**(12), 4481–4489 (2011)
48. L. Zhu, Y. Wang, Z. Fang, Y. Sun, Q. Huang, An effective heat dissipation method for densely packed solar cells under high concentrations. *Sol. Energy Mater. Sol. Cells* **94**(2), 133–140 (2010)
49. L. Liu, L. Zhu, Y. Wang, Q. Huang, Y. Sun, Z. Yin, Heat dissipation performance of silicon solar cells by direct dielectric liquid immersion under intensified illuminations. *Sol. Energy* **85**(5), 922–930 (2011)
50. L. Zhu, R.F. Boehm, Y. Wang, C. Halford, Y. Sun, Water immersion cooling of PV cells in a high concentration system. *Sol. Energy Mater. Sol. Cells* **95**(2), 538–545 (2011)
51. X. Han, Y. Wang, L. Zhu, H. Xiang, H. Zhang, Mechanism study of the electrical performance change of silicon concentrator solar cells immersed in de-ionized water. *Energy Convers. Manag.* **53**(1), 1–10 (2012)
52. H. Xiang, Y. Wang, L. Zhu, X. Han, Y. Sun, Z. Zhao, 3D numerical simulation on heat transfer performance of a cylindrical liquid immersion solar receiver. *Energy Convers. Manag.* **64**, 97–105 (2012)
53. Y. Sun, Y. Wang, L. Zhu, B. Yin, H. Xiang, Q. Huang, Direct liquid-immersion cooling of concentrator silicon solar cells in a linear concentrating photovoltaic receiver. *Energy* **65**, 264–271 (2014)
54. X. Han, Y. Wang, L. Zhu, The performance and long-term stability of silicon concentrator solar cells immersed in dielectric liquids. *Energy Convers. Manag.* **66**, 189–198 (2013)
55. G. Xin, Y. Wang, Y. Sun, Q. Huang, L. Zhu, Experimental study of liquid-immersion III–V multi-junction solar cells with dimethyl silicone oil under high concentrations. *Energy Convers. Manag.* **94**, 169–177 (2015)
56. X. Han, Q. Wang, J. Zheng, J. Qu, Thermal analysis of direct liquid-immersed solar receiver for a high concentrating photovoltaic system. *Int. J. Photoenergy* (2015)
57. X. Kang, Y.P. Wang, G.C. Xin, X.S. Shi, Experiment and simulation study on silicon oil immersion cooling densely-packed solar cells under high concentration ratio. *Int. J. Energy Power Eng.* **5**(3), 90–96 (2016)
58. X. Kang, Y. Wang, Q. Huang, Y. Cui, X. Shi, Y. Sun, Study on direct-contact phase-change liquid immersion cooling dense-array solar cells under high concentration ratios. *Energy Convers. Manage.* **128**, 95–103 (2016)
59. Y. Wang, C. Wen, Q. Huang, X. Kang, M. Chen, H. Wang, Performance comparison between ethanol phase-change immersion and active water cooling for solar cells in a high concentrating photovoltaic system. *Energy Convers. Manage.* **149**, 505–513 (2017)
60. Y. Wang, X. Shi, Q. Huang, Y. Cui, X. Kang, Experimental study on direct-contact liquid film cooling simulated dense-array solar cells in the high concentrating photovoltaic system. *Energy Convers. Manage.* **135**, 55–62 (2017)
61. Y. Wang, L. Zhou, X. Kang, Q. Huang, X. Shi, C. Wang, Experimental and numerical optimization of direct-contact liquid film cooling in high concentration photovoltaic system. *Energy Convers. Manage.* **154**, 603–614 (2017)
62. L. R. Glicksman, R. L. R. J. Phillips, Forced-convection, liquid cooled; microchannel heat sinks for high power-density microelectronics, in *Proceedings of the International Symposium on Cooling Technology for Electronic Equipment* (1987), pp. 295–316

63. A.M. Adham, N. Mohd-Ghazali, R. Ahmad, Thermal and hydrodynamic analysis of micro-channel heat sinks a review. *Renew. Sustain. Energy Rev.* **21**(21), 614–622 (2013)
64. J. A. A. Ortegón, J. P. Cassiano, E. M. Cardoso, J. B. C. Silva, CFD analysis of a microchannel heat sink cooling system for high concentration photovoltaic systems, in *Cilamce*, Florianópolis, SC, Brazil, November, 5–8 (2017)
65. M.D.H. Capua, R. Escobar, A.J. Diaz, A.M. Guzmán, Enhancement of the cooling capability of a high concentration photovoltaic system using microchannels with forwarding triangular ribs on sidewalls. *Appl. Energy* **226**, 160–180 (2018)
66. K. Vafai, L. Zhu, Analysis of two-layered micro-channel heat sink concept in electronic cooling. *Int. J. Heat Mass Transf.* **42**(12), 2287–2297 (1999)
67. X. Wei, Y. Joshi, Stacked microchannel heat sinks for liquid cooling of microelectronic components. *J. Electron. Packag.* **126**(1), 60–66 (2004)
68. A. Radwan, M. Ahmed, The influence of microchannel heat sink configurations on the performance of low concentrator photovoltaic systems. *Appl. Energy* **206**, 594–611 (2017)
69. I. A. Siyabi, K. Shanks, T. Mallick, S. Sundaram, Thermal analysis of a multi-layer micro-channel heat sink for cooling concentrator photovoltaic (CPV) cells, in *AIP Conference Proceedings*, vol. 1881, No. 1 (AIP Publishing, 2017), Ottawa, Canada, p. 070001
70. J.H. Ryu, D.H. Choi, S.J. Kim, Three-dimensional numerical optimization of a manifold microchannel heat sink. *Int. J. Heat Mass Transf.* **46**(9), 1553–1562 (2003)
71. E. Kermani, S. Dessiatoun, A. Shooshtari, M. M. Ohadi, Experimental investigation of heat transfer performance of a manifold microchannel heat sink for cooling of concentrated solar cells, in *Electronic Components and Technology Conference, 2009. ECTC 2009. 59th* (IEEE, 2009), San Diego, California, USA pp. 453–459
72. K. Yang, C. Zuo, A novel multi-layer manifold microchannel cooling system for concentrating photovoltaic cells. *Energy Convers. Manag.* **89**, 214–221 (2015)
73. J. Dong, X. Zhuang, X. Xu, Z. Miao, B. Xu, Numerical analysis of a multi-channel active cooling system for densely packed concentrating photovoltaic cells. *Energy Convers. Manag.* **161**, 172–181 (2018)
74. A. Radwan, M. Ahmed, S. Ookawara, Performance enhancement of concentrated photovoltaic systems using a microchannel heat sink with nanofluids. *Energy Convers. Manag.* **119**, 289–303 (2016)
75. A. Radwan, S. Ookawara, S. Mori, M. Ahmed, Uniform cooling for concentrator photovoltaic cells and electronic chips by forced convective boiling in a 3D-printed monolithic double-layer microchannel heat sink. *Energy Convers. Manag.* **166**, 356–371 (2018)
76. B. W. Webb, C. F. Ma, Single-phase liquid jet impingement heat transfer, in *Advances in Heat Transfer*, vol. 26 (Elsevier, 1995), Salt Lake City, Utah, USA, pp. 105–217
77. D.Y. Lee, K. Vafai, Comparative analysis of jet impingement and microchannel cooling for high heat flux applications. *Int. J. Heat Mass Transf.* **42**(9), 1555–1568 (1999)
78. M. Ahmed, M. Eslamian, Laminar forced convection of a nanofluid in a microchannel: effect of flow inertia and external forces on heat transfer and fluid flow characteristics. *Appl. Therm. Eng.* **78**, 326–338 (2015)
79. C. Huh, M.H. Kim, An experimental investigation of flow boiling in an asymmetrically heated rectangular microchannel. *Exp. Thermal Fluid Sci.* **30**(8), 775–784 (2006)
80. L. Yin, R. Xu, P. Jiang, H. Cai, L. Jia, Subcooled flow boiling of water in a large aspect ratio microchannel. *Int. J. Heat Mass Transf.* **112**, 1081–1089 (2017)
81. W. Lin, Z. Ma, P. Cooper, M.I. Sohel, L. Yang, Thermal performance investigation and optimization of buildings with integrated phase change materials and solar photovoltaic thermal collectors. *Energ. Buildings* **116**, 562–573 (2016)
82. A. Hasan, S.J. McCormack, M.J. Huang, B. Norton, Characterization of phase change materials for thermal control of photovoltaics using differential scanning calorimetry and temperature history method. *Energy Convers. Manag.* **81**, 322–329 (2014)
83. M.J. Huang, P.C. Eames, B. Norton, Phase change materials for limiting temperature rise in building integrated photovoltaics. *Sol. Energy* **80**(9), 1121–1130 (2006)

84. M.J. Huang, P.C. Eames, B. Norton, N.J. Hewitt, Natural convection in an internally finned phase change material heat sink for the thermal management of photovoltaics. *Sol. Energy Mater. Sol. Cells* **95**(7), 1598–1603 (2011)
85. U. Stritih, Increasing the efficiency of PV panel with the use of PCM. *Renew. Energy* **97**, 671–679 (2016)
86. S. Preet, B. Bhushan, T. Mahajan, Experimental investigation of water-based photovoltaic/thermal (PV/T) system with and without phase change material (PCM). *Sol. Energy* **155**, 1104–1120 (2017)
87. T. Klemm, A. Hassabou, A. Abdallah, O. Andersen, Thermal energy storage with phase change materials to increase the efficiency of solar photovoltaic modules. *Energy Procedia* **135**, 193–202 (2017)
88. Z. Luo, Z. Huang, N. Xie, X. Gao, T. Xu, Y. Fang, Z. Zhang, Numerical and experimental study on temperature control of solar panels with form-stable paraffin/expanded graphite composite PCM. *Energy Convers. Manag.* **149**, 416–423 (2017)
89. S. Nižetić, M. Arıcı, F. Bilgin, F. Grubišić-Čabo, Investigation of pork fat as potential novel phase change material for passive cooling applications in photovoltaics. *J. Clean. Prod.* **170**, 1006–1016 (2018)



Thermal Energy Storage Systems Based on Metal Hydride Materials

10

Claudio Corgnale and Bruce Hardy

Contents

10.1	Introduction	284
10.2	Metal Hydrides as Heat Processing Systems	285
10.3	Metal Hydride-Based High-Temperature Thermal Energy Storage Systems	290
10.4	Techno-Economic Analysis of Metal Hydride Thermal Energy Storage Systems	296
10.4.1	Economic Model	296
10.4.2	Exergetic Efficiency Model	299
10.4.3	Metal Hydride Thermal Energy Storage Systems Techno-Economic Performance	301
10.5	Transport Phenomena Modeling of Metal Hydride Thermal Energy Storage Systems	304
10.5.1	Thermal Energy Storage Coupled Metal Hydrides	304
10.5.2	Metal Hydride System Transport Model	305
10.5.3	Laboratory Scale Test Results	308
10.6	Outlook and Summary	311
	References	312

Author Contribution

The paper was entirely written by CC and BH. Figures and charts were supplied and edited by CC. The final draft was reviewed and edited by BH.

C. Corgnale (✉)

Greenway Energy, LLC, Aiken, SC, USA

Savannah River National Laboratory, Aiken, SC, USA

e-mail: claudio.corgnale@greenway-energy.com

B. Hardy

Savannah River National Laboratory, Aiken, SC, USA

Abstract

A comprehensive techno-economic analysis of candidate metal hydride materials, used for thermal energy storage applications, is carried out. The selected systems show the potential to exceed the performance of latent heat or phase change heat storage systems and can closely approach the US Department of Energy targets for concentrating solar power plant applications. A paired metal hydride system is selected as possible thermal energy storage to be integrated with high-temperature steam power plants. Its performance is simulated adopting a finite element-based detailed transport phenomena model. Results show the ability of the system to achieve the required operating temperatures and to store and release thermal energy appropriately.

10.1 Introduction

Concentrating solar power plants, integrated with either steam plants or gas power plants (e.g., supercritical carbon dioxide (CO₂) power plants), represent one of the main options to produce electric power without local greenhouse gas emissions. Concentrating solar plant systems are positioned to become a major source of renewable-generated electricity in the United States [1]. This is especially due to their high potential for providing dispatchable power among all the different renewable options [2–5]. However, these plants need to be equipped with thermal energy storage systems to reach or closely approach the United States Department of Energy SunShot Initiative solar electricity production target of <0.05 US dollar per kilowatt-hour (\$/kWh) [6] and compete with the performance of conventional power plants [3, 7]. The three types of storage systems, being developed today, can store thermal energy as (1) sensible heat, (2) latent heat from material phase change, or (3) thermochemical energy, using the heat released (or absorbed) during chemical reactions occurring inside the material [3, 8].

Among the third typology, metal hydride-based systems are a very attractive choice, showing strong potential to achieve the SunShot Initiative thermal energy storage targets [9, 10], which include exergetic efficiency, operating temperature, cost, and volumetric energy density. Compared to other systems the metal hydride-based technology has several attractive features, including full reversibility, high gravimetric and volumetric energy density on the order of 200–600 kilowatt-hour of thermal heat per cubic meter (kWhth/m³) [9]. Although some metal hydride systems can be costly, due to the price of the material, the use of hydrogen and the required thermal management, recent material discoveries allow for a significant reduction in system cost [9]. One of the most studied classes of metal hydrides for thermal energy storage in concentrating solar power plant applications is the magnesium hydride (MgH₂) based materials, which have a reported gravimetric energy density approximately 18 times higher than that of molten salts together with a low material cost [9, 11]. However, magnesium (Mg)-based materials are usually employed for low to medium temperatures (i.e., 300–500 °C or 573.15–773.15 K), which is consistent

with nonsupercritical steam power plant operating conditions. Other recently discovered materials, described in the following sections, can also be employed for higher temperature applications, suitable for Brayton cycle power plants.

To effectively design and build a thermal energy storage system based on metal hydride materials, different processes need to be examined in detail using models that include momentum, mass, and energy transport, coupled with the kinetics and thermodynamics of the reacting materials. In addition, experimental support is needed to collect material property data (such as kinetics, thermodynamics, hysteresis, and stability with cycling, etc.) and to develop new materials or modify existing materials for the specific conditions. Experiments also need to be carried out to verify the performance of the material under different operating conditions and for extended operating periods (e.g., cycling capacity).

In the following sections a general overview of the basic principles of metal hydride materials, focusing on the engineering and system aspects, is given. A review of the use of metal hydrides as thermochemical reservoirs, being able to provide heat/cooling power or to store thermal energy at different temperatures, is also provided. Previous work on metal hydride thermal energy storage systems is also discussed, providing information and results available from the literature. Techno-Economic analysis of available metal hydride thermal energy storage systems, with the inclusion of recently developed materials, is conducted and the results are discussed. The aim of the analysis is to give useful criteria to (1) select candidate materials, which have the potential to meet technical targets or can be adopted for a specific application and (2) evaluate the performance of the selected materials under different operating conditions. In addition, the results provide a useful guide for experimental efforts in needed material modifications. The results from a high-level techno-economic analysis are necessary, as the first step of a detailed performance analysis focused on a restricted number of candidate materials displaying a high potential for successful operation. However, the use of screening tools does not take the place of more detailed numerical simulations and experimental studies needed to fully evaluate and describe the thermal energy storage system. A thermal energy storage system, based on a relatively newly developed material (namely sodium magnesium hydride fluoride, NaMgH_2F), was selected to be coupled with an ultra-supercritical steam power plant. The system was simulated on a laboratory scale level, performing detailed transport modeling analysis to show its potential for efficient integration into concentrating solar power plants.

10.2 Metal Hydrides as Heat Processing Systems

Metal hydrides are materials that can react with hydrogen in a nearly reversible manner. The hydrogenation reaction, the formation of the hydride, is an exothermic reaction, while the dehydrogenation reaction, decomposition of the hydride and the accompanying release hydrogen, is an endothermic reaction. The pressure – composition – temperature (PCT) profiles define the thermodynamic equilibrium

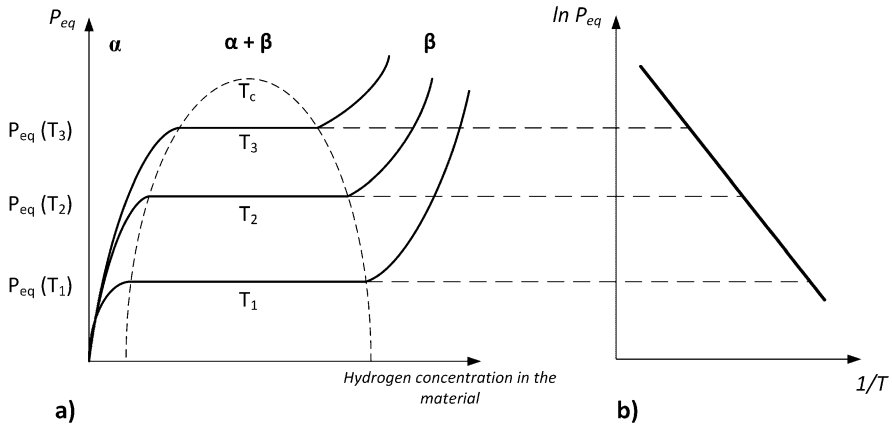


Fig. 10.1 Pressure composition temperature (PCT) qualitative profile (a) and corresponding qualitative Van't Hoff plot (b)

conditions of hydrogenation and dehydrogenation, correlating absorption and desorption reactions with the equilibrium pressure, temperature, and hydrogen concentration.

A qualitative PCT profile and, the corresponding van't Hoff plot are shown in Fig. 10.1a and b, respectively. The PCT of the metal hydrides is characterized by three regions: the α phase, the $(\alpha + \beta)$ phase, and the β phase. The α phase is the phase in which the molecular hydrogen dissociates into individual atoms and diffuses into the unreacted metal lattice. For small hydrogen concentrations in the solid, which is the condition in the α phase region, the hydrogen concentration in the solid can be expressed as proportional to the square root of pressure, using the (simplified) Sievert's law:

$$C_H = \frac{1}{K} \sqrt{P_{eq}(T)} \quad (10.1)$$

with C_H being the atomic hydrogen concentration in the solid ($\text{mol}_H/\text{mol}_{\text{Metal}}$), K is temperature dependent constant (dimensionless) and $P_{eq}(T)$ the equilibrium pressure (atm), function of the temperature, $T(\text{K})$. As the hydrogen pressure is increased, saturation occurs as the hydrogen and metal react to form a metal hydride, thus going from the α into the $(\alpha + \beta)$ phase.

The Gibbs function, ΔG_{at} (J/mol_H), for the atomic hydrogen can be expressed, in the $(\alpha + \beta)$ phase, as a function of only the equilibrium temperature (in kelvin):

$$\Delta G_{at} = \frac{1}{2} RT \ln \frac{P_{eq}(T)}{P_0} \quad (10.2)$$

with $P_0(\text{Pa})$ being the reference pressure (atmospheric pressure $[\text{atm}] = 101,325 \text{ Pa}$). The Van't Hoff equation, for the atomic hydrogen, can be expressed from the Gibbs function equation:

$$\frac{1}{2} \ln \frac{P_{eq}(T)}{P_0} = \frac{\Delta H_{at}}{RT} - \frac{\Delta S_{at}}{R} \quad (10.3)$$

The plateau pressure $P_{eq}(T, \text{atm})$ of the two-phase region is the equilibrium dissociation pressure of the hydride and is a measure of the stability of the hydride, which is usually referred to as β phase.

After completing the reaction between hydrogen and metal in the two-phase region, any addition of hydrogen results in a high increase in pressure required to diffuse hydrogen into the metal hydride. The intermediate ($\alpha + \beta$) phase is the region of interest for practical applications of metal hydrides, such as hydrogen storage system [12–15], hydrogen compression systems [15–18], hydrogen purification [19–21], or thermal processing systems [22–25]. The conversion of α to β phase occurs with the change hydrogen concentration in the solid at a nearly constant equilibrium pressure, corresponding to a constant temperature, ideally denoted by a flat plateau. However, the ($\alpha + \beta$) region is always characterized by sloped transition causing a pressure variation (with the slope dependent on the material) at a constant temperature. The length of the plateau represents the amount of hydrogen that can be stored reversibly with small pressure variation. The exploitation of this region is the primary focus of research for all the metal hydride-based applications as it ensures the transfer of hydrogen at near constant operating conditions. Concurrently, the extension of the plateau region is the primary focus of the development of new metal hydride materials. At operating temperatures higher than the critical temperature (T_c), the two-phase plateau region disappears. Empirical formulations are usually adopted to account for the PCT curve in the β region.

In the plateau region, the equilibrium pressure can be evaluated adopting the Van't Hoff relationship, suitably modified to account for the specific material morphology. In general, the correction factor is a function of hydrogen concentration and temperature, to be evaluated for the specific material, but for many cases, a linear correction factor can be adopted [26].

Another important aspect to be taken into consideration is the hysteresis effect that occurs during charging and discharging of hydrogen. This behavior is modeled by having two Van't Hoff equations, one for the charging and one for the discharging process. A hysteresis factor is introduced to account for the material hysteresis. This factor is:

$$\frac{1}{2} \ln \frac{P_{eqa}(T)}{P_{eqd}(T)} = \frac{\Delta G_{atHyst}}{RT} \quad (10.4)$$

with $P_{eqa}(\text{atm})$ being the absorption equilibrium pressure, $P_{eqd}(\text{atm})$ the desorption equilibrium pressure, and ΔG_{atHyst} (J/mol_H) the sorption hysteresis Gibbs free

energy for the atomic hydrogen, where R ($8.314 \text{ JK}^{-1} \text{ mol}^{-1}$) is the universal gas constant and T is the temperature (K).

The hysteresis factor is characteristic of a specific metal hydride system and needs to be determined experimentally.

In practical applications, the material reaction enthalpy (ΔH , J/mol) and entropy (ΔS , $\text{Jmol}^{-1} \text{ K}^{-1}$) are usually expressed in terms of molecular hydrogen (H_2). Therefore $\Delta H = 2 \Delta H_{\text{at}}$ and $\Delta S = 2 \Delta S_{\text{at}}$. From the Van't Hoff plot (Fig. 10.1b), the negative slope and the intercept on the temperature axis are proportional to the reaction enthalpy (ΔH) and entropy (ΔS), respectively.

In many practical applications of metal hydrides, the kinetics associated with absorption and desorption plays a fundamental role in attaining effective and low-cost configurations. The kinetics and the mechanisms underpinning the hydrogen/metal interactions were examined and highlighted in many papers [16, 27]. In general, depending on the material (e.g., intermetallic or complex hydrides, single or multiple reaction plateaus) specific kinetics expressions should be developed. However, for the majority of the available metal hydrides, a first-order kinetics expression can model and replicate with an excellent agreement the experimental charging and discharging kinetics process. The first order expression has the typical form shown in Eq. 10.5, expressed in terms of molecular hydrogen concentration:

$$\frac{dX}{dt} = \begin{cases} C_a \exp\left(-\frac{E_a}{RT}\right) \ln\left(\frac{P}{P_{eq}}\right) (X_M - X), & P > P_{eq} \\ C_d \exp\left(-\frac{E_d}{RT}\right) \left(\frac{P - P_{eq}}{P_{eq}}\right) (X - X_m), & P < P_{eq} \end{cases} \quad (10.5)$$

with $C_a(\text{s}^{-1})$ and $C_d(\text{s}^{-1})$ being the pre-exponential kinetics factors, $E_a(\text{J/mol})$ and $E_d(\text{J/mol})$ being the activation energies for H_2 absorption and desorption, respectively, and $X_M(\text{mol}_{\text{H}_2}/\text{m}^3)$ and $X_m(\text{mol}_{\text{H}_2}/\text{m}^3)$ being respectively the maximum and minimum molar concentrations of H_2 within the metal hydride material. The first expression of Eq. 10.5 represents the hydrogen absorption kinetics at pressures higher than the equilibrium pressure, while the second expression represents the hydrogen desorption kinetics when pressures are lower than the equilibrium pressure. Other kinetics expressions adopted specially to model the behavior of complex hydrides (e.g., sodium aluminum hydride, NaAlH_4 kinetics) can be found in several modeling publications [28, 29].

Metal hydrides can be used as a single material system, in which the hydrogen operating conditions (temperature and pressure) can be modified by exchanging heat with external sources at required conditions. They can be used in hydrogen storage systems, absorbing and desorbing hydrogen at the required operating pressures modifying the temperature of the material. Metal hydrides can also be used to compress or purify hydrogen, essentially operating pressure/temperature swing absorption and desorption processes. For this type of application two (or more) metal hydride tanks need to be used in parallel, to assure continuous operation of the overall process.

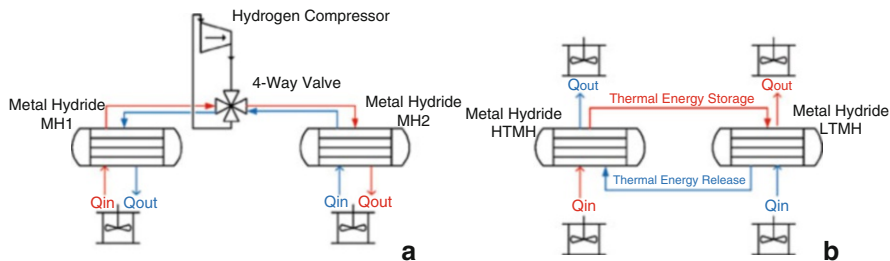


Fig. 10.2 Heat processing metal hydride systems: (a) compressor driven heat pump system, (b) thermal energy storage system

Metal hydrides can also be paired together and used as thermal machines, which can function in conjunction with power production systems (e.g., heating and cooling systems) or can store thermal energy. In these applications a quantity of hydrogen is moved between two metal hydride beds, each having PCT characteristics consistent with the particular application. Figure 10.2 shows a simplified schematics of paired metal hydride systems that can produce heating/cooling power (Fig. 10.2a) or store thermal energy (Fig. 10.2b).

Several layouts and configurations can be established for the paired metal hydride system working as a heating/cooling system. The first work on compressor-driven hydride heat pumps was described in a technical paper by Saul Wolf [30] of the US Navy in 1975 and a patent on the basic concept was granted to McClaine in 1977 and assigned to the Navy [31]. The configuration, shown in Fig. 10.2a, is comprised of two reactors [Metal hydride x](MH1 and MH2), which can be filled with the same material or with different metal hydride formulations, connected by a compressor [32]. The process starts with one material fully saturated with hydrogen and the other metal hydride unsaturated. In the first half cycle (red circuit in Fig. 10.2a) the unsaturated material (high-temperature tank, MH2) absorbs hydrogen, providing high-temperature heating (Q) power (Q_{out} from MH2) and the other material (the low-temperature tank, MH1) desorbs hydrogen providing cooling power (Q_{in} for MH1). In the second half cycle (blue circuit in Fig. 10.2a) the process is reversed and MH1 is the high-temperature tank, providing high-temperature heating power and MH2 is the low-temperature tank providing cooling power. The hydrogen needs to be compressed (either mechanically, thermally, or electrochemically) to assure the absorption at higher pressures (i.e., at higher temperatures) in the high-temperature tank.

The system is also simple, compact, and reliable. Depending on the material thermodynamics and kinetics, as well as on the performance of the heat transfer system, the process can be realized reaching cycling times on the order of 5–10 min each cycle. This results in high efficiencies (e.g., coefficients of performance higher than 3) and low costs, due to the reduced amount of metal hydride required to absorb/desorb hydrogen [32].

Another application of paired metal hydride systems is to store thermal energy. The basic principle of metal hydride-based thermal energy storage is the same as for

the heat pump concept. As shown in Fig. 10.2b, two materials are paired together: the high-temperature metal hydride (HTMH) tank working at high temperatures and the low-temperature metal hydride (LTMH) tank working at low temperatures. The system can work either continuously or discontinuously depending on the thermal energy storage capacity and reaction rate. The red circuit and the blue circuit in Fig. 10.2b represent the thermal storage and the thermal release operations, respectively. During thermal energy storage (red color circuit in Fig. 10.2b) a high-temperature thermal source provides the high-temperature heat to the HTMH (Q_{in} in the HTMH), which desorbs hydrogen. The hydrogen is absorbed in the LTMH, which releases low-temperature heat (Q_{out} in the LTMH), exchanged with a low-temperature external unit. During thermal energy release, the process is reversed (blue circuit in Fig. 10.2b). A low-temperature external source provides heat to the LTMH (Q_{in} in the LTMH) to release the hydrogen previously absorbed. The hydrogen is charged in the HTMH system, which provides heat at high temperature (Q_{out} in the HTMH), exchanged with the external high-temperature system. By this approach, having two materials operating at a reasonable temperature difference (resulting from different reaction enthalpies) the hydrogen is exchanged between the two materials adjusting only the operating temperature (and correspondingly the operating pressure) of the LTMH tank. The basic principles and the performance of selected materials, used for high-temperature thermal energy storage in a concentrating solar power plant, will be described and discussed in the next sections.

10.3 Metal Hydride-Based High-Temperature Thermal Energy Storage Systems

Two main power plants are currently the baseline systems to be integrated with a high-temperature solar source: (1) steam power plants, including also the hypercritical steam power plants, operating at temperatures, in general <650 °C [923.15 K] and (2) supercritical CO₂ [sCO₂, 304.25 K and 72.9 atm] gas power plants, operating at temperatures >700 °C [973.15 K]. The steam power plant is more advanced system, while the sCO₂ plants require additional development for large market penetration, related especially to the gas turbine [33–35]. The solar plant, shown in Fig. 10.3, is comprised of the solar collection and concentrating section, the thermal energy storage section (based on the metal hydride system concept), and the power plant (based on a steam Rankine cycle). The same metal hydride-based thermal energy storage concept can be adapted for use with other power plants (e.g., Brayton cycle), with only a few minor variations.

The power plant is designed to operate continuously. The thermal energy storage system stores and releases the thermal energy needed to maintain continuous operation of the power section. The metal hydride storage system shown in Fig. 10.3 is comprised of two metal hydride materials operating at different temperatures.

During the day (“Sun available” in Fig. 10.3), the surplus solar power is stored in the thermal energy storage system. The high-temperature metal hydride has a high

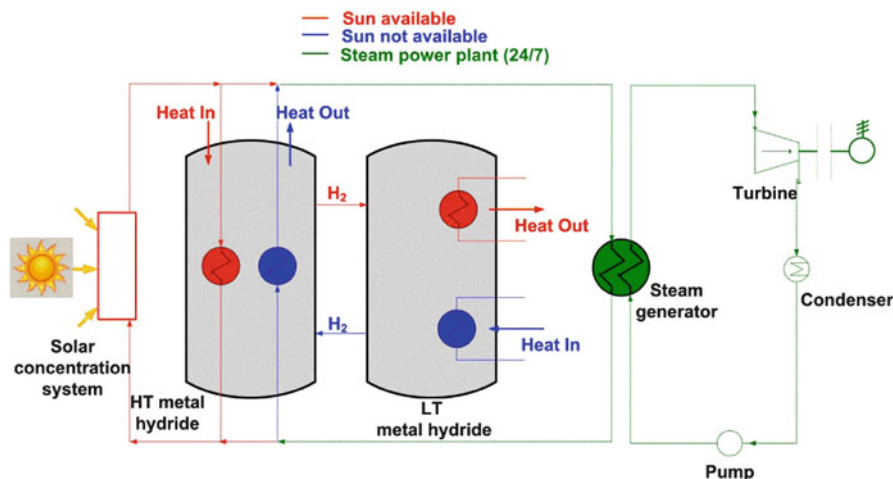


Fig. 10.3 Schematic of a Rankine cycle based concentrating solar power plant with a thermal energy storage system comprised of a high temperature (HT) metal hydride paired with a low temperature (LT) metal hydride

reaction enthalpy (ΔH) value and works at high temperature, allowing a large amount of heat to be stored by using solar heat to release hydrogen (endothermic process, $+\Delta H$) and store it in the low-temperature metal hydride. As the material absorbs hydrogen (exothermic process, $-\Delta H$), it releases low-temperature heat, which is extracted from the thermal energy storage system. During the night or times when additional power is required to run the power plant (“Sun not available” in Fig. 10.3), the process is reversed. Hydrogen flows from the low-temperature metal hydride and is absorbed by the high-temperature metal hydride exothermally providing the needed heat at high temperature to the power plant. The energy density that can be provided by the use of metal hydride systems has been shown to have values on the order of 15–20 times higher than molten salts-based thermal energy storage systems [9]. This can substantially lower the size and capital cost of many thermal energy storage systems. Using only small pressure changes, hydrogen can be transferred from one metal hydride system to another to exchange large quantities of heat at high temperature with the external heat transfer fluid. Hydrogen moves between the two beds by the pressure gradients generated after heating or cooling the system through suitable thermal management and choosing suitable material pairs. This simple exchange results in a thermally self-sustaining system, without the use of additional hydrogen compression systems that would increase the electric power consumption.

The use of hydride materials for high temperature solar thermal energy storage is of great interest due to their unique material properties. Lithium (Li) material was one of the first hydrides examined for this purpose. Caldwell et al. [36] proposed at the end of 1960s the integration of lithium hydride (LiH)-based solar thermal energy storage system with solar parabolic concentrator systems. The proposed system was

designed to provide continuous heat to a satellite power conversion system deployed in near-earth orbit. Experimental tests (with a metal hydride bed of about 0.45 kg of LiH) were conducted for 190 h highlighting a good performance of the thermal energy storage system. A maximum temperature of 760 °C [1033.15 K] was achieved during the tests. The authors concluded that the LiH-based thermal energy storage system would be very attractive for space applications or to balance the solar source availability when only solar energy is available. The main limiting factor of the Li-based storage concept is relative to its cost, as highlighted by Caldwell et al. [36]. Hanold and Johnston [37] proposed the use of Li material-based thermal energy storage systems for power plants and, more particularly, as a thermal energy storage system for a Stirling cycle engine. A conical concentrator, producing temperatures around 700 °C [973.15 K], was designed and connected to the thermal energy storage and integrated with the Stirling engine. Different materials were tested and lithium compounds such as lithium hydroxide, lithium fluoride, and particularly lithium hydride seemed to be the best materials due to their high hydrogenation temperatures (>700 °C or 973.15 K) and their high energy densities, with the heat of reaction around 3500 kJ/kg [37].

More recently, the attention has shifted to magnesium (Mg)-based solar thermal energy storage systems, due to the lower cost of Mg materials relative to Li hydride. After conducting an overview of methods for solar energy storage, Bogdanovic et al. [11] concluded that among the reversible metal-hydride-metal systems, the magnesium hydride (MgH₂) system is particularly attractive. This is due to its high hydrogen capacity and the high formation enthalpy of the Mg-H bond. Experimental results of heat storage were obtained by coupling a storage system based on MgH₂ with a low-temperature metal hydride storage system (i.e., MischMetal-Ni₅ material, where MischMetal is composed approximately of 50% cerium, 25% lanthanum with varying percent of neodymium, praseodymium, and other rare earth metals) [11], highlighting a good performance of the system. Two other aspects, namely, the catalytic hydrogenation and the doping of magnesium powders, were emphasized by Bogdanovic et al. [11] as important aspects of the system. Several studies were carried out to compare the performance of nickel (Ni)-doped MgH₂ system against the performance of un-doped MgH₂ material for high-temperature solar energy storage. After an analysis of different possible doping techniques, Bogdanovic et al. [38] concluded that the mechanical mixing of Mg powder with Ni powder in the dry state “turned out to be by far the simplest and least expensive doping method.” Bogdanovic et al. [39] showed that Ni-doped Mg-MgH₂ materials had excellent cyclic stability and high hydrogenation rates suitable for applications such as the solar generation of heat and cold, heat pumps, and hydrogen storage. They showed [39] that the material can be used as an economic option for the purpose of reversible thermochemical storage of high-temperature heat in the temperature range of 450–500 °C [723.15–773.15 K]. The material reached heat storage capacities of 0.6–0.7 kWh/kg-Mg (2160–2520 kJ/kg-Mg) [39].

Felderhoff and Bogdanovic [40] described two possible applications of the MgH₂-based storage system for high-temperature CSP plants. The first system describes the direct integration of the MgH₂ bed with a steam generator for use in

a Rankine cycle. The volume of the experimental device is about 19 L with 14.5 kg of Ni-doped Mg. The maximum operating temperature is 450 °C [723.15 K] with a maximum pressure of 50 bar (49.34 atm) and a maximum thermal power of 4 kW exchanged to produce steam [41]. The MgH_2 bed is paired both with low-temperature hydrogen pressure tank and with a low-temperature metal hydride material based on titanium-iron-chromium-manganese (Ti-Fe-Cr-Mn) [41].

The second application described in Reference [40] investigated the utilization of Mg-based TES systems in conjunction with Stirling engines (Fig. 10.4). This is an evolution of the previous concept, with the high-temperature hydride system providing the needed heat when sunlight is unavailable. A preliminary small solar power station system was built at the Max Plank Institute during the 1990s [40, 42]. The main components are a solar radiation concentrator, a cavity radiation receiver, a heat pipe system for heat transfer, a Stirling engine, and an MgH_2 storage system coupled with a hydrogen pressure tank or a low-temperature metal hydride tank based on titanium-iron-chromium-vanadium-manganese (Ti-Fe-Cr-V-Mn) material [42]. To transfer the heat two potassium heat pipes were used [42]. The first prototype test systems contained about 20 kg of Mg powder with a storage capacity of about 12 kilowatt-hours of thermal heat (kWhth) and reached operating temperatures in the range 300–480 °C [573.15–753.15 K] [42].

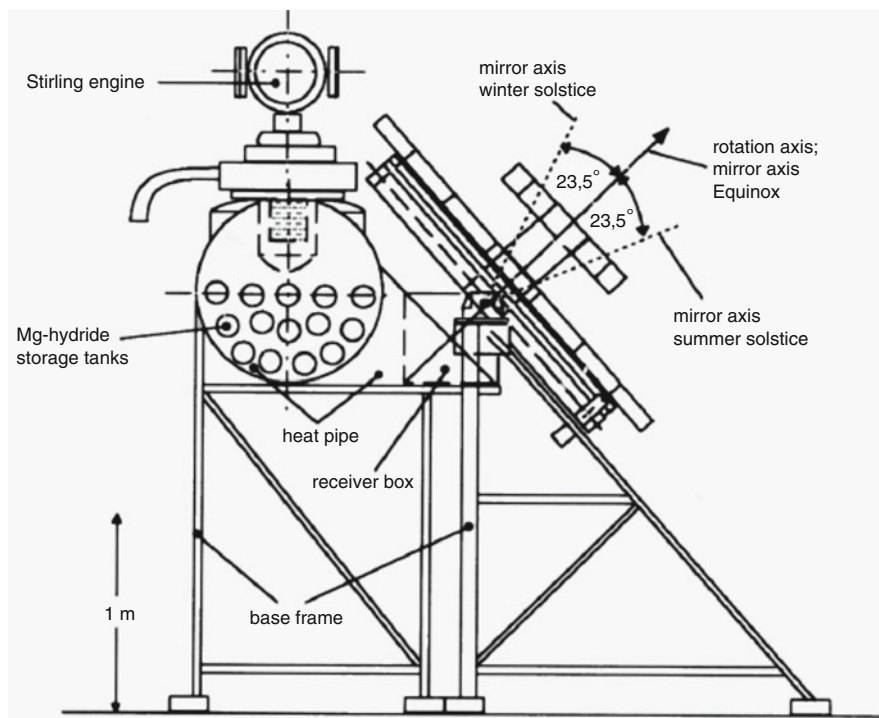


Fig. 10.4 Solar driven Stirling engine with Mg-hydride based thermal energy storage [42]

Other possible Mg-based materials have recently been investigated as possible components of high-temperature metal hydride solar thermal energy storage systems. These materials include Mg-Fe hydride, Mg-Ni hydride, Mg-Co-based hydride [43], and Na-Mg hydride [44]. The Mg-Ni/Mg₂NiH₄ material demonstrated good cyclic stability with a hydrogen weight capacity of about 3% and reaching energy densities of 916 kJ/kg at temperatures of 230–330 °C [503.15–603.15 K] [11]. The Mg-Fe/Mg₂FeH₆ material showed good cyclic stability at temperatures of 480–550 °C [753.15– 823.15 K], corresponding to a pressure range of about 60–100 bar and achieved weight hydrogen capacities on the order of 5.4% [43]. Magnesium cobalt hydride (Mg-Co-H) material has a theoretical weight capacity on the order of 4–4.5%, depending on the hydrides formed in the Mg-Co-H system [43]. However, two plateau regions were found by Reiser et al. [43]: the first plateau has hydrogen content up to 2.5%, while the second plateau provides an additional 2.5% to about 3.7% hydrogen weight capacity. The operating temperatures are on the order of 450–550 °C with pressures on the order of magnesium iron (MgFe)-based hydride [43]. A comparison among Mg-Fe, Mg-Ni, and Mg-Co materials resulted in identifying the Mg-Fe compound as the most promising material for high-temperature thermal energy storage applications, due to its operating conditions, low material cost, and high material weight capacity [43, 45]. A more detailed investigation of the potential of Mg-Fe material as a high-temperature storage material was given by Bogdanovic et al. [45]. The performance of the material is shown in Reference [45] and reported excellent cycling stability at around 500 °C [773.15 K]. The authors [45] also compared the performance of different Mg-Fe materials that were prepared to start from different initial Fe/MgH₂ ratios. More recently, sodium magnesium hydride (NaMgH₃) has garnered interest for use as a low-cost material for a high-temperature storage system. Sheppard et al. [44] performed experimental tests to assess the performance of the perovskite-type hydride, NaMgH₃ under high-temperature CSP plant conditions. The optimal use of NaMgH₃ hydride is at temperatures around 580–600 °C [853.15–873.15 K] with a one-step reaction, corresponding to pressures (on the order of tens of bar) lower than the other Mg-based materials [44]. More recent activities highlighted the possibility of using a modified NaMg-based metal hydride, namely, sodium magnesium fluoride (NaMgH₂F) hydride, for higher temperature applications, on the order of 550–650 °C [823.15–923.15 K]. The material has appealing thermodynamic properties for solar thermal energy storage applications, with high reaction enthalpy values (96.8 kJ/mol_{H₂}) and relatively high weight capacities (almost 3 wt %), and potential for low costs [46–49].

Calcium (Ca)-based hydrides have also been investigated to store high temperature solar thermal energy. Due to its very high enthalpy of formation (at 950 °C or 1223.15 K the heat released during hydrogen absorption is 4494 kJ/kg [9]), there was early interest in using calcium hydride for thermochemical energy storage. Reference [50] describes a proposal, made in the late 1970s, to construct a solar power plant with a 700 kWe output, which used a sodium loop to transfer the heat from the solar concentrator to the hydride system. A solar plant using calcium hydride as the storage material with a continuous output of 100 kWe system coupled

to a Stirling engine has recently been investigated in Australia [50]. However, calcium hydride (CaH_2) material poses very challenging issues in terms of vessel material corrosion, which is difficult to overcome. Recent work highlighted the potential of calcium aluminum (CaAl_2), as well as other Ca-based hydrides (e.g., calcium-silicon (Ca-Si) hydrides) for low cost and efficient thermal energy storage systems. Calcium aluminum (CaAl_2) showed the presence of two plateaus and excellent PCT profiles to work at operating temperatures on the order of 600–650 °C [873.15–923.15 K] [51]. Ca-based materials still require additional research and development to be used as thermal energy storage systems at large scale but have very high potential to meet the US Department of Energy (DOE) techno-economic targets.

Possible candidate low-temperature materials, to be paired with the corresponding high-temperature material, are usually selected from the AB_5 , AB, and AB_2 type materials. The AB_5 materials, based on MishMetal or Rare Earth materials (e.g., Lanthanum-Nickel (LaNi_5) materials), are materials with excellent stability and cycling performance at low temperature (around 25 °C or 298.15 K) with weight capacities on the order of 1–2%. The adoption of these materials as low-temperature metal hydride materials has been demonstrated in several solar applications [40, 52]. Another possible AB_5 hydride is based on CaNi_5 material. Yonezu et al. [52] proposed dual low-temperature metal hydride beds with CaNi_5 coupled to MmNi_5 through a heat pipe-based heat exchanger. More recently, Chumphongphan et al. [53] demonstrated better stability of Al-doped CaNi_5 relative to undoped material at 85 °C (358.15 K) and 20 bar (19.73 atm). The intermetallic AB and AB_2 type materials, which are Ti-based low-temperature metal hydride materials, are more economically advantageous than AB_5 materials. Their specific material cost is generally lower than the AB_5 formulations and has approximately the same weight capacities (around 1.5 wt %) and the same reaction enthalpies (about 25–30 kJ/mol $_{\text{H}_2}$). Libowitz [54, 55] reported on one of the first applications of AB materials for solar thermal energy storage systems. This report shows the use of titanium iron (TiFe) material for low-temperature solar systems, analyzing the behavior under different operating conditions and for different configurations. The AB class of materials has excellent cycling properties with operating temperatures on the order of ambient temperature and weight capacities around 1–2% [54]. The titanium iron hydride (TiFeH_2) has recently been proposed as one of the best low-temperature hydrides to be paired with CaH_2 high-temperature material by Harries et al. [56]. A new class of low-cost complex hydrides, sodium alanates (NaAlH_4), has been the focus of extensive research as hydrogen storage materials since Bogdanovic and Swickardi [57] demonstrated the reversibility of the reaction by catalyzing the reaction. This material is characterized by two-plateau pressure-composition-temperature profiles (i.e., two sequential chemical reactions) occurring for two different equilibrium temperatures and pressures [57]. Depending on the application, sodium alanate can be used as a low-cost hydride, either employing both plateaus or by operating with only one reaction. Sodium alanate has several properties that make the compound very attractive for several thermal energy storage application, as long as the required operating temperatures can be satisfied.

10.4 Techno-Economic Analysis of Metal Hydride Thermal Energy Storage Systems

The two unknowns involved in the analysis of metal hydride-based thermal energy storage system techno-economic performance are: (1) the installed cost of the proposed system and (2) the exergetic efficiency of the system. The model has been applied to coupled metal hydride systems for high-temperature thermal energy storage, but it can easily be used to assess the techno-economic performance of any other coupled metal hydride energy system.

10.4.1 Economic Model

The specific installed cost of the thermal energy storage system, C_S (\$/kWh), can be assessed accounting for: (1) the cost of the metal hydride materials, C_M (\$), (2) the cost of the heat transfer system, C_{HE} (\$), and (3) the cost of the pressure vessel walls, C_{PV} (\$). Therefore:

$$C_S = \frac{(C_M + C_{HE} + C_{PV})}{E_{th}} \quad (10.6)$$

The overall thermal energy stored in the thermal energy storage system, E_{th} (kWh), is:

$$E_{th} = \frac{(W_{el}\Delta t_s)}{(\eta_{PP}PCF)} \quad (10.7)$$

with W_{el} (W) being the average electric power produced by the plant during the year. Δt_s (h) the storage time, η_{PP} the power plant efficiency, and PCF the plant capacity factor.

The installed cost of the metal hydride material (C_M) is given by:

$$C_M = C_{RM} + C_{AM} \quad (10.8)$$

The term C_{RM} (\$) is the raw metal hydride material cost. The second term, C_{AM} (\$) accounts for all the additional material synthesis work cost, manufacturing cost, and handling costs needed to locate the material (in the right configuration and shape) inside the tank. Based on experience and data available for small scale stationary applications using similar metal hydride formulations, C_{AM} has been assumed equal to 20% of the raw cost of the material (C_{RM}) [58].

The shell and tube heat exchanger concept has been assumed as the baseline heat transfer system to evaluate the cost of the heat transfer system (C_{HE}).

A simplified steady state one-dimensional (1D) radial model was developed using cylindrical coordinate geometry. The storage tank was modeled as a series of cylindrical structures filled with the metal hydride materials and with the fluid

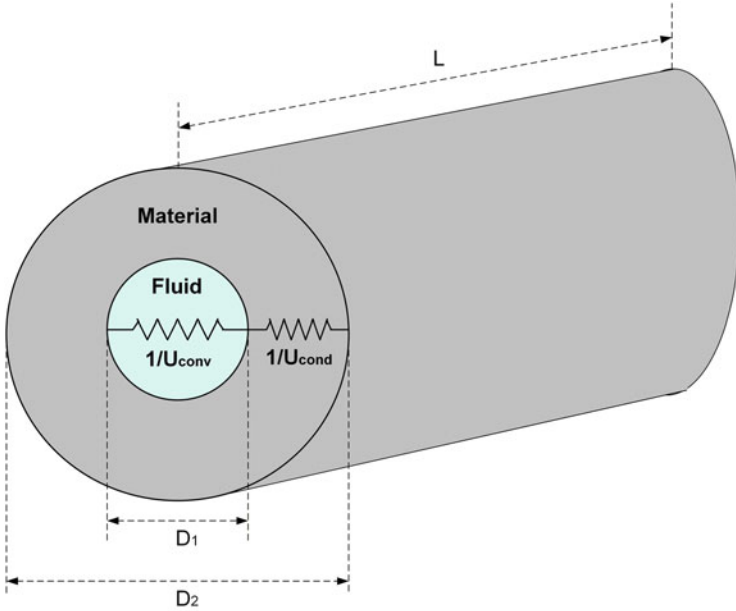


Fig. 10.5 Model of the tube (Fluid) and metal hydride (Material) structure for a cylindrical geometry, with the material packed around the heat transfer fluid tube

flowing inside tubes located inside the material structures (Fig. 10.5 shows the single cylindrical structure). The thermal resistance offered by the heat transfer fluid tube wall (usually made of highly conductive materials) was assumed negligible compared to the other resistances.

The overall heat flux W_{th} (W) can be expressed as a function of the conductive heat transfer coefficient, U_{cond} ($W/m^2\cdot K$), convective heat transfer coefficient, U_{conv} ($W/m^2\cdot K$), number of tubes, n_T , heat transfer fluid tube diameter, D_1 (m), length of the heat exchanger, L (m), and logarithmic mean temperature difference between the fluid and the material, ΔT (K):

$$W_{th} = \left(\frac{1}{\frac{1}{U_{cond}} + \frac{1}{U_{conv}}} \right) n_T \pi D_1 L (\Delta T) \quad (10.9)$$

The conductive coefficient can be assessed as a function of the material thermal conductivity, k ($W/m\cdot K$), heat transfer fluid tube diameter, D_1 (m), and the single metal hydride material diameter, D_2 (m). Fixed temperatures at the heat transfer fluid tube diameter (D_1) and at the material tube diameter (D_2) have been assumed as boundary conditions of the problem:

$$U_{cond} = \frac{2k}{D_1 \ln\left(\frac{D_2}{D_1}\right)} \quad (10.10)$$

The convective heat transfer coefficient can be assessed using the known Dittus & Boelter's expression, assuming a turbulent regime (i.e., $Re > 10,000$, dimensionless unit):

$$U_{conv} = \frac{k_{fluid}}{D_1} 0.023 Re^{0.8} Pr^n \quad (10.11)$$

with k_{fluid} (W/m-K) being the fluid heat thermal conductivity. Re and Pr (dimensionless) numbers are calculated for the heat transfer fluid properties (density, specific heat, thermal conductivity, viscosity, and velocity) and having the diameter D_1 as the characteristic length in the Re . Pr number exponential factor, n , is equal to 0.3 for heating fluid and 0.4 for cooling fluid.

The volume occupied by the metal hydride, determined by the solar plant and material properties, gives an additional constraint to solve the equations of the problem.

The data and the assumed degrees of freedom of the problem are D_1 , k , U_{conv} , ΔT , and L . The unknown quantities are D_2 and n_T .

The heat transfer area, A (m^2), which is the most significant parameter in the assessment of the heat exchanger costs, is given by:

$$A = n_T \pi D_1 L \quad (10.12)$$

The installed cost of the shell and tube heat exchanger can be estimated using traditional factored method approaches [59]. The component cost, C_{HE} , is given by:

$$C_{HE} = C_{FHE} + C_{AHE} \quad (10.13)$$

The component "free on board" cost, C_{FHE} (\$), was evaluated from the cost of a reference heat exchanger. The reference heat exchanger cost depends on its area, A , and its operating conditions (1 bar operating pressure, carbon steel material, and straight tube geometry heat exchanger). To evaluate the "free on board" cost, the initial reference cost was modified adopting suitable cost factors. These cost factors account for the actual heat exchanger working conditions (i.e., operating pressure), materials, and heat exchanger geometry. Stainless Steel (SS) has been assumed to be the current baseline material for the specific system. However, other materials, capable of withstanding higher temperature can be considered when needed. Straight tube heat exchanger geometry has been assumed for all systems. The reference cost and the additional cost factors have been assessed using the ASPEN In-Plant Cost Estimator, based on databases developed for metal hydrides and hydrogen energy applications [60, 61], and suitably modified to match the operating conditions and configuration of the actual system.

The term C_{AHE} (\$) includes the installation costs of the component such as piping, instrumentation, concrete, and insulation, as well as labor [59]. The component cost (C_{HE}) can be expressed as a function of the “free on board” cost, with an installation factor (f) >1:

$$C_{HE} = fC_{FHE} \tag{10.14}$$

The installation factor (f) accounts for the additional costs associated with the installation of the component.

For the specific application, an installation factor (f) equal to approximately 1.5 (dimensionless unit) has been used. This value is based on available databases [60] and on the size of the heat exchangers as well as on previous experience gained from small scale stationary metal hydride bed applications [58].

The pressure vessel cost has been assessed by applying the same factored method approach used for the heat exchangers. The pressure vessel “free on board” cost, C_{PV} (\$), has been evaluated as a function of working conditions (pressure), vessel material (SS is the baseline material), and the size of the vessel (diameter and length) using the ASPEN In-Plant Cost Estimator and the databases available in References [60, 61]. An additional 25% void volume has been included when estimating the vessel dimensions to allow for the expansion/contraction of the metal hydride material during the charging and discharging process, following best practices [26, 58].

10.4.2 Exergetic Efficiency Model

Figure 10.6 shows the metal hydride storage system interfaced with the high-temperature heat transfer fluid. Figure 10.6a shows the heat storage process when excess thermal power is available with hydrogen moving from the high-temperature metal hydride to the low-temperature metal hydride. The exergetic input (Bth_s) is the thermal exergy related to the high-temperature heat transfer fluid. The chemical

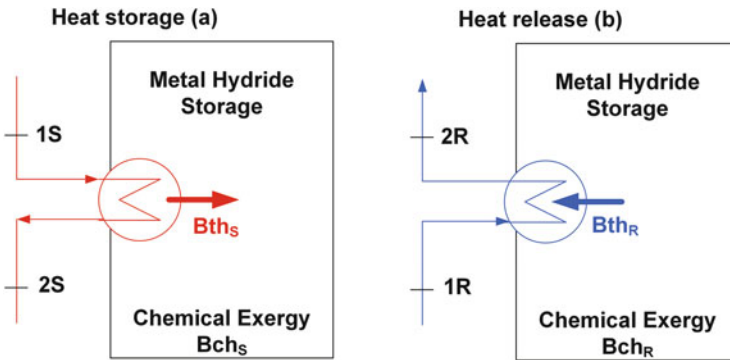


Fig. 10.6 Metal hydride thermal energy storage system exergy (B) quantities: (a) heat storage, (b) heat release

exergy related to the endothermic hydrogen discharge reaction in the high-temperature system (Bch_S) represents the exergy available in the thermal energy system. Figure 10.6b shows the heat release process with hydrogen moving from the low-temperature metal hydride to the high-temperature material. In this case, the exergetic input (Bch_R) is the chemical exergy from the hydrogen charging reaction in the high-temperature metal hydride.

The heat transfer fluid thermal exergy (Bth_R) represents the exergy available from the thermal energy storage system.

For a stationary thermal energy storage process, the exergetic efficiency (η_{BS}) is given by:

$$\eta_{BS} = \frac{Bch_S}{Bth_S} \quad (10.15)$$

with η_{BS} being the exergetic efficiency of the heat storage process, Bch_S (J) being the total chemical exergy stored in the metal hydride bed, Bth_S (J) being the total exergetic input available from the high-temperature heat transfer fluid during thermal storage. The two exergy terms (Bch_S and Bth_S) can be written in terms of the change in the Gibbs energy between the initial and final states.¹ The thermal exergy (Bth_S) is:

$$Bth_S = m_S \Delta t_S (h_{2S} - h_{1S} - T_0 (s_{2S} - s_{1S})) \quad (10.16)$$

The term m_S (kg/h) is the heat transfer fluid mass flow rate and Δt_S (h) is the storage time. The Gibbs function is expressed in terms of enthalpy variation between point 2S, h_{2S} (J/kg), and point 1S, h_{1S} (J/kg), and entropy variation between point 2S, s_{2S} (J/kg-K), and point 1S, s_{1S} (J/kg-K). T_0 (298 K) represents the reference temperature.

The chemical exergy term (Bch_S) is evaluated as shown in Eq. 10.17:

$$Bch_S = M_{H_2} (\Delta H_S - T_0 \Delta S_S) \quad (10.17)$$

M_{H_2} indicates the mass of stored hydrogen (kg) and ΔH (J/kg_{H₂}) and ΔS (J/kg_{H₂}-K) represent the reaction enthalpy and entropy during the heat storage process (i.e., hydrogen discharging).

The exergetic efficiency for heat released from the thermal storage system (η_{BR}) can be written as:

$$\eta_{BR} = \frac{Bth_R}{Bch_R} \quad (10.18)$$

¹The kinetics energy term as well as potential term, referred to the reference exergetic state, have been assumed negligible

with η_{BR} being the exergetic efficiency of the heat release process, Bch_R (J) being the total chemical exergy available from the high-temperature metal hydride charging, Bth_R (J) being the total thermal exergy available in the heat transfer fluid during thermal release. The two exergy terms (Bch_R and Bth_R) can be written in terms of the change in the Gibbs energy between the initial and final states.² The thermal exergy (Bth_S) is:

$$Bth_R = m_R \Delta t_R (h_{2R} - h_{1R} - T_0 (s_{2R} - s_{1R})) \quad (10.19)$$

The term m_R (kg/h) is the heat transfer fluid mass flow rate during thermal energy release and Δt_R (h) is the release time. The Gibbs function is expressed in terms of enthalpy variation between point 2R, h_{2R} (J/kg) and point 1R, h_{1R} (J/kg), and entropy variation between point 2R, s_{2R} (J/kg-K) and point 1R, s_{1R} (J/kg-K).

The chemical exergy term, Bch_R (J) can be evaluated as follows:

$$Bch_R = M_{H_2} (\Delta H_R - T_0 \Delta S_R) \quad (10.20)$$

M_{H_2} is the mass of stored hydrogen (kg) and ΔH (J/kg_{H2}) and ΔS (J/kg_{H2}-K) represent the reaction enthalpy and entropy during the heat release process (i.e., hydrogen charging).

The final total exergetic efficiency (η_B) of the system is:

$$\eta_B = \eta_{BS} \eta_{BR} = \frac{Bch_S}{Bth_S} \frac{Bth_R}{Bch_R} \quad (10.21)$$

10.4.3 Metal Hydride Thermal Energy Storage Systems Techno-Economic Performance

Existing candidate high-temperature metal hydride materials are reported in Table 10.1, which includes the properties needed for the screening analysis. These materials represent currently available metal hydride materials for high-temperature solar applications, with the potential to achieve low cost and high efficiency.

The best high-temperature candidates have: (1) high reaction enthalpy; (2) high working temperatures, which affect the efficiency of the power plant; (3) high hydrogen capacity, which determines the mass (i.e., cost) of the material; and (4) low raw material cost. Other existing materials, such as potassium aluminum (KAl)-based and zirconium manganese (ZrMn)-based hydrides, have not been included as potential candidates due to their high raw material cost. Some of the recently discovered materials require additional development for large scale solar applications. The bulk density of the materials is computed from their crystal density,

²The kinetics energy term as well as potential term, referred to the reference exergetic state, have been assumed negligible

Table 10.1 High-temperature metal hydrides characteristics (ΔH and ΔS are absolute values)

	Temp/Press (°C/bar)	ΔH (kJ/molH ₂)	ΔS (kJ/molH ₂ K)	Theoretical wf (wt % H ₂)	Bulk density (kg/m ³)	Raw material cost (\$/kg)	References
MgH ₂	300–500/10–200	75	0.136	7.6	870	2.9	[9, 62, 63]
Mg ₂ FeH ₆	350–550/10–200	77	0.137	5.5	1300	1.9	[43, 63]
NaMgH ₃	400–600/10–80	88	0.132	4.0	1000	4.2	[44, 63, 64]
LiH	950–1150/0.1–1.5	190	0.135	12.6	500	70.0	[63, 65]
TiH _{1.72}	650–950/0.5–10	142	0.130	3.5	1600	12.0	[63, 65]
CaH ₂	900–1100/0.1–1.5	171	0.126	5.0	890	6.0	[63, 65]
NaH	400–600/0.5–70	130	0.165	4.2	750	4.0	[63, 65]
NaMgH ₂ F	500–650/3–33	96.8	0.134	3.0	1390	1.7	[46]

assuming a void fraction on the order of 0.5, which is a typical value for metal hydride applications. The hydrogen weight capacities reported in Table 10.1 refer to the theoretical material capacity. However, practical values were used in the techno-economic analysis and were based on data reported in the literature and on previous experience with particular materials (e.g., a practical capacity of 7% has been considered for MgH_2 material, based on Ref. [62]).

The thermal conductivity (k) of all materials was assumed to be 7 W/mK with the inclusion of 10 wt % expanded natural graphite in each compacted metal hydride system [66, 67].

Pressurized gases (helium or air) have been assumed as the baseline heat transfer fluids. Based on previous work carried out for similar applications, these gases have relatively high convection heat transfer coefficients [68]. A Log Mean Temperature Difference value of 25 °C [298.15 K] for the heat exchanger design was assumed in the calculations.

The techno-economic analysis was carried out by examining the integration of the thermal energy storage systems, comprised of the different metal hydrides shown in Table 10.1, with a 100 megawatt electrical (MWe) power plant, having a power plant efficiency of 45%, and a plant capacity factor of 63%, produced by storage capacity yielding a duration of 13 h.

The exergetic efficiency analysis was also carried out assuming no hysteresis in the selected metal hydrides (see Eq. 10.4). This assumption was made because, with few exceptions (e.g., MgH_2), there is no data on hysteresis for the majority of the materials shown in Table 10.1.

The specific installed costs and exergetic efficiencies of the proposed high-temperature metal hydrides are shown in Fig. 10.7.

Figure 10.7a reports the economic analysis results, showing the specific installed cost of (only) the high-temperature metal hydride system, with the contribution of the hydride material specific installed cost and the heat transfer and pressure vessel specific installed cost. The results show that the heat transfer system and pressure vessel cost significantly influences the overall cost of the low price and high-pressure materials (Mg and Na family of materials). More than 60% of the

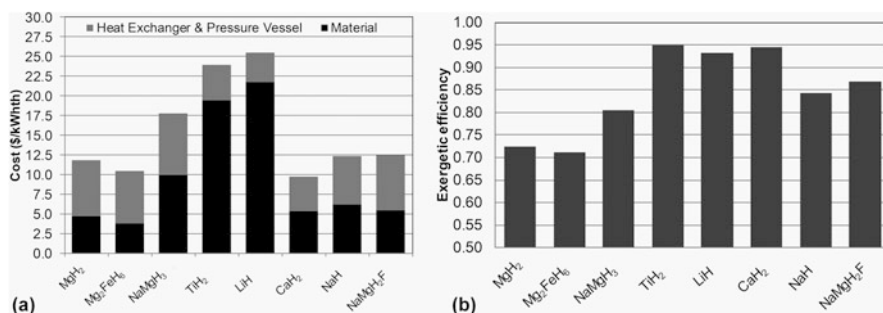


Fig. 10.7 Techno-economic performance of the selected high-temperature metal hydride (stand-alone) systems. Specific cost (a) and exergetic efficiency (b) of the high-temperature materials

overall high-temperature system cost is due to the heat transfer system and pressure vessel cost for MgH_2 and Mg_2FeH_6 materials. For the Na-based materials, the overall cost is affected by the cost of the heat exchanger and pressure vessel on the order of 45–50%. Results for the NaMgH_2F system show that the cost of the heat exchanger and pressure vessel represents almost 57% of the overall system cost. For low-pressure materials, like the less expensive Ca-based system, the results show that the heat exchanger and pressure vessel contribute to the overall cost by approximately 45–50%. Conversely, for the more expensive low-pressure materials (Li and Ti-based metal hydrides), the system cost is mainly affected by the material cost, with percentages on the order of 80–85%. Figure 10.7b shows that three classes of materials can be identified. The first material class (lowest operating temperatures) is comprised of Mg and Mg-Fe-based materials. Their exergetic efficiency (for temperatures on the order of 500 °C or 773.15 K) is on the order of 70–75%. These values can be higher at lower operating temperatures but at the expense of decreased power plant efficiency. The second material class is comprised of Na-based materials, and it is characterized by higher operating temperatures, on the order of 500–650 °C [773.15–923.15 K]. Typical exergetic efficiencies of these systems are around 85%. The last class of materials includes the very high-temperature materials, with operating temperatures exceeding 700 °C (73.15 K with some having operating temperatures greater than 1000 °C or 273.15 K). This class includes Ti, Li, and Ca materials and has the highest exergetic efficiencies (on the order of 95%). However, these materials operate at low pressures (on the order of 1–5 bar) making the pairing with low-temperature metal hydrides challenging without the presence of hydrogen compression systems. The high-temperature hydride will need to be paired with a suitable low-temperature metal hydride material, to be selected based on the specific application and on the operating conditions. In the following section, a specific application is described, with a coupled metal hydride system integrated with an ultra-supercritical steam power plant.

10.5 Transport Phenomena Modeling of Metal Hydride Thermal Energy Storage Systems

Based on the results of the techno-economic analysis carried out for the selected high-temperature materials, NaMgH_2F hydride, paired with a suitable low-temperature metal hydride, is one of the best candidates to be integrated into a high-temperature steam power plant.

10.5.1 Thermal Energy Storage Coupled Metal Hydrides

The thermal energy storage system, comprised of NaMgH_2F hydride, was integrated with a solar driven high-temperature steam power plant (e.g., ultra-supercritical steam plant), operating at temperatures on the order of 600–650 °C [873.15–923.15 K].

The choice of a low-temperature hydride, to be paired with the NaMgH₂F system, is critical since the conditions of hydrogen uptake and discharge must be compatible with both the operating conditions of the high-temperature metal hydride (especially the NaMgH₂F hydrogenation pressure) and the temperature and rate of waste heat released from the power plant. The low-temperature metal hydride should work at pressures on the order of 50 bar, required to hydrogenate the NaMgH₂F material, and at temperatures on the order of 15–30 °C [288.15–303.15 K]. These conditions allow the heat rejected from the steam power plant to be internally recovered to drive the low-temperature material hydrogen desorption. To realize a thermally self-sustaining plant concept, the following condition needs to be satisfied [69]:

$$\Delta H_{LTMH} < \Delta H_{HTMH}(1 - \eta_{PP}) \quad (10.22)$$

with ΔH being the enthalpy of reaction (J/mol_{H₂}) of the high-temperature metal hydride (HTMH) and low-temperature metal hydride (LTMH) systems and η_{PP} being the efficiency of the power plant.

The constraint given by Eq. 10.22 was obtained for the thermal energy release process (i.e., hydrogen absorption in the high-temperature material) under the following assumptions: (1) the hydrides operate at constant temperature during the thermal energy release, (2) no additional losses (in the connecting equipment, tubing, etc.) are included, (3) all of the waste heat from the power plant can be recovered and used in the storage system.

The above condition is necessary, but not sufficient. It ensures that the waste heat, rejected by the steam plant condenser at a constant temperature, can desorb hydrogen from the low-temperature material and hydrogenate properly the NaMgH₂F bed as required by the power plant. The NaMgH₂F material has a reaction enthalpy of 96.8 kJ/molH₂ (Table 10.1) and a typical ultra-supercritical steam power plant can reach cycle efficiencies on the order of 45–50% [70]. Therefore, the low-temperature material needs to have reaction enthalpies at least lower than 45–50 kJ/molH₂. Titanium chromium manganese [TiCr_{1.6}Mn_{0.2}] was selected as the low-temperature hydride. The material meets the required operating conditions and has a relatively low cost, relative to other low-temperature hydrides [9]. The heat available from the power plant condenser is recovered to release hydrogen from the low-temperature hydride, during the thermal energy release, or is rejected to the environment during the thermal energy storage process.

10.5.2 Metal Hydride System Transport Model

A novel detailed transport phenomena model was developed to simulate coupled metal hydride systems. The model is comprised of mass, momentum, and energy balance equations, with additional ancillary equations to evaluate the properties of the gaseous hydrogen. Suitable kinetics expressions have also been included to simulate the charging and discharging process for both the high- and low-temperature metal hydrides, based on the kinetics in Eq. 10.5. The differential

equations were developed using a finite element approach and were solved using COMSOL Multiphysics[®]. The model is very general and simulates a metal hydride system. It can be applied to every metal hydride-based system, either using coupled materials or single hydride concepts.

The differential equation of the mass balance for hydrogen in a gaseous state within the porous materials is expressed as follows:

$$\varepsilon \frac{\partial \rho}{\partial t} + \nabla(\rho \vec{v}_s) = -S \quad (10.23)$$

with ρ being the density of the H₂ gas (kg/m³), ε (dimensionless) being the porosity of the MH bed, and $\vec{v}_s = \varepsilon \vec{v}$ being the superficial gas velocity (m/s). The net mass rate of hydrogen gas uptake (positive during hydrogen absorption/MH charging) is expressed as:

$$S = MW_{H_2} \frac{\partial X}{\partial t} \quad (10.24)$$

with MW_{H_2} being the molecular weight of hydrogen and X being the local concentration of H₂ absorbed within the metal hydride (mol_{H₂}/m³).

The mass balance equation of hydrogen flowing in the free volume without porous media and without mass sources has the following expression:

$$\frac{\partial \rho}{\partial t} + \nabla(\rho \vec{v}) = 0 \quad (10.25)$$

with \vec{v} being the hydrogen velocity (m/s).

The differential form of momentum balance equation (Brinkman equation) for hydrogen flowing inside the media under laminar flow conditions is expressed as follows:

$$\begin{aligned} \frac{\rho}{\varepsilon} \frac{\partial \vec{v}_s}{\partial t} + \left(\frac{\mu}{\kappa} + \frac{S}{\varepsilon^2} \right) \vec{v}_s = & -\vec{\nabla} P + \nabla \left[\frac{\mu}{\varepsilon} \left(\vec{\nabla} \vec{v}_s + \vec{\nabla} \vec{v}_s^T \right) \right] \\ & - \nabla \left[\left(\frac{2\mu}{3} - \eta_d \right) \frac{1}{\varepsilon} (\nabla \vec{v}_s) \underline{I} \right] \end{aligned} \quad (10.26)$$

with P being the pressure (Pa), μ being the dynamic viscosity (Pa s), and η_d being the dilatational viscosity of the H₂ gas (Pa s).

This equation also includes the viscous stress term expressed in terms of velocity components, taking into account the viscosity of the media as well.

For open channel flow, in the absence of a porous medium, the momentum balance equation is expressed as:

$$\rho \frac{\partial \vec{v}}{\partial t} = -\vec{\nabla} P + \nabla \underline{\underline{\tau}} \quad (10.27)$$

with $\underline{\tau}$ (Pa) being the viscous stress tensor.

The energy balance of the porous system, comprising the metal hydride material and gas phase hydrogen, is expressed as:

$$\rho_{MH} C_{MH} \frac{\partial T}{\partial t} - \nabla k \left(\vec{\nabla} T \right) = -\varepsilon \rho_{H_2} C_{H_2} \left(\frac{\partial T}{\partial t} + \vec{v} \cdot \vec{\nabla} T \right) + \varepsilon \frac{\partial P}{\partial t} + C_{H_2} T \cdot S + S \cdot \Delta H MW_{H_2} + Q \quad (10.28)$$

with ρ_{MH} (kg/m³) being the bulk metal hydride density, C_{MH} (J/kg-K) being the specific heat of the metal hydride, k (W/m-K) being the thermal conductivity, ΔH being the enthalpy of reaction (J/mol_{H₂}), and Q (W/m³) being the contribution of volumetric heat sources.

The energy balance, given by Eq. 10.28, was derived for both the solid and gas phases and includes the effects of chemical reactions between them, along with pressure work and viscous dissipation. Because of the nature of the flow, the contribution of gravitational work and kinetic energy were assumed to be negligible.

For hydrogen flowing in an open channel, in the absence of a porous or reacting medium, the energy balance equation is expressed as:

$$\rho \frac{\partial h}{\partial T} \frac{\partial T}{\partial t} - \nabla k \left(\vec{\nabla} T \right) = -\rho \frac{\partial h}{\partial T} \vec{v} \cdot \vec{\nabla} T - \frac{T}{\rho} \frac{\partial \rho}{\partial T} \left(\frac{\partial P}{\partial t} + \vec{v} \cdot \vec{\nabla} P \right) - \underline{\tau} : \vec{\nabla} \vec{v} \quad (10.29)$$

with ρ being the density of the H₂ gas (kg/m³) and h the enthalpy (J/kg) of hydrogen gas.

The equation of state for hydrogen, as adopted in the model, is given in terms of its compressibility factor as:

$$P = Z(P, T) \rho RT \quad (10.30)$$

The compressibility factor (dimensionless unit) function was obtained by fitting to the NIST database hydrogen data [71].

First-order kinetics expressions (Eq. 10.5) were used to represent the metal hydride hydrogenation and dehydrogenation rates. Parameters in Eq. 10.5 were obtained from experimental measurements using metal hydride powders, thus implicitly capturing the effects of both the local reaction kinetics and diffusion rates for the particles.

The hydrogen equilibrium pressure for the metal hydrides was assessed adopting the van't Hoff equation with molar enthalpy and entropy changes.

The current model assumed no slope in the ($\alpha + \beta$) region and no hysteresis for the absorption/desorption process.

Table 10.2 Thermodynamic and physical and chemical properties of the high-temperature material (NaMgH₂F) and low-temperature material (TiCr_{1.6}Mn_{0.2}) (ΔH and ΔS are absolute values)

	ΔH (kJ/molH ₂)	ΔS (kJ/molH ₂ K)	wf (wt %)	Bulk density (kg/m ³)	Specific heat (J/kg-K)	Thermal conductivity (W/m-K)	Porosity	References
NaMgH ₂ F	96.8	0.138	2.5	1390	1300	0.5	0.5	[46]
TiCr _{1.6} Mn _{0.2}	28.0	0.129	1.5	3123	500	0.6	0.5	[72, 73]

Table 10.3 Kinetics parameters (baseline kinetics expressions in Eq. 10.5)

	Ca (1/s)	Ea (J/molH ₂)	Cd (1/s)	Ed (J/molH ₂)	X _M (molH ₂ /m ³)	X _m (molH ₂ /m ³)	References
NaMgH ₂ F	120,000	102,500	1,000,000	151,500	17,375	0	[46, 69]
TiCr _{1.6} Mn _{0.2}	25	21,500	15.5	19,000	23,423	0	[72, 73]

The thermodynamic and physical-chemical properties of the high-temperature metal hydride (NaMgH₂F) and paired low-temperature metal hydride (TiCr_{1.6}Mn_{0.2}) are shown in Table 10.2. The kinetic parameters are shown in Table 10.3.

10.5.3 Laboratory Scale Test Results

The model was applied to simulate a laboratory scale paired system developed in-house by Greenway Energy and Savannah River National Laboratory.

Figure 10.8 shows a view of one of the bench-scale experimental reactors (Fig. 10.8a), the corresponding three-dimensional (3D) model geometry (Fig. 10.8b), the two-dimensional (2D) axial symmetric geometry of the two coupled reactors (high temperature metal hydride, HTMH, and low temperature metal hydride, LTMH) that was used in the Comsol Multiphysics model (Fig. 10.8c), and the dimensions of a single reactor (Fig. 10.8d).

The volumes occupied by the metal hydrides were determined so that both vessels have the same maximum hydrogen storage capacity while maintaining a free gas space in each reactor at least equal to 20% of the volume. The high-temperature metal hydride material volume was set to $L_{HTMH} = 0.8L_v = 0.122$ m, resulting in a low temperature material fill length of $L_{LTMH} = 0.0905$ m and a theoretical H₂ storage capacity of 1.04 molH₂.

During the discharge process, the outer surface of the (hydrogen discharge) vessel was thermally insulated while a volumetric heat source, Q , was applied to the material to represent the effects of the heaters used in the bench-scale experimental apparatus. During charging, a constant and uniform temperature was imposed on the outer wall and bottom of the vessel, replicating the experimental conditions.

The thermal energy storage and release time were assumed to equal to 1.5 h for each process, resulting in a cycle time of 3 h.

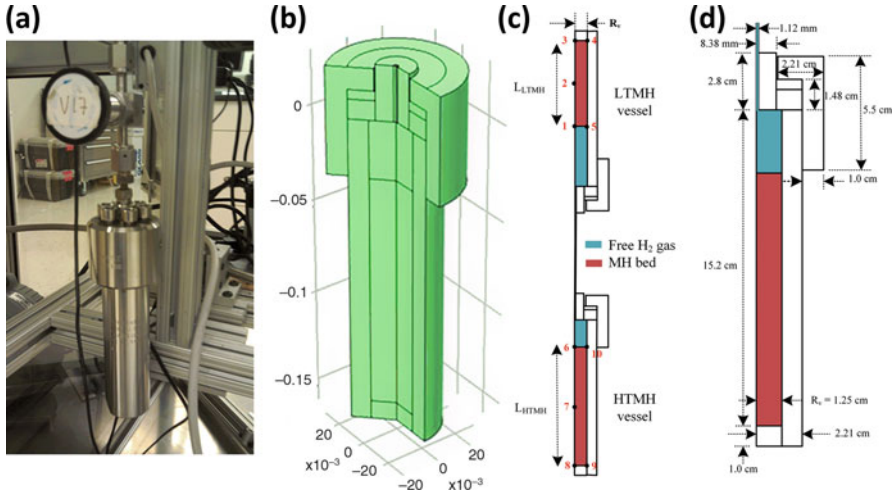


Fig. 10.8 Bench-scale reactors – Picture of the bench-scale experimental reactor (a) – 3D modeling geometry of a single reactor (b) – Coupled high temperature metal hydride (HTMH) vessel and low temperature metal hydride (LTMH) vessel in a 2D axisymmetric configuration as used in the numerical simulation (c) – 2D view of a single vessel with the main dimensions (d)

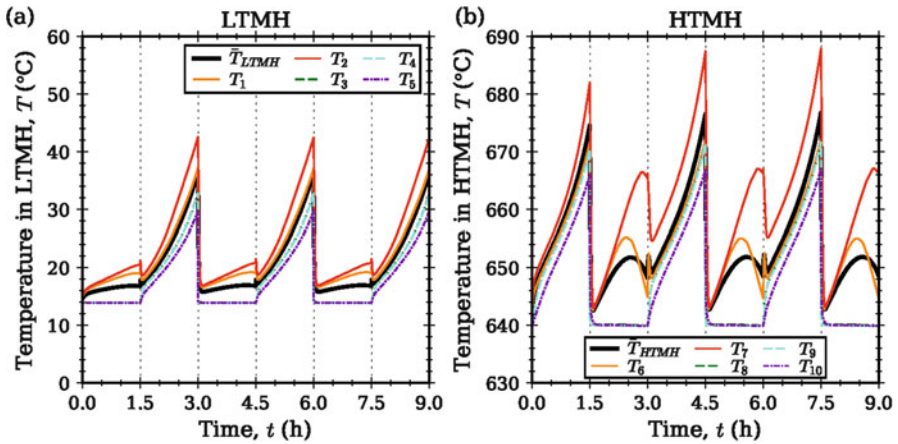


Fig. 10.9 Average temperature (\bar{T}) and selected location temperature profiles for (a) the low temperature metal hydride (LTMH) and (b) the high temperature metal hydride (HTMH) systems

Results of the simulations are shown in Figs. 10.9, 10.10, and 10.11. Figure 10.9 shows the average temperature (\bar{T}) and local temperatures at selected locations within (a) the low temperature metal hydride (locations 1–5 shown in Fig. 10.8c) and (b) the high temperature metal hydride (locations 6–10 shown in Fig. 10.8c). The temperatures ranged from 14 °C to 43 °C [287.15–316.15 K] in the low-temperature bed and from 640 °C to 689 °C [316.15–962.15 K] in the high-temperature bed. In

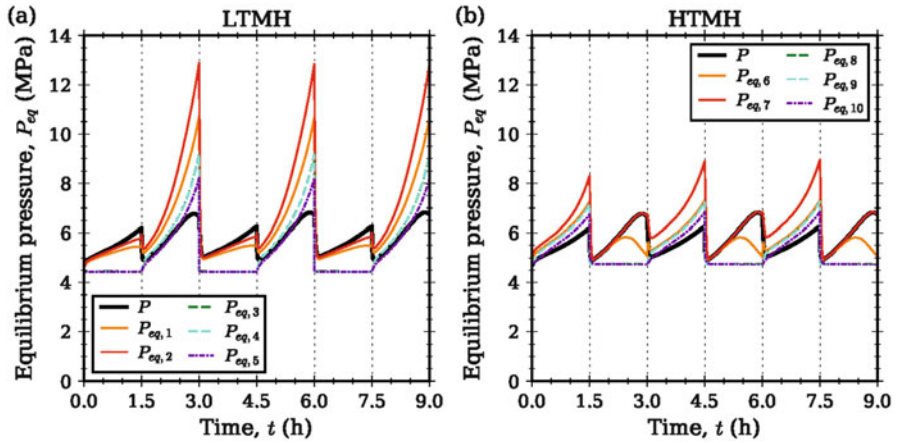
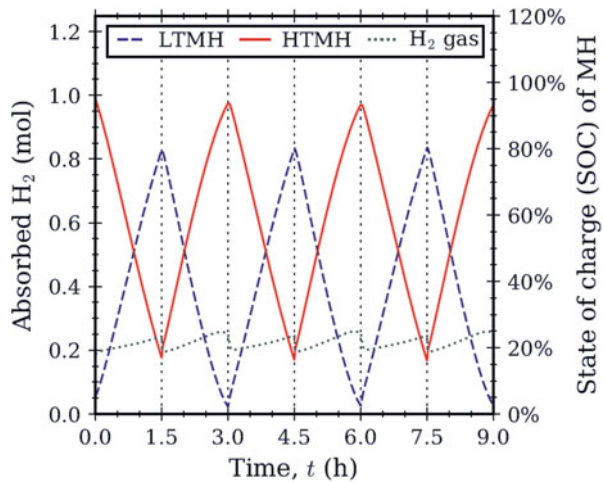


Fig. 10.10 Hydrogen gas pressure (P) and selected location equilibrium pressure profiles for (a) the low-temperature metal hydride (LTMH) and (b) the high-temperature metal hydride (HTMH) systems

Fig. 10.11 Mass of hydrogen absorbed in the high-temperature metal hydride (HTMH), low-temperature metal hydride (LTMH), and as free gas, with the corresponding state of charge (SOC) of the metal hydride (MH)



general, the temperature along the outer surface of the bed was close to uniform and significantly cooler than the interior of the metal hydride bed. In fact, the temperatures at the two locations in contact with the end of the vessel were nearly identical (<0.3% relative difference), so these curves overlap in the figure.

Each MH bed steadily rose in temperature throughout its discharging step due to the heater input, modeled as a punctual heat source in the metal hydride system. The predicted temperature increase during the desorption process is likely higher than the actual temperature variation in the experimental system. However, results suggest the need for heat transfer enhancement systems (e.g., inclusion of finned tubes or

expanded natural graphite) in the high-temperature metal hydride, in order to maintain the maximum temperature at values on the order of 650 °C [923.15 K].

Figure 10.10 shows the local equilibrium pressures at selected locations within (a) the low-temperature material (LTMH) and (b) the high-temperature material (HTMH) as well as the gas pressure (P) as functions of time. The equilibrium pressure evolution at each location qualitatively resembles the temperature evolution, since the two quantities are linked via the van't Hoff equation.

Figure 10.11 shows the amount of hydrogen absorbed in the low-temperature metal hydride (LTMH), the high-temperature metal hydride (HTMH), and the gas as functions of time. The corresponding state of charge (SOC) of the metal hydride (MH) is also displayed in the right axis of Fig. 10.11. The thermal energy release step (i.e., hydrogenation of the high-temperature hydride) nearly saturates the high temperature material and almost completely depletes the hydrogen content of the low-temperature hydride, while the thermal energy storage step (i.e., low-temperature hydride charging step) reaches approximately 80% of the high-temperature material capacity and lowers the low-temperature hydride content to approximately 16% of capacity. Overall, about 77% of the system capacity was cycled resulting in a balanced system that yielded consistent and steady-state cycling behavior after the first cycles.

10.6 Outlook and Summary

A comprehensive techno-economic analysis of candidate high-temperature metal hydride materials used to store solar thermal energy was carried out. Results obtained for the high-temperature hydrides demonstrated that many high-temperature materials can achieve costs on the order of 10–13 \$/kWhth. When paired with suitable low-temperature materials, the overall thermal energy storage system reaches costs on the order of 25–30 \$/kWhth [9] thus meeting and possibly exceeding molten salt-based thermal energy storage costs, on the range of 25–40 \$/kWhth [74]. The majority of the selected metal hydrides can also achieve high exergetic efficiencies on the order of 85–95%. Among the selected materials, a novel hydride (NaMgH₂F) was identified to be paired with a low-temperature Ti-based material (TiCr_{1.6}Mn_{0.2}) and integrated into a high-temperature steam power plant. A detailed transport phenomena model was developed to simulate the paired metal hydride system and assess its technical performance as a storage system. Results, obtained for a laboratory scale paired system, showed excellent behavior of the selected metal hydrides, with the ability to exchange almost 80% of the available hydrogen and achieve the required operating temperatures. Additional work is still required to identify suitable configurations and systems for commercial scale. The research and development should mainly focus on (1) material development and (2) heat transfer optimization. The selected material, as well as other new Ca-based metal hydrides, already demonstrated good behavior when paired with low-temperature metal hydrides. However, the material formulations require adjustments and optimization, in order to achieve long-term cycling stability at the

required operating conditions. The heat transfer and containment systems require enhancement and optimization (e.g., including finned tubes, expanded natural graphite) to reduce the thermal gradients currently shown in the modeling results.

Acknowledgments This material is based upon work supported by the Department of Energy, Office of Energy Efficiency and Renewable Energy (EERE), under Award Number DE-EE0007118. The authors wish to acknowledge Dr. L. Irwin, Mr. M. Lausten, PE, and Dr. A. Schultz, who were the US Department of Energy managers, for their useful discussions and direction. The authors also wish to thank Drs. R. Zidan and A. d'Entremont (Savannah River National Laboratory, USA), Dr. T. Motyka (Greenway Energy, USA), Drs. C. Buckley and D. Sheppard (both Curtin University, Australia), and Mr. S. Sullivan (Brayton Energy, USA).

Disclaimer “This report was prepared as an account of work sponsored by an agency of the United States Government. Neither the United States Government nor any agency thereof, nor any of their employees, makes any warranty, express or implied, or assumes any legal liability or responsibility for the accuracy, completeness, or usefulness of any information, apparatus, product, or process disclosed, or represents that its use would not infringe privately owned rights. Reference herein to any specific commercial product, process, or service by trade name, trademark, manufacturer, or otherwise does not necessarily constitute or imply its endorsement, recommendation, or favoring by the United States Government or any agency thereof. The views and opinions of authors expressed herein do not necessarily state or reflect those of the United States Government or any agency thereof.”

References

1. <https://www.seia.org/initiatives/concentrating-solar-power>. Accessed Mar 2019
2. A. Gil, M. Medrano, I. Martorell, A. Lazaro, P. Dolado, B. Zalba, et al., State of the art on high-temperature thermal energy storage for power generation. Part 1 – concepts, materials, and modellization. *Renew. Sust. Energ. Rev.* **14**, 31–55 (2010)
3. J. Stekli, L. Irwin, R. Pitchumani, Technical challenges and opportunities for concentrating solar power with thermal energy storage. *J. Therm. Sci. Eng. Appl.* **5**, 021011-1-12 (2013)
4. S. Izquierdo, C. Montanes, C. Dopazo, N. Fueyo, Analysis of CSP plants for the definition of energy policies: the influence on electricity cost of solar multiples, capacity factors, and energy storage. *Energy Policy* **38**(10), 6215–6221 (2010)
5. P. Denholm, M. Hand, Grid flexibility and storage required to achieve very high penetration of variable renewable electricity. *Energy Policy* **39**(3), 1817–1830 (2011)
6. <https://www.energy.gov/eere/solar/sunshot-2030>. Accessed Mar 2019
7. R. Dominguez, L. Baringo, A. Conejo, An optimal strategy for a concentrating solar power plant. *Appl. Energy* **98**, 316–325 (2012)
8. S. Kuravi, J. Trahan, Y. Goswami, M.M. Rahman, E.K. Stefanakos, Thermal energy storage technologies and systems for concentrating solar power plants. *Prog. Energy Combust. Sci.* **39**(4), 285–319 (2013)
9. C. Corgnale, B. Hardy, T. Motyka, R. Zidan, J. Teprovich, B. Peters, Screening analysis of metal hydride based thermal energy storage systems for concentrating solar power plants. *Renew. Sust. Energ. Rev.* **38**, 821–833 (2014)
10. D.A. Sheppard, M. Paskevicius, T.D. Humphries, M. Felderhoff, G. Capurso, J. Bellosta von Colbe, et al., Metal hydrides for concentrating solar thermal power energy storage. *Appl. Phys. A* **122**, 395 (2016)
11. B. Bogdanovic, A. Ritter, B. Spliethoff, Active MgH₂-Mg systems for reversible chemical energy-storage. *Angew. Chem. Int. Ed. Engl.* **29**(3), 223–234 (1990)

12. L. Schlapbach, A. Züttel, Hydrogen-storage materials for mobile applications. *Nature* **414**, 353–358 (2002)
13. L. Schlapbach, Hydrogen-fuelled vehicles. *Nature* **460**, 809–811 (2009)
14. B. Sakintuna, F. Lamari-Darkrim, M. Hirscher, Metal hydride materials for solid hydrogen storage: a review. *Int. J. Hydrog. Energy* **32**(9), 1121–1140 (2007)
15. J. Bellosta von Colbe, J.R. Ares, J. Barale, M. Baricco, C. Buckley, G. Capurso, et al., Application of hydrides in hydrogen storage and compression: achievements, outlook, and perspectives. *Int. J. Hydrog. Energy* **44**(15), 7780–7808 (2019)
16. M.V. Lototskyy, V.A. Yartys, B.G. Pollet, R.C. Bowman, Metal hydride hydrogen compressors: a review. *Int. J. Hydrog. Energy* **39**(11), 5818–5851 (2014)
17. P.M. Golben, J.M. Rosso: Hydrogen compressor. US Patent US4402187A, published 1983
18. C. Corgnale, M. Sulic, Techno-economic analysis of high-pressure metal hydride compression systems. *Metals* **8**(6), 469 (2018)
19. X.Y. Chen, L.X. Wei, L. Deng, F.S. Yang, Z.X. Zhang, A review on the metal hydride based hydrogen purification and separation technology. *Appl. Mech. Mater.* **448**, 3027–3036 (2014)
20. P. Chen, Z. Xiong, J. Luo, J. Lin, K. Lee Tan, Interaction of hydrogen with metal nitrides and imides. *Nature* **420**, 302–304 (2002)
21. G.J. Grashoff, C.E. Pilkington, C.W. Corti, The purification of hydrogen. *Platin. Met. Rev.* **27**(4), 157–169 (1983)
22. N.C. Srivastava, I.W. Eames, A review of adsorbents and adsorbates in solid–vapor adsorption heat pump systems. *Appl. Therm. Eng.* **18**(9–10), 707–714 (1998)
23. T. Nishizaki, M. Miyamoto, K. Miyamoto, K. Yoshida, K. Yamaji, Y. Nakata: Metal hydride heat pump system. US Patent US4523635A, published 1985
24. P. Mathukumar, M. Groll, Metal hydride based heating and cooling systems: a review. *Int. J. Hydrog. Energy* **35**(8), 3817–3831 (2010)
25. M. Mohan, M. Sharma, S.V. Kumar, E. Anil Kumar, A. Satheesh, P. Muthukumar, Performance analysis of metal hydride based simultaneous cooling and heat transformation system. *Int. J. Hydrog. Energy* **44**(21), 10906–10915 (2019)
26. C. Corgnale, T. Motyka, S. Greenway, J. Perez-Berrios, A. Nakano, I. Ito, Metal hydride bed system model for renewable source driven regenerative fuel cell. *J. Alloy Compd.* **580**(1), S406–S409 (2013)
27. J. Bloch, M.H. Mintz, Kinetics and mechanisms of metal hydride formation – a review. *J. Alloys Compd.* **253**, 529–541 (1997)
28. B.J. Hardy, D.L. Anton, Hierarchical methodology for modeling hydrogen storage systems. Part I: Scoping models. *Int. J. Hydrog. Energy* **34**, 2269–2277 (2009)
29. B.J. Hardy, D.L. Anton, Hierarchical methodology for modeling hydrogen storage systems. Part II: Detailed models. *Int. J. Hydrog. Energy* **34**, 2992–3004 (2009)
30. S. Wolf: Hydrogen sponge heat pump. 10th Intersociety Energy Conversion Engineering Conf. (IECEC), Paper 759196 (1975)
31. A.W. McClaine: Method and apparatus for heat transfer, using metal hydrides. US Patent 4,039,023 (1977)
32. K.J. Kim, K.T. Feldman Jr, G. Lloyd, A. Razani, Compressor-driven metal-hydride heat pumps. *Appl. Therm. Eng.* **17**(6), 551–560 (1997)
33. Z. Ma, C. Turchi: Advanced supercritical carbon dioxide power cycle configurations for use in concentrating solar power systems. Conference Paper NREL/CP-5500-50787 March 2011
34. J.N. Phillips: Supercritical CO₂ Brayton power cycles, in *5th International Supercritical CO₂ Power Cycles Symposium* March 30, 2016
35. A. Rimpel, N. Smith, J. Wilkes, H. Delgado, T. Allison, R.A. Bidkar, et al. Test rig design for large supercritical CO₂ turbine seals, in *The 6th International Supercritical CO₂ Power Cycles Symposium* March 27–29, 2018, Pittsburgh, Pennsylvania
36. R.T. Caldwell, J.W. McDonald, A. Pietsch, Solar-energy receiver with lithium-hydride heat storage. *Sol. Energy* **9**, 48–60 (1965)

37. R.J. Hanold, R.D. Johnston: Power plant heat storage arrangement. US Patent US3029596 (1962)
38. B. Bogdanovic, T.H. Hartwig, B. Spliethoff, The development, testing, and optimization of energy-storage materials based on the MgH₂-Mg system. *Int. J. Hydrog. Energy* **18**(7), 575–589 (1993)
39. B. Bogdanovic, H. Hofmann, A. Neuy, A. Reiser, K. Schlichte, Ni-doped versus undoped Mg–MgH₂ materials for high-temperature heat or hydrogen storage. *J. Alloys Compd.* **292**, 57–71 (1999)
40. M. Felderhoff, B. Bogdanović, High-temperature metal hydrides as heat storage materials for solar and related applications. *Int. J. Mol. Sci.* **10**, 325–344 (2009)
41. B. Bogdanović, A. Ritter, B. Spliethoff, K. Straßburger, A process steam generator based on the high-temperature magnesium hydride/magnesium heat storage system. *Int. J. Hydrog. Energy* **20**, 811–822 (1995)
42. M. Wierse, R. Werner, Magnesium hydride for thermal energy storage in a small-scale solar-thermal power station. *J. Less Common Met.* **172–174**(3), 1111–1121 (1991)
43. A. Reiser, B. Bogdanovic, K. Schlichte, The application of Mg-based metal-hydrides as heat energy storage systems. *Int. J. Hydrog. Energy* **25**, 425–430 (2000)
44. D. Sheppard, M. Paskevicius, C. Buckley, Thermodynamics of hydrogen desorption from NaMgH₃ and its application as a solar heat storage medium. *Chem. Mater.* **23**, 4298–4300 (2011)
45. B. Bogdanović, A. Reiser, K. Schlichte, B. Spliethoff, B. Tesche, Thermodynamics and dynamics of the Mg-Fe H system and its potential for thermochemical thermal energy storage. *J. Alloys Comp.* **345**, 77–89 (2002)
46. D. Sheppard, C. Corgnale, B. Hardy, T. Motyka, R. Zidan, M. Paskevicius, et al., Hydriding characteristics of NaMgH₂F with preliminary technical and cost evaluation of magnesium-based metal hydride materials for concentrating solar power thermal storage. *RSC Adv.* **4**, 26552–26562 (2014)
47. P. Ward, C. Corgnale, J. Teprovich, T. Motyka, B. Hardy, B. Peters, et al., High-performance metal hydride based thermal energy storage systems for concentrating solar power applications. *J. Alloys Compd.* **645**(1), S374–S378 (2015)
48. C. Corgnale, B. Hardy, T. Motyka, R. Zidan, Metal hydride based thermal energy storage system requirements for high performance concentrating solar power plants. *Int. J. Hydrog. Energy* **41**(44), 20217–20230 (2016)
49. T.D. Humphries, D.A. Sheppard, M.R. Rowles, M.V. Sofianos, C.E. Buckley, Fluoride substitution in sodium hydride for thermal energy storage applications. *J. Mater. Chem. A* **4**, 12170–12178 (2016)
50. D. Harries, A novel thermochemical energy storage technology, in *Proceedings of EcoGeneration Conf.* Sydney, Australia (2010)
51. P.A. Ward, J.A. Teprovich, Y. Liu, J. He, R. Zidan, High-temperature thermal energy storage in the CaAl₂ system. *J. Alloys Compd.* **735**, 2611–2615 (2018)
52. I. Yonezu, K. Nasako, N. Honda, T. Sakai, Development of thermal energy storage technology using metal hydrides. *J. Less Common Met.* **89**(2), 351–358 (1983)
53. S. Chumphongphan, M. Paskevicius, D. Sheppard, C. Buckley, Effect of Al and Mo substitution on the structural and hydrogen storage properties of CaNi₅. *Int. J. Hydrog. Energy* **38**, 2325–2331 (2013)
54. G.G. Libowitz: Thermal energy storage systems employing metal hydrides. US Patent: US4040410 (1977)
55. G. Libowitz, Z. Blank, Solid metal hydrides: properties relating to their application in solar heating and cooling, in *Solid State Chemistry of Energy Conversion and Storage*, ed. by J. B. Goodenough, M. S. Whittingham, (ACS, Washington, DC, 1976), pp. 271–283
56. D. Harries, M. Paskevicius, D. Sheppard, T. Price, C. Buckley, Concentrating solar thermal heat storage using metal hydrides. *Proc. IEEE* **100**, 539–549 (2012)

57. B. Bogdanovic, M. Schwickardi, Ti-doped alkali metal aluminum hydrides as potential novel reversible hydrogen storage materials. *J. Alloys Compd.* **253–254**, 1–9 (1997)
58. T. Motyka: Savannah River National Laboratory Regenerative Fuel Cell Project. SRNL-STI-2008-00388, Nov. 11, 2008 (2008)
59. K.M. Guthrie, Data and techniques for preliminary capital cost estimating. *Chem. Eng. Prog.* **76** (6), 114–142 (1969)
60. E. Douglas, *Industrial Chemical Process Design* (McGraw-Hill Professional Engineering, New York (USA) 2003)
61. <https://www.aspentech.com/en/products/pages/aspentech-in-plant-cost-estimator>. Accessed Mar 2019
62. A. Chaise, P. De Rango, P. Marty, D. Fruchart, Experimental and numerical study of a magnesium hydride tank. *Int. J. Hydrog. Energy* **35**, 6311–6322 (2010)
63. <https://agmetalmminer.com/metal-prices/>. Accessed Mar 2019
64. P. Di Pietro, E. Skolnik: Analysis of the sodium hydride-based hydrogen storage system, in *Proceedings of the 2000 Hydrogen Program NREL/CP-570-28890*, Washington DC (USA), (2000)
65. W. Mueller, J. Blackledge, G. Libowitz, *Metal Hydrides* (Academic, New York/London, 1968)
66. C. Corgnale, B.J. Hardy, D.A. Tamburello, S.L. Garrison, D.L. Anton, Acceptability envelopes for metal hydride-based hydrogen storage systems. *Int. J. Hydrog. Energy* **37**, 2812–2824 (2012)
67. J.M. Pasini, C. Corgnale, B. van Hassel, T. Motyka, S. Kumar, K. Simmons, Metal hydride material requirements for automotive hydrogen storage systems. *Int. J. Hydrog. Energy* **38**(23), 9755–9765 (2013)
68. C. Corgnale, W. Summers, Solar hydrogen production by the hybrid sulfur process. *Int. J. Hydrog. Energy* **36**(18), 11604–11619 (2011)
69. A. d’Entremont, C. Corgnale, B. Hardy, R. Zidan, Simulation of high-temperature thermal energy storage system based on coupled metal hydrides for solar driven steam power plants. *Int. J. Hydrog. Energy* **43**(2), 817–830 (2018)
70. F. Czesla, J. Bewerunge, A. Senzel: Lunen – state of the art Ultra Supercritical Steam Power Plant under construction. POWER-GEN Europe 2009, Cologne, Germany (2009). Available online at <https://www.energy.siemens.com/nl/pool/hq/power-generation/power-plants/steam>. Accessed Jan 2019
71. Website: <http://webbook.nist.gov/chemistry/fluid/>. Accessed Nov 2016
72. T. Gamo, Y. Moriwaki, N. Yanagihara, T. Yamashita, T. Iwaki, Formation and properties of titanium-manganese alloy hydrides. *Int. J. Hydrog. Energy* **19**(1), 39–47 (1985)
73. T.A. Zotov, R.B. Sivov, E.A. Movlaev, S.V. Mitrokhin, V.N. Verbetsky, IMC hydrides with high hydrogen dissociation pressure. *J. Alloys Compd.* **509S**, 839S–843S (2011)
74. G. Kolb, C. Ho, T. Mancini, J. Gary: Power tower technology roadmap and cost reduction plan. Sandia Report SAND2011-2419, April 2011 (2011)



Advanced Coupling of Energy Storage and Photovoltaics

11

Ashim Gurung, Ke Chen, and Qiquan Qiao

Contents

11.1	Introduction	318
11.2	Conventional Versus Integrated Coupling of Photovoltaics and Energy Storage	319
11.3	Integration of Supercapacitors with Photovoltaics	319
11.3.1	Photo-Charging Supercapacitors Using Integrated Silicon Photovoltaics	320
11.3.2	Photo-Charging Supercapacitors Using Integrated Dye-Sensitized Photovoltaics	321
11.3.3	Photo-Charging Supercapacitors Using Organic Photovoltaics	325
11.3.4	Photo-Charging Supercapacitors Using Integrated Perovskite Photovoltaics	326
11.4	Integration of Batteries with Photovoltaics	327
11.4.1	Photo-Charging Batteries Using Integrated Silicon Photovoltaics	328
11.4.2	Photo-Charging Batteries Using Integrated Dye-Sensitized Photovoltaics	331
11.4.3	Photo-Charging Batteries Using Perovskite Photovoltaics	334
11.4.4	Other Advanced Integrated Battery-Photovoltaic Designs	334
11.5	Key Challenges, Opportunities, and Outlook	336
11.5.1	Material and Device Compatibility	336
11.5.2	Capacity, Energy, and Power Densities	338

Author Contributions

A. Gurung wrote the section on batteries, K. Chen on supercapacitors and Q. Qiao reviewed and edited the submitted draft as well as research from his own research group.

Ashim Gurung and Ke Chen contributed equally with all other contributors.

A. Gurung · K. Chen · Q. Qiao (✉)

Center for Advanced Photovoltaics, Department of Electrical Engineering and Computer Sciences, South Dakota State University, Brookings, SD, USA

e-mail: qiquan.qiao@sdstate.edu

11.5.3	Device Efficiency	340
11.5.4	Material and Device Stability	342
11.5.5	System Scalability and Cost-Effectiveness	343
References	344

Abstract

As the demand of energy has skyrocketed, there is an urgent need for development of energy self-sufficient power systems. Devices for energy generation such as solar/photovoltaic and energy storage such as supercapacitors and batteries are key technologies suitable for meeting the growing energy demand. This chapter introduces the integration of photovoltaic and electrochemical storage processes into one device to build miniaturized and energy self-sufficient power pack. The notable advances in this integration concept based on silicon, dye-sensitized, and perovskite such as photovoltaic technologies with supercapacitors and batteries such as energy storage technologies are presented and discussed along with the challenges and future directions of the technology.

11.1 Introduction

Energy is the key, driving our everyday activities. Consumer smart electronics, electric vehicles, and renewable electric grids are three major thriving energy technologies. Consumer smart electronics are driven by energy storage devices, mostly batteries which are energy-limited [1]. This demands the frequent recharging of smart electronics. The conventional way of recharging is by a wired connection to electric plug-ins which is inconvenient. Use of solar or photovoltaics to accomplish this recharging can be an efficient approach.

Electric vehicles have attracted much attention as a potential key contributor towards achieving sustainable clean energy. However, they are being charged using electric grids which are being powered by fossil-fuel generation. Furthermore, the large-scale development of electric vehicles is also restrained by a number of charging stations [2]. These issues can be addressed by using photovoltaics distributed generation for charging the electric vehicles.

Electric grids are being revived by the integration of renewable electricity generation. Among the renewables, photovoltaic is being recognized to be the most promising as cost continues to decline. Major investments in solar module manufacturing leading to an oversupply of modules and competitive procurement via auctions for utility-based photovoltaics are the major reasons [3]. Photovoltaic is intermittent in nature due to the coupling of output power with the availability of sunlight. The fluctuations in output power due to its intermittency leads to an unreliable power supply that is a huge concern for electric grid stability. This demands the use of energy storage in conjunction with photovoltaics [4]. The energy storage has the capability to store excess energy and release the stored energy when needed. Energy storage can facilitate peak power saving and meet the designated ramp rates of photovoltaic integration into the electric grid [5].

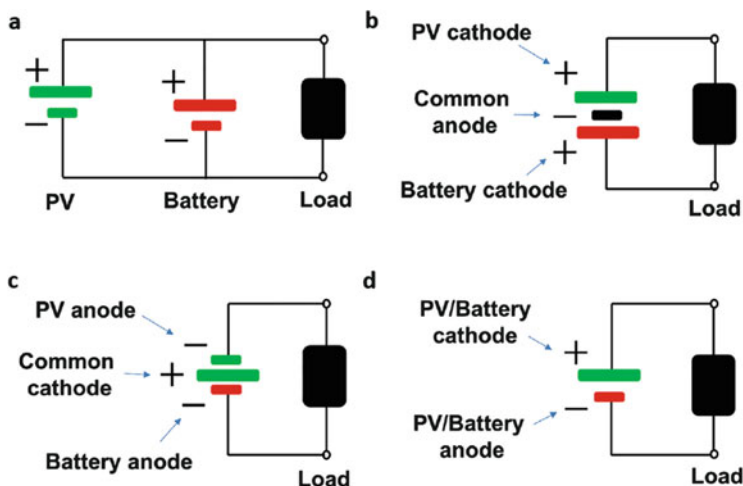


Fig. 11.1 Circuit schematic showing coupling of photovoltaics and energy storage systems (e.g., Batteries). (a) Conventional discrete system. (b–d) Integrated system: (b) three-electrode system with a common anode, (c) three-electrode system with a common cathode, (d) two-electrode system. (Figures (a–d) adapted with permission from Ref. [6], Cell Press)

11.2 Conventional Versus Integrated Coupling of Photovoltaics and Energy Storage

The conventional practice of coupling of photovoltaics and energy storage is the connection of separate photovoltaic modules and energy storage using long electric wires (Fig. 11.1a). This approach is inflexible, expensive, undergoes electric losses, and possesses a large areal footprint. An advanced approach would be to combine the two systems into one and develop an integrated design. This integrated device would be compact, efficient, and accomplish lesser packaging requirements and small footprint. This integrated design can potentially be an inexpensive alternative to the current designs.

The integration of the solar cell and energy storage can be achieved with two types of systems: (1) three-electrode system sharing a common electrode either anode (Fig. 11.1b) or cathode (Fig. 11.1c) and (2) two-electrode system where the same electrode performs as photoelectrode and battery electrode (Fig. 11.1d). Among these configurations, the two-electrode system is the most representative of the integration approach and is the most challenging.

11.3 Integration of Supercapacitors with Photovoltaics

Supercapacitors have advantages of fast charge/discharge capability resulting in high power density and exceptional cycling stability [7]. It typically consists of two electrodes which are electronically separated by a separator and impregnated in the electrolyte. On the basis of charge storage mechanisms, supercapacitors can be

categorized into two types: electrochemical double layer capacitor (EDLC) and pseudocapacitor. EDLCs store charges by reversible ion adsorption at the electrode-electrolyte interface physically, while pseudocapacitor store charges through a chemical redox reaction at the vicinity of the electrode surface. The most common material for EDLCs is activated carbon, while pseudocapacitors usually use metal oxides or conductive polymers as electrode [8].

11.3.1 Photo-Charging Supercapacitors Using Integrated Silicon Photovoltaics

A capacitive energy storage device can be built by transferring the unused part of silicon (Si) in Si solar cell. Based on this concept, a Si solar supercapacitor was reported by Westover et al. [9] Fig. 11.2a shows the Si solar supercapacitor fabrication schematic. After removing the Al back contact of a commercial polycrystalline Si solar cell panel, the backside of Si solar cell was etched to be porous to assemble a

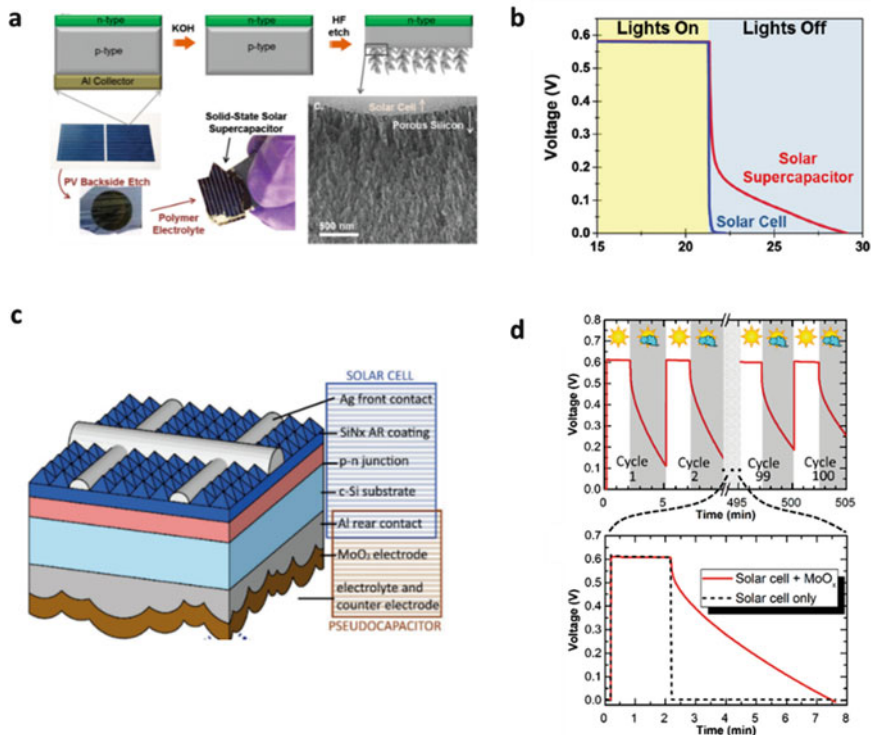


Fig. 11.2 Photo-charging supercapacitors using integrated silicon photovoltaics. (a–b) All Si Solar supercapacitor: (a) fabrication schematic (b) photo-charging/discharging curves. (c–d) Si solar supercapacitor with anodic MoO_x electrode: (c) cell structure, (d) photo-charging/discharging curves. (Figures (a–d) adapted with permission from Ref. [9], American Institute of Physics (a–b); Ref. [10], Wiley (c–d))

silicon supercapacitor. When the light is off, the energy stored in Si supercapacitor can be released, and it also demonstrated that a constant current load can be maintained even with intermittent illumination (Fig. 11.2b). Another work was reported with the integration of a molybdenum trioxide (MoO_3)-based pseudocapacitor deposited onto the Al rear contact of the Si solar cell [10]. This led to minimization in a performance loss of the silicon solar cell (Fig. 11.2c). Light-induced anodization method was used to deposit the amorphous MoO_3 . The solar supercapacitor could maintain its capacitance of 34 mF cm^{-2} after 100 cycles (Fig. 11.2d). A laser scribed porous reduced graphene oxide has also been integrated with a c-Si solar cell with a demonstration of long self-discharge time up to 10 days [11].

11.3.2 Photo-Charging Supercapacitors Using Integrated Dye-Sensitized Photovoltaics

Integrated dye-sensitized solar cell (DSSC)/supercapacitor with a two-electrode design was first reported by Miyasaka et al. [12] which consisted of dye-coated titania (TiO_2) layer, a hole-trapping layer, and two activated carbon layers separated by a porous separator (Fig. 11.3a). This integrated device only showed a charging voltage of 0.5 V and a capacitance of 0.69 F cm^{-2} . This design was constrained by high internal resistance. The same group later developed a three-electrode design where an activated carbon layer coated on one side of the platinum plate was used as the third electrode (Fig. 11.3b) [13]. During photo-charging, the generated electrons and holes were stored separately on the two carbon electrodes as a double layer capacitor. Compared to the previous two-electrode configuration, this design facilitates efficient electrons and holes transfer during the charge and discharge processes. This design led to a higher charging voltage of 0.8 V and five times the higher energy density of $47 \text{ } \mu\text{Wh cm}^{-2}$ compared to the two-electrode design (Fig. 11.3c).

One of the most common materials used as an internal electrode in a three-electrode integrated DSSC/supercapacitor is carbon owing to its compatibility for both the systems. Other materials such as conductive polymer [14, 15], titanium nitride/titanium (TiN/Ti) mesh [16], metal oxide [17], TiO_2 nanotube arrays [18], and silicon (Si) wafer [19] have also been explored. Figure 11.3d, e show the structure and energy level diagram of a three-electrode integration structure based on Si as the internal electrode, respectively. This device was built on a double side etched Si wafer, which served as a counter electrode for DSSC while functioning as an electrode for supercapacitor. The overall efficiency of 2.1% was achieved for this integrated design (Fig. 11.3f) [19].

Wire-type integrated DSSC/supercapacitors have been developed by researchers with various kinds of structures. These “energy wires” usually have a common wire electrode with another wire or sheet electrode then either twisted or coaxially wrapped [20–22]. The first “energy wire” was proposed by Bae et al. [23]. It included a mechanical energy harvesting part, a DSSC solar energy part and a supercapacitor part, which were all built on a single $\sim 200 \text{ } \mu\text{m}$ diameter polymethyl methacrylate (PMMA) fiber (Fig. 11.4a). Figure 11.4b, c show the performance of

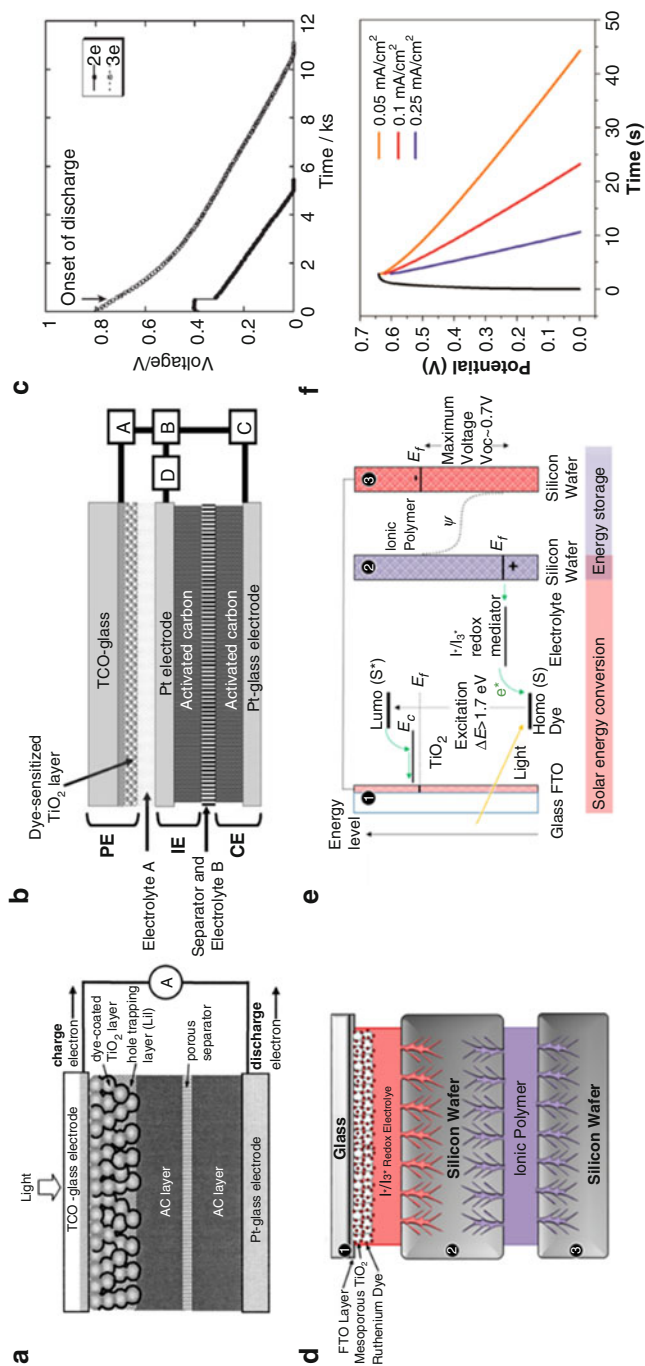


Fig. 11.3 Planar-type integrated dye-sensitized photovoltaics/supercapacitor. (a) Solar supercapacitor based on a two-electrode design. (b–c) Solar supercapacitor based on a three-electrode design. (b) device structure, (c) Comparison of discharge curves between two-electrode and three-electrode solar supercapacitors. (d–f) Three-electrode solar supercapacitor with Si water as an internal electrode: (d) device structure, (e) energy band diagram, (f) photocharge/galvanostatic discharge curves at different discharge currents. (Figures (a–f) adapted with permission from Ref. [12], American Institute of Physics (a); Ref. [13], Royal Society of Chemistry (b–c); Ref. [19], American Chemical Society (d–f))

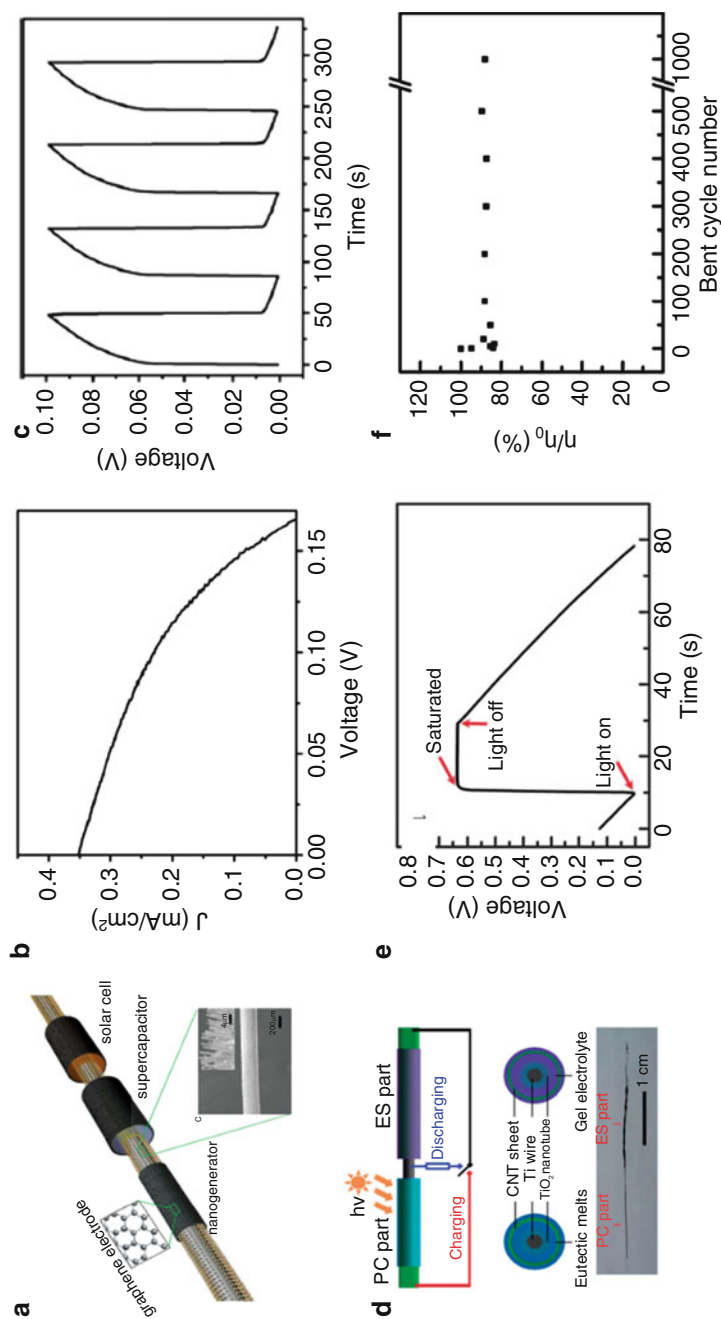


Fig. 11.4 Wire-type integrated dye-sensitized solar photovoltaics/supercapacitor. (a–c) Wire-type multi-energy device comprising of a nanogenerator, a DSSC, and a supercapacitor: (a) device structure, (b) J-V curve of the DSSC, (c) Charge/discharge voltage profiles of the supercapacitor. (d–f) Wire-type solar supercapacitor with coaxial structure: (d) device structure, (e) photo-charge/galvanostatic-discharge curves, (f) bending stability test of the integrated wire. (Figures (a–f) adapted with permission from Ref. [23], Wiley (a–c); Ref. [21], Royal Society of Chemistry (d–f))

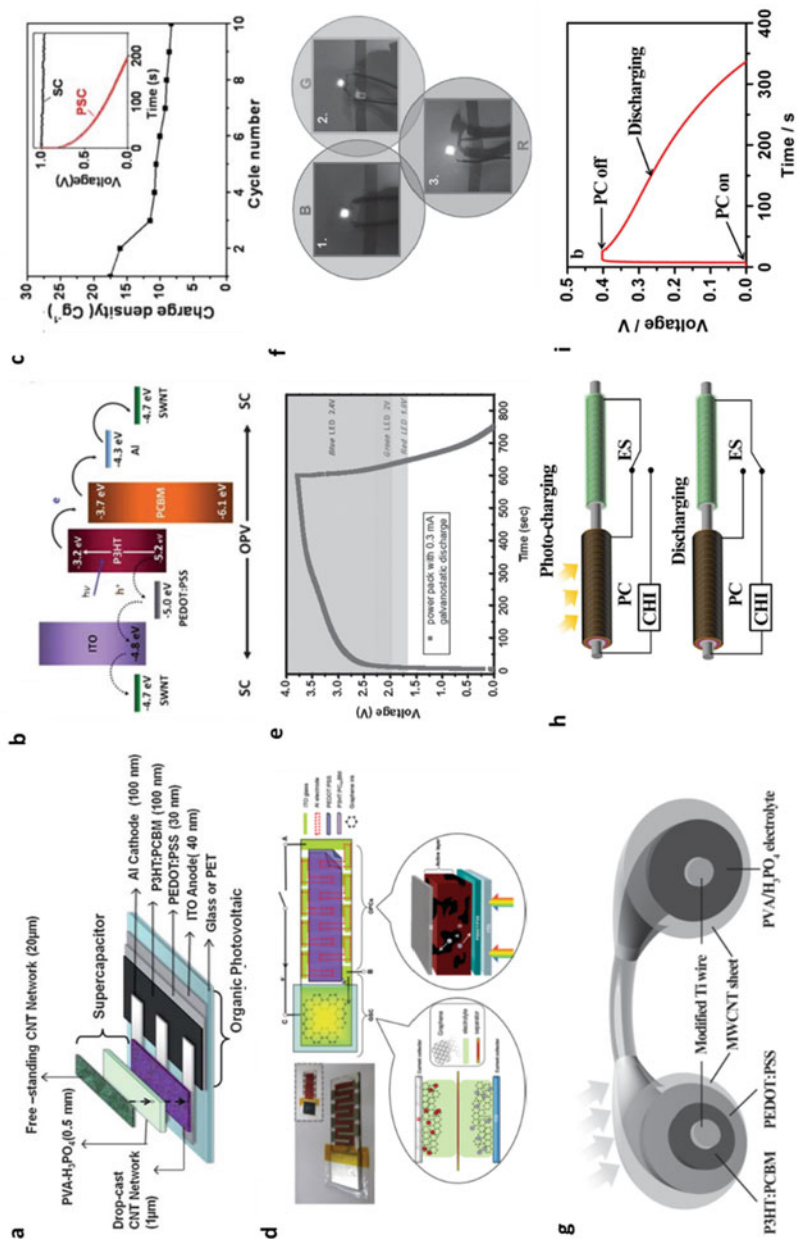


Fig. 11.5 (continued)

the DSSC and the photo-charge supercapacitor. However, this device only showed a photoconversion efficiency of 0.02%. Figure 11.4d shows a coaxial “energy wire” which comprises a photoconversion (PC) part and an energy storage (ES) part [21]. The wire-type integrated device shared a Ti wire as the common electrode. The PC part had N719 dye attached TiO₂ nanowires as photoanode, the carbon nanotubes (CNT) sheet as photocathode and gel electrolytes. For the ES part, the supercapacitor was constructed using another CNT sheet as the counter electrode. During the “energy-wire” operation, charges generated from the PC part under illumination could be transferred through the external circuit and common electrode and stored in the ES part by switching to the red wire. While discharging by turning the switch to the blue wire, the stored energy could be used to power external loads. Furthermore, this “energy-wise” was flexible and the overall efficiency could be maintained at 88.2% after 1000 bending cycles with an initial overall efficiency of 2.73% (Fig. 11.4e, f).

11.3.3 Photo-Charging Supercapacitors Using Organic Photovoltaics

A printable solar supercapacitor with the integration of an organic solar cell and supercapacitor was reported by Wee et al. [24] (Fig. 11.5a–c). Single-walled carbon nanotubes (CNTs) network was used as an electrode of the supercapacitor and bridge connection to reduce the internal resistance. By comparing the voltage drop in the integrated cell and wire-connected cell, the internal resistance was found to reduce from 200 to 115 Ω . Under illumination of 100 mWcm⁻² for 70 s, the solar supercapacitor yielded a specific capacitance of 28 Fg⁻¹ when discharged in dark and a capacitance of 79.8 F g⁻¹ by using tandem polymer solar cell. To obtain a higher output voltage of the solar capacitor, Chien et al. [25] explored another option by serially connecting eight organic solar cells (Fig. 11.5d). A high system voltage of 4 V was reached, which is suitable to drive red, green, and blue light emitting diodes (LEDs) (Fig. 11.5e–f). However, these two designs are limited with the planar flat structure that increases the device area, making it difficult to fit into more compact and small area portable devices.

A foldable solar supercapacitor was designed by employing laminated freestanding poly(3,4-ethylenedioxythiophene): polystyrene sulfonate (PEDOT: PSS) as the common electrode for both organic solar cell and supercapacitor [26]. This inte-



Fig. 11.5 Photo-charging supercapacitors using integrated organic photovoltaics. (a–c) Organic solar cell integrated with CNT supercapacitor: (a) device structure, (b) energy band diagram, (c) cycling stability. (d–f) Eight series-connected organic solar cells integrated with graphene supercapacitor: (d) device structure, (e) photo-charge/discharge voltage curve, (f) integrated cell powering red, green, and blue LEDs. (g–i) Integrated organic solar cell/supercapacitor “energy wire”: (g) device structure, (h) working schematic, (i) photo-charge/discharge voltage curve. (Figures (a–i) adapted with permission from Ref. [24], Royal Society of Chemistry (a–c); Ref. [25], Wiley (d–f); Ref. [27], Wiley (g–i))

grated solar supercapacitor achieved an overall efficiency of 2% without performance decay for 100 photo-charge/galvanostatic cycles. Peng's group developed a flexible "energy fiber" integrated with photovoltaic conversion (PC) and energy storage (ES) (Fig. 11.5g–i). A TiO₂ modified Ti wire was used as a support electrode and the common electrode in the center along with organic solar cell and supercapacitor built coaxially on Ti wire consequently [27]. Notably, the overall efficiency only decreased by less than 10% after 1000 bending cycles. This design enabled a flexible fiber shape solar supercapacitor which has promising application in textiles.

11.3.4 Photo-Charging Supercapacitors Using Integrated Perovskite Photovoltaics

Perovskite solar cells (PSCs) are the emerging third generation photovoltaic technology that promises excellent photovoltaic performance while accomplishing low-cost manufacturability [28, 29]. Perovskite solar cells have already demonstrated power conversion efficiency of 25.2% at cell level which outperforms multi-crystalline silicon and other thin film technologies [30]. Therefore, PSCs can be an efficient source of photo charging supercapacitors. Xu et al. proposed the first solar supercapacitor which contained a MAPbI₃-based PSC and a polypyrrole-based supercapacitor [31]. The design consisted of a separation between the PSC and supercapacitor, thus was able to reach a high overall efficiency of 10%. A more compact stacked three-electrode structure of PSC and supercapacitor was later developed which used poly (3, 4-ethylenedioxythiophene) (PEDOT)-carbon electrode as a common electrode (Fig. 11.6a–c) [32]. The design demonstrated an overall efficiency of 4.7%. To solve the supercapacitor liquid electrolyte leakage issue, a solid-state supercapacitor was integrated with PSC [33]. The design used the intermediate carbon layer to serve as a counter electrode in PSC and cathode in supercapacitor with gel electrolyte and obtained an overall efficiency of 7.1%.

Intrinsic material and device instability of PSCs in response to humidity, ambient air, and continuous illumination is a critical concern for the implementation of PSC integrated solar supercapacitors [34]. One of the approaches used to address this stability issue is the use of inorganic perovskites. Taking the advantage of high tolerance of such inorganic PSC to the environment, an integrated design consisting of cesium lead(II) bromide (CsPbBr₃)-based inorganic PSC and inorganic silica-gel-electrolyte-based supercapacitor was reported (Fig. 11.6d–f) [35]. The integration was accomplished by using a nanocarbon layer as the common electrode. A power conversion efficiency of 6.1% along with a high open circuit voltage of 1.22 V was obtained for the CsPbBr₃-based inorganic PSC. This assisted the integrated device to achieve an overall efficiency of 5.1% that was maintained even after 1000 photo-charge/galvanostatic discharge cycles.

Sun et al. [36] developed a simple method to connect supercapacitors into different patterns with tunable capacitance by fusing and integrating with PSC (Fig. 11.6g–i). These fusible supercapacitors were fabricated using aligned carbon nanotubes (CNT)/self-healing polymer (SHP). The CNT sheet and ladder structure make the fusible energy devices available to be connected in series or parallel, and

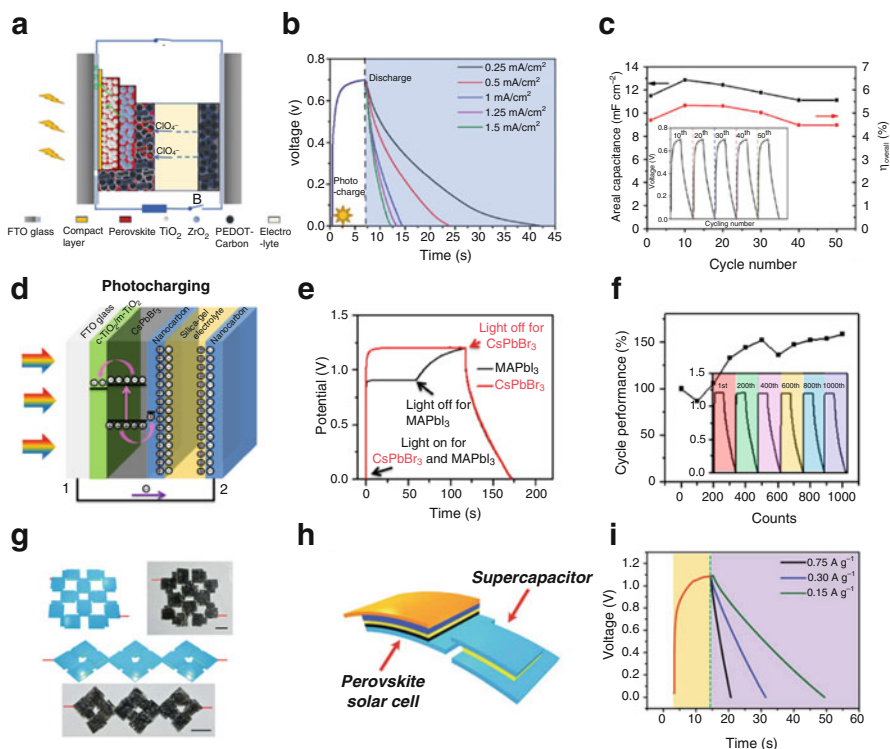


Fig. 11.6 Photo-charging supercapacitors using integrated perovskite photovoltaics. (a–c) Three-electrode integrated cell-based on MAPbI₃-based PSC and PEDOT-carbon supercapacitor: (a) device structure, (b) photo-charge/discharge voltage curves, (c) cycling stability. (d–f) Integrated CsPbBr₃ PSC/supercapacitor with gel electrolyte: (d) device working schematic of photo-charging, (e) photo-charge/discharge voltage curves comparing integrated MAPbI₃ PSC/supercapacitor and CsPbBr₃ PSC/supercapacitor, (f) cycling stability of CsPbBr₃ PSC/supercapacitor. (g–i) Fusible integrated PSC/supercapacitor: (g) schematic illustrations and photographs for 12 supercapacitors fused by different formats. (h) schematic showing a fusible PSC/supercapacitor, (i) photo-charge/discharge curves at different current densities. (Figures (a–i) adapted with permission from Ref. [32], Wiley (a–c); Ref. [35], Elsevier (d–f); Ref. [36], Royal Society of Chemistry (g–i))

the SHP layer fuses them into a patterned structure. In this way, supercapacitors can be connected in different patterns and integrated with PSC. The output voltage and capacitance can be controlled by varying the number of PSCs and supercapacitors, for example, 1.82 and 3.65 V of discharging voltage could be achieved when connecting 4 and 8 units, respectively.

11.4 Integration of Batteries with Photovoltaics

Batteries are electrochemical devices that have the capability to store much higher energy than supercapacitors. Lithium-ion, consisting of intercalation graphite as anode and lithium transition metal oxides [lithium cobalt oxide, (LiCoO₂), lithium

nickel manganese cobalt oxide (NMC), lithium nickel cobalt aluminum oxide, (NCA)] as a cathode, is the dominant battery technology in the consumer electronics industry. This commercial Li-ion chemistry provides an energy density up to 200–250 Whkg⁻¹. State-of-the-art intercalation cathodes have a low specific capacity (e.g., LiCoO₂ ~ 160 mAhg⁻¹). Advanced battery chemistries such as lithium-sulfur (Li-S) using sulfur cathode and lithium-oxygen (Li-O₂) using oxygen cathode have been investigated that can deliver a high theoretical energy density of 2500 Whkg⁻¹ and 3500 Whkg⁻¹ respectively. These chemistries can deliver much higher practical energy density > 600 Whkg⁻¹. While for large-scale energy applications such as electric grids, redox flow battery technology is suitable as it facilitates scalability to store a much larger amount of bulk energy scale energy [37]. A typical redox-flow battery consists of two compartments with electrolytes (catholyte and anolyte) as an energy storage medium separated by an ion-exchange membrane. The electrolytes are stored in external tanks circulated by pumps and the amount of energy can be controlled by the amount of electrolyte stored. The size of the electrolyte reservoir controls the energy and the size of the electrochemical cell or stack controls the power of the redox flow battery. An all-vanadium redox flow battery is a state-of-the-art and commercially available system.

11.4.1 Photo-Charging Batteries Using Integrated Silicon Photovoltaics

Monolithic integration of lithium-ion battery with crystalline silicon was demonstrated by Um et al. [38] (Fig. 11.7a–c). The integration consisted of 24 series-interconnected units of Si mini-solar cells with a bipolar solid-state lithium-ion battery fabricated on top of the aluminum (Al) metal contact of the photovoltaic module. The photovoltaic module was able to provide a power conversion efficiency of 15.8% with a 14.1 V output voltage. The bipolar solid-state lithium-ion battery was prepared by an ultraviolet curing-assisted printing process which helped to achieve a higher voltage and hence a higher battery energy storage capacity. The integrated power pack was able to demonstrate a high overall efficiency of 7.61% with a rapid photo-charging of fewer than 2 min. The group also demonstrated the charging of smartphones and motion picture experts group layer-3 (MP3) players using the integrated power pack, validating its practicality.

Use of silicon as photoelectrode has also been demonstrated for photo charging redox flow batteries. A solar rechargeable flow battery comprising of dual-silicon photoelectrodes with redox couple of quinone/bromine was reported by Liao et al. [39] (Fig. 11.7d–e). Narrow bandgap silicon helped to achieve efficient light harvesting. Platinum was used as cocatalyst on the surface of Si wafers to improve the semiconductor/redox-couple interfacial charge transfer kinetics. Furthermore, the redox couple that comprised of quinones and halogens facilitated fast reaction kinetics. These combinations led to the high overall efficiency of 3.2% with a discharge capacity of 730 mAhL⁻¹ and photo-charge voltage to

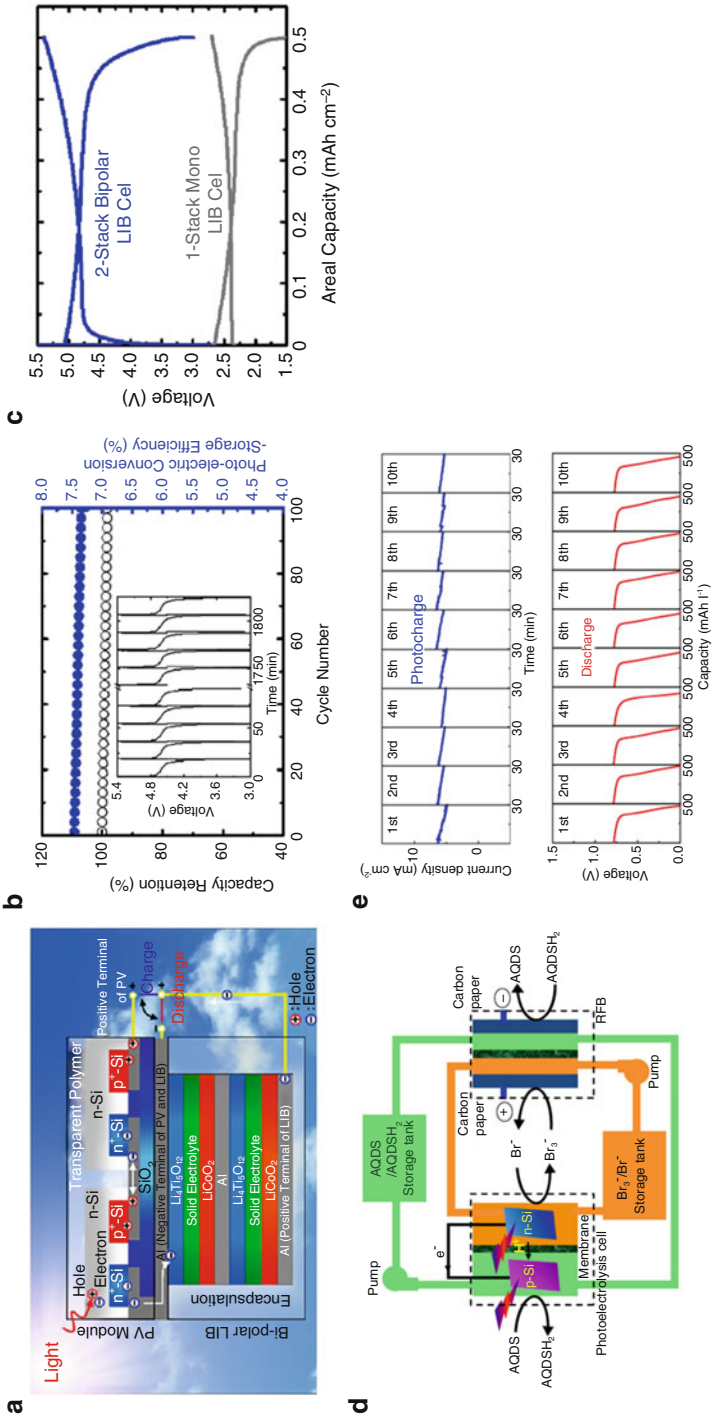


Fig. 11.7 Photo-charging batteries using integrated silicon photovoltaics. **(a–c)** Silicon solar cell-lithium ion battery integrated device: **(a)** device schematic, **(b)** photo-charging/discharging performance, **(c)** charge/discharge voltage curves of mono and bipolar configurations of lithium-ion battery. **(d–e)** Solar rechargeable redox flow battery: **(d)** device schematic, **(e)** photo-charge/discharge voltage profiles. (Figures **(a–e)** adapted with permission from Ref. [38], Royal Society of Chemistry **(a–c)**; Ref. [39], Springer Nature **(d–e)**)

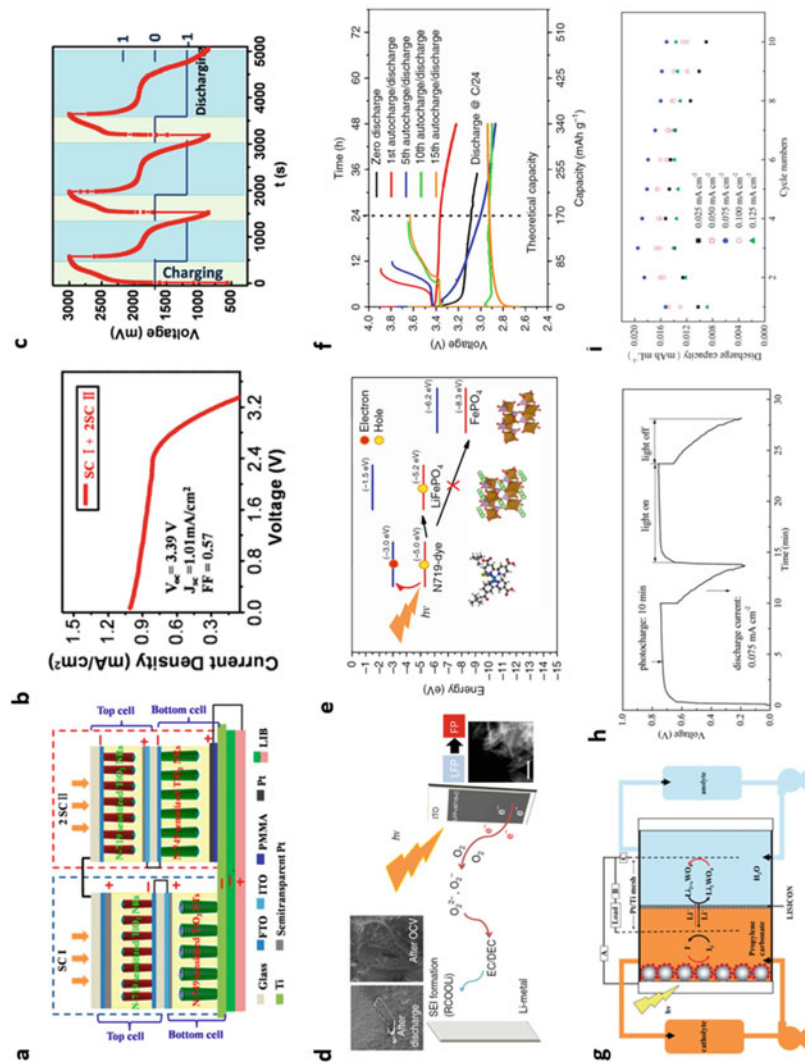


Fig. 11.8 (continued)

0.8 V. A tandem design incorporating silicon as photoanode and photocathode with a redox flow battery was demonstrated by Li et al. [40]. The redox flow battery composed of aqueous quinone-based all-organic redox couples based on 9,10-anthraquinone-2,7-disulfonic acid (AQDS) as catholyte/1,2-benzoquinone-3,5-disulfonic acid (BQDS) as anolyte quinone-based organic redox couple. The integrated system demonstrated an overall efficiency of 1.7% with a discharge capacity of 3500 mAhL^{-1} and photo-charge voltage to 0.41 V.

11.4.2 Photo-Charging Batteries Using Integrated Dye-Sensitized Photovoltaics

Integration of a lithium-ion battery with dye-sensitized photovoltaics was first reported by Wang et al. (Fig. 11.8a, c) [41]. The integration was based on the use of titanium nanotubes grown on the same titanium metal substrate. The solar part consisted of series connected three tandem DSSCs on top of the titanium metal. While the storage part consisted of a lithium-ion battery with titanium nanotubes anode and lithium cobalt oxide (LiCoO_2) cathode fabricated on the other side of the metal. During the photo charging process, photogenerated electrons from the TiO_2 /dye film causes lithiation in the TiO_2 nanotubes battery anode. The tandem DSSCs was able to produce V_{oc} of 3.39 V that helped to charge the lithium-ion battery from 0.55 to 2.996 V in 440 s. The integrated power pack exhibited an overall efficiency of 0.82% with a discharge capacity of 33.89 μAh .

A solar rechargeable lithium-ion battery based on dye-sensitized photoelectrode in a two-electrode configuration was reported by Paoletta et al. (Fig. 11.8d–f) [42]. The integrated device consisted of photocathode in the form of dye-coated lithium iron phosphate (LiFePO_4) nanocrystals and anode in the form of lithium metal rinsed in lithium hexafluorophosphate (LiPF_6)-based organic electrolyte. During photo-charging, the photo-generated holes facilitate photo-oxidation causing delithiation of LiFePO_4 into iron(III) phosphate (FePO_4). Meanwhile, the photo-generated electrons from reduced oxygen species. These reduced species in the form of peroxides and/or superoxides react with the carbonate-based electrolyte and form solid electrolyte interphase (SEI). A similar mechanism occurs in a typical Li-O_2 battery. The integrated device delivered an overall efficiency of 0.06–0.08% with a



Fig. 11.8 Photo-charging batteries using integrated dye-sensitized photovoltaics. (a–c) Three-electrode integration using series tandem solar cell and lithium-ion battery: (a) device configuration, (b) J–V curve of the series tandem solar cell, (c) photo-charge/discharge voltage profiles of the integrated device. (d–f) Two-electrode solar rechargeable battery using dye-sensitized LiFePO_4 photoelectrode against lithium metal: (d) device schematic, (e) energy level alignment and proposed a photoelectrochemical process, (f) photo-charge/discharge voltage profiles. (g–i) Integration of dye/ TiO_2 photoelectrode with redox flow battery: (g) device schematic, (h) photo-charge/discharge voltage curves, (i) cycling performance vs. current densities. (Figures (a–i) adapted with permission from Ref. [41], American Chemical Society (a–c); Ref. [42], Springer Nature (d–f); Ref. [44], Royal Society of Chemistry (g–i))

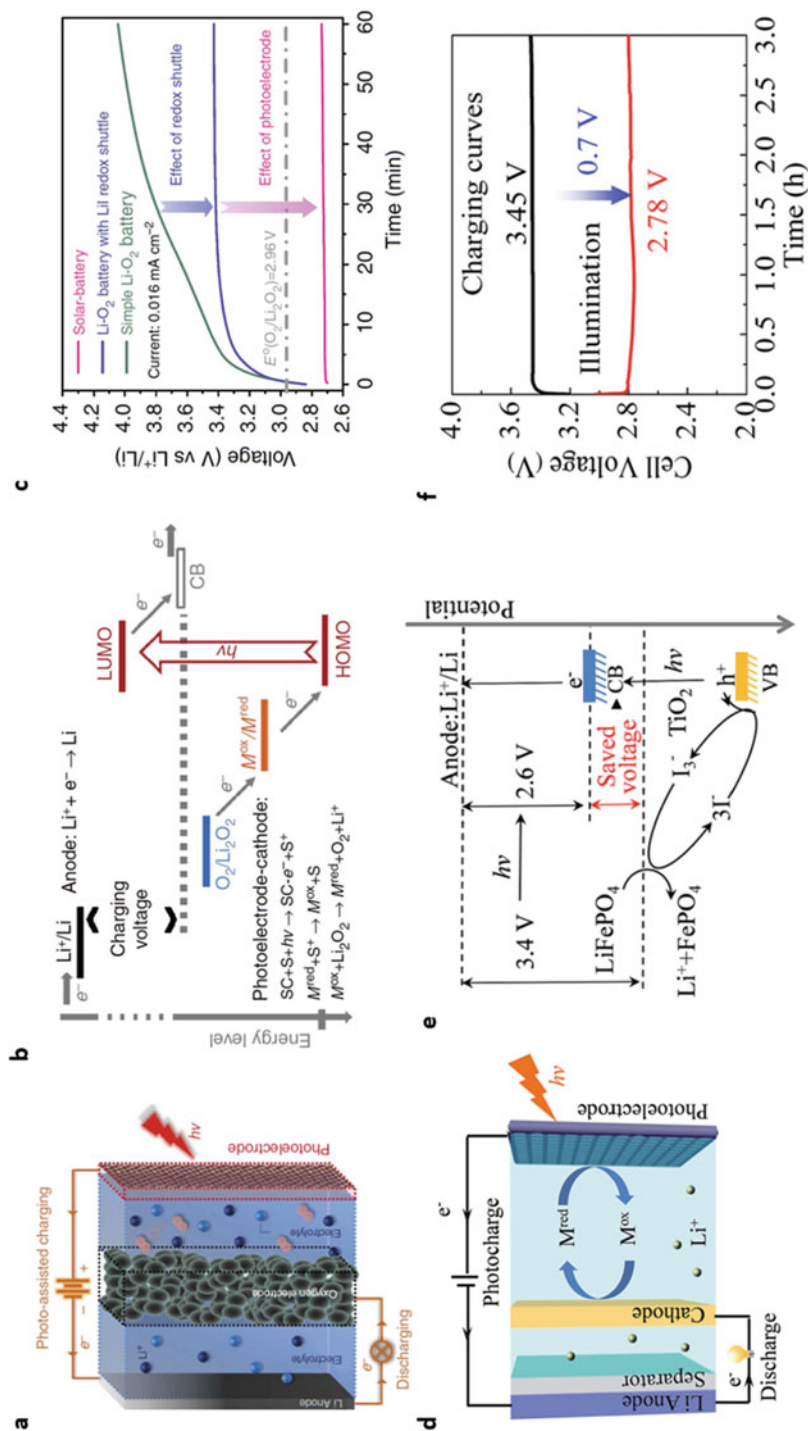


Fig. 11.9 (continued)

discharge capacity of 340 mA h g^{-1} . It was found that the photo-oxidation only occurred for colloidal LiFePO_4 nanocrystals with a large surface area of $24 \text{ m}^2 \text{ g}^{-1}$ but not for hydrothermally obtained microcrystals with $5 \text{ m}^2 \text{ g}^{-1}$ surface area. It should also be noted that the device would operate only in an oxygen environment.

Photo-charging of redox flow battery was demonstrated using a TiO_2 -based DSSC photoelectrode with two redox couples of tri-iodate/iodide (I_3^-/I^-) and decamethylferrocene (DMFc^+) cation/decamethylferrocene [$\text{DMFc}^+/\text{DMFc}$] in organic solvents [43]. The design involved two electrolyte circuit loops where the two redox couples enter the DSSC during charging and enter the redox flow battery during discharge. The photo sharing takes place by oxidation of I^- to I_3^- ions at the photoelectrode with simultaneous reduction of DMFc^+ to DMF at the platinum cathode side. However, the integrated device exhibited an overall efficiency of only 0.05% with DSSC power conversion efficiency of 0.15%. The low DSSC efficiency was attributed to the use of large device area and thick inorganic separator. Another study was reported demonstrating a combination of the aqueous electrolyte with monolithium tungsten oxide (LiWO_4) redox couple (anolyte) and an organic electrolyte with iodine redox couple (catholyte) coupled with a dye-sensitized photoelectrode (Fig. 11.8g–i) [44]. The photosharing leads to oxidation of I^- to I_3^- ions and dilithium tungsten oxide (Li_2WO_4) to $\text{Li}_{2+x}\text{WO}_4$, while the discharging involves the reduction to the original states of I^- and Li_2WO_4 . The TiO_2 /dye-based photoelectrodes do not exhibit high efficiency. Furthermore, stability becomes an issue as these iodine-based systems suffer from chemical deterioration due to a corrosive characteristic of iodine.

Several reports on using the photo-integration approach to partially assist the battery charging process have been claimed. Yu et al. employed this photo-assisted integration to charge a lithium-oxygen battery where a dye-sensitized photoelectrode was used against an oxygen electrode in a triiodide/iodide redox couple (Fig. 11.9a–c) [45]. During photo-charging, the triiodide ions are reduced at the photoelectrode, then diffuse to the oxygen electrode and oxidize lithium peroxides. This photo-assisted integration helped to reduce the high charging overpotential found in lithium-oxygen battery from 3.6 to 2.7 V. Similar photo-assisting approach to reducing the charging potential was demonstrated by Li et al. in a system consisting of lithium iron phosphate (LiFePO_4) cathode, lithium anode, and a TiO_2 photoelectrode coupled with iodide-based redox couple (Fig. 11.9d–f) [46]. Upon light exposure, the photogenerated holes oxidize the iodide ions forming triiodide ions that further oxidizes the LiFePO_4 into iron(III) phosphate (FePO_4), meanwhile, the photogenerated electrons reduce the Li^+ ions into Li metal. This photo-charging



Fig. 11.9 Photo-assisted charging batteries using integrated dye-sensitized photovoltaics. (a–c) Lithium-oxygen battery integrated with dye/ TiO_2 photoelectrode: (b) Device structure, (b) energy level diagram showing the proposed photoelectrochemical process, (c) charging voltage curves with and without photo-charging. (d–f) Photo-assisted charging of Li/ LiFePO_4 lithium-ion battery integrated with a TiO_2 photoelectrode: (d) device schematic, (e) energy level alignment and proposed a photoelectrochemical process, (f) photo-charging voltage profiles. (Figures (a–f) adapted with permission from Ref. [45], Springer Nature (a–c); Ref. [46], Royal Society of Chemistry (d–f))

scheme helps to reduce the battery's charging voltage to 2.78 V from 3.45 V, which is even lower than the 3.41 V discharge potential. Thus, it results in an energy saving of $\sim 20\%$ compared to traditional lithium-ion batteries. A photo-assisted design using similar charging mechanism was demonstrated with aqueous lithium iodide (Li-I) solar flow battery that involves the use of a dye-sensitized TiO_2 photoelectrode linking triiodide/iodide catholyte with a platinum (Pt) counter electrode [47]. The decrease in the charging voltage from 3.3 to 2.9 V was achieved which translated into a similar energy saving of $\sim 20\%$.

11.4.3 Photo-Charging Batteries Using Perovskite Photovoltaics

Perovskite solar cells (PSCs) can be an efficient photo-charging source to photo-charge batteries due to their excellent photovoltaic performance. Discrete systems where PSCs have been used to charge lithium-ion batteries have been demonstrated. Four PSCs connected in series were employed to charge a lithium iron phosphate \ lithium titanate ($\text{LiFePO}_4/\text{Li}_4\text{Ti}_5\text{O}_{12}$) lithium-ion battery (Fig. 11.10a, b) [2]. The PSCs produced an open circuit voltage of 3.84 V with a power conversion efficiency of 12.65%. The photosharing system demonstrated an overall efficiency of 7.36% at 0.5°C along with an energy storage efficiency of 60%. Our group also demonstrated a discrete design using a single PSC to charge a lithium cobalt oxide/lithium titanate ($\text{LiCoO}_2/\text{Li}_4\text{Ti}_5\text{O}_{12}$) lithium-ion battery (Fig. 11.10c, d) [48]. The higher voltage required to charge the battery was obtained by using a direct current-direct current (DC-DC) boost converter. The converter also facilitated maximum power point tracking of the power generated by the PSC. The overall efficiency of 9.36% was achieved along with the storage efficiency of 77.2% at 0.5°C .

Perovskite has been demonstrated as a bifunctional material that can simultaneously harvest energy and store it. Recently, a two-electrode solar rechargeable battery was demonstrated with a two-dimensional lead halide perovskite coupled with a lithium metal (Fig. 11.11a–c) [49]. During photo charging, the photo-generated holes are responsible for pushing the Li ions out of the perovskite towards the lithium metal. Meanwhile, the photogenerated electrons through the external circuit reduce the Li ions at the lithium metal. Capacity fading was observed for the solar rechargeable battery. Possible reasons include perovskite morphology deterioration after lithiation/delithiation cycle, the formation of an unstable solid electrolyte interphase (SEI) layer, and formation of poorly reversible lead (Pb).

11.4.4 Other Advanced Integrated Battery-Photovoltaic Designs

A solar rechargeable battery based on advanced lithium-based battery technology in the form of lithium-sulfide (Li-S) was reported using a platinum Pt-modified cadmium sulfide (CdS) as a photocatalyst (Fig. 11.12a) [50]. The photosharing was realized by oxidation of sulfur anion (S^{2-}) ions to polysulfide ions in aqueous solution with photogenerated holes from the photocatalyst. The Li-S battery delivered a specific capacity of 792 mAhg^{-1} after 2 h of photo-charging. However, most cathode materials in lithium-ion batteries are unable to be directly oxidized by photoexcited holes as they

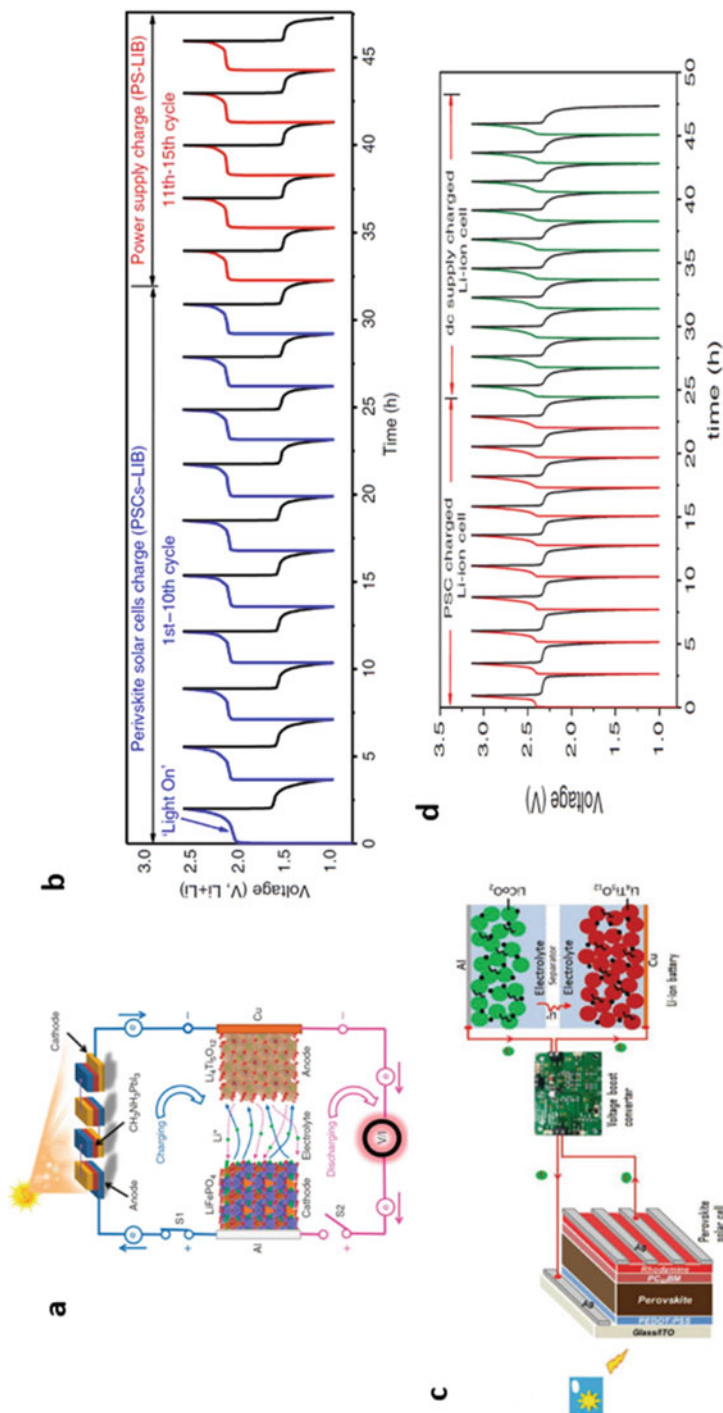


Fig. 11.10 Photo-charging batteries using discrete perovskite photovoltaics. (a–b) Four series-connected PSCs photo charging a LiFePO₄/Li₄Ti₅O₁₂ lithium-ion battery: (a) design schematic, (b) photo-charge/discharge voltage profiles. (c–d) Single PSC photo charging of LiCoO₂/Li₄Ti₅O₁₂ lithium-ion battery enabled by a DC-DC converter: (c) design schematic, (d) photo-charge/discharge voltage profiles. (Figures (a–d) adapted with permission from Ref. [2], Springer Nature (a–b); Ref. [48], Wiley (c–d))

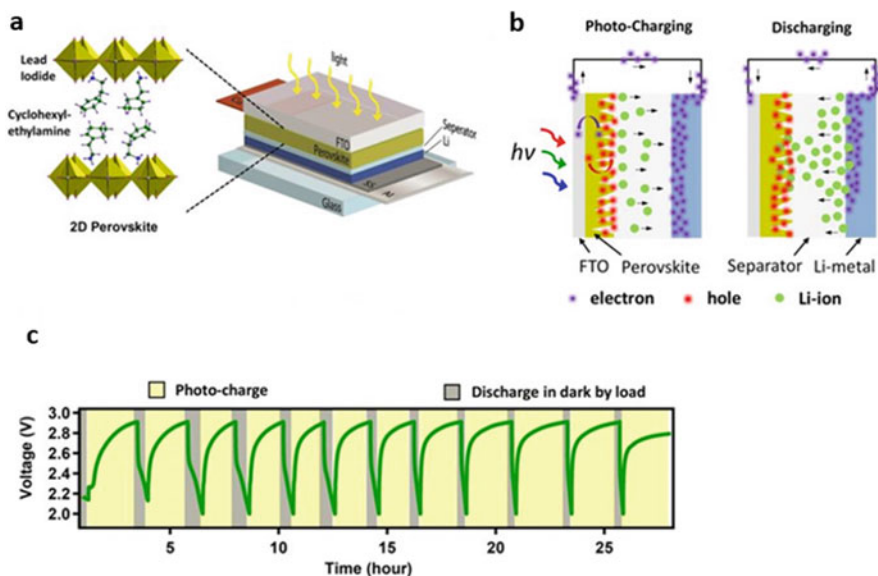


Fig. 11.11 Photo-charging batteries using integrated perovskite photovoltaics. (a–c) Two-electrode coupling of perovskites photoelectrode coupled with lithium: (a) device structure, (b) photo-charging and discharging schematics, (c) photo-charge/discharge curves. (Figures (a–c) adapted with permission from Ref. [49], American Chemical Society)

are insulating and insoluble in organic/aqueous electrolytes. Recently, a monolithic solar rechargeable device was demonstrated by using highly efficient and high-photovoltage tandem III–V solar cells and high-voltage of the redox couples 4-hydroxy-2,2,6,6-tetramethylpiperidin-1-oxyl (4-OH-TEMPO) and methyl viologen (MV) as the shuttle in the redox flow battery (Fig. 11.12b) [51]. A record overall power conversion and energy storage efficiency of 14.1% was observed for the design. One of the contributors to the high efficiency was the high-power conversion efficiency of the Indium gallium phosphide/gallium arsenide/germanium [InGaP/GaAs/Ge] tandem solar cell of 26.1%. The other contributor was the 4-OH-TEMPO/MV redox couple that enables the highest cell voltage (1.25 V) among the aqueous organic redox flow batteries. A maximum power point voltage mismatch was observed for the design which suggested the use of a redox couple with even higher cell voltage. These types of solar rechargeable systems can be employed in off-grid electrification at remote places.

11.5 Key Challenges, Opportunities, and Outlook

11.5.1 Material and Device Compatibility

Materials compatibility is a key component for integration of photogeneration and storage components. Stable photoelectrode should be designed especially in a two-electrode integrated system where the photoelectrode is in physical contact

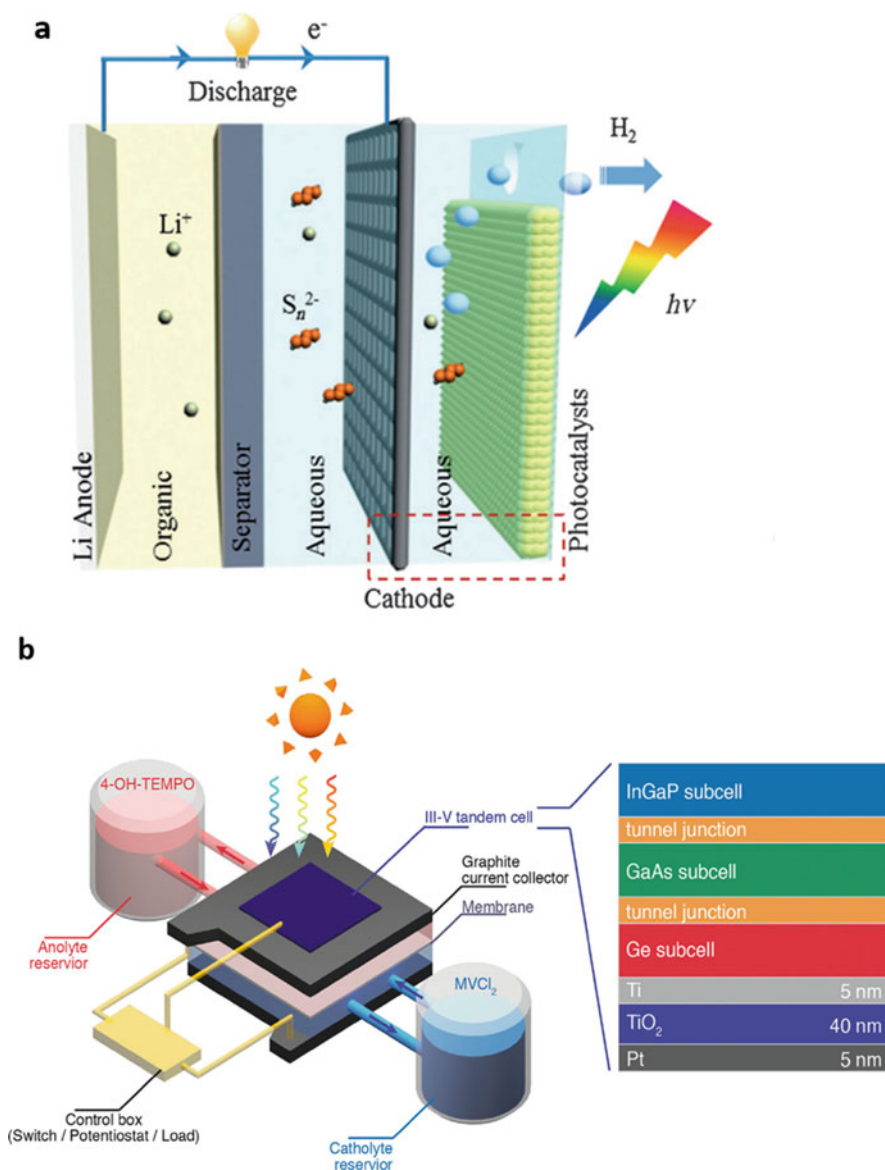


Fig. 11.12 Schematics of other advanced photo-charging designs. (a) Integration of Li-S battery with Pt-modified CdS as a photocatalyst. (b) Integration of III-V (InGaP/GaAs/Ge) tandem solar cell with a redox flow battery (4-OH-TEMPO/MVCl₂ as redox couples). (Figures (a–b) adapted with permission from Ref. [50], Wiley (a); Ref. [51], Cell Press (b))

with corrosive liquid electrolytes of the electrochemical storage system. A suitable thin barrier layer can be designed on top of the photoelectrode to make the semiconductor/liquid interface chemically stable. The focus should be on the use of “common” current collectors, electrodes, and electrolytes of the two systems. For

example, aluminum (Al) is a metal electrode used in solar cells and is employed as an anode in Al-ion battery. The integrated design should also incorporate bifunctional materials (e.g., silicon) which have the capability of both photoelectric conversion and energy storage. Perovskites can also be implemented as bifunctional material as it has been reported to host a high concentration of lithium-ions [52]. The focus should be on chemical stability and electrochemical compatibility between electrodes and electrolytes. Meanwhile, modeling and simulation investigations should be implemented to better assist the selection process of materials.

Aqueous supercapacitors can be charged using a single junction solar cell. However, nonaqueous supercapacitors and batteries would require a higher voltage than a single junction solar cell can deliver. This demands the use of more than one solar cell in series or multi-junction solar cells to acquire a higher output voltage. A simpler alternative design is to use DC-DC boost converters that would deliver the higher output voltage using a single junction solar cell. However, the use of a multi-junction solar cell can offer higher power conversion efficiency. Incorporation of DC-DC converters along with tandem solar cells is another option.

11.5.2 Capacity, Energy, and Power Densities

Batteries can offer higher energy density while supercapacitors offer higher power density. Lithium-ion, consisting of intercalation graphite as anode and lithium transition metal oxides as a cathode, is the dominant battery technology. This commercial Li-ion chemistry provides an energy density of 200–250 Whkg⁻¹. This limited energy density is not enough to satisfy the ever-increasing energy demand of advanced smart electronics, electric vehicles, and smart grids. Advanced anode materials such as silicon that can accommodate lithium ions greater than ten times have been pursued to replace graphite. The silicon anode coupled with NMC intercalation cathode can achieve an energy density of ~400 Whkg⁻¹ [53]. However, cells based on silicon anode undergo rapid capacity fading due to large volume change that silicon experiences during lithiation/de-lithiation. In an attempt to alleviate this issue, nanostructures (e.g., nanowires), carbon matrix, carbon coating, and porous silicon have been investigated. Spin-off companies such as Amprius has already commenced commercializing its lithium-ion batteries based on silicon anode. Silicon can be a bifunctional electrode that can function as photoelectrode as well as a battery electrode. One of the concerns would be the amorphousization that silicon undergoes after lithiation/delithiation processes as crystallinity plays a significant role in silicon photovoltaic performance. The detailed study might be useful in this case.

Lithium metal is the ideal anode candidate due to its high theoretical specific capacity of 3860 mAhg⁻¹ and the lowest negative electrochemical potential (−3.040 V vs. standard hydrogen electrode). Battery-based on lithium metal coupled with NMC intercalation cathode can achieve an even higher energy density of ~500 Whkg⁻¹ [53]. However, the practical implementation of lithium metal as an anode is inhibited by its high reactivity leading to aggressive electrolyte decomposition that

leads to the growth of lithium dendrites. The formation of these dendrites presents safety hazards with the possibility of short-circuits causing a fire. Considerable efforts have been reported to address this issue that includes the use of protective interface [54–56], 3D porous copper (Cu) [57], electrolyte additives [58, 59], and lithium hosts [60, 61]. For lithium metal to be implemented as a common electrode in the integrated system, lithium metal film deposition by heating and melting might be an issue as the temperature of ~ 180 °C is used. Evaporation of the lithium metal is an alternative. Meanwhile, it can be used in the form of a separate metal foil as an electrode if not used as the common electrode.

Advanced battery chemistries that couple lithium metal with high capacity cathodes such as lithium sulfide (Li-S) and lithium dioxide (Li-O₂) can be employed to achieve much higher practical energy density > 600 Whkg⁻¹. However, these advanced chemistries are plagued with several problems. Lithium sulfide (Li-S) batteries undergo polysulfide dissolution, large volume change, and have low electronic and ionic conductivity in sulfur cathodes. However, effective approaches addressing these issues have been reported that include embedding sulfur in carbon [62, 63], use of hollow sulfur [64, 65] and lithiated sulfur Li₂S as starting cathodes [66, 67]. Lithium dioxide (Li-O₂), on the other hand, is much more challenging as much less understanding of its underlying electrochemistry exists. Problems such as sluggish kinetics of oxygen reduction reaction and oxygen evolution reaction at the cathode and large charging overpotential exist for Li-O₂ cells [68]. Implementing electrolytes with high donor number, solution oxidation mediators and stable porous gas diffusion cathodes have been some of the solution strategies [69].

Multi-valent batteries such as Al-ion can deliver higher volumetric capacity (8056 mAh.cm⁻³) than that of Li-ion (2042 mAh.cm⁻³) [70–72] owing to each Al ion carrying three charges. Aluminum-ion batteries have the advantage of resource availability as aluminum is the most abundant metal on the Earth, while lithium-ion is restrained with lithium availability [73]. Al-ion battery employs Al metal as its anode. Meanwhile, Al is also a common metal electrode employed in solar cells (silicon, perovskite). Consequently, Al can be used as the common anode for integration of silicon or perovskite solar cell and Al-ion battery. Major research in Al-ion batteries is focused on suitable host material for Al ions. Recently, a carbon material such as layered graphite has been reported to be an excellent host displaying 2 V discharge voltage, fast charging, and cycle life up to 5000 cycles [74, 75], but with a specific capacity of only 100 mAhg⁻¹. Therefore, the development of cathode materials with high capacity and high working potential is imperative to fulfill the gap between multi-valent battery technologies and state-of-art Li-ion. In addition, the development of a suitable electrolyte for multi-charge ions conduction is crucial.

Integrated systems with supercapacitors would be more suitable for high power applications. Supercapacitors have a low energy density (< 10 Whkg⁻¹) compared to lithium-ion battery technology [7]. This demands the research on novel materials for supercapacitor electrodes that possess high surface area. Recent research has been focused on metal-organic frameworks (MOFs) and covalent organic frameworks (COFs) that have the capability of controllable pore size and surface area [76, 77]. Furthermore, two-dimensional materials such as black phosphorene and

two-dimensional (2-D) titanium carbide MXene core ($\text{Ti}_3\text{C}_2\text{T}_x$) shell can be used to achieve high capacitance [78–80]. Meanwhile, exploring new organic electrolytes that facilitate high operation voltage should be encouraged. On the other hand, a lithium-ion capacitor can be a new avenue that couples the high energy density of the lithium-ion battery and the high-power density of supercapacitor [81, 82].

11.5.3 Device Efficiency

The overall efficiency is the ratio of energy storage discharge energy to the incident light energy. Therefore, it is a product of photovoltaic power conversion efficiency and energy storage efficiency. This implies that the maximum overall efficiency of the integrated photovoltaic-energy storage system is the photovoltaic power conversion efficiency. One of the factors that directly impact the overall efficiency of the integrated system is the amendment done in photovoltaic and energy storage components to build the integrated system. The alteration is even more pronounced in a two-electrode integrated system; consequently, the overall efficiency is lower in comparison to the three-electrode system. Therefore, the challenge is to keep the modifications to the pristine structure of the photovoltaic and energy storage to a minimum.

The use of tandem photovoltaics can be employed to achieve higher power conversion efficiency than the single junction counterpart. The 46% efficient four-junction epitaxially grown III–V tandem solar cell can be applied; however, this type of tandem solar cell is expensive and therefore limited to space applications. An inexpensive tandem design would be a silicon-perovskite tandem. A power conversion efficiency of 23.6% has already been achieved with a tandem structure employing silicon heterojunction with cesium-doped formamidinium (FA) lead tribromide iodide [$\text{Cs}_{0.17}\text{FA}_{0.83}\text{Pb}(\text{Br}_{0.17}\text{I}_{0.83})_3$] perovskite [83]. The transparent electrodes tin oxide (SnO_2), zinc tin oxide (ZTO), indium tin oxide (ITO) enabled minimizing parasitic absorption and protection of perovskite layer from ITO sputter damage. Further optimization has led to achievement of 25.0% [84] by (1) reducing reflection with lower thickness of ITO top electrode and polydimethylsiloxane pyramidal structure as scattering layer, and (2) employing poly[bis(4-phenyl)(2,4,6-trimethylphenyl)amine] (PTAA) as hole transport material replacing nickel oxide (NiO_x) and wider bandgap perovskite $\text{Cs}_{0.25}\text{FA}_{0.75}\text{Pb}(\text{Br}_{0.2}\text{I}_{0.8})_3$. Spin-off companies such as Oxford Photovoltaics is pursuing commercialization of such perovskite-silicon tandem modules.

Perovskite-perovskite or all-perovskite tandem is another avenue to simultaneously achieve higher efficiency and low-cost fabrication. As the first 2-terminal monolithic all-perovskite tandem, a high bandgap perovskite methylammonium lead tribromide (MAPbBr_3 , $E_g \sim 2$ eV) and a conventional methylammonium lead triiodide (perovskite (MAPbI_3 , $E_g \sim 1.6$ eV) were laminated to each other, that resulted in an efficiency of 10.4% [85]. With the advancement of perovskite research, tandem perovskites have also observed much growth. Notable advances in 2-terminal monolithic design include perovskites combinations of mixed A-site cation methylammonium (MA)/formamidinium (FA) lead halides such as

$\text{Cs}_{0.15}\text{FA}_{0.85}\text{Pb}(\text{I}_{0.3}\text{Br}_{0.7})_3/\text{MAPbI}_3$ with efficiency of 18.1% [86], $\text{FA}_{0.83}\text{Cs}_{0.17}\text{Pb}(\text{I}_{0.5}\text{Br}_{0.5})_3/\text{FA}_{0.75}\text{Cs}_{0.25}\text{Sn}_{0.5}\text{Pb}_{0.5}\text{I}_3$ with efficiency of 16.9% [87] and $\text{MA}_{0.9}\text{Cs}_{0.1}\text{Pb}(\text{I}_{0.6}\text{Br}_{0.4})_3/\text{MAPb}_{0.5}\text{Sn}_{0.5}\text{I}_3$ with efficiency of 18.5% [88]. The highest efficiency of 18.5% was achieved by using low bandgap 1.2 eV lead-tin-based perovskite as the rear sub-cell, along with device engineering with reduction of nonradiative recombination to achieve the lowest photovoltage loss. One limitation of the tandem design is that the high and low bandgap PSCs exhibit lower power conversion efficiencies compared to conventional 1.6 eV perovskites. Research advances for high bandgap perovskites have been on the use of mixed cations (e.g., formamidinium (FA)/cesium (Cs)) [89, 90], improvement of perovskite film conditions [91], and partial replacement of lead (Pb^{2+}) with tin (Sn^{2+}) cations [92]. Similarly, for low bandgap sub-cell, the focus has been on implementing reducing agents [93–95], mixed organic cations [96], 2D layered/3D perovskite [97], and Sn-Pb metal cations [98, 99]. Competitive power conversion efficiencies of 17.6% [100] and 18.03% [101] have already been achieved for low bandgap perovskite solar cells using mixed metal cations of Sn and Pb.

Carbon-based materials have been used as top contact electrodes for perovskite solar cells which makes it compatible for supercapacitor integration with perovskite solar cells. Significant advances have been achieved with carbon-based top electrodes for perovskite solar cells demonstrating high efficiency >19% [102, 103]. These carbon-based perovskite solar cell device structures should be considered for supercapacitor integration.

For a real-field application of the integrated photovoltaic-storage device, the photovoltaic part must operate at maximum power point to harvest optimum energy. For the integrated system to operate at the maximum power point of the photovoltaic power generation, the ratio of the input photovoltaic power during storage charging to the maximum photovoltaic power should be equivalent to 1. To achieve this, the integrated design should consider matching energy storage voltage plateau as closely as possible with the photovoltaic maximum power point voltage. This requires selecting energy storage chemistries that is compatible with the photovoltaic voltage. Alternately, external power electronics can be employed that offers the advantage of the maximum power point tracking of the photovoltaic power. In addition, it can facilitate energy storage management such as overvoltage/undervoltage and thermal protection. Further, DC-DC converters can provide voltage boosting to enable the use of simpler designs such as single junction solar cells.

Energy efficiency of the energy storage system also plays an equally important role in determining the overall efficiency of the integrated system. Energy storage efficiency depends on (a) the charging overpotential over discharging and (b) difference between charging and discharging capacities (coulombic efficiency). The charging overpotential over discharging increases when higher charge and discharge rates are used. Therefore, the amount of current generated (charging current) by the photovoltaic part will play an important part in determining the energy storage efficiency and should be considered as a design criterion for the integrated system.

11.5.4 Material and Device Stability

Operational stability is a major concern for the integrated system to realize commercialization. Stability has been a major concern for transforming emerging photovoltaics such as perovskites technology towards commercialization. Hybrid perovskites are chemically susceptible to moisture, oxygen, heat, and ultraviolet light. However, promising and significant progress has been achieved towards making stable perovskites. Incorporation of inorganic component (e.g., Cs cation) into the conventional methylammonium (MA)/formamidinium (FA) (MAFA) system, engineering of perovskite/charge transport layer interfaces, use of protection layers, and proper encapsulation have been some major highlights [34, 104, 105]. In addition, all-inorganic PSCs, which are more resistant towards their ambience should be employed for the integrated designs. The photoelectrode in contact with liquid redox couples should be electrochemically stable. Suitable thin barrier layers such as TiO_2 can be employed to reduce the potential corrosion of the photoelectrodes.

Conventional electrolytes in liquid form provide high conductivity and efficient charge transfer kinetics owing to its superior wetting of energy storage electrode surface. However, these liquid electrolytes, in addition to being flammable, undergo unwanted decomposition at the electrode interfaces that forms an unstable SEI layer. This problem is more pronounced in lithium metal-based batteries, eventually presenting a safety hazard [106]. Use of solid-state electrolytes is the ultimate solution to replace the liquid electrolytes. Despite the safety advantage solid-state storage presents, incorporation of this technology also brings other challenges. One of the fundamental challenges is ionic conductivity of such solid-state electrolytes [107]. However, intense research has led to the development of solid-state electrolytes with ionic conductivity comparable or even higher than the state-of-the-art liquid electrolyte. Especially, the ceramic oxide-based and sulfide-based electrolytes have been promising. Different classes of ceramic electrolytes such as perovskite, antiperovskite, sodium (Na) Super Ionic CONductor (NASICON), Garnet (Thio-), Lithium Super Ionic CONductor (LISICON), Argyrodite, and lithium sulfide-phosphorus sulfide ($\text{Li}_2\text{S-P}_2\text{S}_5$) systems have been explored [107]. The sulfide-based solid ceramic electrolyte lithium germanium phosphorus sulfide ($\text{Li}_{10}\text{GeP}_2\text{S}_{12}$, LGPS) has demonstrated the highest room temperature ionic conductivity of $\sim 12 \text{ mS cm}^{-1}$ comparable to conventional organic solvent-based liquid electrolyte [108]. However, sulfide-based electrolytes face challenges of the hygroscopic nature of sulfides and poor electrochemical stability [107]. Additionally, these sulfide-based electrolytes do not provide a stable interface against lithium metal. In contrast, garnet-type solid electrolytes such as lithium lanthanum zirconium oxide ($\text{Li}_7\text{La}_3\text{Zr}_2\text{O}_{12}$, LLZO) have high ionic conductivity $\sim 1 \text{ mS cm}^{-1}$ and exhibit superior air and electrochemical stability along with stable interface against lithium metal.

The other challenge is a large interfacial resistance of solid-state electrolytes with the electrodes. A full cell solid-state battery development would require small interfacial impedance between the solid-state electrolyte and anode as well as

cathode. Some of the applied approaches to improve the cathode interface include the use of thin film vacuum deposited cathodes [109], surface coatings [110, 111], adding low melting point additives [112, 113] and interphase [114]. Meanwhile, for the anode interface, one of the approaches used is heating/melting lithium metal [115]. However, the degree of reduction in interfacial resistance is not satisfactory. The other approaches include using an ultrathin layer coating (alumina, Al_2O_3) on the solid-state electrolyte [116] and forming an intermediary Li-metal alloy at the interface [117]. This enhances its wettability and stability, thus drastically reducing the interfacial resistance.

Both the photovoltaic and storage components of the integrated system must be thermally stable during continuous sunlight exposure. Volatile solvents in conventional liquid energy storage would not be suitable with constant exposure to the heat. However, solid-state electrolytes usually demonstrate superior performance at higher temperatures, therefore, in situ external thermal heating of the energy storage during photo-charging could be an advantage.

11.5.5 System Scalability and Cost-Effectiveness

One of the factors limiting new technologies to become a commercial success is the capital cost. The transformation of the new technology into a commercial product demands huge capital investments if the fabrication processing does not adopt the current existing industrial manufacturing processes. This, in turn, leads to higher product prices that cannot compete with the existing commercial products. Taking this into consideration, the integrated system should be compatible with the existing industrial manufacturing processes. For the emerging photovoltaic technology such as perovskites, emphasis should be given to scalable solution phase deposition techniques such as screen printing [118], spray coating [119], blade coating [120], inkjet printing [122], and slot-die coating [121]. Additionally, emerging metal-based batteries and solid-state energy storage systems should also implement coating practices that exist in current battery manufacturing.

Traditionally, the integration of multi-function into one unit to achieve miniaturization has been a successful commercial approach in the electronics industry and low system cost has been one of the beneficial outcomes. The integration of the two functions of photoelectric conversion and energy storage also adopts a similar theme. Consequently, it is expected to result in a low-cost system compared to the conventional system of using separate photovoltaic and energy storage system. However, detailed economic analysis on transferring from the conventional system of using separate photovoltaic and energy storage system to the integrated system should be encouraged. The economic analysis should also take system maintenance and lifetime into consideration.

Innovations in material and device designs will be crucial in further advancement of the integrated photo rechargeable storage system and the above-discussed strategies should play a major part. It cannot be denied that the advances in the two individual fields of photovoltaic and energy storage will be significant in further

advancing the integrated system. This implies that optimal advantage should be taken of the state-of-the-art developments made in the two research domains by implementing them into the integrated designs.

Acknowledgments The project was benefitted from US-Egypt and Science Technology Joint Fund from USAID through NAS (2000007144). This article is derived from the Subject Data funded in whole or part by NAS and USAID, and any opinions, findings, conclusions, or recommendations expressed in this article are those of the authors alone and do not necessarily reflect the views of USAID or NAS.

References

1. M.M. Thackeray, C. Wolverton, E.D. Isaacs, Electrical energy storage for transportation – approaching the limits of, and going beyond, lithium-ion batteries. *Energy Environ. Sci.* **5**, 7854–7863 (2012)
2. J. Xu, Y. Chen, L. Dai, Efficiently photo-charging lithium-ion battery by perovskite solar cell. *Nat. Commun.* **6**, 8103 (2015)
3. IRENA. Renewable Power Generation Costs in 2017. (International Renewable Energy Agency, Abu Dhabi, 2018)
4. N.S. Lewis, Research opportunities to advance solar energy utilization. *Science* **351**, aad1920 (2016)
5. B. Dunn, H. Kamath, J.-M. Tarascon, Electrical energy storage for the grid: a battery of choices. *Science* **334**, 928–935 (2011)
6. A. Gurung, Q. Qiao, Solar charging batteries: advances, challenges, and opportunities. *Joule* **2**, 1217–1230 (2018)
7. Z.N. Yu, L. Tetard, L. Zhai, J. Thomas, Supercapacitor electrode materials: nanostructures from 0 to 3 dimensions. *Energy Environ. Sci.* **8**, 702–730 (2015)
8. F.X. Wang et al., Latest advances in supercapacitors: from new electrode materials to novel device designs. *Chem. Soc. Rev.* **46**, 6816–6854 (2017)
9. A.S. Westover et al., Direct integration of a supercapacitor into the backside of a silicon photovoltaic device. *Appl. Phys. Lett.* **104**, 213905 (2014)
10. Z. Ouyang et al., Monolithic integration of anodic molybdenum oxide pseudocapacitive electrodes on screen-printed silicon solar cells for hybrid energy harvesting-storage systems. *Adv. Energy Mater.* **7**, 1602325 (2017)
11. L.V. Thekkekara et al., On-chip energy storage integrated with solar cells using a laser scribed graphene oxide film. *Appl. Phys. Lett.* **107**, 031105 (2015)
12. T. Miyasaka, T.N. Murakami, The photocapacitor: an efficient self-charging capacitor for direct storage of solar energy. *Appl. Phys. Lett.* **85**, 3932–3934 (2004)
13. T.N. Murakami, N. Kawashima, T. Miyasaka, A high-voltage dye-sensitized photocapacitor of a three-electrode system. *Chem. Commun.* **5**, 3346–3348 (2005)
14. H.W. Chen et al., Plastic dye-sensitized photo-supercapacitor using electrophoretic deposition and compression methods. *J. Power Sources* **195**, 6225–6231 (2010)
15. C.Y. Hsu, H.W. Chen, K.M. Lee, C.W. Hu, K.C. Ho, A dye-sensitized photo-supercapacitor based on PProDOT-Et-2 thick films. *J. Power Sources* **195**, 6232–6238 (2010)
16. N.F. Yan, G.R. Li, G.L. Pan, X.P. Gao, TiN nanotube arrays as electrocatalytic electrode for solar storable rechargeable battery. *J. Electrochem. Soc.* **159**, A1770–A1774 (2012)
17. M. Skunik-Nuckowska et al., Integration of solid-state dye-sensitized solar cell with metal oxide charge storage material into the photoelectrochemical capacitor. *J. Power Sources* **234**, 91–99 (2013)
18. J. Xu et al., Integrated photo-supercapacitor based on bi-polar TiO₂ nanotube arrays with selective one-side plasma-assisted hydrogenation. *Adv. Funct. Mater.* **24**, 1840–1846 (2014)

19. A.P. Cohn et al., All silicon electrode photocapacitor for integrated energy storage and conversion. *Nano Lett.* **15**, 2727–2731 (2015)
20. Y. Fu et al., Integrated power fiber for energy conversion and storage. *Energy Environ. Sci.* **6**, 805–812 (2013)
21. X. Chen et al., A novel “energy fiber” by coaxially integrating dye-sensitized solar cell and an electrochemical capacitor. *J. Mater. Chem. A* **2**, 1897–1902 (2014)
22. T. Chen et al., An integrated “energy wire” for both photoelectric conversion and energy storage. *Angew. Chem. Int. Ed.* **51**, 11977–11980 (2012)
23. J. Bae et al., Single-Fiber-based hybridization of energy converters and storage units using graphene as electrodes. *Adv. Mater.* **23**, 3446–3449 (2011)
24. G. Wee, T. Salim, Y.M. Lam, S.G. Mhaisalkar, M. Srinivasan, Printable photo-supercapacitor using single-walled carbon nanotubes. *Energy Environ. Sci.* **4**, 413–416 (2011)
25. C.T. Chien et al., Graphene-based integrated photovoltaic energy harvesting/storage device. *Small* **11**, 2929–2937 (2015)
26. (a) Y.Z. Jin et al., Laminated free standing PEDOT: PSS electrode for solution-processed integrated photocapacitors via hydrogen-bond interaction. *Adv. Mater. Interfaces* **4**, 1700704 (2017). (b) Liu et al., Beyond metal oxides: introducing low-temperature solution-processed ultrathin layered double hydroxide nanosheets into polymer solar cells toward improved electron transport. *Solar RRL* **3**, 1970025 (2019); (c) Sai-Anand et al., Additive assisted morphological optimization of photoactive layer in polymer solar cells. *Sol. Energy Mater. Sol. Cells* **182**, 246–254 (2018); (d) Xu et al., Improving photovoltaic properties of P3HT:IC60BA through the incorporation of small molecule. *Polymers MDPI* **10**, 121 (2018); (e) Elshobaki et al., Tailoring nanoscale morphology of polymer:fullerene blends using electrostatic field. *ACS Appl. Mater. Interfaces* **9**, 2678–2685 (2017); (f) Zhen et al., Ethanol-amine-functionalized fullerene as an efficient electron transport layer for high-efficiency inverted polymer solar cells. *J. Mater. Chem. A* **4**, 8072–8079 (2016); (g) Sai-Anand et al., Electrostatic nanoassembly of contact interfacial layer for enhanced photovoltaic performance in polymer solar cells. *Sol. Energy Mater. Sol. Cells* **153**, 148–163 (2016); (h) Kumar et al., Origin of photogenerated carrier recombination at metal – active layer interface in polymer solar cells. *Phys. Chem. Chem. Phys.* **17**, 27690–27697 (2015); (i) Mohammad et al., Improved performance for inverted organic photovoltaics via spacer between benzodithiophene and benzothiazole in polymers. *J. Phys. Chem. C* **11**, 18992–19000 (2015); (j) Ngo et al., Enhanced lifetime of polymer solar cells by surface passivation of metal oxide buffer layers. *ACS Appl. Mater. Interfaces* **7**, 16093–16100 (2015); (k) Venkatesan et al., Critical role of domain crystallinity, domain purity and domain interface sharpness for reduced bimolecular recombination in polymer solar cells. *Nano Energy* **12**, 457–467 (2015)
27. Z.T. Zhang et al., Integrated polymer solar cell and electrochemical supercapacitor in a flexible and stable Fiber format. *Adv. Mater.* **26**, 466–470 (2014)
28. M.A. Green, A. Ho-Baillie, H.J. Snaith, The emergence of perovskite solar cells. *Nat. Photonics* **8**, 506–514 (2014)
29. (a) H.J. Snaith, Present status and future prospects of perovskite photovoltaics. *Nat. Mater.* **17**, 372 (2018); (b) H. Elbohy et al., Tuning hole transport layer using urea for high-performance perovskite solar cells. *Adv. Funct. Mater.* 1806740 (2019); (c) K.M. Reza et al., Tailored PEDOT:PSS hole transport layer for higher performance in perovskite solar cells: enhancement of electrical and optical properties with improved morphology. *J. Energy Chem.* (2019), in press; (d) S. Mabrouk et al., Higher efficiency perovskite solar cells using additives of LiI, LiTFSI and BMIm in the PbI₂ precursor. *Sustain. Energy Fuels* **1**, 2162–2171 (2017); (e) G. Wang et al., Improving photovoltaic performance of carbon-based CsPbBr₃ perovskite solar cells by interfacial engineering using P3HT interlayer. *J. Power Sources* **432**, 48–54 (2019); (f) Vickers et al., Improving charge carrier delocalization in perovskite quantum dots by surface passivation with conductive aromatic ligands. *ACS Energy Lett.* **3**, 2931–2939 (2018); (g) Wu et al., Inverted current–voltage hysteresis in perovskite solar cells, *ACS Energy Lett.* **3**, 2457–2460 (2018); (h) Wu et al., Bias-dependent normal and inverted J–V hysteresis in

- perovskite solar cells. *ACS Appl. Mater. Interfaces* **10**, 25604–25613 (2018); (i) Wu et al., Influence of nonfused cores on the photovoltaic performance of linear triphenylamine-based hole-transporting materials for perovskite solar cells. *ACS Appl. Mater. Interfaces* **10**, 17883–17895 (2018); (j) Gangadharan et al., Aromatic alkylammonium spacer cations for efficient two-dimensional perovskite solar cells with enhanced moisture and thermal stability. *Solar RRL* **2**, 1700215 (2018); (k) K.M. Reza, S. Mabrouk, Q. Qiao, A review on tailoring PEDOT: PSS layer for improved performance of perovskite solar cells. *Proc. Nat. Res. Soc.* **2(1)**, 02004 (2018)
30. NREL, Best Research-Cell Efficiencies (2018), <https://www.nrel.gov/pv/assets/images/efficiency-chart.png>
 31. X.B. Xu et al., A power pack based on organometallic perovskite solar cell and supercapacitor. *ACS Nano* **9**, 1782–1787 (2015)
 32. J. Xu, Z.L. Ku, Y.Q. Zhang, D.L. Chao, H.J. Fan, Integrated photo-supercapacitor based on PEDOT modified printable perovskite solar cell. *Adv. Mater. Technol.* **1**, 1600074 (2016)
 33. J. Liang et al., Integrated perovskite solar capacitors with high energy conversion efficiency and fast photo-charging rate. *J. Mater. Chem. A* **6**, 2047–2052 (2018)
 34. M. Asghar, J. Zhang, H. Wang, P. Lund, Device stability of perovskite solar cells—a review. *Renew. Sust. Energ. Rev.* **77**, 131–146 (2017)
 35. J. Liang et al., An all-inorganic perovskite solar capacitor for efficient and stable spontaneous photocharging. *Nano Energy* **52**, 239–245 (2018)
 36. H. Sun et al., Energy harvesting and storage devices fused into various patterns. *J. Mater. Chem. A* **3**, 14977–14984 (2015)
 37. P. Alotto, M. Guarnieri, F. Moro, Redox flow batteries for the storage of renewable energy: a review. *Renew. Sust. Energ. Rev.* **29**, 325–335 (2014)
 38. H.-D. Um et al., Monolithically integrated, photo-rechargeable portable power sources based on miniaturized Si solar cells and printed solid-state lithium-ion batteries. *Energy Environ. Sci.* (2017)
 39. S. Liao et al., Integrating a dual-silicon photoelectrochemical cell into a redox flow battery for unassisted photocharging. *Nat. Commun.* **7**, 11474 (2016)
 40. W. Li et al., Integrated photoelectrochemical solar energy conversion and organic redox flow battery devices. *Angew. Chem. Int. Ed.* **55**, 13104–13108 (2016)
 41. W. Guo, X. Xue, S. Wang, C. Lin, Z.L. Wang, An integrated power pack of dye-sensitized solar cell and Li battery based on double-sided TiO₂ nanotube arrays. *Nano Lett.* **12**, 2520–2523 (2012)
 42. A. Paoletta et al., Light-assisted delithiation of lithium iron phosphate nanocrystals towards photo-rechargeable lithium-ion batteries. *Nat. Commun.* **8**, 14643 (2017)
 43. P. Liu et al., A solar rechargeable flow battery based on photoregeneration of two soluble redox couples. *ChemSusChem* **6**, 802–806 (2013)
 44. (a) N.F. Yan, G.R. Li, X.P. Gao, Solar rechargeable redox flow battery based on Li₂WO₄/LiI couples in dual-phase electrolytes. *J. Mater. Chem. A* **1**, 7012–7015 (2013); (b) Ma et al., Fe_{1-x}CoxS₂ solid solutions with tunable energy structures to enhance the performance of triiodide reduction in dye-sensitized solar cells. *ChemNanoMat* **4**, 1043 (2018); (c) Elbohy et al., Creation of oxygen vacancy to activate WO₃ for higher efficiency dye-sensitized solar cells. *Sustain. Energy Fuels* **2**, 403–412 (2018); (d) Abdulkarim et al., Urea treated electrolytes for higher efficiency dye-sensitized solar cells. *J. Phys. Chem. C* **121(39)**, 21225–21230 (2017); (e) Huang et al., Synergistically enhanced electrochemical performance of Ni₃S₄-PtX (X=Fe, Ni) heteronanorods as heterogeneous catalysts in dye sensitized solar cells. *ACS Appl. Mater. Interfaces* **9**, 27607–27617 (2017); (f) He et al., The role of Mott–Schottky heterojunctions in Ag–Ag₈SnS₆ as counter electrodes in dye-sensitized solar cells. *ChemSusChem* **8**, 817–820 (2015); (g) Awuah et al., New pyran dyes for dye-sensitized solar cells. *J. Photochem. Photobiol. A Chem.* **224**, 116–122 (2011); (h) Sigdel et al., Dye-sensitized solar cells based on spray-coated carbon nanofiber/TiO₂ nanoparticle composite counter electrodes. *J. Mater. Chem. A* **2**, 11448–11453 (2014); (i) Elbohy et al., Graphene-embedded carbon nanofibers

- decorated with Pt nanoneedles for higher efficiency dye-sensitized solar cells. *J. Mater. Chem. A* **3**, 17721–17727 (2015); (j) Zhou et al., Graphene-beaded carbon nanofibers with incorporated Ni nanoparticles as efficient counter electrode for dye-sensitized solar cells. *Nano Energy* **22**, 558–563 (2016); (k) Ma et al., Electrospun carbon nano-felt derived from alkali lignin for cost-effective counter electrodes of dye-sensitized solar cells. *RSC Adv.* **6**, 11481–11487 (2016)
45. M. Yu, X. Ren, L. Ma, Y. Wu, Integrating a redox-coupled dye-sensitized photoelectrode into a lithium-oxygen battery for photoassisted charging. *Nat. Commun.* **5**, 5111 (2014)
 46. Q. Li, N. Li, M. Ishida, H. Zhou, Saving electric energy by integrating a photoelectrode into a Li-ion battery. *J. Mater. Chem. A* **3**, 20903–20907 (2015)
 47. M. Yu et al., Aqueous lithium–iodine solar flow battery for the simultaneous conversion and storage of solar energy. *J. Am. Chem. Soc.* **137**, 8332–8335 (2015)
 48. A. Gurung et al., Highly efficient perovskite solar cell photocharging of lithium ion battery using DC-DC booster. *Adv. Energy Mater.* **7**, 1602105 (2017)
 49. S. Ahmad, C. George, D.J. Beesley, J.J. Baumberg, M. De Volder, Photo-rechargeable organo-halide perovskite batteries. *Nano Lett.* **18**, 1856–1862 (2018)
 50. N. Li, Y. Wang, D. Tang, H. Zhou, Integrating a photocatalyst into a hybrid lithium–sulfur battery for direct storage of solar energy. *Angew. Chem. Int. Ed.* **54**, 9271–9274 (2015)
 51. W. Li, H.-C. Fu, Y. Zhao, J.-H. He, S. Jin, 14.1% efficient monolithically integrated solar flow battery. *Chem* **4**, 2644–2657 (2018)
 52. N. Vicente, G. Garcia-Belmonte, Methylammonium lead bromide perovskite battery anodes reversibly host high Li-ion concentrations. *J. Phys. Chem. Lett.* **8**, 1371–1374 (2017)
 53. (a) S. Chu, Y. Cui, N. Liu, The path towards sustainable energy. *Nat. Mater.* **16**, 16 (2017); (b) A. Gurung et al., Tin selenide – multi-walled carbon nanotubes hybrid anodes for high performance lithium-ion batteries. *Electrochim. Acta* **211**, 720–725 (2016); (c) Z. Zhou et al., Binder free hierarchical mesoporous carbon foam for high performance lithium ion battery. *Sci. Rep.* **7**, 1440 (2017); (d) S. J. P. Varapragasam et al., Kirkendall growth of hollow Mn₃O₄ nanoparticles upon galvanic reaction of MnO with Cu²⁺ and evaluation as anode for lithium-ion batteries. *J. Phys. Chem. C* **121**, 11089–11099 (2017); (e) R. Naderi et al., Activation of passive nanofillers in composite polymer electrolyte for higher performance lithium-ion batteries. *Adv. Sustain. Syst.* **1**, 1700043 (2017); (f) A. Gurung et al., A review on strategies addressing interface incompatibilities in inorganic all-solid-state lithium batteries. *Sustain. Energy Fuels* (2019), in press; (g) R. Pathak et al., Self-recovery in Li-metal hybrid lithium-ion batteries via WO₃ reduction. *Nanoscale* **10**, 15956–15966 (2018)
 54. A.C. Kozen et al., Stabilization of lithium metal anodes by hybrid artificial solid electrolyte interphase. *Chem. Mater.* **29**, 6298–6307 (2017)
 55. (a) N.W. Li, Y.X. Yin, C.P. Yang, Y.G. Guo, An artificial solid electrolyte interphase layer for stable lithium metal anodes. *Adv. Mater.* **28**, 1853–1858 (2016); (b) K. Chen et al., Flower-shaped lithium nitride as a protective layer via facile plasma activation for stable lithium metal anodes. *Energy Storage Mater.* **18**, 389–396 (2019); (c) R. Pathak et al., Ultrathin bilayer of graphite/SiO₂ as solid interface for reviving Li metal anode. *Adv. Energy. Mater.* **9**, 1901486 (2019)
 56. G. Zheng et al., Interconnected hollow carbon nanospheres for stable lithium metal anodes. *Nat. Nanotechnol.* **9**, 618 (2014)
 57. C.-P. Yang, Y.-X. Yin, S.-F. Zhang, N.-W. Li, Y.-G. Guo, Accommodating lithium into 3D current collectors with a submicron skeleton towards long-life lithium metal anodes. *Nat. Commun.* **6**, 8058 (2015)
 58. H. Zhang et al., Electrolyte additives for lithium metal anodes and rechargeable lithium metal batteries: progress and perspectives. *Angew. Chem. Int. Ed.* **57**, 15002–15027 (2018)
 59. Q. Pang, X. Liang, A. Shyamsunder, L.F. Nazar, An in vivo formed solid electrolyte surface layer enables stable plating of Li metal. *Joule* **1**, 871–886 (2017)
 60. D. Lin et al., Layered reduced graphene oxide with nanoscale interlayer gaps as a stable host for lithium metal anodes. *Nat. Nanotechnol.* **11**, 626 (2016)

61. R. Zhang et al., Coralloid carbon fiber-based composite lithium anode for robust lithium metal batteries. *Joule* **2**, 764–777 (2018)
62. X. Ji, K.T. Lee, L.F. Nazar, A highly ordered nanostructured carbon-sulfur cathode for lithium-sulfur batteries. *Nat. Mater.* **8**, 500 (2009)
63. H. Wang et al., Graphene-wrapped sulfur particles as a rechargeable lithium-sulfur battery cathode material with high capacity and cycling stability. *Nano Lett.* **11**, 2644–2647 (2011)
64. W. Li et al., Understanding the role of different conductive polymers in improving the nanostructured sulfur cathode performance. *Nano Lett.* **13**, 5534–5540 (2013)
65. W. Li et al., High-performance hollow sulfur nanostructured battery cathode through a scalable, room temperature, one-step, bottom-up approach. *Proc. Natl. Acad. Sci.* **110**, 7148–7153 (2013)
66. Z.W. Seh et al., Facile synthesis of Li_2S -polypyrrole composite structures for high-performance Li_2S cathodes. *Energy Environ. Sci.* **7**, 672–676 (2014)
67. Z.W. Seh et al., High-capacity Li_2S -graphene oxide composite cathodes with stable cycling performance. *Chem. Sci.* **5**, 1396–1400 (2014)
68. K.-N. Jung et al., Rechargeable lithium-air batteries: a perspective on the development of oxygen electrodes. *J. Mater. Chem. A* **4**, 14050–14068 (2016)
69. D. Aurbach, B.D. McCloskey, L.F. Nazar, P.G. Bruce, Advances in understanding mechanisms underpinning lithium-air batteries. *Nat. Energy* **1**, 16128 (2016)
70. S.K. Das, S. Mahapatra, H. Lahan, Aluminium-ion batteries: developments and challenges. *J. Mater. Chem. A* **5**, 6347–6367 (2017)
71. F. Ambroz, T.J. Macdonald, T. Nann, Trends in aluminium-based intercalation batteries. *Adv. Energy Mater.* **7**, 1602093 (2017)
72. Z.A. Zafar et al., Cathode materials for rechargeable aluminum batteries: current status and progress. *J. Mater. Chem. A* **5**, 5646–5660 (2017)
73. G.A. Elia et al., An overview and future perspectives of aluminum batteries. *Adv. Mater.* **28**, 7564–7579 (2016)
74. D.Y. Wang et al., Advanced rechargeable aluminum ion battery with a high-quality natural graphite cathode. *Nat. Commun.* **8**, 14283 (2017)
75. M.C. Lin et al., An ultrafast rechargeable aluminum-ion battery. *Nature* **520**, 325–328 (2015)
76. C.R. DeBlase et al., Rapid and efficient redox processes within 2D covalent organic framework thin films. *ACS Nano* **9**, 3178–3183 (2015)
77. L. Liu, Y. Yan, Z.H. Cai, S.X. Lin, X.B. Hu, Growth-oriented Fe-based MOFs synergized with graphene aerogels for high-performance supercapacitors. *Adv. Mater. Interfaces* **5**, 1701548 (2018)
78. X. Xiao et al., Freestanding mesoporous VN/CNT hybrid electrodes for flexible all-solid-state supercapacitors. *Adv. Mater.* **25**, 5091–5097 (2013)
79. M. Ghidui, M.R. Lukatskaya, M.Q. Zhao, Y. Gogotsi, M.W. Barsoum, Conductive two-dimensional titanium carbide ‘clay’ with high volumetric capacitance. *Nature* **516**, 78–U171 (2014)
80. C.X. Hao et al., Flexible all-solid-state supercapacitors based on liquid-exfoliated black-phosphorus nanoflakes. *Adv. Mater.* **28**, 3194–3201 (2016)
81. C. Liu, C. Zhang, H. Fu, X. Nan, G. Cao, Exploiting high-performance anode through tuning the character of chemical bonds for Li-ion batteries and capacitors. *Adv. Energy Mater.* **7**, 1601127 (2017)
82. P. Wang et al., Porous niobium nitride as a capacitive anode material for advanced Li-ion hybrid capacitors with superior cycling stability. *J. Mater. Chem. A* **4**, 9760–9766 (2016)
83. K.A. Bush et al., 23.6%-efficient monolithic perovskite/silicon tandem solar cells with improved stability. *Nat. Energy* **2**, 17009 (2017)
84. K.A. Bush et al., Minimizing current, and voltage losses to reach 25%-efficient monolithic two-terminal perovskite-silicon tandem solar cells. *ACS Energy Lett.* **3**, 2173–2180 (2018)
85. J.H. Heo, S.H. Im, $\text{CH}_3\text{NH}_3\text{PbBr}_3\text{-CH}_3\text{NH}_3\text{PbI}_3$ perovskite-perovskite tandem solar cells with exceeding 2.2 V open circuit voltage. *Adv. Mater.* **28**, 5121–5125 (2016)

86. D. Forgács et al., Efficient monolithic perovskite/perovskite tandem solar cells. *Adv. Energy Mater.* **7**, 1602121 (2017)
87. G.E. Eperon et al., Perovskite-perovskite tandem photovoltaics with optimized bandgaps. *Science* **354**, 861–865 (2016). <https://doi.org/10.1126/science.aaf9717>
88. A. Rajagopal et al., Highly efficient perovskite–perovskite tandem solar cells reaching 80% of the theoretical limit in photovoltage. *Adv. Mater.* **29**, 1702140 (2017)
89. D.P. McMeekin et al., A mixed-cation lead mixed-halide perovskite absorber for tandem solar cells. *Science* **351**, 151–155 (2016)
90. K.A. Bush et al., Compositional engineering for efficient wide band gap perovskites with improved stability to photoinduced phase segregation. *ACS Energy Lett.* (2018)
91. M. Hu, C. Bi, Y. Yuan, Y. Bai, J. Huang, Stabilized wide bandgap MAPbBr_{1–x}I_x perovskite by enhanced grain size and improved crystallinity. *Adv. Sci.* **3**, 1500301 (2016)
92. Z. Yang et al., Stabilized wide bandgap perovskite solar cells by tin substitution. *Nano Lett.* **16**, 7739–7747 (2016)
93. M.H. Kumar et al., Lead-free halide perovskite solar cells with high photocurrents realized through vacancy modulation. *Adv. Mater.* **26**, 7122–7127 (2014)
94. K. Marshall, M. Walker, R. Walton, R. Hatton, Enhanced stability and efficiency in hole-transport-layer-free CsSnI₃ perovskite photovoltaics. *Nat. Energy* **1**, 16178 (2016)
95. W. Liao et al., Lead-free inverted planar formamidinium tin triiodide perovskite solar cells achieving power conversion efficiencies up to 6.22%. *Adv. Mater.* **28**, 9333–9340 (2016)
96. Z. Zhao et al., Mixed-organic-cation tin iodide for lead-free perovskite solar cells with an efficiency of 8.12%. *Adv. Sci.* **4**, 1700204 (2017)
97. S. Shao et al., Highly reproducible Sn-based hybrid perovskite solar cells with 9% efficiency. *Adv. Energy Mater.* **8**, 1702019 (2018)
98. Y. Li et al., 50% Sn-based planar perovskite solar cell with power conversion efficiency up to 13.6%. *Adv. Energy Mater.* **6**, 1601353 (2016)
99. F. Hao, C.C. Stoumpos, R.P. Chang, M.G. Kanatzidis, Anomalous band gap behavior in mixed Sn and Pb perovskites enables broadening of an absorption spectrum in solar cells. *J. Am. Chem. Soc.* **136**, 8094–8099 (2014)
100. D. Zhao et al., Low-bandgap mixed tin-lead iodide perovskite absorbers with long carrier lifetimes for all-perovskite tandem solar cells. *Nat. Energy* **2**, 17018 (2017)
101. G. Xu et al., Integrating ultrathin bulk-heterojunction organic semiconductor intermediary for high-performance low-bandgap perovskite solar cells with low energy loss. *Adv. Funct. Mater.* **28**, 1804427 (2018)
102. X. Liu et al., 17.46% efficient and highly stable carbon-based planar perovskite solar cells employing Ni-doped rutile TiO₂ as the electron transport layer. *Nano Energy* **50**, 201–211 (2018)
103. H. Zhang et al., Self-adhesive macroporous carbon electrodes for efficient and stable perovskite solar cells. *Adv. Funct. Mater.* **28**, 1802985 (2018)
104. G. Niu, X. Guo, L. Wang, Review of recent progress in chemical stability of perovskite solar cells. *J. Mater. Chem. A* **3**, 8970–8980 (2015)
105. J. Chen et al., Recent progress in stabilizing hybrid perovskites for solar cell applications. *J. Power Sources* **355**, 98–133 (2017)
106. J.C. Bachman et al., Inorganic solid-state electrolytes for lithium batteries: mechanisms and properties governing ion conduction. *Chem. Rev.* **116**, 140–162 (2015)
107. L. Fan, S. Wei, S. Li, Q. Li, Y. Lu, Recent progress of the solid-state electrolytes for high-energy metal-based batteries. *Adv. Energy Mater.* **8**, 1702657 (2018)
108. N. Kamaya et al., A lithium superionic conductor. *Nat. Mater.* **10**, 682 (2011)
109. S. Ohta, T. Kobayashi, J. Seki, T. Asaoka, Electrochemical performance of an all-solid-state lithium ion battery with garnet-type oxide electrolyte. *J. Power Sources* **202**, 332–335 (2012)
110. A. Sakuda et al., All-solid-state lithium secondary batteries with metal-sulfide-coated LiCoO₂ prepared by thermal decomposition of dithiocarbamate complexes. *J. Mater. Chem.* **22**, 15247–15254 (2012)

111. K. Takada et al., Interfacial phenomena in solid-state lithium battery with sulfide solid electrolyte. *Solid State Ionics* **225**, 594–597 (2012)
112. S. Ohta et al., All-solid-state lithium-ion battery using garnet-type oxide and Li_3BO_3 solid electrolytes fabricated by screen-printing. *J. Power Sources* **238**, 53–56 (2013)
113. K. Park et al., Electrochemical nature of the cathode interface for a solid-state lithium-ion battery: an interface between LiCoO_2 and garnet- $\text{Li}_7\text{La}_3\text{Zr}_2\text{O}_{12}$. *Chem. Mater.* **28**, 8051–8059 (2016)
114. F. Han et al., Interphase engineering enabled all-ceramic lithium battery. *Joule* **2**, 497–508 (2018)
115. Y. Jin, P.J. McGinn, Bulk solid-state rechargeable lithium-ion battery fabrication with Al-doped $\text{Li}_7\text{La}_3\text{Zr}_2\text{O}_{12}$ electrolyte and $\text{Cu}_{0.1}\text{V}_2\text{O}_5$ cathode. *Electrochim. Acta* **89**, 407–412 (2013)
116. X. Han et al., Negating interfacial impedance in garnet-based solid-state Li metal batteries. *Nat. Mater.* **16**, 572 (2017)
117. K.K. Fu et al., Toward garnet electrolyte-based Li metal batteries: an ultrathin, highly effective, artificial solid-state electrolyte/metallic Li interface. *Sci. Adv.* **3**, e1601659 (2017)
118. A. Priyadarshi et al., A large area (70 cm^2) monolithic perovskite solar module with high efficiency and stability. *Energy Environ. Sci.* **9**, 3687–3692 (2016)
119. J.H. Heo, M.H. Lee, M.H. Jang, S.H. Im, Highly efficient $\text{CH}_3\text{NH}_3\text{PbI}_{3-x}\text{Cl}_x$ mixed halide perovskite solar cells prepared by re-dissolution and crystal grain growth via spray coating. *J. Mater. Chem. A* **4**, 17636–17642 (2016)
120. M. Yang et al., Perovskite ink with a wide processing window for scalable high-efficiency solar cells. *Nat. Energy* **2**, 17038 (2017)
121. T. Qin et al., Amorphous hole-transporting layer in slot-die coated perovskite solar cells. *Nano Energy* **31**, 210–217 (2017)
122. S.-G. Li et al., Inkjet printing of $\text{CH}_3\text{NH}_3\text{PbI}_3$ on a mesoscopic TiO_2 film for highly efficient perovskite solar cells. *J. Mater. Chem. A* **3**, 9092–9097 (2015)



Design, Engineering, and Evaluation of Porphyrins for Dye-Sensitized Solar Cells **12**

Wenhui Li, Mahmoud Elkhalfifa, and Hongshan He

Contents

12.1	Introduction	352
12.1.1	Working Principles and Challenges	353
12.1.2	Characteristics of Porphyrin Dyes	356
12.1.3	Porphyryns for DSCs	358
12.1.4	Synthetic Methods for Porphyrin Dyes	367
12.2	Porphyryn Dyes with Different Anchoring Groups	370
12.2.1	Carboxylic and Cyanoacetic Acids	371
12.2.2	Phosphonic Acids	373
12.2.3	Pyridyl Groups	373
12.2.4	Other Anchoring Groups	374
12.3	Summary	375
	References	376

Abstract

Dye-sensitized solar cells (DSCs) have attracted worldwide attention due to their low cost and versatility. Porphyrins have broad and intense absorption in the

The original version of this chapter was revised. Correction to this chapter can be found at https://doi.org/10.1007/978-3-662-59594-7_18

Author Contribution

W. Li wrote the manuscript related to the solar properties, M. Elkhalfifa the synthesis section, and H. He revised the second draft.

W. Li

School of Information Engineering, Jiangxi University of Science and Technology, Ganzhou, Jiangxi, China

M. Elkhalfifa · H. He (✉)

Department of Chemistry and Biochemistry, Eastern Illinois University, Charleston, IL, USA

e-mail: hhe@eiu.edu

© Springer-Verlag GmbH Germany, part of Springer Nature 2019, corrected publication 2023

T. A. Atesin et al. (eds.), *Nanostructured Materials for Next-Generation Energy Storage and Conversion*, https://doi.org/10.1007/978-3-662-59594-7_12

visible region, versatility in tuning the molecular structure. Early porphyrin dyes are generally β -functionalized *meso*-tetraarylporphyrins. In the late 2000s, several groups began to pay their attention to *meso*-functionalized porphyrins. In 2010, the *meso*-functionalized porphyrin dye with donor- π -acceptor structure, achieved an efficiency of 11%. Since then, dozens of donor- π -acceptor porphyrin dyes with >10% efficiency have been reported. In 2014, the energy conversion efficiency of 13% was reached. However, some challenges still exist including inefficient photon capture in the regions around 520 nm and >700 nm, severe aggregation because of porphyrin's planar structure and rich π electrons, and poor long-term stability resulting from the weak binding capability of the anchoring group. In this chapter, we will provide readers the operation principles of DSC, an evolution of porphyrin dyes as the best candidates for DSCs, and challenges facing porphyrin dyes for DSCs. Different design strategies, synthetic protocols, as well as their photovoltaic performance of representative dyes will be discussed.

12.1 Introduction

Humans have used fossil fuels that took around 400 million years to form and store underground. To meet the increasing energy demand, new energy sources need to be found. Solar energy has attracted much attention due to its abundant, clean, and sustainable properties. We can use the thermal solar collector to convert solar energy to heat, which is efficient and low cost, but heat is difficult to store. We can also use solar cells to convert solar energy into electricity, which is more expensive than a thermal solar collector, but the electricity is easy to transport and store making this method more attractive.

Solar cells have gone through three generations since their discovery. The first generation was made using crystalline silicon (c-Si). This type of cell has a high energy conversion efficiency of up to 25% [93] but requires extremely pure silicon; therefore, the production cost is high. The second generation is thin film solar cells, which are low cost. Amorphous silicon (a-Si), cadmium telluride (CdTe), copper indium gallium selenide (CIGS) belong to this type. Amorphous silicon (a-Si) was first introduced by D. Carlson in 1976 [9]. A power conversion efficiency of 2.4% was achieved in a-Si [positive-type, intrinsic undoped, and negative-type semiconductor] *p-i-n* structure. Up to now, the energy conversion efficiency of this type of solar cell has reached 10.2% [24]. However, the energy conversion efficiency is still low compared to c-Si solar cells. In addition, long-term stability is also poor. Alternatively, thin film solar cells, such as cadmium telluride (CdTe) and copper indium gallium selenide (CIGS), were developed to booster energy conversion efficiency. The highest efficiencies of CdTe and CIGS were 21.0% and 21.7%, respectively [24]. However, due to the toxic property or limited resources, their application is impeded. Dye-sensitized solar cells (DSCs) have been widely regarded as next-generation solar cells for providing electricity at lower cost with more versatility. An overall light-to-electricity energy conversion efficiency above 11% has been obtained using ruthenium dyes [7, 20, 69], but the limited resources and the environmental issue of ruthenium provide opportunities for other organic dyes, such

as porphyrin dyes. Extensive studies showed that porphyrin dyes have great potential to level the economic cost of DSC devices due to their versatile structural modification and excellent light-harvesting capability. Recently, an energy conversion efficiency of greater than 13% has been reached using a donor- π -acceptor porphyrin dye [63].

There are several challenges for porphyrin sensitized solar cell. The first is that the absorption of porphyrin dyes is not broad enough to capture all photons in the visible and near-infrared regions. Most porphyrin dyes have no absorption above 700 nm, leading to significant loss of photons in the near-infrared region. In addition, the absorption capability in the green light region is also weak. Several fused porphyrin dyes and porphyrin dimers have been developed to address this challenge with an absorption edge up to 900 nm; however, their photovoltaic performance was not competitive to porphyrin monomers due to dye aggregation and energy mismatch. The second one is the weak binding capability of the anchoring group on the surface of titania (TiO_2) nanoparticles. Currently carboxylic acid and benzoic acid are two anchoring groups that have been extensively explored. Although they can chelate to Ti atoms readily, the binding strength is not strong enough. The anchoring group can dissociate slowly from TiO_2 surface into electrolyte medium, resulting in complete loss of energy conversion ability of devices.

12.1.1 Working Principles and Challenges

In DSCs, light is absorbed by a sensitizer, which is anchored to the surface of a wide band semiconductor, such as TiO_2 nanoparticles. Charge separation takes place at the interface via photo-induced electron injection from the excited state of the dye into the conduction band of the semiconductor. Carriers are transported in the conduction band of the semiconductor to the charge collector. So far, the most common state-of-the-art DSC is titanium dioxide nanoparticles-based electrochemical device, in which interconnected TiO_2 nanoparticles in the anatase phase are randomly packed on a substrate, such as fluorine-tin-oxide (FTO)-coated transparent conducting glass (TCO glass).

The operation of a DSC is shown in Fig. 12.1. The first step is dye molecules absorb light and get excited as $S + h\nu \rightarrow S^*$, where S represents the ground state of the sensitizer, and S^* is the excited state of the sensitizer. Then electrons from dyes in the excited states are injected into the TiO_2 conduction band as $S^* \rightarrow S + e^- (\text{TiO}_2)$, in which S^+ is the oxidized state of the sensitizer. After charge separation, electrons transport through a network of interconnected TiO_2 particles to the TCO layer to the external circuit as $e^- (\text{TiO}_2) \rightarrow e^- (\text{PE})$, in which PE is the photoelectrode. The oxidized dyes are reduced by the electrons from electrolyte as $2S^+ + 3I^- (\text{electrolyte}) \rightarrow 2S + 3I^- (\text{electrolyte})$. The biggest difference between DSCs and inorganic solar cells is that in DSCs the function of light absorption and charge carrier transport are separated [22].

Besides the desired pathways of the electron transfer processes, there are several undesirable electron recombination processes, which are shown by red lines in Fig. 12.2. One is the direct recombination of the excited dye to the ground state (process 2). The second is injected electrons in the conduction band of TiO_2 with

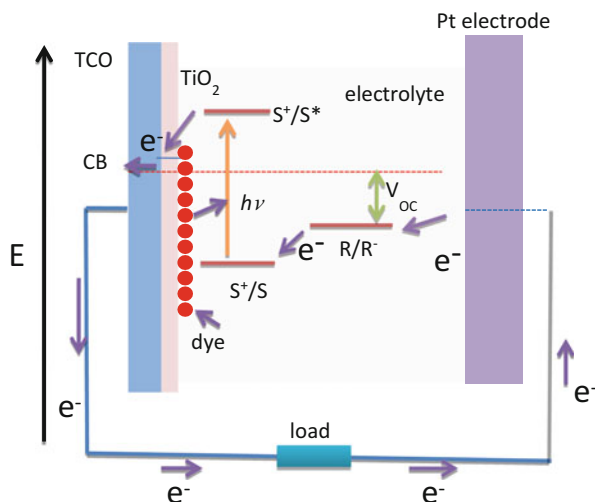


Fig. 12.1 An operation principle of DSC. S: ground state, S*: excited state, R/R⁻: redox couple

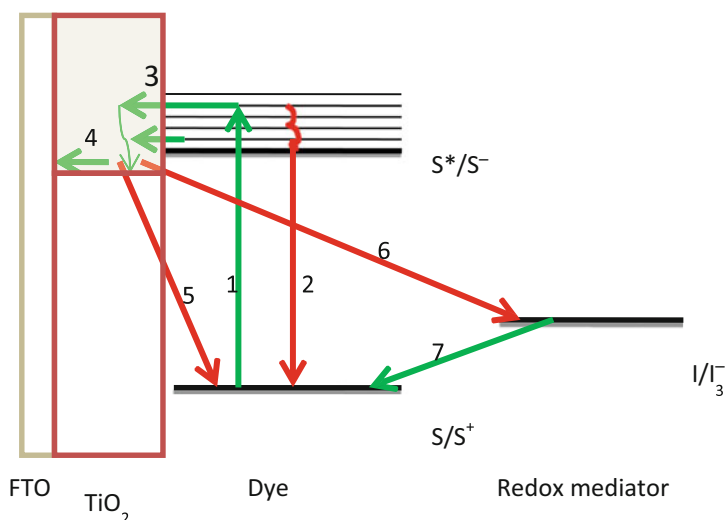


Fig. 12.2 Electron transport processes in photoanode of DSC. S: ground state, S*: excited state, R/R⁻: redox couple

electrolyte (process 6), and third is the recombination of injected electrons with oxidized dyes (process 5) [25].

Process 2 is the fluorescence, usually in the nanosecond time scale for porphyrin dyes, while process 3 occurs in a femtosecond time scale, which is fast enough to compete with process 2. In principle, electron transfer to the electrolyte (process 6) can occur either at the interface between the nanocrystalline oxide and the electrolyte or in areas of the anode contact that are exposed to the electrolyte. In practice, the second

route can be suppressed by using a compact blocking layer of oxide deposited on the anode by spray pyrolysis or spin coating. To reduce the electron recombination process at the interface, charge separation at the interface can be enhanced by molecular engineering of the sensitizers. The structural features of the dye should match the requirements for current rectification. Unidirectional electron flow from the electrolyte through the junction and into the oxide results from photo-excitation of the sensitizer. The reverse charge flow, i.e., recapture of electrons by the electrolyte can be impaired by judicious design of the sensitizer. The latter should form a tightly packed insulating monolayer to block the dark current. If dye molecules have long side chains, when it adsorbed on TiO_2 surface, the long chains will expand in the electrolyte and form a blocking layer of electrolyte, as shown in Fig. 12.3. Thus, high charge collection in the electrode will be expected.

The gain in the open-circuit voltage (V_{OC}) can be calculated from the following equation,

$$V_{OC} = \frac{nkT}{q} \ln\left(\frac{J_{sc}}{J_0}\right) = \frac{nkT}{q} \ln\left(\frac{I_{sc}}{I_0}\right) = 0.059nlg \frac{I_{sc}}{I_0}$$

where n is the ideality factor whose value is between 1 and 2 for the DSC and I_0 is the saturation current (A), where, J_0 , q , k , and T stands for photogenerated current density, electronic charge, Boltzmann's constant, and operating temperature of the organic solar cell. The kT/q term is the thermal voltage at 300 K ($=0.02586$ V), J_{sc} the short circuit current density (A/cm^2), and I_{sc} = short circuit current (the current at $V = 0$) and I_0 the saturation current. Thus, for each order of magnitude decrease in the dark current, the gain in V_{OC} would be 59 mV at room temperature. Work in this direction is needed to raise the efficiency of DSC significantly over the 15% limit with the currently employed redox electrolytes. DSCs efficiency varies with light harvesting ability and loss-in-potential, which is a term used to express the drive energy loss when electron transfer from a higher level to lower level. As shown in Fig. 12.4 [79], when the absorption onset exceeds 700 nm, the potential loss will domain the overall conversion efficiency. While if the loss-in-potential is reduced to 0.2 eV, and absorption onset reaches to 1110 nm, the power conversion efficiency can reach a maximum of 25.6%. However, alternatives to

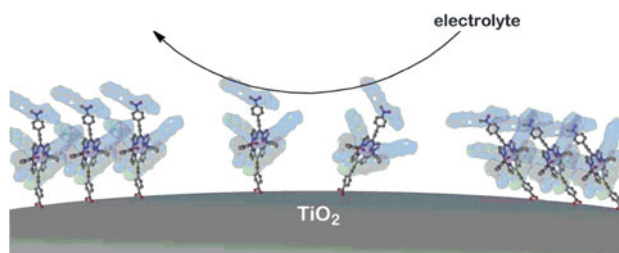


Fig. 12.3 Long alkoxy/alkyl chains enveloped with porphyrin cores on the TiO_2 surface. The colored surfaces represent the long alkoxy/alkyl chains. (Reproduced with permission from C-L Wang et al. [86] Copyright (2012) Royal Society Chemistry)

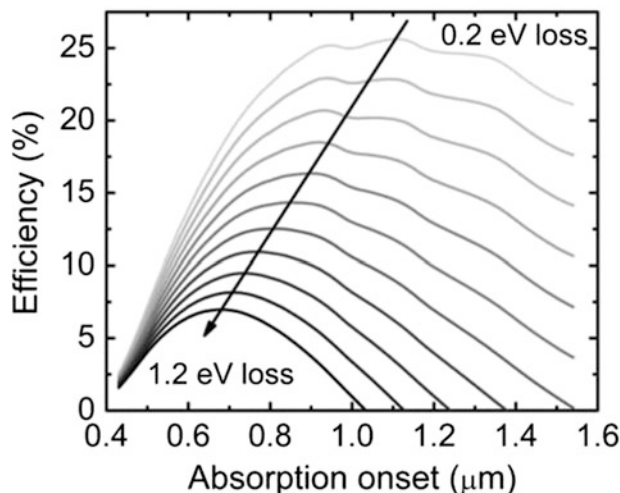


Fig. 12.4 Estimated efficiency of solar cell versus absorption onset and loss in dye-sensitized solar cells. (Reproduced with permission from Snaith [79] Copyright (2009) John Wiley and Sons)

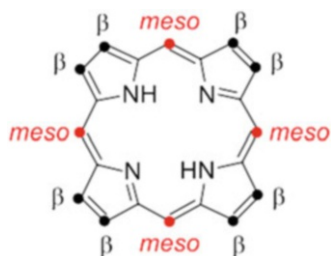
TiO₂ may need to allow electron transfer from lower bandgap sensitizers. In current DSCs, the loss-in-potential is around 0.8 eV, so the peak efficiency absorption onset is around 800 nm.

The ideal dyes for DSC applications should fulfill several essential characteristics. (1) The spectra of dyes should cover the whole visible region and part of the near-infrared region. This is because the visible region and near-infrared region accounts for ~44% and ~37% of the whole solar radiation energy, respectively. (2) The lowest unoccupied molecular orbital (LUMO) of the dye should be sufficiently higher than the conduction band edge of TiO₂. There is still debate about the minimum driving force for sufficient electron injection. Nonetheless, Kohjiro Hara and coworkers have reported that the energy gap of 0.2 eV should be sufficient for effective electron injection [43]. Electronic coupling between LUMO and TiO₂ nanoparticles is also crucial for electron injection, which is mediated by anchoring groups. In this regard, carboxylate is the most widely used anchoring groups. (3) The HOMO (highest occupied molecular orbital) of the dye should be sufficiently lower than the redox potential of the electrolyte or the hole conductor so that the dye can be regenerated efficiently. (4) The dye should be elaborately designed to suppress the unfavorable energy/charge transfer pathways such as dye aggregation and charge recombination [13, 72, 87]. (5) To obtain 20 years of cell life, the dye should be stable enough to undergo 10⁸ turnover cycles [23].

12.1.2 Characteristics of Porphyrin Dyes

The porphyrin is one class of tetrapyrrole compounds. Its core structure is shown in Fig. 12.5. The porphyrin ring has two different sites for functionalization, i.e., eight

Fig. 12.5 Active sites for functionalization on a porphyrin ring



β -positions and four *meso*-positions. In general, *meso*-positions are the most reactive sites in all types of reactions. The relative reactivities of the β - and *meso*-positions can be qualitatively explained by the frontier orbital theory. In this model, the coefficients of the frontier orbitals are used as the indices for the relative reactivities of individual reaction centers. Theoretical calculations reveal that two frontier orbitals exhibit maximum coefficients on the *meso*-positions [19]. Based on their easy accessibility, researchers have focused on *meso*-functionalized porphyrin dyes. After decades of development, both β - and *meso*-positions can undergo nearly all types of reactions such as oxidations, reductions, intramolecular and intermolecular cycloadditions, electrophilic substitution, and nucleophilic reactions. The discussion of these typical reactions is out of the scope of this chapter, and readers are referred to two reviews of Mathias O. Senge [34, 76]. Instead, this chapter will outline C-C and C-N cross-couplings in Sect. 12.3.3 because of their importance in the synthesis of push-pull porphyrin dyes, which is the state-of-the-art structural model in DSCs.

Porphyrins possess two characteristic absorption bands in the visible region [D_{4h} symmetry]. The intense band locating at 400–450 nm is called B band or the Soret band; the moderate ones at 500–650 nm are Q bands. Generally, the molar extinction coefficient of B band is several $10^5 \text{ mol}^{-1} \text{ cm}^{-1}$; the intensity of Q bands is ~ 10 times weaker than B bands. But as shown in Fig. 12.6, Q bands are still comparable to organic dyes and much stronger than ruthenium (Ru) dyes. This is meaningful from points of lowering the cost and raising the cell performances. Inorganic or Ru dyes-based DSCs, a $\sim 10 \mu\text{m}$ -thick transparent TiO_2 film, are required for saturated absorption; while it can be reduced to $\sim 2 \mu\text{m}$ for porphyrins-based cells because of their strong absorption in the visible region. Furthermore, studies on the effect of TiO_2 electrodes have revealed that thinner TiO_2 films are good for higher V_{OC} [38, 83].

Earlier studies have established that the absorption spectra of metalloporphyrins can be tuned by central metal ions. In fact, nearly all metals on the periodic table can be coordinated to the porphyrin ligand. This provides a wide room for researchers to tune porphyrin's optical properties. Unfortunately, only free base and Zn (II) porphyrins have shown competitive photovoltaic performances [5, 54, 66].

The inferior performance of other metalloporphyrins origins from their much shorter singlet excited-state lifetimes. The decay kinetics of excited states has a significant effect on electron injection, and it strongly depends on the nature of the central metal ions in the case of porphyrins [14]. Generally, free base and zinc [Zn(II)] porphyrins have ns scaled singlet excited-state lifetimes [14], which is

Fig. 12.6 Absorption spectra of typical a porphyrin dye, a ruthenium dye, and an organic dye

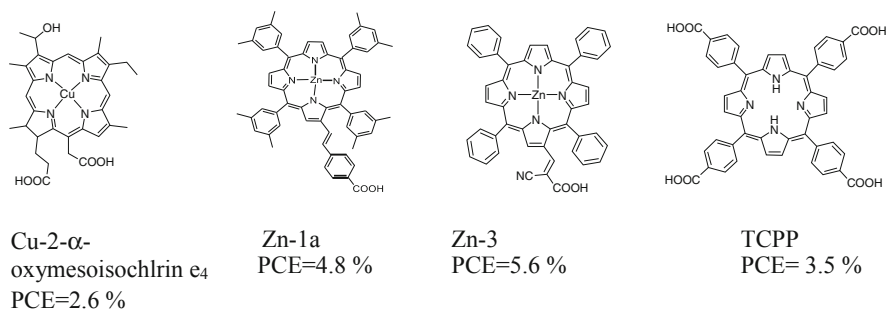
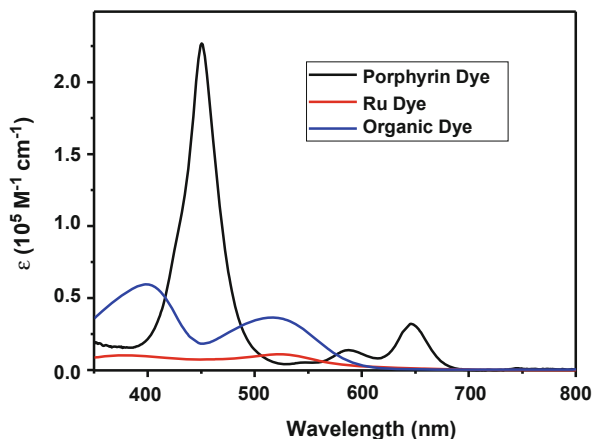


Fig. 12.7 Four representative porphyrin dyes from early studies and their energy conversion efficiency

long enough for effective electron injection (in ps scale). Other metalloporphyrins such as palladium [Pd(II)], copper [Cu(II)], and nickel [Ni(II)] exhibit much shorter-lived excited state (sub-ps to ps) because of strong interactions between porphyrin ligands and metal ions.

12.1.3 Porphyrins for DSCs

12.1.3.1 Discovery of Porphyrin Dyes for DSCs

Early porphyrin dyes were mainly based on the β -functionalized *meso*-tetraarylporphyrins and natural porphyrin derivatives [12, 41, 68, 84]. Several typical porphyrin dyes of this stage are shown in Fig. 12.7. In spite of their broad absorption in the visible region, these porphyrin dyes showed no competitive performance as compared to ruthenium dyes. The relatively low efficiency of these porphyrin dyes is

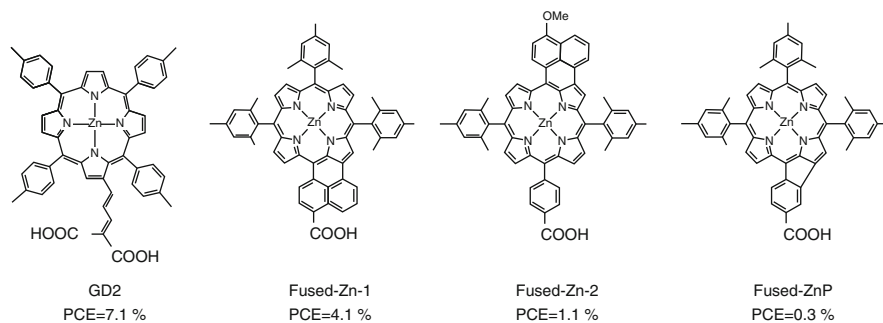


Fig. 12.8 Four representative β -functionalized porphyrins dyes and their energy conversion efficiency

ascribed to their strong dye aggregations on the TiO_2 surface and fast charge recombination at the TiO_2 /electrolyte interface.

In the late 2000s, the research of porphyrin dyes fell into two categories. On the one hand, works on β -functionalized porphyrins were continued. To get red-shifted absorption spectra, David L. Officer and co-workers further extended the π system in the β -positions, and an impressive PCE of 7.1% was obtained by dye GD2 (Fig. 12.8) [6]. Inspired by this work, Imahori group reported several fused porphyrin dyes (Fig. 12.8) [26, 27, 81]. The extended π system and lowered symmetry indeed caused significant red-shifted absorption spectra for these fused dyes. But their efficiencies were limited to 0.3–4.1% because of severe dye aggregation and/or too much low LUMOs. On the other hand, comprehensive studies were focused on the fundamental understandings of *meso*-functionalized porphyrin dyes such as substitutions on *meso*-phenyl groups [18, 36], substitution position of the carboxyl group on phenyl groups [73], spacers between porphyrin rings and anchoring groups [16, 56, 57, 73]. Based on these exhaustive works, several basic guidelines for designing *meso*-functionalized porphyrin dyes can be obtained. Those include (1) substitution at *ortho* positions of *meso*-phenyl groups could induce larger steric repulsion between porphyrin rings and phenyl rings and thereby hamper dye aggregations, (2) the carboxyl groups attached at the *para* positions of the phenyl groups are more favorable for both dye coverage and retarding the charge recombination between electrons in TiO_2 and oxidized dyes, (3) adding an ethynyl group between porphyrin ring and the spacers at the anchoring end is suggested, and (4) long alkyl/alkoxy chains should be introduced to the peripheral groups to retard the charge recombination between electrons in the TiO_2 and electron acceptors in the electrolyte.

Promoted by the development of palladium (Pd)-catalyzed cross-couplings, porphyrin dyes with push-pull structures were also studied in the late 2000s. This type of dyes consists of an electron donor group and an electron-withdrawing group. The interest in push-pull type porphyrin dyes is because of their broad and red-shifted absorption spectra as well as the long-lived charge-separated state. In 2009, Diao and co-workers reported a push-pull porphyrin dye YD1 [48]. As shown in Fig. 12.9, YD1 incorporated 3,5-di-*tert*butylphenyl groups to 5,15-*meso*-positions to suppress

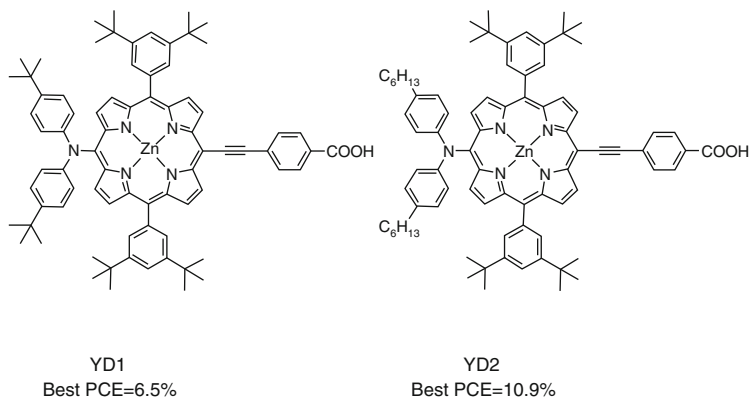


Fig. 12.9 Structures of YD1 and YD2 and their energy conversion efficiency

the dye aggregation, and a bis(4-(*tert*-butyl)phenyl)amine as an electron donor was attached to 20-*meso*-positions. In comparison with other dyes, YD1 outperformed those β -functionalized porphyrin dyes with a conversion efficiency of 6.1%. To improve the stability, authors subsequently replaced the *tert*-butyl groups on the donor with *n*-hexyl groups, obtaining dye YD2 (Fig. 12.9) [58]. Comparing to YD1, YD2 exhibited slightly higher PCE (6.8% vs. 6.5%). In 2010, the performance of YD2 was further improved to nearly 11% by cooperation with Michael Grätzel group [3]. This is the first porphyrin dye achieving a PCE >10%.

Inspired by the success of YD2, push-pull structured porphyrins have dominated the studies on porphyrin dyes since 2010, and dozens of dyes with efficiencies >10% have been reported [82]. It can be concluded that nearly all these highly efficient porphyrin dyes containing two *ortho* long alkyloxy groups at 5,15-*meso*-phenyl groups. Diao and co-workers proposed that the long *ortho* alkyloxy chains could wrap the porphyrin ring in a shape that prevents dye aggregation effectively and forms a blocking layer on the TiO₂ surface [10, 86]. As a result, dye YD2-*o*-C8 exhibited higher PCE than the counterpart YD2 (11.9% vs. 8.4%) in a cobalt-based electrolyte [90]. After co-sensitization with the organic dye Y123, YD2-*o*-C8 achieved an unprecedented PCE of 12.3% [90], surpassing the best ruthenium dyes and organic dyes at the same time. Since then, the long *ortho* alkyloxy chains have seemed to be the “standard” equipment for porphyrin dyes. Another structural improvement for porphyrin dyes is proposed by Grätzel and co-workers in 2014. As shown in the molecular structures of dyes SM315 and GY50 (Fig. 12.10) [63, 91], an electron acceptor 2,1,3-benzothiadiazole (BTD) was introduced as a spacer between porphyrin ring and benzoic acid forming a D- π -A-A structure. This modification induces dual effects which are favorable for light harvesting: the absorption onset is red-shifted and the valley between the Soret band and the Q bands is filled because of the splitting of the B band. As a result, SM315 achieved a 13% PCE without co-sensitization. Grätzel et al. pointed out that the phenyl group between BTD and the carboxyl anchoring group is essential for cell performance [91]. The electron lifetime was decreased significantly for the

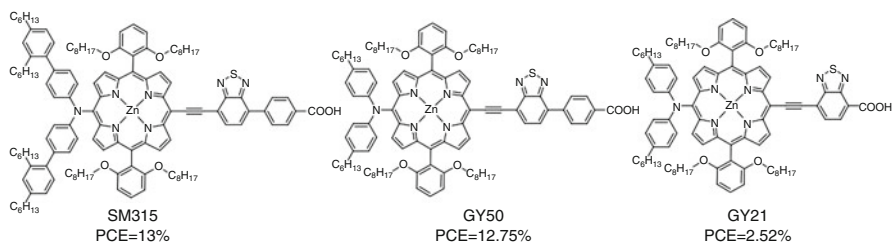


Fig. 12.10 Molecular structures of SM315, GY50, and GY21

counterpart dye without the phenyl group (GY21 in Fig. 12.10), resulting more than five times lower PCE in a cobalt-based electrolyte.

12.1.3.2 Challenges for Porphyrin Dyes

Inefficient Photon Capture

The match between the absorption spectrum of the dye and the solar spectrum is essential to efficient power conversion. It can be seen from Fig. 12.11 that porphyrin dyes have weak or no absorption in the near-infrared region. Besides, there is a valley between the Soret band and the Q bands. Thus, numerous efforts have been devoted to the design and synthesis of dye with broad light absorption.

As shown in Fig. 12.12c, the Q bands and the B band arise from the transitions from the ground state S_0 to the excited states S_1 and S_2 , respectively. Furthermore, S_1 and S_2 are given as results of the configuration interaction of four excited states generated by the transitions between two HOMOs (as c_1 and c_2 in Fig. 12.12b) and two LUMOs (b_1 and b_2 in Fig. 12.12b). Here, we use b_1c_1 to denote the singlet state produced by the transition $b_1 \rightarrow c_1$, and the rest three can be done in the same manner. Among these four excited states, b_1c_1 and b_2c_2 have similar symmetry and are y -polarized. Also, b_1c_2 have similar symmetry to b_2c_1 and both are x -polarized. Thus, the results of the configuration interaction will be represented by:

$$B_y^0 = \frac{1}{\sqrt{2}}(b_1c_1 + b_2c_2); B_x^0 = \frac{1}{\sqrt{2}}(b_1c_2 + b_2c_1)$$

$$Q_y^0 = \frac{1}{\sqrt{2}}(b_1c_1 - b_2c_2); Q_x^0 = \frac{1}{\sqrt{2}}(b_1c_2 - b_2c_1)$$

where B_y and B_x represent the constructive effect of the transition dipoles giving rise to the strongly allowed B band. In the case of Zn(II) porphyrins who has D_{4h} symmetry, x and y components are equivalent. Similarly, Q_y and Q_x represent the destructive effect of the transition dipoles giving rise to the Q bands. It may be noted that the value of $(b_1c_1 - b_2c_2)$ and $(b_1c_2 - b_2c_1)$ should be equal to zero because b_1 and b_2 , as well as c_1 and c_2 , are degenerate. This means that Q bands are theoretically forbidden.

Fig. 12.11 Absorption spectrum of YD2-*o*-C8 and AM1.5 solar spectrum
 AM1.5 solar spectrum
 [~1000 W/m²]

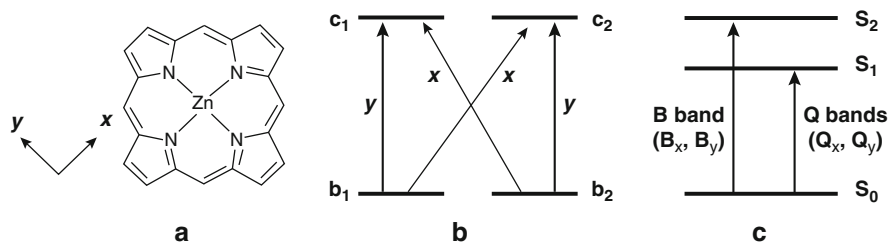
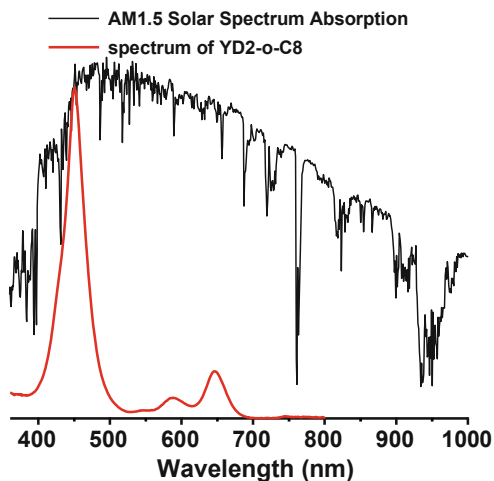


Fig. 12.12 (a) *x* and *y* directions of the Zn(II) porphyrin; (b) HOMOs and LUMOs of Zn(II) porphyrins, the transitions are also included; (c) Energy states of Zn(II) porphyrins

But the molecular vibrations within the porphyrin ring marginally lift the degeneracy of b_1 and b_2 so that Q bands become weakly allowed. Their weakness allows one to identify two vibrational peaks, i.e., $Q(0,0)$ and $Q(0,1)$, as shown in Fig. 12.13.

Based on the electronic fundamentals of porphyrins absorption, B and Q bands could be broadened and red-shifted through structural modifications which cause the splitting of frontier orbitals, namely, elongating the π system and reducing the symmetry.

1. **Fused porphyrins.** In 2007, Imahori and co-workers reported the naphthyl-fused porphyrin dye fused-Zn-1 (the molecular structure is in Fig. 12.8) [81]. This unsymmetrically π -elongated porphyrin exhibited a 130 nm red-shift comparing with the unfused counterpart Zn-1, and the splitting of B band was also observed. As a result, dye fused-Zn-1 achieved a significantly higher PCE than Zn-1 (4.1% vs. 2.8%). Other bigger aromatic groups such as anthracene [2], perylene [59], porphyrin ring [60] were also fused to porphyrin rings, but none of them have shown PCE > 1% because of their too low LUMOs. Thus, fusing groups should be chosen with cautions to avoid inefficient electron injection.

Fig. 12.13 Absorption spectrum of zinc tetraphenylporphyrin (ZnTPP)

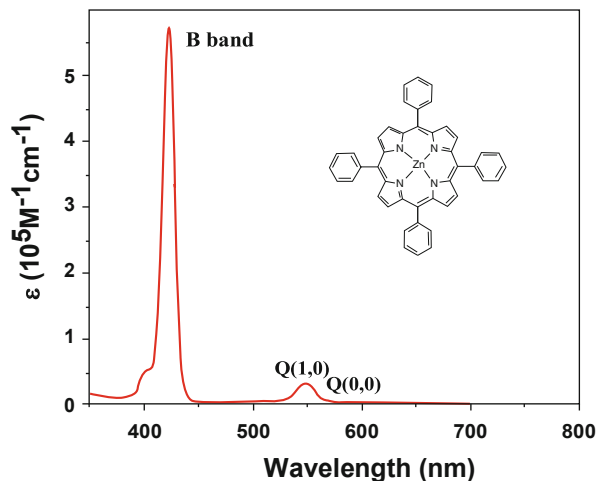
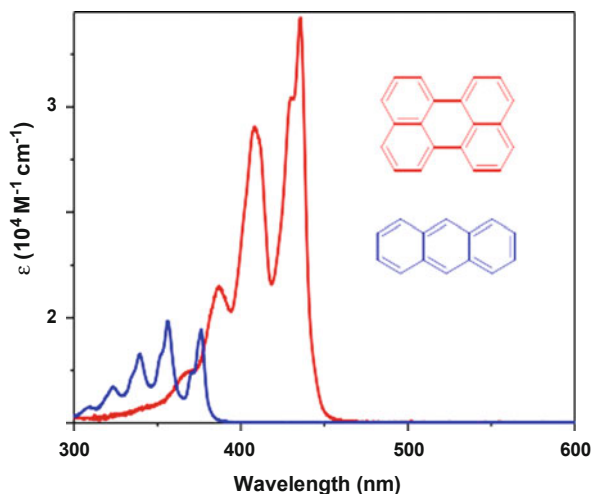
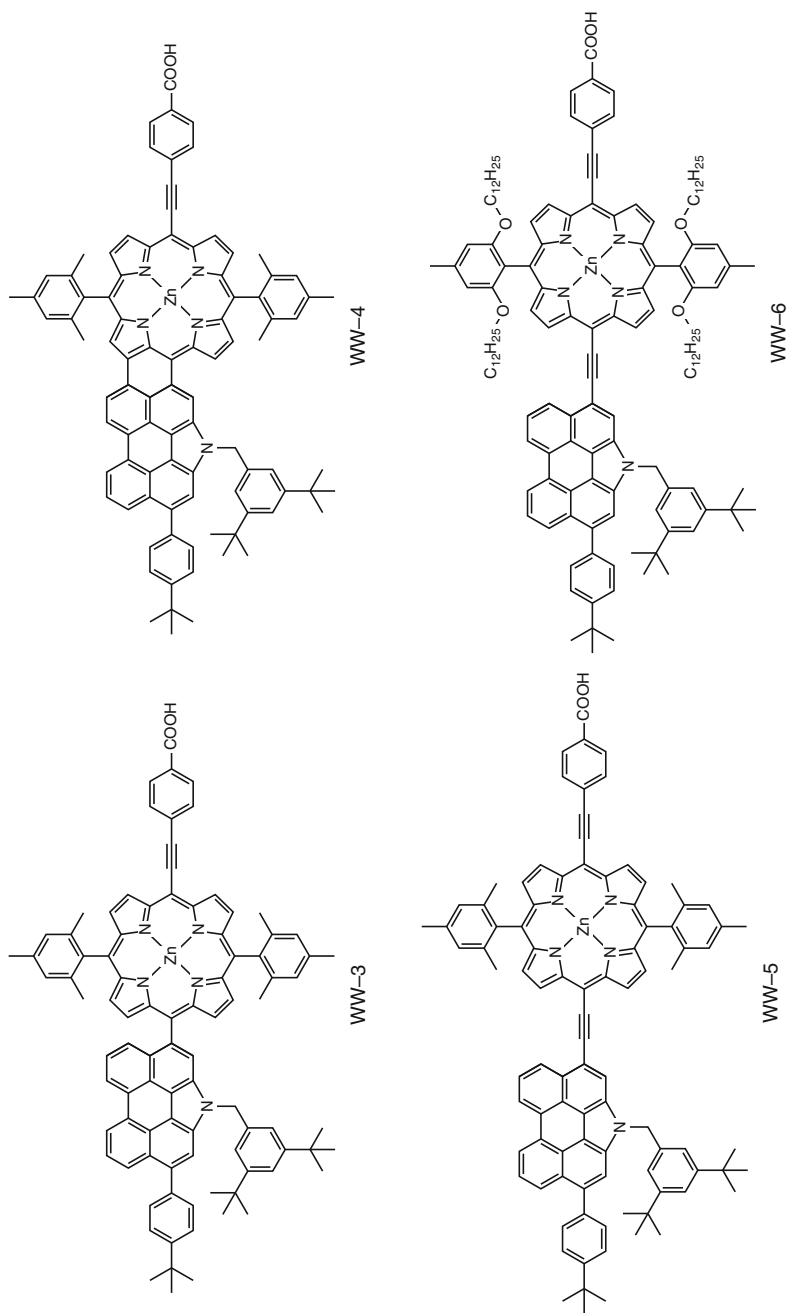


Fig. 12.14 Absorption spectra of perylene and anthracene



2. **Introducing auxiliary chromophore.** Aromatic groups with extended π systems such as perylene and anthracene usually have characteristic absorption bands at around 400 nm (see Fig. 12.14). Thus, attachment of these chromophores to porphyrin rings in a conjugated mode (i.e., through ethynyl linker) may result in enhanced light harvesting ability [54, 59, 60, 78, 85]. Wu and co-workers reported a series of porphyrins dyes with N-annulated perylene was attached to the porphyrin through direct linkage (WW-3), fusing (WW-4), or ethynyl linker (WW-5, WW-6) [59]. The molecular structures of these dyes are depicted in Fig. 12.15. As compared to WW-3, the strong coupling between the perylene

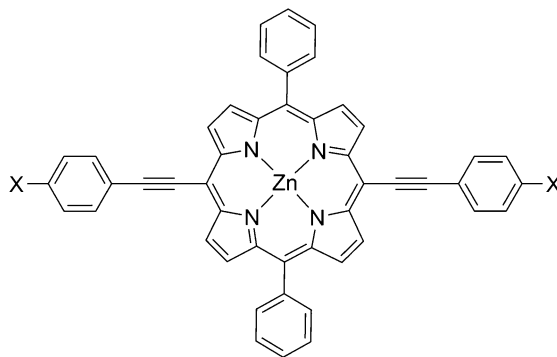


group and the porphyrin ring in WW-5 and WW-6 gives rise to the red-shifted Q bands and significantly broadened B band. One drawback of this strategy is the enhanced dye aggregation caused by the elongated π system.

- Multiple electron donors.** The symmetry has a strong effect on the absorption spectra of porphyrins. A typical example is the free base porphyrin that has reduced symmetry comparing with Zn(II) porphyrins. With the same peripheral substituents, the former one has significantly broadened and red-shifted Q bands [94]. To reduce the symmetry of porphyrin dyes, the strategy adopted by Hiroshi Imahori and co-workers is to introduce two diarylamino groups into the *meso*-positions in a low-symmetry manner [37, 45]. As expected, these dyes exhibited enhanced light-harvesting in the visible region. Moreover, the best dye ZnPBAT showed a PCE of 10.1% [45], which was higher than the reference dye YD2.
- Enhancing the donor/acceptor strength.** In a push-pull porphyrin, the degeneracy of HOMOs and LUMOs will be affected by the strength of the donor and acceptor, respectively [47]. By using the model shown in Fig. 12.16, Lecours et al. found that the energy gap between the HOMO-1 (the *au*-orbital) and HOMO (*bu* or *b1u* orbital) decreases from 0.269 eV to 0.101 eV as the substituent X is varied from NMe_2 to NO_2 ; on the other hand, the splitting of LUMO and LUMO+1 increases with the acceptor strength. Accordingly, Grätzel and co-workers designed dye SM315 (see Fig. 12.10) by inserting a strong electron acceptor BTB between the porphyrin and the benzoic acid and achieved a PCE up to 13% because of its panchromatic absorption in the visible region [63].

Solar cells with broad light absorption can also be achieved by co-sensitization with complementary dyes [17, 29, 46]. As compared to the difficulties in design and synthesis of panchromatic porphyrin dyes, co-sensitization seems to be a convenient method through the combination of two or more dyes sensitized on semiconductor films together. In addition, the dye aggregation

Fig. 12.16 Model used for the study of effects of electron/acceptor strength on the porphyrin's frontier orbitals



of porphyrin dyes could also be reduced by co-sensitization [49]. Another two considerations should be taken into accounts except for the complementary spectra. Firstly, the co-sensitizers should have a high molar extinction coefficient. In a co-sensitization manner, both/all dyes would have reduced dye-loadings comparing to single dye-sensitized cells. Thus, co-sensitizers should have intense absorption to obtain saturated light-harvesting. Secondly, the co-sensitizers itself should have a strong ability to suppress the charge recombination. By reviewing the literature concerning co-sensitizations, it is found that the co-sensitized cells generally exhibit a V_{OC} between the single dye-sensitized cells [46]. In this regard, the cell based on the co-sensitizer itself should have higher V_{OC} than the porphyrin-based cell.

Severe Aggregation

Because of their planar structure and rich π electrons, porphyrins have a strong tendency to form aggregates in solutions or on semiconductor films. For DSCs applications, the presence of dye aggregates may results in serious deterioration in electron injection due to self-quenching of photoexcited state. In other words, aggregation is a critical factor that should be well controlled. Several methods have been reported to tackle this problem, including co-sensitization with small molecules [15], growing an ultrathin transparent metal oxide coating [62]. The following section will focus on the topic of how to suppress dye aggregation via elaborate molecular design.

Generally, alkyl/alkoxy chains have been introduced to suppress the dye aggregation because they can retard charge recombination and enhance long-term stability simultaneously. Diao and co-workers have conducted exhaustive studies on the effect of alkyl/alkoxy chains appended to the *meso*-phenyl groups [10, 86]. The results revealed that the four *ortho* dodecyloxy groups at the two *meso*-phenyl groups have the strongest ability to reduce the dye aggregation [86]. For dyes with extended π systems, especially those have two ethynyl units at *meso*-positions [35, 52], more severe aggregation was observed despite the already present alkyl/alkoxy chains on the porphyrin ring and/or electron donor. Thus, extra chains are suggested to place on the π unit. But factors such as numbers, length, and positions should be taken under deliberation to practically exploit the steric hindrance of alkyl/alkoxy chains. Otherwise, extra chains may induce more aggregates because of the van der Waals interactions between the chains [31, 51]. Dye aggregates can also be reduced by using electron donors with nonplanar configurations, such as diarylamine [35], phenothiazine [89]. For a comprehensive review of electron donors, one can refer to the articles on organic dyes by Kim [42], Chen [53], and Giribabu [39].

Poor Stability

Porphyrins themselves have good thermal, light, and chemical stabilities. However, the binding between the carboxylic anchoring group and TiO_2 surface is relatively

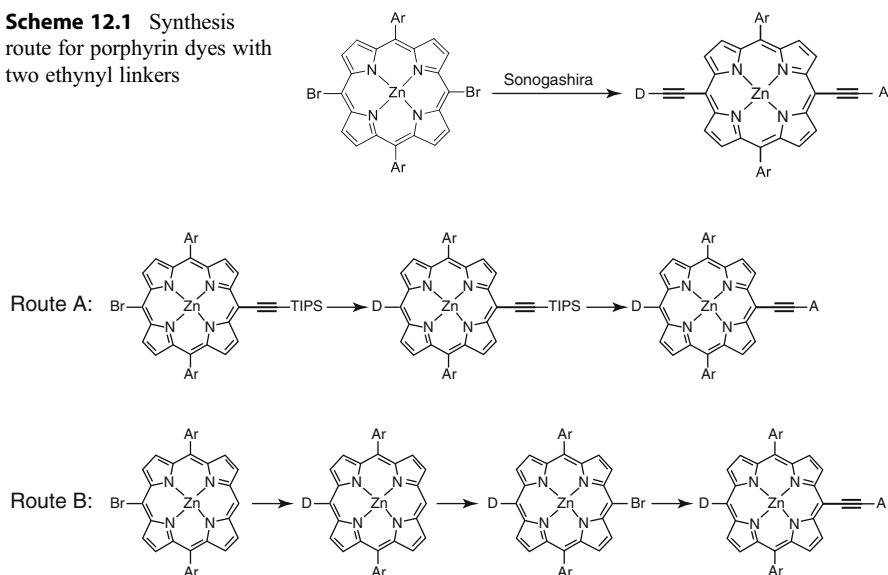
weak in the presence of trace water, resulting in desorption of dyes. To obtain water-stable binding, multiple carboxylic acid groups can be introduced to porphyrin dye. Alternative anchoring groups with a superior TiO_2 binding capability to a carboxylic acid group were also developed. The detailed discussion on anchoring groups will be given in Sect. 12.2.

12.1.4 Synthetic Methods for Porphyrin Dyes

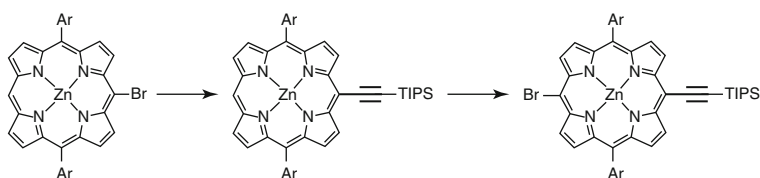
In principle, there are three different synthetic approaches to obtain unsymmetrical porphyrins: (a) mixed condensations involving pyrrole and dipyrrole chemistry, (b) total synthesis via bilanes, and (c) subsequent functionalization by organolithium reactions or transition metal-catalyzed coupling reactions [75]. For the first method, it is frequently limited by unsatisfied yields and/or various isomers [55]. Moreover, the acidic conditions involved in the condensation reactions are often not compatible with some functional groups. Therefore, bridges between the porphyrin ring and function groups (e.g., carboxyl anchoring group) are confined to aromatic groups such as benzene and thiophene, resulting in insufficient electronic coupling for charge transfer. In the total synthesis route, porphyrins bearing four different *meso*-substituents are accessible. Nevertheless, the acid-catalyzed scrambling in combination with the necessity of high temperature has limited its application. The step-wise functionalization of more available reagents, such as 5,15-diarylporphyrins, could lead to more appreciable results and the reactions are compatible with more functional groups. For porphyrin dyes, the involved step-wise functionalizations are mainly C-N and C-C couplings for linkages of the electron donor and acceptor. It has been demonstrated that electronic coupling is essential for electron injection. Thus nearly all efficient porphyrin dyes possess an ethynyl linker between the porphyrin ring and the electron acceptor. The linkage between the electron donor and the porphyrin ring is more various. It can be realized by triple bond or direct C-C/C-N bonding. In this sense, the synthesis routes for push-pull porphyrins are more dependent on the linking mode of the donor.

For the porphyrin dye with two ethynyl linkers, it can be obtained via the route in Scheme 12.1, where Sonogashira cross-couplings are the main protocols. To synthesize porphyrin dyes with direct C-C/C-N bonding mode, two routes can be followed (Scheme 12.2). The difference lies in the role of the porphyrin intermediates in the final Sonogashira cross-couplings. In route A, the ethynyl group is positioned at the porphyrin ring. Therefore, another two more steps are needed to obtain the starting material 5-bromo-15-(triisopropylsilyl)ethynyl-10,20-diarylporphyrin (Scheme 12.3). In contrast, the route B seems to be more efficient as the starting material is the more accessible 5-bromo-10,20-diarylporphyrin. It can be seen from Scheme 12.1 and Scheme 12.2 that all three routes start with a brominated porphyrin. So, we will first describe the bromination of porphyrins in the following sections. Then, protocols for further C-N and C-C couplings will be outlined.

Scheme 12.1 Synthesis route for porphyrin dyes with two ethynyl linkers



Scheme 12.2 Synthesis routes for porphyrin dyes with one ethynyl linker

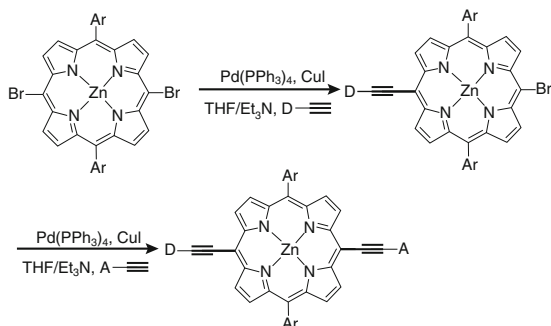


Scheme 12.3 Synthesis route for 5-bromo-15-(triisopropylsilyl)ethynyl-10,20-diarylporphyrin

12.1.4.1 Bromination of Porphyrins

Similar to the situations in other reactions, bromination exclusively happens at *meso*-positions unless all four *meso*-positions are substituted or electron-withdrawing groups are presented at *meso*-positions [8, 74]. The bromination of 5,15-diarylporphyrins is typically realized with N-bromosuccinimide (NBS) in methylene chloride (CH_2Cl_2) at 0 °C [71]. For 10,20-dibromo-5,15-diarylporphyrins, yields >90% can be obtained with 2 equivalents of NBS. After reducing the NBS content to 0.9–1.0 equivalent, the same method can also be used for the production of *meso*-monobrominated 5,15-diarylporphyrins. But the yields are usually reduced to ~60% because of the **co-existence** of 10,20-dibromo-5,15-diarylporphyrins and unreacted 5,15-diarylporphyrins. It was also noted that the *meso*-monobromination of 5,15-bis(3,5-di-*tert*-butylphenyl)porphyrin was made tedious by the difficulty of separating the reaction mixture [40].

Scheme 12.4 Synthesis protocols for porphyrin dyes with ethynyl groups at 10,20-positions



Sonogashira Cross-Couplings

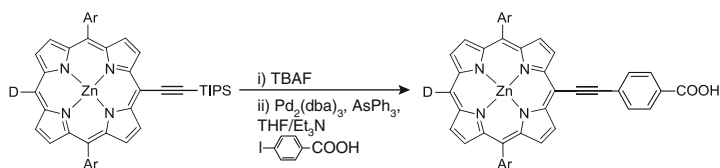
For porphyrin dyes like LD14, XW-4, and WW-5, there are two ethynyl groups at the 10,20-positions. As shown in Scheme 12.4, these dyes can be obtained via two sequential Sonogashira couplings using tetrakis(triphenylphosphine)palladium(0)/copper(I) iodide $[[\text{Pd}(\text{PPh}_3)_4]/\text{CuI}]$ catalytic system at 40–50 °C, and a relatively long reaction time (~20 h) is necessary. The dibrominated porphyrins are firstly subjected to the coupling with an ethynylated donor. Yields between 17–35% have been reported for this step [10, 88]. After chromatographic separation on silica gel, the donor-modified intermediate is coupled to an ethynylated acceptor through a second Sonogashira coupling, and the yield of this step is much higher (~65%).

Ethynylated porphyrins can also be synthesized from the reaction between monobrominated porphyrin and (triisopropylsilyl)acetylene using the same catalytic system and solvents. In this reaction, the temperature can be elevated to the boiling point, and thus can be completed in a much shorter time (~4 h). But in the following Sonogashira coupling with halogenated groups (e.g., 4-iodobenzoic acid, see Scheme 12.5), the catalytic system should be replaced with tris(dibenzylideneacetone)dipalladium(0) / triphenylarsine $[\text{Pd}_2(\text{dba})_3/\text{AsPh}_3]$ to avoid the homogenous coupling of the ethynylated porphyrin in copper(I) iodide (CuI) system.

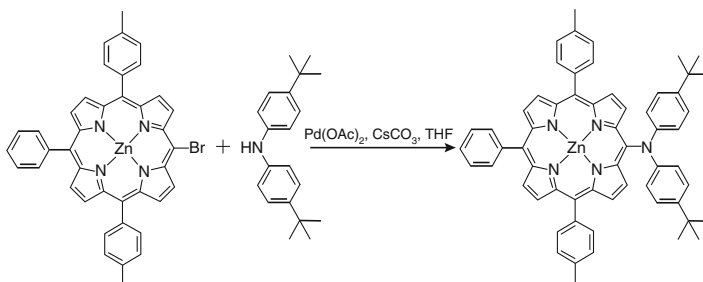
12.1.4.2 C-N Cross-Couplings

In 2017, Mathias O. Senge and co-workers optimized the Buchwald-Hartwig amination of monobrominated porphyrin by using bis(4-*tert*-butylphenyl)amine as substrate [64]. In this study, best results were obtained when using palladium(II) acetate $[\text{Pd}(\text{OAc})_2]$, 2,2'-bis(diphenylphosphino)-1,1'-binaphthyl [BINAP], and cesium carbonate $[\text{Cs}_2\text{CO}_3]$ in tetrahydrofuran (THF, Scheme 12.6). It was noted that in all cases a significant amount of debrominated starting material was observed. Further optimization was then conducted by stirring the base and the amine for 30 min under reaction conditions before the addition of other reagents.

Beside the Pd-catalyzed Buchwald-Hartwig amination, the C-N bond can also be formed through the iodine(III)-mediated nucleophilic substitution reactions (Scheme 12.7) [37, 77]. The yield was much lower (~20%) than the Buchwald-Hartwig coupling. But this approach has advantages as the reactions can be performed in mild conditions (air, room temperature) and short reaction time (~15 min).



Scheme 12.5 Reaction conditions for the Sonogashira cross-coupling of ethynylated porphyrins



Scheme 12.6 Optimized reaction conditions for the Buchwald-Hartwig amination

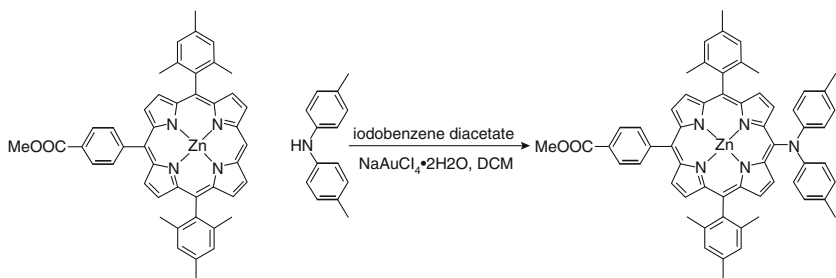
Moreover, many bulky amines such as bis(9,9-dihexyl-9H-fluorene-7-yl)amine can also be attached to the porphyrin ring under this protocol [50], while no desired product was obtained under Buchwald-Hartwig conditions.

Suzuki-Miyaura Cross-Couplings

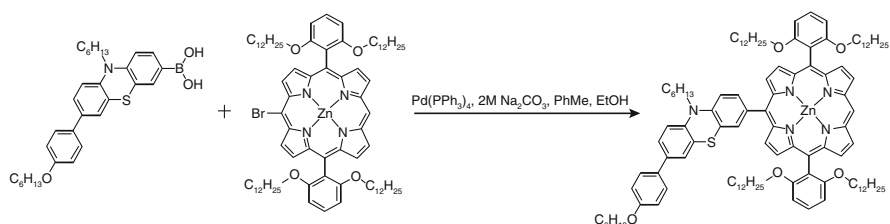
In 2015, Xie and co-workers designed and synthesized a porphyrin dye XW9 [89]. In this dye, the electron donor phenothiazine was introduced to the porphyrin ring via the Suzuki-Miyaura cross-coupling between the boronic acid and brominated porphyrin, as shown in Scheme 12.8. Suzuki-Miyaura cross-couplings can also be used to synthesize [59] porphyrins as a precursor. By using pinacolborane as the transmetallating agent, the *meso*-boronyl-diarylporphyrins can be synthesized from a brominated porphyrin in the presence of trimethylamine and bis(triphenylphosphine)palladium (II) dichloride (TEA/[Pd(PPh₃)₂Cl₂]) in 1,2-dichloroethane (C₂H₄Cl₂) at 85 °C for 1 h [92]. In the further cross-coupling reaction with halogenated groups, the *meso*-boronyl-diarylporphyrins can be transformed into the desired product in a mild yield [59].

12.2 Porphyrin Dyes with Different Anchoring Groups

One of the persistent challenges that need to be effectively addressed is the lack of thermal stability of DSCs. Despite the efficiencies of ~12% which have been reached under standard AM 1.5 conditions by iodide/triiodide (I⁻/I³⁻) or cobalt(II)/cobalt(III) [Co²⁺/Co³⁺]⁻ based liquid electrolytes, the stabilities under certain outdoor conditions



Scheme 12.7 An example for the iodine(III)-mediated C-N bonding



Scheme 12.8 Suzuki-Miyaura cross-coupling between the boronic acid and brominated porphyrin

have prevented DSCs from competing commercially [67]. There are several components that simultaneously determine the stability of DSCs under thermal stress. These components include the dye's molecular structure, the TiO₂ semiconductor/electrolyte interface, and the dye's proneness to degrade [1]. Moreover, the anchoring group plays one of the most crucial roles in maintaining the device performance under light exposure [11, 33, 80]. Aside from enabling the dye's bond to the semiconductor and facilitating the electron injection process, the anchoring group plays a central role in preventing dye desorption.

12.2.1 Carboxylic and Cyanoacetic Acids

The carboxylic acid anchor is one of the most widely used anchors in DSCs. In 2017, Chakraborty et al. employed a carboxyl anchor in three porphyrin dyes, LS-01, LS-11, and H2PE1 and investigated their thermal stabilities (Fig. 12.17) [95]. After 1000 h of irradiation, the H2PE1, LS-01, and LS-11 cells experienced a 31%, 54%, and 46% decrease in their power conversion efficiencies, respectively. The electron-donating group of LS-11 was shown to increase the overall cell efficiency while limiting long-term stability. In 2016, Krishna et al. utilized a cyanoacetic acid anchor

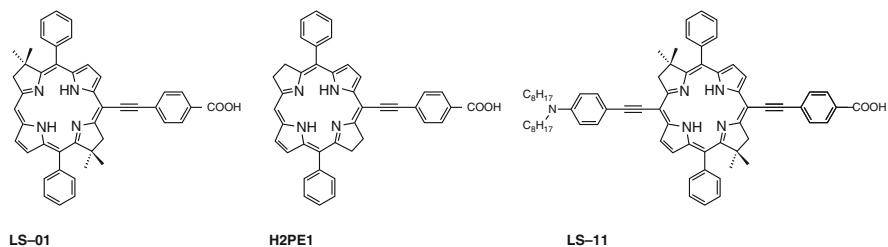


Fig. 12.17 Molecular structures of LS-01, LS-11, and H2PE1

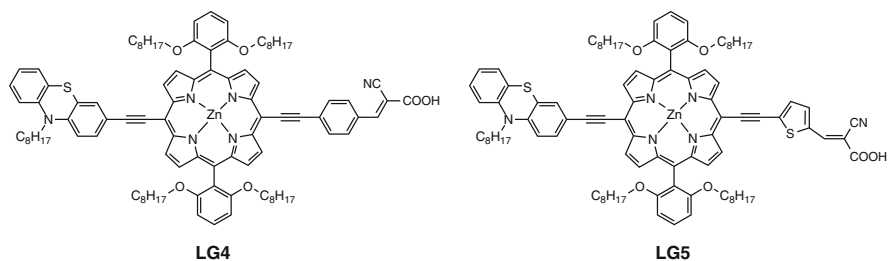


Fig. 12.18 Molecular structures of LG4 and LG5

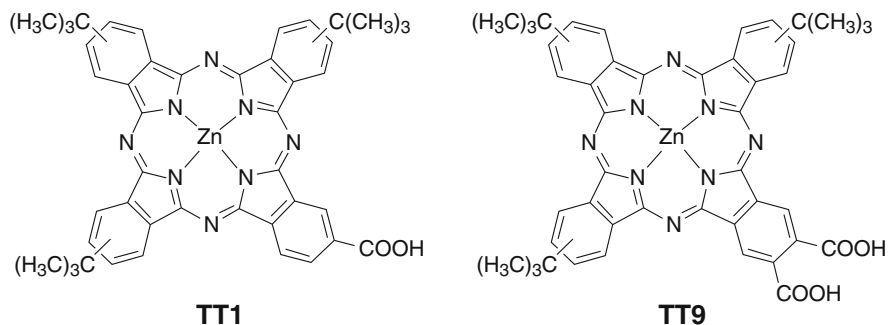


Fig. 12.19 Molecular structures of TT1 and TT9

in two D- π -A porphyrins, LG4 and LG5 (Fig. 12.18) [44]. Their thermal stabilities were assessed via thermogravimetric analysis and compared to a series of their carboxyl-anchored analogs. Porphyrins were found to withstand temperatures of up to 200 °C. LG5, which yielded the greatest efficiency, was found to retain 80% of its initial power conversion efficiency after 1000 h of irradiation in a low volatility electrolyte solution. Adding the number of carboxyl anchors is also found to be good

for stability. In 2011, Tomás Torres et al. reported an unsymmetrical zinc phthalocyanine (TT9) dye that consists of three tert-butyl and two carboxylic acid groups (Fig. 12.19) [21]. After being soaked in light at 60 °C, TT9 sensitized solar cell retained 80% of the initial efficiency. By contrast, the reference dye with only one carboxyl anchor (TT1) lost 50% of its initial value under the same conditions.

12.2.2 Phosphonic Acids

As compared to carboxylic acid anchors, phosphonate groups can provide much stronger anchoring stability. A comparison conducted by Grätzel et al. has shown that the adsorption strength of phosphonic acid was estimated to be approximately 80 times higher than that of the carboxylic acid and the desorption of phosphonated dye in the presence of water was negligible [70]. Unfortunately, phosphonated porphyrins generally exhibit lower IPCE than the carboxylated counterparts, resulting in **deteriorated** power conversion efficiency [4, 68]. The reasons may be the titled adsorption geometry of the phosphonate anchoring group, and/or the slower electron injection [4, 65].

12.2.3 Pyridyl Groups

After carboxylic acids, pyridyl groups may be the most widely studied anchors for porphyrin dyes. It was reported that the formation of coordinate bonds between the pyridine ring and the Lewis acid sites of the TiO₂ surface can provide efficient electron injection owing to good electron communication between them. In 2015, Chi-Lun Mai et al. assessed the performance of their pyridine-anchored MH3 (Fig. 12.20) porphyrin and compared its performance to its carboxyl-anchored YD2-*o*-C8 (Fig. 12.20) [61]. MH3 performed competitively and yielded a power conversion efficiency of 8.2%, similar to YD2-*o*-C8. The

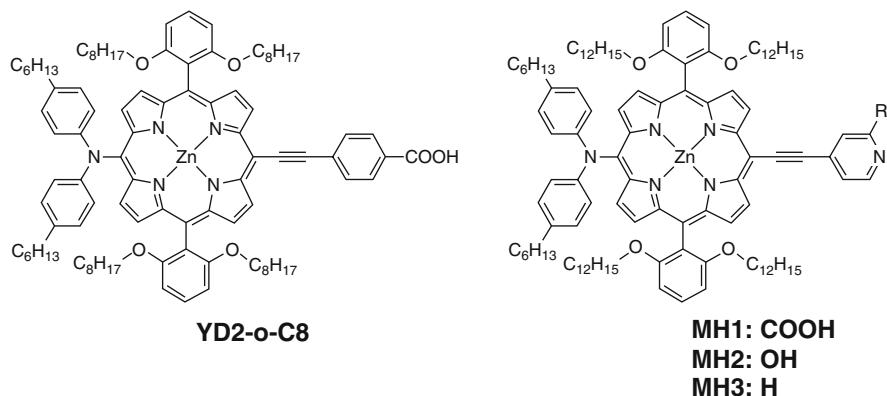


Fig. 12.20 Molecular structures of YD2-*o*-C8, MH-1, MH2, and MH3

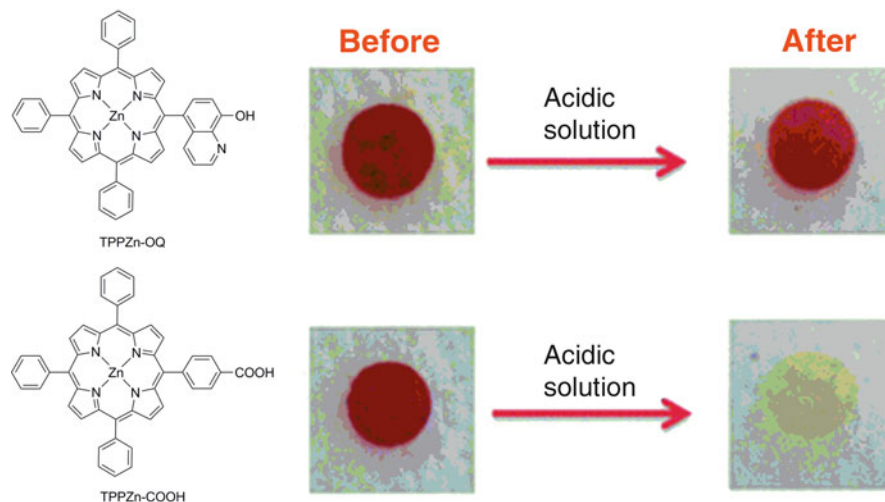


Fig. 12.21 Optical images of TPPZn-OQ and TPPZn-COOH coated TiO₂ nanoparticle films before and after immersion in a 28 mM acetic acid-acetonitrile solution at room temperature for 3 h. (Reproduced with permission from He et al. (2012) Copyright (2012) Royal Society Chemistry)

performances and stabilities of MH1 (Fig. 12.20) and MH2 (Fig. 12.20) were also investigated. Porphyrins MH1 and MH2 employed a 2-carboxypyridine and 2-hydroxypyridine anchor, respectively. Their photovoltaic performances were nearly identical to those of MH3. The long-term stability of each dye was assessed via an ionic-liquid based electrolyte and simulated AM 1.5 G (100 mW cm⁻²) at 60 °C. After 1000 h of irradiation, MH1 and MH2 retained 90% and 69% of their original efficiencies. The results were compared to the carboxyl-anchored porphyrin, YD2-*o*-C8, which retained 85% of its initial power conversion efficiency.

He et al. reported a porphyrin dye TPPZn-OQ using 8-hydroxyquinoline (OQ) as an anchoring group (Fig. 12.21) [28]. As evident from DFT calculations on a dinuclear model compound [Ti₂O₂(OH)₂(H₂O)₄]²⁺, both oxygen and nitrogen atoms on the OQ groups were bound to the titanium atoms. This anchoring mode made TPPZn-OQ more stable on the TiO₂ surface.

As shown in Fig. 12.21, the carboxyl analog, TPPZn-COOH, dissociated from the TiO₂ nanoparticle film after being immersed in an acetic acid solution (28 mM) for 3 h; whereas no obvious dissociation of the TPPZn-OQ sensitized film was observed.

12.2.4 Other Anchoring Groups

By replacing the carboxylic acid anchoring group in YD2-*o*-C8 with tropolone and hydroxamic acid (Fig. 12.22), Imahori and co-workers developed two durable porphyrins, YD2-*o*-C8T and YD2-*o*-C8HA [30, 32]. As implicated by

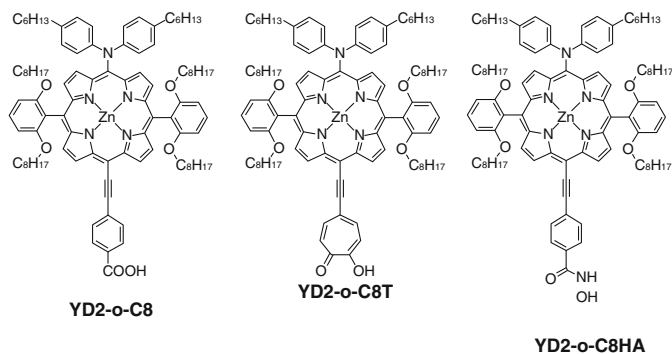


Fig. 12.22 Molecular structures of YD2-*o*-C8, YD2-*o*-C8T, and YD2-*o*-C8HA

desorption experiments in the acid or base solutions, both YD2-*o*-C8T and YD2-*o*-C8HA sensitized electrodes retained more than 90% absorbance in 8 h. Long-term stability of the cells based on YD2-*o*-C8T and YD2-*o*-C8HA were also evaluated under continuous white-light illumination (100 mW cm^{-2}) condition at 25°C . Inconsistent with the desorption experiments, long-term stability tests indicated the advantages of tropolone and hydroxamic acid anchoring groups in terms of long-term durability.

12.3 Summary

Solar energy has attracted much attention due to its abundant, clean, and sustainable properties. A solar cell is a device to convert solar energy into electricity. Crystalline silicon solar cells have higher efficiency and excellent stability compared to other photovoltaic technologies. However, they have high production costs due to the requirement of extremely pure silicon. Dye-sensitized solar cells have been widely regarded as next-generation solar cells for providing electricity at a lower cost with more versatility. Several types of porphyrin dyes have been investigated for DCSs by many groups. Porphyrins with an anchoring group attached to the β -position of porphyrin ring were found to have limited narrow band absorption. Porphyrin dyes with an anchoring group and an additional donor-acceptor group attached to the *meso*-position of porphyrin ring were found to provide broader absorption, with an efficiency of 13%. However, this dye had no absorption in the green and near infrared (IR) regions and detached from the TiO_2 surface reducing the long-term stability of the cells. Numerous attempts have been made to addressing these concerns; none of them was very successful in solving all problems in a single dye. From this perspective, it would be beneficial if multiple dyes are used to co-sensitizer TiO_2 films for high efficiency.

Acknowledgments HH thanks Department of Chemistry & Biochemistry, Eastern Illinois University, for the support of this work.

References

1. M.I. Asghar, K. Miettunen, J. Halme, P. Vahermaa, M. Toivola, K. Aitola, P. Lund, Review of stability for advanced dye solar cells. *Energy Environ. Sci.* **3**(4), 418–426 (2010). <https://doi.org/10.1039/B922801B>
2. J.M. Ball, N.K.S. Davis, J.D. Wilkinson, J. Kirkpatrick, J. Teuscher, R. Gunning, H.L. Anderson, H.J. Snaith, A panchromatic anthracene-fused porphyrin sensitizer for dye-sensitized solar cells. *RSC Adv.* **2**(17), 6846–6853 (2012). <https://doi.org/10.1039/C2RA20952G>
3. T. Bessho, S.M. Zakeeruddin, C.Y. Yeh, E.W. Diau, M. Grätzel, Highly efficient mesoscopic dye-sensitized solar cells based on donor-acceptor-substituted porphyrins. *Angew. Chem. Int. Ed. Engl.* **49**(37), 6646–6649 (2010). <https://doi.org/10.1002/anie.201002118>
4. B.J. Brennan, M.J. Llansola Portolés, P.A. Liddell, T.A. Moore, A.L. Moore, D. Gust, Comparison of silatrane, phosphonic acid, and carboxylic acid functional groups for attachment of porphyrin sensitizers to TiO₂ in photoelectrochemical cells. *Phys. Chem. Chem. Phys.* **15**(39), 16605–16614 (2013). <https://doi.org/10.1039/c3cp52156g>
5. W.M. Campbell, A.K. Burrell, D.L. Officer, K.W. Jolley, Porphyrins as light harvesters in the dye-sensitized TiO₂ solar cell. *Coord. Chem. Rev.* **248**(13), 1363–1379 (2004). <https://doi.org/10.1016/j.ccr.2004.01.007>
6. W.M. Campbell, K.W. Jolley, P. Wagner, K. Wagner, P.J. Walsh, K.C. Gordon, L. Schmidt-Mende, M.K. Nazeeruddin, Q. Wang, M. Grätzel, Highly efficient porphyrin sensitizers for dye-sensitized solar cells. *J. Phys. Chem. C* **111**(32), 11760–11762 (2007). <https://doi.org/10.1021/jp0750598>
7. Y. Cao, B. Yu, Q. Yu, Y. Cheng, S. Liu, S. Dong, F. Gao, P. Wang, Dye-sensitized solar cells with a high absorptivity ruthenium sensitizer featuring a 2-(hexylthio)thiophene conjugated bipyridine. *J. Phys. Chem. C* **113**(15), 6290–6297 (2009). <https://doi.org/10.1021/jp9006872>
8. C.M. Carcel, J.K. Laha, R.S. Loewe, P. Thamyongkit, K. Schweikart, V. Misra, D.F. Bocian, J.S. Lindsey, Porphyrin architectures tailored for studies of molecular information storage. *J. Org. Chem.* **69**(20), 6739–6750 (2004). <https://doi.org/10.1021/jo0498260>
9. D.E. Carlson, C.R. Wronski, Amorphous silicon solar cells. *IEEE Trans. Electron Devices* **36**(12), 2775–2780 (1976). <https://doi.org/10.1063/1.88617>
10. Y.C. Chang, C.L. Wang, T.Y. Pan, S.H. Hong, C.M. Lan, H.H. Kuo, C.F. Lo, H.Y. Hsu, C.Y. Lin, E.W. Diau, A strategy to design highly efficient porphyrin sensitizers for dye-sensitized solar cells. *Chem. Commun.* **47**(31), 8910–8912 (2011). <https://doi.org/10.1039/C1CC12764K>
11. C. Chen, X. Yang, M. Cheng, F. Zhang, L. Sun, Degradation of cyanoacrylic acid-based organic sensitizers in dye-sensitized solar cells. *ChemSusChem* **6**(7), 1270–1275 (2013). <https://doi.org/10.1002/cssc.201200949>
12. S. Cherian, C.C. Wamser, Adsorption and photoactivity of tetra(4-carboxyphenyl)porphyrin (TCPP) on nanoparticulate TiO₂. *J. Phys. Chem. B* **104**(104), 3624–3629 (2000). <https://doi.org/10.1021/jp994459v>
13. J.N. Clifford, E. Martínez-Ferrero, A. Viterisi, E. Palomares, Sensitizer molecular structure-device efficiency relationship in dye-sensitized solar cells. *Chem. Soc. Rev.* **40**(3), 1635–1646 (2011). <https://doi.org/10.1039/b920664g>
14. J.R. Darwent, P. Douglas, A. Harriman, G. Porter, M.C. Richoux, Metal phthalocyanines and porphyrins as photosensitizers for reduction of water to hydrogen. *Coord. Chem. Rev.* **44**(1), 83–126 (1982). [https://doi.org/10.1016/S0010-8545\(00\)80518-4](https://doi.org/10.1016/S0010-8545(00)80518-4)
15. H. Deng, Y. Zhou, H. Mao, Z. Lu, The mixed effect of phthalocyanine and porphyrin on the photoelectric conversion of a nanostructured TiO₂ electrode. *Synth. Met.* **92**(92), 269–274 (1998). [https://doi.org/10.1016/S0379-6779\(98\)80096-9](https://doi.org/10.1016/S0379-6779(98)80096-9)
16. S. Eu, S. Hayashi, T. Umeyama, A. Oguro, M. Kawasaki, N. Kadota, Y. Matano, H. Imahori, Effects of 5-membered heteroaromatic spacers on structures of porphyrin films and photovoltaic

- properties of porphyrin-sensitized TiO₂ cells. *J. Phys. Chem. C* **111**(8), 3528–3537 (2007). <https://doi.org/10.1021/jp067290b>
17. S. Fan, X. Lu, H. Sun, G. Zhou, Y.J. Chang, Z.S. Wang, Effect of the co-sensitization sequence on the performance of dye-sensitized solar cells with porphyrin and organic dyes. *Phys. Chem. Chem. Phys.* **18**(2), 932–938 (2016). <https://doi.org/10.1039/c5cp05986k>
 18. A. Forneli, M. Planells, M.A. Sarmentero, E. Martinezferrero, B.C. O'Regan, P. Ballester, E. Palomares, The role of para-alkyl substituents on meso-phenyl porphyrin sensitized TiO₂ solar cells: control of the eTiO₂/electrolyte⁺ recombination reaction. *J. Mater. Chem.* **18**(14), 1652–1658 (2008). <https://doi.org/10.1039/B717081E>
 19. J.H. Fuhrhop, The reactivity of the porphyrin ligand. *Angew. Chem. Int. Ed. Engl.* **13**(5), 321–335 (1974). <https://doi.org/10.1002/anie.197403211>
 20. F. Gao, Y. Wang, D. Shi, J. Zhang, M. Wang, X. Jing, R. Humphry-Baker, P. Wang, S.M. Zakeeruddin, M. Grätzel, Enhance the optical absorptivity of nanocrystalline TiO₂ film with high molar extinction coefficient ruthenium sensitizers for high performance dye-sensitized solar cells. *J. Am. Chem. Soc.* **130**(32), 10720–10728 (2008). <https://doi.org/10.1021/ja801942j>
 21. M. Garcíaiglesias, J.H. Yum, R. Humphrybaker, S.M. Zakeeruddin, P. Péchy, P. Vázquez, E. Palomares, M. Grätzel, M.K. Nazeeruddin, T. Torres, Effect of anchoring groups in zinc phthalocyanine on the dye-sensitized solar cell performance and stability. *Chem. Sci.* **2**(6), 1145–1150 (2011). <https://doi.org/10.1039/C0SC00602E>
 22. M. Grätzel, Dye-sensitized solar cells. *J Photochem Photobiol C: Photochem Rev* **4**(2), 145–153 (2003). [https://doi.org/10.1016/S1389-5567\(03\)00026-1](https://doi.org/10.1016/S1389-5567(03)00026-1)
 23. M. Grätzel, Photovoltaic performance and long-term stability of dye-sensitized mesoscopic solar cells. *C. R. Chim.* **9**(5), 578–583 (2006). <https://doi.org/10.1016/j.crci.2005.06.037>
 24. M.A. Green, Y. Hishikawa, W. Warta, E.D. Dunlop, D.H. Levi, J. Hohl-Ebinger, A.W.H. Ho-Baillie, Solar cell efficiency tables (version 50). *Prog. Photovolt. Res. Appl.* **25**(7), 668–676 (2017). <https://doi.org/10.1002/pip.2909>
 25. A. Hagfeldt, G. Boschloo, L. Sun, L. Kloo, H. Pettersson, Dye-sensitized solar cells. *Chem. Rev.* **110**(11), 6595–6663 (2010). <https://doi.org/10.1021/cr900356p>
 26. S. Hayashi, Y. Matsubara, S. Eu, H. Hayashi, T. Umeyama, Y. Matano, H. Imahori, Fused five-membered porphyrin for dye-sensitized solar cells. *Chem. Lett.* **37**(8), 846–847 (2008). <https://doi.org/10.1246/cl.2008.846>
 27. S. Hayashi, M. Tanaka, H. Hayashi, S. Eu, T. Umeyama, Y. Matano, Y. Araki, H. Imahori, Naphthyl- fused π -elongated porphyrins for dye-sensitized TiO₂ cells. *J. Phys. Chem. C* **112**(39), 15576–15585 (2008). <https://doi.org/10.1021/jp805122z>
 28. H. He, A. Gurung, L. Si, 8-Hydroxyquinoline as a strong alternative anchoring group for porphyrin-sensitized solar cells. *Chem. Commun.* **48**(47), 5910–5912 (2012). <https://doi.org/10.1039/c2cc31440a>
 29. H. He, A. Gurung, L. Si, A.G. Sykes, A simple acrylic acid functionalized zinc porphyrin for cost-effective dye-sensitized solar cells. *Chem. Commun.* **48**(61), 7619–7621 (2012). <https://doi.org/10.1039/c2cc33337f>
 30. T. Higashino, Y. Fujimori, K. Sugiura, Y. Tsuji, S. Ito, H. Imahori, Tropolone as a high-performance robust anchoring group for dye-sensitized solar cells. *Angew. Chem. Int. Ed. Engl.* **54**(31), 9052–9056 (2015). <https://doi.org/10.1002/anie.201502951>
 31. T. Higashino, K. Kawamoto, K. Sugiura, Y. Fujimori, Y. Tsuji, K. Kurotobi, S. Ito, H. Imahori, Effects of bulky substituents of push-pull porphyrins on photovoltaic properties of dye-sensitized solar cells. *ACS Appl. Mater. Interfaces* **8**(24), 15379–15390 (2016). <https://doi.org/10.1021/acsami.6b03806>
 32. T. Higashino, Y. Kurumisawa, C. Ning, Y. Fujimori, Y. Tsuji, S. Nimura, D. Packwood, J. Park, H. Imahori, A hydroxamic acid anchoring group for durable dye-sensitized solar cells with a cobalt redox shuttle. *ChemSusChem* **10**(17), 3347–3351 (2017). <https://doi.org/10.1002/cssc.201701157>

33. A. Hinsch, J.M. Kroon, R. Kern, I. Uhlenndorf, J. Holzbock, A. Meyer, J. Ferber, Long-term stability of dye-sensitized solar cells. *Prog. Photovolt. Res. Appl.* **9**(6), 425–438 (2001). <https://doi.org/10.1002/pip.397>
34. S. Horn, K. Dahms, M.O. Senge, Synthetic transformations of porphyrins – Advances 2004–2007. *J. Porphyrins Phthalocyanines* **12**(10), 1053–1077 (2008). <https://doi.org/10.1142/S108842460800042X>
35. C.P. Hsieh, H.P. Lu, C.L. Chiu, C.W. Lee, S.H. Chuang, C.L. Mai, W.N. Yen, S.J. Hsu, W.G. Diao, C.Y. Yeh, Synthesis and characterization of porphyrin sensitizers with various electron-donating substituents for highly efficient dye-sensitized solar cells. *J. Mater. Chem.* **20**(6), 1127–1134 (2010). <https://doi.org/10.1039/b919645e>
36. H. Imahori, S. Hayashi, H. Hayashi, A. Oguro, S. Eu, T. Umeyama, Y. Matano, Effects of porphyrin substituents and adsorption conditions on photovoltaic properties of porphyrin-sensitized TiO₂ cells. *J. Phys. Chem. C* **113**(42), 18406–18413 (2009). <https://doi.org/10.1021/jp907288h>
37. H. Imahori, Y. Matsubara, H. Iijima, T. Umeyama, Y. Matano, S. Ito, M. Niemi, N.V. Tkachenko, H. Lemmetyinen, Effects of the meso-diarylamino group of porphyrins as sensitizers in dye-sensitized solar cells on optical, electrochemical, and photovoltaic properties. *J. Phys. Chem. C* **114**(23), 686–694 (2010). <https://doi.org/10.1021/jp102486b>
38. S. Ito, S.M. Zakeeruddin, R. Humphry-Baker, P. Liska, R. Charvet, P. Comte, M.K. Nazeeruddin, P. Pèchy, M. Takata, H. Miura, High-efficiency organic-dye-sensitized solar cells controlled by nanocrystalline-TiO₂ electrode thickness. *Adv. Mater.* **18**(9), 1202–1205 (2006). <https://doi.org/10.1002/adma.200502540>
39. R.K. Kanaparthi, J. Kandhadi, L. Giribabu, Metal-free organic dyes for dye-sensitized solar cells: recent advances. *Tetrahedron* **44**(6), 8383–8393 (2013). <https://doi.org/10.1016/j.tet.2012.06.064>
40. A. Kato, R.D. Hartnell, M. Yamashita, H. Miyasaka, S. K-i, D.P. Arnold, Selective meso-monobromination of 5,15-diarylporphyrins via organopalladium porphyrins. *J. Porphyrins Phthalocyanines* **8**(10), 1222–1227 (2009). <https://doi.org/10.1142/S108842460400057X>
41. A. Kay, M. Grätzel, Artificial photosynthesis. I. Photosensitization of titania solar cells with chlorophyll derivatives and related natural porphyrins. *J. Phys. Chem.* **97**(23), 6272–6277 (1993). <https://doi.org/10.1021/j100125a029>
42. B.G. Kim, K. Chung, J. Kim, Molecular design principle of all-organic dyes for dye-sensitized solar cells. *Chem. Eur. J.* **19**(17), 5220–5230 (2013). <https://doi.org/10.1002/chem.201204343>
43. H. Kohjiro, S. Tadatake, K. Ryuzi, F. Akihiro, O. Yasuyo, S. Akira, S. Sadaharu, S. Kazuhiro, S. Hideki, A. Hironori, Molecular design of coumarin dyes for efficient dye-sensitized solar cells. *J. Phys. Chem. B* **107**(2), 597–606 (2003). <https://doi.org/10.1021/jp026963x>
44. N. Krishna, K.J. Vamsi, S. Venkata, S. Singh, G.L. Prakash, L. Han, I. Bedja, R. Gupta, I.A. Kumar, Donor- π -acceptor based stable porphyrin sensitizers for dye-sensitized solar cells: effect of π -conjugated spacers. *J. Phys. Chem. C* **121**(12), 6464–6477 (2017). <https://doi.org/10.1021/acs.jpcc.6b12869>
45. K. Kurotobi, Y. Toude, K. Kawamoto, Y. Fujimori, S. Ito, P. Chabera, V. Sundström, H. Imahori, Highly asymmetrical porphyrins with the enhanced push-pull character for dye-sensitized solar cells. *Chem. Eur. J.* **19**(50), 17075–17081 (2013). <https://doi.org/10.1002/chem.201303460>
46. C.M. Lan, H.P. Wu, T.Y. Pan, C.W. Chang, W.S. Chao, C.T. Chen, C.L. Wang, C.Y. Lin, W.G. Diao, Enhanced photovoltaic performance with co-sensitization of porphyrin and an organic dye in dye-sensitized solar cells. *Energy Environ. Sci.* **5**(4), 6460–6464 (2012). <https://doi.org/10.1039/c2ee21104a>
47. S.M. Lecours, S.G. Dimagno, M.J. Therien, Exceptional electronic modulation of porphyrins through meso-Arylethynyl groups. Electronic spectroscopy, electronic structure, and electrochemistry of [5,15-Bis[(aryl)ethynyl]-10,20-diphenylporphinato]zinc(II) complexes. X-ray crystal structures of [5,15-Bis[(4'-fluorophenyl) ethynyl]-10,20-diphenylporphinato] zinc (II) and 5,15-Bis[(4'-methoxyphenyl) ethynyl]-10,20-

- diphenylporphyrin. *J. Am. Chem. Soc.* **118**(47), 11854–11864 (1996). <https://doi.org/10.1021/ja962403y>
48. C.W. Lee, H.P. Lu, C.M. Lan, Y.L. Huang, Y.R. Liang, W.N. Yen, Y.C. Liu, Y.S. Lin, E.W. Diau, C.Y. Yeh, Novel zinc porphyrin sensitizers for dye-sensitized solar cells: synthesis and spectral, electrochemical, and photovoltaic properties. *Chem. Eur. J.* **1035**(6), 400–406 (2013). <https://doi.org/10.1002/chem.200801572>
 49. L.L. Li, E.W. Diau, Porphyrin-sensitized solar cells. *Chem. Soc. Rev.* **42**(1), 291 (2013)
 50. W. Li, L. Si, Z. Liu, H. Wu, Z. Zhao, Y.B. Cheng, H. He, Bis(9,9-dihexyl-9H-fluorene-7-yl) amine (BDFA) as a new donor for porphyrin-sensitized solar cells. *Org. Electron.* **15**(10), 2448–2460 (2014). <https://doi.org/10.1016/j.orgel.2014.07.006>
 51. W. Li, L. Si, Z. Liu, Z. Zhao, H. He, K. Zhu, B. Moore, Y.B. Cheng, Fluorene functionalized porphyrins as broadband absorbers for TiO₂ nanocrystalline solar cells. *J. Mater. Chem. A* **2** (33), 13667–13674 (2014). <https://doi.org/10.1039/c4ta01954g>
 52. W. Li, Z. Liu, H. Wu, Y.B. Cheng, Z. Zhao, H. He, Thiophene-functionalized porphyrins: synthesis, photophysical properties, and photovoltaic performance in dye-sensitized solar cells. *J. Phys. Chem. C* **119**(10), 5265–5273 (2015). <https://doi.org/10.1021/jp509842p>
 53. M. Liang, J. Chen, Arylamine organic dyes for dye-sensitized solar cells. *Chem. Soc. Rev.* **42** (8), 3453–3488 (2013). <https://doi.org/10.1039/c3cs35372a>
 54. C.Y. Lin, C.F. Lo, M.H. Hsieh, S.J. Hsu, H.P. Lu, W.G. Diau, Preparation and photovoltaic characterization of free-base and Metallo carboxyphenylethynyl porphyrins for dye-sensitized solar cells. *J. Chin. Chem. Soc.* **57**(5B), 1136–1140 (2010). <https://doi.org/10.1002/jccs.201000162>
 55. J.S. Lindsey, Synthetic routes to meso-patterned porphyrins. *Acc. Chem. Res.* **43**(2), 300–311 (2010). <https://doi.org/10.1021/ar900212t>
 56. Y. Liu, N. Xiang, X. Feng, P. Shen, W. Zhou, C. Weng, B. Zhao, S. Tan, Thiophene-linked porphyrin derivatives for dye-sensitized solar cells. *Chem. Commun.* **18**(18), 2499–2501 (2009). <https://doi.org/10.1039/b821985k>
 57. C.F. Lo, L. Luo, E.W. Diau, I.J. Chang, C.Y. Lin, Evidence for the assembly of carboxyphenylethynyl zinc porphyrins on nanocrystalline TiO₂ surfaces. *Chem. Commun.* **13**(13), 1430–1432 (2006). <https://doi.org/10.1039/b516782e>
 58. H.P. Lu, C.Y. Tsai, W.N. Yen, C.P. Hsieh, C.W. Lee, C.Y. Yeh, W.G. Diau, Control of dye aggregation and electron injection for highly efficient porphyrin sensitizers adsorbed on semiconductor films with varying ratios of adsorbate. *J. Phys. Chem. C* **113**(49), 20990–20997 (2009). <https://doi.org/10.1021/jp908100v>
 59. J. Luo, M. Xu, R. Li, K.W. Huang, C. Jiang, Q. Qi, W. Zeng, J. Zhang, C. Chi, P. Wang, N-annulated perylene as an efficient electron donor for porphyrin-based dyes: enhanced light-harvesting ability and high-efficiency Co(II/III)-based dye-sensitized solar cells. *J. Am. Chem. Soc.* **136**(1), 265–272 (2014). <https://doi.org/10.1021/ja409291g>
 60. C.L. Mai, W.K. Huang, H.P. Lu, C.W. Lee, C.L. Chiu, Y.R. Liang, E.W. Diau, C.Y. Yeh, Synthesis and characterization of porphyrin sensitizers for dye-sensitized solar cells. *Chem. Commun.* **46**(5), 809–811 (2010). <https://doi.org/10.1039/b917316a>
 61. C.L. Mai, T. Moehl, C.H. Hsieh, J.D. Décoppet, S.M. Zakeeruddin, M. Grätzel, C.Y. Yeh, Porphyrin sensitizers bearing a pyridine-type anchoring group for dye-sensitized solar cells. *ACS Appl. Mater. Interfaces* **7**(27), 14975–14982 (2015). <https://doi.org/10.1021/acsami.5b03783>
 62. V.S. Manthou, E.K. Pefkianakis, P. Falaras, G.C. Vougioukalakis, Co-adsorbents: a key component in efficient and robust dye-sensitized solar cells. *ChemSusChem* **8**(4), 588–599 (2015). <https://doi.org/10.1002/cssc.201403211>
 63. S. Mathew, A. Yella, P. Gao, R. Humphrybaker, B.F. Curchod, N. Ashariastani, I. Tavernelli, U. Rothlisberger, M.K. Nazeeruddin, M. Grätzel, Dye-sensitized solar cells with 13% efficiency achieved through the molecular engineering of porphyrin sensitizers. *Nat. Chem.* **6**(3), 242 (2014). <https://doi.org/10.1038/NCHEM.1861>

64. A. Meindl, S. Plunkett, A.A. Ryan, K.J. Flanagan, S. Callaghan, M.O. Senge, Comparative synthetic strategies for the generation of 5,10- and 5,15-substituted push-pull porphyrins. *Eur. J. Org. Chem.* **2017**(25), 3516–3516 (2017). <https://doi.org/10.1002/ejoc.201700093>
65. R.L. Milot, C.A. Schmuttenmaer, Electron injection dynamics in high-potential porphyrin photoanodes. *Acc. Chem. Res.* **48**(5), 1423–1431 (2015). <https://doi.org/10.1021/ar500363q>
66. R.L. Milot, G.F. Moore, R.H. Crabtree, G.W. Brudvig, C.A. Schmuttenmaer, Electron injection dynamics from photoexcited porphyrin dyes into SnO₂ and TiO₂ nanoparticles. *J. Phys. Chem. C* **117**(42), 21662–21670 (2015)
67. S. Mozaffari, M.R. Nateghi, M.B. Zarandi, An overview of the challenges in the commercialization of dye-sensitized solar cells. *Renew. Sust. Energy Rev.* **71**, 675–686 (2016). <https://doi.org/10.1016/j.rser.2016.12.096>
68. M.K. Nazeeruddin, R. Humphry-Baker, D.L. Officer, W.M. Campbell, A.K. Burrell, M. Grätzel, Application of metalloporphyrins in nanocrystalline dye-sensitized solar cells for conversion of sunlight into electricity. *Langmuir* **20**(15), 6514–6517 (2004). <https://doi.org/10.1021/la0496082>
69. M.K. Nazeeruddin, F. De Angelis, F. Simona, S. Annabella, G. Viscardi, P. Liska, S. Ito, T. Bessho, M. Grätzel, Combined experimental and DFT-TDDFT computational study of photoelectrochemical cell ruthenium sensitizers. *J. Am. Chem. Soc.* **127**(48), 16835 (2005). <https://doi.org/10.1021/ja0524671>
70. P. Péchy, F.P. Rotzinger, M.K. Nazeeruddin, O. Kohle, S.M. Zakeeruddin, R. Humphrybaker, M. Grätzel, Preparation of phosphonated polypyridyl ligands to anchor transition-metal complexes on oxide surfaces: application for the conversion of light to electricity with nanocrystalline TiO₂ films. *J. Chem. Soc. Chem. Commun.* **1**(1), 65–66 (1995). <https://doi.org/10.1039/C39950000065>
71. T. Ripolles-Sanchis, B.C. Guo, H.P. Wu, T.Y. Pan, H.W. Lee, S.R. Raga, F. Fabregat-Santiago, J. Bisquert, C.Y. Yeh, E.W. Diau, Design and characterization of alkoxy-wrapped push-pull porphyrins for dye-sensitized solar cells. *Chem. Commun.* **48**(36), 4368–4370 (2012). <https://doi.org/10.1039/c2cc31111a>
72. N. Robertson, Optimizing dyes for dye-sensitized solar cells. *Angew. Chem.* **37**(27), 2338–2345 (2006)
73. J. Rochford, D. Chu, A. Hagfeldt, E. Galoppini, Tetrachelate porphyrin chromophores for metal oxide semiconductor sensitization: effect of the spacer length and anchoring group position. *J. Am. Chem. Soc.* **129**(15), 4655–4665 (2007). <https://doi.org/10.1021/ja068218u>
74. T.E.O. Screen, K.B. Lawton, G.S. Wilson, N. Dolney, R. Ispasoiu, T.G. Iii, S.J. Martin, D.D.-C. Bradley, H.L. Anderson, Synthesis and third-order nonlinear optics of a new soluble conjugated porphyrin polymer. *J. Mater. Chem.* **11**, 312–320 (2001). <https://doi.org/10.1039/B007250H>
75. M.O. Senge, Stirring the porphyrin alphabet soup—functionalization reactions for porphyrins. *Chem. Commun.* **47**(7), 1943–1960 (2011). <https://doi.org/10.1039/c0cc03984e>
76. M.O. Senge, J. Richter, Synthetic transformations of porphyrins – advances 2002–2004. *J. Porphyrins Phthalocyanines* **8**(07), 934–953 (2005). <https://doi.org/10.1142/S1088424604000313>
77. D.M. Shen, C. Liu, X.G. Chen, Q.Y. Chen, Facile and efficient hypervalent iodine(III)-mediated meso- functionalization of porphyrins. *J. Org. Chem.* **74**(1), 206–211 (2009). <https://doi.org/10.1021/jo801855d>
78. J.W. Shiu, Y.C. Chang, C.Y. Chan, H.P. Wu, H.Y. Hsu, C.L. Wang, C.Y. Lin, E.G. Diau, Panchromatic co-sensitization of porphyrin-sensitized solar cells to harvest near-infrared light beyond 900 nm. *J. Mater. Chem. A* **3**(4), 1417–1420 (2014). <https://doi.org/10.1039/C4TA06589A>
79. H.J. Snaithe, Estimating the maximum attainable efficiency in dye-sensitized solar cells. *Adv. Funct. Mater.* **20**(1), 13–19 (2010). <https://doi.org/10.1002/adfm.200901476>

80. P.M. Sommeling, M. Späth, H.J.P. Smit, N.J. Bakker, J.M. Kroon, Long-term stability testing of dye-sensitized solar cells. *J. Photochem. Photobiol. A* **164**(1), 137–144 (2004). <https://doi.org/10.1016/j.jphotochem.2003.12.017>
81. M. Tanaka, S. Hayashi, S. Eu, T. Umeyama, Y. Matano, H. Imahori, Novel unsymmetrically pi-elongated porphyrin for dye-sensitized TiO₂ cells. *Chem. Commun.* **20**(20), 2069–2071 (2007). <https://doi.org/10.1039/B702501G>
82. M. Urbani, M. Grätzel, M.K. Nazeeruddin, T. Torres, Meso-substituted porphyrins for dye-sensitized solar cells. *Chem. Rev.* **114**(24), 12330–12396 (2014)
83. Z.S. Wang, H. Kawauchi, T. Kashima, H. Arakawa, Significant influence of TiO₂ photo-electrode morphology on the energy conversion efficiency of N719 dye-sensitized solar cell. *Coord. Chem. Rev.* **248**(13–14), 1381–1389 (2004). <https://doi.org/10.1016/j.ccr.2004.03.006>
84. Q. Wang, W.M. Campbell, E.E. Bonfantani, K.W. Jolley, D.L. Officer, P.J. Walsh, K. Gordon, R. Humphrybaker, M.K. Nazeeruddin, M. Grätzel, Efficient light harvesting by using green Zn-porphyrin-sensitized nanocrystalline TiO₂ films. *J. Phys. Chem. B* **109**(32), 15397–15409 (2005). <https://doi.org/10.1021/jp052877w>
85. C.L. Wang, Y.C. Chang, C.M. Lan, C.F. Lo, W.G. Diao, C.Y. Lin, Enhanced light harvesting with π -conjugated cyclic aromatic hydrocarbons for porphyrin-sensitized solar cells. *Energy Environ. Sci.* **4**(5), 1788–1795 (2011). <https://doi.org/10.1039/C0EE00767F>
86. C.L. Wang, C.M. Lan, S.H. Hong, Y.F. Wang, T.Y. Pan, C.W. Chang, H.H. Kuo, M.Y. Kuo, W.G. Diao, C.Y. Lin, Enveloping porphyrins for efficient dye-sensitized solar cells. *Energy Environ. Sci.* **5**(5), 6933–6940 (2012). <https://doi.org/10.1039/c2ee03308a>
87. Y. Wu, W. Zhu, Organic sensitizers from D- π -A to D-A- π -A: effect of the internal electron-withdrawing units on molecular absorption, energy levels, and photovoltaic performances. *Chem. Soc. Rev.* **42**(5), 2039–2058 (2013). <https://doi.org/10.1039/C2CS35346F>
88. C.H. Wu, T.Y. Pan, S.H. Hong, C.L. Wang, H.H. Kuo, Y.Y. Chu, E.W. Diao, C.Y. Lin, A fluorene-modified porphyrin for efficient dye-sensitized solar cells. *Chem. Commun.* **48**(36), 4329–4331 (2012). <https://doi.org/10.1039/c2cc30892d>
89. Y. Xie, Y. Tang, W. Wu, Y. Wang, J. Liu, X. Li, H. Tian, W.H. Zhu, Porphyrin cosensitization for a photovoltaic efficiency of 11.5%: a record for non-ruthenium solar cells based on iodine electrolyte. *J. Am. Chem. Soc.* **137**(44), 14055–14058 (2015). <https://doi.org/10.1021/jacs.5b09665>
90. A. Yella, H.W. Lee, H.N. Tsao, C. Yi, A. Chandiran, M. Nazeeruddin, E. Diao, C.Y. Yeh, S. Zakeeruddin, M. Grätzel, Porphyrin-sensitized solar cells with cobalt (II/III)-based redox electrolyte exceed 12 percent efficiency. *Science* **334**(6056), 629–634 (2011). <https://doi.org/10.1126/science.1209688>
91. A. Yella, C.L. Mai, S.M. Zakeeruddin, S.N. Chang, C.H. Hsieh, C.Y. Yeh, M. Grätzel, Molecular engineering of push-pull porphyrin dyes for highly efficient dye-sensitized solar cells: the role of benzene spacers. *Angew. Chem. Int. Ed. Engl.* **126**(11), 3017–3021 (2014). <https://doi.org/10.1002/anie.201309343>
92. L. Yu, K. Muthukumar, I.V. Sazanovich, C. Kirmaier, E. Hindin, J.R. Diers, P.D. Boyle, D.F. Bocian, D. Holten, J.S. Lindsey, Excited-state energy-transfer dynamics in self-assembled triads composed of two porphyrins and an intervening bis(dipyrrinato)metal complex. *Inorg. Chem.* **42**(21), 6629–6647 (2003). <https://doi.org/10.1021/ic034559m>
93. J. Zhao, A. Wang, M.A. Green, F. Ferrazza, 19.8% efficient “honeycomb” textured multicrystalline and 24.4% monocrystalline silicon solar cells. *Appl. Phys. Lett.* **73**(14), 1991–1993 (1998). <https://doi.org/10.1063/1.122345>
94. W. Zheng, N. Shan, L. Yu, X. Wang, UV-visible, fluorescence and EPR properties of porphyrins and metalloporphyrins. *Dyes Pigments* **77**(1), 153–157 (2008). <https://doi.org/10.1016/j.dyepig.2007.04.007>
95. S. Chakraborty, H.-C. You, C.-K. Huang, B.-Z. Lin, C.-L. Wang, M.-C. Tsai, C.-L. Liu, C.-Y. Lin, meso-Diphenylbacteriochlorins: Macrocyclic dyes with rare colors for dye-sensitized solar cells. *J. Phys. Chem. C* **121**(13), 7081–7087 (2017). <https://doi.org/10.1021/acs.jpcc.7b00097>



Insights into the Application of Metal-Organic Frameworks for Molecular Photovoltaics

13

Matthew C. Kessinger and Amanda J. Morris

This chapter is dedicated to Professor Peter J. Derrick who passed away during the writing of this chapter.

Contents

13.1	Introduction	384
13.2	What Are Metal-Organic Frameworks?	384
13.3	The Advantages of MOFSCs	386
13.4	Potential Considerations of MOFSCs	387
13.5	Fundamental Studies on Charge Separation	388
13.6	Charge Transfer and Redox Hopping	390
13.7	Literature Examples of MOFSCs	393
13.8	Conclusions and Future Outlook	403
	References	404

Abstract

Within the area of state-of-the-art photovoltaics, organic photovoltaics, and, more specifically, polymer-based photovoltaics have gained significant interest as novel molecular photovoltaic materials. As a subset of traditional polymers, multi-dimensional metal coordination polymers, known as metal-organic frameworks (MOFs), have shown promise as sensitizers for molecular photovoltaics. These state-of-the-art devices have been termed metal-organic framework solar cells (MOFSCs) and represent an emerging alternative to traditional photovoltaic

Author Contribution

The first draft was written by Matthew Kessinger. The final draft was reviewed and edited by Dr. Amanda J. Morris and Matthew Kessinger.

M. C. Kessinger · A. J. Morris (✉)
Virginia Tech, Blacksburg, VA, USA
e-mail: kessm05@vt.edu; ajmorris@vt.edu

materials. In this chapter, an overview of the application of MOFs as a sensitizer for MOFSCs is explored including their advantages and limitations when compared to molecular dyes, the origin of electronic transport in MOF materials, and a selection of the proof-of-concept studies illustrating the feasibility of MOFSCs in bulk applications.

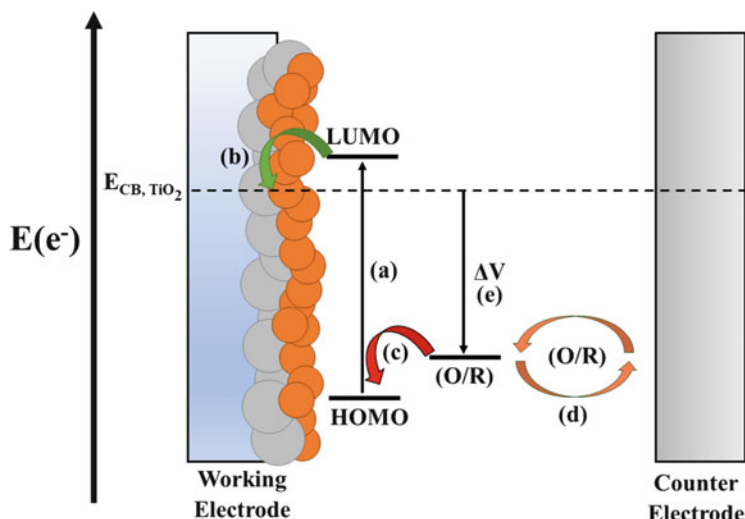
13.1 Introduction

This book chapter will focus on the preparation and use of metal-organic frameworks (MOFs) as a new class of sensitizers for dye-sensitized solar cells (DSSCs). The chapter will begin with a discussion of the fabrication and operational mechanism of DSSCs. Following this, a discussion of MOFs and their characteristic properties will be presented outlining the benefits and considerations for the implementation of metal-organic framework sensitized solar cells (MOFSCs). Finally, the chapter will provide examples and analysis of frameworks used in MOFSCs. Currently, there is only a select handful of MOFSCs in the literature, which primarily provide proof-of-concept experiments on the working principles of MOFSCs. Each of these examples will be discussed in detail to reiterate and demonstrate the current challenges associated with MOFSCs, and the unique solutions researchers are currently investigating to meet these challenges. The chapter will then be concluded with a prospectus on the outlook and challenges of MOFSCs as an emerging class of state-of-the-art molecular photovoltaics.

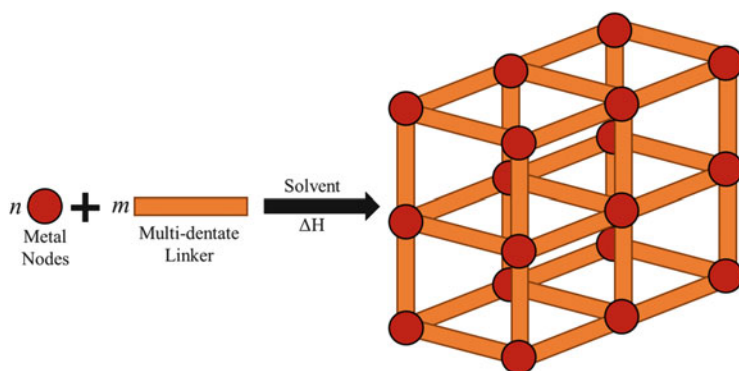
Before examining the finer details of MOFSCs, it is first useful to discuss their predecessor: the dye-sensitized solar cell (DSSC). Dye-sensitized solar cells are second-generation photovoltaic devices based on the original design of Grätzel. In this cell architecture, the absorption of sunlight by a dye-sensitizer or chromophore leads to the generation of free charge carriers, which then power an external load [31]. The typical device architecture for a DSSC consists of three main components: a working electrode or photoanode, a counter electrode, and a liquid or solid-state electrolyte. The working electrode is composed of a sensitizing chromophore chemisorbed onto a wide bandgap semiconductor, usually titanium dioxide (TiO_2) deposited on a conductive glass substrate such as fluorine-doped tin oxide (FTO). The working electrode is responsible for the absorption of sunlight and ultimately, the generation of a charge-separated state. Opposite the working electrode is the counter electrode. This electrode is typically a platinum-coated conductive glass substrate. The two electrodes are separated by a polymer spacer creating an interelectrode space. This void space is then filled with a redox-active electrolyte, which is responsible for regenerating the chromophore during operation and carrying photogenerated holes to the counter electrode. The general operational mechanism for a DSSC is summarized in Scheme 13.1.

13.2 What Are Metal-Organic Frameworks?

Metal-organic frameworks represent a unique class of coordination polymers in which organic linkers coordinate to metal ions or metal-oxo clusters to form highly ordered and tunable two- or three-dimensional assemblies (Scheme 13.2) [47]. Specifically, MOFs



Scheme 13.1 Operational mechanism of a conventional DSSC. (a) Absorption of sunlight by a chromophore promotes an electron from the highest occupied molecular orbital of the dye (HOMO) to its lowest unoccupied molecular orbital (LUMO). (b) Due to the energy differential between the energy of the LUMO of the chromophore and the energy of the conduction band of the TiO_2 (dashed line), the excited electron is injected into the titania (TiO_2) conduction band. (c) The chromophore is then regenerated by electron transfer from a redox couple in the electrolyte. (d, e) The now oxidized redox couple diffuses to the counter electrode where it accepts an electron generating photovoltage



Scheme 13.2 Schematic representation of the solvothermal synthesis of metal-organic frameworks. Multi-dentate organic linkers (orange rods) and metal nodes (red circles) allow for the self-assembly of three-dimensional frameworks under solvothermal conditions

possess four main advantageous properties. First, the coordination of symmetric, repeating units of metal nodes and organic linkers leads to the formation of highly ordered and porous frameworks. Second, MOFs are modular and tunable structures, whose pore size and distribution can be controlled synthetically through variation of the organic linker and to some extent the metal node [27]. Third, some MOF structural motifs, such as the

series developed at the University in Oslo (UiO), represent a robust class of frameworks which display a high degree of stability under a wide range of conditions, especially when using small organic linkers [45]. Finally, MOFs are easily processible with highly crystalline materials being readily prepared from the reaction of metal precursors and organic linkers.

13.3 The Advantages of MOFSCs

The advantages afforded by MOFs can also be applied to DSSCs to overcome the current limitations of molecular dye assemblies. To begin, the porous and highly ordered nature of MOFs allows for the fabrication of thin film devices with exceptional dye loading, reducing both the weight and cost of the device. Expanding on this, if the structure of the MOF can be optimized to allow for fast and efficient exciton transport, the ability to incorporate multiple chromophores into the framework allows for the fabrication of high surface area, thin film, panchromatic electrodes. This, in turn, provides a device which possesses superior dye-loading and spectral overlap when compared to traditional DSSC photoanodes.

In addition, the orientation of the chromophore can be controlled for enhanced energy transfer in processes such as triplet-triplet annihilation-based upconversion (TTA-UC), as well as Förster resonance energy transfer (FRET) and Dexter energy transfer pathways [20, 22, 35, 48]. On a related note, the incorporation of the molecular sensitizer into the organic backbone of the MOF can significantly reduce the detrimental effects of dye aggregation, which is known to shift the absorption of the HOMO-LUMO gap of molecular sensitizers up to 270 meV [13, 41]. Similarly, interactions between neighboring chromophores can lead to static quenching, reducing the quantum yield of the sensitizer emission.

Finally, locking the chromophore into a rigid MOF scaffold allows for exhaustive control over the identity of the chromophore within the sensitizing layer with near molecular precision through a solution processible layer-by-layer (LBL) synthesis also known as liquid phase epitaxy. While LBL growth of MOF films is the most appealing strategy for controlling film thickness and chromophore identity, not all MOFs can be readily fabricated by such methods. Notable examples of some MOFs that can be grown via LBL growth include Hong Kong University of Science and Technology-1 (HKUST-1), surface-integrated metal-organic frameworks (SURMOFs), copper coordinated 5,15-di(*p*-benzoato)porphyrin, $C_{36}H_{24}N_4O_2[O^-]_2$ $[Cu_x(dbc)_y]$ or zinc coordinated 1,4-benzenedicarboxylate ($C_8H_4O_2[O^-]_2$) $[Zn_x(bdc)_y]$ frameworks, and layered frameworks consisting of porphyrin units supported on molecular “columns” by bridging ligands such as 4,4'-bipyridine ($C_{10}H_8N_2$).

Preliminary examples of such LBL film growth include a mixed-valency ruthenium-based MOF grown via adsorption of ruthenium (III) chloride ($RuCl_3$) precursor and 1,3,5-benzenetricarboxylate ($C_6H_3O_3[O^-]_3$) precursor onto an amine functionalized glass substrate [23]. In addition, LBL deposition has been used to grow the zinc-based framework with (1,4-naphthalene dicarboxylate, $C_{12}H_6O_2[O^-]_2$) and (1,4-diazabicyclo(2.2.2)octane, $C_6H_{12}N_2$) as linkers $[Zn_2(ndc)_2(dabco)_n]$ perfectly

oriented on top of the copper variant, $\text{Cu}_2(\text{ndc})_2(\text{dabco})_n$. In this instance, the copper-based framework acts as a template for orienting the zinc-based framework [38]. It is worth noting that in the above example, the placement of the copper framework was necessary to achieve directed growth along the (001) crystallographic plane. When only $\text{Zn}_2(\text{ndc})_2(\text{dabco})_n$ was used during the deposition, no unidirectional growth was observed. It will be of interest for future studies to develop new methods which allow for the growth of additional frameworks by LBL methods as it allows for both fine controls over the electrode thickness while maintaining a strong electronic contact with the conductive substrate.

13.4 Potential Considerations of MOFSCs

To date, MOFSCs have displayed maximum power conversion efficiencies (power conversion efficiency, PCEs, or η) of $\sim 2.1\%$ PCE in which a cobalt-based framework acts as both a light absorber and hole conducting solid-state electrolyte [1]. More traditional MOFSCs based on liquid junction device architectures typically display efficiencies less than 1%. These stunted efficiencies are directly linked to a few potential challenges, which must be considered when designing MOFSCs. One such challenge involves the diffusion and effusion of the liquid electrolyte within the porous framework. As with current DSSC technology, it is expected that the performance of MOFSCs are dependent on mass transport of the redox electrolyte through the MOF material, with a diffusion of the electrolyte throughout the framework being significantly slower than in bulk solution. The rate of diffusion will be directly dependent on a variety of factors such as the pore size and distribution inherently associated with the MOF material as well as the viscosity, surface tension, and fluid dynamics of the chosen electrolyte.

Yet, despite diffusion being a key challenge for the implementation of MOFSCs, most studies have only looked at the transport of small molecules through MOFs [14, 17, 37, 43]. In these studies, it has been shown that diffusion within the porous framework can be up to four orders of magnitude slower than in bulk solution, commonly taken to be between 5×10^{-5} and 1×10^{-6} cm^2/s [4]. For example, the diffusion of Ce^{4+} within an iridium-modified UiO-67 framework was found to be 1.52×10^{-11} cm^2/s under low concentrations (< 1 mM) and as low as 4.6×10^{-13} cm^2/s at higher concentrations (~ 7 mM) [43]. These values have been attributed in large part to self-exchange between individual Ce^{4+} ions. In addition, these results are in line with molecular dynamics simulations of a lanthanide-copper iodide framework with isonicotinate ($\text{C}_6\text{H}_4\text{NO}[\text{O}^-]$) and dimethylformamide ($\text{C}_3\text{H}_7\text{NO}$) as linkers or coordinative units ($[\text{Ln}_3(\text{Cu}_4\text{I}_4)(\text{ina})_9(\text{DMF})_4] \cdot \text{DMF}_n$, where Ln = praseodymium, Pr; and terbium, Tb), which displayed a calculated diffusion coefficient of I_2 in acetonitrile of 3.8×10^{-9} cm^2/s though no experimental diffusion coefficients were calculated for the MOF [17].

13.5 Fundamental Studies on Charge Separation

Another primary consideration for MOFSC materials involves transport of the photogenerated electron from the site of charge separation through the MOF material to the back contact. While MOFs have displayed the presence of a charge-separated state and photocatalytic activity, they lack an extended band structure typical of other semiconductors like titanium dioxide or zinc oxide [40]. As such, extended electronic communication in MOFs involves a redox hopping mechanism, where a charge is transferred through self-exchange between redox-active linkers. Explanations of the origin of the charge-separated state in some MOF materials have involved simple charge trapping between the metal node and organic linker. In addition, no study has calculated the mobility of free charge carriers during the charge-separated state. Since electronic communication plays an important role in MOFSCs, a discussion of the fundamental studies on both charge separation and redox hopping will follow, below.

We will begin by discussing the former case first. One of the key properties necessary for photovoltaic applications is the ability of the MOF to undergo photo-induced charge separation. Examples of such a charge-separated state can be found in studies probing Metal-organic-framework-5 (MOF-5), Material Institut Lavoisier-125 [MIL-125(Ti), consisting of Ti and terephthalic acid] and its amine-functionalized derivative MIL-125(Ti)-NH₂ [3, 10] (Fig. 13.1). In the case of MOF-5, the presence of a charge-separated state was characterized by visible light irradiation in the presence of methyl viologen (C₁₂H₁₄[Cl⁻][N⁺]₂, V²⁺) dichloride, a well-known electron acceptor whose radical cation (V^{•+}) can be monitored by its distinct absorption spectrum. Upon light irradiation of an aqueous suspension of MOF-5, the characteristic blue color of V^{•+} was detected, demonstrating that MOF-5 is capable of undergoing photoinduced charge-separation.

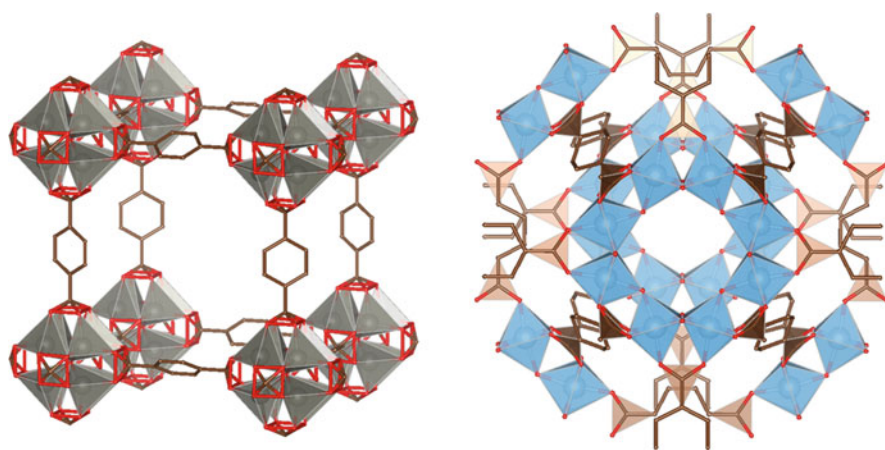


Fig. 13.1 Crystallographic structure of MOF-5 (left) and Mil-125(Ti) (right)

As a follow up to these studies, the highest occupied molecular orbital-lowest unoccupied molecular orbital (HOMO-LUMO) gap of MOF-5 was calculated from diffuse reflectance data and found to be 3.4 eV, only 200 meV larger than the optical bandgap of anatase titania ((TiO₂) (a-TiO₂)), the most commonly used semiconductor support in DSSCs. In addition, the LUMO energy could be estimated from photovoltaic cells prepared using MOF-5 supported on fluorine-doped tin oxide (FTO) as a photoanode, in contact with an iodide/triiodide I^-/I_3^- redox electrolyte. During operation of liquid junction DSSCs, the open circuit potential is dictated by the difference in energy between the standard reduction potential of the redox electrolyte, taken to be 300 meV for I^-/I_3^- and the Fermi level energy of electrons in the TiO₂, which can be approximated to the conduction band energy of the semiconductor during normal operation [5]. This same approximation was applied to cells prepared with MOF-5 as the photosensitizer. The open circuit voltage (V_{OC}) of cells prepared using MOF-5 were found to be 300 mV lower than cells prepared with TiO₂. By using TiO₂ reference cells as a standard, with the conduction band energy of TiO₂ taken at -0.1 V versus normal hydrogen electrode (NHE), the conduction band energy of MOF-5 was estimated to be 0.2 V versus NHE. The HOMO energy of MOF-5 was then extracted from the LUMO energy and the diffuse reflectance data and calculated to be 3.6 eV versus NHE. Incidentally, this study suggests the ability of a MOF scaffold to act as a tunable alternative to TiO₂ in photovoltaic devices, where MOFs can accommodate additional sensitizers, which are otherwise limited by their inability to inject excitons into TiO₂.

Regarding MIL-125(Ti) and MIL-125(Ti)-NH₂, the charge-separated states of these frameworks were first characterized by their activity towards alcohol oxidation [9]. Where, adsorption of alcohols (R-OH) into the pores of the framework, followed by ultraviolet (UV) excitation, produced a prominent dark blue color within the sample indicating the formation of titanium (Ti³⁺). The corresponding alcohol oxidation products were detected via infrared spectroscopy (IR). To identify the active species in this oxidation reaction, electron spin resonance spectroscopy (ESR) was used to probe for the presence of varying metal oxidation states. Interestingly, a Ti³⁺ species was detected after alcohol adsorption and UV excitation, suggesting two possible mechanisms for alcohol oxidation. In the first mechanism, oxidation could occur directly at the Ti⁴⁺ nodes through reduction of the Ti⁴⁺ node to Ti³⁺. In the second mechanism, a photogenerated charge-separated state is generated where Ti⁴⁺ is reduced to Ti³⁺, and the hole is centered on the organic linker, which then oxidizes the adsorbed alcohol.

Despite these studies, it wasn't until 2012 that the photophysical properties of this class of frameworks were examined. Garcia et al. began their investigation with transient absorption (TA) techniques and observed that the transient decay of all excited species within the spectrum was coincident, meaning each signal decayed with the same kinetics [10]. The significance of this suggested that the observed spectral features corresponded to either a single species or if multiple species are present, as would be the case if photogenerated electrons were present in the sample, they decayed through interrelated processes such as recombination or annihilation. In addition, the transient species of Mil-125(Ti)-NH₂ decay on the microsecond

timescale, which provides strong evidence for the presence of a charge-separated state [40]. To explore the possibility that such a recombination process was occurring, a simple oxygen quenching study was conducted. In the presence of oxygen, both a decrease in the signal intensity and lifetime of the observed transients was recorded. By taking into consideration the types of species readily quenched by oxygen such as triplet excited states, carbon-centered radicals, and free electrons, it was concluded that the observed transient species was most likely due to photo-generated electrons within the framework. The proposed mechanism for the generation of the charge-separated state is as follows: UV light absorption leads to a charge-separated state with positively charged holes centered on the organic linker, followed by the trapping of photogenerated electrons in the Ti^{4+} node, subsequently reduced to Ti^{3+} . In conjunction with these spectroscopic studies, the presence of a long-lived charge-separated state was again confirmed in the MIL-125(Ti)- NH_2 sample using both methyl viologen ($\text{C}_{12}\text{H}_{14}[\text{Cl}^-][\text{N}^+]_2$) and N, N, N', N'-tetramethyl-p-phenylenediamine (TMPD, $\text{C}_{10}\text{H}_{16}\text{N}_2$) as molecular probes for reduction and oxidation, respectively. As observed in MOF-5, the presence of each corresponding radical cation was detected with both molecular probes.

13.6 Charge Transfer and Redox Hopping

Given the lack of band structure in these materials, it is likely that any photocatalytic activity requiring extended charge transport is promoted by self-exchange or “redox hopping” between redox active moieties incorporated into the MOF scaffold. A schematic representation is illustrated in Fig. 13.2.

Examples of charge transport via a redox hopping mechanism have been observed before in polymer materials [19, 34] and examples of such charge transfer mechanisms within MOFs are readily available in the literature [2, 7, 15, 16, 26]. The first reported example of redox hopping in MOFs was by Morris et al. who demonstrated the electrical conduction of a cobalt framework with [5,10,15,20-tetra(4-carboxyphenyl)porphyrin, $\text{Co}^{\text{III}}\text{TCPP}$, $\text{C}_{45}\text{H}_{30}\text{N}_4\text{O}_8$] secondary building units, and $\text{Co}^{\text{III}}\text{TCPP}$ struts bound by linear trinuclear Co^{II} -carboxylate film [$\text{Co}(\text{RCOO})_n$, CoPIZA] in the form of ($\text{Co}^{3+/2+}\text{TCPP}/\text{CoPIZA}$), deposited on fluorine-doped tin oxide substrate (FTO). The CoPIZA/FTO could not be explained by a simple band theory argument. Instead, the observed electrical conductivity was attributed to redox hopping between CoTCPP units, which act as support struts for the CoPIZA framework [2]. For such a mechanism to exist, it relies on two assumptions. First, the active redox centers which participate in charge transport must have the same or similar redox potentials for electron transfer to occur. Second, the redox active sites must lie in close enough proximity to allow for efficient redox hopping. If both conditions are met, then the electrical conductivity of the material can be described by charge hopping from one redox center to another, giving rise to Fickian diffusion of electrons through the material.

Characterization of such materials is commonly conducted using electrochemical methods. For any redox active species, such as those immobilized in the CoPIZA

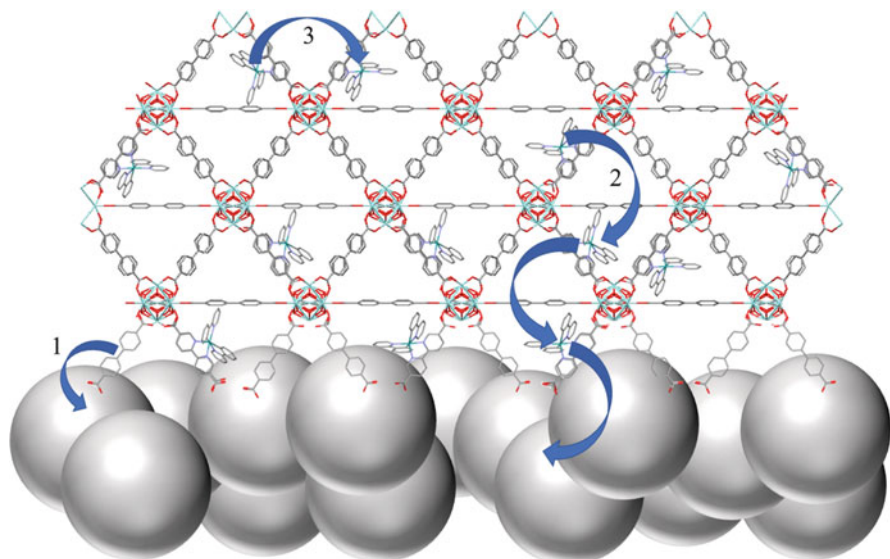


Fig. 13.2 The generation of charge-separated states via the redox hopping mechanism. In this case, a ruthenium coordination complex Ruthenium(II) bis-2,2'-bipyridine [C₁₀H₈N₂] 5,5'-dicarboxy-2,2'-bipyridine [C₁₂H₈N₂O] (Ru(bpy)₂(dcbpy)²⁺) has been incorporated into the backbone of the MOF scaffold. Charge separation occurs through two processes: the direct excitation of the 5,5'-dicarboxy-2,2'-bipyridine linker which then injects directly into the titania (TiO₂) semiconductor (process 1), or through excitation and injection of a ruthenium species incorporated into the backbone of the MOF scaffold (process 2). Exciton diffusion throughout the framework typically occurs through redox hopping between the incorporated ruthenium centers before injection or recombination with a positively charged hole (process 3)

framework, the electrochemical response is dependent upon the diffusion coefficient of the redox active species (D), and thus for an immobilized species, the rate of charge transfer (k_{ct} , unit s^{-1}). For such materials, there exist three regimes: (i) the rate of charge transfer (k_{ct}) is faster than the experiment sweep rate (ν , unit mV/s) or $k_{ct} > \nu$, (ii) $k_{ct} \approx \nu$, and (iii) $k_{ct} < \nu$. The first regime describes rapid charge transport, where for immobilized species, the cyclic voltammogram will display asymmetrical shape ($\Delta E_p = 0$ mV) centered at the reduction potential of the material. Chidsey's work on surface-modified gold electrodes represents a classic example of such work [8]. Since the electrochemical response of the CoPIZA framework exhibits non-zero scan rate dependence across all measured scan rates, it was concluded that for the CoPIZA/FTO film, regime (iii) most accurately describes its electron transfer kinetics. Since the electron transport is sluggish in this regime, the behavior of the cyclic voltammogram exhibits the same behavior for freely diffusing redox active species in solution, and this follows the Randles-Sevcik equation (Eq. 13.1).

$$i_p = 0.4463nFAC \left(\frac{nF\nu D}{RT} \right)^{\frac{1}{2}} \quad (13.1)$$

In the above equation, i_p is the peak current of either the background corrected anodic or cathodic process (A), n is the number of electrons transferred in the redox active process (dimensionless, usually one), F is Faraday's constant ($96485.3 \text{ C mol}^{-1}$), A and C are the active area of the electrode (cm^2) and the bulk concentration of the redox active species (mol/cm^3), v is the scan rate (mV/s), R and T are the ideal gas law constant ($\text{K}^{-1} \text{ mol}^{-1}$), and the temperature (K), and D is the diffusion coefficient of the species (cm^2/s). By varying the scan rate of the cyclic voltammogram, and generating a plot of peak current versus the square root of the scan rate, a linear relationship can be observed whose slope is equal to $2.69 \times 10^5 \text{ ACD}^{1/2}$ for a one-electron redox couple measured at $25 \text{ }^\circ\text{C}$. From this data, the diffusion coefficient can be calculated for the redox active species.

For immobilized species incorporated into the MOF, however, a more reliable method for determining the diffusion coefficient can be employed through the analysis of spectroelectrochemistry. From the spectroelectrochemical data, it was shown that the reduction processes observed within the film were ascribed to both the $\text{Co}^{3+/2+}$ redox couple and the $\text{Co}^{2+/+}$ redox couple. From these results, the apparent diffusion coefficient for redox hopping throughout the CoPIZA film (D_{app} , unit cm^2/s) was measured using time-resolved spectroelectrochemistry data and a modified version of the Cottrell equation (Eq. 13.2). For the CoPIZA material, D_{app} was calculated to be $7.55 (\pm 0.05) \times 10^{-14} \text{ cm}^2/\text{s}$. Ultimately, this value is found to be four to six orders of magnitude lower than for modified polymer films which are typically on the order of $\sim 10^{-8} - 10^{-6} \text{ cm}^2/\text{s}$ [32, 39, 44]. This significant reduction in D_{app} could be attributed to reduced diffusion of ionic species within the framework leading to significant impacts on the rate of charge transport within the MOF film [26].

$$\Delta A = \frac{2A_{\max} D_{app}^{1/2} t^{1/2}}{d\pi^{1/2}} \quad (13.2)$$

Likewise, Hupp et al. showed that charge transport via redox active linkers can be separated from chromophores by incorporation of additional redox active moieties inside the framework itself [15]. By incorporating the ferrocene derivative, ferrocene carboxylic acid, into the open channels of the framework Northwestern University-1000 [NU-1000], the authors demonstrated bias-switchable redox behavior in which oxidation of the tethered ferrocene units selectively blocked cation mobility within the NU-1000 pores. By blocking the pores in such a manner, the authors were able to remove any observable redox chemistry for the pyrene-containing linkers. Upon reduction of these ferrocene units, the cation mobility of the supporting electrolyte was restored, as well as the electrochemical response of the pyrene-containing linker. In a follow-up study, the authors demonstrated that by utilizing host-guest chemistry, the electron transfer kinetics and the apparent diffusion coefficient for redox hopping could be modulated. By taking advantage of the high affinity for β -cyclodextrin ($\beta\text{-CD}$, $\text{C}_{42}\text{H}_{70}\text{O}_{35}$) complexation with ferrocene and the low affinity for

complexation of β -CD with ferrocenium ($C_{10}H_{10}[X^-][Fe^+]$, where X^- is the counter anion), the authors were able to observe $[Fe(C_5H_5)_2]$, modulated redox hopping as a function of β -CD concentration, with a 30-fold reduction of D_{app} at the maximum solubility of the β -CD. The apparent diffusion coefficient can also be directly related to the microscopic rate constant for redox hopping events k_{hop} (Eq. 13.3).

$$k_{hop} = \frac{D_{app}}{r^2} \quad (13.3)$$

In the case of the functionalized NU-1000 framework, inductively coupled plasma mass spectrometry (ICP-MS) and coulometric analysis supports the assumption that one ferrocene molecule is present at each node of the framework. This provides a ferrocene-to-ferrocene separation distance of 1.6 nm, which in turn resulted in a reduction of k_{hop} from 780 s^{-1} in the absence of β -CD, to 23 s^{-1} when the β -CD concentration is 20 mM. However, in either of these cases, the rate of k_{hop} is still dependent on the diffusion of either cations or anions of the electrolyte throughout the framework.

13.7 Literature Examples of MOFSCs

One of the most common frameworks employed in MOFSCs is the pillared porphyrin framework. The most notable entry in this class of MOFs is the pillared porphyrin framework 4 (PPF-4), which consists of layered structure of tetra(carboxyphenyl) porphyrin (TCPP, $C_{48}H_{28}N_4O_8Zn$) linker molecules with planar coordination to zinc (Zn^{2+}) ions and separated by 4,4'-bipyridine ($C_{10}H_8N_2$) linkers (Fig. 13.3). In this configuration, the framework acts as a series of two-dimensional layers of planar Zn-TCPP units joined by vertical bipyridine pillars. One of the most notable studies involving this framework examined the photovoltaic properties of cells prepared with PPF-4 as its sensitizer. The importance of these studies was that the observed photovoltaic response was due solely to the PPF-4 framework acting as the photosensitizer on a TiO_2 scaffold [41]. By using only prewashed nanocrystals of PPF-4 dispersed on a conductive substrate coated with TiO_2 , the authors were able to prepare cells where it was not possible for free linker molecules to coordinate to TiO_2 and contribute to the cell's photocurrent response. This approach differed from traditional methods of film preparation wherein the MOF film is grown in situ solvothermally on the titania/fluorine-doped tin oxide (TiO_2 /FTO) electrode surface, which leads to ambiguity as to whether the framework is acting as the sensitizer in the MOFSC, or if the photovoltaic properties are due to chemisorbed linker molecules on the TiO_2 working electrode.

To begin, nanocrystals of PPF-4 were synthesized in a one-pot reaction from Zn-TCPP, zinc nitrate tetrahydrate [$Zn(NO_3)_2 \cdot 4H_2O$], and 4,4'-bipyridine ($C_{10}H_8N_2$) in 1:3 (v:v) ethanol (C_2H_6O) and diethylformamide (DEF, $HCON(C_2H_5)_2$) solution. The resulting crystals were subsequently collected and washed via centrifugation with DEF and ethanol. These crystals were then dispersed in

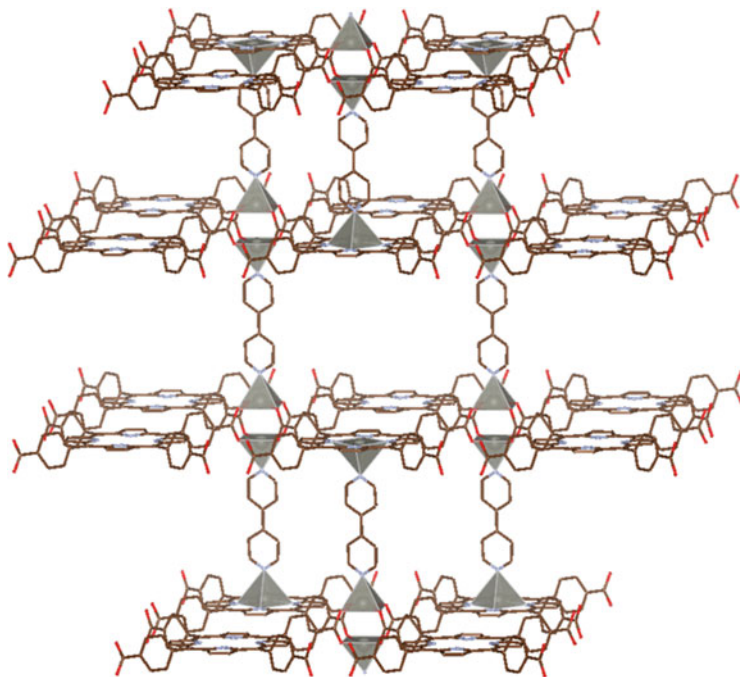


Fig. 13.3 Crystallographic structure of PPF-4 displaying the characteristic layered TCPP units joined by 4,4'-bipyridine pillars

chloroform and drop-cast onto a TiO_2 -coated substrate to form the PPF-4/ TiO_2 working electrode. This working electrode was sealed together with a platinum (Pt)-FTO counter electrode and iodide-based electrolyte. The photovoltaic properties of the prepared cells are shown below (Fig. 13.4).

From the current-voltage plots in Fig. 13.4, a clear increase in photocurrent response is observed by PPF-4 over TiO_2 . When a 450-nm band-pass filter was used to remove the photoresponse from UV-excited TiO_2 , a prominent contribution from the PPF-4 is observed, while the TiO_2 control electrode exhibits a photovoltaic response nearly identical to the prepared PPF-4 cell under dark conditions. Ultimately, due to the absence of a strong electronic contact in this device architecture, the overall cell efficiencies were only $2.3 \times 10^{-3}\%$. In addition to the current-voltage plots, electrical impedance spectra (EIS) demonstrate a reduction in the electron transfer resistance across both PPF-4 MOFSCs and TiO_2 control. However, the cells prepared with PPF-4 as the sensitizer displayed consistently lower electron transfer resistance than those of the TiO_2 control. These results demonstrated unambiguously that the PPF-4 MOF nanocrystals act as the sensitizer for the MOFSC with no additional contributions from adsorbed linker or TiO_2 photoexcitation. More importantly, this study provided the first proof-of-concept MOF/ TiO_2 electrodes for light-absorbing chromophores in photovoltaic applications.

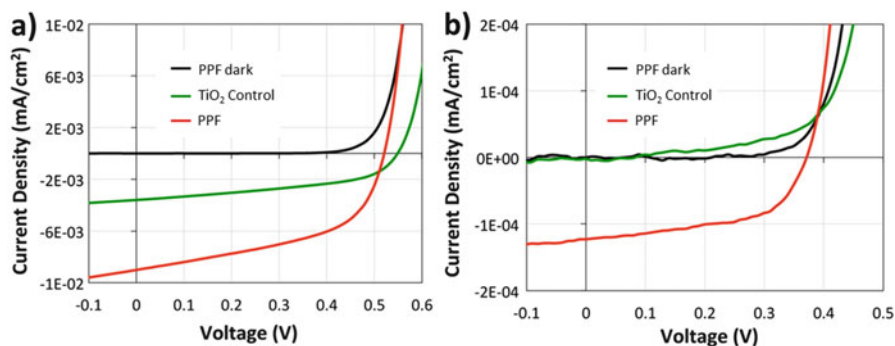
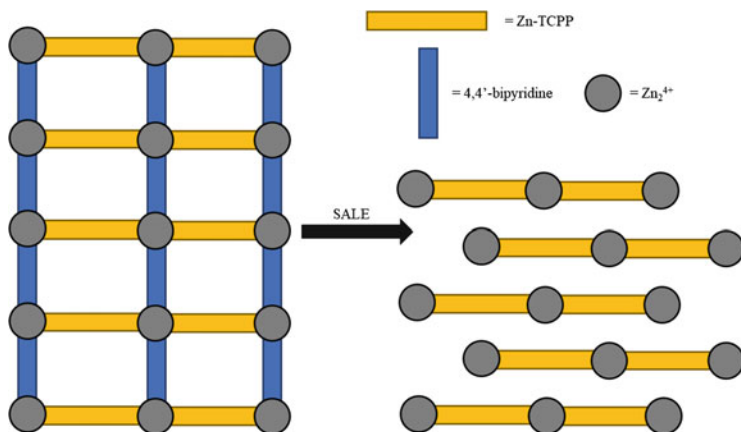


Fig. 13.4 A photovoltaic response of PPF-4 MOFSCs prepared via drop-casting of PPF-4 on TiO₂ under AM 1.5 simulated illumination (a). The photovoltaic response of PPF-4 MOFSCs under 450 nm band-pass filtered illumination to remove UV-excited photoresponse from TiO₂ (b). (Reprinted (adapted) with permission from Spoerke et al. [41]. Copyright 2017 American Chemical Society)

Similar porphyrin-based frameworks aim to alleviate another significant challenge faced by MOFSCs: the reduction of deleterious recombination processes between the redox electrolyte and the photogenerated electrons within the MOF framework [12]. It was, therefore, reasoned that if the photogenerated holes could be quickly and efficiently transported to the periphery of the MOF film where the electrode/electrolyte interface exists, then exclusion of the redox electrolyte from the pores of the MOF would lead to a reduced chance for unwanted electronic recombination. In addition, one of the major considerations for the design of novel frameworks for MOFSCs is the enhancement of the photogenerated electron diffusion distance (L_d). In general, this kind of enhancement can be achieved through two strategies – through the optimization of three-dimensional frameworks to allow for rapid exciton transport through the extended MOF structure, or through collapsing a three-dimensional, layered framework, into a two-dimensional framework. Regardless of which strategy is chosen, the overall goal is the same, to bring the chromophore linkers of the MOF in close Van der Waals contact with one another, allowing for the exchange of excitonic energy more readily.

As one example of the latter strategy, work by Hupp et al. with a derivative of the PPF-4 framework employing metallated zinc(II) meso-tetra(4-carboxyphenyl) porphyrin (Zn-TCPP) was selectively collapsed from its three-dimensional structure into a layered two-dimensional structure using solvent-assisted linker exchange (SALE) [12]. In SALE, the MOF is soaked in a solution containing a separate linker or coordinating unit which can then undergo ligand exchange with some of the organic linkers in the MOF backbone. In this case, a collapse of the framework brings the Zn-TCPP units in closer Van der Waals contact than in the pillared configuration increasing k_{hop} for *inter*-layer electron transfer. That is to say, the rate of electron transfer between two independent layers increases. The increase in the *inter*-layer k_{hop} leads to an increase in L_d , as *inter*-layer electron transfer will bring either a photogenerated electron closer to the TiO₂ scaffold, or a



Scheme 13.3 The collapse of a layer-by-layer Zn-TCPP PPF by SALE to produce a layered two-dimensional MOF

photogenerated hole closer to the electrode/electrolyte interface. In contrast, *intra*-layer hopping, hopping within a single layer between Zn-TCPP units, produces largely no beneficial effect for increasing L_d .

In this instance, the pillared Zn-TCPP framework was soaked in a solution of pyridine to remove the bipyridine pillars. When this process is carried out, the pillared morphology of the framework was collapsed, such that the orientation of the film would resemble that of a layered two-dimensional coordination polymer (Scheme 13.3).

Pyridine was chosen as it possesses a slightly higher pK_a than that of 4,4'-bipyridine (5.25 vs. 4.9), allowing for the near-quantitative exchange of the 4,4'-bipyridine pillars. The *post*-SALE films were characterized by both profilometry and ellipsometry to determine the new film thickness and density. Measurements of the film thickness supported an average decrease from approximately 80 nm to approximately 40 nm after SALE. In addition, collapsing such films led to direct increases in film density and, therefore, the refractive index (n) of the material. Since the refractive index of a porous framework can be estimated as a volume-weighted average of the indices for the framework itself ($n_{\text{MOF}} > 1$, dimensionless) and the corresponding void space within the MOF ($n_{\text{vac}} = 1$), the observed increase in the refractive index from the native structure to the collapsed film (1.4–1.8) indicated an approximate doubling of the film density. For these methods to be expanded upon, it will be crucial in follow-up studies to conduct in-depth materials characterization of the framework *pre*- and *post*-SALE.

To examine the enhanced excitonic transport properties of the collapsed film, a molecular quencher was installed atop the framework prior to collapse. For this purpose, a standout candidate that could easily be incorporated by an LBL approach was the palladium-metallated porphyrin (Pd-TCPP) which is known to quench the excited state of the Zn-TCPP linker [6]. By installing two layers of Pd-TCPP on top

of films prepared with 13 cycles of Zn-TCPP and 4,4'-bipyridine layers, the emission intensity of the Zn-TCPP linkers was quenched by approximately 50%. Post-collapse however, this quenching efficiency increased to approximately 70%, qualitatively indicating an increase in exciton transport distance via *inter*-layer hopping to the Pd-TCPP quenchers. From this assessment, an estimate of L_d was derived by equating the percentage of quenched emission to the percentage of Zn-TCPP linkers capable of being quenched by Pd-TCPP, whether by direct energy transfer or by *inter*-layer hopping between Zn-TCPP units. For this approximation, two assumptions must hold true. The first being that the rate of quenching of the Zn-TCPP units by Pd-TCPP is fast relative to the nonradiative decay of the excited Zn-TCPP units, and the second being the optical density of the film is small enough that the probability of photon absorption by any individual Zn-TCPP unit is independent of its location within the film. Based on these assumptions, prior to film collapse, an exciton could readily diffuse across a maximum of eight layers. Post-collapse however, this number increased to a maximum of 11 layers.

As a follow-up study, Hupp and coworkers have also investigated replacing the 4,4'-bipyridine units of this framework, with smaller bifunctional organic linkers which will maintain the three-dimensional nature of the framework while reducing the distance between individual Zn-TCPP units [11]. In this work, 1,4-diazabicyclo [2.2.2]octane (DABCO) was exchanged with the 4,4'-bipyridine struts through SALE. In doing so, the authors demonstrated that the number of layers the exciton could traverse was increased from 11 layers to 26. This substantial increase was due to the three-dimensional structure of the framework, which forces the Zn-TCPP units to sit facially aligned with each other, while in the collapsed two-dimensional topology, the Zn-TCPP units adopt a staggered arrangement leading to almost no decrease in the electronic coupling distance between porphyrin units. As such, only a marginal increase was observed when pyridine (C_5H_5N) was used to replace 4,4'-bipyridine. Ultimately, these studies clearly demonstrate that post-synthetic modification of current frameworks could be utilized to improve device performance.

In moving away from porphyrin-based MOFs, other investigators have characterized MOFSCs utilizing MOF sensitizers in which the aromatic linker, typically 1,4-benzene dicarboxylic acid (bdc, $C_8H_6O_4$) acted as the light absorber. Probably the most well-studied case for such a system is the commercially available framework aluminum coordinated benzene dicarboxylic acid [$Al_2(bdc)_3$]. The structure of $Al_2(bdc)_3$ can be simply described as a zinc oxide [Zn_4O] cluster bridged by benzene dicarboxylic acid linkers (Fig. 13.5a). However, as discussed earlier, the HOMO-LUMO gap for such a framework is ill-matched to the visible spectrum ca. 3.4 eV [3]. Cells utilizing $Al_2(bdc)_3$ as their sensitizer were fabricated by spin coating $Al_2(bdc)_3$ framework onto a TiO_2 photoanode supported on indium-doped tin oxide (ITO). A hole conducting layer of Spiro-OMeTAD ($C_{81}H_{68}N_4O_8$) was spin-coated on top of the photoactive MOF layer, followed by deposition of a gold counter electrode. Though revolutionary at their introduction, the current-voltage performance of these devices displayed poor percent power conversion efficiencies (% PCE) with a maximum % PCE of ~0.002% for 2.7 μm films (Fig. 13.5b).

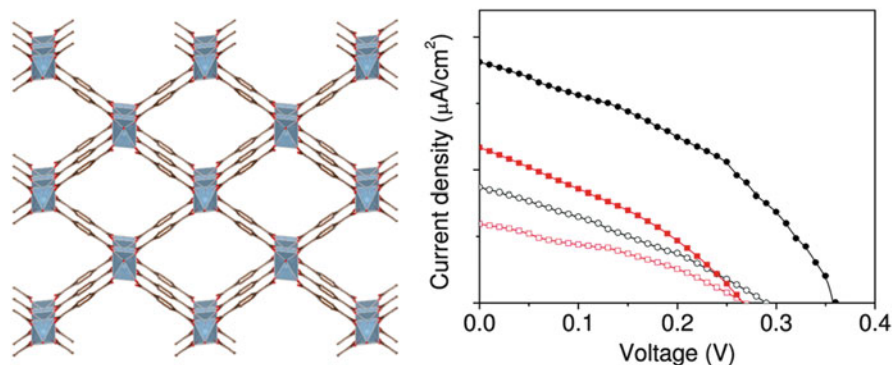
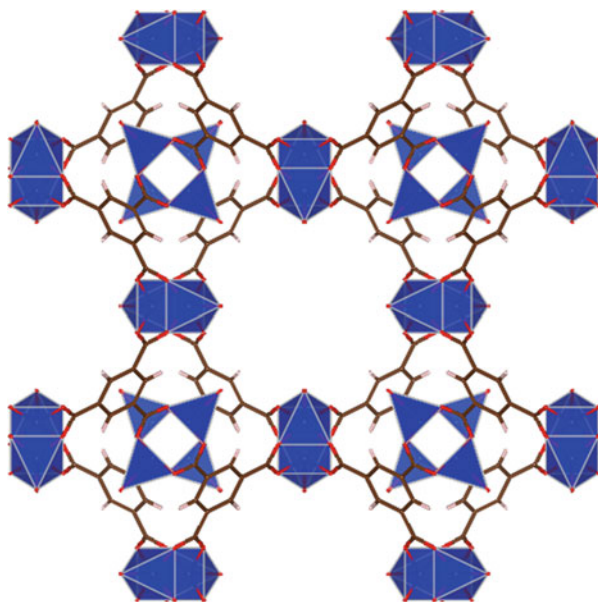


Fig. 13.5 Crystallographic structure of $\text{Al}_2(\text{bdc})_3$ as viewed down the b axis displaying one-dimensional rhombohedral channels (a). Photocurrent response of cells prepared with $\text{Al}_2(\text{bdc})_3$ as the sensitizer and Spiro-OMeTAD as the hole conductor with a gold counter electrode with either $\text{Al}_2(\text{bdc})_3$ sensitizer with a thickness of $2.7 \mu\text{m}$ (red solid squares) or $5.4 \mu\text{m}$ (red open squares) or with $\text{DMB@Al}_2(\text{bdc})_3$ sensitizer with a thickness of $2.7 \mu\text{m}$ (black solid circles) or $5.4 \mu\text{m}$ (black open circles) under AM 1.5 illumination (b). (Reprinted (adapted) with permission from Lopez et al. [49]. Copyright 2011 American Chemical Society)

To mitigate these low efficiencies, $\text{Al}_2(\text{bdc})_3$ was doped with 1,4-dimethoxybenzene (DMB, $\text{C}_8\text{H}_{10}\text{O}_2$) which acts as a hole-trapping agent to produce the framework $\text{DMB@Al}_2(\text{bdc})_3$. By incorporating a hole-trapping agent into the framework, the lifetime of the charge-separated state could be enhanced reducing parasitic recombination within the cell. Indeed, by incorporating DMB into the framework, the lifetime of the transient corresponding to free electrons (optical absorption from 350 to 500 nm) increased markedly. In addition, by incorporating these deep trap states into the framework, an increase in fill factor (ff) was observed for cells prepared with DMB, which increased by 6.62% from 33.84% to 40.46% (Fig. 13.5b). This, in turn, led to a substantial boost in the relative device % PCE up to $\sim 0.005\%$ PCE under optimal conditions. More importantly, this study laid the groundwork for the design of state-of-the-art MOFSCs, leading investigators to consider the modification of the MOF linker as a suitable site for the incorporation of a photosensitizing chromophore to compensate for poor spectral overlap of the framework itself with solar irradiance.

More successful solar cells, however, were prepared with an iodine-doped Cu-MOF, formed by the reaction of $\text{Cu}(\text{NO}_3)_2$ with benzene-1,3,5-tricarboxylate, acting as a replacement for more traditional DSSC chromophores (Fig. 13.6) [24]. By utilizing Cu-MOF as their sensitizer, cells prepared by LBL growth of Cu-MOF on TiO_2 -coated fluorine-doped tin oxide (TiO_2/FTO) substrates displayed % PCEs of 0.008% PCE. To further enhance cell performance, iodine was doped into the framework. The benefit of this additive is twofold. First, incorporation of iodine molecules into the framework switches the electrical conductivity of the framework from the insulating regime to the semiconductive regime through either partial oxidation of the Cu-MOF or conduction through an ordered iodine network in the framework [21, 46]. Impedance spectroscopy

Fig. 13.6 Structure of Cu-MOF as viewed down the crystallographic a axis



was used to determine the effect of iodine doping on the conductivity of the framework. From the EIS spectra, it is clear that doping the framework with iodine significantly improves the conductivity of the framework under solar irradiance (Fig. 13.7a). It was observed that the charge transfer resistance (R_{ct}) of the iodine-doped Cu-MOF is one order of magnitude lower than TiO_2/FTO (Fig. 13.7b), and three orders of magnitude lower than Cu-MOF/ TiO_2/FTO (Fig. 13.7c). Finally, R_{ct} was investigated for iodine-doped Cu-MOF under dark and illuminated conditions (Fig. 13.7d). The drastic decrease in R_{ct} under illumination suggests that upon illumination, iodine-doped Cu-MOF acts as a photosensitizer generating electron-hole pairs on illumination which are rapidly injected into the TiO_2 support.

In addition to the impressive change in conductivity, iodine doping also increased the efficiency of the device by an order of magnitude increasing the % PCE from less than 0.01% PCE to 0.26% PCE. However, there is one major caveat to improving the device performance with iodine, and that is that iodine is well-known to undergo photoinduced dissociation into the radical species (I^\cdot) under visible illumination (Eq. 13.4). In these circumstances, it is unclear whether the Cu-MOF acts independently as a sensitizer for the PV, or if the photogenerated I^\cdot radical contributes appreciably to the device performance by reacting with the TiO_2 semiconductor.



In terms of modifying the MOF linker itself to incorporate various chromophores, few examples exist in the literature. One instance can be found in the work presented

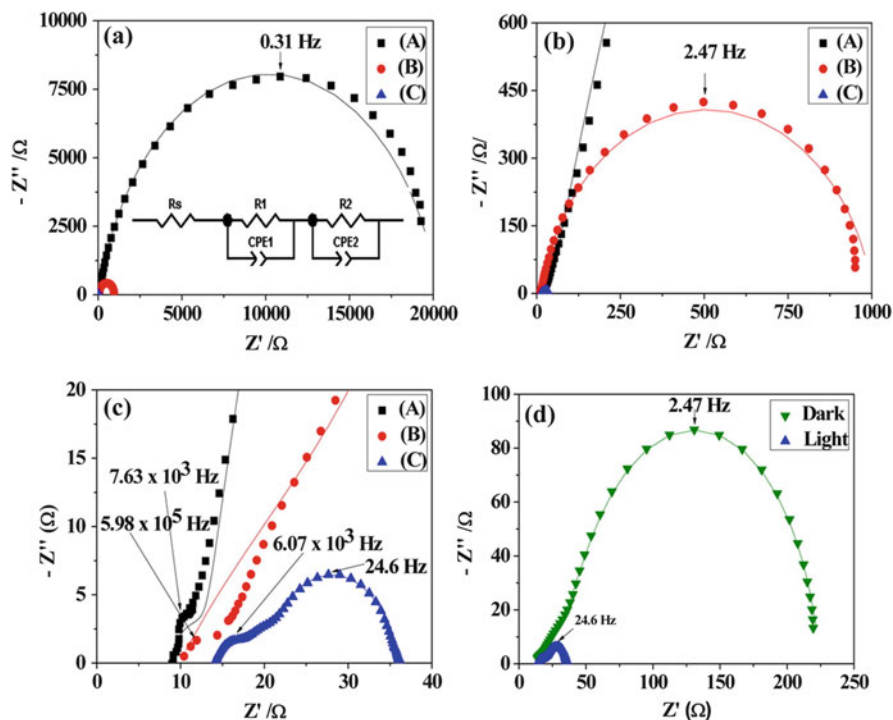


Fig. 13.7 (a) Circuit model and impedance spectrum of cells prepared with either (A) undoped Cu-MOF/TiO₂/FTO (black squares), (B) TiO₂/FTO (red circles), or (C) iodine-doped Cu-MOF/TiO₂/FTO (blue triangles) under simulated AM 1.5 illumination. (b) Zoomed-in impedance spectrum of (A) at higher frequencies emphasizing the insulating nature of the undoped Cu-MOF framework relative to that of TiO₂/FTO. (c) Zoomed-in impedance spectrum of (A) at the highest frequency region. (d) Electrical impedance spectrum of iodine-doped Cu-MOF/TiO₂/FTO cells under dark and simulated AM 1.5 illumination. (Reprinted (adapted) with permission from Lee et al. [24]. Copyright 2014 American Chemical Society)

by Morris et al. utilizing a ruthenium [Ru(II)L₂L'] (L = 2,2'-bipyridine, C₁₀H₈N₂; L' = 2,2'-bipyridine-5,5'-dicarboxylic acid, C₁₂H₈N₂O₄) (RuDCBPY) linker to form a RuDCBPY-doped UiO-67 framework (UiO-67(Ru)) [29]. Cells sensitized with UiO-67(Ru) were prepared using two methods, wherein UiO-67(Ru) was grown either directly via solvothermal synthesis onto TiO₂/FTO, termed UiO-67(Ru)-OP/TiO₂/FTO (OP = one pot), or by post-synthetic modification of pristine UiO-67 grown directly onto TiO₂/FTO by submerging the prepared films in an ethanolic solution of RuDCBPY termed UiO-67(Ru)-PS/TiO₂/FTO (PS = post-synthetic).

When grown directly onto FTO, at low-doping concentrations of RuDCBPY, it was found that the UiO-67(Ru) framework displayed excited-state properties consistent with the RuDCBPY linker dissolved in DMF. These excited-state characteristics include a long-lived metal-to-ligand charge transfer state (MLCT) with a lifetime of $\sim 1.4 \mu\text{s}$ [29]. By increasing the doping concentration, a decrease in the

emission lifetime was observed, corresponding to homogenous energy transfer between RuDCBPY centers [30]. Additionally, this framework readily grows on TiO₂ scaffolds without appreciably changing the energetics of the RuDCBPY linkers relative to RuDCBPY in solution [28]. Based on these observations, this framework represented a strong candidate for use in photovoltaic applications.

Cells prepared using the UiO-67(Ru) framework as a sensitizing material displayed moderate photocurrents with short-circuit current densities (J_{sc}) ranging from 0.03 to 0.54 mA/cm² and open-circuit potentials (V_{OC}) ranging from 370 to 520 mV when utilizing a common I^-/I_3^- electrolyte. In addition, cells displayed higher amounts of charge recombination than traditional DSSCs with the average fill factors (ff) across the cells being 0.50. These ff values were presumably due to partial occlusion of the pores to I^- and I_3^- diffusion as well as large film thickness which can prevent the majority of excitons from reaching the TiO₂ scaffold. Evidence for such an event can be seen in cells prepared using the post-synthetically modified UiO-67(Ru) films. In a post-synthetic modification, only the outermost layers of the UiO-67 framework are likely to undergo efficient linker exchange. This was confirmed by confocal fluorescence microscopy which showed denser populations of RuDCBPY centers along the edges of the UiO-67 crystallites. When such a buildup occurs, the high density of RuDCBPY units along the exterior of the MOF film leads to exclusion of the redox electrolyte from the interior of the MOF, resulting in lower ff values.

Another downfall of these devices was the lack of control over film thickness, which resulted in a reduction in the efficiency of charge collection. For example, the maximum hopping distance for photogenerated electrons in this material can be calculated from k_{hop} (unit Angstrom) by the following equation (Eq. 13.5).

$$k_{hop} = \frac{mD_{RET}}{R_{hop}^2} \quad (13.5)$$

In this equation, m is a dimensional factor (unitless, where $m = 6$ for three-dimensional systems, $m = 4$ for two-dimensional systems, and $m = 2$ for one-dimensional systems), D_{RET} is the diffusion coefficient for energy migration (cm²/s) in crystalline Ru(bpy)₃²⁺ salts [18]. From this data, it was calculated that the maximum hopping distance for RuDCBPY-UiO-67-TiO₂ of 254 Å. This distance was significantly smaller than the average film thickness of ~10 μm as calculated from scanning electron microscopy (SEM) images. As a consequence, the maximum % PCE observed for the prepared cells was only measured to be 0.125%. Notably, however, UiO-67(Ru) outperformed control cells constructed in this study in which RuDCBPY adsorbed directly onto TiO₂ or those in which UiO-67 acted as the sensitizer. This study highlights some of the challenges and future considerations that will be discussed at the end of this chapter. Namely, the need for control of MOF film growth and transport of redox mediators through control of the MOF three-dimensional (3D) structure.

In efforts to minimize the diffusion limitation inherent in many MOF materials, some investigators have shifted their focus toward solid-state MOFSCs. These cells

eschew traditional liquid electrolytes in favor of hole conducting polymers or MOF materials. Possibly one of the most notable efforts to fabricate a MOFSC utilizes a hole-conducting MOF based on the coordination between cobalt (Co^{2+}) ions and a redox active linker, di(3-aminopropyl)-viologen (DAPV, IUPAC Name 1,1'-bis(3-aminopropyl)-[4,4'-bipyridinium] dianion, $\text{C}_{16}\text{H}_{24}[\text{X}^-]_2\text{N}_2[\text{N}^+]_2$), to form the framework Co-DAPV [1]. Hall-type measurements of the Co-DAPV MOF displayed a [positive] *p*-type photoconductance with a hole concentration and hole mobility of $3.35 \times 10^8 \text{ cm}^{-3}$ and $0.017 \text{ cm}^2/\text{V}\cdot\text{s}$ respectively. These mobilities are on par with poly(3-hexylthiophene-2,5-diyl) (P3HT, $(\text{C}_{10}\text{H}_{14}\text{S})_n$) doped with 2,3,5,6-Tetrafluoro-7,7,8,8-tetracyanoquinodimethane (F_4TCNQ , $\text{C}_{12}\text{F}_4\text{N}_4$), an oxidant used to increase the conductivity of organic semiconductors [36]. The origin of such photoconductivity is attributed to metal-to-ligand charge transfer involving the transfer of photoexcited electrons from the cobalt metal center to the DAPV ligand.

Films of Co-DAPV were grown on TiO_2 using LBL techniques, and in doing so, a [positive-negative] p-n heterojunction is prepared, which led to a maximum power conversion efficiency of 2.1% PCE (Fig. 13.8). In terms of device performance, the prepared cells displayed J_{sc} values, ranging from 0.98 to $4.92 \text{ mA}/\text{cm}^2$ for cells prepared with 5 and 15 LBL cycles of Co-DAPV, respectively. Likewise, The V_{OC} values achieved a maximum of 670 mV when 15 layers of Co-DAPV were deposited on the electrode surface. It is worth noting that up to 30 LBL cycles were performed on some devices, but when 15 layers were exceeded, a reduction in J_{sc} was observed, while the V_{OC} values remained unchanged. The increase in J_{sc} , up to 15 cycles and subsequent reduction in J_{sc} above 15 cycles was correlated to a reduction in the charge transport resistance (R_{trans}) within the Co-DAPV film. Ultimately, by combining the light absorbing layer and the hole conducting layer into a single material, the classical challenges of electrolyte diffusion and hole mobility have been

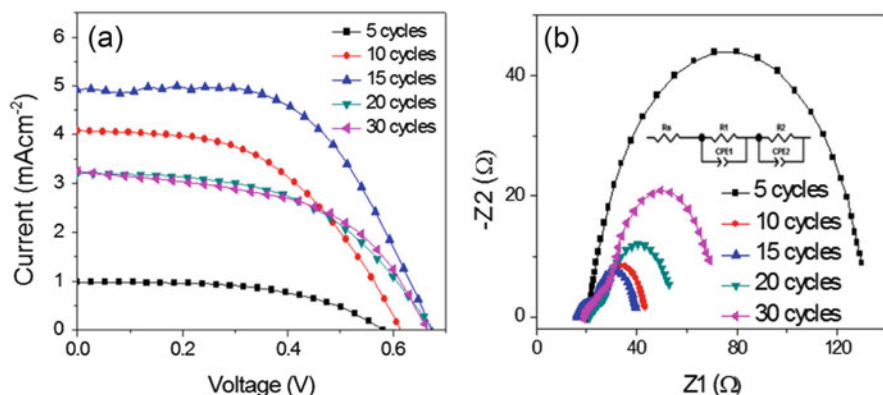


Fig. 13.8 (Left) Photocurrent response of MOFSCs prepared using Co-DAPV as both the sensitizer and hole conductor as a function of layer-by-layer cycles. (Right) Nyquist plot of prepared cells under 0.1 sun illumination displaying the increase in conductivity of the Co-DAPV MOF up to 15 LBL cycles. (Reprinted (adapted) with permission from Ahn et al. [1]. Copyright 2017 American Chemical Society)

alleviated allowing for the preparation of high-efficiency devices. Moving forward, considerable interest should be given to developing and optimizing solid-state MOFSCs as the absence of comparative cells for this architecture is currently lacking within the literature. Additionally, designing novel hole-conducting MOFs capable of fast and efficient redox hopping to improve hole mobility with absorption profiles well-suited for visible and near-infrared light absorption should receive consideration as well.

13.8 Conclusions and Future Outlook

Given the preliminary work discussed herein, it is suitable to provide a perspective of the field and future considerations for MOFSCs and their implementation. To begin, three major challenges must be addressed for the field to advance. First, the development of new MOF materials, which possess efficient exciton transport is essential to improve photogenerated electron and hole transport through the MOF. Significant progress has been made by utilizing dopants such as iodine or redox active ligands like DAPV to improve exciton transport throughout the MOF sensitizer. However, additional studies are needed to fully realize a highly photoconductive material, which possesses satisfactory exciton diffusion. This can be accomplished through the development of modified organic linkers, which possess rapid self-exchange rate constants and long-lived charge-separated states. Likewise, host-guest interactions can also be exploited to promote increased exciton diffusion by incorporating additional trap states, which can reduce exciton recombination and should evolve coincidentally with the design philosophy of increased photo-conductivity.

Second, new studies to enhance the diffusion of the redox electrolyte throughout the MOF are necessary. For rapid and efficient chromophore regeneration, the redox electrolyte must be able to freely diffuse into and out of the framework. As such, framework engineering and design should account for and aim to improve electrolyte diffusion. This can be accomplished through modification of existing frameworks with large channels such as the HKUST-1 and NU-1000 frameworks, or by the development of novel frameworks unlike those presently studied. Considerations such as pore obstruction by incorporated chromophores, channel, pore orientation, and defect density will be primary research goals.

Finally, the growth and modification of MOF films must lead to strong electronic contacts to the TiO₂ scaffold. This is a necessity for rapid injection of electrons into TiO₂ as well as leading to uniform coverage of the TiO₂ scaffold. Most MOFSCs can be prepared by loading the MOF sensitizer onto the TiO₂ either by solvothermal growth, spin coating, or by LBL deposition. While LBL growth is preferred, not all MOFs can be easily fabricated on the surface of TiO₂ through LBL methods. While most other MOFs can be prepared via solvothermal synthesis, this method of film growth affords virtually no control over film thickness. This lack of control only helps to exacerbate the diffusion limitations of prepared devices, despite the presence of strong electronic contacts between MOF film and the conductive substrate.

Contrarily, spin-coating the MOF sensitizer allows for excellent control of film thickness but leads to poor electronic contact between the MOF and TiO₂ as growth is not directly seeded from the surface as it is in both LBL growth and solvothermal synthesis. This leads to poor injection rates for the photogenerated electrons lowering the photocurrent the device can produce. Significant headway in this field could be made if processes were developed which allowed for a wide array of MOF structures to be grown via layer-by-layer growth or other means such as chemical vapor deposition.

In closing, MOFSCs present a unique avenue to the development of new state-of-the-art photovoltaics. The ability to fix chromophores into MOF backbones provides several distinct advantages over dye adsorption onto a nanostructured semiconductor electrode. These advantages include the prevention of dye aggregation and the ability to incorporate multiple chromophores, through variation of the MOF linker during synthesis, with various functionalities and absorption properties into the framework. Despite the challenges that MOFs face as sensitizers, they represent a novel molecular scaffold due to their unmatched synthetic tunability. The number of preliminary experimental results has increased dramatically in the last 5 years, with over one-hundred twenty independent studies exploring MOFs as either photosensitizers directly in MOFSCs, photoconductors, photodetectors, or as an additional component of more traditional DSSCs being published [25, 33, 42]. Compared to only five studies between the years of 2000–2012, this field is rapidly growing and expanding every year. It is feasible then to presume that the development optimization of new MOF materials for light harvesting applications will lead to MOFSCs emerging as one of the most promising candidates in the field of molecular photovoltaics.

Acknowledgments The authors wish to thank the US Department of Energy, Office of Basic Energy Sciences for funding under Award Number DE-SC0012445.

References

1. D.Y. Ahn et al., Novel solid-state solar cell based on hole-conducting MOF-sensitizer demonstrating power conversion efficiency of 21% ACS. Appl. Mater. Interfaces **9**, 12930–12935 (2017). <https://doi.org/10.1021/acsami.7b03487>
2. S.R. Ahrenholtz, C.C. Epley, A.J. Morris, Solvothermal preparation of an electrocatalytic metalloporphyrin MOF thin film and its redox hopping charge-transfer mechanism. J. Am. Chem. Soc. **136**, 2464–2472 (2014). <https://doi.org/10.1021/ja410684q>
3. M. Alvaro, E. Carbonell, B. Ferrer, F.X. Llabrés i Xamena, H. Garcia, Semiconductor behavior of a metal-organic framework (MOF). Chem. Eur. J. **13**, 5106–5112 (2007). <https://doi.org/10.1002/chem.200601003>
4. A.J. Bard, L.R. Faulkner, *Electrochemical Methods: Fundamentals and Applications* (Wiley, Hoboken, 2007)
5. G. Boschloo, A. Hagfeldt, Characteristics of the iodide/triiodide redox mediator in dye-sensitized solar. Cells Acc. Chem. Res. **42**, 1819–1826 (2009). <https://doi.org/10.1021/ar900138m>

6. A.M. Brun, A. Harriman, Energy- and electron-transfer processes involving palladium porphyrins bound to DNA. *J. Am. Chem. Soc.* **116**, 10383–10393 (1994). <https://doi.org/10.1021/ja00102a004>
7. P. Celis-Salazar, S. Ahrenholtz, A. Morris, Structural insight into redox hopping electron transport metal-organic frameworks. *Am. Chem. Soc.*, INOR-244 (2016)
8. C.E.D. Chidsey, C.R. Bertozzi, T.M. Putvinski, A.M. Muijsce, Coadsorption of ferrocene-terminated and unsubstituted alkanethiols on gold: electroactive self-assembled monolayers. *J. Am. Chem. Soc.* **112**, 4301–4306 (1990). <https://doi.org/10.1021/ja00167a028>
9. M. Dan-Hardi, C. Serre, T. Frot, L. Rozes, G. Maurin, C. Sanchez, G. Férey, A new photoactive crystalline highly porous titanium(IV) dicarboxylate. *J. Am. Chem. Soc.* **131**, 10857–10859 (2009). <https://doi.org/10.1021/ja903726m>
10. M. de Miguel, F. Ragon, T. Devic, C. Serre, P. Horcajada, H. García, Evidence of photoinduced charge separation in the metal-organic framework MIL-125(Ti)-NH₂. *ChemPhysChem* **13**, 3651–3654 (2012). <https://doi.org/10.1002/cphc.201200411>
11. S. Goswami, M. Chen, M.R. Wasielewski, O.K. Farha, J.T. Hupp, Boosting transport distances for molecular excitons within photoexcited metal-organic framework films. *ACS Appl. Mater. Interfaces* **10**, 34409–34417 (2018). <https://doi.org/10.1021/acsami.8b14977>
12. S. Goswami, L. Ma, A.B.F. Martinson, M.R. Wasielewski, O.K. Farha, J.T. Hupp, Toward metal-organic framework-based solar cells: enhancing directional exciton transport by collapsing three-dimensional film structures. *ACS Appl. Mater. Interfaces* **8**, 30863–30870 (2016). <https://doi.org/10.1021/acsami.6b08552>
13. B.A. Gregg, M.E. Kose, Reversible switching between molecular and charge transfer phases in a liquid crystalline organic semiconductor. *Chem. Mater.* **20**, 5235–5239 (2008). <https://doi.org/10.1021/cm800813h>
14. T.G. Grissom, C.H. Sharp, P.M. Usov, D. Troya, A.J. Morris, J.R. Morris, Benzene, toluene, and xylene transport through UiO-66: diffusion rates, energetics, and the role of hydrogen bonding. *J. Phys. Chem. C* **122**, 16060–16069 (2018). <https://doi.org/10.1021/acs.jpcc.8b03356>
15. I. Hod et al., Bias-switchable permselectivity and redox catalytic activity of a ferrocene-functionalized, thin-film metal-organic framework compound. *J. Phys. Chem. Lett.* **6**, 586–591 (2015). <https://doi.org/10.1021/acs.jpcclett.5b00019>
16. I. Hod, O.K. Farha, J.T. Hupp, Modulating the rate of charge transport in a metal-organic framework thin film using host: guest chemistry. *Chem. Commun.* **52**, 1705–1708 (2016). <https://doi.org/10.1039/C5CC09695B>
17. Y.-Q. Hu et al., Direct observation of confined I⁻⋯I₂⋯I⁻ interactions in a metal-organic framework: iodine capture and sensing. *Chem. Eur. J.* **23**, 8409–8413 (2017). <https://doi.org/10.1002/chem.201702087>
18. N. Ikeda, A. Yoshimura, M. Tsushima, T. Ohno, Hopping and annihilation of ³MLCT in the crystalline solid of [Ru(bpy)₃]₂X₂ (X = Cl⁻, ClO₄⁻ and PF₆⁻). *Chem. A Eur. J.* **104**, 6158–6164 (2000). <https://doi.org/10.1021/jp0002188>
19. F.B. Kaufman, E.M. Engler, Solid-state spectroelectrochemistry of crosslinked donor bound polymer films. *J. Am. Chem. Soc.* **101**, 547–549 (1979). <https://doi.org/10.1021/ja00497a009>
20. C.A. Kent, D. Liu, T.J. Meyer, W. Lin, Amplified luminescence quenching of phosphorescent metal-organic frameworks. *J. Am. Chem. Soc.* **134**, 3991–3994 (2012). <https://doi.org/10.1021/ja211271m>
21. Y. Kobayashi, B. Jacobs, M.D. Allendorf, J.R. Long, Conductivity, doping, and redox chemistry of a microporous dithiolene-based metal-organic framework. *Chem. Mater.* **22**, 4120–4122 (2010). <https://doi.org/10.1021/cm101238m>
22. C.Y. Lee, O.K. Farha, B.J. Hong, A.A. Sarjeant, S.T. Nguyen, J.T. Hupp, Light-harvesting metal-organic frameworks (MOFs): efficient strut-to-strut energy transfer in bodipy and porphyrin-based MOFs. *J. Am. Chem. Soc.* **133**, 15858–15861 (2011). <https://doi.org/10.1021/ja206029a>
23. D.Y. Lee et al., Layer-by-layer deposition and photovoltaic property of Ru-based metal-organic frameworks. *RSC Adv.* **4**, 12037–12042 (2014a). <https://doi.org/10.1039/C4RA00397G>

24. D.Y. Lee, D.V. Shinde, S.J. Yoon, K.N. Cho, W. Lee, N.K. Shrestha, S.-H. Han, Cu-based metal-organic frameworks for photovoltaic application. *J. Phys. Chem. C* **118**, 16328–16334 (2014b). <https://doi.org/10.1021/jp4079663>
25. Y. Li, C. Chen, X. Sun, J. Dou, M. Wei, Metal-organic frameworks at interfaces in dye-sensitized solar cells. *ChemSusChem* **7**, 2469–2472 (2014). <https://doi.org/10.1002/cssc.201402143>
26. S. Lin, P.M. Usov, A.J. Morris, The role of redox hopping in metal-organic framework electrocatalysis. *Chem. Commun.* **54**, 6965–6974 (2018). <https://doi.org/10.1039/C8CC01664J>
27. W. Lu et al., Tuning the structure and function of metal-organic frameworks via linker design. *Chem. Soc. Rev.* **43**, 5561–5593 (2014). <https://doi.org/10.1039/C4CS00003J>
28. W.A. Maza, S.R. Ahrenholtz, C.C. Epley, C.S. Day, A.J. Morris, Solvothermal growth and photophysical characterization of a ruthenium(II) tris(2,2'-bipyridine)-doped zirconium UiO-67 metal-organic framework thin-film. *J. Phys. Chem. C* **118**, 14200–14210 (2014). <https://doi.org/10.1021/jp5034195>
29. W.A. Maza, A.J. Haring, S.R. Ahrenholtz, C.C. Epley, S.Y. Lin, A.J. Morris, Ruthenium(ii)-polypyridyl zirconium(iv) metal-organic frameworks as a new class of sensitized solar cells. *Chem. Sci.* **7**, 719–727 (2016). <https://doi.org/10.1039/C5SC01565K>
30. W.A. Maza, A.J. Morris, Photophysical characterization of a ruthenium(II) tris(2,2'-bipyridine)-doped zirconium UiO-67 metal-organic framework. *J. Phys. Chem. C* **118**, 8803–8817 (2014). <https://doi.org/10.1021/jp501140r>
31. B. O'Regan, M. Grätzel, A low-cost, high-efficiency solar cell based on dye-sensitized colloidal TiO₂ films. *Nature* **353**, 737 (1991). <https://doi.org/10.1038/353737a0>
32. P.J. Peerce, A.J. Bard, Polymer films on electrodes: part III. A digital simulation model for cyclic voltammetry of electroactive polymer film and electrochemistry of poly(vinyl ferrocene) on platinum. *J. Electroanal. Chem. Interfacial Electrochem.* **114**, 89–115 (1980). [https://doi.org/10.1016/S0022-0728\(80\)80438-4](https://doi.org/10.1016/S0022-0728(80)80438-4)
33. I.R. Perera, C.V. Hettiarachchi, R.J.K.U. Ranatunga, Metal-organic frameworks in dye-sensitized solar cells, in *Advances in Solar Energy Research*, ed. by H. Tyagi, A. K. Agarwal, P. R. Chakraborty, S. Powar, (Springer Singapore, Singapore, 2019), pp. 175–219. https://doi.org/10.1007/978-981-13-3302-6_7
34. P.G. Pickup, R.W. Murray, Redox conduction in mixed-valent polymers. *J. Am. Chem. Soc.* **105**, 4510–4514 (1983). <https://doi.org/10.1021/ja00352a002>
35. J.M. Rowe, J. Zhu, E.M. Soderstrom, W. Xu, A. Yakovenko, A.J. Morris, Sensitized photon upconversion in anthracene-based zirconium metal-organic frameworks. *Chem. Commun.* **54**, 7798–7801 (2018). <https://doi.org/10.1039/C8CC01893F>
36. D.T. Scholes, S.A. Hawks, P.Y. Yee, H. Wu, J.R. Lindemuth, S.H. Tolbert, B.J. Schwartz, Overcoming film quality issues for conjugated polymers doped with F₄TCNQ by solution sequential processing: hall effect, structural, and optical measurements. *J. Phys. Chem. Lett.* **6**, 4786–4793 (2015). <https://doi.org/10.1021/acs.jpcclett.5b02332>
37. C.H. Sharp, J. Abelard, A.M. Plonka, W. Guo, C.L. Hill, J.R. Morris, Alkane–OH hydrogen bond formation and diffusion energetics of n-butane within UiO-66. *J. Phys. Chem. C* **121**, 8902–8906 (2017). <https://doi.org/10.1021/acs.jpcc.7b01351>
38. O. Shekha et al., MOF-on-MOF heteroepitaxy: perfectly oriented [Zn₂(ndc)₂(dabco)]_n grown on [Cu₂(ndc)₂(dabco)]_n thin films. *Dalton Trans.* **40**, 4954–4958 (2011). <https://doi.org/10.1039/C0DT01818J>
39. K. Shigehara, N. Oyama, F.C. Anson, Electrochemical responses of electrodes coated with redox polymers. Evidence for control of charge-transfer rates across polymeric layers by electron exchange between incorporated redox sites. *J. Am. Chem. Soc.* **103**, 2552–2558 (1981). <https://doi.org/10.1021/ja00400a011>
40. C.G. Silva, A. Corma, H. García, Metal-organic frameworks as semiconductors. *J. Mater. Chem.* **20**, 3141–3156 (2010). <https://doi.org/10.1039/B924937K>
41. E.D. Spoerke et al., MOF-sensitized solar cells enabled by a pillared porphyrin framework. *J. Phys. Chem. C* **121**, 4816–4824 (2017). <https://doi.org/10.1021/acs.jpcc.6b11251>

42. V. Stavila, A.A. Talin, M.D. Allendorf, MOF-based electronic and optoelectronic devices. *Chem. Soc. Rev.* **43**, 5994–6010 (2014). <https://doi.org/10.1039/C4CS00096J>
43. C. Wang, J.-L. Wang, W. Lin, Elucidating molecular iridium water oxidation catalysts using metal-organic frameworks: a comprehensive structural, catalytic, spectroscopic, and kinetic study. *J. Am. Chem. Soc.* **134**, 19895–19908 (2012). <https://doi.org/10.1021/ja310074j>
44. H.S. White, J. Leddy, A.J. Bard, Polymer films on electrodes. 8. Investigation of charge-transport mechanisms in Nafion polymer modified electrodes. *J. Am. Chem. Soc.* **104**, 4811–4817 (1982). <https://doi.org/10.1021/ja00382a013>
45. S. Yuan et al., Stable metal-organic frameworks: design, synthesis, and applications. *Adv. Mater.* **30**, 1704303 (2018). <https://doi.org/10.1002/adma.201704303>
46. M.-H. Zeng, Q.-X. Wang, Y.-X. Tan, S. Hu, H.-X. Zhao, L.-S. Long, M. Kurmoo, Rigid pillars and double walls in a porous metal-organic framework: single-crystal to single-crystal, controlled uptake, and release of iodine and electrical conductivity. *J. Am. Chem. Soc.* **132**, 2561–2563 (2010). <https://doi.org/10.1021/ja908293n>
47. H.-C. Zhou, J.R. Long, O.M. Yaghi, Introduction to metal-organic frameworks. *Chem. Rev.* **112**, 673–674 (2012). <https://doi.org/10.1021/cr300014x>
48. J. Zhu, S. Shaikh, N.J. Mayhall, A.J. Morris, Energy transfer in metal-organic frameworks, in *Elaboration and Applications of Metal-Organic Frameworks* (Singapore, World Scientific), (2017), pp. 581–654. https://doi.org/10.1142/9789813226739_0014
49. HA. Lopez, A. Dhakshinamoorthy, B. Ferrer, P. Atienzar, M. Alvaro, H. Garcia Photochemical Response of Commercial MOFs: Al₂(BDC)₃ and Its Use As Active Material in Photovoltaic Devices *The Journal of Physical Chemistry C* **115**, 22200–22206 (2011). <https://doi.org/10.1021/jp206919m>



Industry-Specific Utilization of Solar Industrial Process Heat (SHIP)

14

Shahjadi Hisan Farjana, Nazmul Huda, and M. A. Parvez Mahmud

This chapter is dedicated to Professor Peter J. Derrick who passed away in March 2017 during the writing of this chapter.

Contents

14.1	Solar Industrial Process Heat (SHIP)	410
14.2	Existing Studies on SHIP	411
14.3	Industrial Processes with SHIP	413
14.3.1	Cleaning Process with SHIP	414
14.3.2	Drying Process with SHIP	414
14.3.3	Pasteurization with SHIP	419
14.3.4	General Process Heating with SHIP	419
14.3.5	Cooking with SHIP	425
14.3.6	Cooling Processes with SHIP	425
14.3.7	Surface Treatment with SHIP	427
14.3.8	Other Processes with SHIP	428
14.4	SHIP Plants in the World	429
14.5	Conclusion	436
	References	437

Author Contribution

The first draft was written by SHF. The data in the figures and charts was supplied by SHF. The final draft was reviewed and edited by MAPM and NH.

S. H. Farjana · N. Huda (✉) · M. A. P. Mahmud
Sustainable Energy Systems Engineering Group, Macquarie University, Sydney, Australia
e-mail: Nazmul.huda@mq.edu.au

Abstract

Solar industrial process heating systems have become very promising for the industrial sectors as replacement of fossil fuel generation sources to supply heat for industrial scale water heating, air drying, cleaning, food processing, metal refining, and various other uses. The potential of solar industrial process heating systems varies depending on the availability of solar resources and the government policy towards process heat utilization. Though solar driven industrial heating systems may reduce the environmental burdens to a great extent, the feasibility of integration due to the system design requirements and capital cost should be considered systematically. This book chapter will discuss some of the processes which are currently using solar industrial process heating systems and outlines about the leading countries who are utilizing solar industrial process heating systems on a large scale.

14.1 Solar Industrial Process Heat (SHIP)

Industrial process heat is generated based on renewables and nonrenewable sources of energy for various uses in the industrial sectors. The process heat generation sources from the renewable resources promote a sustainable operation and reduction of greenhouse-gas emissions. Solar process heat utilized in industrial processes is the best solution for sustainability problems, irrespective of the higher capital costs associated with their implementation. However, many industrial sectors are currently relying on solar process heat for thermal energy generation with or without energy storage systems for off-peak hours. The implementation of these systems principally depends on the capital costs of the industry, availability of solar energy, and the government policy. The process heat generated from solar resources which are used in industrial operations is termed as “solar heat for industrial processes (SHIP).” Process heat is generated using solar power and the combination of suitable solar collector technologies. The design of solar collector technology varies based on the design criteria such as the selection of suitable collector, number or combination of collectors, collector size and area, the position of installation, working fluid, thermal power, storage volume, and the temperature range for a chosen industrial process.

Solar heat for industrial processes (SHIP) is currently growing throughout the world with solar energy potential. According to the SHIP plants database, 303 plants are in operation in conjunction with industrial processes. Mostly these SHIP plants are of relatively small sized, running for low-temperature industrial processes. SHIP plants are on the focus of researchers, industrialists, government, and policy makers to utilize the immense potential of the abundant source of renewable energy while reducing the environmental burdens associated with massive scale consumption of fossil fuels. To achieve the sustainable development goal for 2050, solar heat for industrial processes (SHIP) can play a vital role. Though many SHIP plants are already in operation, enormous potential exists in many industrial sectors and countries which required to be identified and analyzed to take necessary steps towards successful implementation of SHIP plants.

Industrialized and developed countries are already using SHIP plants in their industrial sectors like agriculture, mining, manufacturing of food, meat, tobacco, textile, leather, wood, paper, chemical, pharmaceutical, rubber, computer, machinery, vehicle, furniture, and so on. Countries who are successfully operating the SHIP plants in the abovementioned industrial sectors are Australia, Austria, Peoples Republic of China (China herein), Chile, Germany, Greece, India, Oman, Qatar, Romania, South Africa, Spain, Sweden, Switzerland, Turkey, United Arab Emirate, and the United States of America (USA herein). Researchers also analyzed the country-specific SHIP potential for India, Australia, the United States, Spain, Portugal, Austria, China, Germany, South Africa, Mexico, Turkey, Pakistan, and Chile. In addition, there is an increasing focus on design methodology of SHIP plants based on software simulation and experimental investigation. The design optimization and performance assessment of SHIP plants are also analyzed based on design methodology.

In this article, Sect. 14.2 illustrates the previous literature studies based on country-specific prospects of SHIP plants, their industries, and industrial processes. Section 14.3 will describe the key industrial processes which are utilizing solar process heat, based on their country, industrial sector information, and solar collector specifications. Section 14.4 will discuss the summary of the present condition of the SHIP plants based on collector area, type of collectors, collector's summary based on industry type, and country-specific SHIP installation summary. Section 14.5 gives the concluding remark.

14.2 Existing Studies on SHIP

There are several studies in the form of research papers, review papers, and scientific reports which analyzed the potentiality of SHIP plants based on their location (country), industry, or process/operation. Analyzing the SHIP plants database information about operating SHIP plants in the world, the 12 most influential countries for SHIP are India, Austria, Germany, the USA, Spain, China, South Africa, Mexico, France, and Greece.

In India, the dominant industrial sectors that are utilizing SHIP are agriculture, food, tobacco, textile, wearing apparel, leather, paper, chemical metals, electrical equipment, and transport equipment. With the growing demand for renewable energy resources, solar radiation in India has an average of around 250 clear sunny days which created immense opportunities for using SHIP plants. However, still many industrial sectors lack using solar process heat. According to the existing literature, SHIP plants in India are in the area of food, paper, and dairy industries. Palappanian described an energy network named Planters Energy Network (PEN), that is a nongovernment organization (NGO) for drying processes using solar process heat utilized for drying rubber, leaves, pulses, fish, or grains. These units are operating in conjunction with conventional process heating systems [1]. Sharma et al. conducted several review works based on the potential of SHIP in the paper and dairy industries in India based on the SHIP plants design requirements like process

heat, thermal energy, and solar collector design. They conducted a survey based on the location of paper industries in India and their requirements [2–5]. Suresh et al. developed a solar industrial process heating system integration methodology through matching process heating requirements and solar collector technologies. They considered the dominant industries in India while addressing the economic and developmental parameters [6].

In Austria, the dominant industrial sectors are food, beverages, leather, chemical, metals, and furniture. Austria developed and used solar collector systems in the building and industrial processes from the last two decades. However, industrial sectors like paper, electronics, wood, pulp, etc. are still in lack of attention which is also major industrial sectors in Austria. Very few research works or reports are available based on SHIP plants in Austria in the open literature. Kranzl et al. analyzed the overview of prospects of renewable energy in Austria until 2030, especially in the upper region of Austria [7].

For Germany, the economy is ruled by the industrial sectors utilizing SHIP plants like agriculture, food, beverage, textiles, chemicals, and metals. SHIP plants used in Germany are mostly low-temperature process heating systems while few are high-temperature industrial processes. Lauterbach reviewed existing potential studies in the field of solar process heat used in Germany with a focus on their industrial processes. According to their research, there are 11 potential industrial sectors which hold solar process heat integration feasibilities. The temperature range determined by their work in 100–200 degree Celsius ($^{\circ}\text{C}$) through the comparison among theoretical and technical feasibility studies [8]. Frey analyzed a textile factory which has solar industrial process heating systems installed in it located in Germany and practically analyzed their design parameters, system requirements, and optimized results [9].

In the United States, the vital industrial sectors which are operating in conjunction with SHIP plants are agriculture, food, textiles, and beverages. Many industrial sectors like chemical, metal, mining, and electrical equipment-based industries are still in the lack of attention, where the potential for solar process heating systems integration exists. Kurup et al. conducted several studies based on solar process heating system integration focus in the United States of America. They were focused on five top industrial sectors, while they conducted their research based on food industries and SHIP potential. They worked through analyzing solar resources availability, energy requirements in industrial processes, and temperature range of solar collectors [10, 11].

For Spain, the SHIP plants are operating in conjunction with agriculture, food, textiles, wood, metals, and motor vehicle. However, Spain also has great potential to integrate SHIP plants in the industrial sectors like pharmaceutical, chemical, and automobile industries. Schweiger et al. conducted a review work based on solar process heat integration potential of Spain and Portugal. They studied the recent developments of medium temperature and high-temperature industrial collectors and processes and gave an outline for future trend [12, 13]. Silva et al. studied the SHIP plants installed in the food industries while prime attention is on parabolic-trough solar collectors [14–16].

In the Peoples Republic of China, the SHIP operated industrial sectors are agriculture, food, beverage, textiles, chemicals, and leathers. The dominant industries in China are mining, ore processing, and automobiles; so undoubtedly, immense

potential still exists for solar process heat integration in these industries: mining, ore processing, and automobiles. Though the SHIP plants in operation are mostly low-temperature and medium-temperature process heating application where mining industries require not only low and medium temperature but also high-temperature process heating systems. Sturm et al. analyzed different types of steam generation systems while focusing on renewable energy integration based on their energy requirements [17]. Liu et al. studied energy consumption in Chinese industrial sectors through an economic input-output analysis based on 29 types of industries [18]. Jia et al. studied SHIP plants installed in P.R. China based on their energy consumption, SHIP integration, and solar collector technologies. They have also analyzed 26 SHIP cases from 10 industrial sectors in China [19].

For South Africa, SHIP driven industrial sectors are mining, food, beverages, machinery, and motor vehicles. However immense potential still exists to integrate solar process heat in automobile and electronic equipment industries which are identified as major industries in South Africa. The existing SHIP plants in South Africa are mostly low-temperature process heat applications, while medium and high-temperature process heating systems are also in operation due to the huge availability of solar resources. There are few research works based on SHIP plants in South Africa. Brent et al. studied concentrating on solar water heating systems to identify the potential for South Africa [20]. Joubert et al. analyzed 89 large-scale solar thermal systems in South Africa based on their industries sectors, economics, and application areas [21]. Uhlig et al. analyzed the potentialities of high-temperature solar process heat applications based on concentrating solar thermal technologies [22].

In Mexico, solar process heat is used mostly in the agriculture and food industries. Mexico has a good number of solar industrial process heating systems in operation while mostly they are low and medium temperature solar thermal systems. Only a few research works exist which analyzed the potentiality of SHIP plants in Mexico. Ramos et al. studied parabolic-trough solar collector technologies to be considered for the textile and food industries of Mexico [23].

In France, the food, beverage, and metal industries are utilizing solar process heat. However, no significant research works or review studies have been reported which have analyzed the potential of SHIP plants located in France.

In Greece, SHIP plants are operating in the industrial sectors like food, beverage, textiles, pharmaceuticals, and leather industries. There are a few studies regarding the SHIP potentiality analysis in respect of Greece. Karagiorgas et al. studied solar thermal systems and compared with conventional thermal systems based on their energy equivalency [24].

14.3 Industrial Processes with SHIP

This subsection will elaborate on the major industrial processes which are already integrated with SHIP plants throughout the world. The subsections are organized based on the industries processes with operating SHIP plants information. The processes are cleaning, drying, pasteurization, general process heating, cooking,

cooling processes, surface treatment, and other processes (evaporation, blanching, sterilization, heating of production hall, cooling of production hall, melting, extraction, bleaching, painting, and retaining [25, 26]). Among the 303 SHIP plants information collected in the SHIP plants database, 237 plants are in operating in the abovementioned industrial processes. Rest of the 66 SHIP plants are operating with other process heating conditions which are excluded from this study. Most of the SHIP plants with widely integrated industrial processes are currently under consideration. In these subsections, the tables describe the name of the SHIP plants, industry information, country, solar collector specifications, and installed thermal power requirements. Plants information are placed alphabetically, irrespective of their design specifications and capacity.

14.3.1 Cleaning Process with SHIP

For the industrial cleaning processes, 61 plants are reported to date according to the SHIP plants database information, while the industries are food, beverage, meat, textile, mining, dairy, fish, transport, chemical, and manufacturing. The dominant industrial sector is the food industries where 30 SHIP plants are operating with the solar-driven cleaning process. Countries which are utilizing solar process heat for industrial cleaning operations are Israel, Greece, the United States of America, South Africa, Mexico, France, Germany, India, Austria, Portugal, Canada, Spain, and Saudi Arabia. The leading countries are Austria (9 plants), Germany (6 plants), Greece (5 plants), Mexico (11 plants), South Africa (6 plants), and United States (5 plants). Among these plants, 45 plants are operating with flat-plate solar collector technologies where mostly are low-temperature industrial processes. The other types of solar collectors are parabolic trough collector and evacuated tube collectors. The highest capacity SHIP plant with solar cleaning operation is Prestige Food located in the United States, where the average solar collector area is 7804 m², installed thermal power is 5462.8 kWh, and storage volume is 946 m³. Table 14.1 showed the SHIP plants summary based on solar driven industrial cleaning operations and their key details.

14.3.2 Drying Process with SHIP

For the industrial drying processes, 33 plants are reported to date according to the SHIP plants database information, while the industries are agriculture, textile, furniture, food, transportation, tobacco, mineral, rubber, beverage, paper, and metal. The dominant industrial sector is the food industries where 10 SHIP plants are operating with the solar-driven drying process. Countries which are utilizing solar process heat for industrial cleaning operations are India, the United States, Romania, Mexico, Austria, Germany, Costa Rica, Panama, China, Argentina, Thailand, Indonesia, Canada, Spain, and Portugal. The leading countries are the United States of America (8 plants), Germany (3 plants), Austria (3 plants), Mexico (3 plants), and India (4 plants). Among these plants, 18 plants are operating with air

Table 14.1 Summary of the SHIP operated-industrial cleaning processes [27]

Plant name	Country	Industry	Collector technology (temperature range)	Installed collector area (gross), m ²	Installed thermal power (actual), kWth	Storage volume, m ³
1 Of Tov Hatching Farm	Israel	Food	FPC (~65)	313.5	212.4	20
Achaia Clauss S.A.	Greece	Beverage	FPC (45~60)	308.0		15
Adams Farm Slaughterhouse	USA	Meat		297.0	207.9	
Allegro S.A. Children's Clothing Manufacturer	Greece	Textile	FPC (33~60)	70	49	3.5
Anglo Plat – Brakfontein	South Africa	Mining	FPC	540	378	42
Anglo Plat – Middelport	South Africa	Mining	FPC	180	126	14.2
BHP Billiton Wolwekrans Colliery	South Africa	Mining	FPC (~60)	390	273	40
Bonaprime Slaughterhouse	Mexico	Meat	FPC (65~70)	65	45.5	3
Battenkill Valley Creamery	USA	Dairy	FPC	53	37.1	
Bonilait Dairy	France	Dairy	FPC (~80)	1500	1050	30
Bourdouil	France	Beverage	FPC (15~70)	105	52	6
Brauerei Hald (brewery for beverages)	Germany	Beverage	FPC (~60)	25.1	19.6	3
Brown's Brewing Co	USA	Beverage	FPC	53	37.1	4
Carnes La Laguna Slaughterhouse	Mexico	Meat	ETC (65~80)	99	69	6
Carnes Muma	Mexico	Meat	ETC (60~80)	72	50	5
Carnes Selectas DE Mexico SA DE CV	Mexico	Meat	FPC (55~85)	175	122.5	5
Caritas-Werkstätten: Wäscherei	Germany		FPC (20~90)	80	56	5.6
Carnes Selectas de Sonora S.A. de C.V.	Mexico	Meat	PTC (20~70)	89.48	22.2	3

(continued)

Table 14.1 (continued)

Plant name	Country	Industry	Collector technology (temperature range)	Installed collector area (gross), m ²	Installed thermal power (actual), kWth	Storage volume, m ³
Centro Lechero Cooperativo de los Altos SCL	Mexico	Dairy	PTC (19~92)	422	94.5	9.5
Chalmar Beef Pty (Ltd)	South Africa	Food	FPC	121.2	39	
Clean Park	Germany		FPC (20~90)	24	16.8	0.85
Dausa Milk	India	Dairy	FPC (75~85)	110	77	5
Edmund Merl - Gourmet Foods	Germany	Food	FPC (20~60)	568	397.6	30
Eisvogel Hubert Bernegger	Austria	Fish	FPC	44	30.8	2.5
Gangl Fruit Juices	Austria	Beverage	FPC (95~105)	60	42	21.9
Golan Winery	Israel	Food	FPC (~85)	244	246	30
Hammerer	Austria		FPC (20~60)	180	126	6
Harita Seatings Systems Limited	India	Transport	ETC (55~60)	754.8	360	
Izra'el's Kitchen	Israel		FPC (~85)	120	123	5
Kibbutz Urim	Israel		FPC (~80)	40.6	30.5	5
Knorr Best Foods S.A.	Portugal	Food	FPC (40~45)	440	308	10
L'Oreal Pune	India	Chemical	FPC (~55)	640	448	32
Laiterie Chagnon SHIP	Canada	Dairy	PTC Montesano – Canary Islands	82	46	
MAPAG	Austria	Chemical	FPC (~60)	42	29.4	2.5
Metbraueri Neuwirth	Austria	Beverage	FPC (50~95)	20	14	0.85
Mevgal S.A.	Greece	Food	Multiple	1	0.7	10

Moguntia Spice Making	Austria	Food	FPC	220	154	20
Montesano – Canary Islands	Spain	Food	FPC (40~60)	290	203	23
Montesano – Jerez de los Caballero	Spain	Meat	FPC (40~45)	252	176.4	30
Mother Dairy	India	Dairy	Multiple (70~90)	1520	1064	
Mr. Wash Mannheim	Germany	Transportation	ETC	197	137.9	
Nestle Waters	Saudi Arabia	Beverage	FPC	515	460.5	15
New York City Subway Washing Plant	USA	Transportation	ETC	164	85	
Northam Platinum's Booyensdal Mine	South Africa	Mining	FPC (~60)	192	134.4	30
Procame Slaughterhouse "A"	Mexico	Meat	FPC (65~75)	110	77	6
Procame Slaughterhouse "B"	Mexico	Meat	ETC (65~80)	96	67	5
Parkings Service S.A.	Spain	Other	FPC (20~80)	510	357	40
Peitler Vineyard	Austria	Beverage	FPC	100.8	70.56	4
Plektomboriki Kritis S.A.	Greece	Food	FPC (40~90)	50	35	2
Prestage Foods	USA	Food	FPC (60~)	7804	5462.8	946
Rainbow Industries	India	Other		25	17.6	
Santa Anita Dairy	Mexico	Dairy	ETC (60~70)	68	47	3.5
Sukame Slaughterhouse	Mexico	Meat	ETC (70~80)	195	136	10
Sukame Slaughterhouse – Mexicali	Mexico	Meat	FPC	100	70	5
Siddharth Surgicals	India	Textile	PTC (~110)	263	184.1	

(continued)

Table 14.1 (continued)

Plant name	Country	Industry	Collector technology (temperature range)	Installed collector area (gross), m ²	Installed thermal power (actual), kWth	Storage volume, m ³
Sona Koyo	India	Manufacturing	ETC	560	210	
Stadtreinigung Dresden GmbH	Germany	Other	FPC	151	105.7	10
Sunwash Gratwein	Austria	Other	FPC (20~90)	43	30.1	3
Sunwash Köflach	Austria	Other	FPC (20~90)	43	30.1	3
Tyras S.A.	Greece	Food	FPC (20~80)	1040	728	50
Xstrata Elands Mine	South Africa	Mining	ETC (~60)	504	352.8	60

collector technologies where mostly are low-temperature industrial processes. The other types of solar collectors are a flat-plate collector and evacuated-tube collectors. The highest capacity SHIP plant with solar drying operation is Habau-concrete component production located in Austria, where the average solar collector area is 1500 m², installed thermal power is 1050 kWh, and storage volume is 80 m³. Another similar one is Parc Solaire Alain Lemaire located in Canada, where the average solar collector area is 1490 m² and installed thermal power is 800 kWh. Table 14.2 showed the SHIP plants summary based on solar driven industrial drying operations and their key details.

14.3.3 Pasteurization with SHIP

For the industrial pasteurization processes, 16 plants are reported to date according to the SHIP plants database information, while the industries are dairy, beverage, and manufacturing industries. The dominant industrial sector is the dairy industries where 11 SHIP plants are operating with solar-driven pasteurization process. Countries which are utilizing solar process heat for industrial pasteurization operations are India, Mexico, Morocco, Czech Republic, and Austria. The leading countries are Mexico (9 plants) and India (4 plants). Among these plants, ten plants are operating with parabolic-trough solar collector technologies where mostly are low-temperature industrial processes. The other types of solar collectors are flat-plate collector and multiple collectors. The highest capacity SHIP plant with solar pasteurization operation is Solar Pasteurization (Lechera Guadalajara Sello Rojo) located in Mexico, where the average solar collector area is 1641.25 m², installed thermal power is 240 kWh, and storage volume is 50 m³. Another similar one is Nestle Dairy Plant Lagos De Moreno located in Mexico, where the average solar collector area is 1327.59 m² and installed thermal power is 137 kWh, the storage volume is 5 m³. Milma dairy located in India have installed collector area of about 1440 m² and installed thermal power is 1008 kWh, the storage volume is 60 m³. Table 14.3 showed the SHIP plants summary based on solar driven industrial pasteurization operations and their key details.

14.3.4 General Process Heating with SHIP

For the general process heating operations, 56 plants are reported to date according to the SHIP plants database information, while the industries are metal, manufacturing, dairy, food, chemical, agriculture, pharmaceutical, beverage, transport, mining, animal, textile, vegetable, etc. The dominant industrial sector is the food industries where 23 SHIP plants are operating with solar-driven general process heating operations. Countries which are utilizing solar process heat for general process heating Germany, Mexico, Greece, Spain, Ukraine, Chile, Egypt, Switzerland, India, Netherlands, Jordan, and Portugal. The leading countries are Mexico (30 plants), Spain (4 plants), and India (5 plants). These plants are operating with parabolic-trough solar collector technologies or flat-plate solar collector technologies, where most are low-temperature industrial

Table 14.2 Summary of the SHIP-operated industrial drying processes [27]

Plant name	Country	Industry	Collector technology (temperature range)	Installed collector area (gross), m ²	Installed thermal power (actual), kWth	Storage volume, m ³
AMR Dal mill	India	Agriculture	Air collector (65~75)	230	161	
Acme McCrary	USA	Textile	FPC	743	520.1	1
Aroma Plant Romania	Romania	Agriculture	Air collector	80	56	1
CIATEQ	Mexico	Professional	FPC (60~90)	80	56	4
Carpentry Hammingner	Austria	Furniture	FPC (~60)	88	61.6	14
Carriers & Sons	USA	Food	Air collector (~43)	300	210	1
Cologne Transit Authority (Kölner VKB)	Germany	Transportation	ETC	237	165.9	25.2
Coopeldos	Costa Rica	Food	Air collector (40~45)	860	602	1
Duran Coffee	Panama	Food	Air collector (40~45)	900	630	1
FengLi Fruit Drying	China	Food	Air collector (50~70)	55.7	38.99	1
Grammer Solar Argentina	Argentina	Tobacco	Air collector	737	515.9	1
Habau - Concrete Component Production	Austria	Mineral	FPC (16~25)	1500	1050	80
Hofigal S.A.	Romania	Agriculture	Air collector	60	42	1
Inter Rubber Latex Co. Ltd.	Thailand	Rubber	Air collector	80	56	1
Kaveri Agri-Care Pvt. Ltd.	India	Food	Air collector (~105)	414	289.8	1
Keyawa Orchards	USA	Food	Air collector (~43)	864	604.8	1
Kreher's Poultry Farms	USA	Food	Air collector (~43)	50.4	35.28	1
Krimmer	Germany	Agriculture	FPC (~35)	150	105	42

(continued)

Table 14.2 (continued)

Plant name	Country	Industry	Collector technology (temperature range)	Installed collector area (gross), m ²	Installed thermal power (actual), kWth	Storage volume, m ³
Lackiererei Vogel	Germany	Repair	ETC	43	30.1	3
Leitl Beton GmbH	Austria	Mineral	FPC	315	220.5	36
Malabar Tea Drying	Indonesia	Food	Air collector (~35)	600	420	1
Neumarkter Lammsbräu	Germany	Beverage	Air collector (~60)	72.5	50.75	1
PSG Hospital Laundry	India	Human health	PTC (~150)	50	35	
Parc Solaire Alain Lemaire	Canada	Paper	PTC (120~140)	1490	800	
Pincasa	Spain	Metal	Various ETC (~180)	180	26	
Rockland County	USA	Waste	Air collector	743	520.1	1
Silampos, S. A.	Portugal	Metal	PTC (50~160)	450	67	
Surprise Ship for sewage sludge drying	USA	Waste	PTC (90~100)	151	98	
Sonoma County Herb Exchange	USA	Agriculture	Air collector	10	7	1
Sunsweet Dryers	USA	Food	Air collector	110	77	1
Ultramarine Pigments	India	Chemical	Other (~140)	570	399	
Zacatecas Termosolar Drying Plant – Air Collectors	Mexico	Agriculture	Air collector (55~120)	120	84	
Zacatecas Termosolar Drying Plant – Flate Plate	Mexico	Agriculture	FPC (70~85)	125	87	12

Table 14.3 Summary of the SHIP-operated industrial pasteurization processes [27]

Plant name	Country	Industry	Collector technology (temperature range)	Installed collector area (gross), m ²	Installed thermal power (actual), kWth	Storage volume, m ³
B.G. Chitale	India	Dairy	Various	320	224	
Bevco, S. de R.L. de C.V.	Mexico	Beverage	PTC (20~90)	33.43	15.05	2.5
COPAG (rooftop)	Morocco	Dairy	PTC (80~90)	110	61	
Casa Cuervo S. A de C.V.	Mexico	Beverage	PTC (30~90)	577.13	123.55	9.6
Cider house Hostetin	Czech Republic	Beverage	FPC	36	25.2	9
Durango Dairy Company (Productos Lácteos COVBARS)	Mexico	Dairy	PTC (80~90)	265.68	46.2	7
HP Dairy State	India	Dairy	FPC	120	84	6
Indian Institute of Horticulture	India	Manufacturing	Various	42	29.4	
Krispl Fruit Juice	Austria	Manufacturing	FPC (~80)	112	78.4	20
Lácteos Mojica	Mexico	Dairy	PTC (20~95)	132	59.88	4.5
Milma dairy	India	Dairy	FPC	1440	1008	60
Nestle Dairy Plant Chapa De Corzo	Mexico	Dairy	PTC (~90)	460	126	5
Nestle Dairy Plant Lagos De Moreno	Mexico	Dairy	PTC (~90)	1327.59	137	5
Qesera Lacteos Ticoy, S.A. de C.V	Mexico	Dairy	PTC (~90)	250	42	6
Qesos La Doñita	Mexico	Dairy	PTC	66	22.2	1.5
Solar Pasteurization (Lechera Guadalajara Sello Rojo)	Mexico	Dairy	PTC (~85)	1641.25	240	50

processes. The other types of solar collectors are an unglazed collector or air collectors. The highest capacity SHIP plant with general process heating operation is Codelco Gabriela Mistral located in Chile, where the average solar collector area is 39,300 m², installed thermal power is 27,510 kWth, and storage volume is 4300 m³. Table 14.4

Table 14.4 Summary of the SHIP operated general process heating operations [27]

Plant name	Country	Industry	Collector technology (temperature range)	Installed collector area (gross), m ²	Installed thermal power (actual), kWth	Storage volume, m ³
Alanod Solar	Germany	Metal	PTC (~143)	108	75.6	
Alimentos y Productos para Ganado Lechero	Mexico	Manufacturing	PTC (~60)	1031.25	179.85	24.4
Alpino S.A.	Greece	Dairy	FPC (20~70)	740	518	25
Autolavados Carte S.A.	Spain	Other	FPC (40~70)	138	96.6	12
Barcel	Mexico	Food	FPC (60~70)	172	120	12
BASF Mexico	Mexico	Chemical	FPC (60~70)	30	21	1.5
Bermejillo Chapin	Mexico	Agriculture	FPC (60~75)	200	140	9
Biotecnología Mexicana de Microalgas S.A. de C.V.	Mexico	Pharmaceutical	PTC (55~75)	110	31.67	10
Brewery Radoy	Ukraine	Beverage	FPC	216	151.2	15
COFICAB	Mexico	Transport	FPC (60~90)	25	17.5	2
Codeco Gabriela Mistral	Chile	Mining	FPC	39,300	27,510	4300
El NASR Pharamaceutical	Egypt	Pharmaceutical	PTC	1900	1330	
Emmi Dairy Saignelégier	Switzerland	Dairy	PTC	627	360	15
Frito Lay	USA	Food	PTC	5068	3547.6	1
Futtermittel Fixkraft	Austria	Animal	FPC	324	226.8	6
Gamesa-Quaker Pepsico Mexico	Mexico	Food	FPC (60~70)	64	45	4
Gatorade Mexico	Mexico	Beverage	FPC (60~70)	56	39	3
General Electric Queretaro	Mexico	Manufacturing	FPC (60~90)	24	16.8	2
Glaxo Smithkline Mexico	Mexico	Pharmaceutical	FPC (70~80)	360	252	25
Grupo BIMBO	Mexico	Food	FPC (60~80)	232	162	15
Guetermann Polygal	Mexico	Textile	FPC (55~85)	450	315	20
Gatorade	USA	Beverage	FPC (~35)	4221	2954.7	114
Grammer Solar Vietnam	Vietnam	Textile	Air collector	480	336	1
IER UNAM	Mexico		FPC (70~95)	75	52.5	
ITEC Culiacan	Mexico		FPC (75~110)	60	42	
India Tobacco Division	India	Tobacco	Various	900	220	

(continued)

Table 14.4 (continued)

Plant name	Country	Industry	Collector technology (temperature range)	Installed collector area (gross), m ²	Installed thermal power (actual), kWth	Storage volume, m ³
Industria Alimnetaria Alcoyana	Spain	Food	FPC (40~130)	151	105.7	12
KOF Mixcoac	Mexico	Beverage	FPC (50~70)	125	87.5	10
KOF Tlanepantla	Mexico	Beverage	FPC (50~75)	45	31.5	2.5
Körner KVK	Austria	Metal	FPC (~80)	86	60.2	10
L'oreal Mexico	Mexico	Pharmaceutical	FPC (55~75)	154	107	8
Lavin Industries	Mexico	Pharmaceutical	FPC (60~75)	525	367	20
Liomont Laboratories	Mexico	Pharmaceutical	FPC (60~80)	75	52.5	4
Laguna	Germany		FPC (20~90)	57	39.9	3.3
Lesa Dairy	Switzerland	Dairy	PTC	115	67	0.01
Marinela CDMX	Mexico	Food	FPC (60~70)	164	114	9
Mexlub	Mexico	Chemical	FPC (60~75)	50	35	3
Minera El Rob Peñoles	Mexico	Mining	FPC (60~80)	330	231	15
Matatlan Dairy	Mexico	Dairy	PTC	64	46.2	2.5
Metadero Montesierra	Spain	Food	FPC (50~60)	79	55.3	5
Nestle Chiapas	Mexico	Food	FPC (~90)	650	455	25
Nestle. Toluca	Mexico	Food	Unglazed (~37)	3700	2590	500
Peñoles Totolapan I	Mexico	Mining	FPC (60~70)	60	42	3
Peñoles Totolapan II	Mexico	Mining	FPC (65~75)	160	112	8
Peñoles Totolapan III	Mexico	Mining	FPC (65~85)	45	31.5	3
Panchmahal Dairy	India	Dairy	FPC	472	330.4	20
Perfetti van Melle	Netherlands	Dairy	FPC	2400	1680	95
RAM Pharma	Jordan	Pharmaceutical	Fresnel (160~165)	550	222	2
SANA Internacional	Mexico	Food	FPC (55~75)	240	168	7.5
Salem District Cooperative Milk Producers Union	India	Dairy	Various (~95)	338	236.6	
Simoa S.A.	Portugal	Food	FPC (~30)	670	469	
Stapleton-Spence Fruit Packing Co.	USA	Vegetable	Unglazed	2637	1845.9	50
Synthokem Labs	India	Pharmaceutical	ETC	288	201.6	10
TE-PE S.A.	Spain	Food	FPC (40~130)	260	182	20

(continued)

Table 14.4 (continued)

Plant name	Country	Industry	Collector technology (temperature range)	Installed collector area (gross), m ²	Installed thermal power (actual), kWth	Storage volume, m ³
Tapi Foods	India	Vegetable	Various	93	65.1	
Unison	Mexico	Education	Various (50~70)	254	177.8	

showed the SHIP plants summary based on solar driven industrial pasteurization operations and their key details.

14.3.5 Cooking with SHIP

For the solar cooking operations, 13 plants are reported to date according to the SHIP plants database information, while the industries are food, meat, manufacturing, and vegetables. The dominant industrial sector is the food industries where 7 SHIP plants are operating with solar-driven cooking operations. Countries which are utilizing solar process heat for industrial cooking are Mexico, India, Austria, and Spain. The leading country is Mexico (10 plants). These plants are operating with parabolic-trough solar collector technologies or flat-plate solar collector technologies, where most are low-temperature industrial processes. The other types of solar collectors are a combination of different type of solar collectors. The highest capacity SHIP plant for solar cooking operation is Procesadora de Alimentos Integrales-Paisa located in Mexico, where the average solar collector area is 577.13 m², installed thermal power is 116.12 kWh, and storage volume is 3 m³. Table 14.5 showed the SHIP plants summary based on solar driven cooking operations and their key details.

14.3.6 Cooling Processes with SHIP

For the solar cooling operations, 12 plants are reported to date according to the SHIP plants database information, while the industries are food, construction, beverage, manufacturing, and so on. The dominant industrial sector is the manufacturing industries where three SHIP plants are operating with solar-driven cooling operations. Countries which are utilizing solar are United Arab Emirates (UAE), South Africa, Germany, Tunisia, and Spain. The leading country is UAE (2 plants) and Germany (2 plants). These plants are operating with Fresnel collector technologies, where most are low-temperature industrial processes. The other types of solar collectors are a parabolic-trough collector, flat-plate collector, or a combination of different type of solar collectors. The highest

Table 14.5 Summary of the SHIP operated solar cooking operations [27]

Plant name	Country	Industry	Collector technology (temperature range)	Installed collector area (gross), m ²	Installed thermal power (actual), kWth	Storage volume, m ³
Agriculture University Tamil Nadu	India	Food	Various	250	175	
Barcel S.A DE C.V.	Mexico	Food	PTC (35~164)	529.2	77.9	0.15
Conservas del Norte S.A de C.V.	Mexico	Food	PTC (25~95)	660	104.81	9
Fleischwaren Berger	Austria	Meat	FPC (30~95)	1067	746.9	60
Grupo Mirasol de Occidente SA de CV	Mexico	Meat	PTC (21~95)	396	64.83	5
Grupo Mosa la Luz SA de CV	Mexico	Food	PTC (55~110)	693	92.61	9.6
IMATEC Tortilla Dough Factory	Mexico	Manufacturing	FPC (65~85)	125	87.5	5
INDUSTRIA MAIZ	Mexico	Food	FPC (65~80)	72	50.4	3.5
INDUSTRIAS CRICOTL	Mexico	Food	FPC (55~85)	72	50	3
Nutrición Marina	Mexico	Manufacturing	PTC	310	97.2	7.5
Papes Safor S.L.	Spain	Vegetable	PTC (200~250)	175	134	
Procesadora de Alimentos Integrales – PAISA	Mexico	Manufacturing	PTC (~95)	577.13	116.02	3
San Pablo Villa Tortilla Dough Factory	Mexico	Food	FPC (70~85)	70	49	5

capacity SHIP plant for solar cooling operation is the Fédération Internationale de Football Association (FIFA, Soccer) World Cup Solar Cooled Demonstration Stadium located in Qatar, where the average solar collector area is 2000 m², installed thermal power is 790 kWh, and storage volume is 40 m³. Table 14.6 showed the SHIP plants summary based on solar driven cooling operations and their key details.

Table 14.6 Summary of the SHIP operated solar cooling operations [27]

Plant name	Country	Industry	Collector technology (temperature range)	Installed collector area (gross), m ²	Installed thermal power (actual), kWth	Storage volume, m ³
Bergamo	Italy	Manufacturing	Fresnel	183	74	
Canelas S.A. de C.V.	Mexico	Food	PTC (25~80)	577.13	118	2
FIFA world cup solar cooled demonstration stadium	Qatar	Construction	Fresnel (7~15)	2000	790	40
GICB Wine Cellars	France	Beverage	ETC (70~90)	216.2	151	1
Gerhard Rauch Ges.mbH	Austria	Metal Manufacturing	FPC	264	184.8	12
Masdar City Solar Field	UAE	Other	Other (180~165)	44	21	16
Masdar Demonstration Project	UAE	Other	Fresnel	185	74	
Solar cooling for the data center	South Africa	Information	Fresnel (6~32)	678	272	42
Solar cooling for stainless steel pipe industry	Germany	Metal Manufacturing	Fresnel (7~12)	678	272	
Solar refrigeration in the food industry	Germany		Fresnel (-5~ - 10)	123	49	
University of Sevilla	Spain	Education	Fresnel (7~15)	493	198	
Winery Grombalia	Tunisia	Beverage	Fresnel (-10~7)	132	49.5	1

14.3.7 Surface Treatment with SHIP

For the solar driven surface treatment operations, 11 plants are reported to date according to the SHIP plants database information, while the industries are a computer, vehicle, machinery, metal, and manufacturing. The dominant industrial sector is the metal-based industries where five SHIP plants are operating with solar-driven surface treatment operations. Countries which are utilizing solar process heat for industrial cooling are Sweden, Spain, Austria, Germany, Mexico, India, and Switzerland. The leading country is Mexico (2 plants), Spain (2 plants), and India (2 plants). These plants are operating with flat-plate collector technologies, where most are low-temperature industrial processes. The other types of solar collectors are

Table 14.7 Summary of the SHIP operated solar driven surface treatment operations [27]

Plant name	Country	Industry	Collector technology (temperature range)	Installed collector area (gross), m ²	Installed thermal power (actual), kWth	Storage volume, m ³
Bomans Lackering	Sweden	Computer	PTC (~160)	100	40	
FASA Valladolid	Spain	Vehicle	FPC (~50)	243.6	170.52	15
Hoval Marchtrenk	Austria	Machinery	FPC	202	141.4	6
Hustert Galvanic	Germany	Metal	ETC (~80)	221	154.7	
Industrias MOSO	Mexico	Manufacturing	FPC (60~80)	110	77	5
Industrias Verona Galvanoplasty	Mexico	Metal	FPC (70~85)	64	44	3.5
Julius Blum	Austria	Metal	ETC (85~60)	460	322	8
Kangaroo India Limited	India	Metal	FPC	506	354.2	65
Nissan Avila	Spain	Vehicle	FPC	530	370	40
SKF Technologies Mysore	India	Metal	PTC	400	72	95
Zehnder Group AG	Switzerland	Machinery	ETC	395.2	276.64	

a parabolic-trough collector or evacuated-tube solar collectors. The highest capacity SHIP plant for solar driven surface treatment operation is Nissan Avila located in Spain, where the average solar collector area is 530 m², installed thermal power is 370 kWh, and storage volume is 40 m³. Table 14.7 showed the SHIP plants summary based on solar operated surface treatment processes and their key details.

14.3.8 Other Processes with SHIP

The other type of industrial processes which have few plants already in operation is evaporation, blanching, sterilization, heating, and cooling of production hall, melting, extraction, bleaching, painting, and retaining. In the case of the solar-operated evaporation process, the industries are a beverage, water supply, and chemical industries which are in Mexico, the United States, and China. For the evaporation process, heat is supplied through parabolic-trough solar collector technologies. The highest capacity SHIP plant integrated with evaporation process is the Solar steam boiler for Procter & Gamble (Tianjin) located in China with the installed collector area 4600 m² and installed thermal power is

1050 kWh. For the blanching process, the only SHIP plant is operating at Malaysia named Poultry Processing Malaysia PPNJ which is a meat factory with installed collector area 181.35 m^2 , installed thermal power is 163.2 kWh, and storage volume is 8 m^3 . Solar process heat is used for the sterilization process in two plants located in Switzerland and China for food and dairy industries built on the parabolic-trough collector and evacuated-tube collector. The largest one is Crema SA in Switzerland with installed collector area 581 m^2 , installed thermal power is 330 kWh. Among the three operating SHIP plants for heating of production hall, the largest one is Lhasa vegetable greenhouse located in China with installed collector area 2150 m^2 and installed thermal power 440 kWh. For the cooling of production hall, two SHIP plants are in operation from which the larger one is Sarantis S.A. located in Greece with installed collector area 2700 m^2 , installed thermal power 1890 kWh, and storage volume is 66 m^3 . For the solar melting operation, the only SHIP plant is in Switzerland named Colar Yverdon-Les-Bains, with installed collector area 197 m^2 , installed thermal power 96 kWh, and storage volume is 90 m^3 . For the extraction process, there are five SHIP plants in metal, food, and mining industries of which Hellenic copper mine in Cyprus is the highest capacity SHIP plant using solar driven extraction process. The installed collector area is 760 m^2 , installed thermal power 532 kWh, and storage volume is 100 m^3 . In case of the bleaching operation, there are five operating SHIP plants in apparel and textile industries located in India, P.R. China, Greece, and Vietnam of which the largest one is on China named Daly textile with installed collector area $13,000 \text{ m}^2$, installed thermal power 9000 kWh, and storage volume is 900 m^3 .

Similarly, five SHIP plants are operating with solar driven painting operation of chemical, vehicle, textile, and machinery industries located in South Africa, Spain, Germany, and India. The largest one is Wheels India with installed collector area 1365 m^2 and installed thermal power 955.5 kWh. For the retaining operation, eight SHIP plants are operating in the leather industries of Thailand, Austria, P.R. China, India, Kenya, Vietnam, and Greece. The largest one is Atutthaya tannery located in Thailand with installed collector area 1890 m^2 , installed thermal power 1323 kWh, and storage volume 80 m^3 . Table 14.8 showed the SHIP plants summary based on different types of solar-operating processes and their key details.

14.4 SHIP Plants in the World

According to the SHIP plants database, there are 12 countries which have many successfully installed and operated solar-driven industrial process heating plants for different types of industrial operations. So far, 303 SHIP plants have been reported throughout the world. The country-wise scenario for the highest number of installed SHIP plant statistics is presented below to identify the leading countries in this field. Table 14.9 describes the country-based statistics for installed and operating SHIP plants information. According to the results presented in Table 14.9.

Table 14.8 Summary of the SHIP operated different types of processes [27]

Operation	Plant name	Country	Industry	Collector technology (temperature range)	Installed collector area (gross), m ²	Installed thermal power (actual), kWth	Storage volume, m ³
Evaporation	Casa Armando Guillermo Prieto S.A de C.V.	Mexico	Beverage	PTC (21~90)	816.75	136.79	9.9
	Destileria 501 S.A de C.V	Mexico	Beverage	PTC (19~99)	610	94.6	8
	Panoche County Desalination	USA	Water supply	PTC	690	480	
Blanching	Solar steam boiler for Procter & Gamble (Tianjin)	China	Chemical	PTC (~130)	4600	1050	
	Poultry Processing Malaysia PPNJ	Malaysia	Meat	ETC (70~75)	181.35	163.2	8
Sterilization	Cremo SA	Switzerland	Dairy	PTC (~150)	581	330	
	Meihao Food Processing	China	Food	ETC (~80)	395	276.5	
Heating of production hall	Buena Vista Greenhouse	Mexico	Agriculture	PTC	112	36	2.5
	Lhasa vegetable greenhouse	China	Food	ETC	2150	400	
Cooling of the production hall	Telekom Rotweil	Germany	Information	ETC	503	352.1	20
	Honeywell Technology Solutions	India	Manufacturing	PTC	821	574.7	
Melting	Sarantis S.A.	Greece	Pharmaceutical	FPC (7~45)	2700	1890	66
	Colas Yverdon-les-Bains	Switzerland	Construction	Various (50~90)	197	96	90

Extraction	Gillich Galavanic	Austria	Metal	ETC	9	6.3	1.5
	Hellenic Copper Mines	Cyprus	Mining	FPC (20~50)	760	532	100
Bleaching	Kwality Walls Ice Cream	India	Food	FPC	120	84	11
	Minera Constanza	Chile	Mining	FPC	440	308	
	Chelsea Jeans	India	Apparel	FPC	943	660.1	60
	Daly Textile	China	Textile	FPC (20~60)	13,000	9000	900
	Kastrinogiannis S.A.	Greece	Textile	FPC (40~90)	174	121.1	10
	Saitex Jeans	Vietnam	Apparel	ETC	705	493.5	20
Painting	Sharman Shawls	India	Textile	FPC (100~)	360	252	8
	BMW Manufacturing	South Africa	Vehicle	ETC (~90)	200	140	24.2
	Harlequin	Spain	Textile	FPC	47.15	33	5
	Penzkofer Autolackiererei	Germany	Chemical	Air collector	20.1	14.07	1
	Solar Process Heat for Car Paintshop	Germany	Vehicle	Fresnel (~220)	185	66	
	Wheels India	India	Machinery	ETC (~75)	1365	955.5	80
Retanning	Ayuthaya tannery	Thailand	Leather	ETC (~80)	1890	1323	80
	Gerberer Kölblinger	Austria	Leather	FPC	77	53.9	40
	Heshan Bestway Leather	China	Leather	ETC (~70)	630	441	60
	Leo Leather	India	Leather	FPC	300	210	15
	Nairobi tannery	Kenya	Leather	ETC	580	406	
	Sadesa Leather	Thailand	Leather	ETC (~80)	540	378	35
	Saigon Tanteo	Vietnam	Leather	ETC (~70)	1000	700	70
	Tripou – Katsouris Leather Treatment Factory	Greece	Leather	FPC (48~84)	300	210	15

Table 14.9 Country-based analysis of SHIP plants [27]

Country name	Number of SHIP plants	Industrial sectors using SHIP
Mexico	80	Agriculture, mining, food, tobacco, textile, wearing apparel, leather, paper, chemical, metals, electrical equipment, transport equipment
India	46	Agriculture, food, tobacco, textile, wearing apparel, leather, paper, chemical, metals, electrical equipment, transport equipment
Austria	27	Food, beverages, leather, chemicals, metals, furniture
Germany	26	Agriculture, food, beverages, textiles, chemicals, metals
United States	19	Agriculture, food, beverages, textiles,
Spain	16	Agriculture, food, textiles, wood, metals, motor vehicle
China	12	Agriculture, food, beverages, textiles, chemicals, leather
South Africa	10	Mining, food, beverages, machinery, motor vehicles
Greece	10	Food, beverages, textiles, Pharmaceuticals, leather
Switzerland	6	Construction, dairy, machinery
France	4	Food and beverages, metals
Israel	4	Food, accommodation, and others

According to the analysis results presented in Tables 14.1, 14.2, 14.3, 14.4, 14.5, 14.6, 14.7, and 14.8, SHIP plants vary among them based on process temperature requirements, installed gross area, number of systems, installed capacity, and size categories. Fig. 14.1 describes the brief relationship among these parameters in terms of installed SHIP plants by March 2018 [28]. According to the results presented here, SHIP plants with gross solar collector size above 30,000 m² is 125 MWth valued 250,000 m² while for SHIP plants of solar collector size from 1000 to 30,000 m² is 54 MWth valued 100,000 m². Hence, SHIP plants with gross solar collector size from 500 to 1000 m² are 16 MWth valued around 250,000 m². SHIP plants with gross solar collector size above from 100 to 500 m² is 17 MWth valued 50,000 m². SHIP plants with gross solar collector size below 100 m² are 2 MWth valued below 50,000 m². The installed capacity is largest for the first category of collectors with gross size above 30,000 m².

Figure 14.2 describes the installed collector area, number of systems, and installed capacity of the SHIP plants based on the type of solar collectors or their combinations. The chart represents seven types of solar collectors: flat-plate collector, parabolic-trough collector, evacuated-tube collector, other or various collector, air collector, unglazed collector, and Fresnel collector. According to the SHIP plants database information and International Energy Agency (IEA) Solar heating & Cooling Programme (SHC) Task 49, there are around 124 plants with the flat-plate collector of installed collector area around 100,000 m², and installed capacity 71 MWth. Forty-nine SHIP plants with parabolic-trough collector with installed collector area around 250,000 m² and installed capacity 111 MWth. Forty-six SHIP plants are operating with evacuated-tube collector with installed collector

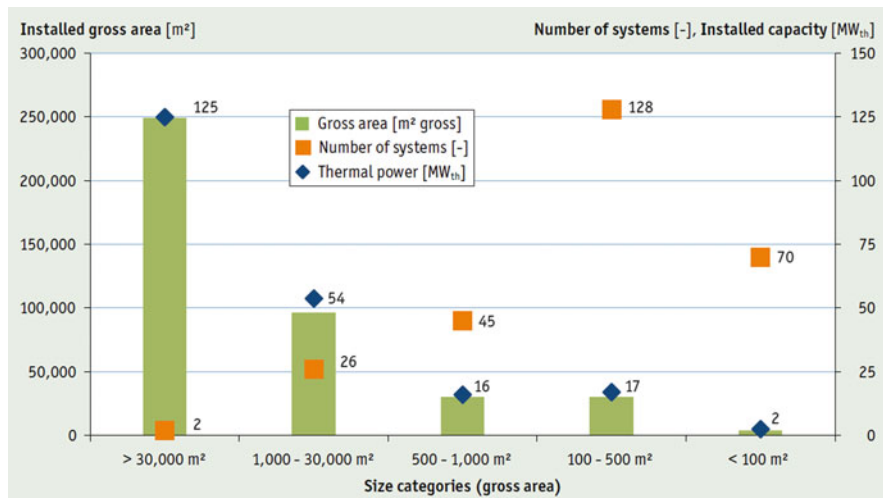


Fig. 14.1 Global SHIP plants in operation based on capacity and collector area [28]

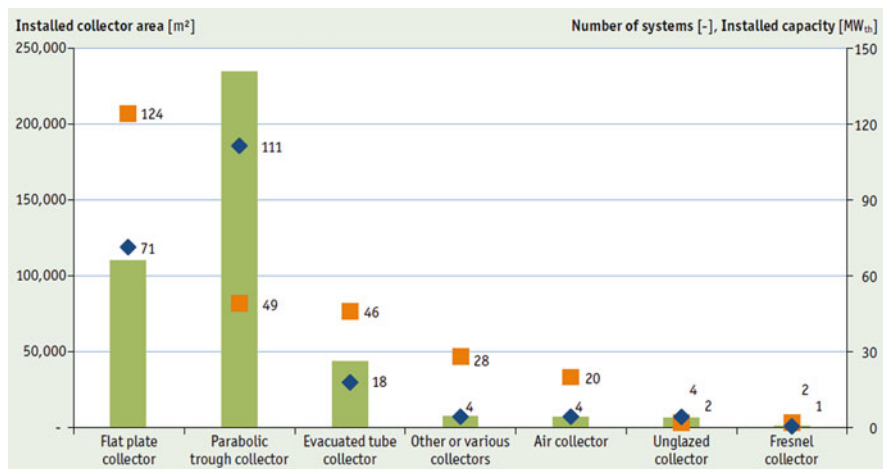


Fig. 14.2 Global SHIP plants in operation based on collector type [28]

area around 50,000 m² and installed capacity 18 MWth. Twenty-eight SHIP plants have a combination of different type collectors while installing collector area is around 10,000 m² with installed capacity 4 MWth. Similarly, 20 SHIP plants have air collectors with installed collector area around 10,000 m² and installed capacity 4 MWth. For the unglazed and Fresnel collectors, these statistics are very low.

Figure 14.3 describes the SHIP plants design specifications based on their respective industrial sector. The diagram is subdivided into ten segments based

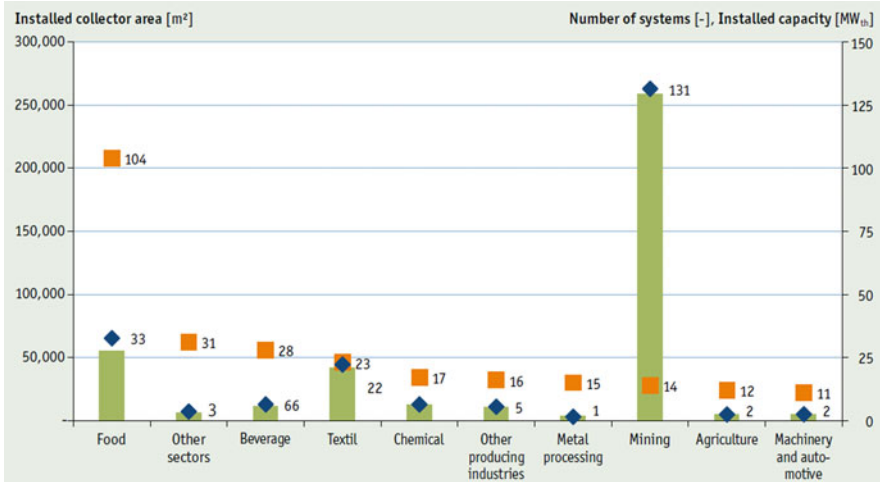


Fig. 14.3 Global SHIP plants in operation based on industrial area [28]

on the industrial sector: food, other sectors, beverage, textile, chemical, other producing industries, metal processing, mining, agriculture, machinery, and automotive. The food industry has 104 systems with installed collector area above 50,000 m² and installed capacity 33 MWth. The other sectors have 31 systems with installed collector area above 10,000 m² and installed capacity 3 MWth. The beverage industry has 28 systems with installed collector area above 20,000 m² and installed capacity 66 MWth. The textile industry has 23 systems with installed collector area above 40,000 m² and installed capacity 22 MWth. The chemical sector has 17 systems with installed collector area above 20,000 m². The other producing sectors have 16 systems with installed collector area above 15,000 m² and installed capacity 5 MWth. The metal processing sectors have 15 systems with installed collector area above 5000 m² and installed capacity 1 MWth. The mining sectors have 14 systems with installed collector area around 250,000 m² and installed capacity 131 MWth. The agriculture industry has 12 systems with installed collector area around 5000 m² and installed capacity 2 MWth. Similarly, the machinery and automotive industry have installed capacity 2 MWth. and installed collector area 5000 m² while the number of the system is 11.

Figure 14.4 describes the installed gross collector area, number of systems, and installed capacity of the SHIP plants installed in the world based on their country-specific locations. The chart represents 17 countries which use solar process heat for industrial use. According to the results presented here, the leading SHIP operated countries are Mexico, India, Austria, Germany, the USA, Spain, China, Greece, South Africa, and Chile. Only the SHIP plants with the gross area above 1000 m² and installed capacity above 0.7 is considered here for analysis.

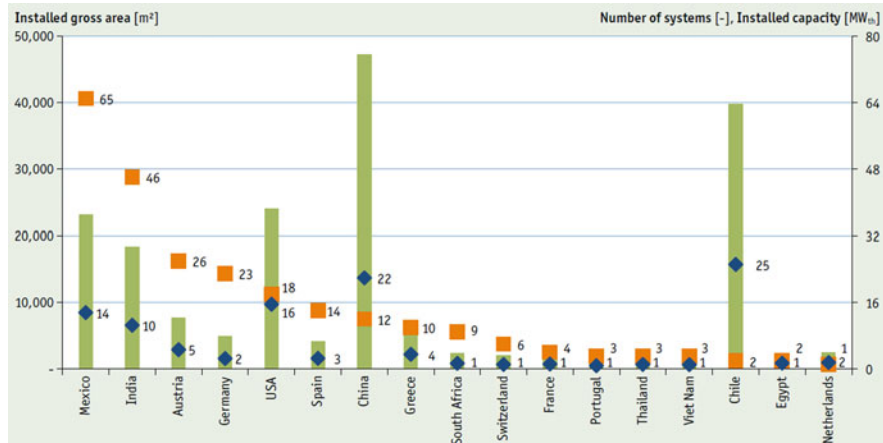


Fig. 14.4 Global SHIP plants in operation based on the country [28]

In Mexico, the number of SHIP plants is 65, installed area around 23,000 m², and installed capacity 14 MWth. In the case of India, the number of SHIP plants is 46, installed area around 19,000 m², and installed capacity 10 MWth. In Austria, the number of SHIP plants is 26, installed area around 8000 m², and installed capacity 5 MWth. In Germany, the number of SHIP plants is 23, installed area around 5000 m², and installed capacity 2 MWth. In the USA, the number of SHIP plants is 18, installed area around 25,000 m², and installed capacity 16 MWth. In Spain, the number of SHIP plants is 14, installed area around 5000 m², and installed capacity 3 MWth.

In China, the number of SHIP plants is 22, installed area around 48,000 m², and installed capacity 12 MWth. In Greece, the number of SHIP plants is 10, installed area around 8000 m², and installed capacity 4 MWth. In South Africa, the number of SHIP plants is 9, installed area around 3000 m², and installed capacity 1 MWth. In Chile, the number of SHIP plants is 25, installed area around 40,000 m², and installed capacity 2 MWth.

Table 14.10 describes the solar collector-related information and a carbon dioxide (CO₂) reduction of the leading countries with operating SHIP plants in the current world in their order of installed SHIP plants in operation. The parameters presented here are total collector area in m², total capacity in MWth, collector yield in GWh/a, and CO₂ reduction in t_{CO₂e}/a. According to the statistics presented here, China has the largest installed solar collector area of 413,600,000 m², total capacity 289,520 MW_{th}, collector yield 231,838 GWh/a, and CO₂ reduction 80,435,787 tones of carbon dioxide equivalence per annum [t_{CO₂e}/a]. The second position goes to United States with installed solar collector area of 24,279,331 m², total capacity 16,996 MWth, collector yield 10,925 GWh/a, and CO₂ reduction 3,790,555 t_{CO₂e}/a. Next comes Germany with installed solar collector area of 18,256,700 m², total

Table 14.10 SHIP plant design parameters in the leading countries

Country name	Total collector area [m ²] [28]	Total capacity [MW _{th}] [28]	Collector yield [GWh/a] [28]	CO ₂ reduction [t _{CO_{2e}/a] [28]}
Mexico	2,817,077	1972	1612	559,127
India	7,451,900	5216	6435	2,232,502
Austria	5,161,798	3613	2087	724,070
Germany	18,256,700	12,780	7434	2,579,104
United States	24,279,331	16,996	10,925	3,790,555
Spain	3,450,433	2415	2409	835,901
China	413,600,000	289,520	231,838	80,435,787
South Africa	1,650,050	1155	1178	408,709
Greece	4,286,300	3000	2986	1,035,865
Switzerland	1,484,640	1039	586	203,423

capacity 12,780 MWth, collector yield 7434 GWh/a, and CO₂ reduction 2,579,104 t_{CO_{2e}/a}. At next consequentially comes India, Austria, Greece, Spain, Mexico, South Africa, and Switzerland. Though, according to these statistics, the position of Mexico is far lags China, United States, India, and Germany, Mexico is the leading country in the world with the largest number of installed SHIP plants in operation

14.5 Conclusion

This book chapter studies the present condition of the installed SHIP plants based on their industrial processes under consideration, country-based location, and solar collector specifications. This chapter also studied the present condition of solar collector installation in the leading SHIP-operated countries and their CO₂ reduction scenario. Furthermore, this chapter presented the industrial sectors with the potentiality of SHIP integration in the leading countries. Further research should be carried out in those countries where SHIP integration in the industrial processes has not been started yet. In addition, identification of the low-temperature processes is required to extend the scope of SHIP integration in the world.

Acknowledgments The authors would like to thank the editors for the invitation to contribute in this book and their tireless effort for bringing this book into its final form. The first author would like to acknowledge the scholarship support received from Macquarie University through the International Macquarie University Research Training Pathway (iMQ RTP) scholarship scheme.

Acronyms

FPC	Flat-plate collector
PTC	Parabolic-trough collector
ETC	Evacuated-tube collector
SHIP	Solar heat for industrial processes

References

1. C. Palaniappan, Perspectives of solar food processing in India. Int Solar Food Processing Conf. January Indore, India. (2009), pp. 14–16
2. A.K. Sharma, C. Sharma, S.C. Mullick, T.C. Kandpal, Solar industrial process heating: a review. *Renew. Sust. Energ. Rev.* **78**, 124–137 (2017). December 2016
3. A. Sharma, C.R. Chen, N. Vu Lan, Solar-energy drying systems: a review. *Renew. Sust. Energ. Rev.* **13**(6–7), 1185–1210 (2009)
4. A.K. Sharma, C. Sharma, S.C. Mullick, T.C. Kandpal, Potential of Solar Energy Utilization for Process Heating in Paper Industry in India: A Preliminary Assessment. *Energy Procedia* **79**, 284–289 (Elsevier B.V., 2015)
5. A.K. Sharma, C. Sharma, S.C. Mullick, T.C. Kandpal, Carbon mitigation potential of solar industrial process heating: paper industry in India. *J. Clean. Prod.* **112**, 1683–1691 (2016)
6. N.S. Suresh, B.S. Rao, Solar energy for process heating: a case study of select indian industries. *J. Clean. Prod.* **151**, 439–451 (2017)
7. L. Kranzl et al., Renewable energy in the heating sector in Austria with particular reference to the region of Upper Austria. *Energy Policy* **59**, 17–31 (2013)
8. C. Lauterbach, B. Schmitt, U. Jordan, K. Vajen, The potential of solar heat for industrial processes in Germany. *Renew. Sust. Energ. Rev.* **16**(7), 5121–5130 (2012)
9. P. Frey, S. Fischer, H. Drück, K. Jakob, Monitoring results of a solar process heat system installed at a textile company in southern Germany. *Energy Procedia* **70**, 615–620 (2015)
10. P. Kurup, C. Turchi, Potential for solar industrial process heat in the United States, in *SolarPACES 2015*, vol. 110001, 2015
11. P. Kurup, C. Turchi, Initial investigation into the potential of CSP industrial process heat for the southwest United States, *NREL Tech. Rep.*, vol. NREL/TP-6A, no. November, 2015
12. H. Schweiger et al., The potential of solar heat in industrial processes. A state of the art review for Spain and Portugal, proceedings of *Eurosun2000*, Copenhagen, Denmark, 2000
13. W. Weiss, H. Schweiger, R. Battisti, Market potential and system designs for industrial solar heat applications. *Heat Treatment* **95**, 105 (2006)
14. R. Silva, F.J. Cabrera, M. Pérez-García, Process heat generation with parabolic trough collectors for a vegetables preservation industry in Southern Spain. *Energy Procedia* **48**, 1210–1216 (2014)
15. R. Silva, M. Berenguel, M. Pérez, A. Fernández-García, Thermo-economic design optimization of parabolic trough solar plants for industrial process heat applications with memetic algorithms. *Appl. Energy* **113**, 603–614 (2014)
16. R. Silva, M. Pérez, M. Berenguel, L. Valenzuela, E. Zarza, Uncertainty and global sensitivity analysis in the design of parabolic-trough direct steam generation plants for process heat applications. *Appl. Energy* **121**, 233–244 (2014)
17. B. Sturm et al., Process intensification and integration of solar heat generation in the Chinese condiment sector – a case study of a medium sized Beijing based factory. *Energy Convers. Manag.* **106**, 1295–1308 (2015)
18. M. Liu, S. Wang, K. Li, Study of the solar energy drying device and its application in traditional chinese medicine in drying. *Int. J. Clin. Med.*, 271–280 (2015)
19. T. jia, J. Huang, R. Li, P. He, Y. Dai, Status and prospect of solar heat for industrial processes in China. *Renew. Sust. Energ. Rev.* **90**, 475–489 (2018)
20. A.C. Brent, M. Pretorius, Industrial and commercial opportunities to utilise concentrating solar thermal systems in South Africa. *J. Energy S. Afr.* **22**(4), 15–30 (2011)
21. E.C. Joubert, S. Hess, J.L. Van Niekerk, Large-scale solar water heating in South Africa: status, barriers and recommendations. *Renew. Energy* **97**, 809–822 (2016)
22. R. Uhlig, L. Amsbeck, R. Buck, B. Gobereit, P. Schwarzbözl, Potential high-temperature industrial process heat applications for concentrating solar technology in South Africa. 3rd Southern African Solar Energy Conference, South Africa, 11–13 May, (2015)
23. C. Ramos, R. Ramirez, J. Beltran, Potential assessment in Mexico for solar process heat applications in food and textile industries. *Energy Procedia* **49**, 1879–1884 (2013)

24. M. Karagiorgas, A. Botzios, T. Tsoutsos, Industrial solar thermal applications in Greece: economic evaluation, quality requirements and case studies. *Renew. Sust. Energ. Rev.* **5**(2), 157–173 (2001)
25. S.H. Farjana, N. Huda, M.A.P. Mahmud, R. Saidur, Solar process heat in industrial systems – a global review. *Renew. Sust. Energ. Rev.* **82**, 2270–2286 (2018)
26. S.H. Farjana, N. Huda, M.A.P. Mahmud, R. Saidur, Solar industrial process heating systems in operation – current SHIP plants and future prospects in Australia. *Renew. Sust. Energ. Rev.* **91** (2018)
27. http://ship-plants.info/?industry_sector=2
28. W. Weiss, F. Mauthner, Solar Heat Worldwide, AEE INTEC and IEA SolarHeating and Cooling Programme, (2010), p. 94



Comparative Analysis of Water Quality of Different Types of Feed Water in Solar Energy Based Desalting System

15

Arunkumar Thirugnanasambantham, Jiaqiang Wang, and David Denkenberger

Contents

15.1	Introduction	440
15.2	Natural Water Resources	441
15.2.1	Type of Water Quality Problems	441
15.2.2	Water Quality of Rivers, Lakes, Groundwater, and Domestic Water	441
15.3	Water Quality Analysis of Solar Still Designs	442
15.4	Summary of Water Quality Results	445
15.5	Conclusion	445
	References	453

Abstract

In this chapter, desalinated water quality analyses from various solar stills are examined. Many authors have performed experiments in solar stills along with the testing of physical and chemical water quality examinations for feed water and desalinated water. This was performed on different types of feed water,

Author Contribution

T. Arunkumar wrote the first draft, D. Denkenberger compiled the data for the tables and J. Wang completed the final review of the manuscript.

A. Thirugnanasambantham · J. Wang (✉)

National Center for International Research on Photoelectric and Energy Materials, Yunnan Provincial Collaborative Innovation Center of Green Chemistry for Lignite Energy, Yunnan Province Engineering Research Center of Photocatalytic Treatment of Industrial Wastewater, The Universities' Center for Photocatalytic Treatment of Pollutants in Yunnan Province, School of Chemical Sciences and Technology, Yunnan University, Kunming, China
e-mail: tarunkumarsolar@163.com; jqwang@ynu.edu.cn

D. Denkenberger

Mechanical Engineering and the Alaska Center for Energy and Power, University of Alaska Fairbanks, Fairbanks, AK, USA
e-mail: david.denkenberger@gmail.com

namely, ocean water, bore well water, water from lakes, tap water, and synthetic water from the laboratory are investigated. This research is important to understand solar still performance for a variety of different water types. Based on the investigation, the potential of hydrogen (pH) and total dissolved solids (TDS) value (before and after treatment) of the synthetic water, brackish water, groundwater, lake water, and seawater are improved and is compliant with WHO-2017 and BIS-2010 water quality standards. Water quality results of dissolved macro minerals (before and after treatment) in the water are discussed and useful conclusions are drawn.

Abbreviations

AT	After treatment
BIS	Bureau of Indian Standards
BT	Before treatment
DSSS	Double slope solar still
EC	Electrical conductivity, $\mu\text{S}/\text{cm}$
ETU	Ethylene thiourea unit
NTU	Nephelometric turbidity unit
PCM	Phase change material
SSSS	Single slope solar still
TCU	True color units
TDS	Total dissolved solids, ppm
The EPA	United States Environmental Protection Agency
TWAD	Tamilnadu Water Supply and Drainage
WHO	World Health Organization

15.1 Introduction

Water is the most crucial fluid on Earth; survival without water is impossible. Water is the source of life on Earth since it is required for biological processes. Because of its abundant presence and physical and chemical characteristics, water has a stabilizing effect on interplanetary and earthly processes. Civilizations typically start near water. Many people in India store water in copper vessels for drinking purposes. Recently, researchers from the Indian Institute of Science (IISc), Bangalore, have developed a water filter with copper to make drinking water safe. They proposed that the water stored in the copper coated vessels for 16 h killed pathogenic bacteria such as *Escherichia coli* (*E. coli*) and *Vibrio cholerae*. This is because of the anti-bacterial property of the copper [23].

Researchers have enhanced fresh water production in different ways, including solar stills with dye in the basin [26, 72], wick on the basin [29, 35–37, 40, 50, 57, 60, 69, 73], charcoal pieces [53], rubber scraps [5], internal reflectors [43, 74],

sponge cubes [1, 7, 21], porous basin [47], spherical solar still [10], tubular solar still [8, 12, 13, 15], concentrator assisted solar still [16, 17, 18], solar still with phase change material (PCM) [11], solar still with heater [51], solar still with air blower [39], photovoltaic thermal hybrid solar collector (PV-T) solar still [52], solar still with bubble-wrap insulation [19], and solar still with heat exchanger [38].

Some misconceptions that distilled water is not good for health is not right. A few important organizations such as the World Health Organization (WHO), US Environmental Protection Agency (EPA), and Bureau of Indian Standards prescribe the water quality standards for safe drinking water. The published water quality results of different feed water intake and desalinated water samples in the solar stills are examined. Many research works have been conducted by authors on solar stills to enhance fresh water productivity. A collection of a compact review on recent advances is essential for researchers to prioritize further work. The present review focuses on water quality standards and their relevance in the light of recent research findings. Based on the literature survey, it is found that very few review studies have been performed in water quality analysis in solar stills to the best of authors' knowledge.

15.2 Natural Water Resources

15.2.1 Type of Water Quality Problems

Upon reaching the surface, precipitation either percolates into the soil, becoming groundwater or runs off along the surface in rivulets, streams, and rivers. Minerals dissolve in both surface and groundwater, but greater contact with soil and minerals generally results in higher dissolved-salt concentration in groundwater. Chemical impurities that are commonly found in water in significant quantities include calcium, magnesium, sodium, potassium, bio-carbonate, chloride, sulfate, and nitrate. Traces of lead, copper, arsenic, manganese, and a wide spectrum of organic compounds are also found. The organic compounds are mainly from four sources; (1) decaying plant and animal matter, (2) agricultural run-off, (3) wastewater, and (4) improper management of hazardous waste discharges.

15.2.2 Water Quality of Rivers, Lakes, Groundwater, and Domestic Water

The main source of water for public, industrial, and commercial uses are either from rivers or lakes. Many rivers and lakes are badly polluted due to the disposal of domestic and industrial waste. Conservation of groundwater is essential because, during the summer, it is the only option to provide the water for many places. Groundwater pollution is more dangerous than surface water pollution because groundwater contamination lasts much longer. Among all the uses of water, domestic use of water has prime importance. Safe and wholesome water can be defined as

Table 15.1 The physical and chemical water quality parameters according to the World Health Organization (WHO)-2017, Bureau of Indian Standards (BIS)-2010 and Environmental Protection Agency (EPA)-2014 standards

S. No.	Physical parameters	WHO standard-2017	BIS standard-2010 [22]	EPA standard-2014 [31]
1	Color	15 true color units	5 true color units	–
2	pH value	<8.0	6.5–8.5	≥6.5 and ≤ 9.5
3	Turbidity	5 NTU	1 NTU	1 NTU
4	Total dissolved solids (TDS), mg/L	1000	500	500
	Chemical parameters			
5	Arsenic, mg/L	0.01	0.01	0.01
6	Copper, mg/L	2	0.05	2.0
7	Fluoride, mg/L	1.5	1.5	0.8
8	Manganese, mg/L	0.5	0.1	0.05
9	Nitrate (as NO ₃ ⁻), mg/L	50	45	50
10	Aluminum, mg/L	0.2	0.03	0.2
11	Ammonia, mg/L	1.5	0.5	0.30
12	Chloride, mg/L	250	250	250
13	Iron, mg/L	0.3	0.3	0.2
14	Sulfate, mg/L	250	200	250
15	Chlorine, mg/L	0.6–1.0	0.2	0.5
16	Hardness	200	200	200

uncontaminated water free from an excessive amount of minerals and free from poisonous substances (see Table 15.1).

15.3 Water Quality Analysis of Solar Still Designs

Kumar et al. [46] experimentally studied the DSSS under Bareilly (India) climatic conditions. The synthetic samples were tested in the Sam Higginbottom Institute of Agricultural Technology & Sciences. The synthetic samples such as sodium carbonate (Na₂CO₃), sodium hydrogen carbonate (NaHCO₃), calcium chloride (CaCl₂), and magnesium iodide (MgI₂) are prepared and fed into the double slope solar still (DSSS). The distilled water passed the standards of WHO-2017 and BIS-2010 standards.

Ahsan et al. [2, 6] studied the arsenic contaminated water in the single slope solar still (SSSS). The arsenic water samples are fed into the solar still and the distillate underwent water quality tests (i.e., pH (potential of Hydrogen), redox potential, EC (electrical conductivity), and *E. coli* colony count). The “LaMotte Arsenic kit” was used to test the presence of arsenic in the water. *Escherichia coli* is the pathogenic bacteria which may cause diarrhea. The quality values show compliance with the WHO-2017 standard. Palpandi and Raj [55] experimentally studied the SSSS with

PCM for seawater and bore well water distillation. The water quality tests were carried out in the TWAD (Tamilnadu Water Supply and Drainage) board. The physical examination (appearance of water, color, odor, turbidity, and total dissolved solids (TDS)); electrical conductivity, (EC); and chemical examination (pH, alkalinity, total hardness, and mineral content analyses of calcium (Ca), magnesium (Mg), sodium (Na), potassium (K), manganese (Mn), ammonia (NH₃), chlorine (Cl), fluorine (F), sulfate (SO₄), and phosphate (PO₄)) were carried out. The physical and chemical examination values after distillation were found to be in the acceptable range of WHO-2017 and BIS-2010 standards.

Al-Hassan and Algarni [3] studied three identical pyramid type solar stills for saline water distillation. The results of TDS and pH shows compliance with the WHO-2017 standard. Siddiqui et al. [70] studied water quality before and after distillation. The water samples were tested at Sobhasaria Engineering College, Sikar, India. The pH, EC, and TDS tested values were compliant with WHO-2017 standards. Abhishek and Navneet [64] studied SSSS for water desalination. The pH and TDS values were in acceptable range by EPA-2014 standards. Raza et al. [61] experimented on a hexagonal tomb type solar still. The pH, EC, TDS, and total hardness of water were tested. The test values were compliant with WHO-2017 prescriptions. Almuhanha [4] experimentally studied an SSSS integrated with a condenser for distillation. The output water collected from the SSSS was tested for the water quality. The physical and chemical water quality (pH, TDS, total hardness, and EC) values were compliant with the WHO-2017 standards. Bilal et al. [34] studied an SSSS integrated with a photovoltaic thermal hybrid solar collector (PV/T) system. The output water from the SSSS was collected and tested for water quality (pH, TDS, and EC). The physical and chemical water examination result revealed that the values were well within the WHO-2017 water quality standard. Vinoth Kumar and Kasturi Bai [75] experimentally studied an SSSS for tap water and sea water distillation. The physical and chemical water quality test results complied with the EPA-2014 standard.

Gurmu et al. [33] analyzed the output distillate water obtained from a solar still. The tested quality values were acceptable according to the WHO-2017 and EPA-2014 standards. Ahsan et al. [2] experimentally studied the TSS for synthetic and sea water distillation. The pH, redox potential, EC, TDS, and salinity were studied for seawater and synthetic water. The quality results were that the tested values complied with the WHO-2017 standard. Eltawil and Zhengming [30] studied an SSSS integrated with a wind turbine for groundwater desalination. The output water collected from the SSSS was tested for physical and chemical water qualities. The results followed the WHO-2017 standard.

Kumar and Tiwari [45] have studied a photovoltaic thermal (PV/T) system for groundwater distillation. The physical and chemical water quality tests such as appearance, odor, pH, TDS, total hardness, Cl, and SO₄ were conducted. The result showed that the water quality after distillation was found suitable for drinking purposes [76]. Sampathkumar and Senthilkumar [62] tested single basin solar still integrated with a solar water heater for groundwater distillation. Four different water samples were collected in Coimbatore, and physical and chemical water quality

examinations were carried out. The water quality followed WHO-2017 and BIS-2010 standards.

Arunkumar et al. (2012) experimentally studied hemispherical solar still for tap water distillation. The pH, TDS, and EC of the water quality tests were performed. The water quality results complied with the WHO-2017 standard. Arunkumar et al. [14] tested a concentrator coupled hemispherical basin solar still for tap water distillation. The pH, TDS, EC, and chloride parameters were tested, and the results complied with the WHO-2017 standard. Omara et al. [54] studied the wick type solar still with an evacuated solar water heater. Water quality analyses were done before and after distillation (pH and TDS). The water quality lay in the acceptable range of the WHO-2017 standard. Agouz [28] investigated stepped solar still for seawater and saline water distillation. The physical and chemical water quality tests were conducted for the two input water type samples. The results of quality analysis reveal that the values lie in the acceptable range of WHO-2017. Dev et al. [25] testing inverted absorber solar still for seawater and laboratory sample distillation. Seawater samples in the still were tested with different depth and water quality was analyzed. The results showed that the output water values followed the WHO-2017 standard. Kaushal et al. [44] developed a vertical single solar still for saline water distillation. The before and after distillation water samples were tested for TDS and pH analysis. The after values found complied with the WHO-2017 standard.

Flendrig et al. [32] experimentally studied an SSSS of area 1.34 m². The purification performance test such as TDS, pH, and EC were conducted. The results showed that the still produced safe drinking water in an economical way. Asadi et al. [20] investigated an SSSS with brackish water distillation. The TDS and EC quality parameters were tested for the desalinated water. The water quality results complied with the WHO-2017 standard. Pillai et al. [56] studied an SSSS for saline water distillation. The pH, TDS, and EC of before and after treated water were acceptable by the WHO-2017 and BIS-2010 standards. Sengar et al. [66] studied an SSSS for tap water distillation. The pH, EC, and chlorine level in the water were tested and their results were compared with the WHO-2017 standard.

Sengar et al. [65] experimentally studied a wick type solar still for tap water and saline water distillation. The water quality results complied with the WHO-2017 standard. Edwin and Sekar [27] investigated the SSSS for saline water distillation. The chemical water quality examinations were conducted, and they complied with the WHO-2017 standard. Saha et al. [59] experimentally investigated the SSSS for municipal and sea water distillation. The water quality results complied with the WHO-2017 standard. Kalbande et al. [42] tested a solar still for groundwater distillation. Four different water samples were collected near Akola, India, and the physical and chemical water quality was examined. The result showed that the water quality after distillation was found suitable for drinking purposes [76]. Shatat et al. [68] investigated a solar still for synthetic water distillation. The pH, TDS, and EC were tested for before and after water collected from a solar still. The values after distillation were acceptable according to the WHO-2017 water quality standard.

Mashaly et al. [49] investigated three different feed water types in a solar still namely ground water, sea water, and drainage water. The detailed physical and chemical examinations were acceptable under WHO-2017 water quality standards. Chendake et al. [24] experimentally studied the inverted pyramid solar still for brackish water distillation. The pH and TDS results were measured before and after distillation. The outcome of the after tested results showed compliance with the standards of WHO-2017. Madhlopa [48] experimentally studied a solar still with a separate condenser for bore well water distillation. The pH, EC, and TDS of the distilled water were acceptable according to the WHO-2017 standard. Shanmugasundaram [67] investigated the pyramid type solar still for bore well water distillation. The pH, TDS, and EC tested values of distilled water were found to be in the acceptable range of BIS-2010. Hansen and Murugavel [63] experimentally studied an SSSS and an inclined solar still for water distillation. The result showed that the water quality after distillation was found suitable for drinking purposes [76]. Riahi et al. [58] conducted experiments in SSSS for lake water distillation. The physical and chemical water quality examination revealed that the water was acceptable according to the WHO-2017 standard. Sivakumar and Sundaram [71] experimentally studied the SSSS for saline and sea water distillation. The detailed physical and chemical water quality results were found to be in the acceptable range of WHO-2017 drinking water quality standards.

The quality of different types of feed water such as bore well water, tap water, lake water, sea water, and laboratory synthesized water has been tested. The results of physical and chemical water quality examinations (before and after treatment) are shown in Tables 15.2 and 15.3.

15.4 Summary of Water Quality Results

Figure 15.1 shows the desalinated values for different feed water used in the solar still. The pH and TDS value (before and after treatment) of the synthetic water, brackish water, groundwater, lake water, and seawater are presented. The results reveal that the quality of desalinated water improved and is compliant with WHO-2017 and BIS-2010 water quality standards.

15.5 Conclusion

In this chapter, water quality examination results in solar stills are discussed. The significance of the present work is to reveal the misconceptions that distilled water is not good for health, is not right. A few important organizations such as the World Health Organization (WHO), US Environmental Protection Agency (EPA), and Bureau of Indian Standards prescribe the water quality standards for safe drinking water. The

Table 15.2 Tested results of desalinated water samples

S. N#	Author, country, and water type	Test parameters											
		pH		TDS (ppm)		Total hardness (mg/L)		Electrical conductivity (μ S/cm)		Alkalinity (mg/L)		Chloride content (mg/L)	
		BT	AT	BT	AT	BT	AT	BT	AT	BT	AT	BT	AT
1	Kumar et al. [46], India/synthetic water	8	7.2	×	×	433	51	×	×	642	76	388	32
2	Ahsan et al. [2, 6], Malaysia/lake water	8	5.72	185.4	89.6	×	×	286.1	138.2	148	71.7	×	×
3	Palpandi and Raj [55], India/sea water	8.06	6.8	16,078	52	3420	26	23,997	73	112	16	8050	10
4	Bore well water	7.31	6.5	398	40	178	18	577	54	142	14	87	7
		7.35	5.94	15,120	193.4	×	×	×	×	×	×	×	×
5	Al-Hassan and Algami [3], Syria/brackish water	8.25	7.06	325	40	×	×	13,000	3000	×	×	×	×
6	Saxena and Deval [64], India/tap water	8.9	7.7	290	21	×	×	×	×	×	×	×	×
7	Raza et al. (2014), Pakistan/brackish water	9.1	6.1	3640	225	320	38	5.20	0.31	×	×	×	×
8	Almuhanna [4], Saudi Arabia/brackish water	8.1	7.9	1370	30.9	×	×	1436	43.4	×	×	×	×
9	Bilal et al. (2016), Pakistan/brackish water	6.92	6.1	1250	105	×	×	3.5	0.15	×	×	×	×
11	Vinoth Kumar and Kasturi Bai [75], India/tap water	6.9	7.8	428.2	110.3	268	44	822	149	×	×	32.66	17.04
12	Sea water	8.2	6.9	39,350	153	4480	53	76	271	×	×	12,666	42.06
		8.6	7.1	1390	8.9	308.4	16.4	×	×	344.2	21.4	×	×

13	Ahsan et al. [2], Malaysia/sea water	8.7	7.7	28,110	7.52	×	×	43.37	11.6	22.49	6.01	×	×
	Synthetic water (3% salt)	8.18	7.29	25,310	3.28	×	×	39.05	5.06	20.25	2.62	×	×
14	Eltawil and Zhengming et al. [30], China/tap water	8.09	6.78	317	6.5	×	×	586	13.29	0.3	0	×	×
15	Kumar and Tiwari [45], India/ground water	7.68	6.32	724	0.32	456	0.84	×	×	376	0.06	282	0.46
16	Sampathkumar and Senthilkumar [62], India/Ravathur city water	8	6.98	5355	150	1470	43	×	×	780	68	1500	12
	Kannampalayam city water	7.75	7.2	5172	13	1340	38	×	×	770	62	1500	10
	Sulur city water	7.86	7.1	2492	100	650	33	×	×	380	65	670	8
	Karadivavi city water	7.86	6.7	744	90	266	28	×	×	200	55	176	5
17	Arunkumar et al. (2012), India/tap water	7.60	7.32	320	40	×	×	1000	100	×	×	×	×
18	Arunkumar et al. [14], India/tap water	6.92	7.26	430	124	255	51	850	210	×	×	×	×
19	Omara et al. [54], Egypt/brackish water	8.9	7.1	732	72	×	×	×	×	×	×	×	×
20	El-Agouz et al. [28], Egypt/sea water	8.25	6.6	40,772	41	3900	16	57,100	62	183	0.5	21,300	10.8
	Saline water	8.15	5.9	1681	27	460	9	2370	41	162	0	369	2.4
21	Dev et al. [25], India/sea water (1 cm SS water depth)	7.64	6.52	×	×	×	×	55,200	137.1	×	×	×	×
	Sea water (2 cm water depth)	7.35	6.15	×	×	×	×	94,600	984	×	×	×	×
	Sea water (3 cm water depth)	7.14	6.31	×	×	×	×	60,600	893	×	×	×	×
	Sea water	6.86	6.24	7010	580	×	×	13,890	45.1	×	×	×	×
	Sea water (38,000 ppm)	7.37	6.66	37,200	540	×	×	45,400	431	×	×	×	×
22	Kaushal et al. [44], India/tap water	7.5	5.8	574	30	×	×	×	×	×	×	×	×
23	Flendrig et al. [32], The Netherlands/contaminated water	9.6	5.5	2925	40	×	×	6130	26	×	×	×	×

(continued)

Table 15.2 (continued)

S. N#	Author, country, and water type	Test parameters											
		pH		TDS (ppm)		Total hardness (mg/L)		Electrical conductivity ($\mu\text{S}/\text{cm}$)		Alkalinity (mg/L)		Chloride content (mg/L)	
		BT	AT	BT	AT	BT	AT	BT	AT	BT	AT	BT	AT
24	Asadi et al. [20], Iran/brackish water	×	×	2221	140	×	×	3704	233	×	×	×	×
25	Pillai et al. [56], India/brackish water	7.58	6.82	154	19.48	×	×	×	×	×	×	×	×
26	Sengar et al. [66], India/brackish water	7.8	7.0	×	×	×	×	100	0.8	×	×	1.6	0
27	Sengar et al. [65], India/tap water	7.63	7.0	×	×	×	×	1,60,000	70,000	×	×	1.5	0
	Saline water	9.3	7.02	35,780	790	×	×	7,24,000	90,590	×	×	0	0
28	Edwin and Sekar (2015), India/saline water	×	×	38,790	810	210	0.36	34,100	520	×	×	18,971	18
29	Saha et al. [59], Iraq/municipality water	×	×	547	33	×	×	×	×	×	×	×	×
	Sea water	×	×	33,500	3920	×	×	×	×	×	×	×	×
30	Kalbande et al. [42], India/College of Agricultural Engineering and Technology (CAET) Akola- water	7.02	7.01	953.60	19.2	4.66	0.04	×	×	×	×	22	2
	Akola hostel water	7.03	6.98	960	25.6	5.22	0.04	×	×	×	×	24	2
	Shivni location water	7.31	6.99	1536	25.6	6.52	0.12	×	×	×	×	40	5.4
	Mothumri location water	7.23	6.88	1954	38.4	6.9	1.12	×	×	×	×	48	5.7
31	Shatat et al. [68], USA/synthetic water	8	7.5	2500	22	×	×	3050	34.5	×	×	×	×

Table 15.3 Water quality results of dissolved macrominerals in the water

S. no	Author, country, and water type	Test parameters of inorganic compounds															
		Ca (mg/L)		Mg (mg/L)		Na (mg/L)		K (mg/L)		Fe (mg/L)		NO ₃ (mg/l)		F (mg/L)		PO ₄ (mg/L)	
		BT	AT	BT	AT	BT	AT	BT	AT	BT	AT	BT	AT	BT	AT	BT	AT
1	Palpandi and Raj [55], India/sea water	880	6	293	1	3480	7	660	1	0	0	6	1	0.8	0.2	0.08	0.01
	Bore well water	44	2	16	1	48	4	12	1	0	0	1	1	0	0	0.06	0.01
2	Eltawil and Zhengming et al. [30], China/tap water	19.29	1.36	90.4	0.37	×	×	8.2	0.4	8.2	0.4	×	×	×	×	×	×
3	Sampathkumar and Senthilkumar [62], India/Ravathur city water	392	18	118	6	1180	8	120	2	0	0	154	23	0.8	0	0.03	0
	Kannampalayam city water	358	15	1070	6	1320	9	130	1.5	0.04	0	152	28	0.8	0	0.01	0
	Sulur city water	174	16	52	4	270	8	30	1.5	0	0	61	14	0.6	0	0.01	0
	Karadivavi city water	71	10	21	2	108	4	10	0.5	0	0	16	6	0.6	0	0	0

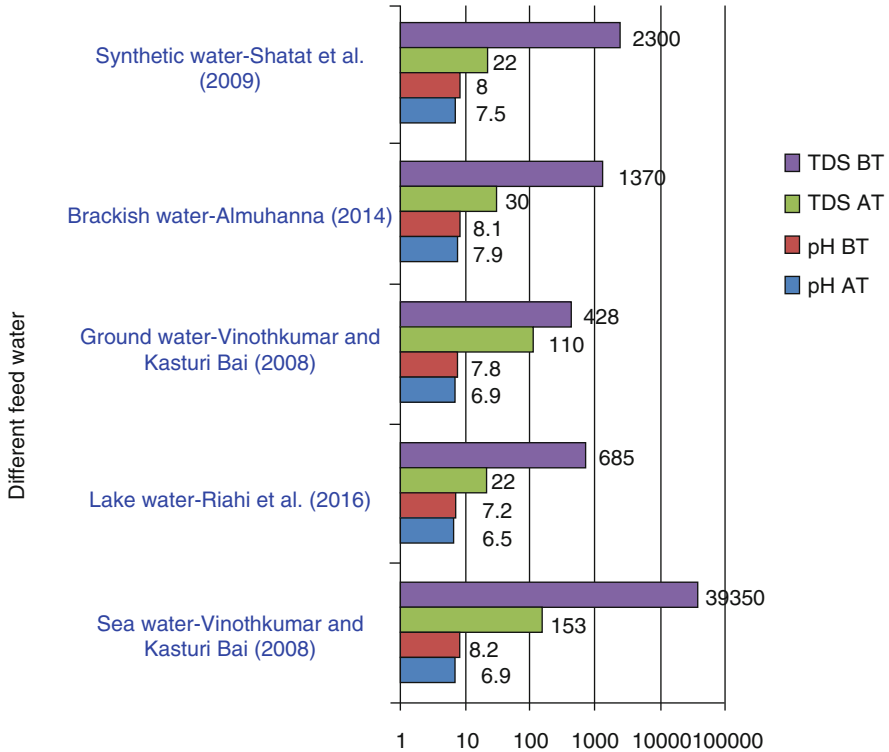


Fig. 15.1 Treated water results of different types of feed water

published water quality results of different feed water intake and desalinated water samples in the solar stills are examined and the following conclusions can be drawn:

- Solar stills can produce good quality of potable water from most types of feed water, basically anything with nonvolatile contaminants. The physical and chemical testing reveals that the desalinated water quality is in the acceptable range of the WHO-2017 and BIS-2010 standards.
- The pH and TDS value (before and after treatment) of the synthetic water, brackish water, groundwater, lake water, and seawater are presented. The results reveal that the quality of desalinated water improved and is compliant with WHO-2017 and BIS-2010 water quality standards.
- Water quality results of dissolved macro minerals (before and after treatment) in the water are reviewed. The inorganic compounds in the water such as Ca, Mg, Fe, Na, K, F, and PO_4 are shown in good agreement with prescribed water quality standards suggested by WHO-2017 and BIS-2010.

Acknowledgments We thank all the researchers and their contributions which were cited in this article.

References

1. B.A./K. Abu-Hijleh, H.M. Rababa'h, Experimental study of a solar still with sponge cubes in the basin. *Energy Convers. Manag.* **44**(9), 1411–1418 (2003). [https://doi.org/10.1016/S0196-8904\(02\)00162-0](https://doi.org/10.1016/S0196-8904(02)00162-0)
2. A. Ahsan, M. Imteaz, U.A. Thomas, M. Azmi, A. Rahman, N.N. Nik Daud, Parameters affecting the performance of low cost solar still. *Appl. Energy* **114**, 924–930 (2014). <https://doi.org/10.1016/j.apenergy.2013.08.066>
3. G.A. Al-Hassan, S.A. Algarni, Exploring of water distillation by single solar still basins. *Am. J. Clim. Chang.* **2**, 57–51 (2013)
4. E.A. Almuhanna, Evaluation of single slope solar still integrated with an evaporative cooling system of brackish water desalination. *J. Agric. Sci.* **6**, 48–48 (2014)
5. A.O. Al-Sulttani, A. Ahsan, A.N. Hanoon, A. Rahman, N.N.N. Daud, S. Idrus, Hourly yield prediction of a double-slope solar still hybrid with rubber scrapers in low-latitude areas based on the particle swarm optimization technique. *Appl. Energy* **203**, 280–303 (2017). <https://doi.org/10.1016/j.apenergy.2017.06.011>
6. A. Amimul, N. Syuhada, E. Jolhi, M.D. Kh, K.R. Md, J. Md, S. Shafie, A.H. Ghazali, Assessment of distillate water quality parameters produced by solar still for portable usage. *Fresenius Environ. Bull.* **23**(3 A), 859–866 (2014)
7. T.V. Arjunan, H.Ş. Aybar, N. Nedunchezihan, Effect of sponge liner on the internal heat transfer coefficients in a simple solar still. *Desalin. Water Treat.* **29**, 271–284 (2011)
8. T. Arunkumar, A.E. Kabeel, Effect of phase change material on concentric circular tubular solar still-integration meets enhancement. *Desalination* **414**, 46–50 (2017). <https://doi.org/10.1016/j.desal.2017.03.035>
9. T. Arunkumar, R. Jayaprakash, D. Denkenberger, A. Ahsan, M.S. Okundamiya, S. kumar, H. Tanaka, H.Ş. Aybar, An experimental study on a hemispherical solar still. *Desalination* **286**, 342–348 (2012). <https://doi.org/10.1016/j.desal.2011.11.047>
10. T. Arunkumar, K. Vinothkumar, A. Ahsan, R. Jayaprakash, S. Kumar, Experimental study on various solar still designs. *ISRN Renew. Energ.*, 1–10 (2012). <https://doi.org/10.5402/2012/569381>
11. T. Arunkumar, D. Denkenberger, A. Ahsan, R. Jayaprakash, The augmentation of distillate yield by using concentrator coupled solar still with phase change material. *Desalination* **314**, 189–192 (2013). <https://doi.org/10.1016/j.desal.2013.01.018>
12. T. Arunkumar, R. Jayaprakash, A. Ahsan, D. Denkenberger, M.S. Okundamiya, Effect of water and air flow on concentric tubular solar water desalting system. *Appl. Energy* **103**, 109–115 (2013). <https://doi.org/10.1016/j.apenergy.2012.09.014>
13. T. Arunkumar, J. Rajan, A. Ahsan, V. Kandasamy, Effect of air flow on tubular solar still efficiency. *Iran. J. Environ. Health Sci. Eng.* **10**(31) (2013). <https://doi.org/10.1186/1735-2746-10-31>
14. T. Arunkumar, D. Denkenberger, R. Velraj, R. Sathyamurthy, H. Tanaka, K. Vinothkumar, Experimental study on a parabolic concentrator assisted solar desalting system. *Energy Convers. Manag.* **105**, 665–674 (2015). <https://doi.org/10.1016/j.enconman.2015.08.021>
15. T. Arunkumar, R. Velraj, A. Ahsan, A.J.N. Khalifa, S. Shams, D. Denkenberger, R. Sathyamurthy, Effect of parabolic solar energy collectors for water distillation. *Desalin. Water Treat.* **57**(45), 21234–21242 (2016). <https://doi.org/10.1080/19443994.2015.1119746>
16. T. Arunkumar, R. Velraj, D.C. Denkenberger, R. Sathyamurthy, Influence of crescent-shaped absorber in water desalting system. *Desalination* **398**, 208–213 (2016). <https://doi.org/10.1016/j.desal.2016.07.039>
17. T. Arunkumar, R. Velraj, D. Denkenberger, R. Sathyamurthy, K.P. Vinothkumar, A. Ahsan, Effect of heat removal on the tubular solar desalting system. *Desalination* **379**, 24–33 (2016). <https://doi.org/10.1016/j.desal.2015.10.007>
18. T. Arunkumar, R. Velraj, D.C. Denkenberger, R. Sathyamurthy, K. Vinoth Kumar, A. Ahsan, Productivity enhancements of compound parabolic concentrator tubular solar stills. *Renew. Energy* **88**, 391–400 (2016). <https://doi.org/10.1016/j.renene.2015.11.051>

19. T. Arunkumar, A.E. Kabeel, K. Raj, D. Denkenberger, R. Sathyamurthy, P. Ragupathy, Productivity enhancement of solar still by using porous absorber with bubble-wrap insulation. *J. Clean. Prod.* **195**, 1149–1161 (2018). <https://doi.org/10.1016/J.JCLEPRO.2018.05.199>
20. R.Z. Asadi, F. Suja, F. Mashhoon, S. Rahimi, Feasibility studies for using a solar still on Sarkhon gas refinery wastewater recovery. *Desalin. Water Treat.* **30**(1–3), 154–160 (2011). <https://doi.org/10.5004/dwt.2011.1948>
21. R. Bhardwaj, M.V. Ten Kortenaar, R.F. Mudde, Maximized production of water by increasing area of condensation surface for solar distillation. *Appl. Energy* **154**, 480–490 (2015). <https://doi.org/10.1016/j.apenergy.2015.05.060>
22. BIS water quality standard report-2010. [http://bis.org.in/sf/fad/FAD25\(2047\)C.pdf](http://bis.org.in/sf/fad/FAD25(2047)C.pdf)
23. S. Bose, Antibacterial property of copper coated membrane (2018). <http://www.thehindu.com/sci-tech/science/iisc-copper-coated-membrane-makes-drinking-water-safe/article19524569.ece>
24. A. Chendake, S. Patil, P. Kamble, A. Mane, S. Mane, Design and performance evaluation of inverted pyramid type solar still distillation unit. *Int. J. Sci. Res. Dev.* **4**, 19–12 (2016)
25. R. Dev, S.A. Abdul-Wahab, G.N. Tiwari, Performance study of the inverted absorber solar still with water depth and total dissolved solids. *Appl. Energy* **88**(1), 252–264 (2011). <https://doi.org/10.1016/j.apenergy.2010.08.001>
26. D.K. Dutt, A. Kumar, J.D. Anand, G.N. Tiwari, Performance of a double-basin solar still in the presence of dye. *Appl. Energy* **32**(3), 207–223 (1989). [https://doi.org/10.1016/0306-2619\(89\)90030-5](https://doi.org/10.1016/0306-2619(89)90030-5)
27. M. Edwin, S. Joseph Sekhar, Performance and chemical analysis of distilled saline water production using solar distillation system. *Int. J. ChemTech Res.* **8**(4), 1632–1637 (2015)
28. S.A. El-Agouz, Experimental investigation of stepped solar still with continuous water circulation. *Energy Convers. Manag.* **86**, 186–193 (2014). <https://doi.org/10.1016/j.enconman.2014.05.021>
29. A.A. El-Sebaii, S.M. Shalaby, Parametric study and heat transfer mechanisms of single basin v-corrugated solar still. *Desalin. Water Treat.* **55**(2), 285–296 (2015). <https://doi.org/10.1080/19443994.2014.913998>
30. M.A. Eltawil, Z. Zhengming, Wind turbine-inclined still collector integration with solar still for brackish water desalination. *Desalination* **249**(2), 490–497 (2009). <https://doi.org/10.1016/j.desal.2008.06.029>
31. EPA water quality standard report -2014. https://www.epa.ie/pubs/advice/drinkingwater/2015_04_21_ParametersStandaloneDoc.pdf
32. L.M. Flendrig, B. Shah, N. Subrahmaniam, V. Ramakrishnan, Low cost thermoformed solar still water purifier for d&e countries. *Phys. Chem. Earth* **34**(1–2), 50–54 (2009). <https://doi.org/10.1016/j.pce.2008.03.007>
33. D. Gummu, B.W. Chala, B. Melese, Experimental evaluation of basin type solar still for saline and fluoride water purification (a case on Giby-Deep Well Water, Dupti, Afar-Ethiopia). *Am. J. Environ. Resour. Econ.* **2**(1), 27–36 (2017). <https://doi.org/10.11648/j.ajere.20170201.14>
34. B. Hamza, A. Ghafoor, A. Munir, Desalination of brackish water using dual acting solar still. *J. Eng. Res.* **4**(4), 178–193 (2016)
35. R. Hansen, C. Samuel, S. Narayanan, K. Kalidasa Murugavel, Performance analysis on inclined solar still with different new wick materials and wire mesh. *Desalination* **358**, 1–8 (2015). <https://doi.org/10.1016/j.desal.2014.12.006>
36. B. Janarthanan, J. Chandrasekaran, S. Kumar, Evaporative heat loss and heat transfer for open and closed-cycle systems of floating tilted wick solar still. *Desalination* **180**(1–3), 291–305 (2005). <https://doi.org/10.1016/j.desal.2005.01.010>
37. B. Janarthanan, J. Chandrasekaran, S. Kumar, Performance of floating cum tilted-wick type solar still with the effect of water flowing over the glass cover. *Desalination* **190**(1–3), 51–62 (2006). <https://doi.org/10.1016/j.desal.2005.08.005>
38. P. Joshi, G.N. Tiwari, Energy matrices exergo-economic and enviro-economic analysis of active single slope solar still integrated with a heat exchanger: a comparative study. *Desalination* **443**, 85–98 (2018)

39. N. Joy, A. Antony, A. Anderson, Experimental study on improving the performance of solar still using air blower. *Int. J. Ambient Energy* **39**, 613–616 (2018). <https://doi.org/10.1080/01430750.2017.1324817>
40. A.E. Kabeel, Performance of solar still with a concave wick evaporation surface. *Energy* **34**(10), 1504–1509 (2009). <https://doi.org/10.1016/j.energy.2009.06.050>
41. A.E. Kabeel, Y.A.F. El-Samadony, W.M. El-Maghlany, Comparative study on the solar still performance utilizing different PCM. *Desalination* **432**, 89–96 (2018)
42. S.R. Kalbande, S. Deshmukh, V.P. Khambalkar, Evaluation study of solar water desalination system for saline track area of Vidharba region. *Int. J. Appl. Nat. Sci. (IJANS)* **6**(1), 55–64 (2017)
43. M.R. Karimi Estahbanati, A. Ahsan, M. Feilizadeh, K. Jafarpur, S.S.A. Mansour, M. Feilizadeh, Theoretical and experimental investigation on internal reflectors in a single-slope solar still. *Appl. Energy* **165**, 537–547 (2016). <https://doi.org/10.1016/j.apenergy.2015.12.047>
44. A.K. Kaushal, M.K. Mittal, D. Gangacharyulu, Development and experimental study of an improved basin type vertical single distillation cell solar still. *Desalination* **398**, 121–132 (2016). <https://doi.org/10.1016/j.desal.2016.07.017>
45. S. Kumar, G.N. Tiwari, Life cycle cost analysis of single slope hybrid (PV/T) active solar still. *Appl. Energy* **86**(10), 1995–2004 (2009). <https://doi.org/10.1016/j.apenergy.2009.03.005>
46. A. Kumar, P. Anthony, M.A. Zaidi, Distillate water quality analysis and economic steady of passive solar still. *Recent Res. Sci. Technol.* **6**, 128–130 (2014)
47. A.A. Madani, G.M. Zaki, Yield of solar stills with porous basins. *Appl. Energy* **52**(2–3), 273–281 (1995). [https://doi.org/10.1016/0306-2619\(95\)00044-S](https://doi.org/10.1016/0306-2619(95)00044-S)
48. A. Madhlopa, n.d.Ph.D. Thesis, Development of an advanced passive solar still with a separate condenser. University of Strathclyde Glasgow, United Kingdom, 2009
49. A.F. Mashaly, A.A. Alazba, A.M. Al-Awaadh, Assessing the performance of a solar desalination system to approach near-ZLD under hyper-arid environment. *Desalin. Water Treat.* **57**(26), 12019–12036 (2016). <https://doi.org/10.1080/19443994.2015.1048738>
50. A.N. Minasian, A.A. Al-Karaghoul, An improved solar still: the wick-basin type. *Energy Convers. Manag.* **36**(3), 213–217 (1995). [https://doi.org/10.1016/0196-8904\(94\)00053-3](https://doi.org/10.1016/0196-8904(94)00053-3)
51. S. Mohamed Iqbal, K. Karthik, J.J. Michael, Performance analysis on improved efficiency in a hybrid solar still and solar heater. *Int. J. Ambient Energy* (2018). <https://doi.org/10.1080/01430750.2018.1517685>
52. M. Naroqi, F. Sarhaddi, F. Sobhnamayan, Efficiency of a photovoltaic-thermal stepped solar still: experimental and numerical analysis. *Desalination* **441**, 87–95 (2018)
53. C.E. Okeke, S.U. Egarievwe, A.O.E. Animalu, Effects of coal and charcoal on solar-still performance. *Energy* **15**(11), 1071–1073 (1990). [https://doi.org/10.1016/0360-5442\(90\)90035-Z](https://doi.org/10.1016/0360-5442(90)90035-Z)
54. Z.M. Omara, M.A. Eltawil, E.S.A. ElNashar, A new hybrid desalination system using wicks/solar still and evacuated solar water heater. *Desalination* **325**, 56–64 (2013). <https://doi.org/10.1016/j.desal.2013.06.024>
55. K. Palpandi, R. Prem Raj, Performance test on solar still for various TDS water and phase change materials. *Int. J. Innov. Res. Sci. Eng. Technol.* **4**, 451–461 (2015)
56. R. Pillai, A.T. Libin, M. Mani, Study into solar-still performance under sealed and unsealed conditions. *Int. J. Low-Carbon Technol.* **10**(4), 354–364 (2015). <https://doi.org/10.1093/ijlct/ctt045>
57. T. Rajaseenivasan, K. Kalidasa Murugavel, T. Elango, Performance and exergy analysis of a double-basin solar still with different materials in the basin. *Desalin. Water Treat.* **55**(7), 1786–1794 (2015). <https://doi.org/10.1080/19443994.2014.928800>
58. A. Riahi, K. Wan Yusof, B.S. Mahinder Singh, M.H. Isa, E. Olisa, N.A.M. Zahari, Sustainable potable water production using a solar still with a photovoltaic modules-ac heater. *Desalin. Water Treat.* **57**(32) (2016). <https://doi.org/10.1080/19443994.2015.1070285>
59. S. Saha, N. Mistry, I. Husein, J. Nilesh, Design and construction of solar water distillation system. *Int. J. Sci. Res. Sci. Eng. Technol.* **3**, 606–610 (2017)

60. M. Sakthivel, S. Shanmugasundaram, T. Alwarsamy, An experimental study on a regenerative solar still with energy storage medium – jute cloth. *Desalination* **264**(1–2), 24–31 (2010). <https://doi.org/10.1016/j.desal.2010.06.074>
61. R. Saleem, K.C. Mukwana, M.M. Tunio, Experimental study of desalination technologies and timer-based solar PV tracking system. *Quaid-E-Azam Univ. Res. J. Eng. Sci. Technol.* **13**(1), 1–6 (2014)
62. K. Sampathkumar, P. Senthilkumar, Utilization of solar water heater in a single basin solar still an experimental study. *Desalination* **297**, 8–19 (2012). <https://doi.org/10.1016/j.desal.2012.04.012>
63. R. Samuel Hansen, K. Kalidasa Murugavel, Enhancement of integrated solar still using different new absorber configurations: an experimental approach. *Desalination* **422**, 59–67 (2017). <https://doi.org/10.1016/j.desal.2017.08.015>
64. A. Saxena, N. Deval, A high rated solar water distillation unit for solar homes. *J. Eng. (United States)* (2016). <https://doi.org/10.1155/2016/7937696>
65. S.H. Sengar, A.G. Mohod, Y.P. Khandetod, S.P. Modak, D.K. Gupta, Design and development of wick type solar distillation system. *J. Soil Sci. Environ. Manag.* **2**(7), 125–133 (2011). <http://www.academicjournals.org/JSEM>
66. S.H. Sengar, Y.P. Khandetod, A.G. Mohod, New innovation of low-cost solar still. *Eur. J. Sustain. Dev.* **1**(2), 315–352 (2012)
67. K. Shanmugasundaram, Experimental study on different designs of solar still and its uses. *Int. J. Trend Res. Dev.* **32**, 559–562 (2016)
68. M.I.M. Shatat, K. Mahkamov, K. Johnson, n.d. Experimental and theoretical investigations of a performance of multi-stage solar still water desalination unit coupled with an evacuated tube solar collector, in *2008 Proceedings of the 2nd International Conference on Energy Sustainability, ES 2008*, 2 (2009), pp. 655–664
69. S.K. Shukla, V.P.S. Sorayan, Thermal modeling of solar stills: an experimental validation. *Renew. Energy* **30**(5), 683–699 (2005). <https://doi.org/10.1016/j.renene.2004.03.009>
70. M.T. Siddiqui, Satyapal, A. Jain, Analysis of solar still with a reflector. *Int. J. Technol. Res. Eng.* **2**, 1211–1216 (2015)
71. V. Sivakumar, E. Ganapathy Sundaram, Experimental studies on quality of desalinated water derived from single slope passive solar still. *Desalin. Water Treat.* **57**(57), 27458–27468 (2016). <https://doi.org/10.1080/19443994.2016.1176963>
72. M.S. Sodha, A. Kumar, G.N. Tiwari, G.C. Pandey, Effects of dye on the performance of a solar still. *Appl. Energy* **7**, 147–162 (1980). [https://doi.org/10.1016/0306-2619\(80\)90055-0](https://doi.org/10.1016/0306-2619(80)90055-0)
73. P.K. Srivastava, S.K. Agrawal, Experimental and theoretical analysis of single sloped basin type solar still consisting of multiple low thermal inertias floating porous absorbers. *Desalination* **311**, 198–205 (2013). <https://doi.org/10.1016/j.desal.2012.11.035>
74. H. Tanaka, Solar thermal collector augmented by flat plate booster reflector: optimum inclination of collector and reflector. *Appl. Energy* **88**(4), 1395–1404 (2011). <https://doi.org/10.1016/j.apenergy.2010.10.032>
75. K. Vinoth Kumar, R. Kasturi Bai, Performance study on solar still with enhanced condensation. *Desalination* **230**(1–3), 51–61 (2008). <https://doi.org/10.1016/j.desal.2007.11.015>
76. WHO water quality standard report-2017.: <http://apps.who.int/iris/bitstream/10665/254637/1/9789241549950-eng.pdf>



Toward Economically Rational Hydrogen Production from Solar Energy: From Battery Versus Hydrogen to Battery × Hydrogen

16

Michihisa Koyama

Contents

16.1	Introduction	458
16.2	Trend of Renewable Capacities	458
16.3	Trend of the Levelized Cost of Electricity	460
16.4	Fermi Estimate for Energy Storage Options	462
16.5	Integrating Storage Measures to Photovoltaic Power Generation	464
16.6	Summary and Future Perspective	466
	References	468

Abstract

The use of renewable energy as a main primary energy source can be perceived as a common target of all the countries in the world to reach a sustainable society late in this century. Toward the sustainable goal, the photovoltaic and wind power generations are expected to play important roles in coming decades. To counter the intermittency of their power outputs, economically feasible energy storage measures are necessary. In this chapter, the storage technologies as key technologies for making intermittent renewable energies a main power generation option are discussed focusing on the battery and hydrogen energy systems. The rationality of hydrogen energy as a long-term storage measure is first discussed by a Fermi estimate formula proposed by Hasegawa. Then the rationality of

Author Contribution

The manuscript was fully written by MK.

M. Koyama (✉)

Center for Green Research on Energy and Environmental Materials, National Institute for Materials Science, Tsukuba, Ibaraki, Japan

Research Initiative for Supra-Materials, Shinshu University, Nagano, Japan

Graduate School of Engineering, Hiroshima University, Higashi-Hiroshima, Japan

e-mail: michihisakoyama3@gmail.com

integrating battery with hydrogen production from solar energy is discussed. A concrete example of the integrated system optimization is introduced to clearly show that the integration will lead to the realization of an economically viable hydrogen production from solar energy.

16.1 Introduction

Future energy vision cannot be separable from the global warming problems. Until Kyoto protocol agreed in 1997, demand-side energy savings and a reduction of greenhouse gas (GHG) emission associated with electricity generation have been major directions. Early in this century, nuclear power attracted much expectations and new plant constructions have been promoted in many countries, which is called as “Nuclear Renaissance.” Severe accident in Fukushima Daiichi Nuclear Power Plant in March 11, 2011 (hereafter, 3.11) has changed this paradigm drastically. It has become difficult to locate the nuclear power as a major option for the GHG emission reduction and better energy security especially in Japan [1]. This shift can be clearly seen, for example, from the energiewende in Germany [2] and fourth strategic energy plan of Japan published in 2014 [3] as an update of the third published in 2010, before 3.11 [4].

Two major world directions have been published in 2015: sustainable development goals (SDGs) [5] by United Nations in September and The Paris Agreement [6] adopted at the twenty-first Conference of the Parties in December. In Paris Agreement, Japan has promised 26% GHG emission reduction by 2030 compared to 2013 [7]. In 2016, Japan’s cabinet published the Plan for Global Warming Countermeasures [8], in which 80% GHG reduction by 2050 is targeted as a long-term goal. The 2030 target is set on the basis of reasonable bases, and thus, its achievement will be realized by promoting the measures in the course of present trends. However, many recognize 2050 target as unachievable by the extrapolations of present trends. In fact, Japan’s fifth strategic energy plan published in 2018 [9] describes “It is difficult to foresee a long-term perspective of 2050 with a certain rational due to the possibilities and uncertainties of technology innovations as well as a lack of transparencies of geopolitical situations.”

In this chapter, the author would like to discuss the future directions and present the possibilities of hydrogen production from solar energy toward the massive utilization of intermittent renewable energy.

16.2 Trend of Renewable Capacities

Toward the deep decarbonization for the world to meet key climate goals by 2050, we only have three options for primary energy: nuclear energy, renewable energy, and fossil fuels implemented with carbon capture, utilization, and storage (CCUS) measures as illustrated in Fig. 16.1. If we regard a nuclear fusion as a nuclear energy, no other option exists, thus those three options are the

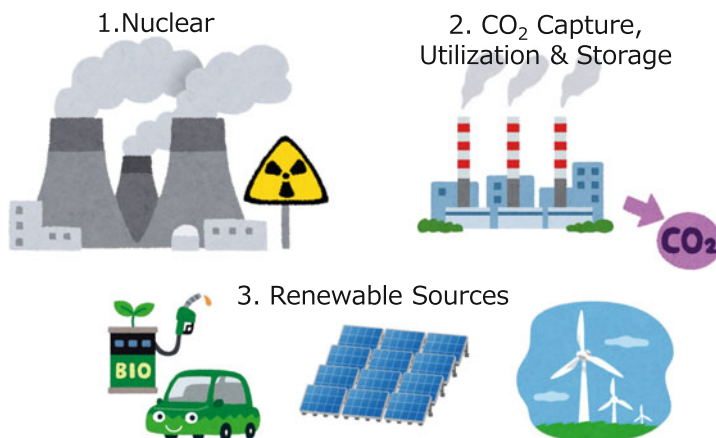


Fig. 16.1 Three primary energy options for future deep decarbonization

first-principles for considering the deep decarbonization. As discussed in the introduction, illustrating a realistic pathway to increase the contribution from nuclear power is difficult especially in developed countries. CCUS is an important and necessary option especially considering the deep decarbonization in chemical and steel-making industries [10–12]. Even if the high cost and low social acceptance outstanding presently as technology challenges are solved in future, this option is associated with fossil fuel depletion. In addition, a present trend of divestment from fossil fuel-based technologies should be recognized as a risk for this option. Therefore, it would be preferable to minimize the dependence on this option as possible. As a result, maximizing the contribution from renewable energy is essentially required for the deep decarbonization as well as massive energy savings at the demand side [13].

Total capacity of renewable energy systems in the world has reached more than 2350 GW in 2018 [14] as shown in Fig. 16.2. Hydropower's capacity is ca. 1172 GW, accounting for approximately half of the total capacity. Those of wind and solar energy are 564 and 486 GW, respectively. When we focus on the increase ratio from 2009 to 2018 rather than the present capacity, rapid increase of solar energy is noticed. Solar increased by ca. 2000%, and wind energy increased by 300%. On the other hand, hydropower increased by ca. 30%. From the projection of this trend, it is expected that wind and solar energies will play central roles in future deep decarbonation. As is well known, wind and solar energies are intermittent by nature and cannot adjust their outputs to the power demand in a timely manner required for the stable operation of the electricity grid system. In addition, due to low capacity ratios of wind and solar energies, total capacities will become much larger than the maximum peak demand when one envisions a fully renewable power supply system [15]. Therefore, storage measures must be massively implemented together with wind and solar energy systems in order to supply a major part of the energy in future.

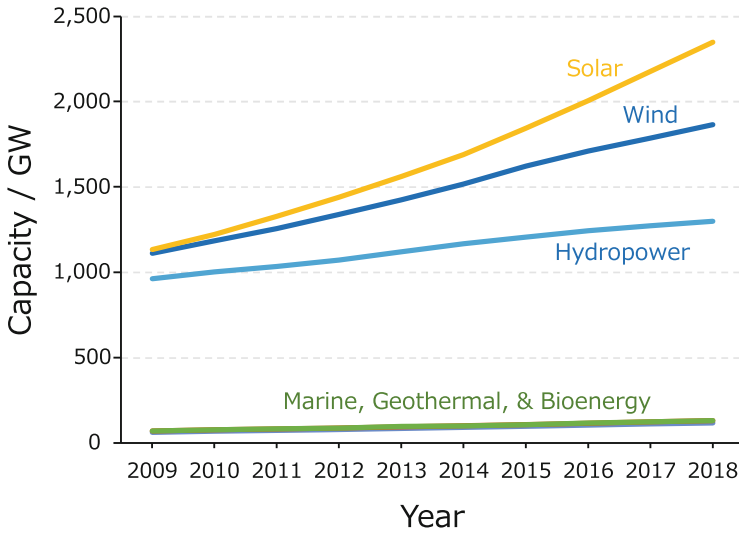


Fig. 16.2 Capacities of renewable energy systems [14]

16.3 Trend of the Levelized Cost of Electricity

World trend of the levelized cost of electricity (LCOE) is summarized in the LAZARD's report [16]. Unsubsidized mean LCOE's of coal are 0.111 and 0.102 US \$/kWh, in 2009 and 2018, respectively, and those of gas combined cycle are, respectively, 0.083 and 0.058 US \$/kWh. Mean LCOE of nuclear decreased from 0.123 US \$/kWh in 2009 to 0.095 US \$/kWh in 2011, then increased to 0.151 US \$/kWh in 2018, from which one can see the shift of paradigm from Nuclear Renaissance to Safety-first after 3.11. Those of crystalline photovoltaic (PV) and wind power plants decrease from 0.359 to 0.043, and from 0.135 to 0.042 US \$/kWh, respectively, during the same period. To see more closely the trend, the author summarized the LCOE of selected power generation options focusing on Japan as shown in Fig. 16.3 [17–22]. Horizontal and vertical axes of the figure correspond to the LCOE associated with plant and fuel, respectively. Vertical axis value of nuclear includes the front end, reprocessing, back end costs. That for LNG and Coal consists of fuel and GHG countermeasure costs. From the figure, nuclear increases its LCOE associated with the power plant, especially after 3.11. General trends in Coal and LNG are the increase in LCOE associated with fuel, in line with the future prospects of current and new policy scenarios of IEA [23]. Note that recent sustainable development scenario of IEA [23] may influence those estimates. Compared to other countries in the world, the LCOE of the PV is much higher in Japan. The deployment of PV in Japan is accelerated by Feed-in Tariff actuated in July 2012, leading to a rapid decrease of its LCOE from 2013 to 2017. The value of 2040 is estimated to be 3.7 JPY/kWh. Crossover with nuclear, coal, LNG is expected to

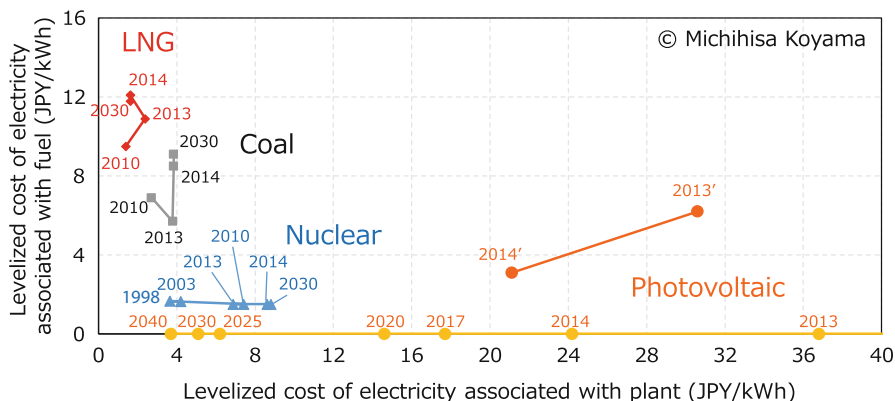


Fig. 16.3 Levelized cost of electricity of representative power generation options in Japan. The LCOE's of nuclear power plants estimated for 1998 [17], 2003 [18], 2010 [19], 2013 [20], 2014 [21], 2030 [21], coal and LNG combustion power plants for 2010 [19], 2013 [20], 2014 [21], 2030 [21], and non-residential photovoltaic power plants for 2013 [20], 2014 [21], 2017 [22], 2025 [22], 2030 [22], 2040 [22], 2040' and 2014' for photovoltaic are the different plots of 2013 and 2014. In references [20, 21], the unsubsidized LCOE and the procurement price of Feed-in Tariff scheme are explicitly considered. The latter is a policy-incentive cost corresponding to internal rate of return, which is proportional to the electricity generated. This policy-incentive is assigned to horizontal axis values for 2013 and 2014 while it is assigned to vertical axis values for 2013' and 2014'. (This policy-incentive is not explicitly described in reference [22].) Copyright retained by the author

occur between 2020 and 2025. The LCOE of renewable technologies under Feed-in Tariff is controversial. In Fig. 16.3, the plot of setting the policy incentive corresponding to the internal ratio of return as the vertical value of the PV with the unsubsidized LCOE as the horizontal axis is also shown. From Fig. 16.3, three distinct trends are clearly seen. One is the horizontally increasing trend of the nuclear. The second is the vertically increasing trend of the Coal and LNG, and the third is horizontally decreasing trend of the PV. Under the trend of the nuclear, one may assume a background paradigm: No incentive to increase the conversion efficiency; high incentive to increase the capacity ratio for easier capital investment recovery. Actually, no increase in efficiency is found in references [17–21]. The trend of the coal and LNG will evoke a different background paradigm: High incentive to increase the conversion efficiency even with some increased capital investment costs; the simultaneous importance of energy savings at the demand side to reduce the total GHG emission because the increase in supply capacity will result in the increase in the total GHG emission, also accepting the decrease in the capacity ratio to a certain extent. A future paradigm expected from the trend of the PV's LCOE in Fig. 16.3 can be free from all of the above. Energy savings may not be important after massive deployment and decreased LCOE of PV in future, especially during a sunny daytime. This means that measures with lower thermal or exergy efficiency but with better economic rationality may increase their importance in future.

Also, one can see the transition of relative locations of the PV, nuclear, coal, and LNG power generation systems in the context of energy security, environmental protection, and economic efficiency (3E). The nuclear was favorable in all aspects of 3E. The coal was the worst in terms of environmental protection, while it was the second better choice from the other two aspects. The PV was too unfavorable to consider in terms of economic efficiency. After 3.11, 3E and Safety (3E + S) was set as a new paradigm of the energy systems. This makes the nuclear less favorable economically, but still favorable compared to the coal and LNG partly due to the increase in the fossil fuel prices. Focusing on 2030, most economically favorable option is expected to be the PV, followed by the nuclear, coal, and LNG in this order. It is needless to mention that the PV is also favorable in terms of the energy security, environmental protection, and safety. Therefore, one may imagine a future humanity freed by the economically efficient future PV from the depletion and geopolitical risks associated with fossil fuels, which have often been a cause of wars historically. Of course, one may point out a serious concern of the intermittency of PV, which is not explicitly considered in the values shown in Fig. 16.3. Therefore, I would like to discuss the storage options and their integration with PV in the subsequent sections.

16.4 Fermi Estimate for Energy Storage Options

Only studying the future investment costs of storage measures is insufficient because the levelized cost of storage depends on the role of storage. A system integration of storage measures to counter the intermittency of renewable energies has been intensively studied [24–29]. Schmidt et al. investigated the levelized costs of storage and showed valuable global map for technology options suitable for specific existing application targets [24]. When we assume the existing application targets, deep understanding of the present system and paradigm is important. By contrast, it is important to consider the system configuration itself, free from a priori assumptions when designing future systems that do not exist in the course extrapolated from the present trends and paradigm. However, it should be noted that even when we design future energy systems, one should place a highest priority on economic rationality. Therefore, it is ideal attitude to consider the economic rationality of future energy systems even early in the conceptual design phase.

Hasegawa has proposed a Fermi estimate formula to calculate the crossover storage time at a given set of costs related to technologies considered [30]. Fermi estimate means the estimate of approximate values, which cannot be easily investigated, based on a certain clues and logics, named after Enrico Fermi's estimate of the strength of the atomic bomb [31]. Such an approach is also known as an order estimate or a back-of-the-envelope calculation.

Hasegawa focused on the hydrogen energy-based and lithium ion battery (LIB)-based energy storage system (ESS) for renewable electricity in his first study [30]. The LIB is an electrochemical device that stores electrical energy as chemical energy through the charge-transfer reaction at the interface between the active material and electrolyte. Therefore, the LIB itself is equipped with functions of

Table 16.1 Comparison between LIB and hydrogen ESS [30]

	LIB ESS	Hydrogen ESS
Energy conversion cost Cost per power (\$/kW)	Low $A (\equiv 0)$	High C
Energy storage cost Cost per storage (\$/kWh)	High B	Low D

both energy conversion and storage. On the contrary, a high-pressure tank for hydrogen storage only has a function of energy storage. Therefore, energy conversion functions, i.e., to convert electricity to hydrogen and vice versa, are needed externally to the tank. He assumed a set of water electrolyzer and fuel cell (FC) systems. Because the storage function is independent from the energy conversion function in the hydrogen ESS, the system's economic rationality is determined by the cost for storage, i.e., the high-pressure tank when the stockpile is infinitely large. Oppositely, the economic rationality is determined by the cost for energy conversions when the stockpile is small. In the case of LIB, the cost is apparently proportional to the storage.

Table 16.1 shows a conceptual comparison of LIB and hydrogen ESS. Because the energy conversion function is inherently equipped with LIB, the cost for energy conversion can be defined to be zero. Energy storage cost of LIB can be regarded to be expensive compared to high-pressure tank because the former needs 1 mol of functional compounds to store 1 mol of electrons while the latter requires vacuum space for hydrogen storage and the metallic alloy or carbon fiber composing high-pressure tank as a shell. The energy conversion cost of hydrogen ESS is expensive compared to that of LIB ESS, which is zero.

Crossover time for storage, at which the costs of LIB and hydrogen ESS's become equal, can then be derived as follows.

$$A \times P + B \times P \times t = C \times P + D \times P \times t \quad (16.1)$$

P and t are the rated power of ESS (kW) and storage time (h), respectively. A is zero by its definition, and given that B , C , and D are independent from P , t is expressed as

$$t = C / (B - D). \quad (16.2)$$

For an initial estimate in this chapter, I updated values of B , C , and D , by referring available technology information. The battery cost of 125 \$/kWh can be found as United States Department of Energy (US DOE) Project target [32] and 50 \$/kWh is indicated as cost of advanced battery in 2030 [33]. Because those are for the battery pack, the doubled cost is assumed for LIB-based ESS cost: i.e., \$100–250/kWh for B . US DOE's cost target is 53 \$/kW for FC power plant, on a condition of 500,000 units annual production of 100 kW-FCs [34]. 50,000 JPY/kW (ca. 455 \$/kW) as a cost target of the water electrolyzer plant can be found in the report of CO₂ free hydrogen working group, the Ministry of Economy, Trade, and

Industry, Japan [35]. Considering that a balance of plants cost for integrating FC, electrolyzer, and high-pressure tank is necessary, 1000 \$/kW for C is assumed: an approximately doubled cost of the summation of the cost targets of FC and electrolyzer plants. The cost for hydrogen tank is estimated by US DOE's project: 14.8 \$/kWh for 700 bar baseline tank system at a manufacturing volume of 500,000 systems/year [36]. Also, doubled cost is assumed for high-pressure tank, meaning 30 \$/kWh for D .

Assigning those values to Eq. (16.2) will give us a crossover time of 4.5 and 14.3 h for the battery cost of 250 and 100 \$/kWh, respectively. If we assume a good advancement of battery and retarded advancement of the FC and electrolyzer, i.e., 100 \$/kWh for B and 10,000 \$/kW for D , crossover time is calculated to be 143 h, still shorter than a week. Fermi estimates here mean that the crossover time will be in the order of 10^1 – 10^2 h, and hydrogen ESS will show the economic rationality over LIB ESS for the energy storage period longer than the estimated crossover time. Schmidt et al. assumes that LIB and hydrogen will be major options for energy storage in future [24]. Their detailed estimation of levelized cost of storage showed a crossover time of ca. 30–40 h. One can see how the Fermi estimate formula proposed by Hasegawa works well.

16.5 Integrating Storage Measures to Photovoltaic Power Generation

The discussion in the previous section is to show the rationality of hydrogen energy as a long-term storage measure for renewable electricity. However, a simple combination of hydrogen and PV will not result in the economically feasible system due to the low capacity ratio of the PV, hindering a capital recovery within a reasonable depreciation period. So far, various studies have been conducted under the concept of the Power-to-Gas [37]. Recently, hybridization possibility of the battery with hydrogen production from the PV was discussed by Gillissen et al. [28]. They considered technology options such as the LIB and redox-flow battery with the technology levels around 2030 to conclude that the system without battery is most economically feasible, even assuming an electricity cost of zero. This result is in line with our apparent intuition that the system becomes more expensive by incorporating the expensive battery into the expensive hydrogen production from the PV. Then, is there no solution in this direction, and should one consider different directions to realize a sustainable energy supply system based on the PV?

In this section, let me consider the system configuration free from a priori assumptions or background knowledge. An extreme of the free electricity assumed in [28] does not provide a solution because it does not directly solve the difficulty of the capital recovery due to the low capacity ratio. Therefore, another extreme of battery cost of zero, i.e., sufficiently low cost in a practical context, will be discussed. When we do not need any investment to install a battery system, sufficiently large capacity of battery can be installed to PV system. In this extreme end, all the

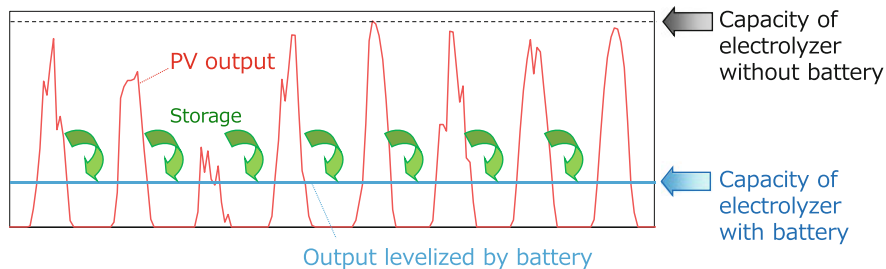


Fig. 16.4 Schematic of the power generation profile of PV and electrolyzer capacity with sufficiently large capacity of battery

electricity generated by the PV is once charged to the battery, then discharged to the electrolyzer with a constant output power as schematically illustrated in Fig. 16.4. When the battery is not installed, the capacity of the electrolyzer is determined by referring the capacity of PV, leading to a low capacity ratio of the electrolyzer. On the contrary, the capacity of the electrolyzer is designed to the discharge output of the battery in the extreme case discussed here. In addition, the capacity ratio becomes 100% meaning much easier capital recovery. Assuming that the capacity ratio of 12% for PV and the battery charge/discharge efficiency of 100%, the discharge output will become 12% of the PV capacity, then the capacity of the electrolyzer can be 12%, ca. one-eighth, compared to that without battery. From this estimate, one can understand that the battery installation is economically beneficial when the investment cost of the battery is smaller than the benefit by decreasing the investment cost and increasing the capacity ratio of the electrolyzer. Here, let's assume the reference system of 1 kW of PV equipped with 1 kW of electrolyzer. When the electrolyzer cost is 500 \$/kW, the reference system requires 500\$ to install the electrolyzer of 1 kW capacity. On the other hand, the necessary electrolyzer capacity is 120 W when the sufficiently large capacity of the battery is installed, meaning that the necessary investment for the electrolyzer is only 60 \$. The difference, 440 \$, can be used to invest for the battery. When the battery cost is 100 \$/kWh, 4.4 kWh can be installed. The question will be the expected increase of the capacity ratio by installing the 4.4 kWh battery, which can only be estimated by referring the actual power generation profile of PV.

Kikuchi et al. have optimized the system integration of the PV, battery, and electrolyzer [27]. Figure 16.5 shows a schematic system configuration of a battery-assisted hydrogen production from solar energy. The electricity generated by PV is transferred to the energy management system (EMS). The EMS determines the appropriate operation mode from the options of direct input to the electrolyzer, charging excess electricity to the battery, discharging from the battery to meet the electricity deficiency, and rejecting the electricity. When the costs of the PV, battery, and electrolyzer, as well as a solar irradiance profile are given, an operational mode and capacities (ratio) of the PV, battery, and electrolyzer, minimizing the levelized cost of hydrogen (LCOH₂), can be determined.

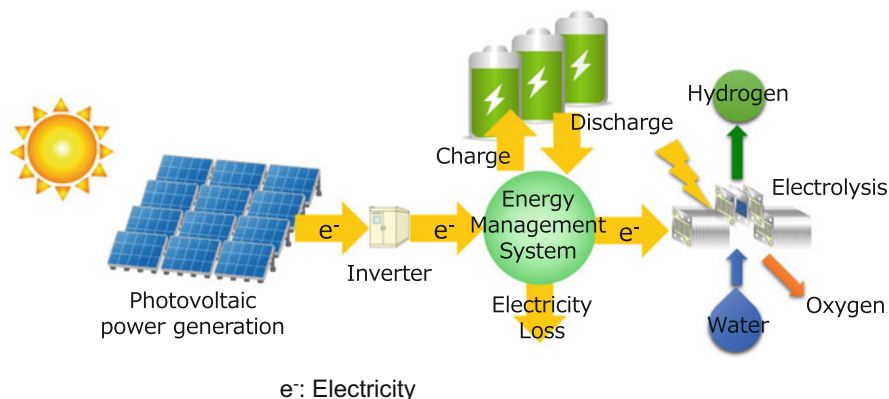


Fig. 16.5 Schematic system configuration of a battery-assisted hydrogen production from solar energy [38]

Figure 16.6a shows the breakdown of the optimized LCOH_2 when the LCOE of the PV and electrolyte investment cost is 7 JPY/kWh and 50,000 JPY/kW, respectively. When the battery unit cost is 20,000 JPY/kWh, LCOH_2 becomes ca. 50 JPY/Nm³, indicating that the system will be economically viable against the present gasoline price. One can see that the PV electricity occupies the large part of the cost, followed by the electrolyzer including investment, operation and maintenance. As the unit cost of the battery becomes cheaper down from 20,000 JPY/kWh, the ratio of the battery cost in the total cost increases. Below the unit cost of around 14,000 JPY/kWh, the ratio of the battery cost decreases as the unit cost decreases. To see more details, the ratio of the battery and electrolyzer capacities is plotted against the battery unit cost in Fig. 16.7. When the unit cost of the electrolyzer ($\text{CAPEX}_{\text{ely}}$ in the figure) is 50,000 JPY/kW, the relative battery capacity increases steadily as the battery unit cost decreases from 20,000 JPY/kWh. Below 14,000 JPY/kWh, the relative capacity increases only slightly. The cost of the installed battery is given as the product of the unit cost and installed capacity. The increase of the installed capacity explains the increase of the battery cost in Fig. 16.6a even if the unit cost decreases from 20,000 to 14,000 JPY/kWh, while the plateau of installed capacity will explain the decrease of battery cost as the unit cost decrease below down to 14,000 JPY/kWh. Figure 16.6b shows the breakdown of the LCOH_2 when the LCOE of PV and the battery unit cost is 2 JPY/kWh and 5000 JPY/kWh, respectively. It can be seen that the LCOH_2 is ca. 20 JPY/Nm³ when the electrolyzer unit cost is 20,000 JPY/kW.

16.6 Summary and Future Perspective

In this chapter, the author introduced the discussion focusing mainly on the storage technologies as key technologies for making intermittent renewable energies a main power generation system of the future. From the trend analysis of LCOE's of the PV,

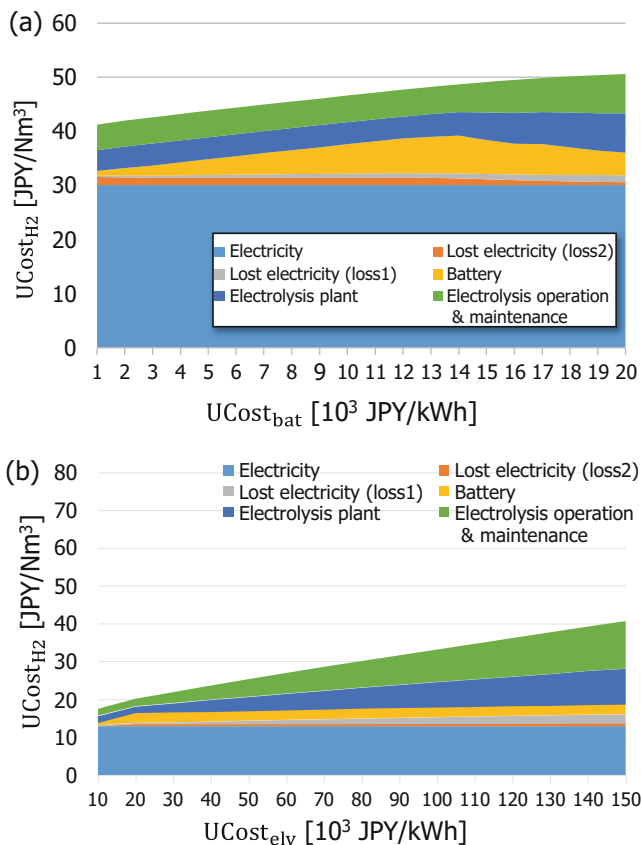


Fig. 16.6 Examples of estimated levelized cost of hydrogen for a battery-assisted hydrogen production from solar energy: (a) the LCOE of PV and electrolyzer unit cost is 7 JPY/kWh and 50,000 JPY/kW, respectively, and (b) the LCOE of PV and the battery unit cost is 2 JPY/kWh and 5000 JPY/kWh, respectively. (Reprinted from Int. J. Hydrogen Energy, 44/3, Y. Kikuchi, T. Ichikawa, M. Sugiyama, M. Koyama, Battery-assisted low-cost hydrogen production from solar energy: Rational target setting for future technology systems, 1451–1465, Copyright 2019, with permission from Elsevier)

nuclear, coal, and LNG, future paradigm of power generation options was discussed. As an option for long-term storage, rationality of hydrogen against battery was discussed by referring a Fermi estimate formula by Hasegawa. The rationality of integrating battery with hydrogen production from solar energy was discussed. By considering the rationality of the system from scratch, it was derived that the investment cost of the electrolyzer can be one-eighth of the system without the battery. Examples of the system optimization were introduced. By the appropriate integration of the battery into the system, an economic competitiveness of the hydrogen production from the solar energy was clearly shown especially when the future technology costs were assumed.

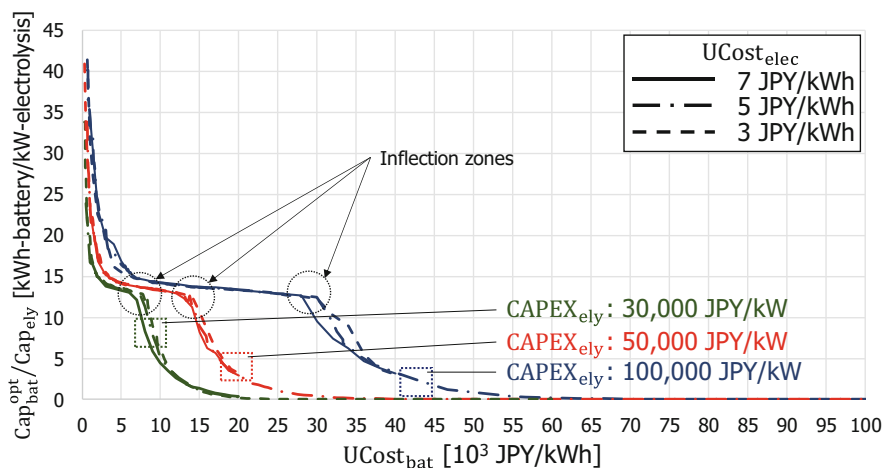


Fig. 16.7 Profiles of ratio of the battery capacity against electrolyzer capacity. (Reprinted from *Int. J. Hydrogen Energy*, 44/3, Y. Kikuchi, T. Ichikawa, M. Sugiyama, M. Koyama, Battery-assisted low-cost hydrogen production from solar energy: Rational target setting for future technology systems, 1451–1465, Copyright 2019, with permission from Elsevier)

Promoting the research and development to make the PV and electrolyzer cost-competitive toward the economically viable hydrogen production is important beyond controversy. However, one should be reminded that even if the electrolyzer becomes more efficient and less expensive, the issue of a low capacity ratio of the PV, which makes the capital recovery of the electrolyzer difficult, remains outstanding. The investment to the battery may increase the economic rationality of the expensive hydrogen production from the PV. The battery and hydrogen have been often discussed as “battery vs hydrogen,” as if they are incompatible competitors. An example discussed in this chapter is a trial of the discussion free from such context. Harmonic integration of battery and hydrogen, i.e., “battery × hydrogen”, will be a key toward a renewable energy-centered energy system in future.

Acknowledgments The author would like to thank the fruitful discussion with Dr. Takuya Hasegawa (NISSAN Motor Co. Ltd.) and Dr. Takahide Haneda (Tokyo Gas Co. Ltd.). Part of the research is financially supported by MEXT Program for Integrated Materials Development.

References

1. M. Koyama, S. Kimura, Y. Kikuchi, T. Nakagaki, K. Itaoka, Present status and points of discussion for future energy systems in Japan from the aspects of technology options. *J. Chem. Eng. Jpn.* **47**(7), 499–513 (2014)
2. O. Renn, J.P. Marshall, Coal, nuclear and renewable energy policies in Germany: from the 1950s to the “Energiewende”. *Energy Policy* **99**, 224–232 (2016)
3. Fourth strategic energy plan of Japan (2014). Available from https://www.enecho.meti.go.jp/en/category/others/basic_plan/pdf/4th_strategic_energy_plan.pdf

4. Third strategic energy plan of Japan (2010). Available from <http://warp.da.ndl.go.jp/info:ndljp/pid/1079811/www.enecho.meti.go.jp/topics/kihonkeikaku/100618honbun.pdf>
5. <https://sustainabledevelopment.un.org/>
6. <https://unfccc.int/resource/docs/2015/cop21/eng/109r01.pdf>
7. https://japan.kantei.go.jp/97_abe/statement/201611/1219866_11019.html
8. <https://www.env.go.jp/en/headline/2238.html>
9. Fifth strategic energy plan of Japan, (2018). Available from https://www.meti.go.jp/english/press/2018/0703_002.html
10. I. Taniguchi, K. Itaoka, CO₂ capture, transportation, and storage technology, in *Energy Technology Roadmaps of Japan -Future Energy Systems Based on Feasible Technologies Beyond 2030*, ed. by Y. Kato, M. Koyama, Y. Fukushima, T. Nakagaki, (Springer, Tokyo, Japan, 2016), pp. 343–358
11. T. Setoyama, Chemical industry, in *Energy Technology Roadmaps of Japan -Future Energy Systems Based on Feasible Technologies Beyond 2030*, ed. by Y. Kato, M. Koyama, Y. Fukushima, T. Nakagaki, (Springer, Tokyo, Japan, 2016), pp. 369–379
12. Y. Ujisawa, S. Tomomura, N. Ishiwata, Y. Nabeshima, K. Saito, CO₂ breakthrough program by COURSE50 in Japanese steel industry sector, in *Energy Technology Roadmaps of Japan -Future Energy Systems Based on Feasible Technologies Beyond 2030*, ed. by Y. Kato, M. Koyama, Y. Fukushima, T. Nakagaki, (Springer, Tokyo, Japan, 2016), pp. 431–439
13. Global energy transformation: A roadmap to 2050 (2019 edition), International Renewable Energy Agency (2019)
14. Capacity Statistics 2019, International Renewable Energy Agency (2019)
15. Y. Izui, M. Koyama, Future energy and electric power systems and smart technologies. IEEJ Trans. Electr. Electron. Eng. **12**, 453–462 (2017)
16. LAZARD’s leveled cost of energy analysis, version 12.0, LAZARD (2018)
17. Economic efficiency of nuclear power plants (Genshiryoku Hatsuden No Keizaisei Ni Tsuite) 70th Nuclear Energy Subcommittee, Advisory Committee for Energy, Agency for Natural Resources and Energy, Ministry of Economy, Trade, and Industry, Japan (1999)
18. “Comparison of leveled cost of electricity of each power generation system based on model estimation (Moderu Shisan Niyoru Kaku Dengen No Hatsuden Kosuto Hikaku)” 8th Subcommittee to Study Costs and Other Issues, Electricity Industry Committee, Advisory Committee for Natural Resources and Energy, Agency for Natural Resources and Energy, Ministry of Economy, Trade, and Industry, Japan (2003)
19. Report of Committee to Study Costs and Other Issues, Energy and Environment Council, Japan (2011)
20. K. Tokushige, K. Akimoto, J. Oda, F. Sano, Latest estimate of power generation costs by power source, and cost-benefit analysis of alternative power sources, Research Institute of Innovative Technology for the Earth (RITE), Kyoto, Japan (2014). Available from http://www.rite.or.jp/system/global-warming-ouyou/download-data/E-PowerGenerationCost_estimates_20141020.pdf
21. “Report of verification of power generation cost for Long-term Energy Demand and Supply Projection Subcommittee (Tyouki Enerugi Jukyu Mitooshi Syou Iinkai Ni Taisuru Hatsuden Kosuto Touno Kensyo Ni Kansuru Houkoku)”, Power generation cost verification working group, Long-term Energy Demand and Supply Projection Subcommittee, Strategic Policy Committee, Advisory Committee for Natural Resources and Energy, Agency for Natural Resources and Energy, Ministry of Economy, Trade, and Industry, Japan (2015)
22. Future Issues toward Renewable Energy as Main Power Source (Saiseikanou Enerugi No Syuryokudengenka Ni Muketa Kongo No Ronten), Renewable energy large-scale introduction, next-generation electricity network subcommittee, Committee on Energy Efficiency and Renewable Energy/Electricity and Gas Industry Committee, Advisory Committee for Natural Resources and Energy, Agency for Natural Resources and Energy, Ministry of Economy, Trade, and Industry, Japan (2018)
23. World energy outlook 2017, International Energy Agency (2017)
24. O. Schmidt, S. Melchior, A. Hawkes, I. Staffell, Projecting the future leveled cost of electricity storage technologies. *Joule* **3**, 81–100 (2019)

25. S. Comello, S. Reichelstein, The emergence of cost effective battery storage. *Nat. Commun.* **10**, 2038 (2019)
26. M. Baumann, M. Weil, J.F. Peters, N. Chibeles-Martins, A.B. Moniz, A review of multi-criteria decision making approaches for evaluating energy storage systems for grid applications. *Renew. Sust. Energ. Rev.* **107**, 516–534 (2019)
27. Y. Kikuchi, T. Ichikawa, M. Sugiyama, M. Koyama, Battery-assisted low-cost hydrogen production from solar energy: rational target setting for future technology systems. *Int. J. Hydrog. Energy* **44**(3), 1451–1465 (2019)
28. B. Gillissen, H.U. Heinrichs, P. Stenzel, J. Linssen, Hybridization strategies of power-to-gas systems and battery storage using renewable energy. *Int. J. Hydrog. Energy* **42**, 13554–13567 (2017)
29. M. Uhriga, S. Koeniga, M.R. Suriyaha, T. Leibfried, Lithium-based vs. vanadium redox flow batteries – a comparison for home storage systems. *Energy Procedia* **99**, 35–43 (2016)
30. T. Hasegawa, Economic rationality of long-term energy storage systems for renewable energies. Paper presented at ISPIM Connects Fukuoka, Fukuoka, Japan (2018); T. Hasegawa, M. Koyama, T. Haneda (2019); Abstract of IMPRES2019, accepted
31. Los Alamos National Laboratory, Eyewitnesses to trinity. *Nucl. Weapons J.* **2**, 45 (2005)
32. Vehicle Technologies Office, USDOE (US Department of Energy). Overview of the DOE VTO advanced battery R&D program. Available from https://www.energy.gov/sites/prod/files/2016/06/f32/es000_howell_2016_o_web.pdf
33. G. Berckmans, M. Messagie, J. Smekens, N. Omar, L. Vanhaverbeke, J. Van Mierlo, Cost projection of state of the art lithium-ion batteries for electric vehicles up to 2030. *Energies* **10**(9), 1314 (2017)
34. US Department of Energy, DOE hydrogen and fuel cells program record (2016). Available from https://www.hydrogen.energy.gov/pdfs/16020_fuel_cell_system_cost_2016.pdf
35. CO₂ free hydrogen working group (2017). Available from <http://www.meti.go.jp/press/2016/03/20170307003/20170307003.html> (in Japanese)
36. US Department of Energy, DOE Hydrogen and Fuel Cells Program Record (2015). Available from https://www.hydrogen.energy.gov/pdfs/15013_onboard_storage_performance_cost.pdf
37. M. Gotz, J. Lefebvre, F. Mors, A.M. Koch, F. Graf, S. Bajohr, R. Reimert, T. Kolb, Renewable power-to-gas: a technological and economic review. *Renew. Energy* **85**, 1371–1390 (2016)
38. <https://www.nims.go.jp/eng/news/press/2018/12/201812130.html>



Postface: China in the New Policies Scenario 17

Yongjun Gao, Yuliang Zhang, Jingbo Louise Liu, and Sajid Bashir

Contents

17.1	Introduction	472
17.2	Evolution of Decentralized Energy Policy	473
17.3	Policy Implementation: Illustration from Southern China	479
17.4	New Policy Scenario	484
17.5	Photovoltaics as a Model of Deregulated and Redistributed Energy	486
17.6	From Yesterday to Today to Tomorrow: Lessons Learned, What to Expect Next?	487
	References	492

Author Contribution

G. Yongjun did all the internal data analyses from NEA, NRDC, and the five-year plans, including select figures; J. Liu translated some documents in English and completed the additional figures; and S. Bashir wrote the English draft and incorporated IEA, CAIT, non-China-based data sets. All authors reviewed the manuscript, which was submitted by J. Liu.

Y. Gao (✉) · Y. Zhang

Zhejiang Triangle Qing Energy Enterprise Management Co., Ltd., Hangzhou, People's Republic of China

Zhejiang Yangtze River Delta Clean Energy, Conservation and Environmental Protection Development Research Center, Hangzhou, People's Republic of China

e-mail: gyj@3ecube.cn

J. L. Liu

Department of Chemistry, Texas A&M University-Kingsville, Kingsville, TX, USA

Department of Chemistry, Texas A&M University (TAMU), College Station, TX, USA

e-mail: kfjll00@tamuk.edu

S. Bashir (✉)

Department of Chemistry, Texas A&M University-Kingsville, Kingsville, TX, USA

e-mail: br9@tamuk.edu

Abstract

The rise of China since World War II has been centralized in the form of a series of five-year plans. These plans affected society at all levels and have now reached a zenith in terms of ecological, environmental, energy, and economic outcomes. A new power law was enacted to govern the Chinese Electricity sector. The central government intent is to decentralize energy generation, transmission, and storage through the formulation of policies which affect energy generation through tighter supervisory controls, through innovation and economic rebates and aid. These new provisions are targeted to slow down the rate of energy consumption and enable the transition of China to an electricity generator based on renewables including hydro-electric, biomass natural gas, and nuclear with a lesser reliance on coal-fired electricity generation. The policies are derived from earlier noticed in area of electricity generation, transmission, and environmental protection. The formulated policies using southern China as a test case migrated from general pronouncements to specific policy outcomes; the acceptance of which is based on the level of gain, fairness, and transparency. Heavy electricity users can buy directly from the power generator competitive rates; however, the social justice principle ensures that users who do not choose to participate in the electricity market are quoted prices that are not at far higher levels than high volume users. Also, there needs to be tighter integration between the supply and return of investment or rebates either at the government or province-level to ensure transparency and fairness to supply. To meet the ambitious targets of decarbonization and environmental goal's, the policymakers have allowed the local municipalities meet the projected targets using local knowledge, expertise, and resources; however, more research and development (R&D), technical assistance, and workforce training are required to meet the new policies scenario by 2040.

17.1 Introduction

Energy policymaking in the People's Republic of China (China) is coordinated by the State Council [1], but the practical implementations are decentralized through a number of entities in the form of a national action plan [2]. This plan lays out performance targets in the form of five-year plans which recently have included renewable energy with traditional energy portfolios, such as nuclear power, coal-fired power stations, methane, and methane hydrates [3]. The rise of China as an industrial power is aligned with its rise as an economic power like the United States or European Union political trading block of 28 countries (EU28) and is shown in Fig. 17.1 [4, 5, 6, 7].

The plot shows a positive correlation between carbon dioxide emissions and industrial production as measured in the gross domestic product, as well as a steady rise in atmospheric carbon dioxide levels. China is currently the world's largest electricity generator and energy consumer, as well as a carbon emitter [8].

Under the five-year master plan, China's electric power law coordinates energy services between state-owned enterprises and province or regional government entities that purchase using a decentralized approach [9]. The State Council formulates union which is delineated by the National People's Congress in the form of published articles. For example the 1995 National People's Congress (NPC) articles 35 and

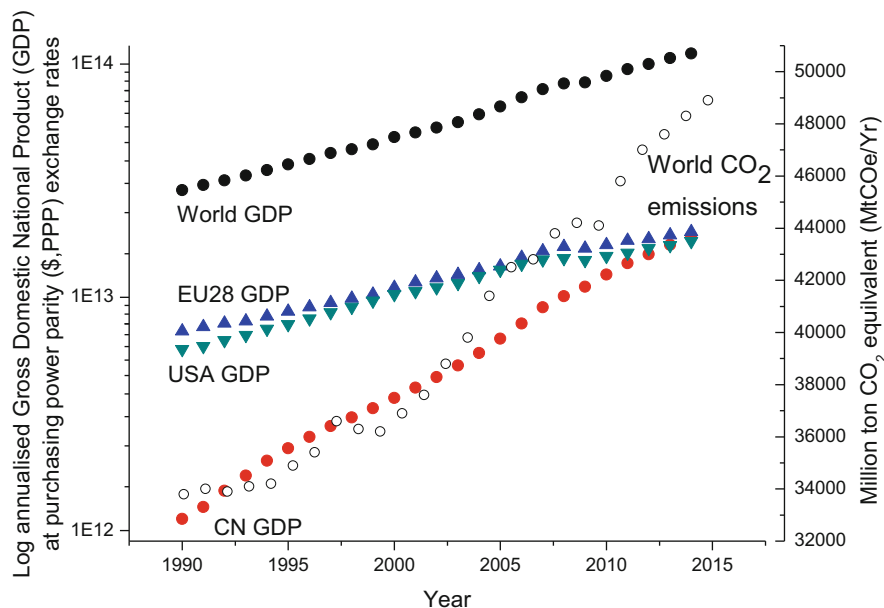


Fig. 17.1 Summary of the world, EU28, the United States, and China (CN) gross domestic product based on purchasing power parity (GDP, PPP) on the left axis superimposed with world carbon dioxide emissions (million-ton coal equivalent on the right axis). (Source: CAIT [7] and World Bank [6])

36 guarantee investment returns through price caps as a means of attracting “private sector” financing and meeting the energy demands set forth in the quinquennial five-year plan; the latest iteration is the 13th five-year plan (State Council [10–13]).

The early five-year plans emphasized a catch-up mentality to Japan, a regional competitor and a potential hostile foe, the United States as a Pacific dominant power, and Europe. These plans enable the Central Planner to meet the performance targets by enabling sectors such as manufacturing and heavy industries to have the power as required [14]. From the tenth to the current plan, a slight re-think was emphasized particularly during the Olympics held in Beijing to tackle grid inefficiencies, waste, greenhouses gas (GHG) emissions, and particulate matter which can cause serious health issues particularly to the millennials who are expected to carry the intellectual and practical burden into the next three decades [15–23].

In the early five-year plans, the purpose was to catch up after an internal civil war and a war against Japan to rebuild and rebuild fast using the Soviet planning model. To accomplish the energy requirements, a high investment in coal-fired generators was initiated from near 90% to around 70% to 40% around 2040 [24–26].

17.2 Evolution of Decentralized Energy Policy

It can be seen that the country’s energy generation capacity and consumption are closely aligned, with an increase in consumption of 5.9%, the fastest since 2014 (Fig. 17.4). The new policy scenario envisages a transition to a more robust

renewable portfolio by 2040 from the current 58% (coal-fired electricity generation) to 32% (Fig. 17.5) [27, 28]. A close look at electricity consumption over the last five-year plan is shown in Table 17.1. The per capita electricity consumption for 2017 is summarized in Table 17.2 by sector consumption. The total per capita usage was 4589 kW/h of which the domestic sector accounted for 628 kW/h with a corresponding increase of 268 kW/h from 2016. The total nationwide usage was 63,625 kW/h (Figs. 17.2 and 17.3).

Electricity consumption in the whole country was 636.25 TW/h with an annual growth rate of 6.6% or a relative increase of 2.7% relative to 2016 [30–34]. These successive increases indicate that the expected industrial output due to the steel tariffs imposed by the Trump Administration either have not taken effect or have not slowed the economy significantly to affect energy consumption, with heavy industry contributing toward the largest increase in the share [35].

The five-year plans from 2005 have stressed self-sufficiency in energy, as well as manufacturing and a managed transition to renewables, and to lower greenhouse gas emissions and improve the air quality in large metropolitan cities of China [36–41]. This can only be accomplished if the reliance on coal-fired power stations is diminished (cf. Fig. 17.5).

The current mix is summarized in Table 17.3. This transition can be better managed by placing new environmental standards in the coal sector through policy reforms [42–44]. One is the modernization of older coal-power stations or early

Table 17.1 Summary of installed capacity and corresponding growth rate

Year	The installed capacity of power generation (kW × 10)	Growth rate (%)	The per capita installed capacity of power generation (1 × 10 ³ adults, kW/h)	Growth rate (%)
2010	96,641	10.6	0.85	11.9
2011	106,253	9.9	0.79	9.3
2012	114,676	7.9	0.86	8.9
2013	125,768	9.7	0.93	8.1
2014	137,018	8.9	1.02	9.7
2015	152,527	10.6	1.10	7.8
2016	165,051	8.2	1.19	8.2
2017	177,708	7.7	1.28	7.6

Table 17.2 Summary of installed capacity and corresponding growth rate by the end user for 2017

	Electricity consumption (×1 × 10 ⁹ , kW/h)	Growth rate (%)
Primary industry electricity	1175	7.5
Secondary industry electricity	44,922	5.5
Electric power in the tertiary industry	8825	10.7
Electricity consumption for urban and rural residents	8703	7.7

<http://www.cec.org.cn/guihuayutongji/tongjixinxi/niandushuju/2019-01-22/188396.html>

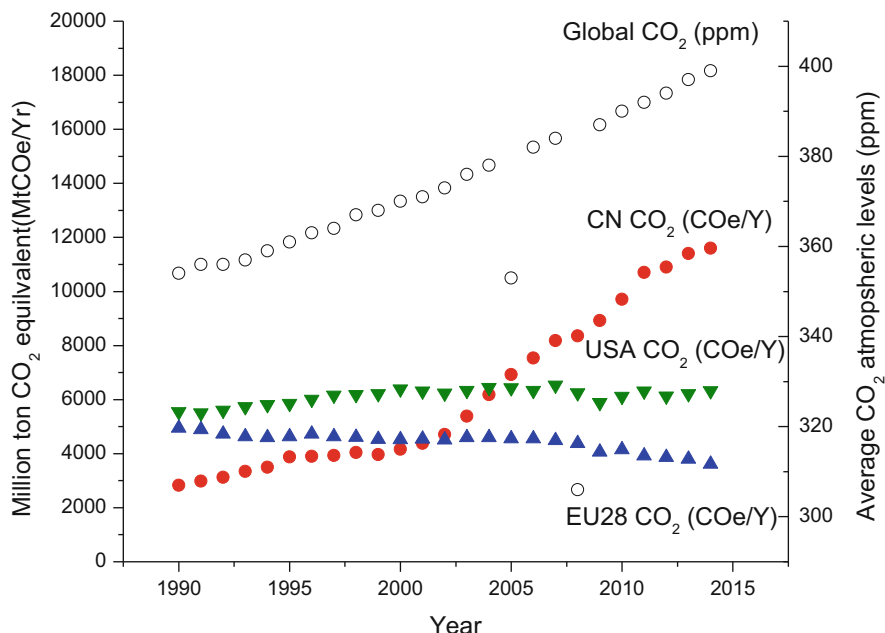


Fig. 17.2 Summary of annualized carbon dioxide emissions for EU28, the United States, and China (CN) in millions of tons of carbon dioxide equivalent per year on the left axis superimposed with world carbon dioxide atmospheric levels (in parts per million (ppm) on the right axis) (Source: World Bank [7] and NOAA [29])

retirements as solar, wind, and hydroelectric have increased their share. The second factor related to price and energy mix adjustment is related to the cancellation of projected commissions from the 12th five-year plan. Lastly, the third factor related to changes in energy policy is loosening of state controls in terms of pricing, to promote trade and competitiveness between power utilities and manufacturers as directed by the State Council in 2015 [25]. Collectively, these three factors are designed to increase efficiencies, enable fast transitions in use of the energy portfolio and minimize excess capacity.

The total installed capacity of non-fossil energy (non-thermal) power generation was 688.5 TW/h (37.8%), as renewables of the new policy scenario sustainable mix (wind power, solar energy) installed account for 16.5% [30].

This has enabled investment on renewables (excluding hydro, Eyre et al. [46]) to increase as their share of the total product portfolio increases. To promote efficiencies within the grid, the new price controls have resulted in reduced tariffs, saving regulatory costs and top-down supervision and enabling localities to better manage their production and demand. These State Council articles and local management have enabled China to be responsive at the local level while maintaining top-down control [47]. The policy makers within the State Council recognize that the cost of doing business should also factor in environmental and health costs associated with

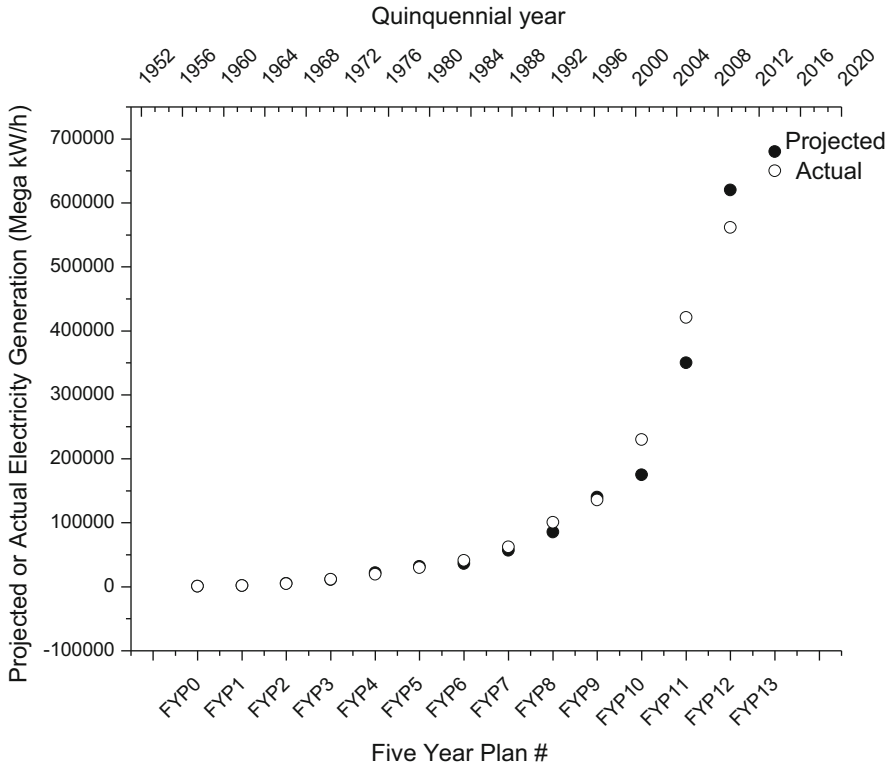


Fig. 17.3 Summary of annualized planned and actual electricity generation as outlined in the quinquennial five-year plans (bottom axis) and the corresponding years (to axis). (Source: IEA [30], USCC [16, 17], Sun et al. [45, 31, 32])

higher greenhouse gas emission and particulate matter. Since much of the electricity is dominated by coal-fired power stations, reform of the electricity system is logical as is the transition from a planned economy to a service economy, where the energy generators negotiate directly with the large energy consumers. The justification for this transition is based on the greater responsiveness and adaptability to changing circumstances from the bottom-up as opposed to the traditional top-down [48].

The goal of the current five-year plan to increase renewables (excluding hydro) to 15% by 2020 and to 20% by 2030 is designed to meet the environmental goals of all major 338 cities meeting the air quality standards. In 2016, only 84 major cities met the air quality standard [49, 50]. To lower both carbon and particulate emissions the dependence on central large thermal power stations needs to be better managed and aligned with local entities such that the power is transmitted from great distance to the desired location, and that better coordination is required over the use and

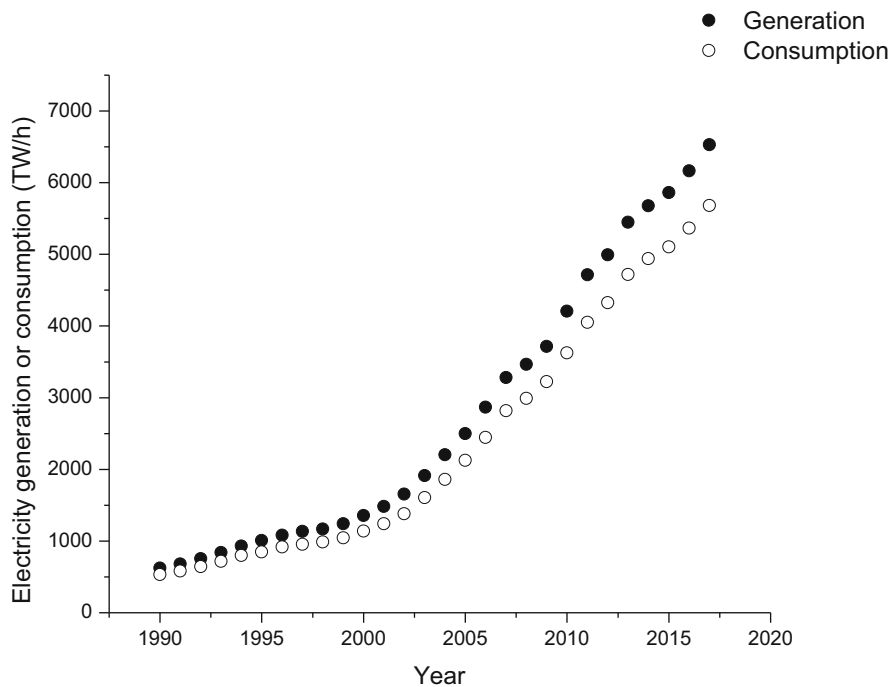


Fig. 17.4 Summary of annualized electricity generation and consumption (TW/h). (Source: yearbook.enerdata.net, 2017)

Install Power Capacity by Source (2016) Installed Power Capacity by Source (2040)

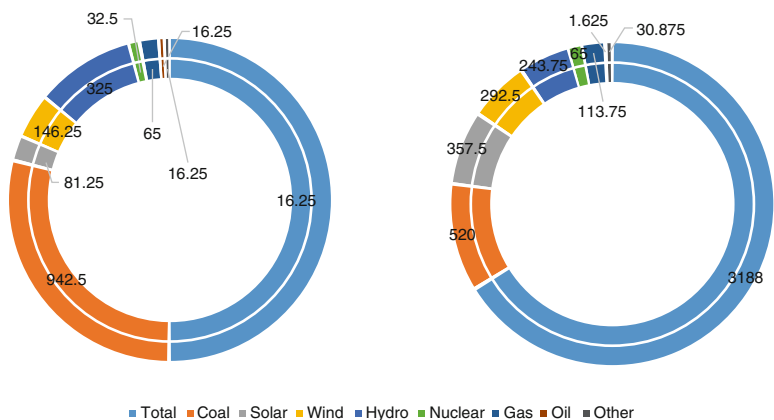


Fig. 17.5 Summary of the installed power capacity in China today (2016, left) and anticipated by 2040 (right) by energy source. (Source: IEA [30])

Table 17.3 Summary of energy from renewables and percent change from 2016 to 2017

Power generation installation structure	Percentage ratio (%)	
	2016	2017
Thermal (coal)	64.3	62.2
Hydropower	20.1	19.3
Wind power	8.9	9.2
Solar power generation	4.7	7.3
Nuclear power	2.0	2.0

<http://www.cec.org.cn/d/file/guihuayutongji/tongjixinxi/niandushuju/2019-01-22/4fedb4c956f6059c5998913b10a6233a.pdf>

Table 17.4 Summary of installed power capacity by energy type for 2017

	Installed capacity kW($\times 10$)	Percentage ratio (%)
Coal-fired power generation	98,000	55.2
Gas power generation	7570	4.3
Yu Wen, residual pressure, residual gas power generation	2989	1.7
Biomass power generation	1651	0.9

<http://www.cec.org.cn/d/file/guihuayutongji/tongjixinxi/niandushuju/2018-12-19/b386d97a65996f9e3520b9d63b4ba634.xls>

management of the power grid, summarized in Table 17.4 [51]. In reference to Table 17.4, it can be seen that relative to 2016, the consumption of energy from large centralized thermal units or thermal power stations decreased by 2.2%, in spite of an overall increase of gas power station by 8% [52].

By the end of 2017, the national installed capacity of full-caliber power generation was 1.777 billion kilowatts, up from the previous year by 7.7%. In addition, by the end of 2017, the per capita installed was 1.28 kilowatts, an increase of 0.09 kilowatts over the previous year, an increase of 7.6%, slightly above the world average (<http://english.cec.org.cn/No.110.1481.htm>).

In Fig. 17.6 and Table 17.5 it is clear that use of large thermal units and thermal power stations will remain a dominant mix of the energy portfolio for some substantial time, although transition to renewables (excluding hydroelectric) has resulted in a slight decrease of thermal consumption from 72% to 71% from a high consumption of 82.5% in 2010 [30, 53].

An example of the State Council (top-down) and local city planners (bottom-up) approach is how the City of Shenzhen (southern China) has managed its energy needs. According to the State Council article 9 [13, 25] and in coordination with the National Development and Reform Commission [54–56], a repricing of electricity and use of the transmission grid was initiated in 2015 [25].

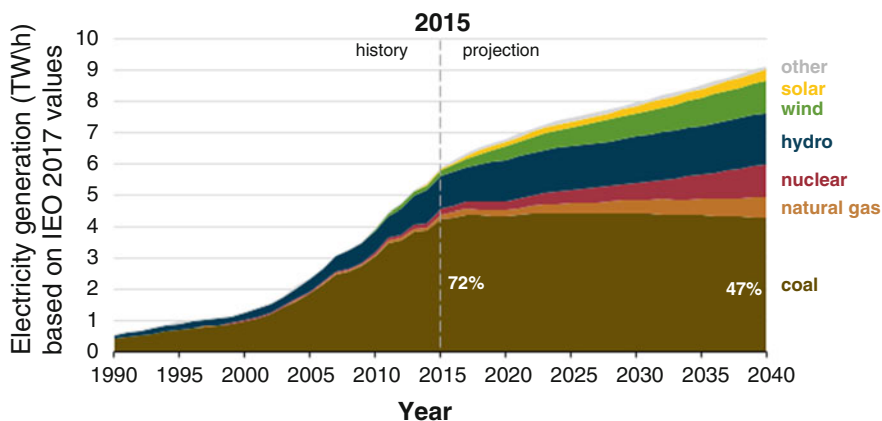


Fig. 17.6 Electricity generation (TW/h) based on IEO 2017 values for 2005–2040. (Source: EIA [32])

Table 17.5 Summary of installed percentage change of power capacity between 2016 and 2017

Generation	Percentage ratio (%)	
	2016	2017
Thermal (coal)	71.8	71.0
Hydropower	19.5	18.6
Wind power	4.0	4.7
Nuclear power	3.5	3.9
Solar power generation	1.1	1.8

17.3 Policy Implementation: Illustration from Southern China

The work plan for Shenzhen is shown in Fig. 17.6. Briefly, the State Council formulates the framework policy through assurances of articles [57, 58]. The provincial or municipalities formulate these articles at the local level based on need and available resources or access [59]. The aim of article six of the State Council circular is to improve efficiencies in energy production and transmission and is not focused on a single inflection point. The circular deals with several factors, which can be classed as either strengthening or improving supervision of energy production, technical improvements in the areas of energy generation or economic support to enable provinces to migrate to cleaner energies whilst meeting the energy targets. These include but are not limited to subsidies which yield tax discounts to manufacturers of solar cells who utilize the solar panels for light-harvesting and generation of electricity. A more common approach is to encourage the city planners to promote the purchase and use of local photovoltaic components, materials, and assemblies to provide energy at a local level. While the subsidies are modest at

Table 17.6 Summary of subsidies offered to entities in southern China business based on energy type per kW/h of generated electricity

Type	Cost (RMB)
Thermal	0.2~0.3
Hydropower	0.25~0.3
Onshore wind power	0.2~0.35
Photovoltaic power station	0.3~0.4
Nuclear power	0.45~0.5

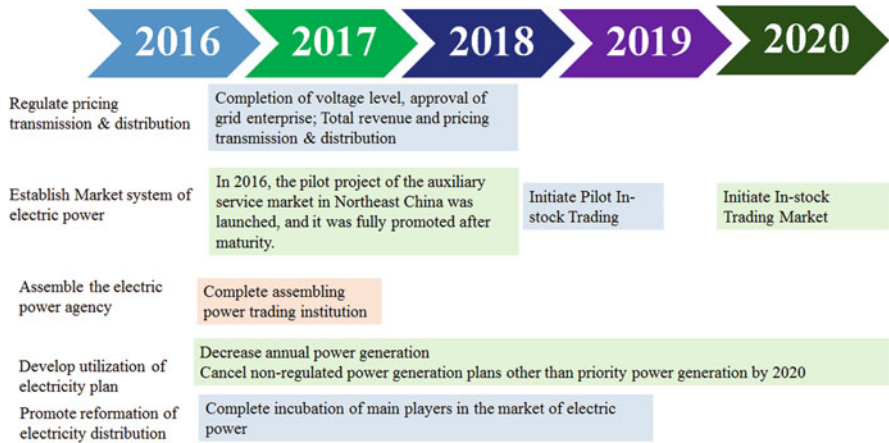


Fig. 17.7 Summary of the State Council policies driven at the local level using policy implementation and policy instruments at the City of Shenzhen as a test case

<0.3 yuan/kWh (cf. Table 17.6 for a range of tax credits), they promote local innovation and increase the non-renewable portfolio in line with the State Council articles [27, 43, 44, 60].

An analysis of approximately 32 major cities or administrative centers in southern China (such as Guangdong, Guangxi, or Hainan) shows an equal implementation of the three reforms (supervision, technical, or economic) [49, 61] (Fig. 17.7).

A common problem faced by policy planners is central versus decentral. Does the state consolidate and invest in a few but large energy producing or consuming entities, or does the state decentralize and have numerous but lower capacity generating or consuming entities [62]. In China, during the first few five-year plans, the earlier models were based on centralized management and quotas as developed by the Soviet System, that took less account of local needs, resources, and know-how. The current five-year plans have migrated towards more subsidiarity, enabling localities to develop solutions which impact the entire nation, such as the environment, economy, healthcare or energy. The five-year plans concerning energy have increased the sustainable mix and governance or implementation of directives via a more deregulated model. Deregulated energy thus

relies on renewables at the local level, lowering transport costs and improving responsiveness to local energy needs and lowering the likelihood of blackouts or brownouts during peak emergencies as the grid is decentralized, including a stop on authorized construction projects [63, 64]. The first advantage of such a deregulated approach is fostering of adaptability to dynamic energy needs. Some of the older sustainable energies such as hydroelectric imply automation without heavy human involvement, while other newer sustainable energies such as PV and to a lesser degree wind suggest human involvement and capital costs providing near zero emitting carbon energy sources [55]. A number of policy instruments have been issued and adopted to promote deregulated energy to lower the barrier to market, promote market penetration, as well as lower carbon emissions and increase high technology products manufactured in China. These policies often have been contradictory and not consistently applied as the focus of successive five-year plans has not been the same, as macro-incentive policies have shifted depending on the specifically stated goal. Between November 2015 and July 2018, the NDRC issued a series of policies designed to reform the electricity generation and distribution in southern China [54, 56, 94]. At the end of 2016, the renewable portfolio accounted for 36% of the total electric installation with photovoltaic and wind energies contributing the highest kW/h in the world, although the relative ratio to the total energy demand in China is modest. Through the introduction of subsidies, preferential trading policies (cf. Fig. 17.8), and grants, the anticipation has been that uptake in renewables will increase [30].

The redistributed energy policy has three broad goals: the first is the reduction of electricity from coal-powered utilities, and the second is local planning, input, and implementation of central policy directives, based on local need and resources to provide clean, safe, reliable (high up-time), and sustainable energy to industry and local population centers [47].

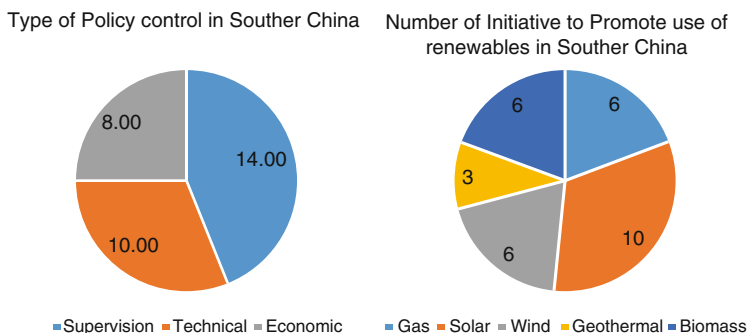


Fig. 17.8 Summary of policy types in southern China, such as enhancement of supervision and training, technical innovation and modernization or economic or infrastructure assistance (left) from the central government and number of policy subsidies or changes at the local level (southern China) to promote renewables (right)

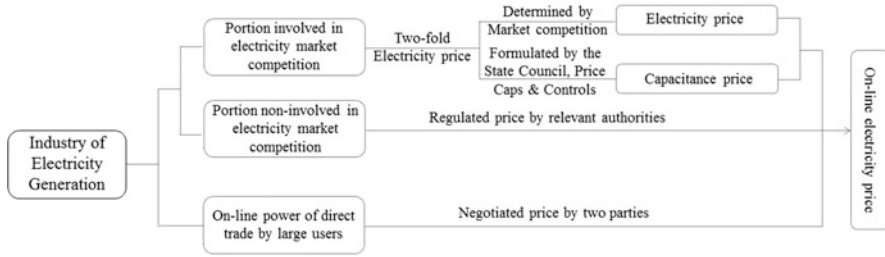


Fig. 17.9 Summary of classification of electricity price related to power generation enterprises

The second is to enable the local municipalities to have a greater say in which renewable energy portfolio is their focus based on financial strength, local resources, and need, such as photovoltaics (PV), wind, and hydroelectric. Lastly, is the minimization of long-distance or high-voltage transmission of energy from central thermal plants reducing cost, waste, loss, and cost of installation, maintenance management, training and safety upgrades. These initiatives are designed to lower power loss due to transmission but also increase the renewable energy mix portfolio [65].

In Shenzhen, the NDRC policy implementation has not resulted in price changes, but has enabled: (a) participation of high volume energy users in the power market to compete for feed-in electricity price adjustments from power generation enterprises; (b) increased participation of power generation enterprises to supply feed-in electricity at fixed prices, which were not competing before due to long-term fixed contracts with guaranteed price caps; and (c) the ability for direct negotiation between energy generator and user for more competitive rates, regardless of volume of energy usage. While these reforms have not altered the price category band, the new round of power system reform has altered how the market is managed and is summarized in Fig. 17.9 [66].

The new policy directives have four modalities “off-grid, on-grid, grid-connected without power injection, and grid connected with power injection.” In the off-grid modality, local energy services are provided without transmission from a central source; whereas on-grid, electrical power is supplied locally to the grid and then to a source with air-conditioning and steam supplied locally, with the grid supplying on-demand peak loads [67]. A series of reforms are tailored to enable renewable resources to be better managed and be price competitive with coal, where price caps, tariffs, and rebates have generated a pricing mechanism which generates a sales price band to ensure “fairness” and “equity” to both end users who enter the market to price competitive transactions and also for users who choose not to enter the market but rely on fixed price long-term contracts [1, 68, 95]. The charge caps within each price band take into account a form of social justice or “the protection of people’s livelihood” as well as being responsive to large combines who are major consumers of energy. This mechanism allows them to conduct strategic planning and budgeting, as the prices are fixed using long-term contracts for a definitive period, summarized in Fig. 17.10 [69, 70].

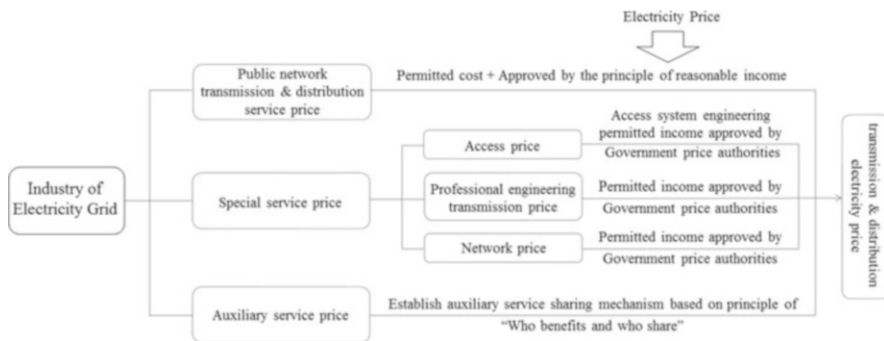


Fig. 17.10 Classification of electricity price related to related manufacturers or heavy energy consumers

The oil crisis focused policymakers on energy security, on the turn of the millennium, and environment dimension was added for minimizing climate change through a balanced energy approach of combining renewable energy, clean energy, and traditional fossil fuels [71]. The transition has also offered an opportunity for workforce training and new revenue lines. The State Council articles of 2016 [27, 60] are designed for stabilizing energy, reducing greenhouses gas emissions, and controlling air pollution. The reforms in the power sector incorporate elements of a regulated market in the decision making, a process in which the energy sector was opened to both domestic and foreign investments and capital and on/off-grid electricity tariffs, price caps, and subsidies [44]. The 2015 reforms [25] were build upon the 1985 reforms [57] with power generation sector using the concept of energy justice and social equity formulated in articles [“Chapter V Electricity Rates and Fees Article 35 The electricity rates herein refer to the rates charged to the power-generating enterprises for incorporation into the power network, the rates of mutual supply between different power networks and the sales rates of electricity supplied to consumers”. “The rates of electricity shall be based on a centralized policy, fixed in accordance with a unified principle and administered at different levels. Article 36 Establishment of electricity rates shall be based on the principles of reasonable compensation of cost and reasonable determination of profits, legal incorporation of taxes, fairly shared burdens and promotion of electric power construction”] [13], which enshrine the concept of a guaranteed return on investment and also controlled inflation and capped the returns for investors. These early reforms enabled local and state entities to invest in the power generation sector to meet new growth targets. The relationship between electricity generation, consumption, and price controls is summarized in Figs. 17.10 and 17.11 [72].

In practical terms, direct trading between major energy users to buy electricity at competitive prices has expanded. While the pricing mechanism to determine the unit purchase price of heavy users has not been substantially been changed, the policy tweak has enabled the voice of small to intermediate energy users to be factored into the overall pricing model, along with the choice of renewable energy mix into long term strategic planning [73]. Through this reform, market bid to transactions of energy units has

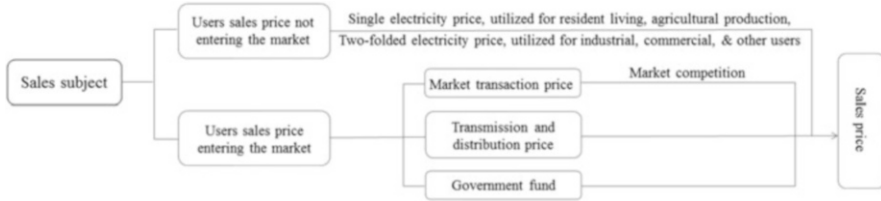


Fig. 17.11 Classification of electricity price related to electricity sales companies

increased, while maintaining price structure similar to pre-reform approach, for end-users who did not enter the price competitive bidding process. The purpose of these market-based reforms is to make the electricity generation to market process more responsive to local needs across different regions of South China, whilst maintaining the concept of ‘social justice’ [74]. The rollout of reforms is not consistent or uniform across the region; some cities are able to implement the reform policy quicker, while there is a lag in adoption in other municipalities. The pre-reform trading includes large users who directly buy [66–110 kW/h] electricity or greater users such as heavy industrial and commercial manufacturers and power generation enterprises who trade directly with local commercial consumers [75]. Power generation enterprises will sell electricity to the power grid to sell to end users and a third to heavy users who bid directly to the power generating entity. The price band is designed to provide an equitable settlement, with the power grid enterprises ensuring a guaranteed power supply services and also minimum length contracts to stop end users from shopping for a power supplier too frequently [45, 76].

17.4 New Policy Scenario

This triad approach is designed to simultaneously increase the power supply from renewables, by fostering local actors to build local power generation capacity from domestic and foreign investors, who are guaranteed higher on-grid tariffs to entice their investment and allow a maximum return on investment [77]. The role of foreign investment or higher returns may not be politically beneficial at the State Council level, but by deferring to local municipalities, the political penalty is by-passed as a greater foreign share of power generation in China is decentralized, limiting the probability of one foreign actor dominating the China power-generating market [73, 78]. The electric power law has pivoted China to consolidate the infrastructure phase and maintain annual growth of 1% in contrast to an annualized growth of 4.5% over the last two five-year plans. The stabilization of growth is equivalent to an improvement of 3.4% gain in energy on a per capita basis which is expected to increase until 2040 [30, 33]. The growth model also predicts that China will overtake the EU28 by 2035 in per capita energy consumption [79]. The energy law promotes “newenergy” through the generation of electricity from renewable resources such as natural gas, and nuclear, and hydropower while lessening the reliance on coal. This

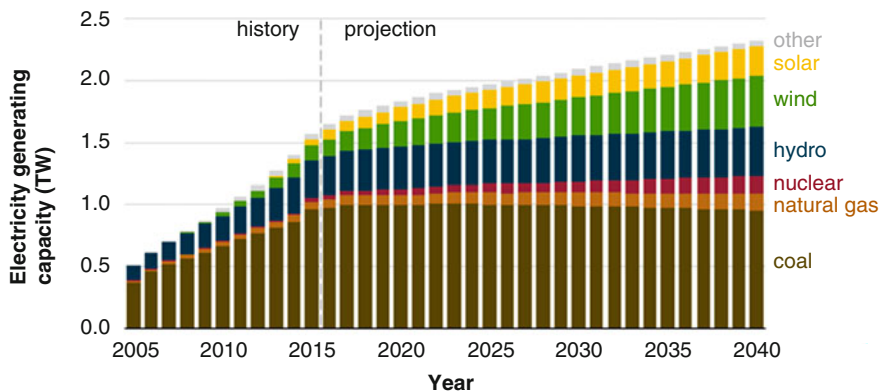


Fig. 17.12 Electricity generating capacity (2005–2040) using IEO2017 as a reference (Source EIA [32])

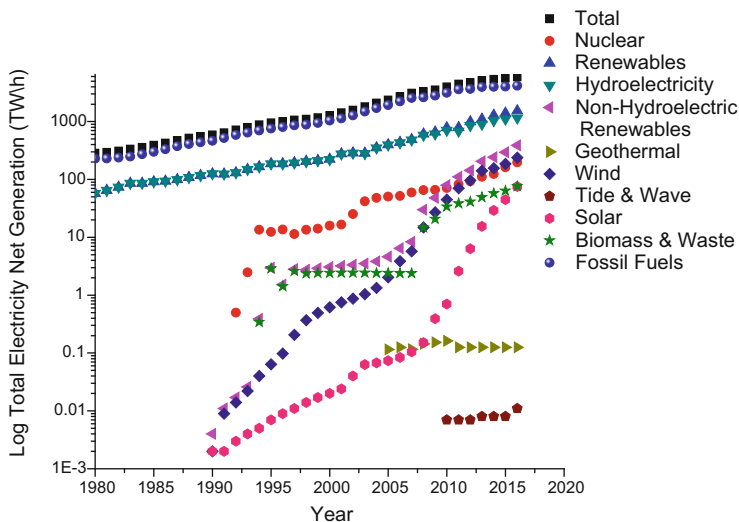


Fig. 17.13 Net electricity generating capacity by type. (Source: EIA [31, 32])

diversification in the energy mix is expected to continue for at least the next 3–4 five-year plans (cf. Fig. 17.12; [30, 80]). The renewable portfolio is also used for energy storage related to heating and transport. If the current trend is continued, electricity as an energy carrier will be the dominant form of energy consumption rather than natural gas or petroleum or coal [81]. The cross over is expected to occur around 2025–2030 for both coal and oil as photovoltaics, biomass, and wind provide energy for domestic, light energy, and battery/and hydrogen for transport (cf. Fig. 17.13). A total of 150 GW of new coal capacity has been postponed until 2020, in addition to

the retirement of 20 GW of older coal-fired plants and technological upgraded to 1 TW of current coal-fired power stations and is expected with natural gas and petroleum to be significant until 2040 [30, 33].

17.5 Photovoltaics as a Model of Deregulated and Redistributed Energy

New Power Law of China is designed to formulate a distributed energy system through administrative controls [52]. These controls consist of the top-down State Council policies which apply to all state and private agencies, the Ministry of Industry and Information Technology for industrial entities, and other area-specific ministries such as the Ministry of Science and Technology. These State Control entities also offer directly or through the province assistance to promote and use renewable energy resources in the form of tariffs, feed-in tariffs, power generation, or installation subsidies, in addition to state grants, tax rebates, preferential loans, on-grid tariffs, and guaranteed minimum returns in the form of articles, notices, or interim measures as the communication instrument [82]. At the top level, the National Energy Administration (NEA) supervises the province or special administrative unit power generation capacity. The province dictates the scale and scope of implementations of the power capacity scale, requiring state-owned enterprises or other actors to buy power generation rights from large thermal power stations [83].

To encourage and lower the cost of business, financial loans, subsidies, and heavy rebates were implemented; however, this rate of investment cannot continue and is likely to be tapered off, as some businesses generate less income than anticipated, while others are unable to meet the current financial obligations (as subsidies are lowered). Return back to the province may not be accounted for until 2–5 years after the initial construction phase was completed; lastly, the quality of the electricity generation and feed into the grid varies with load [83]. Photovoltaics (PV) and wind is intermittent, and some power generation units are not appropriately grounded or produce a lower voltage with a broad frequency distribution which can affect the quality of the grid voltage [84]. The device storage capacity, grounding, voltage level steady output, connections, type of inverters, and frequency/voltage filters are important factors in addition to power generation prior to grid injection [85].

Both wind and solar have significantly increased their share over the last 3 years with a relative rate increase of 20% in 2017 from 2016 in terms of installed capacity. In 2017 an additional 103 GWh was installed a capacity increase of 29.4% year, a record high [30, 33]. The photovoltaic (PV) surge is occurring in China, the United States, Japan, and India as the ‘big four players’ in the PV market, who account for more than 80% of the available capacity, the installed capacity of 53.06 GW, 10.6 GW, 331 9.63 GW, and 7.2 G W, respectively. As the world’s largest photovoltaic market, China has installed more than half of the world’s capacity in 2017, and the Chinese market has largely swayed global market trends in the past 2 years, with newly installed increments in the Chinese market in the 2016 and 2017 accounting for 70% and 82% of the global market increase [33].

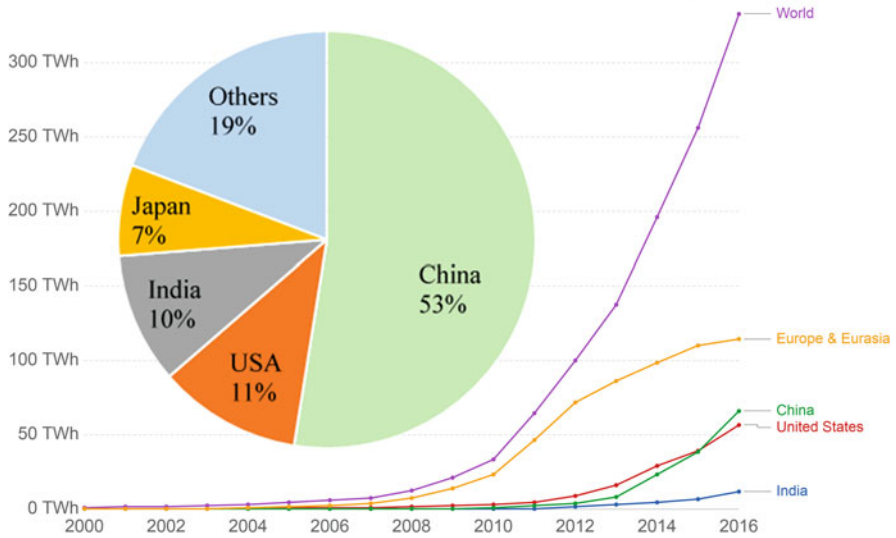
China's photovoltaic new grid capacity in the first three quarters of 2018 was 34.5 GW, a decline of 19.6% relative to the same period in 2017. A starting capacity of 19.6%, at 17.4 GW from the province's power generating entities, to 10.92 GW over the previous year, which was a decline of 37% in generating PV capacity. This slowdown may be a reflection of the implementation of the new policy scenario rebalancing. The off-grid capacity in the province of southern China was 17.1 GW, an increase of 12% from the previous year with 13% in off-grid usage [30]. The overall decline in state-owned enterprise capacity is balanced by an increase in installation, and usage by new businesses and heavy energy users and also installation in provinces previously identified as being below the poverty line are consistent with State Policy regarding "social justice" and "equity" and opening up of markets to new players particularly in financially depressed regions or provinces [13]. The current photovoltaic construction and installation in southern China are expected to be capped at 30–40 GW, although private non-subsidized projects are likely to increase leading to grid injection and lower output from coal-powered power utilities. The combined subsidized and non-subsidized PV installed capacity is expected to reach 45–50 GW by the end of 2019. One reason for the increased participation of smaller companies in the PV market without subsidies is the lowering of market entry as the cost of PV has continued to decline. While power generation from PV is less than 2% of the global total energy (~333 vs. 16,894 TW/h or 1.97%, [34]), it is likely to increase as the cost of PV continues to fall and the environmental costs of coal-based electricity generation are expected to rise, not in the generation of electricity but in environment-related cleanup costs, related to acid rain and greenhouse gas emissions. In southern China, the cost of photovoltaic electricity is about 31% higher than that of coal, without subsidies. With increased marketization, the cost of photovoltaic power generation is expected to be lower than coal by 2021 years, and continue to decrease or taper off. It is expected that the share of photovoltaic power generation will gradually rise to 10% by 2040, while photovoltaic and wind energy will account for 37% of the total installed capacity of electricity generation in southern China by 2040, which will be a fourfold increase (cf. Fig. 17.14 and insert). "Solar photovoltaic (PV) module prices (measured in 2016 US\$ per watt-peak) versus cumulative installed capacity (measured in megawatts-peak, MWp). This represents the 'learning curve' for solar PV and approximates a 22% reduction in price for every doubling of cumulative capacity" (Our Word in Data and Fig. 17.15 including insert).

17.6 From Yesterday to Today to Tomorrow: Lessons Learned, What to Expect Next?

The early five-year plans emphasized self-sufficiency and today's plan are no different in ensuring that there is energy security in China. The consumption of energy outstripped capacity, resulting in the fifth five-year plan promoting an increase in coal-fired power stations to meet and exceed demand. This trend has continued until the ninth five-year plan. The economy in the 1990s focused on

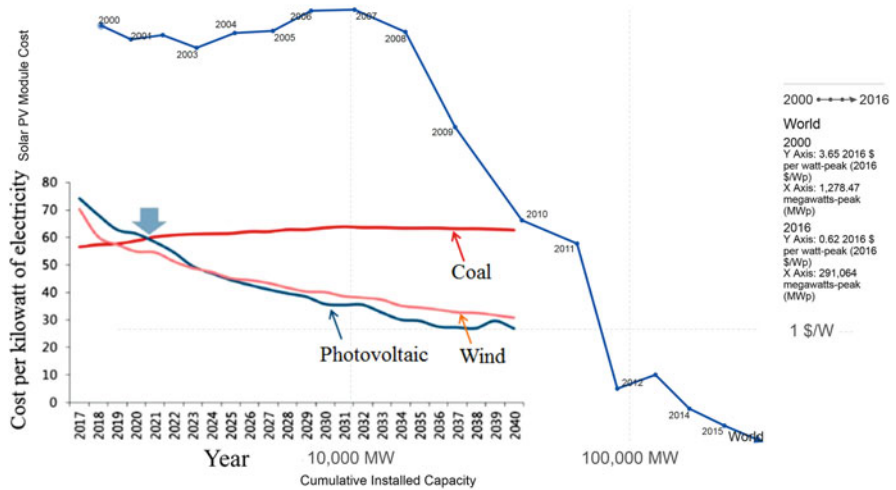
Solar PV energy consumption, terawatt-hours per year

Total solar photovoltaic (PV) energy consumption by country or region, measured in terawatt-hours (TWh) per year.



Source: BP Statistical Review of Global Energy

Fig. 17.14 Solar PV consumption by country. (Source: Our World in Data)



Source: Lafond et al. (2017); IRENA; SolarServer

Fig. 17.15 Solar PV module price versus cumulative capacity, 2000 to 2016. (Source: Our World in Data)

expectation and actuality in the tenth five-year plan which slowed the construction of new coal plants. To meet this “shortfall,” the planners at the province level continued to build plants or look at renewables. Also, the early market reforms of 2002 decoupled generation and transmission with a state-owned enterprise quintopoly to compete with each other and other private sector actors in the power generation sector [58]. These reforms were supplemented in 2004 by “generation rights” whereby construction of thermal plants (heat and power from coal) required prior approval from the national development and reform commission [64], due to decoupling between central planning and performance targets for the 11th and 12th five-year plans, resulting in a divergence between projected and actual growth or generation of electricity. As China was developing, little attention was paid to tangential issues regarding workflow training, safety, and environmental impact, but the emphasis shifted in the 13th five-year plan to incorporate societal and environmental goals into industrial output and energy targets. For example, the plan placed a 5 billion metric tons of coal cap [12] as a means to lower carbon emission to 15–18% [27, 60] in addition to particulate matter. These new requirements resulted in older coal power stations being retired equating 20 GW [27], as well as newer and cleaner manufacturing techniques [43, 54]. The current plan emphasizes on three aspects: supervision, technical innovation, and economic aid. It is likely the latter aspect will taper off as newer generating capacity including non-hydro renewables become more prominent, to meet China’s ecological and environmental goals. The proportion of non-fossil energy installed capacity in China will exceed 40% by 2020 and will continue to surpass that of the European Union and the United States over the next 20 years [30]. This is both clean [coal, natural gas, and nuclear] and [wind, solar, wave, geothermal] renewable energy. The downward trend in carbon and greenhouses gas is related to market reform and stricter [NDRC] control of the scale of coal power development and the quick elimination of “dirty” production capacity forming the supervisory arm [44, 55, 56]. The development of new wind, PV, and thermal storage including batteries has enabled smaller firms to participate directly in the electricity market as purchases of electricity or as buy-to-sell entities, which has been implemented with varying degrees of vigor within southern China, promoting grid flexibility. Lastly, economic aid to clean up or replace coal-based electricity generation and/or utilization of clean electricity has resulted in an increased rate of renewables. Technical innovations and deployment of intelligent power systems improvements in load-leveling have contributed to increasing efficiencies in available electricity and decreased the requirement for transmission over large distances from large thermal units. Unrelated directly to the generation of electricity, but tangentially involved in the incorporation of elements from information technology to provide technical support for the intelligent development of the power system [86]. Other allied areas of incorporation are the use of cloud computing, big data, Internet of the Things, mobile Internet, and deep integration between the smart grid and appliances. Specific applications include communication between electric vehicles, wireless charging, and other fields of rapid technological breakthroughs that rely on electricity [87]. These have promoted distributed energy using an intelligent supply system to increase responsiveness to load changes at high efficacy and low transmission loss. Third, the internationalization of

electric power development, particularly at the province level, is an important component in attracting outside (foreign or out of province) investment, both as importers and exporters related to “Belt and Road” initiatives. This implies that Chinese business related to energy will be exported to nearest neighbor countries as well as attracting outside investment and research and development. These R&D efforts are based both within China and also at “technology hubs” in select cities in the United States, Canada, Europe, Australia, Africa, and the Middle East. This research includes both devices, software, and artificial intelligence tools; thus China can export and promote both products [solar panels] and solutions [intelligence, cell phone-based apps, smart algorithms] to improve its economy, aid its workforce in high technology, and open up new markets in Africa, Asia, Eurasia, and Latin America [88]. The internal marketization within China will continue in the form of institutional mechanisms. : A new round of power system reform, from power generation, transmission, distribution, to electricity sales, and user’s service. These reforms include provisions from the State Council circular which are promulgated in the form of articles, notices, and interim measures, reflecting varying degrees of ‘implementation urgency’. The application of State circulars conforms to the multi-mode pilot level of multi-level integration reflecting both human (‘vertical’) and capital/technical (‘horizontal’) resources type of amalgamation. The above reform involves comprehensive promotion across local, provincial and national areas of administration to make stakeholder aware and to enable planners to implement the provisions uniformly across the energy mix portfolio. The steel and good tariffs imposed on China by the Trump Administration resulted in a focused attention on the internal market, which was often obscured by the drive “to go outside” [89]. Heavy energy users can directly buy electricity within their province or cross-provincial bidding, promoting the province-to-province retail transactions which are beginning to increase in the proportion of total market share. With the gradual maturation of this business model, both light and heavy industries can take advantage of competitive pricing, driving innovation and leading the development of the power industry in a new direction and fostering potential new revenue streams as export products and solutions [90].

The five-year plan is a blueprint which is not implemented consistently or uniformly as drivers are different from province to province. The Electric Power Law has attempted to unify both social justice, equity, and energy security to maintain the high electricity generating capacity to meet the high energy needs. This has been accomplished using both administrative supervision changes, technical innovation, and economic aid. The end result is for China to continue to be a world leader in electricity consumption, but to generate electricity from renewables including hydro and nuclear. This is expected to keep prices low (controlling inflation) and lower the carbon emission as cleaner coal stations are brought on-line and renewables take up a greater share of the total energy mix [91].

In southern China (Guangzhou Province), the electricity generation sector played an important role in delivering the state policy outcomes from upper administration, although the actual implementation was varied based on local needs and resources. The decarbonization process of the sector was accomplished through increased photovoltaic, wind, and biomass usage, as well as pricing deregulation to manage

the local sector [92]. This has resulted in improved efficiencies and savings, gives each heavy energy user a stake, and is more transparent as end users are aware of the price structure and how they can contribute and gain financially through grid-injection or off-line consumption [93]. In general five approaches have been observed which contributed toward the decarbonization process: (a) Policy deregulation enabling each municipality to manage its energy needs has allowed heavy energy users to buy directly from local energy generators and has each user to strategically plan on how best to manage their resources, using a market price mechanism [95]. (b) Diversity in the energy mix: Allowing each municipality to generate electricity using local resources, as diversified energy generation. While solar and PV are the more dominant forms of renewables, others include biomass, thermal storage, as well as clean coal for heating and cooling, to lower the carbon footprint, restricting unauthorized electricity from coal [94]; (c) the use of targeted subsidies to enable high-cost items such as construction of energy plants to progress on-time and on-budget. Subsidies, tax rebates, and in-feed pricing should promote renewables through issuance of green electricity certificates [68], which are seen as a price competitive advantage relative to energy from large thermal units [96] (d) technical innovation in construction and energy production is important in driving costs down due to incorporation of new technology, improvement of current technologies, and availability of expertise from the “research hubs” to promote local businesses to become more energy efficient [97]; and fifthly, (e) the decoupling of generation and transmission. The last ‘structural’ change requires constant monitoring and adjustment to avoid excess capacity or brown-outs. The promotion of local generation and off-grid storage is tailored towards a smart grid approach using sensors and artificial intelligence that self-manage load and energy balance in real-time by making the appropriate electric power adjustments at each node as an energy device injects or feeds electricity The five-year plan has a provision for a smart grid development plan to distribute medium and low voltages and is expected to be deployable around 2020 [98].

In summary, China is today a world leader in power generation and power consumption and will be a world leader if calculated on a per-capita basis by 2040. To continue with its “social justice” program, the policymakers need to examine their approach to decentralize and distribute energy to incorporate an element of subsidiarity and diversity. Subsidiarity is enabling local municipalities to manage how the target goals are met and when they are met over the five-year plan projected targets. Diversity is using different energy mixes, from solar, hydro, nuclear, wind, tidal, biomass, or thermal storage. The policy instruments should continue with adaptable supervision, technical innovation, and economic incentives and tighter integration between on-grid injection and payback of subsidies.

Acknowledgments This work is supported by the Petroleum Research Fund of the American Chemical Society (53827-UR10) and the Robert Welch Foundation (AC-0006). We thank the program chairs of the ENFL and COLL divisions of the America Chemical Society for the opportunity to run or moderate symposia at the technical sessions. Lastly Springer Science+Business Media, LLC technical staff are acknowledged for their assistance in copy editing this and other book chapters.

References

1. E.S. Downs, The Chinese energy security debate. *The China Quarterly* **177**, 21–41 (2004)
2. Z. Liu, D. Guan, D. Crawford-Brown, Q. Zhang, K. He, J. Liu, Energy policy: a low-carbon road map for China. *Nature* **500**(7461), 143 (2013)
3. J.J. Schreifels, Y. Fu, E.J. Wilson, Sulfur dioxide control in China: policy evolution during the 10th and 11th five-year plans and lessons for the future. *Energy Policy* **48**, 779–789 (2012)
4. P. Crompton, Y. Wu, Energy consumption in China: past trends and future directions. *Energy Econ.* **27**(1), 195–208 (2005)
5. World Bank, GDP (2018), https://data.worldbank.org/indicator/NY.GDP.MKTP.CD?end=2014&locations=CN-US-EU&name_desc=false&start=1990
6. World Bank, GDP, PPP (current international \$) (2018), https://data.worldbank.org/indicator/ny.gdp.mktp.pp.cd?end=2014&start=1990&year_high_desc=true
7. CAIT, CAIT historical GHG emissions (2019), <https://www.climatewatchdata.org/ghg-emissions>
8. C. Wang, J. Chen, J. Zou, Decomposition of energy-related CO₂ emission in China: 1957–2000. *Energy* **30**(1), 73–83 (2005)
9. X. Yuan, J. Zuo, Transition to low carbon energy policies in China-from the five-year plan perspective. *Energy Policy* **39**(6), 3855–3859 (2011)
10. State Council, A speech made by Premier Li Keqiang at a Meeting on Functional Transformation and Institutional Reform of Local Government (2013), http://www.gov.cn/guowuyuan/2013-11/08/content_2591026.htm
11. State Council, Notice of the State Council on Issuing the 12th Five-Year Plan for Energy Development, No. 2, 2013 (2013)
12. State Council, The 13th Five-Year Plan for Economic and Social Development of the People's Republic of China (2016), http://www.gov.cn/xinwen/2016-03/17/content_5054992.htm
13. The National People's Congress of the People's Republic of China (NPC), Electric Power Law of the People's Republic of China (2007), http://www.npc.gov.cn/englishnpc/Law/2007-12/12/content_1383731.htm
14. A.G. Hu, The five-year plan: a new tool for energy saving and emissions reduction in China. *Adv. Clim. Chang. Res.* **7**(4), 222–228 (2016)
15. S. Shao, T. Huang, L. Yang, Using a latent variable approach to estimate China's economy-wide energy rebound effect over 1954–2010. *Energy Policy* **72**, 235–248 (2014)
16. United States-China Commission (USCC) (2011), www.uscc.gov/sites/default/files/Research/12th-FiveYearPlan_062811.pdf
17. United States-China Commission (USCC) (2017), <https://www.uscc.gov/Research/13th-five-year-plan>
18. The University of Southern California at Annenberg (USC), 11th Five Year Plan on Energy Development (2007), <https://china.usc.edu/national-development-and-reform-commission-%E2%80%9C11th-five-year-plan-energy-development%E2%80%9D-April-2007>
19. The United Nations Public Administration Network (UNPAN), China: Summary of the Tenth Five-Year Plan (2001–2005) (2001), <http://unpan1.un.org/intradoc/groups/public/documents/apcity/unpan022769.pdf>
20. China.Org, The 2nd Five-Year Plan (1958–1962) (2019), <http://www.china.org.cn/english/MATERIAL/157606.htm>
21. China.Org, The 3rd Five-Year Plan (1966–1970) (2019), <http://www.china.org.cn/english/MATERIAL/157608.htm>
22. China.Org, The 4th Five-Year Plan (1971–1975) (2019), http://www.china.org.cn/archive/2006-02/27/content_1157612.htm
23. China.Org, The 5th Five-Year Plan (1976–1980) (2019), <http://www.china.org.cn/english/MATERIAL/157615.htm>
24. W. Zhengyi, Conceptualizing economic security and governance: China confronts globalization. *Pac. Rev.* **17**(4), 523–545 (2004)

49. Ministry of Ecology and Environment of the People's Republic of China (MEE), Ministry of Environmental Protection announces China State of the Environment Bulletin 2016 (2016), http://www.translatetheweb.com/?ref=SERP&br=ro&mkt=en-US&dl=en&lp=ZH-CHS_EN&a=http%3a%2f%2fwww.mee.gov.cn%2fgkml%2fbbb%2fq%2f201706%2f20170605_415442.htm
50. G. Liu, Z. Yang, B. Chen, Y. Zhang, M. Su, S. Ulgiati, Prevention and control policy analysis for energy-related regional pollution management in China. *Appl. Energy* **166**, 292–300 (2016)
51. Z. Guo, L. Ma, P. Liu, I. Jones, Z. Li, A multi-regional modeling and optimization approach to China's power generation and transmission planning. *Energy* **116**, 1348–1359 (2016)
52. M. Zeng, Y. Yang, L. Wang, J. Sun, The power industry reform in China 2015: policies, evaluations, and solutions. *Renew. Sust. Energ. Rev.* **57**, 94–110 (2016)
53. W. Xiong, Y. Wang, B.V. Mathiesen, H. Lund, X. Zhang, Heat roadmap China: new heat strategy to reduce energy consumption towards 2030. *Energy* **81**, 274–285 (2015)
54. National Development and Reform Commission and National Energy Administration (NDRC), Notice on Promoting the Proper Development of China's Coal Power Generation, No. 565, 2016 (2016)
55. National Development and Reform Commission and National Energy Administration (NDRC), The 13th Five-year Plan for Electricity Development (2016–2020) (2016)
56. National Development and Reform Commission and National Energy Administration (NDRC), Notice on Further Controlling the Pace of Constructing Electric Power Projects, No. 1698, 2016 (2016)
57. State Council, Interim Provisions of the State Council on Encouraging Fund-Raising for Power Construction and Implementing Differentiated On-grid Tariffs, No. 72, 1985 (1985)
58. State Council, Scheme of Reforming the Electric Power System, No. 5, 2002 (2002)
59. L. Yingjian, Y.A. Abakr, Q. Qi, Y. Xinkui, Z. Jiping, Energy efficiency assessment of fixed asset investment projects—a case study of a Shenzhen combined-cycle power plant. *Renew. Sust. Energ. Rev.* **59**, 1195–1208 (2016)
60. State Council, Notice on Issuing the Work plan to Control Greenhouse Gas Emissions During the 13th Five-Year Period, No. 61, 2016 (2016)
61. B. Rioux, P. Galkin, F. Murphy, A. Pierru, How do price caps in China's electricity sector impact the economics of coal, power, and wind? Potential gains from reforms. *Energy J.* **38**, 63–75 (2017)
62. State Council, The Decision of the State Council on Reforming the Investment System, No. 20, 2004 (2004)
63. A. Boute, H. Zhang, The role of the market and traditional regulation in decarbonising China's energy supply. *J. Environ. Law* **30**(2), 261–284 (2017)
64. State Council, Notice of the State Council's Approval and Written Reply to the Opinion of the National Development and Reform Commission on Resolutely Stopping the Disordered Construction of Power Generation Station, No. 32, 2004 (2004)
65. M.M. Zhang, D.Q. Zhou, P. Zhou, H.T. Chen, Optimal design of subsidy to stimulate renewable energy investments: the case of China. *Renew. Sust. Energ. Rev.* **71**, 873–883 (2017)
66. Q. Y. Yan, Q. Zhang, L. Yang, X. Wang, Overall review of the feed-in tariff and renewable portfolio standard policy: a perspective of China. In *IOP Conference Series: Earth and Environmental Science*, vol. 40, No. 1 (IOP Publishing, 2016), p. 012076
67. Z. Ming, O. Shaojie, S. Hui, G. Yujian, Q. Qiqi, Overall review of distributed energy development in China: status quo, barriers, and solutions. *Renew. Sust. Energ. Rev.* **50**, 1226–1238 (2015)
68. Q. Zhang, G. Wang, Y. Li, H. Li, B. McLellan, S. Chen, The substitution effect of renewable portfolio standards and renewable energy certificate trading for a feed-in tariff. *Appl. Energy* **227**, 426–435 (2018)
69. H. Wang, S. Zheng, Y. Zhang, K. Zhang, Analysis of the policy effects of downstream Feed-In Tariff on China's solar photovoltaic industry. *Energy Policy* **95**, 479–488 (2016)

70. J. Lin, F. Kahrl, J. Yuan, Q. Chen, X. Liu, Economic and carbon emission impacts of electricity market transition in China: a case study of Guangdong Province. *Appl. Energy* **238**, 1093–1107 (2019)
71. K.J. Chalvatzis, K. Rubel, Electricity portfolio innovation for energy security: the case of a carbon-constrained China. *Technol. Forecast. Soc. Chang.* **100**, 267–276 (2015)
72. J. Shen, C. Luo, Overall review of renewable energy subsidy policies in China—contradictions of intentions and effects. *Renew. Sust. Energ. Rev.* **41**, 1478–1488 (2015)
73. L. Yang, B. Lin, Carbon dioxide-emission in China’s power industry: evidence and policy implications. *Renew. Sust. Energ. Rev.* **60**, 258–267 (2016)
74. W. Geng, Z. Ming, P. Lilin, L. Ximei, L. Bo, D. Jinhui, China’s new energy development: Status, constraints, and reforms. *Renew. Sust. Energ. Rev.* **53**, 885–896 (2016)
75. L. Zhang, J. Yu, B.K. Sovacool, J. Ren, Measuring energy security performance within China: toward an inter-provincial prospective. *Energy* **125**, 825–836 (2017)
76. X. Sun, B. Zhang, X. Tang, B. McLellan, M. Höök, Sustainable energy transitions in China: renewable options and impacts on the electricity system. *Energies* **9**(12), 980 (2016)
77. M. den Elzen, H. Fekete, N. Höhne, A. Admiraal, N. Forsell, A. F. Hof, . . . , H. van Soest, Greenhouse gas emissions from current and enhanced policies of China until 2030: can emissions peak before 2030?. *Energy Policy* **89**, 224–236 (2016)
78. M.J. Herreras, A. Cuadros, D. Luo, Foreign versus indigenous innovation and energy intensity: further research across Chinese regions. *Appl. Energy* **162**, 1374–1384 (2016)
79. J. Kaivo-oja, J. Vehmas, J. Luukkanen, Trend analysis of the energy and climate policy environment: comparative electricity production and consumption benchmark analyses of China, the Euro area, the European Union, and the United States. *Renew. Sust. Energ. Rev.* **60**, 464–474 (2016)
80. L. Wang, P.L. Patel, S. Yu, B. Liu, J. McLeod, L.E. Clarke, W. Chen, Win-Win strategies to promote air pollutant control policies and non-fossil energy target regulation in China. *Appl. Energy* **163**, 244–253 (2016)
81. W. Chen, X. Yin, H. Zhang, Towards low carbon development in China: a comparison of national and global models. *Clim. Chang.* **136**(1), 95–108 (2016)
82. G.L. Luo, C.F. Long, X. Wei, W.J. Tang, Financing risks involved in distributed PV power generation in China and analysis of countermeasures. *Renew. Sust. Energ. Rev.* **63**, 93–101 (2016), Routledge (Taylor & Francis Group)
83. B. M. Owen, S. Sun, W. Zheng, China’s competition policy reforms: the Anti-monopoly Law and beyond, in *Law and the Market Economy in China*, Routledge (Taylor & Francis Group), pp. 121–155 (2017)
84. X. Guo, X. Guo, China’s photovoltaic power development under policy incentives: a system dynamics analysis. *Energy* **93**, 589–598 (2015)
85. K. Zeb, I. Khan, W. Uddin, M. Khan, P. Sathishkumar, T. Busarello, . . . , Kim, H., A review on recent advances and future trends of transformerless inverter structures for single-phase grid-connected photovoltaic systems. *Energies* **11**(8), 1968 (2018)
86. M. Moretti, S.N. Djomo, H. Azadi, K. May, K. De Vos, S. Van Passel, N. Witters, A systematic review of environmental and economic impacts of smart grids. *Renew. Sust. Energ. Rev.* **68**, 888–898 (2017)
87. M.A. Ponce-Jara, E. Ruiz, R. Gil, E. Sancristóbal, C. Pérez-Molina, M. Castro, Smart grid: assessment of the past and present in developed and developing countries. *Energy Strat. Rev.* **18**, 38–52 (2017)
88. W. Chen, S. Wu, Y. Lei, S. Li, Interprovincial transfer of embodied energy between the Jing-Jin-Ji area and other provinces in China: a quantification using interprovincial input-output model. *Sci. Total Environ.* **584**, 990–1003 (2017)
89. Z.X. Wang, H.H. Zheng, L.L. Pei, T. Jin, Decomposition of the factors influencing export fluctuation in China’s new energy industry based on a constant market share model. *Energy Policy* **109**, 22–35 (2017)

90. X.J. Yang, H. Hu, T. Tan, J. Li, China's renewable energy goals by 2050. *Environ. Dev.* **20**, 83–90 (2016)
91. C. Cheng, F. Chen, G. Li, Q. Tu, Market equilibrium and impact of market mechanism parameters on the electricity price in Yunnan's electricity market. *Energies* **9**(6), 463 (2016)
92. Y. Li, Z. Lukszo, M. Weijnen, The impact of inter-regional transmission grid expansion on China's power sector decarbonization. *Appl. Energy* **183**, 853–873 (2016)
93. B. Gilley, Local governance pathways to decarbonization in China and India. *China Q.* **231**, 728–748 (2017)
94. State Council, Notice of the General Office of the State Council on Clearing the Power Generation Projects and Recent Work on Construction, No. 8, 2005 (2005)
95. S. Zhang, P. Andrews-Speed, S. Li, To what extent will China's ongoing electricity market reforms assist the integration of renewable energy? *Energy Policy* **114**, 165–172 (2018)
96. D. Zhang, J. Wang, Y. Lin, Y. Si, C. Huang, J. Yang, . . . , W. Li, Present situation and future prospect of renewable energy in China. *Renew. Sust. Energ. Rev.* **76**, 865–871 (2017)
97. G. Brunekreeft, M. Buchmann, C. Dänekas, X. Guo, C. Mayer, M. Merkel, . . . , M. Stadler, Recommended approaches for smart grid development in China, in *Regulatory Pathways For Smart Grid Development in China* (Springer Vieweg, Wiesbaden, 2015), pp. 79–117
98. Routledge, R. Yuan, P. Behrens, A. Tukker, J.F. Rodrigues, Carbon overhead: the impact of the expansion in low-carbon electricity in China 2015–2040. *Energy Policy* **119**, 97–104 (2018)



Correction to: Design, Engineering, and Evaluation of Porphyrins for Dye-Sensitized Solar Cells

Wenhui Li, Mahmoud Elkhalfa, and Hongshan He

Correction to: Chapter 12 “Design, Engineering, and Evaluation of Porphyrins for Dye-Sensitized Solar Cells ” in: T. A. Atesin et al. (eds.), *Nanostructured Materials for Next-Generation Energy Storage and Conversion*, https://doi.org/10.1007/978-3-662-59594-7_12

The original version of this chapter was revised. The chapter was inadvertently published with an incorrect spelling of the author’s name as Mahamoud Elkhaklifa whereas it should be Mahmoud Elkhalfa.

The correction to this chapter is available at https://doi.org/10.1007/978-3-662-59594-7_18

The updated original version of this chapter can be found at https://doi.org/10.1007/978-3-662-59594-7_12

Index

A

After treatment (AT) ,445, 452
Alumina/Aluminum oxide (Al_2O_3), 17, 18, 100, 167, 192, 193, 259, 263, 264, 328, 343
Aluminum-doped zinc oxide (AZO), 152, 205–207
5-Ammoniumvaleric acid (5-AVA), 198
Amorphous silicon (a-Si), 10, 12, 13, 143, 166, 189, 206, 320, 352
Analysis of variance (ANOVA), 154
Anisotropic dielectric functions, 91
Anisotropy of energy transfer, 118, 119
9,10-Anthraquinone-2,7-disulfonic acid (AQDS), 331
Average visible transmittance (AVT), 172–175, 177, 186, 205, 206, 208

B

Before treatment (BT) ,445, 452
4,5-Benzoquinone-1,3-disulfonic acid (BQDs) ,331
Bilayer nickel oxide (BL-NiO), 237
4,4'-Bipyridine ($\text{C}_{10}\text{H}_8\text{N}_2$), 386, 393, 394, 396, 397
2,2'-Bipyridine-5, 5'-dicarboxylic acid ($\text{C}_{12}\text{H}_8\text{N}_2\text{O}_4$) (RuDCBPY), 400, 401
2,2'-bis(diphenylphosphino)-1,1'-binaphthyl (BINAP), 369
Bismuth telluride (Bi_2Te_3), 91–108
Bureau of Indian Standards (BIS), 441, 442

C

Cadmium sulfide (CdS), 47, 123, 125, 129, 148, 152, 156, 157, 230, 334, 337
Cadmium telluride (CdTe), 11, 12, 47, 140, 352
Calcinated, 24

Carbazole ($\text{C}_{12}\text{H}_9\text{N}$), 235
Carbon nanotubes (CNTs), 186, 188, 191–197, 202, 212, 325, 326
Ce-doped TiO_2 nanoparticles (CTO NPs) ,22–38
Cerium oxide (CeO), 21, 23
Cesium lead(II) bromide (CsPbBr_3), 326, 327, 345
Chemical bath deposition (CBD), 145, 154, 156, 230, 231, 234
China's electric power law, 472
Chromophoric linkers, 131
Coal capacity, 485
Coal-fired power stations, 11, 13, 472, 474, 476, 486, 487
Cobalt (Co^+), 19, 370, 390, 402
Colonies per milliliter (CFU/mL), 27
Computational fluid dynamics (CFD), 253, 256, 260
Concentrated solar power (CSP), 15, 142, 253, 292, 294
Concentration ratio (CR) ,248–250, 252, 254–259, 261, 264, 273
Concentrator photovoltaics (CPV), 247–276
Conductive tin oxide, 12
Conjugate gradient (CG) ,48
Conversion efficiency, 112, 142, 143, 149–152, 154, 155, 157, 248, 352, 353, 355, 358–360, 371–374, 387, 397, 402, 461
Copper indium gallium selenide (CIGS), 12, 13, 140, 141, 166, 176, 205, 206, 352
Copper indium gallium sulfur selenide (CIGsSe), 156
Copper indium selenide (CIS), 12
Copper nanowires, 186
Copper zinc cadmium tin sulfide (CZCTS) ,150, 151

- Copper zinc tin sulfide ($\text{Cu}_2\text{ZnSnS}_4$) (CZTS), 139, 140, 144, 149, 150, 152, 154, 155
- Copper zinc tin sulfide selenide (CZTSSe), 144, 147–156
- Covalent organic frameworks (COFs), 339
- Crystalline silicon (c-Si), 10, 140, 189, 203, 205, 328, 352
- CuInGaSe_2 (CIGS), 45–72
- CuIn metallic alloys, 47
- CuInSe_2 , 47, 52–57, 61–64
- Current density-voltage (J-V), 149–151, 169, 173
- Czochralski process, 12
- D**
- Decamethylferrocene (DMF), 333, 400
- Density functional theory (DFT), 47, 48, 52, 152, 374
- Density of states (DOS), 48
- Desorption equilibrium, 287
- Dexter energy transfer, 116, 117
- 1,4-Diazabicyclo(2.2.2)octane ($\text{C}_6\text{H}_{12}\text{N}_2$) (DABCO), 386
- Dielectric-metal-dielectric (DMD), 174–177
- Dielectric tensor, 92–95
- Dimethylformamide ($\text{C}_3\text{H}_7\text{NO}$), 387
- 1-(4,5-dimethylthiazol-2-yl)-3,5-diphenylformazan (MTT), 21
- Dipyrromethene bodypy, 116
- Direct current (DC), 10, 11, 156
- Direct current magnetron co-sputtering, 153
- Direct normal irradiance (DNI), 7, 258
- Double slope solar still (DSSS), 442
- Dye-sensitized solar cell (DSSC), 17, 143, 167, 169, 321, 351–375, 384
- E**
- Economic support, 479
- Effective cluster interactions (ECIS), 49, 64
- Electrical conductivity, $\mu\text{S}/\text{cm}$ (EC), 170, 172, 390, 398, 442, 443
- Electrochemical double layer capacitor (EDLC), 320
- Electron mobilities, 120, 228–233, 239
- Electron spin resonance spectroscopy (ESR), 389
- Electron transport medium (ETM), 202
- Energy-dispersive X-ray spectroscopy (EDX), 155, 187
- Energy mix, 10, 475, 482, 483, 485, 490, 491
- Energy storage (ES), 189, 283–312, 317–344, 410, 462–464
- Energy targets, 479, 489
- Equation of state (EOS), 49, 307
- Evacuated-tube collector (ETC), 414, 419, 428, 429, 432
- Exciton splitting, 112, 113, 116–120
- Extinction coefficients (k), 7, 93
- F**
- Field emission scanning electron microscopy (FESEM), 25, 104, 152, 153
- Finite-difference-time-domain method (FDTD), 95, 101
- First principle calculation, 47–49, 64, 71
- Five-year plan, 472–476, 480, 481, 484, 487, 489–491
- Flat-plate collector (FPC), 419, 427
- Fluorinated hydrocarbons, 142
- Fluorine-doped tin oxide (FTO), 154, 167, 173, 198, 228, 384, 389, 393, 398
- Formamidinium (FA), 114, 115, 167, 205, 206, 340–342
- Förster resonance energy transfer (FRET), 113, 386
- G**
- Generalized gradient approximation (GGA), 48, 52
- Generalized stacking fault energies (GSF), 54–56
- Gibbs free energy (ΔG), 49, 50, 61, 62
- Gibbs function, 286, 300, 301
- Global energy demands, 9, 112
- Global normal irradiance (GNI), 7
- Gram-negative bacteria, 22, 33–35
- Gram-positive bacteria, 22, 26, 33–35
- Greenhouses gas (GHG), 458, 460, 461, 473, 483
- Grid, 10, 34, 172, 186, 187, 318, 328, 336, 338, 459, 473, 475, 478, 481–484, 486, 487, 489, 491
- H**
- Heliostat concentrator photovoltaic (HCPV), 251
- Heterointerfaces, 48, 152, 157
- Heterojunction (HJ), 47, 48, 157, 198, 206, 207, 232, 237, 340, 402
- Hierarchical boron nitride (hBN), 91
- Highest occupied molecular orbital (HOMO), 234, 237, 356, 365, 385, 389

- High-resolution transmission electron microscopy (HRTEM), 47
- High temperature metal hydride (HTMH), 290, 291, 294, 300–303, 305, 308–311
- Hole transport material (HTM), 167, 170, 171, 178, 191, 198, 237, 340
- 4-Hydroxy-2,2,6,6-tetramethylpiperidin-1-oxyl (4-OH-TEMPO), 336
- Hyperbolic material, 91, 94, 108
- Hyperbolic phonon polaritons (HPPS), 94, 97
- I**
- Indium gallium arsenide (InGaAs), 56, 249
- Indium gallium phosphide (InGaP), 249, 336, 337
- Indium(III) sulfide (In₂S₃), 156, 157
- Indium Tin Oxide (ITO), 12, 172, 185, 186, 203, 205, 206, 228, 340
- Infrared spectroscopy (IR), 389
- Interface state density (N_{SS}), 157
- Iron(III) phosphate (FePO₄), 331, 333
- L**
- Lanthanum (La)-doped barium stannate (BaSnO₃) (LBSO), 230
- Layer-by-layer (LBL), 113, 121, 122, 131, 386, 387, 396, 398, 402–404
- Lead iodide (PbI₂), 168, 199, 200
- Lead-iodide perovskites, 113, 237
- Lithium cobalt oxide (LiCoO₂), 327, 328, 331, 334, 335
- Lithium dioxide (LiO₂), 339
- Lithium germanium phosphorus sulfide (Li₁₀GeP₂S₁₂) (LGPS), 342
- Lithium iron phosphate (LiFePO₄), 331, 333–335
- Lithium lanthanum zirconium oxide (Li₇La₃Zr₂O₁₂) (LLZO), 342
- Lithium nickel cobalt aluminum oxide (NCA), 328
- Lithium nickel manganese cobalt oxide (NMC), 327–328
- Lithium sulfide (LiS), 334, 339, 342
- Lithium super ionic conductor (LISICON), 342
- Local density of states (LDOS), 66, 67
- Local power dissipation density (RCWA), 95
- Lowest unoccupied molecular orbital (LUMO), 233, 356, 359, 361, 362, 365, 385, 389, 397
- Low temperature metal hydride (LTMH), 290–293, 295, 299, 300, 304, 305, 308–311
- M**
- Maxwell's equations, 95
- Mercaptopropionic acid (MPA), 149
- Mercury (Hg⁺), 8, 19
- meso-functionalized porphyrin dyes, 357, 359
- Mesoporous alumina, 167
- Mesoscopic scaffold, 151
- Metal hydrides, 283–312
- Metalloporphyrins, 116–119, 357, 358
- Metal organic chemical vapor deposition (MOEVD), 103
- Metal-organic frameworks (MOFs), 112, 113, 115, 155, 339, 383–404
- Methylammonium (MA⁺) cation, 114
- Methylammonium formamidinium (MAFA), 342
- Methylammonium lead iodide (MaPbI₃), 114, 115, 167, 171–173, 197, 198, 205, 237
- Methylene blue (MB), 22, 26, 31, 38
- Methyl viologen (MV), 336, 388, 390
- Metric tons of oil equivalent (TOE), 3
- Minimum sustainable price (MSP), 76–78, 80, 81, 83–85, 87
- Mixed organic cation perovskites, 114–115
- Mo/CIS interface, 47
- Molecular beam epitaxy (MBE), 103
- Molybdenum disulfide flakes (MoS), 17
- Molybdenum trioxide (MoO₃), 173, 174, 177, 189, 236, 321
- Monto Carlo (MC), 48
- Multi walled carbon nanotubes (MWCNTs), 193
- N**
- Nanomaterials, 20–22, 31, 38, 112, 113, 115, 122, 167, 180, 254
- Nanoparticles (NPs), 19, 20, 22–26, 28, 31, 34, 38, 148, 154, 155, 185, 186, 194, 197, 202, 205, 233, 234, 264, 353, 356, 374
- Nano-pyramid, 92, 94–102, 107, 108
- Nanostructures, 21, 25, 36, 90–92, 94–96, 98, 101–105, 108, 113, 142, 151, 180, 187, 191, 338
- 1,4-Naphthalene dicarboxylate C₁₂H₆O₂[O⁻]₂, 386
- N-bromosuccinimide (NBS), 368
- Nephelometric turbidity unit (NTU), 442
- Nickel oxide (NiO), 171, 198, 236–237, 239
- Norland optical adhesive (NOA), 177
- Normal hydrogen electrode (NHE), 389
- Nusselt number (Nu_L), 262

O

- Ohmic contact, 185, 233
 Open-circuit voltage (Voc), 47, 232, 235, 238, 326, 334, 355, 389
 Optical bandgap, 208
 Optical density (OD), 26, 34, 397
 Organic photovoltaics (OPVS), 12, 18, 112, 325

P

- Palladium(II) acetate (Pd(OAc)₂), 369
 Parabolic-trough collector (PTC), 425, 428, 429, 432
 Paraffin wax (PCM), 254, 255, 267
 Perdew-Burke-Ernzerhof (PBE), 48
 Perfect absorber, 89–108
 Perovskite solar cells (PSCs), 17, 115, 165–213, 227–239, 326, 334, 339, 341
 Perylene diimides (PDI), 116, 120
 Phase change material (PCM), 249, 254–255, 441, 443
 Phase diagram, 46, 47, 49–52, 59–65
 Phenothiazine, 366, 370
 Phenyl-C-butyric acid methyl ester (PCBM), 173, 178, 179, 185, 205–207, 230, 237
 Photoanode, 155, 325, 331, 354, 384, 386, 389, 397
 Photocatalyticity, 32–33
 Photoconversion (PC), 325
 Photoelectrode, 319, 328, 331, 333, 334, 336–338, 342, 353
 Photogenerated current density, 355
 Photosensitizer, 389, 399
 Photovoltaics (PV), 9–13, 18, 75–87, 90, 113, 131, 140, 142, 143, 151, 166, 167, 169, 172, 180, 191, 203, 213, 228, 229, 237, 239, 317–344, 353, 357, 374, 375, 383–404, 441, 443, 460, 461, 464–466, 479–482, 485–487, 490
 manufacturing system, 75–87
 module, 11, 247–276, 319, 328
 p-i-n structure, 202, 352
 Poly[bis(4-phenyl)(2,4,6-trimethylphenyl)amine] (PTAA), 235, 340
 Poly(ethylene dioxythiophene) (PEDOT), 12
 Polyethylene naphthalate (PEN), 189
 Polyethylenimine (PEIE), 175, 207
 Poly(hexylthiophene) (PHT), 192, 236
 Polymethyl methacrylate (PMMA), 192, 321
 Polysilicon, 79, 85
 Polystyrene sulfonate (PSS), 12, 172, 173, 206, 235

- Polytriarylamine (PTAA), 167, 207, 235
 Porphyrin (C₃₄H₃₄N₄O), 113, 115, 116, 235, 351–375, 386, 395, 397
 Powder diffraction file (PDF), 60
 Power conversion efficiency (PCE), 147, 150, 155, 167, 173, 230, 231, 326, 328, 333, 334, 338, 340, 352, 355, 371–374, 387
 Pressure-composition-temperature (PCT), 285–287, 289, 295
 Price caps, 473, 482, 483
 Primary energy, 3, 4, 458, 459
 Pyridine (C₅H₅N), 373, 396, 397

Q

- Q bands, 357, 360–362, 365
 Quantum dot solar cells (QDSC), 143, 149, 167
 Quantum efficiency, 132
 Quartz crystal microbalance (QCM), 121, 122

R

- Reactive oxygen species (ROS), 19–21
 Redistributed energy policy, 481
 Redox electrolyte, 355, 387, 389, 395, 401, 403
 Reduced tariffs, 475
 Refractive index, 21, 93–97, 99, 100, 396
 Renewable energy resources, 486
 Renewable portfolio, 474, 481, 485
 Reynolds number (Re), 258
 Round pin heat sink (RPHS), 250
 Ruthenium(III) Chloride (RuCl₃), 386

S

- Scanning electron microscopy (SEM), 24, 25, 28, 104, 148, 155, 168, 401
 Selenization, 47, 147, 148, 152–156
 Self-healing polymer (SHP), 326, 327
 Shockley-Queisser limit, 169
 Short-circuit current density (I_{sc}), 173, 229
 Sievert's law, 286
 Signal to noise (S/N), 154
 Silica oxide (SiO₂), 48
 Silicon carbide (SiC), 48, 263
 Silver (Ag⁺), 17, 19, 100, 101, 149, 170, 172, 175–177, 180, 185, 187, 201, 206
 Single slope solar still (SSSS), 442
 Soda-lime glass (SLG), 153, 154, 156
 Solar cell (SC), 12–18, 45–72, 76, 78, 90, 114, 115, 121, 127, 132, 137–157, 165–213, 227–239, 248, 254, 255, 319–321, 325, 326, 336–341, 351–375, 398, 479

- Solar heat for industrial processes (SHIP), 409–436
- Solar heating & Cooling Programme (SHC), 432
- Sol-gel successive ionic layer adsorption and reaction (SILAR), 147
- Solvent-assisted linker exchange (SALE), 395–397
- Soret band region, 116
- Spinodal curve, 61, 62
- Spiro-OMeTAD, 167, 172, 177, 178, 191, 202, 205, 206, 208, 235–238, 397, 398
- State Council, 472, 473, 475, 478–480, 483, 484, 490
- Straight fins heat sink (SFHS), 250
- Supercritical, 290
- Super ionic conductor (NASICON), 342
- Supervision, 475, 479–481, 489–491
- T**
- Tamilnadu Water Supply and Drainage (TWAD), 443
- Tandem solar cells (TSC), 143, 169, 173, 176, 177, 189, 205–207, 231, 234, 331, 336–338, 340
- Tariff, 76–78, 80, 81, 85–87, 474, 475, 482–484, 486, 490
- Tauc plots, 153
- Technical improvements, 479
- 5,10,15,20-Tetra(4-carboxyphenyl)porphyrin (Co^{III}TCPP) (C₄₅H₃₀N₄O₈), 390
- N N N' N'-Tetramethyl-p-phenylenediamine (TMPD) (C₁₀H₁₆N₂), 390
- Tetrahydrofuran (THF), 369
- Tetrapyrrole compounds, 356
- Thermal power stations, 476, 478, 486
- Thiophene (C₄H₄S), 235, 367
- Tin sulfide (SnS), 145, 147, 151, 152
- Titania (TiO₂), 12, 18–24, 27, 28, 31, 34, 36, 38, 151, 155, 167, 168, 171, 172, 178, 186, 191–199, 202, 204, 205, 207–210, 212, 213, 228–234, 239, 321, 325, 326, 331–334, 342, 353, 355–357, 359, 360, 366, 367, 371, 373–375, 384, 385, 389, 391, 393–395, 397–404
- Titania (Anatase), 3, 18–21, 27, 28, 353, 389
- Titania (Brookite), 18
- Titania (Rutile), 3
- Titanium chloride (TiCl₄), 234
- Total density of states (TDOS), 66, 67, 70, 71
- Total dissolved solids (TDS), 442–445, 452
- Total dissolved solids, ppm (TDS), 442
- Transmission electron microscope (TEM), 25, 28, 36, 47, 155
- Transparent conducting oxides (TCOs), 203, 206
- Trichloromonofluoromethane (CCl₃F), 253
- Triethylamine, 124, 128
- Triplet-triplet annihilation-based upconversion (TTA-UC), 386
- True color units (TCU), 442
- Two-dimensional (2D), 92, 151, 250, 308, 334, 339, 340, 393, 395–397, 401
- U**
- Ultraviolet (UV), 5, 8, 13, 21, 141, 143, 228, 230, 231, 328, 342, 389
- Ultraviolet A (UV A), 19, 21
- Ultraviolet B (UV B), 19
- Ultraviolet C (UV C), 19
- Ultraviolet-visible (UV-vis) spectroscopy, 24, 31, 32, 152
- United States Environmental Protection Agency (EPA), 441, 442, 445
- V**
- Valence band energy (VBE), 234, 238
- Valence band maximum (VBM), 232
- Van't Hoff plot, 286, 288
- Vienna ab initio simulation package (VASP), 48
- W**
- Weighted average capital cost (WACC), 76–77, 83–85
- World Health Organization (WHO), 441, 442, 445
- Wurtzite, 47, 66, 144, 152, 155
- X**
- X-ray energy dispersive spectrometer (EDS), 25
- X-ray powder diffraction (XRD), 24, 27–28, 36, 148, 152
- Z**
- Zinc (Zn²⁺), 13, 19, 48, 117, 130, 144, 145, 148, 149, 151–153, 231, 232, 357, 386, 387, 393, 395
- Zinc oxide (ZnO), 47, 48, 152, 178, 185, 186, 205–207, 229, 230, 232–233, 239
- Zinc selenide, 64
- Zinc sulfide (ZnS), 151, 154, 175
- Zinc tin oxide (ZTO), 340